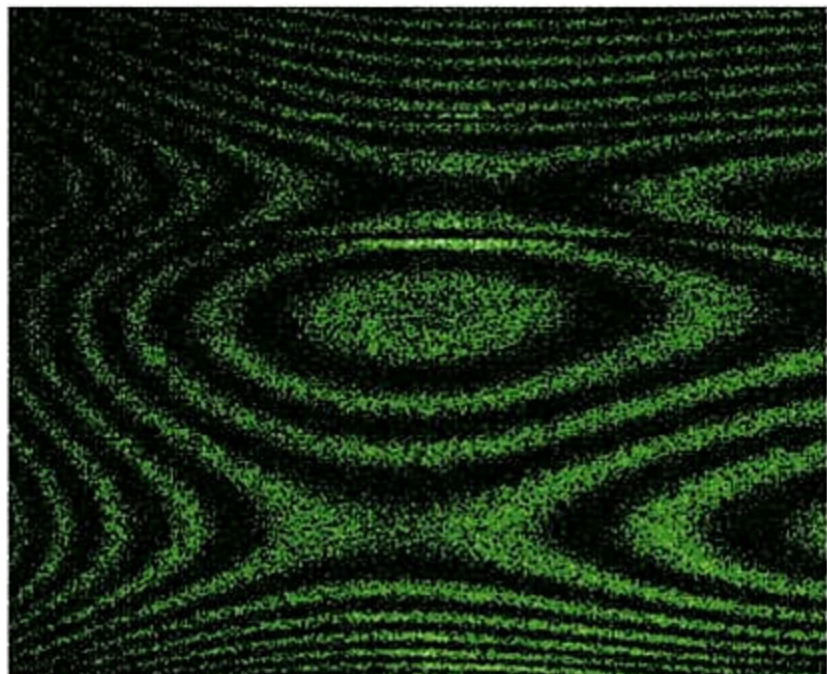


Thomas Kreis

WILEY-VCH

Handbook of Holographic Interferometry

Optical and Digital Methods



Thomas Kreis

Handbook of Holographic Interferometry
Optical and Digital Methods

Thomas Kreis

Handbook of Holographic Interferometry

Optical and Digital Methods



WILEY-VCH Verlag GmbH & Co. KGaA

Author

Dr. Thomas Kreis

BIAS – Bremer Institut für angewandte
Strahltechnik
Klagenfurter Str. 2, 28359 Bremen, Germany
e-mail: kreis@bias.de

All books published by Wiley-VCH are carefully produced. Nevertheless, authors, editors, and publisher do not warrant the information contained in these books, including this book, to be free of errors. Readers are advised to keep in mind that statements, data, illustrations, procedural details or other items may inadvertently be inaccurate.

Library of Congress Card No.: applied for**British Library Cataloging-in-Publication Data:**

A catalogue record for this book is available from the British Library

Cover Picture

Holographic interference pattern of a deformed satellite tank. Deformation caused by variation of internal pressure. Frequency doubled Nd:YAG-laser of 532 nm wavelength used.

Bibliographic information published by**Die Deutsche Bibliothek**

Die Deutsche Bibliothek lists this publication in the Deutsche Nationalbibliografie; detailed bibliographic data is available in the Internet at <<http://dnb.ddb.de>>.

© 2005 WILEY-VCH GmbH & Co. KGaA,
Weinheim

All rights reserved (including those of translation into other languages). No part of this book may be reproduced in any form – nor transmitted or translated into machine language without written permission from the publishers. Registered names, trademarks, etc. used in this book, even when not specifically marked as such, are not to be considered unprotected by law.

Printed in the Federal Republic of Germany
Printed on acid-free paper

Printing Strauss Offsetdruck GmbH, Mörlenbach
Bookbinding Litges & Dopf Buchbinderei
GmbH, Heppenheim

ISBN 3-527-40546-1

Contents

Preface	XI
1 Introduction	1
1.1 Scope of the Book	1
1.2 Historical Developments	3
1.3 Holographic Interferometry as a Measurement Tool	6
2 Optical Foundations of Holography	9
2.1 Light Waves	9
2.1.1 Solutions of the Wave Equation	9
2.1.2 Intensity	12
2.2 Interference of Light	13
2.2.1 Interference of Two Waves with Equal Frequency	13
2.2.2 Interference of Two Waves with Different Frequencies	14
2.2.3 Interference of Two Waves with Different Amplitudes	15
2.3 Coherence	16
2.3.1 Temporal Coherence	17
2.3.2 Spatial Coherence	19
2.4 Scalar Diffraction Theory	21
2.4.1 Fresnel-Kirchhoff Diffraction Formula	21
2.4.2 Fresnel Approximation	23
2.4.3 Fraunhofer Approximation	25
2.4.4 Thin Lens	26
2.4.5 Propagation of Light Waves as a Linear System	29
2.5 Speckles	30
2.5.1 Statistics of Speckle Intensity and Phase	30
2.5.2 Speckle Size	34
2.6 Holographic Recording and Optical Reconstruction	36
2.6.1 Hologram Recording	36
2.6.2 Optical Reconstruction of a Wave Field	40
2.6.3 Holographic Imaging Equations	44
2.6.4 Types of Holograms	47
2.7 Elements of the Holographic Setup	53
2.7.1 Laser	53
2.7.2 Recording Media	58

2.7.3	Optical Components	61
2.7.4	Beam Modulating Components	62
2.8	CCD- and CMOS-Arrays	65
2.8.1	CCD Concept	66
2.8.2	CCD Array Performance Parameters	70
2.8.3	CMOS Image Sensors	73
2.8.4	Spatial Sampling with CCD-Arrays	74
2.8.5	Color Still Cameras	76
3	Digital Recording and Numerical Reconstruction of Wave Fields	81
3.1	Digital Recording of Holograms	81
3.1.1	CCD Recording and Sampling	81
3.1.2	Reduction of the Imaging Angle	84
3.1.3	Reference Waves	89
3.2	Numerical Reconstruction by the Fresnel Transform	93
3.2.1	Wave Field Reconstruction by the Finite Discrete Fresnel Transform	93
3.2.2	Real and Virtual Image	97
3.2.3	Digital Fourier Transform Holography	100
3.2.4	The D.C.-Term of the Fresnel Transform	102
3.2.5	Suppression of the D.C.-Term	105
3.2.6	Suppression of the Twin Image	107
3.2.7	Variation of the Reference Wave	108
3.2.8	Anamorphic Correction	114
3.3	Numerical Reconstruction by the Convolution Approach	115
3.3.1	The Diffraction Integral as a Convolution	115
3.3.2	Size of the Image Field	117
3.3.3	Shifting of the Image Field	118
3.3.4	Scaling of the Image Field	120
3.4	Further Numerical Reconstruction Methods	124
3.4.1	Phase-Shifting Digital Holography	124
3.4.2	Local Amplitude and Phase Retrieval	129
3.4.3	Wavelet Approach to Numerical Reconstruction	132
3.4.4	Comparison of Reconstruction Methods	134
3.4.5	Hologram Recording Using Consumer Cameras	139
3.5	Wave-Optics Analysis of Digital Holography	140
3.5.1	Frequency Analysis of Digital Holography with Reconstruction by Fresnel Transform	141
3.5.2	Frequency Analysis of Digital Holography with Reconstruction by Convolution	148
3.5.3	The Transfer Function as a Filter	151
3.6	Non-Interferometric Applications of Digital Holography	159
3.6.1	Particle Analysis by Digital Holography	160
3.6.2	Microscopy by Digital Holography	169
3.6.3	Data Encryption with Digital Holography	180

4 Holographic Interferometry	185
4.1 Generation of Holographic Interference Patterns	186
4.1.1 Recording and Reconstruction of a Double Exposure Holographic Interferogram	186
4.1.2 Recording and Reconstruction of a Real-Time Holographic Interferogram	188
4.1.3 Time Average Holography	190
4.1.4 Interference Phase Variation Due to Deformation	191
4.1.5 Interference Phase Variation Due to Refractive Index Variation	194
4.1.6 Computer Simulation of Holographic Interference Patterns	196
4.2 Variations of the Sensitivity Vectors	198
4.2.1 Optimization of the Holographic Arrangement	198
4.2.2 Two Reference Beam Holographic Interferometry	201
4.3 Fringe Localization	203
4.3.1 Fringe Formation with Diffusely Scattering Surfaces	203
4.3.2 Fringe Localization with Collimated Illumination	206
4.3.3 Fringe Localization with Spherical Wave Illumination	211
4.3.4 Fringe Localization with Phase Objects	211
4.3.5 Observer Projection Theorem	214
4.4 Holographic Interferometric Measurements	215
4.4.1 Qualitative Evaluation of Holographic Interferograms	215
4.4.2 Holographically Measurable Physical Quantities	216
4.4.3 Loading of the Objects	218
5 Quantitative Determination of the Interference Phase	221
5.1 Role of Interference Phase	221
5.1.1 Sign Ambiguity	222
5.1.2 Absolute Phase Problem	224
5.2 Disturbances of Holographic Interferograms	225
5.2.1 Varying Background Illumination	226
5.2.2 Electronic Noise	226
5.2.3 Speckle Decorrelation	227
5.2.4 Digitization and Quantization	227
5.2.5 Environmental Distortions	228
5.3 Fringe Skeletonizing	229
5.3.1 Pattern Preprocessing	229
5.3.2 Fringe Skeletonizing by Segmentation	231
5.3.3 Skeletonizing by Fringe Tracking	233
5.3.4 Other Fringe Skeletonizing Methods	233
5.3.5 Fringe Numbering and Integration	234
5.4 Temporal Heterodyning	235
5.4.1 Principle of Temporal Heterodyning	235
5.4.2 Technical Realization of Temporal Heterodyning	237
5.4.3 Errors of Temporal Heterodyning	238
5.4.4 Experimental Application of Temporal Heterodyning	240

5.5	Phase Sampling Evaluation	242
5.5.1	Phase Shifting and Phase Stepping	243
5.5.2	Solution of the Phase Sampling Equations with Known Phase Shifts	245
5.5.3	Solution of the Phase Sampling Equations with Unknown Phase Shifts	248
5.5.4	Application of Phase Shift Evaluation Methods	251
5.5.5	Discussion of Phase Shift Evaluation Methods	255
5.6	Fourier Transform Evaluation	256
5.6.1	Principle of the Fourier Transform Evaluation Method	256
5.6.2	Noise Reduction by Spatial Filtering	258
5.6.3	Spatial Filtering and Sign Ambiguity	260
5.6.4	Fourier Transform Evaluation of Phase Shifted Interferograms	261
5.6.5	Spatial Heterodyning	263
5.6.6	Spatial Synchronous Detection	265
5.7	Dynamic Evaluation	266
5.7.1	Principles of Dynamic Evaluation	266
5.7.2	Dynamic Evaluation by a Scanning Reference Beam	268
5.8	Digital Holographic Interferometry	269
5.8.1	Digital Phase Subtraction	269
5.8.2	Enhancement of Interference Phase Images by Digital Filtering	273
5.8.3	Evaluation of Series of Holograms	275
5.8.4	Compensation of Motion Components	278
5.8.5	Multiplexed Holograms Discriminated in Depth	280
5.8.6	Multiplexed Holograms with Discrimination by Partial Spectra	282
5.9	Interference Phase Demodulation	287
5.9.1	Prerequisites for Interference Phase Demodulation	287
5.9.2	Path-Dependent Interference Phase Demodulation	288
5.9.3	Path-Independent Interference Phase Demodulation	289
5.9.4	Interference Phase Demodulation by Cellular Automata	292
5.9.5	Further Approaches to Interference Phase Demodulation	294
6	Processing of the Interference Phase	297
6.1	Displacement Determination	297
6.1.1	Displacement Determination with Known Reference Displacement .	298
6.1.2	Displacement Determination with Unknown Reference Displacement	299
6.1.3	Elimination of Overall Displacement	301
6.1.4	Non-Vibration Isolated Objects	303
6.2	The Sensitivity Matrix	306
6.2.1	Determination of the Sensitivity Vectors	306
6.2.2	Correction of Perspective Distortion	307
6.2.3	Condition of the Sensitivity Matrix	310
6.3	Holographic Strain and Stress Analysis	311
6.3.1	Definition of Elastomechanical Parameters	311
6.3.2	Beams and Plates	314
6.3.3	Numerical Differentiation	317
6.3.4	Fringe Vector Theory	318

6.4	Hybrid Methods	321
6.4.1	Finite Element Methods and Holographic Interferometry	321
6.4.2	Boundary Element Methods and Holographic Interferometry	322
6.4.3	Fracture Mechanics	322
6.5	Vibration Analysis	323
6.5.1	Surface Vibrations	323
6.5.2	Stroboscopic and Real-Time Holographic Interferometry	325
6.5.3	Time Average Holographic Interferometry	326
6.5.4	Temporally Modulated Reference Wave	327
6.5.5	Numerical Analysis of Time Average Holograms	331
6.5.6	Vibration Analysis by Digital Holography	332
6.6	Holographic Contouring	333
6.6.1	Contouring by Wavelength Differences	333
6.6.2	Contouring by Refractive Index Variation	336
6.6.3	Contouring by Varied Illumination Direction	337
6.6.4	Contouring by Light-in-Flight recording	338
6.7	Contour Measurement by Digital Holography	339
6.7.1	Contouring by Digital Holographic Interferometry	340
6.7.2	Contouring by Digital Multi-Wavelength Holography	343
6.7.3	Holographic Contouring by Digital Light-in-Flight Measurement . .	345
6.8	Comparative Holographic Interferometry	349
6.8.1	Principles of Comparative Holographic Interferometry	349
6.8.2	Digital Comparative Holography	353
6.9	Measurement Range Extension	356
6.9.1	Two-Wavelength Holographic Interferometry	357
6.9.2	Holographic Moiré	358
6.9.3	Holographic Interferometry at Rotating Objects	360
6.9.4	Endoscopic Holographic Interferometry	364
6.9.5	Desensitized Holographic Interferometer	365
6.10	Refractive Index Fields in Transparent Media	366
6.10.1	Refraction of Phase Objects	366
6.10.2	Physical Quantities Affecting the Refractive Index Field	370
6.10.3	Two-Dimensional Refractive Index Fields	374
6.10.4	Holographic Interferometry of Circular Symmetric Refractive Index Fields	376
6.10.5	Multidirectional Recording of Asymmetric Refractive Index Fields .	377
6.10.6	Tomographic Reconstruction in the Refractionless Limit	378
6.10.7	Tomographic Reconstruction of Strongly Refracting Fields	382
6.10.8	Analysis of Transparent Media with Digital Holography	384
6.10.9	Resonance Holographic Interferometry	385
6.11	Defect Detection by Holographic Non-Destructive Testing	387
6.11.1	Classification of Defects	387
6.11.2	Data Reduction for Automatic Qualitative Evaluation	389
6.11.3	Neural Network Approach to Qualitative Evaluation	393

7 Speckle Metrology	399
7.1 Speckle Photography	399
7.2 Electronic and Digital Speckle Interferometry	400
7.3 Electro-optic Holography	404
7.4 Speckle Shearography	405
Appendix	
A Signal Processing Fundamentals	409
A.1 Overview	409
A.2 Definition of the Fourier Transform	410
A.3 Interpretation of the Fourier Transform	412
A.4 Properties of the Fourier Transform	415
A.5 Linear Systems	416
A.6 Fourier Analysis of Sampled Functions	420
A.7 The Sampling Theorem and Data Truncation Effects	423
A.8 Interpolation and Resampling	427
A.9 Two-Dimensional Image Processing	429
A.10 The Fast Fourier Transform	434
A.11 Fast Fourier Transform for $N \neq 2^n$	437
A.12 Cosine and Hartley Transform	439
A.13 The Chirp Function and the Fresnel Transform	441
B Computer Aided Tomography	447
B.1 Mathematical Preliminaries	447
B.2 The Generalized Projection Theorem	448
B.3 Reconstruction by Filtered Backprojection	451
B.4 Practical Implementation of Filtered Backprojection	453
B.5 Algebraic Reconstruction Techniques	454
C Bessel Functions	459
Bibliography	463
Author Index	513
Subject Index	527

Preface

The story of this book began in September 2003, when Wiley-VCH asked me to prepare a new edition of my book ‘Holographic Interferometry – Principles and Methods’. Since its publication in 1996 more and more of my colleagues worldwide have used the book in their research, development, and teaching work, as was told to me and which is indicated by a continuous increase in citations. Therefore the demand for an updated new edition became apparent.

However, a new edition gives the impression that only some errors are eliminated, some presentations are streamlined and updated, and some new references are cited. On the other hand, in the last decade in holographic interferometry much substantial progress could be noticed, significant results were published, new interesting applications became possible. Especially, the field of digital holography matured from its infancy as presented in the former book to an established method, offering a lot of options not accessible before. Some of the work in this direction has been performed by my coworkers and me. The emphasis of the former book was on the computer-aided methods in holographic interferometry, so it is a logical consequence to include the methods offered by digital holography as far as they have consequences on holographic interferometry as a metrologic tool. The result is not a further edition of the old book but a totally new book, although many of the basic sections and the general organization are adopted from the former one. Therefore it was given the new title ‘Handbook of Holographic Interferometry’ and the subtitle ‘Optical and Digital Methods’. This title on the one hand makes the big promise to deliver all information needed for solving a typical problem in holographic interferometry – e. g. a nondestructive testing task or an experimental stress analysis job – and on the other hand makes it clear-cut what is not included in this book: All the other applications of holography – e. g. in art, for displaying real or virtual scenes, for security, for general waveform generation etc. – are not considered here. The aim of this book is to present a self-contained treatment of the underlying principles and numerical methods intended to help the physicist or engineer in planning a holographic interferometric measurement, writing the evaluation software, performing the experiments, and interpreting the results of the computer-aided evaluation. The employment of computer power in holographic interferometry should not be restricted to, for example, the determination of interference phase distributions from recorded interference patterns or the numerical generation of the interference phase distribution in digital holography; it also enables numerical feasibility studies, simulations of holographic interferograms, the optimization of a holographic setup with regard to sensitivity and accuracy, automatic control of the measurement process or further processing of the interference phase, for example by numerical strain and stress analysis, by finite element and boundary element methods or by computerized tomography. The book

should provide the fundamentals for making these attempts; where solutions cannot be given – because either they do not yet exist or they would go beyond the scope of this book – it should act as an incentive for further research and development work.

The list of references by no means constitutes a complete bibliography on the subject. Basically I have included those references I have found useful in my own research over the years. Often the use of a particular paper was dictated more by chance than by systematic search. Generally I have not made any attempts to establish historical priorities. No value judgments should be implied by my including or excluding a particular work. I express my apologies to anyone who has been inadvertently slighted or whose work has been overlooked.

It is hoped that this book will help the reader to exploit the various possibilities of holographic interferometry, to make the best choice of methods, and to use successfully the tools and algorithms presented herein. The book aims to present an account of the present state of the methods of holographic interferometric metrology; it must be emphasized that there is a considerable amount of research and development in progress and the subject needs to be kept in constant review. I hope, therefore, that readers will be challenged to think, criticize, read further, and quickly go beyond the confines of this volume.

Of course, I must take the blame for any mistakes, omissions of significant facts, incomprehensible descriptions, residual errors or misprintings. Readers are cordially invited to provide me with any corrections, comments, hints, or suggestions to improve the presentation, which may be realized in the preparation of potential further editions of this book. (Dr. Thomas Kreis, Bremer Institut für Angewandte Strahltechnik – BIAS, Klagenfurter Straße 2, D 28359 Bremen, Germany. E-mail: kreis@bias.de)

Clearly this book would not have been completed without the help of many persons. In the preparation phase of the former book, Prof. Dr. W. Jüptner and Dr. W. Osten helped greatly by critical and stimulating discussions. The former and this present book draw heavily from the research done at BIAS by my past and present colleagues and collaborators, especially M. Adams, T. Baumbach, R. Biedermann, Th. Bischof, J. Geldmacher, D. Holstein, D. Kayser, V. Kebbel, E. Kolenovic, U. Mieth, U. Schnars, S. Seebacher, and M. Wrieden, which is gratefully acknowledged. S. Hotze (n. Knoll) and Chr. Kapitza produced many of the holographic interferograms used to illustrate this book, and most of the photographs have been carefully prepared by B. Schupp. Thanks are due to all colleagues, especially H.-J. Hartmann and Chr. von Kopylow, who made it possible for me to work on the book by relieving me from much of my daily routine. I sincerely appreciate the competent help of the Wiley-VCH staff, especially I want to thank Heike Höpcke, Andreas Thoss and Uwe Krieg who helped a lot in preparing this handbook. Andrew Bacon provided language polishing, making the book more readable for users. Finally thanks go to my wife Elisabeth for her understanding and acceptance when I devoted my spare time to the book.

Thomas Kreis

Bremen, August 2004

1 Introduction

1.1 Scope of the Book

The emerging computer technology of the last decades – increasing processing speed and memory capacity, as well as CCD- and CMOS-camera targets having more and smaller pixels – makes the manifold applications of what can be called ‘computer-aided holographic interferometry’ feasible: In the planning phase of a holographic interferometric experiment the geometry of the setup can be optimized to achieve maximum sensitivity and accuracy. The load to be applied can be optimized in its type, direction, and amplitude by numerical simulation of the holographic interferograms that result from a specific load and geometry. The determination of the interference phase distribution from the recorded interference patterns by refined methods such as phase stepping or Fourier transform evaluation is only possible with powerful computers. Further processing of the interference phase distribution by solving linear equations to obtain displacement fields or by employing computer tomography to calculate refractive index fields can now be effectively carried out. Methods for numerical strain and stress analysis can be combined with computerized holographic interferometry to gain far-reaching knowledge about the behavior of the tested structure with regard to the applied load. Even structural analysis methods such as finite element methods (FEM) or boundary element methods (BEM) can be efficiently associated to holographic interferometry to assist the strain and stress calculations, to optimize the component design process, or to predict the interference patterns for a given load.

Technological progress in the computer field actually also led to an intense use of the concept of digital holography, here understood in the sense of digital recording of the holograms and the numerical reconstruction of the wave fields in a computer. This concept was principally known for a long time, but before broader application it had to wait for the advent of powerful CCD- and CMOS-arrays as well as for fast processing and storing of large data sets. Digital holography avoids many of the drawbacks of the former optical holography and holographic interferometry and furthermore offers some possibilities not given by the optical approach.

The aim of this book is to present the physical principles of holography and interferometry as far as they are needed in this context, as well as the numerical methods for reconstruction of the complex wave fields from digitally recorded holograms and for evaluation of the interference patterns, which constitute the fundamentals of computer-aided holographic interferometry. The emphasis is on quantitative measurements with a sidetlook on the qualitative evaluation of holographic nondestructive testing (HNDT). The present book should provide the background needed for deriving the concepts and writing the programmes to solve prob-

lems in the above mentioned fields. To fulfill these claims but not to become too extensive and to exceed the frame set by the publishers, some topics have been intentionally omitted. The description of technical components – lasers, optics, electro-optic devices, recording media, image processing equipment and methods, computer periphery – is restricted to a very short overview; more details on these topics can be found in more specialized books. The same is true for themes such as digital image processing, or particle and flow-field measurements. These items are addressed here only briefly as far as it seems necessary for a comprehensive presentation. Other applications of holography than interferometric metrology, such as display holography, computer generated holograms, holographic optical elements, color holography, holographic data storage, etc., are excluded intentionally.

The book is organized into seven chapters and three appendices. The main body of the content is contained in Chapters 2, 3, 4, 5, and 6. Chapter 2 presents the physical prerequisites of holography, starting with the wave theory of light, describing such effects as interference, diffraction, coherence, speckle, and how these are employed in holographic recording and reconstruction of optical wave fields. The technical components employed in optical as well as in digital holography and holographic interferometry are introduced.

Chapter 3 presents the techniques of how to record holograms on CCD- and CMOS-arrays, i. e. how to solve the problem imposed by the limited resolution of these detectors. Then the reconstruction of the recorded optical wave field by the numerical Fresnel transform and by the convolution approach is considered. Not only are the reconstruction algorithms presented, but also the various options possible in digital holography, like numerical suppression of the zero diffraction order, are outlined.

In Chapter 4 the fundamentals of holographic interferometric metrology are presented. The quantitative relations for displacements or refractive index variations and the geometric and optical parameters of the holographic setup are introduced. Further discussions center on the role of the sensitivity vectors and the localization of the interference fringes.

Chapter 5 is devoted to methods for determining the interference phase distributions from optically reconstructed intensity images as well as from digitally recorded holograms. Room is given to a thorough treatment of the phase-stepping and the Fourier transform methods as well as to digital holography. Systematic and statistical errors are discussed and a number of approaches for interference phase demodulation are presented.

Chapter 6 describes the further processing of the interference phase distribution. Displacement vector fields, strain and stress distributions, vibration modes, three-dimensional object contours or refractive index fields are determined. Computerized defect detection of holographic nondestructive testing is briefly addressed.

Speckle methods for deformation measurement like ESPI or shearography are closely related to holographic interferometry. These methods first employed analogue electronics, but nowadays they are realized digitally. They differ from digital holography in recording a focused image of a speckled surface and producing correlation fringes on an intensity basis, while in digital holography the whole complex field is reconstructed from the recorded Fresnel or Fraunhofer field. The main speckle methods are discussed briefly in Chapter 7.

The appendices provide the reader with the essentials of Fourier transforms, methods for computerized tomography, and Bessel functions, as far as this seems necessary to understand and implement the related methods of the main chapters.

To make the work with this book more comfortable, the references are given in the sequence of occurrence at the end of the book. This is accompanied by an alphabetically ordered author/coauthor index. A subject index lists a number of terms; these are printed in italics in the text to make their identification easier.

1.2 Historical Developments

Holography got its name from the Greek words ‘holos’ meaning whole or entire and ‘graphein’ meaning to write. It is a means for recording and reconstructing the whole information contained in an optical wavefront, namely amplitude and phase, and not just intensity as ordinary photography does. Holography essentially is a clever combination of interference and diffraction, two phenomena based on the wave nature of light.

Diffraction was first noted by F. M. Grimaldi (1618 – 1663) as the deviation from rectilinear propagation, and the interference generated by thin films was observed and described by R. Hooke (1635 – 1703). I. Newton (1642 – 1727) discovered the composition of white light from independent colors. The mathematical basis for the wave theory describing these effects was founded by Chr. Huygens (1629 – 1695), who further discovered the polarization of light. The interference principle introduced by Th. Young (1773 – 1829) and the Huygens principle were used by A. J. Fresnel (1788 – 1827) to calculate the diffraction patterns of different objects. Since about 1850 the view of light as a transversal wave won against the corpuscular theory. The relations between light, electricity, and magnetism were recognized by M. Faraday (1791 – 1867). These phenomena were summarized by J. C. Maxwell (1831 – 1879) in his well known equations. A medium supporting the waves was postulated as the all pervading ether. The experiments of A. A. Michelson (1852 – 1931), published in 1881, and the work of A. Einstein (1879 – 1955) were convincing evidence that there is no ether.

In 1948 D. Gabor (1900 – 1979) presented holography as a lensless process for image formation by reconstructed wavefronts [1–3]. His goal was to improve electron microscopy, using this new approach to avoid the previous aberrations. However, a successful application of the technique to electron microscopy has not materialized so far because of several practical problems. The validity of Gabor’s ideas in the optical field was recognized and confirmed by, for example, G. L. Rogers [4], H. M. A. El-Sum and P. Kirkpatrick [5], and A. Lohmann [6]. But the interest in holography declined after a few years, mainly because of the poor quality of the holographic images obtained in those days. The breakthrough of holography was initiated by the development of the laser, which made available a powerful source of coherent light. This was accompanied by the solution of the twin-image problem encountered in Gabor’s in-line arrangement. E. N. Leith and Y. Upatnieks [7–9] recognized the similarity of Gabor’s holography to the synthetic aperture antenna problem of radar technology and introduced the off-axis reference beam technique. Y. N. Denisyuk combined the ideas of Gabor and Lippmann in his invention of the thick reflection hologram [10].

Now there was a working method for recording and reconstruction of complete wavefields with intensity and phase, and this also in the visible region of the spectrum. Besides the impressive display of three-dimensional scenes exhibiting effects like depth and parallax, moreover holography found numerous applications based on its unique features. Using the theory describing the formation of a hologram by interference of reference and object wave,

holograms were created by calculation on a digital computer [11]. The result of this calculation was transferred to a transparency by printing or by printing on paper followed by a photographic process that might have included a reduction in scale. Now images of ideal objects not existing in reality could be generated, later on offering ways for interferometric comparison of, for example, optical components to be tested or for fabrication of diffracting elements with predescribed behavior [12, 13]. The way holograms store information in a form of distributed memory has given incentive for research in holographic data storage [14]. Especially three-dimensional storage media, such as photorefractive crystals which are capable of providing Bragg selectivity became the focus of research, eventually yielding solutions to the always increasing demand for data storage capacity in the computer industry [15].

Perhaps the most important application of holography is in interferometric metrology, started by K. Stetson's discovery of holographic interferometry [16, 17]. In holographic interferometry, two or more wave fields are compared interferometrically, at least one of them must be holographically recorded and reconstructed [18]. This technique allows the measurement of changes of the phase of the wave field and thus the change of any physical quantity that affects the phase. The early applications ranged from the first measurement of vibration modes [16, 17], over deformation measurement [19–22], contour measurement [23–28], to the determination of refractive index changes [29, 30]. These developments were accompanied by rigorous investigations of the underlying principles, mainly performed by K. Stetson [31–35].

For certain arrangements of illumination and observation directions the resulting holographic interference fringes can be interpreted in a first approximation as contour lines of the amplitude of the change of the measured quantity. As an example, a locally higher deformation of a diffusely reflecting surface manifests in a locally higher fringe density. So such areas which give hints to possible material faults, risk of damage, or inadequate design, can easily be detected by applying a load of the same type and direction as the intended operational load, but of much less amplitude. This is the field of HNDT – holographic nondestructive testing.

Besides this qualitative evaluation of the holographic interference patterns there has been continuing work to use holographic interferometry for quantitative measurements. Beginning with manual fringe counting [36, 37], soon image processing computers were employed for quantitative evaluation, a process that consists of recording the reconstructed fringe pattern by TV camera, digitizing and quantizing it, calculating the interference phase distribution from the stored intensity values, using geometry data of the holographic arrangement to determine the distribution of the physical quantity to be measured, and the display of the results. The main one of these named tasks is the calculation of the interference phase. The first algorithms doing this resembled the former fringe counting [38]. A significant step forward in computerized fringe analysis was the introduction of the phase shifting methods of classic interferometric metrology [39, 40] into holographic interferometry [41, 42]. Now it was possible to measure – and not to estimate by numerical interpolation – the interference phase between the fringe intensity maxima and minima, and also the sign ambiguity was resolved. However, one had to pay for this increased accuracy by additional experimental effort. An alternative without the need for generating several phase shifted interferograms and also without requiring the introduction of a carrier [43] was presented by the author with the Fourier transform evaluation [44]. This is a flexible tool for fitting a linear combination of harmonic functions to the recorded interferogram, taking into account all intensity values even those between the fringe extrema.

While the evaluation of holographic interferograms by computer was successfully developed, there was still the clumsy work of the fabrication of the interference pattern, which was not amenable to computer. The wet chemical processing of the photographic plates, photothermoplastic film, photorefractive crystals, and other recording media showed their typical drawbacks. So the endeavor to record the primary interfering optical fields by the camera of the image processing system and to perform their superposition and thus the generation of the interferogram in the computer generated two solutions: electronic (ESPI), resp. digital (DSPI) speckle pattern interferometry and digital holography (DH) resp. digital holographic interferometry (DHI).

The imaging of diffusely scattering objects with coherent light always produces speckles, the high-contrast granular structure with which the image of the object appears to be covered. If a mutually coherent reference field is superposed to the field scattered by an object, the resulting speckle fields before and after a variation of the object can be added on an intensity basis and yield correlation fringes of the same form as in holographic interferometry [45]. It was recognized that the speckle patterns have a structure easily recordable by existing image sensors, so this metrologic method was automated by computerized recording and processing [46–48]. Due to the analog TV cameras first employed the method was called TV-holography or electronic speckle pattern interferometry (ESPI); later emphasizing the digital recording and processing the name changed to digital speckle pattern interferometry (DSPI). Its big advance was the computerized real-time fringe generation, but the method suffered from the grainy appearance on the TV screen, i. e. severe speckle noise. In the meantime a number of improvements have been achieved with the result that DSPI now is a mature technique with numerous applications in science and technology. Perhaps the most important contribution was the introduction of phase stepping to speckle interferometry by K. Creath [49] and K. Stetson and W. R. Brohinsky [50], resulting in phase stepping digital speckle pattern interferometry (PSDSPI) where optical phase distributions are calculated and compared.

While in ESPI/DSPI the object is focused onto the recording target and the fringes are correlation fringes on an intensity basis, in digital holography a Fresnel or Fraunhofer hologram is recorded. In the following I will give an admittedly “biased” outline of its development. The earliest publication on digital holography that I have found is by J. W. Goodman and R. W. Lawrence [51] and dates back to 1967, so digital holography is older than ESPI/DSPI. In this classic paper Goodman and Lawrence record a wave field using the lensless Fourier transform geometry with a vidicon whose lens assembly was removed. They write: “The output of the vidicon is sampled in a 256×256 array, and quantized to eight grey levels. To avoid aliasing errors, the object-reference-detector geometry is specifically chosen to assure that the maximum spatial frequency in the pattern of interference [the microinterference constituting the hologram, T. K.] is sampled four times per period.” The reconstruction was done on a PDP 6 computer, the squared modulus of the calculated complex distribution was displayed on a scope. The computation of the 256×256 pixel field lasted 5 minutes, “a time which compares favorably with the processing time generally required to obtain a photographic hologram in the conventional manner” as Goodman and Lawrence wrote in 1967.

A further classic paper [52] by T. S. Huang from 1971 treats both categories of digital holography: computer generated holography and computerized reconstruction from holograms. In this paper Fourier transform holograms as well as Fresnel holograms and their

numerical reconstruction are discussed, also digitization and quantization effects are considered. In 1972 the work of a Soviet group around L. P. Yaroslavsky was presented [53], and in a paper published 1974 T. H. Demetrikopoulos and R. Mittra [54] consider the computer reconstruction of holograms which are recorded at acoustical or microwave frequencies. In 1980 the book of L. P. Yaroslavsky and N. S. Merzlyakov [55] was translated into English; in this book the theory of computer generation of holograms and of computer reconstruction of holograms is thoroughly treated, and the experiments performed worldwide up to this time are described, especially the work done in the Soviet Union is presented in great detail.

Then there began a long phase in which digital holography in the sense of this book was dormant. Computer generated holograms on the one hand and speckle interferometry on the other hand were fields of active research finding numerous applications. The dormancy of digital holography lasted until the beginning of the 1990s. The young scientist U. Schnars in the department led by the author in the institute (BIAS) directed by W. Jüptner was working towards his doctoral dissertation. Starting with the work of Yaroslavsky [55] and using modern CCD-cameras and computer facilities soon the first digital hologram was recorded and numerically reconstructed. All the time it was a known fact that numerically the whole complex wave field can be reconstructed from a digital hologram. But the emphasis in the first experiments [51–53] was on the intensity distribution. Now the potential lying in the numerically reconstructed phase distribution was recognized, leading in 1993 to digital holographic interferometry as a measurement tool [56]. After the first paper [56] of Schnars soon others followed [57–60] and not much later this approach to holographic metrology was taken up by other research groups. One of the first of these was the group around G. Pedrini [61–65], working during the early days of Schnars' development in a joint project with BIAS. In the context of this project [66], Schnars and I presented our first results. Other groups working in digital holography now can be found in Belgium [67–70], Brazil [71], Canada [72–79], China [80,81], Czech Republic [82], France [83–89], Hong Kong [90,91], Italy [92–95], Japan [96–110], Poland [111], Singapore [112–114], Sweden [115–119], Switzerland [120–129], Turkey [130–132], USA [81,97,98,133–151], to name only some countries in alphabetical order.

Digital holography and digital holographic interferometry now are recognized metrologic methods which receive continuously increasing interest [152, 153]. This is indicated by the steadily increasing number of publications per year related to this topic or by the fact that to the knowledge of the author the “Conference on Interferometry in Speckle Light” in Lausanne/Switzerland in 2000 was the first conference with a session entitled and dedicated only to the topic “digital holography”. There is reasonable hope that this technique will yield new interesting results and possibilities, maybe some which are not possible with optical reconstruction. I hope this book will contribute a little bit to the further advance of the promising techniques of digital holography and digital holographic interferometry.

1.3 Holographic Interferometry as a Measurement Tool

In holographic interferometry, two or more wave fields are compared interferometrically, at least one of them must be holographically recorded and reconstructed. The method gives rise to interference patterns whose fringes are determined by the geometry of the holographic

setup via the sensitivity vectors and by the optical path length differences. Thus holographic interference patterns can be produced by keeping the optical path length difference constant and changing the sensitivity vectors, by holding the sensitivity vectors constant and varying the optical path length differences, or by altering both of them between the object states to be compared. Especially the path lengths can be modified by a number of physical parameters. The flexibility and the precision gained by comparing the optical path length changes with the wavelength of the laser light used, make holographic interferometry an ideal means for measuring a manifold of physical quantities [154–156]. The main advantages are:

- The measurements are contactless and noninvasive. In addition to an eventual loading for inducing the optical pathlength changes, the object is only impinged by light waves. The intensities of these waves are well below the level for causing any damage, even for the most delicate of biological objects.
- A reliable analysis can be performed at low loading intensities: the testing remains non-destructive.
- Not only may two states separated by a long time be compared, but furthermore the generation and evaluation of the holographic information can be separated both temporally and locally.
- Measurements can be made through transparent windows. We can therefore make measurements in pressure or vacuum chambers or protect against hostile environments. Due to the measurement of differences of the optical path lengths instead of absolute values, low quality windows do not disturb the results.
- Holographic interferometric measurements can be accomplished at moving surfaces: Short pulse illumination makes the method insensitive to a disturbing motion, vibrations can be investigated, the holographic setup can be made insensitive to specific motion components, and the rotation of spinning objects can be cancelled optically by using an image derotator.
- Deformation measurements can be performed at rough, diffusely reflecting surfaces, which occur frequently in engineering. No specular reflection of the object is required.
- The objects to be examined holographically may be of almost arbitrary shape. Using multiple illumination and observation directions or fiber optics, barely accessible areas can be studied.
- Holographic interferometry is nearly independent of the state of matter: Deformations of hard and soft materials can be measured. Refractive index variations in solids, fluids, gases and even plasmas can be determined.
- Lateral dimensions of the examined subjects may range from a few millimeters to several meters.
- The measurement range extends roughly speaking from a hundredth to several hundreds of a wavelength, for example displacements can be measured from about 0.005 μm to 500 μm .
- The achievable resolution and accuracy of a holographic interferometric displacement measurement permit subsequent numerical strain and stress calculations.

- Two-dimensional spatially continuous information is obtained: local singularities, for example local deformation extrema, cannot go undetected.
- Multiple viewing directions using a single hologram are possible, enabling the application of computerized tomography to obtain three-dimensional fields.

2 Optical Foundations of Holography

This chapter discusses the physical basis of holography and holographic interferometry. The primary phenomena constituting holography are interference and diffraction, which take place because of the wave nature of light. So this chapter begins with a description of the wave theory of light as far as it is required to understand the recording and reconstruction of holograms and the effect of holographic interferometry. In holographic interferometry the variation of a physical parameter is measured by its influence on the phase of an optical wave field. Therefore the dependence of the phase upon the geometry of the optical setup and the different parameters to be measured is outlined.

2.1 Light Waves

2.1.1 Solutions of the Wave Equation

Light is a transverse, electromagnetic wave characterized by time-varying electric and magnetic fields. Since electromagnetic waves obey the Maxwell equations, the propagation of light is described by the wave equation which follows from the Maxwell equations. The *wave equation* for propagation of light in vacuum is

$$\nabla^2 \mathbf{E} - \frac{1}{c^2} \frac{\partial^2 \mathbf{E}}{\partial t^2} = 0 \quad (2.1)$$

where \mathbf{E} is the *electric field strength*, ∇^2 is the *Laplace operator*

$$\nabla^2 = \frac{\partial^2}{\partial x^2} + \frac{\partial^2}{\partial y^2} + \frac{\partial^2}{\partial z^2} \quad (2.2)$$

(x, y, z) are the Cartesian spatial coordinates, t denotes the temporal coordinate, the time, and c is the propagation speed of the wave. The *speed of light* in vacuum c_0 is a constant of nature

$$c_0 = 299\,792\,458 \text{ m s}^{-1} \quad \text{or almost exactly} \quad c_0 = 3 \times 10^8 \text{ m s}^{-1}. \quad (2.3)$$

Transverse waves vibrate at right angles to the direction of propagation and so they must be described in vector notation. The wave may vibrate horizontally, vertically, or in any direction combined of these. Such effects are called *polarization* effects. Fortunately for most applications it is not necessary to use the full vectorial description of the fields, so we can

assume a wave vibrating in a single plane. Such a wave is called *plane polarized*. For a plane polarized wave field propagating in the z -direction the *scalar wave equation* is sufficient

$$\frac{\partial^2 E}{\partial z^2} - \frac{1}{c^2} \frac{\partial^2 E}{\partial t^2} = 0. \quad (2.4)$$

It is easily verified that

$$E(z, t) = f(z - ct) \quad \text{or} \quad E(z, t) = g(z + ct) \quad (2.5)$$

are also solutions of this equation, which means that the wave field retains its form during propagation. Due to the linearity of (2.4)

$$E(z, t) = a f(z - ct) + b g(z + ct) \quad (2.6)$$

is likewise a solution to the wave equation. This *superposition principle* is valid for linear differential equations in general and thus for (2.1) also.

The most important solution of (2.4) is the *harmonic wave*, which in real notation is

$$E(z, t) = E_0 \cos(kz - \omega t). \quad (2.7)$$

E_0 is the *real amplitude* of the wave, the term $(kz - \omega t)$ gives the *phase* of the wave. The *wave number* k is associated to the *wavelength* λ by

$$k = \frac{2\pi}{\lambda}. \quad (2.8)$$

Typical figures of λ for visible light are 514.5 nm (green line of argon-ion laser) or 632.8 nm (red light of helium-neon laser). The *angular frequency* ω is related to the *frequency* ν of the wave by

$$\omega = 2\pi\nu \quad (2.9)$$

where ν is the number of periods per second, that means

$$\nu = \frac{c}{\lambda} \quad \text{or} \quad \nu\lambda = c. \quad (2.10)$$

If we have not the maximum amplitude at $x = 0$ and $t = 0$, we have to introduce the *relative phase* ϕ

$$E(z, t) = E_0 \cos(kz - \omega t + \phi). \quad (2.11)$$

With the *period* T , the time for a full 2π -cycle, we can write

$$E(z, t) = E_0 \cos\left(\frac{2\pi}{\lambda}z - \frac{2\pi}{T}t + \phi\right). \quad (2.12)$$

Figure 2.1 displays two aspects of this wave. Figure 2.1a shows the temporal distribution of the field at two points $z = 0$ and $z = z_1 > 0$, and Fig. 2.1b gives the spatial distribution of

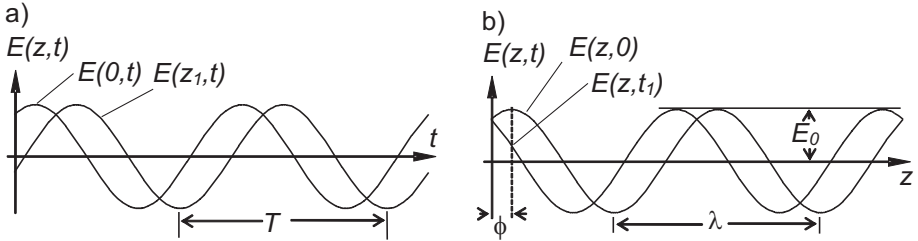


Figure 2.1: Spatial and temporal distribution of a scalar harmonic wave.

two periods for time instants $t = 0$ and $t = t_1 > 0$. We see that a point of constant phase moves with the so called *phase velocity*, the speed c .

The use of trigonometric functions leads to cumbersome calculations, which can be circumvented by using the complex exponential which is related to the trigonometric functions by *Euler's formula*

$$e^{i\alpha} = \cos \alpha + i \sin \alpha \quad (2.13)$$

where $i = \sqrt{-1}$ is the imaginary unit. Since the cosine now is

$$\cos \alpha = \frac{1}{2}(e^{i\alpha} + e^{-i\alpha}) \quad (2.14)$$

the harmonic wave (2.11) is

$$E(z, t) = \frac{1}{2}E_0 e^{i(kz - \omega t + \phi)} + \frac{1}{2}E_0 e^{-i(kz - \omega t + \phi)}. \quad (2.15)$$

The second term on the right-hand side is the complex conjugate of the first term and can be omitted as long as it is understood that only the real part of $E(z, t)$ represents the physical wave. Thus the harmonic wave in complex notation is

$$E(z, t) = \frac{1}{2}E_0 e^{i(kz - \omega t + \phi)}. \quad (2.16)$$

A *wavefront* refers to the spatial distribution of the maxima of the wave, or other surfaces of constant phase, as these surfaces propagate. The wavefronts are normal to the direction of propagation. A *plane wave* is a wave which has constant phase in all planes orthogonal to the propagation direction for a given time t . For describing the spatial distribution of the wave, we can assume $t = 0$ in an arbitrary time scale. Since

$$\mathbf{k} \cdot \mathbf{r} = \text{const} \quad (2.17)$$

is the equation for a plane in three-dimensional space, with the *wave vector* $\mathbf{k} = (k_x, k_y, k_z)$ and the spatial vector $\mathbf{r} = (x, y, z)$, a plane harmonic wave at time $t = 0$ is

$$E(\mathbf{r}) = E_0 e^{i(\mathbf{k} \cdot \mathbf{r} + \phi)}. \quad (2.18)$$

This wave repeats after the wavelength λ in direction \mathbf{k} , which can easily be proved using $|\mathbf{k}| = k = 2\pi/\lambda$ by

$$E\left(\mathbf{r} + \lambda \frac{\mathbf{k}}{k}\right) = E(\mathbf{r}). \quad (2.19)$$

The expression

$$E(\mathbf{r}, t) = E_0 e^{i(\mathbf{k} \cdot \mathbf{r} - \omega t + \phi)} \quad (2.20)$$

describes the temporal dependence of a plane harmonic wave propagating in the direction of the wavevector or

$$E(\mathbf{r}, t) = E_0 e^{i(\mathbf{k} \cdot \mathbf{r} + \omega t + \phi)} \quad (2.21)$$

if the wave propagates contrary to the direction of \mathbf{k} .

Another waveform often used is the *spherical wave* where the phase is constant on each spherical surface. The importance of spherical waves comes from the *Huygens principle* which states that each point on a propagating wavefront can be considered as radiating itself a spherical wavelet.

For a mathematical treatment of spherical waves the wave equation has to be described in polar coordinates (r, θ, ψ) , transformed by $x = r \sin \theta \cos \psi$, $y = r \sin \theta \sin \psi$, $z = r \cos \theta$. Due to the spherical symmetry, a spherical wave is not dependent on θ and ψ . Then the scalar wave equation is

$$\frac{1}{r} \frac{\partial^2}{\partial r^2} (r E) - \frac{1}{c^2} \frac{\partial^2 E}{\partial t^2} = 0. \quad (2.22)$$

The solutions of main interest are the harmonic spherical waves

$$E(r, t) = \frac{E_0}{r} e^{i(kr - \omega t + \phi)}. \quad (2.23)$$

One observes that the amplitude E_0/r decreases proportionally to $1/r$. Furthermore at a long distance from the origin the spherical wave locally approximates a plane wave.

The complex amplitudes of wavefronts scattered by a surface are generally very complicated, but due to the superposition principle (2.6) they can be treated as the sum of plane waves or spherical waves. There are still other solutions to the wave equation. An example are the *Bessel waves* of the class of *nondiffracting beams* [157]. But up to now they have not found applications in holographic interferometry, so here we restrict ourselves on the plane and on the spherical waves.

2.1.2 Intensity

The only parameter of light which is directly amenable to sensors – eye, photodiode, CCD-target, etc. – is the *intensity* (and in a rough scale the frequency as color). Intensity is defined by the energy flux through an area per time. From the Maxwell equations we get

$$I = \varepsilon_0 c E^2 \quad (2.24)$$

where we only use the proportionality of the intensity I to E^2

$$I \sim E^2. \quad (2.25)$$

It has to be recognized that the intensity has a nonlinear dependence on the electric field strength. Since there is no sensor which can follow the frequency of light, we have to integrate over a *measuring time* T_m , the momentary intensity is not measurable. So if $T_m \gg T = 2\pi/\omega$, omitting proportionality constants we define

$$I = E_0 E_0^* = |E_0|^2 \quad (2.26)$$

where $*$ denotes the complex conjugate. The intensity of a general stationary wave field is

$$I(\mathbf{r}) = \langle E E^* \rangle = \lim_{T_m \rightarrow \infty} \frac{1}{T_m} \int_{-T_m/2}^{T_m/2} E(\mathbf{r}, t') E^*(\mathbf{r}, t') dt'. \quad (2.27)$$

This intensity is the limit of the *short time intensity*

$$I(\mathbf{r}, t, T_m) = \frac{1}{T_m} \int_{t-T_m/2}^{t+T_m/2} E(\mathbf{r}, t') E^*(\mathbf{r}, t') dt' \quad (2.28)$$

which is a sliding average of a temporal window centered around t with width T_m . The measuring time T_m always is large compared with the period of the light wave but has to be short in the time scale of the investigated process.

2.2 Interference of Light

2.2.1 Interference of Two Waves with Equal Frequency

The *interference* effect which occurs if two or more coherent light waves are superposed, is the basis of holography and holographic interferometry. So in this *coherent superposition* we consider two waves, emitted by the same source, which differ in the directions \mathbf{k}_1 and \mathbf{k}_2 , and the phases ϕ_1 and ϕ_2 , but for convenience have the same amplitude E_0 and frequency ω and are linearly polarized in the same direction. Then in scalar notation

$$\begin{aligned} E_1(\mathbf{r}, t) &= E_0 e^{i(\mathbf{k}_1 \cdot \mathbf{r} - \omega t + \phi_1)} \\ E_2(\mathbf{r}, t) &= E_0 e^{i(\mathbf{k}_2 \cdot \mathbf{r} - \omega t + \phi_2)}. \end{aligned} \quad (2.29)$$

For determination of the superposition of these waves we decompose the vectors \mathbf{k}_1 and \mathbf{k}_2 into components of equal and opposite directions, Fig. 2.2.: $\mathbf{k}' = (\mathbf{k}_1 + \mathbf{k}_2)/2$ and $\mathbf{k}'' = (\mathbf{k}_1 - \mathbf{k}_2)/2$. If θ is the angle between \mathbf{k}_1 and \mathbf{k}_2 then

$$|\mathbf{k}''| = \frac{2\pi}{\lambda} \sin \frac{\theta}{2}. \quad (2.30)$$

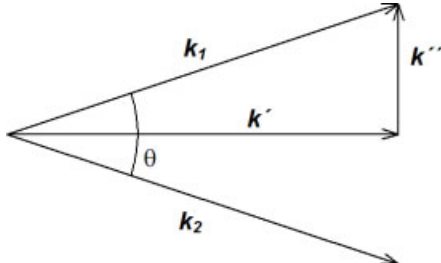


Figure 2.2: Decomposition of wave vectors.

In the same way we define the mean phase $\phi = (\phi_1 + \phi_2)/2$ and the half phase difference $\Delta\phi = (\phi_1 - \phi_2)/2$. Now the superposition gives the field

$$\begin{aligned}
 (E_1 + E_2)(\mathbf{r}, t) &= E_0 e^{i(\mathbf{k}_1 \cdot \mathbf{r} - \omega t + \phi_1)} + E_0 e^{i(\mathbf{k}_2 \cdot \mathbf{r} - \omega t + \phi_2)} \\
 &= E_0 \left\{ e^{i(\mathbf{k}' \cdot \mathbf{r} + \mathbf{k}'' \cdot \mathbf{r} - \omega t + \phi + \Delta\phi)} \right. \\
 &\quad \left. + e^{i(\mathbf{k}' \cdot \mathbf{r} - \mathbf{k}'' \cdot \mathbf{r} - \omega t + \phi - \Delta\phi)} \right\} \\
 &= E_0 e^{i(\mathbf{k}' \cdot \mathbf{r} - \omega t + \phi)} \left\{ e^{i(\mathbf{k}'' \cdot \mathbf{r} + \Delta\phi)} + e^{i(-\mathbf{k}'' \cdot \mathbf{r} - \Delta\phi)} \right\} \\
 &= 2 E_0 e^{i(\mathbf{k}' \cdot \mathbf{r} - \omega t + \phi)} \cos(\mathbf{k}'' \cdot \mathbf{r} + \Delta\phi).
 \end{aligned} \tag{2.31}$$

In this field the exponential term is a temporally varying phase but the cosine term is independent of time. Thus we get the temporally constant intensity

$$\begin{aligned}
 I(\mathbf{r}) &= (E_1 + E_2)(E_1 + E_2)^* \\
 &= 4 E_0^2 \cos^2(\mathbf{k}'' \cdot \mathbf{r} + \Delta\phi).
 \end{aligned} \tag{2.32}$$

This means the intensity is minimal where $\cos^2(\mathbf{k}'' \cdot \mathbf{r} + \Delta\phi) = 0$. These are the loci where

$$\mathbf{k}'' \cdot \mathbf{r} + \Delta\phi = (2n + 1) \frac{\pi}{2} \quad n \in \mathbb{Z}. \tag{2.33}$$

Here the wavefronts are said to be *anti-phase*, we speak of destructive interference. The intensity is maximal where

$$\mathbf{k}'' \cdot \mathbf{r} + \Delta\phi = n \pi \quad n \in \mathbb{Z}. \tag{2.34}$$

Here the wavefronts are *in-phase*, we have constructive interference.

The resulting time independent pattern is called an *interference pattern*, the fringes are called *interference fringes*. For plane waves they are oriented parallel to \mathbf{k}' and have a distance of $\pi/|\mathbf{k}''|$ in the direction \mathbf{k}'' . This is shown in moiré analogy in Fig. 2.3.

2.2.2 Interference of Two Waves with Different Frequencies

In the following we investigate the interference of two waves where not only the propagation directions and the phases but additionally the frequencies $\nu_i = \omega_i/(2\pi)$ are different.

$$\begin{aligned}
 E_1(\mathbf{r}, t) &= E_0 e^{i(\mathbf{k}_1 \cdot \mathbf{r} - 2\pi\nu_1 t + \phi_1)} \\
 E_2(\mathbf{r}, t) &= E_0 e^{i(\mathbf{k}_2 \cdot \mathbf{r} - 2\pi\nu_2 t + \phi_2)}.
 \end{aligned} \tag{2.35}$$

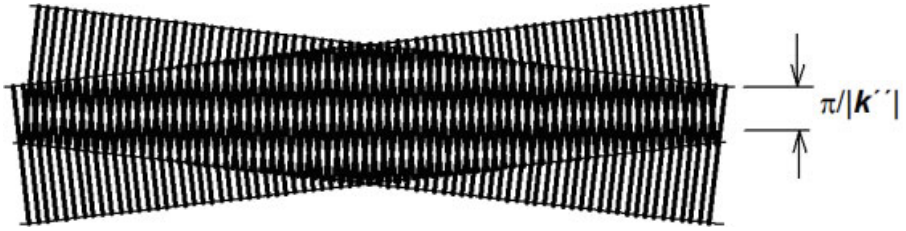


Figure 2.3: Interference fringes constant in time.

Besides the definitions of \mathbf{k}' , \mathbf{k}'' , ϕ and $\Delta\phi$ now let $\nu = (\nu_1 + \nu_2)/2$ and $\Delta\nu = (\nu_1 - \nu_2)/2$. Then we have

$$\begin{aligned}
 (E_1 + E_2)(\mathbf{r}, t) &= E_0 \left\{ e^{i(\mathbf{k}' \cdot \mathbf{r} + \mathbf{k}'' \cdot \mathbf{r} - 2\pi\nu t - 2\pi\Delta\nu t + \phi + \Delta\phi)} \right. \\
 &\quad \left. + e^{i(\mathbf{k}' \cdot \mathbf{r} - \mathbf{k}'' \cdot \mathbf{r} - 2\pi\nu t + 2\pi\Delta\nu t + \phi - \Delta\phi)} \right\} \\
 &= E_0 e^{i(\mathbf{k}' \cdot \mathbf{r} - 2\pi\nu t + \phi)} \left\{ e^{i(\mathbf{k}'' \cdot \mathbf{r} - 2\pi\Delta\nu t + \Delta\phi)} \right. \\
 &\quad \left. + e^{i(-\mathbf{k}'' \cdot \mathbf{r} + 2\pi\Delta\nu t - \Delta\phi)} \right\} \\
 &= 2E_0 e^{i(\mathbf{k}' \cdot \mathbf{r} - 2\pi\nu t + \phi)} \cos(\mathbf{k}'' \cdot \mathbf{r} - 2\pi\Delta\nu t + \Delta\phi)
 \end{aligned} \tag{2.36}$$

and the intensity is

$$\begin{aligned}
 I(\mathbf{r}, t) &= 4E_0^2 \cos^2(\mathbf{k}'' \cdot \mathbf{r} + \Delta\phi - 2\pi\Delta\nu t) \\
 &= 2E_0^2 [1 + \cos(2\mathbf{k}'' \cdot \mathbf{r} + 2\Delta\phi - 4\pi\Delta\nu t)].
 \end{aligned} \tag{2.37}$$

If the frequency difference is small enough, $\nu_1 \approx \nu_2$, a detector can register an intensity at \mathbf{r} oscillating with the *beat frequency* $2\Delta\nu = \nu_1 - \nu_2$. The phase of this modulation is the phase difference $2\Delta\phi = \phi_1 - \phi_2$ of the superposed waves. Contrary to the frequencies of the optical waves the beat frequency can be measured electronically and further evaluated as long as it remains in the kHz or MHz range. The measurement of the beat frequency $\Delta\nu$ enables one to calculate the motion of a reflector via the *Doppler shift* or to determine the phase difference $\Delta\phi$ between different points of an object where the intensity oscillates with the same constant beat frequency.

2.2.3 Interference of Two Waves with Different Amplitudes

If we have plane linearly polarized waves of the same frequency, but different direction and phase and moreover different amplitudes

$$\begin{aligned}
 E_1(\mathbf{r}, t) &= E_{01} e^{i(\mathbf{k}_1 \cdot \mathbf{r} - \omega t + \phi_1)} \\
 E_2(\mathbf{r}, t) &= E_{02} e^{i(\mathbf{k}_2 \cdot \mathbf{r} - \omega t + \phi_2)}
 \end{aligned} \tag{2.38}$$

we get the intensity

$$\begin{aligned}
 I(\mathbf{r}, t) &= (E_{01} e^{i(\mathbf{k}_1 \cdot \mathbf{r} - \omega t + \phi_1)} + E_{02} e^{i(\mathbf{k}_2 \cdot \mathbf{r} - \omega t + \phi_2)}) \\
 &\quad \times (E_{01} e^{-i(\mathbf{k}_1 \cdot \mathbf{r} - \omega t + \phi_1)} + E_{02} e^{-i(\mathbf{k}_2 \cdot \mathbf{r} - \omega t + \phi_2)}) \\
 &= E_{01}^2 + E_{02}^2 + E_{01} E_{02} \{ e^{i(\mathbf{k}_1 \cdot \mathbf{r} - \mathbf{k}_2 \cdot \mathbf{r} + \phi_1 - \phi_2)} \\
 &\quad + e^{i(\mathbf{k}_2 \cdot \mathbf{r} - \mathbf{k}_1 \cdot \mathbf{r} + \phi_2 - \phi_1)} \} \\
 &= E_{01}^2 + E_{02}^2 + 2E_{01} E_{02} \cos(2\mathbf{k}'' \cdot \mathbf{r} + 2\Delta\phi).
 \end{aligned} \tag{2.39}$$

This result can be written as

$$I = I_1 + I_2 + 2\sqrt{I_1 I_2} \cos(2\mathbf{k}'' \cdot \mathbf{r} + 2\Delta\phi) \tag{2.40}$$

or using the identity $\cos \alpha = 2 \cos^2(\alpha/2) - 1$ for comparison with (2.32) as

$$I = E_{01}^2 + E_{02}^2 + 4E_{01} E_{02} \cos^2(\mathbf{k}'' \cdot \mathbf{r} + \Delta\phi) - 2E_{01} E_{02}. \tag{2.41}$$

The special case $E_{01} = E_{02} = E_0$ gives (2.32).

In general the result of superposing two waves consists of one part that is the addition of the intensities and another part, the interference term, (2.40). Up to now we only have investigated *parallelly polarized waves*. The other extreme are *orthogonally polarized waves*. These waves do not interfere, their superposition only consists of the addition of the intensities

$$I = I_1 + I_2. \tag{2.42}$$

For other angles between the polarization directions the field vector has to be decomposed into components of parallel and orthogonal polarizations, the result contains interference parts as well as an addition of intensities.

Reasons for the additive intensity term not only may be mutually oblique polarization directions or different intensities, but also an insufficient coherence of the interfering waves. Because in the superposition of incoherent light we always observe a pure addition of the intensities but no interference, the additive term often is called the *incoherent part*, or we speak of *incoherent superposition*.

The *visibility* or *contrast* of the interference pattern is defined by

$$V = \frac{I_{\max} - I_{\min}}{I_{\max} + I_{\min}}. \tag{2.43}$$

If two parallel polarized waves of the same intensity interfere, we have the maximal contrast of $V = 1$; we have minimal contrast $V = 0$ for incoherent superposition. For example, if the ratio of the intensities of interfering waves is 5:1, the contrast is 0.745.

2.3 Coherence

With sunlight or lamplight we rarely observe interference. Only light of sufficient coherence will exhibit this effect. Roughly speaking coherence means the ability of light waves to interfere. Precisely, coherence describes the correlation between individual light waves. The two aspects of the general spatio-temporal coherence are the temporal and the spatial coherence.

2.3.1 Temporal Coherence

Temporal coherence describes the correlation of a wave with itself as it behaves at different time instants [158, 159]. It is best explained with the help of a *Michelson interferometer*, Fig. 2.4. At a beam splitter the incoming wave field is divided into two parts, one being reflected into the orthogonal direction, one passing the splitter and maintaining the original direction. This type of wavefront division is called *amplitude division*. If we do not have a single beam, but plane waves collimated by properly placed lenses and if there is an extended screen instead of the point-detector, then we speak of a *Twyman-Green interferometer*.

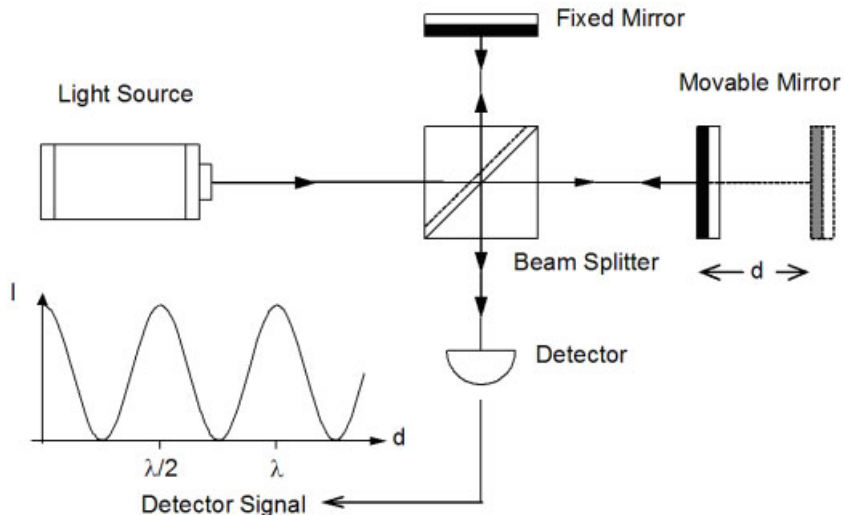


Figure 2.4: Michelson interferometer.

To keep the mathematics easy we assume that the beam splitter of the Michelson interferometer reflects 50 percent of the incident light and transmits the other 50 percent. The reflected wave travels to the fixed mirror, is reflected again and part of it hits the detector or screen for observation, where it meets the other part which was reflected at the movable mirror. At the detector mutually time shifted parts of the wave are superimposed, the time shift can be varied by changing the mirror shift d , Fig. 2.4. If in the Twyman-Green arrangement the mirrors are perfectly orthogonal we see a constant intensity over the screen, but with a minute tilt of one mirror around one axis, we observe fringes parallel to this axis.

Let the waves be E_1 and E_2 . For a fixed point on the screen, or the position of the detector, we have

$$E_2(t) = E_1(t + \tau) \quad \text{or} \quad E_1(t) = E_2(t - \tau) \quad (2.44)$$

where

$$\tau = \frac{2d}{c}. \quad (2.45)$$

We have to recognize that the distance d is travelled forward and backward, therefore the factor 2 in (2.45).

At the observation point we have the superposition

$$E(t) = E_1(t) + E_2(t) = E_1(t) + E_1(t + \tau) \quad (2.46)$$

and see the intensity

$$\begin{aligned} I &= \langle E E^* \rangle \\ &= \langle E_1 E_1^* \rangle + \langle E_2 E_2^* \rangle + \langle E_2 E_1^* \rangle + \langle E_1 E_2^* \rangle \\ &= 2I_1 + 2\text{Re}(\langle E_1 E_2^* \rangle) \end{aligned} \quad (2.47)$$

due to our assumption of equal amplitudes.

According to (2.27) we define the complex *self coherence* $\Gamma(\tau)$ as

$$\begin{aligned} \Gamma(\tau) &= \langle E_1^* E_1(t + \tau) \rangle \\ &= \lim_{T_m \rightarrow \infty} \frac{1}{T_m} \int_{-T_m/2}^{T_m/2} E_1^*(t) E_1(t + \tau) dt \end{aligned} \quad (2.48)$$

which is the autocorrelation of $E_1(t)$. The normalized quantity

$$\gamma(\tau) = \frac{\Gamma(\tau)}{\Gamma(0)} \quad (2.49)$$

defines the *degree of coherence*. Since $\Gamma(0) = I_1$ is always real and the maximal value of $|\Gamma(\tau)|$, we have

$$|\gamma(\tau)| \leq 1 \quad (2.50)$$

and

$$I(\tau) = 2I_1(1 + \text{Re}\gamma(\tau)). \quad (2.51)$$

The degree of coherence or the self coherence are not directly measurable, but it can be shown [159] that for the contrast V , which is easily measurable, we have

$$V(\tau) = |\gamma(\tau)|. \quad (2.52)$$

Now we can discriminate perfectly coherent light with $|\gamma(\tau)| = 1$, which nearly is emitted by a stabilized single-mode laser, incoherent light with $|\gamma(\tau)| = 0$ for all $\tau \neq 0$ where we have a statistically fluctuating phase, e. g. in sunlight, and partially coherent light, $0 \leq |\gamma(\tau)| \leq 1$. Often the contrast $V(\tau)$ decreases monotonically in τ . So we can introduce the *coherence time* τ_c as the time shift at which the contrast is reduced to $1/e$. The time shift is realized in interferometers by different optical pathlengths, so one can define the *coherence length*

$$l_c = c\tau_c. \quad (2.53)$$

If we have a periodic instead of a monotonically decreasing contrast function, e. g. from a two-mode laser, we take the time shift corresponding to the first minimum as the coherence time.

2.3.2 Spatial Coherence

Spatial coherence describes the mutual correlation of different parts of the same wavefront [158, 159] and is explained using *Young's double aperture interferometer*, Fig. 2.5. This type

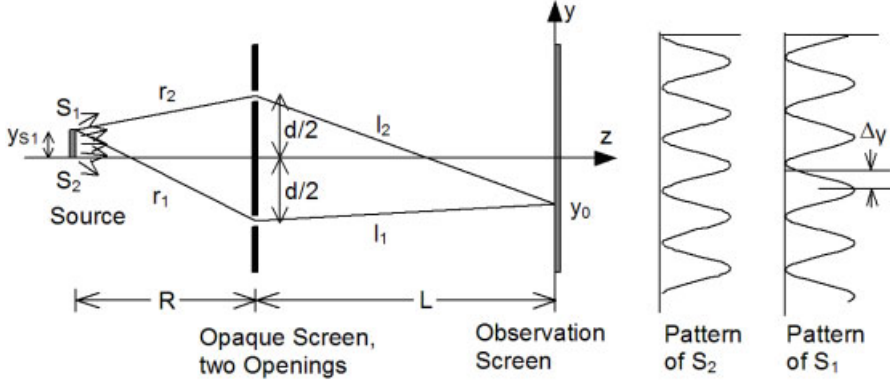


Figure 2.5: Young's interferometer.

of interferometer picks two geometrically different parts of the wavefront and brings them to interference, therefore it is called a *division of wavefront* interferometer. Let an opaque screen contain two small holes or parallel slits with a mutual distance d . For the moment we assume one point $S_1 = (0, y_{S1}, -R - L)$ of an extended source placed at the distance R behind that illuminates the opaque screen. Only the light passing through the holes forms an interference pattern on the observation screen placed some distance L in front of them. The distances of S_1 to the holes are r_1, r_2 , those of the holes to the observation point are l_1, l_2 . We can assume that the intensities of the two spherical waves leaving the holes are equal, therefore the intensity at the observation screen is (2.32)

$$I(x, y) = 4I_0(x, y) \cos^2 \Delta\phi(x, y). \quad (2.54)$$

The half phase difference $\Delta\phi$ is

$$\Delta\phi = \frac{1}{2} \left(\frac{2\pi}{\lambda} \Delta l \right) \quad (2.55)$$

where Δl is the difference in the pathlength of the light from the source S_1 to the observation point $B = (0, y_0, 0)$

$$\begin{aligned} \Delta l &= r_2 + l_2 - r_1 - l_1 \\ &= \sqrt{R^2 + \left(\frac{d}{2} - y_{S1} \right)^2} + \sqrt{L^2 + \left(\frac{d}{2} - y_0 \right)^2} \\ &\quad - \sqrt{R^2 + \left(\frac{d}{2} + y_{S1} \right)^2} - \sqrt{L^2 + \left(\frac{d}{2} + y_0 \right)^2}. \end{aligned} \quad (2.56)$$

Since y_0 , y_{S1} and d are small compared with R and L , the square roots of the form $\sqrt{1+b}$ can be approximated by $1 + b/2$ and we obtain

$$\Delta l = -d \left(\frac{y_{S1}}{R} + \frac{y_0}{L} \right). \quad (2.57)$$

The resulting irradiance now is proportional to

$$I = I_0 \cos^2 \left[\frac{\pi d}{\lambda} \left(\frac{y_{S1}}{R} + \frac{y_0}{L} \right) \right] \quad (2.58)$$

and describes a pattern of fringes parallel to the x -axis with a spacing of $\lambda L/d$ in the y -direction.

Next we investigate an extended source of perimeter l , Fig. 2.5. Source point S_2 on the optical axis emits a spherical wave which reaches the holes with equal phase, so we get an intensity maximum where the optical axis intersects the observation screen. The point S_1 gives rise to a fringe system which is shifted laterally because here r_1 and r_2 do not have equal length. Therefore the phase difference between the two spherical waves originating at the two holes is

$$\phi_1 - \phi_2 = \frac{2\pi}{\lambda} (r_1 - r_2) \quad (2.59)$$

which results in a lateral shift of the interference pattern by the amount

$$\Delta y = \frac{L}{d} (r_1 - r_2). \quad (2.60)$$

If there is a fixed phase relation between S_1 and S_2 , simultaneous emission from S_1 and S_2 will produce an interference pattern similar to the one of one point source alone. If on the other hand we have a randomly fluctuating phase between S_1 and S_2 , in the mean we get the sum of the intensities. As a condition for visibility of the fringes therefore we have to demand a lateral shift Δy less than a half fringe spacing

$$|\Delta y| < \frac{1}{2} \left(\frac{\lambda L}{d} \right) \quad (2.61)$$

or equivalently

$$|r_1 - r_2| < \lambda/2. \quad (2.62)$$

To express this in terms of the optical setup using the same arguments which led to (2.57) we get $|r_1 - r_2| = dl/R$ and thus

$$\frac{dl}{R} < \lambda/2. \quad (2.63)$$

The derivation was carried out for the two points S_1 and S_2 . But since these are the furthest points of the extended source, the condition (2.62), if fulfilled, is valid for all points between.

For points near the optical axis the path lengths from the holes to the observation screen are nearly the same. There the fringe pattern gives us information about the similarity of the wavefront $E(\mathbf{r}_1, t)$ and $E(\mathbf{r}_2, t)$ at the apertures at \mathbf{r}_1 and \mathbf{r}_2 without time shift. This similarity can be expressed by the *spatial coherence function*

$$\Gamma(\mathbf{r}_1, \mathbf{r}_2, 0) = \Gamma_{12}(0) = \langle E(\mathbf{r}_1, t)E^*(\mathbf{r}_2, t) \rangle. \quad (2.64)$$

The general *spatio-temporal coherence function* now is

$$\begin{aligned} \Gamma(\mathbf{r}_1, \mathbf{r}_2, t_1, t_2) &= \Gamma_{12}(t_2 - t_1) = \Gamma(\tau) \\ &= \langle E(\mathbf{r}_1, t + \tau)E^*(\mathbf{r}_2, t) \rangle \end{aligned} \quad (2.65)$$

which can be normalized to give the *mutual degree of coherence*

$$\gamma_{12}(\tau) = \frac{\Gamma_{12}(\tau)}{\sqrt{\Gamma_{11}(0)\Gamma_{22}(0)}} \quad (2.66)$$

where $\Gamma_{11}(0)$ is the intensity at \mathbf{r}_1 , $\Gamma_{22}(0)$ is the intensity at \mathbf{r}_2 .

Spatial coherence of thermal or gas discharge sources is associated primarily with the spatial extent of the source. If we are far enough from the source, R very large, the condition (2.63) is fulfilled. So we receive coherent light from stars, big thermal sources, at the earth, which is used in the field of stellar interferometry. This shows that coherence is not a property of the source, but of the light wave. The spatial coherence of laser light, as used in holographic interferometry, is associated with the transverse mode structure of the resonance cavity. For lasers resonating in the TEM_{00} mode, all points on the wavefront essentially have the same phase, therefore they have extremely good spatial coherence.

2.4 Scalar Diffraction Theory

In holography the light field that is recorded and coded in the hologram is optically reconstructed by diffraction of the reference wave at the hologram, as will be explained in more detail in Section 2.6. Therefore a quantitative description of the reconstructed wave field requires knowledge of the mechanisms of diffraction. However here we aim at a numerical rather than an optical reconstruction, thus a quantitative theory of diffraction is the eminent prerequisite. In this chapter the main results of scalar diffraction theory as they are needed in what follows will be presented. For a rigorous treatment of the theory leading to the diffraction formulas and of the development from the Huygens principle over the contributions of Fresnel, Kirchhoff, and Sommerfeld, to name just a few, the reader is referred to the many books on wave optics, e. g. [160]. Here we concentrate on the different approaches to solve the diffraction formula, namely the Fraunhofer approximation, the Fresnel approximation, and the employment of the convolution theorem when propagation of light waves is viewed as a linear system.

2.4.1 Fresnel-Kirchhoff Diffraction Formula

Let us first recall the formula for finding the diffraction pattern of an aperture which is illuminated by a point source. A detailed discussion of the preliminaries of a scalar diffraction

theory and a rigorous derivation of the diffraction formulas based on Green's functions are given by Goodman [160]. Consider an aperture Σ in an infinite opaque screen, Fig. 2.6. A

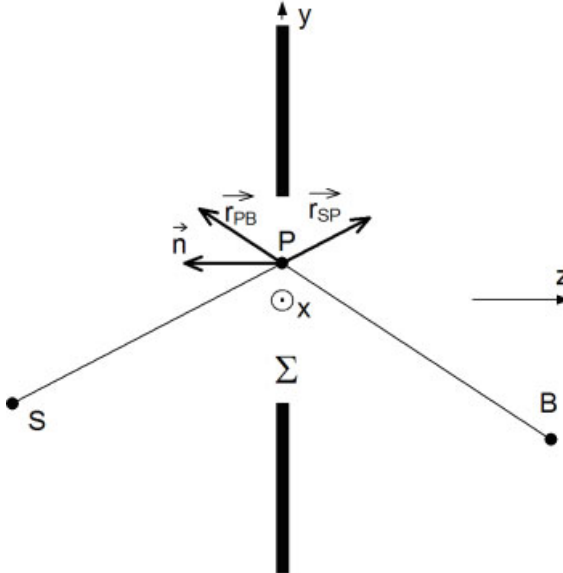


Figure 2.6: Geometry for the Fresnel-Kirchhoff diffraction formula.

radiating point source is at S , B is the observation point. Let P be an arbitrary point of the aperture. The distance from S to P is r_{SP} and that from P to B is r_{PB} . The unit vectors in the corresponding directions are r_{SP} and r_{PB} , and n is the normal to the aperture. The angle between the unit vectors r_{SP} and n is (r_{SP}, n) , the angle (r_{PB}, n) is defined analogously. With these notations the field at the observation point B is given by the *Fresnel-Kirchhoff diffraction formula*

$$E(B) = \frac{iE_0}{\lambda} \iint_{\Sigma} \frac{e^{-ik(r_{SP} + r_{PB})}}{r_{SP}r_{PB}} \left[\frac{\cos(r_{SP}, n) - \cos(r_{PB}, n)}{2} \right] dx dy. \quad (2.67)$$

Here it has been assumed that $k \gg 1/r_{PB}$, meaning an observation point many optical wavelengths apart from the aperture. The obliquity factor $[\cos(r_{SP}, n) - \cos(r_{PB}, n)]$ relates the incident and transmitting angles. For the special case of a light source centrally located with respect to the aperture, or an infinitely distant point source generating normally incident plane wave illumination, the obliquity factor becomes $1 + \cos \theta$, where θ is the angle between vectors n and r_{PB} . If furthermore r_{SP} and r_{PB} are nearly perpendicular to the screen, or equivalently S and B are far away, the obliquity factor becomes approximately 2 and (2.67) formulates to

$$E(B) = \frac{iE_0}{\lambda} \iint_{\Sigma} \frac{e^{ikr_{SP}}}{r_{SP}} \frac{e^{ikr_{PB}}}{r_{PB}} dx dy. \quad (2.68)$$

This equation can be interpreted as a mathematical formulation of Huygens' principle: The integrals sum the contributions of innumerable spherical sources each of amplitude

$E_0 \exp[ikr_{SP}/r_{SP}]$ distributed across the aperture Σ . Hence, if the amplitude distribution of the wave field across the aperture is known, the field E_B at the observation point can be obtained.

2.4.2 Fresnel Approximation

Let us now state the Huygens-Fresnel principle explicitly in rectangular coordinates. The diffracting aperture lies in the $(\xi, \eta, z = 0)$ -plane and is illuminated in the positive z -direction, Fig. 2.7.

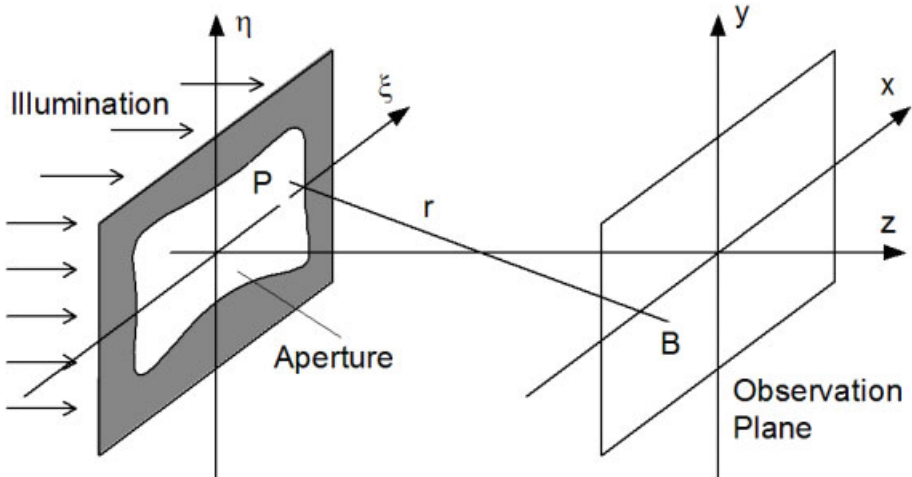


Figure 2.7: Geometry for the Fresnel approximation.

We are interested in the diffracted field in the (x, y) -plane, the observation plane, that is parallel to the (ξ, η) -plane and the distance z apart from it. We assume a finite extent of the diffracting aperture, meaning zero values outside a fixed area. So we can write infinite limits in the integrals. With these conventions the Fresnel-Kirchhoff formula is [160]

$$\begin{aligned} E(x, y, z) &= \frac{1}{i\lambda} \int_{-\infty}^{\infty} \int_{-\infty}^{\infty} U(\xi, \eta) \frac{e^{ikr}}{r} \cos(\theta) d\xi d\eta \\ &= \frac{z}{i\lambda} \int_{-\infty}^{\infty} \int_{-\infty}^{\infty} U(\xi, \eta) \frac{e^{ikr}}{r^2} d\xi d\eta \end{aligned} \quad (2.69)$$

because $\cos \theta = z/r$. The oblique distance r is given by

$$r = \sqrt{(\xi - x)^2 + (\eta - y)^2 + z^2} \quad (2.70)$$

and $U(\xi, \eta)$ denotes the complex field amplitude in the (ξ, η) -plane.

Furthermore it is assumed that the distance z between the diffracting aperture and the image plane is large compared to the lateral distances of the points in the x -, y -, ξ -, and η -directions. Then r in the denominator in (2.69) can be replaced by z . But this replacement is not feasible in the exponential term. The r in the exponent is multiplied by $k = 2\pi/\lambda$ with λ in the sub-micrometer range while r is in the meter range. Thus a minute variation of r would lead to significant phase errors. Therefore a more precise approximation for r in the exponent must be found.

The *Fresnel approximation* uses the binomial expansion of the square root into the series $\sqrt{1+b} = 1 + \frac{1}{2}b - \frac{1}{8}b^2 + \dots$. Omitting all but the constant and the linear terms gives

$$\begin{aligned} r &= \sqrt{z^2 + (\xi - x)^2 + (\eta - y)^2} \\ &= z \sqrt{1 + \left(\frac{\xi - x}{z}\right)^2 + \left(\frac{\eta - y}{z}\right)^2} \\ &\approx z \left[1 + \frac{1}{2} \left(\frac{\xi - x}{z}\right)^2 + \frac{1}{2} \left(\frac{\eta - y}{z}\right)^2 \right]. \end{aligned} \quad (2.71)$$

Now (2.69) is reduced to

$$\begin{aligned} E(x, y, z) &= \frac{1}{i\lambda} \int_{-\infty}^{\infty} \int_{-\infty}^{\infty} U(\xi, \eta) \frac{1}{z} e^{ikz} \left[1 + \frac{1}{2} \left(\frac{\xi - x}{z}\right)^2 + \frac{1}{2} \left(\frac{\eta - y}{z}\right)^2 \right] d\xi d\eta \\ &= \frac{e^{ikz}}{i\lambda z} \int_{-\infty}^{\infty} \int_{-\infty}^{\infty} U(\xi, \eta) e^{\frac{ik}{2z} [(\xi - x)^2 + (\eta - y)^2]} d\xi d\eta. \end{aligned} \quad (2.72)$$

If we perform the multiplication in the exponent and substitute $\nu = x/(z\lambda)$ and $\mu = y/(z\lambda)$ we obtain

$$\begin{aligned} E(\nu, \mu) &= \frac{e^{ikz}}{i\lambda z} \int_{-\infty}^{\infty} \int_{-\infty}^{\infty} U(\xi, \eta) e^{\frac{ik}{2z} [(\xi - x)^2 + (\eta - y)^2]} d\xi d\eta \\ &= \frac{e^{ikz}}{i\lambda z} \int_{-\infty}^{\infty} \int_{-\infty}^{\infty} U(\xi, \eta) e^{\frac{i\pi}{z\lambda} (\xi^2 + \eta^2)} e^{\frac{i\pi}{z\lambda} (x^2 + y^2)} e^{-\frac{2i\pi}{z\lambda} (x\xi + y\eta)} d\xi d\eta \\ &= \frac{e^{ikz}}{i\lambda z} e^{\frac{i\pi}{z\lambda} (x^2 + y^2)} \int_{-\infty}^{\infty} \int_{-\infty}^{\infty} U(\xi, \eta) e^{\frac{i\pi}{z\lambda} (\xi^2 + \eta^2)} e^{-2i\pi (\xi \frac{x}{z\lambda} + \eta \frac{y}{z\lambda})} d\xi d\eta \\ &= \frac{e^{ikz}}{i\lambda z} e^{i\pi z\lambda (\nu^2 + \mu^2)} \int_{-\infty}^{\infty} \int_{-\infty}^{\infty} U(\xi, \eta) e^{\frac{i\pi}{z\lambda} (\xi^2 + \eta^2)} e^{-2i\pi (\xi\nu + \eta\mu)} d\xi d\eta. \end{aligned} \quad (2.73)$$

Apart from the constant intensity factor and the phase factor preceding the integrals this is the Fourier transform of the product of the field $U(\xi, \eta)$ and the two-dimensional chirp function

$$e^{\frac{i\pi}{z\lambda} (\xi^2 + \eta^2)}. \quad (2.74)$$

2.4.3 Fraunhofer Approximation

In (2.71) r was approximated by

$$r \approx z + \frac{x^2 + y^2}{2z} - \frac{x\xi + y\eta}{z} + \frac{\xi^2 + \eta^2}{2z}. \quad (2.75)$$

The Fraunhofer approximation now also omits the term $(\xi^2 + \eta^2)/(2z)$, so that

$$\begin{aligned} E(\nu, \mu) &= \frac{1}{i\lambda z} \int_{-\infty}^{\infty} \int_{-\infty}^{\infty} U(\xi, \eta) e^{ik[z + \frac{x^2+y^2}{2z} - \frac{x\xi+y\eta}{z}]} d\xi d\eta \\ &= \frac{1}{i\lambda z} \int_{-\infty}^{\infty} \int_{-\infty}^{\infty} U(\xi, \eta) e^{\frac{ik}{2z}[2z^2+x^2+y^2-2x\xi-2y\eta]} d\xi d\eta \\ &= \frac{e^{ikz}}{i\lambda z} e^{i\pi z \lambda (\nu^2 + \mu^2)} \int_{-\infty}^{\infty} \int_{-\infty}^{\infty} U(\xi, \eta) e^{-2i\pi(\xi\nu+\eta\mu)} d\xi d\eta. \end{aligned} \quad (2.76)$$

Now despite the phase factors and the intensity factor preceding the integrals the Fresnel-Kirchhoff formula is reduced to the Fourier transform.

It remains to analyze under which conditions the Fresnel approximation and when even the Fraunhofer approximation is permitted. The Fresnel approximation replaces the secondary spherical waves of the Huygens-Fresnel principle by waves with parabolic wavefronts, while the Fraunhofer approximation uses even plane wavefronts. The Fresnel approximation is applicable as long as the quadratic term in the binomial expansion, namely $\frac{1}{8}b^2$, leads to a phase change much less than 1 radian

$$kz \left(\frac{1}{8}b^2 \right) \ll 1 \quad (2.77)$$

or equivalently $b^2 \ll 8/(kz)$. If we take for b again $((\xi - x)/z)^2 + ((\eta - y)/z)^2$ as in (2.71), we obtain

$$\left[\left(\frac{\xi - x}{z} \right)^2 + \left(\frac{\eta - y}{z} \right)^2 \right]^2 \ll \frac{8}{kz} = \frac{4\lambda}{\pi z} \quad (2.78)$$

or

$$\left[(\xi - x)^2 + (\eta - y)^2 \right]^2 \ll \frac{4\lambda}{\pi} z^3 \quad \text{for all } x, y, \xi, \eta. \quad (2.79)$$

For a circular aperture of size 1 cm, a circular observation region of size 1cm, and an assumed wavelength $\lambda = 0.5 \mu\text{m}$, this condition indicates a distance $z \gg 25 \text{ cm}$ for accuracy. As long as the amplitude transmittance and the illumination of the diffracting aperture is smooth and slowly varying, a much less stringent condition can be obtained [160]. But this prerequisite does not hold if we investigate the diffraction at digitally recorded holograms.

To find the region where even the Fraunhofer approximation is valid we investigate the phase induced by the omitted term in (2.75) which should remain much less than 1 radian

$$k \left(\frac{\xi^2 + \eta^2}{2z} \right) \ll 1 \quad (2.80)$$

or $\xi^2 + \eta^2 \ll z\lambda/\pi$. Thus an aperture with width 1 cm and a wavelength $\lambda = 0.5 \mu\text{m}$ requires a distance $z \gg 300 \text{ m}$ for validity of the Fraunhofer approximation. The Fresnel or near field region and the Fraunhofer or far field region are given in Fig. 2.8, but with the distances not exactly scaled.

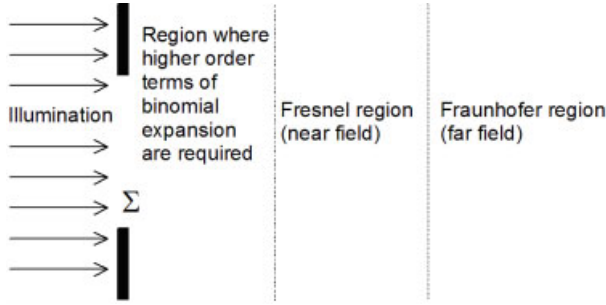


Figure 2.8: Relative positions of Fresnel and Fraunhofer diffraction regions (not exactly scaled).

An observation of the Fraunhofer diffraction patterns in practice is possible without going as far as implied by (2.80) from the diffracting aperture: One has to illuminate the aperture by a spherical wave converging to the observer or a positive lens is placed appropriately between aperture and observer. This last mentioned option deserves a more detailed analysis.

2.4.4 Thin Lens

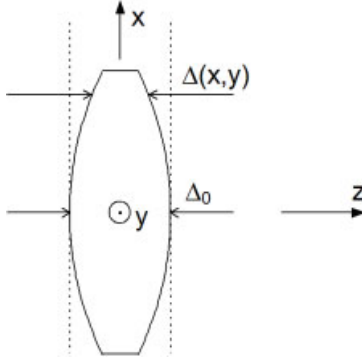
A lens consists of a material optically more dense than air, usually glass with a refractive index of approximately between $n = 1.5$ and $n = 1.9$, in which the propagation velocity of an optical disturbance is less than in air. A lens is considered as a *thin lens* if a ray entering the lens at coordinates (x, y) at one face exits at nearly the same coordinates on the opposite face. Only a delay of the incident wavefront has occurred but no translation of the ray is considered. The delay is proportional to the thickness $\Delta(x, y)$ of the thin lens at coordinates (x, y) , Fig. 2.9. The phase delay $\Delta\phi(x, y)$ of a wave that passes the lens at (x, y) therefore is

$$\begin{aligned} \Delta\phi(x, y) &= kn\Delta(x, y) + k[\Delta_0 - \Delta(x, y)] \\ &= k\Delta_0 + k(n - 1)\Delta(x, y) \end{aligned} \quad (2.81)$$

with Δ_0 denoting the maximum thickness of the lens and n the refractive index of the lens material. The multiplicative phase transformation of such a lens is of the form

$$t_l(x, y) = e^{ik\Delta_0} e^{ik(n-1)\Delta(x, y)}. \quad (2.82)$$

In practice the faces of the lens are spherical surfaces with radii of curvature R_1 and R_2 . Again for practical applications the spheres are approximated by parabolic surfaces. This

**Figure 2.9:** Thickness of a thin lens.

paraxial approximation restricts the analysis to portions of the wavefront that lie near the lens axis, the z -axis of Fig. 2.9. The thickness function $\Delta(x, y)$ now becomes [160]

$$\Delta(x, y) = \Delta_0 - \frac{x^2 + y^2}{2 \left(\frac{1}{R_1} - \frac{1}{R_2} \right)}. \quad (2.83)$$

The lens parameters n, R_1, R_2 are combined with the *focal length* f by

$$f = \frac{1}{(n-1) \left(\frac{1}{R_1} - \frac{1}{R_2} \right)} \quad (2.84)$$

which yields a phase transformation

$$t_l(x, y) = \exp \left[-\frac{ik}{2f} (x^2 + y^2) \right] \quad (2.85)$$

where the constant factor has been omitted [160]. We adopt the convention that a positive focal length f produces a spherical wave converging towards a point on the z -axis a distance f behind the lens if it was illuminated with a plane wave. Such a lens is called a *positive lens* or *converging lens*. On the other hand if f is negative, the plane wave is transformed into a spherical wave diverging from a point on the lens axis a distance $|f|$ in front of the lens, which is now called a *negative* or *diverging lens*, Fig. 2.10. We have to note that the phase transition (2.85) of a lens is described by a chirp function.

Now we can show that a thin positive lens produces a Fraunhofer diffraction pattern in a distance that is far less than that predicted by (2.80). This is equivalent to the statement that a lens performs a two-dimensional Fourier transform of a given input distribution. Let an input in the form of a transparency be pressed against a thin lens and be illuminated by a plane wave, Fig. 2.11. If the input image is represented by the function $U(\xi, \eta)$ then the distribution of light just behind the lens is

$$U_L(\xi, \eta) = U(\xi, \eta) \exp \left[-\frac{i\pi}{\lambda f} (\xi^2 + \eta^2) \right] \quad (2.86)$$

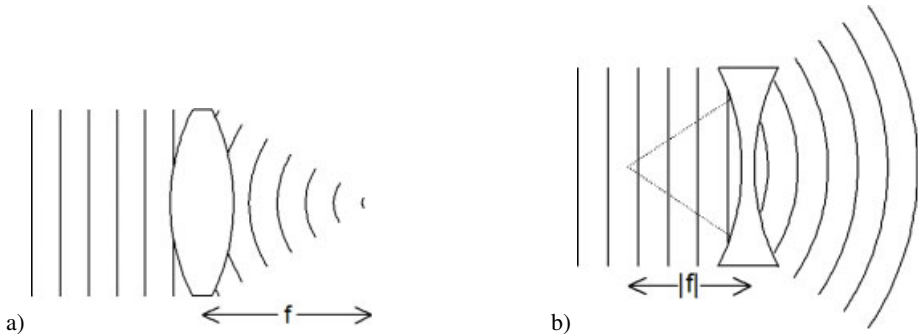


Figure 2.10: Positive (a) and negative (b) lens.

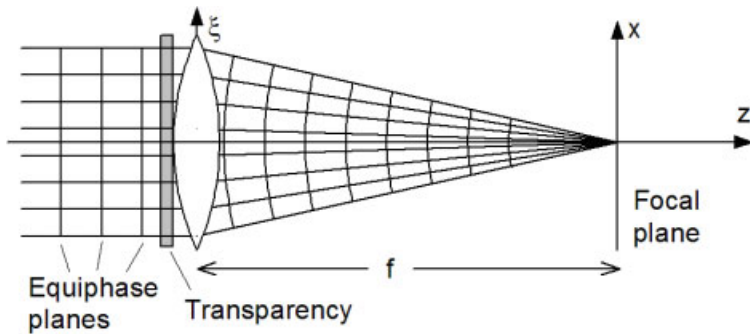


Figure 2.11: Optical Fourier transformation.

where the diameter of the lens is assumed infinite. To find the distribution $E(\nu, \mu, z = f)$ in the back focal plane of the lens, we apply the Fresnel diffraction formula (2.73) and obtain

$$\begin{aligned} E(\nu, \mu, f) &= \frac{e^{ikf}}{i\lambda f} e^{i\pi f \lambda (\nu^2 + \mu^2)} \int_{-\infty}^{\infty} \int_{-\infty}^{\infty} \left[U(\xi, \eta) e^{-\frac{i\pi}{f\lambda}(\xi^2 + \eta^2)} \right] \\ &\quad \times e^{\frac{i\pi}{f\lambda}(\xi^2 + \eta^2)} e^{-2i\pi(\xi\nu + \eta\mu)} d\xi d\eta \quad (2.87) \\ &= \frac{e^{ikf}}{i\lambda f} e^{i\pi f \lambda (\nu^2 + \mu^2)} \int_{-\infty}^{\infty} \int_{-\infty}^{\infty} U(\xi, \eta) e^{-2i\pi(\xi\nu + \eta\mu)} d\xi d\eta. \end{aligned}$$

Except for a factor that does not depend on the specific input function, the pattern in the focal plane is the Fourier transform of the input function, or in other words, we see the Fraunhofer diffraction pattern of the field incident on the lens in a distance equal to the focal length of the lens. This distance is significantly shorter than that demanded by (2.80). The cases of a lens having a finite aperture or those with inputs located at different distances behind and in front of the lens can be found in detailed treatments in [160, 161].

2.4.5 Propagation of Light Waves as a Linear System

The propagation of light from the $(\xi, \eta, z = 0)$ -plane to the parallel plane at nonzero distance z is described by the Fresnel-Kirchhoff formula (2.69). The disturbance $U(\xi, \eta, 0)$ is mapped to the field distribution $E(x, y, z)$. This mapping constitutes a linear system, where linearity is implied by the linearity of the wave equation. Due to linearity the Fresnel-Kirchhoff integral (2.69) can be written as a superposition integral (A.24) in two dimensions

$$E(x, y, z) = \int_{-\infty}^{\infty} \int_{-\infty}^{\infty} U(\xi, \eta, 0) h_z(\xi, \eta, x, y) d\xi d\eta \quad (2.88)$$

where the impulse response is

$$h_z(\xi, \eta, x, y) = \frac{i e^{ikr}}{\lambda r}. \quad (2.89)$$

The obliquity factor $\cos \theta$ can be omitted for large enough z . With (2.70) we get

$$\begin{aligned} h_z(\xi, \eta, x, y) &= \frac{i e^{ik\sqrt{(\xi-x)^2 + (\eta-y)^2 + z^2}}}{\lambda \sqrt{(\xi-x)^2 + (\eta-y)^2 + z^2}} \\ &= h_z(\xi - x, \eta - y). \end{aligned} \quad (2.90)$$

This equality implies that the linear system is shift-invariant: the superposition integral can be written as a convolution of the incident disturbance $U(\xi, \eta, 0)$ with the *impulse response of free-space propagation* $h_z(\xi, \eta)$ over the distance z

$$E(x, y, z) = U(x, y, 0) * h_z(x, y). \quad (2.91)$$

To find the *transfer function* $H_z(\xi, \eta)$ of the system, for its definition see Appendix A.5, one can use the angular spectrum point of view [160] and finally obtains the following expression in spatial frequencies

$$H_z(\xi, \eta) = \begin{cases} \exp \left[-i 2\pi z \sqrt{\frac{1}{\lambda^2} - \xi^2 - \eta^2} \right] & : \xi^2 + \eta^2 \leq 1/\lambda^2 \\ 0 & : \text{otherwise.} \end{cases} \quad (2.92)$$

This *transfer function of free space propagation* is a circularly symmetric complex function. Its magnitude and phase are sketched in Fig. 2.12.

The transfer function is only defined for $\xi^2 + \eta^2 \leq 1/\lambda^2$ for at higher spatial frequencies we get a negative argument in the square root and thus a real transfer function representing an attenuation factor. The wave is then called an *evanescent wave*. The $1/\lambda$ therefore can be regarded as the spatial bandwidth of free space propagation. This means that features contained in spatial frequencies greater than $1/\lambda$, corresponding to details of size finer than λ , cannot be transmitted by an optical wave of wavelength λ over distances much greater than λ [162]. The magnitude is one in the region $\xi^2 + \eta^2 \leq 1/\lambda^2$, the maximum absolute value of the phase is $2\pi z/\lambda$ at $\xi = \eta = 0$.

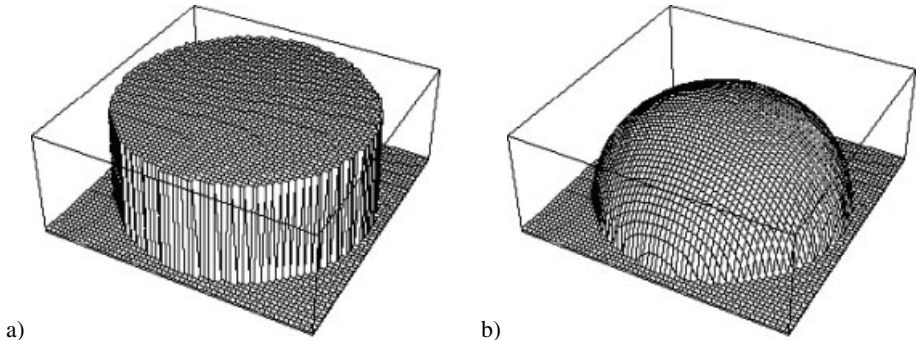


Figure 2.12: Magnitude (a) and phase (b) of the transfer function of free space propagation.

2.5 Speckles

If a randomly scattering object like a diffusely reflecting surface is illuminated with coherent light, all illuminated object points emit spherical waves which can interfere. The resulting wave field in space is called the *speckle field* or *speckle pattern*. The *speckles* form a random pattern in space which is stationary in time but highly fluctuating from point to point. Their appearance is almost independent of the object characteristics, but strongly depends on the optical properties of the viewing system. In holographic interferometry the speckles normally are disturbing, they influence the achievable resolution and accuracy of the measurement. On the other hand a number of related methods employ the speckle effect for solving measurement problems. Some of these methods will be discussed in Chapter 7. In the following a brief summary of the statistics of speckle fields will be given [163].

2.5.1 Statistics of Speckle Intensity and Phase

Let us consider a surface which is rough on the scale of the optical wavelength, Fig. 2.13.

According to the Huygens principle each point of the coherently illuminated rough surface can be treated as emitting a spherical secondary wavelet (2.23)

$$E_n(r_n) = \frac{E'_{0n}}{r_n} e^{i(kr_n + \phi'_n)}. \quad (2.93)$$

The mutual phases are temporally constant but strongly varying with the emission point. Thus at an observation point B in space all the individual field strengths sum up to

$$E(B) = \sum_n \frac{E'_{0n}}{r_n} e^{i(kr_n + \phi'_n)} \quad (2.94)$$

where now r_n are the distances from the surface points to B . This summation is analogous to the *random walk problem* in two dimensions of probability theory. Each spherical wave can be represented as a vector in the complex plane, the resulting field strength is the vector sum, Fig. 2.14. For applying the central limit theorem of probability theory we write

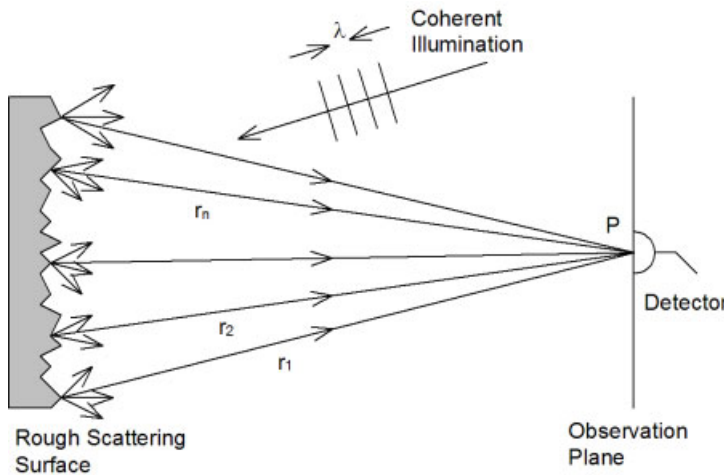


Figure 2.13: Physical origin of speckles, free space propagation.

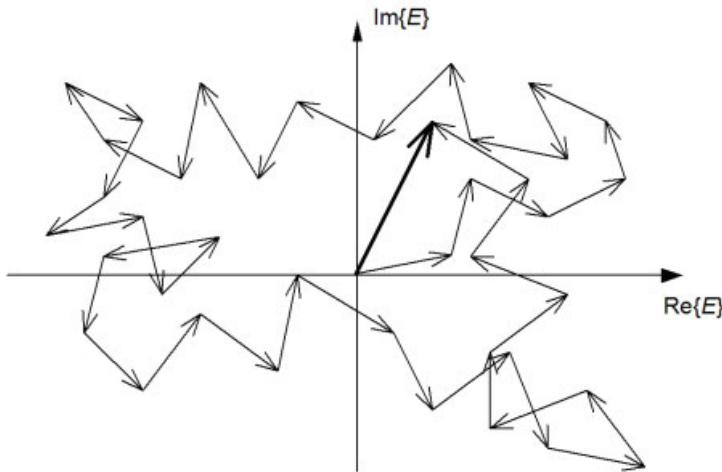


Figure 2.14: Random walk in the complex plane.

$$E_n(r_n) = \frac{1}{\sqrt{N}} |E_{0n}| e^{i\phi_n} \quad (2.95)$$

and make the assumptions that (i) the amplitude E_{0n}/\sqrt{N} and the phase ϕ_n of each wave are statistically independent from each other and from the amplitudes and phases of all other waves and (ii) the phases ϕ_n are uniformly distributed in the interval $[-\pi, \pi]$.

These assumptions are physically justified by the facts that the elementary scattering areas of the surface are unrelated and the strength of a given scattered component bears no relation to its phase (i) and that the surface is rough compared to the wavelength (ii). Phase excursions

more than 2π radians have the same effect as those with the same value modulo 2π .

Let E_r and E_i be the real and imaginary parts of E

$$\begin{aligned} E_r &= \operatorname{Re}\{E\} = \frac{1}{\sqrt{N}} \sum_{n=1}^N |E_{0n}| \cos \phi_n \\ E_i &= \operatorname{Im}\{E\} = \frac{1}{\sqrt{N}} \sum_{n=1}^N |E_{0n}| \sin \phi_n. \end{aligned} \quad (2.96)$$

The average values over an ensemble of macroscopically similar but microscopically different surfaces are

$$\begin{aligned} \langle E_r \rangle &= \frac{1}{\sqrt{N}} \sum_{n=1}^N \langle |E_{0n}| \cos \phi_n \rangle = \frac{1}{\sqrt{N}} \sum_{n=1}^N \langle |E_{0n}| \rangle \langle \cos \phi_n \rangle = 0 \\ \langle E_i \rangle &= \frac{1}{\sqrt{N}} \sum_{n=1}^N \langle |E_{0n}| \sin \phi_n \rangle = \frac{1}{\sqrt{N}} \sum_{n=1}^N \langle |E_{0n}| \rangle \langle \sin \phi_n \rangle = 0. \end{aligned} \quad (2.97)$$

Here the independence of the individual amplitudes from the phases, assumption (i), allows one to take the average over the factors separately. The uniform distribution of the phases in $[-\pi, \pi]$, assumption (ii), gives the zero values for $\langle \cos \phi_n \rangle$ and $\langle \sin \phi_n \rangle$. To calculate the variance and correlation we use

$$\begin{aligned} \langle \cos \phi_n \cos \phi_m \rangle &= \langle \sin \phi_n \sin \phi_m \rangle = \begin{cases} \frac{1}{2} & : n = m \\ 0 & : n \neq m \end{cases} \\ \langle \cos \phi_n \sin \phi_m \rangle &= 0. \end{aligned} \quad (2.98)$$

This gives

$$\begin{aligned} \langle E_r^2 \rangle &= \frac{1}{N} \sum_{n=1}^N \sum_{m=1}^N \langle |E_{0n}| |E_{m0}| \rangle \langle \cos \phi_n \cos \phi_m \rangle = \frac{1}{N} \sum_{n=1}^N \frac{1}{2} \langle |E_{0n}|^2 \rangle \\ \langle E_i^2 \rangle &= \frac{1}{N} \sum_{n=1}^N \sum_{m=1}^N \langle |E_{0n}| |E_{m0}| \rangle \langle \sin \phi_n \sin \phi_m \rangle = \frac{1}{N} \sum_{n=1}^N \frac{1}{2} \langle |E_{0n}|^2 \rangle \\ \langle E_r E_i \rangle &= \frac{1}{N} \sum_{n=1}^N \sum_{m=1}^N \langle |E_{0n}| |E_{m0}| \rangle \langle \cos \phi_n \sin \phi_m \rangle = 0. \end{aligned} \quad (2.99)$$

Altogether we have a complex field with uncorrelated real and imaginary parts of zero mean and identical variances. So we can apply the central limit theorem which states that for $N \rightarrow \infty$, E_r and E_i are asymptotically Gaussian. The joint probability density function is

$$p_{r,i}(E_r, E_i) = \frac{1}{2\pi\sigma^2} e^{-\frac{E_r^2 + E_i^2}{2\sigma^2}} \quad (2.100)$$

with the variance

$$\sigma^2 = \lim_{N \rightarrow \infty} \frac{1}{N} \sum_{n=1}^N \frac{1}{2} \langle |E_{0n}|^2 \rangle. \quad (2.101)$$

Since the intensity I and the phase ϕ of the resultant field are related to the real and imaginary parts by

$$E_r = \sqrt{I} \cos \phi \quad \text{and} \quad E_i = \sqrt{I} \sin \phi \quad (2.102)$$

the joint probability density function $p_{I,\phi}(I, \phi)$ of intensity and phase is

$$p_{I,\phi}(I, \phi) = p_{r,i}(\sqrt{I} \cos \phi, \sqrt{I} \sin \phi) \|J\| \quad (2.103)$$

where $\|J\|$ is the modulus of the determinant of the Jacobian matrix of the transformation (2.102). Substituting (2.102) into (2.100) gives

$$p_{I,\phi}(I, \phi) = \begin{cases} \frac{1}{4\pi\sigma^2} e^{-\frac{I}{2\sigma^2}} & \text{for } I > 0 \text{ and } -\pi \leq \phi < \pi \\ 0 & \text{otherwise.} \end{cases} \quad (2.104)$$

The one-dimensional marginal distributions for the intensity and the phase alone are

$$p_I(I) = \int_{-\pi}^{\pi} p_{I,\phi}(I, \phi) d\phi = \begin{cases} \frac{1}{2\sigma^2} e^{-\frac{I}{2\sigma^2}} & \text{for } I > 0 \\ 0 & \text{otherwise} \end{cases} \quad (2.105)$$

$$p_\phi(\phi) = \int_0^\infty p_{I,\phi}(I, \phi) dI = \begin{cases} \frac{1}{2\pi} & \text{for } -\pi \leq \phi < \pi \\ 0 & \text{otherwise.} \end{cases} \quad (2.106)$$

Thus the *intensity in a speckle pattern* obeys a negative exponential probability distribution and the *speckle pattern phase* is uniformly distributed. Furthermore we see that the intensity and phase are statistically independent

$$p_{I,\phi}(I, \phi) = p_I(I)p_\phi(\phi). \quad (2.107)$$

The n -th moment $\langle I^n \rangle$ of the intensity is

$$\langle I^n \rangle = n!(2\sigma^2)^n = n!\langle I \rangle^n \quad (2.108)$$

especially the mean value is $\langle I \rangle = 2\sigma^2$. By calculating the variance σ_I^2 of the intensity

$$\sigma_I^2 = \langle I^2 \rangle - \langle I \rangle^2 = \langle I \rangle^2 \quad (2.109)$$

we get the result that the standard deviation σ_I of a speckle pattern equals the mean intensity. Since a common measure for the contrast V is

$$V = \sigma_I / \langle I \rangle \quad (2.110)$$

we see that the *contrast of a speckle pattern* is always unity.

Sometimes we are interested in the probability $P(I)$ that the intensity exceeds a threshold I . This probability is

$$P(I) = \int_I^\infty p_I(I') dI' = \int_I^\infty \frac{1}{2\sigma^2} e^{-\frac{I'}{2\sigma^2}} dI' = e^{-\frac{I}{2\sigma^2}} \quad (2.111)$$

which for this special distribution equals the probability density function (2.105) normalized by $\langle I \rangle$. Figure 2.15 shows $\langle I \rangle p_I(I)$ or $P(I)$ against the normalized intensity $I/\langle I \rangle$.

Higher order statistics and the statistics of coherently and incoherently summed speckle patterns can be found in [163].

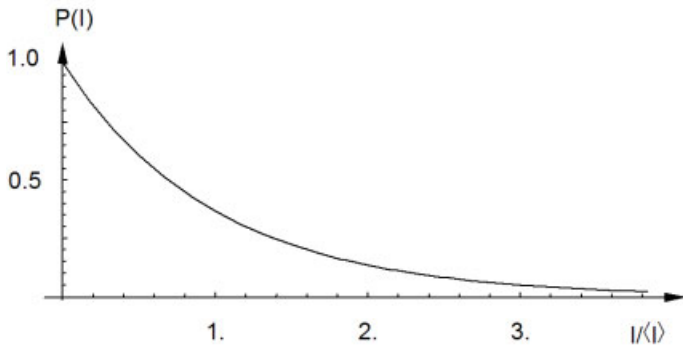


Figure 2.15: Normalized probability density function versus normalized intensity.

2.5.2 Speckle Size

In the context of holographic interferometry we are more interested in the average size of the individual speckles which we can observe. The *speckle size* must be related to the pixel size of CCD-targets recording the patterns and will determine the resolution of measurement methods.

First we consider the free space propagation of the scattered field, Fig. 2.16, without

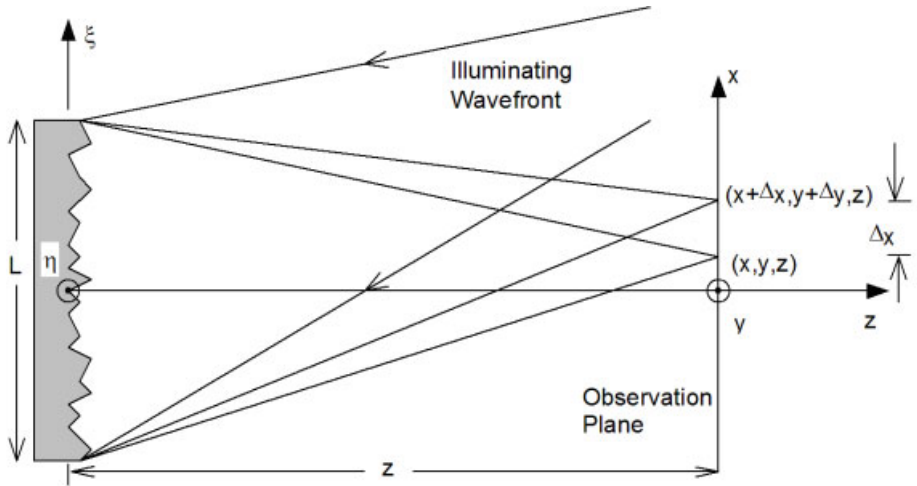


Figure 2.16: Free space propagation speckle formation.

an imaging system. The mean speckle size can be derived over the autocorrelation function $R(x_1, y_1; x_2, y_2)$ of the intensity in the observation plane. The autocorrelation is defined as

$$R(x_1, y_1; x_2, y_2) = R(\Delta x, \Delta y) = \langle I(x_1, y_1)I(x_2, y_2) \rangle. \quad (2.112)$$

In lengthy calculations involving the circular Gaussian distributions and the Huygens-Fresnel principle in [163] the expression

$$R(\Delta x, \Delta y) = \langle I \rangle^2 \left\{ 1 + \left| \frac{\int_{-\infty}^{\infty} \int_{-\infty}^{\infty} |I(\xi, \eta)|^2 e^{i \frac{2\pi}{\lambda z} (\xi \Delta x + \eta \Delta y)} d\xi d\eta}{\int_{-\infty}^{\infty} \int_{-\infty}^{\infty} |I(\xi, \eta)|^2 d\xi d\eta} \right|^2 \right\} \quad (2.113)$$

is derived with $|I(\xi, \eta)|$ denoting the intensity distribution incident on the scattering spot (ξ, η) .

For the special case of a uniformly scattering square area with dimensions $L \times L$, we have

$$|I(\xi, \eta)| = \begin{cases} 1 & \text{for } \left| \frac{\xi}{L} \right| < \frac{1}{2} \quad \text{and} \quad \left| \frac{\eta}{L} \right| < \frac{1}{2} \\ 0 & \text{otherwise} \end{cases} \quad (2.114)$$

and the resulting autocorrelation is

$$R(\Delta x, \Delta y) = \langle I \rangle^2 \left\{ 1 + \operatorname{sinc}^2 \left(\frac{L \Delta x}{\lambda z} \right) \operatorname{sinc}^2 \left(\frac{L \Delta y}{\lambda z} \right) \right\}. \quad (2.115)$$

The average size of a speckle can be taken to be the value of Δx where $\operatorname{sinc}^2(L \Delta x / \lambda z)$ first falls to zero, given by

$$\Delta x_s = \frac{\lambda z \pi}{L}. \quad (2.116)$$

The same result could be derived by taking the two extreme points a distance L apart as the two apertures in the Young's double aperture interferometer, (2.58).

We see that the speckle size at a fixed distance z from the scattering surface increases as the size of the illuminated area decreases. Because the size of these speckles only depends on the scattering surface and the plane where it is viewed, but not on any imaging system, they are called *objective speckles*.

Contrarily we speak of *subjective speckles* if they are formed by an imaging system, Fig. 2.17. Now the spatial distribution of the speckles is additionally determined by the diffraction limit of the imaging system. For this case the autocorrelation function of the intensity in the image plane was found [163] to be

$$R(r) = \langle I \rangle^2 \left\{ 1 + \left| \frac{2 J_1 \left(\frac{\pi D r}{\lambda z} \right)}{\frac{\pi D r}{\lambda z}} \right|^2 \right\} \quad (2.117)$$

where now D is the diameter of the circular lens pupil, J_1 is the Bessel function of first order, z is the distance of the image plane from the lens pupil plane, and $r = \sqrt{\Delta x^2 + \Delta y^2}$. The speckle size can be taken as the separation between the first two minima of J_1 . Since $J_1(x) = 0$ at $x = 1.22\pi$ we get

$$d_{sp} = \frac{2.44 \lambda z}{D}. \quad (2.118)$$

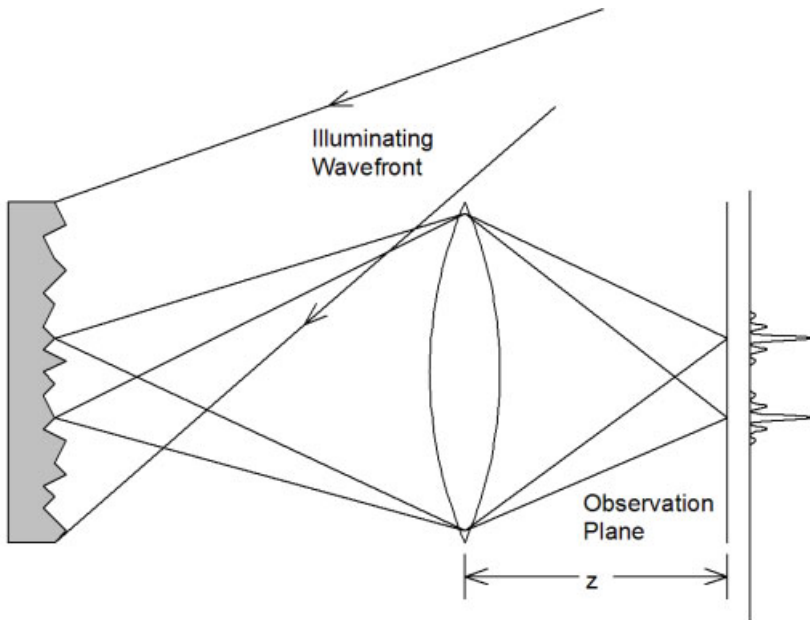


Figure 2.17: Imaging geometry for speckle formation.

The size of image plane speckles thus depends on the imaging system. If the aperture of the viewing lens is decreased, the speckle size will increase. It should be mentioned that the objective speckles exist more or less only theoretically, because we always have an imaging system, at least our own eyes.

The maximum spatial frequency f_{\max} in the speckle pattern is given by the size of the lens aperture and the distance of the lens from the observation plane by [164]

$$\frac{1}{f_{\max}} = \frac{\lambda z}{D}. \quad (2.119)$$

2.6 Holographic Recording and Optical Reconstruction

2.6.1 Hologram Recording

Each optical wave field consists of an amplitude distribution as well as a phase distribution (2.16), but all detectors or recording material like photographic film only register intensities: The phase is lost in the registration process. Now we have seen in (2.32) that if two waves of the same frequency interfere, the resulting intensity distribution is temporally stable and depends on the phase difference $\Delta\phi$. This is used in *holography* where the phase information is coded by interference into a recordable intensity. Clearly, to get a temporally stable intensity

distribution, at least as long as the recording process, $\Delta\phi$ must be stationary, which means the wave fields must be mutually coherent.

It was D. Gabor [1–3] who has shown that by illuminating the recorded interference pattern by one of the two interfering wave fields we can reconstruct the other one: this reconstructed wave field then consists of amplitude and phase distributions, not only the intensity. Figures 2.18 and 2.19 show schematically two basic holographic setups, used for recording the wave field reflected from the object's surface.

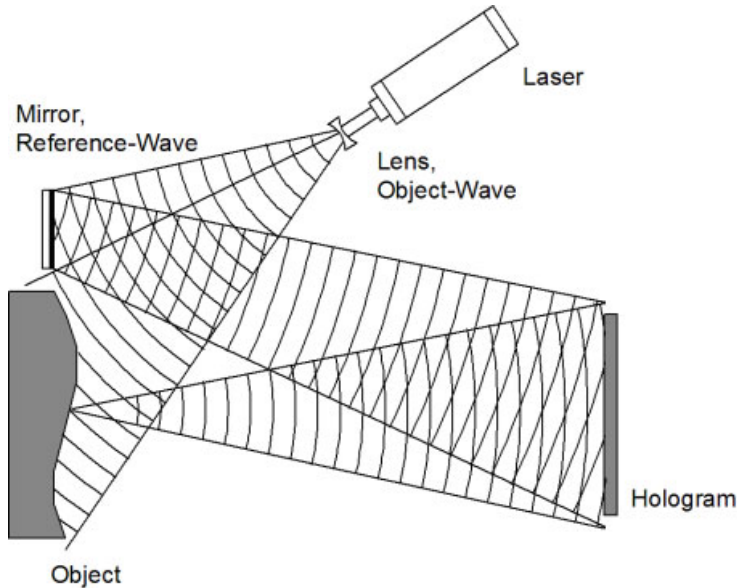


Figure 2.18: Basic holographic setup, wavefront division.

This field is called the object field or object wave, while the other field, necessary for producing the interference, is called the reference field or reference wave. To be mutually coherent, both waves must stem from the same source of coherent light, the laser. The division into object and reference wave can be performed by *wavefront division*, Fig. 2.18, or by *amplitude division*, Fig. 2.19.

The following description uses a point source which does not restrict the generality, because by the superposition principle (2.6) the results can be extended to all points of the object surface. Let the wave reflected by an object surface point P be the spherical wave (2.23), called the *object wave*

$$E_P = \frac{E_{0P}}{p} e^{i(kp + \phi)} \quad (2.120)$$

where p is the distance between the point P and the point $Q = (x, y, 0)$ on the photographic plate. The temporal factor ωt of (2.23) can be omitted. The *reference wave* is assumed to be

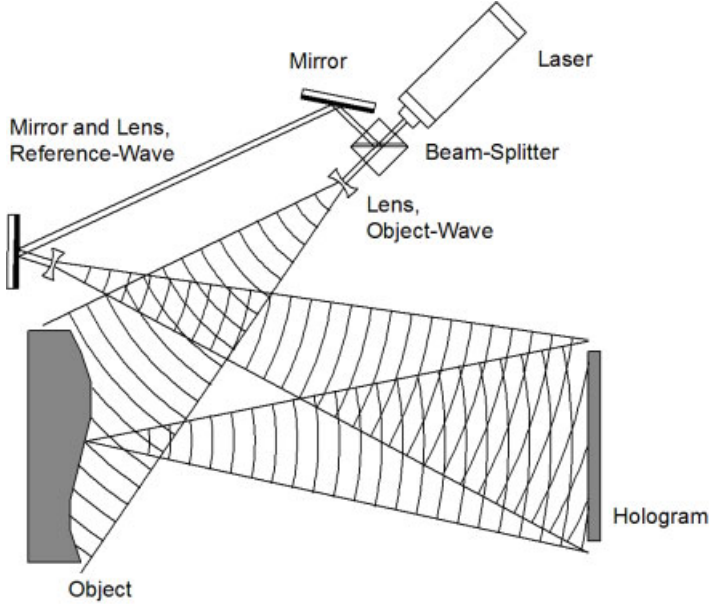


Figure 2.19: Basic holographic setup, amplitude division.

a spherical wave emitted at R

$$E_R = \frac{E_{0R}}{r} e^{i(kr + \psi)} \quad (2.121)$$

with the distance r between R and Q . The photographic plate registers the intensity

$$\begin{aligned} I(x, y) &= |E_P + E_R|^2 = E_P E_P^* + E_R E_R^* + E_P^* E_R + E_P E_R^* \\ &= \frac{E_{0P}^2}{p^2} + \frac{E_{0R}^2}{r^2} + \frac{E_{0P}}{p} e^{-i(kp + \phi)} \frac{E_{0R}}{r} e^{i(kr + \psi)} \\ &\quad + \frac{E_{0P}}{p} e^{i(kp + \phi)} \frac{E_{0R}}{r} e^{-i(kr + \psi)} \\ &= \frac{E_{0P}^2}{p^2} + \frac{E_{0R}^2}{r^2} + \frac{2E_{0P}E_{0R}}{pr} \cos(k(r - p) + \psi - \phi). \end{aligned} \quad (2.122)$$

As long as E_P is a single spherical wave, this intensity distribution, which is spatially varying because $p = p(x, y)$ and $r = r(x, y)$, is the *hologram* of a point source, the phase ϕ of the object wave relative to the phase ψ of the reference wave is coded into the intensity variation. The same applies for a continuum of object surface points according to the superposition principle.

During the *time of exposure* t_B , the photographic plate receives the energy

$$B(x, y) = \int_0^{t_B} I(x, y, t) dt. \quad (2.123)$$

By processing, this energy is translated into a blackening and a change of the refractive index, summarized in the complex *degree of transmission* τ which is generally a spatially varying function

$$\tau = \tau(x, y) = T(x, y)e^{i\theta(x, y)}. \quad (2.124)$$

This contains the cases of the *amplitude hologram*, where $\theta = \text{const}$, or the *phase hologram* with $T = \text{const}$ and θ varying with x and y .

If the exposed plate is processed to produce an amplitude hologram, the real transmission T depends on the received energy B as shown in Fig. 2.20. One has to work in the linear range, where the curve is approximated by the line

$$\begin{aligned} T &= \alpha - \beta B \\ &= \alpha - \beta t_B I \end{aligned} \quad (2.125)$$

for a temporally constant intensity I . α represents a uniform background transmittance and

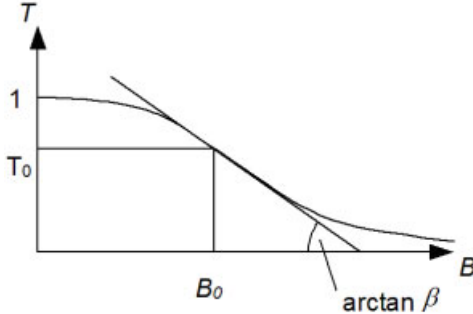


Figure 2.20: Amplitude transmittance versus received energy.

the positive value β is the slope of the amplitude transmittance. The working point B_0 is reached by adjusting the exposure time t_B . To keep the variation around B_0 small, the two wavefronts are given different amplitudes (2.40). The resulting real amplitude transmittance after processing is

$$\begin{aligned} T &= \alpha - \beta t_B(E_P E_P^* + E_R E_R^* + E_P^* E_R + E_P E_R^*) \\ &= \alpha - \beta t_B \left(\frac{E_{0P}^2}{p^2} + \frac{E_{0R}^2}{r^2} \right. \\ &\quad \left. + \frac{E_{0P} E_{0R}}{pr} e^{i(k(r-p) + \psi - \phi)} + \frac{E_{0P} E_{0R}}{pr} e^{-i(k(r-p) + \psi - \phi)} \right) \\ &= T_0 - \beta t_B \frac{E_{0P} E_{0R}}{pr} \left(e^{i(k(r-p) + \psi - \phi)} + e^{-i(k(r-p) + \psi - \phi)} \right) \\ &= T_0 - \frac{\beta t_B E_{0P} E_{0R}}{pr} \cos(k(r-p) + \psi - \phi) \end{aligned} \quad (2.126)$$

where T_0 is the mean transmittance $T_0 = \alpha - \beta t_B(E_{0P}^2/p^2 + E_{0R}^2/r^2)$.

If we produce a phase hologram, we must remain in the linear range of the curve describing the effective phase shift θ against exposure, Fig. 2.21.

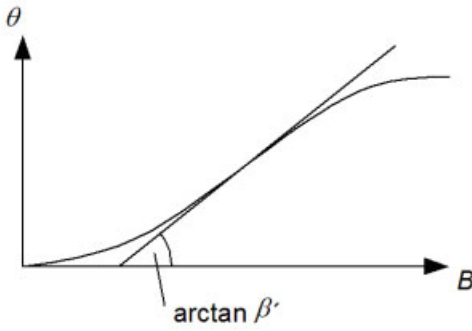


Figure 2.21: Phase shift versus received energy.

Again we have a range where we approximate by a line

$$\theta = \alpha' + \beta' t_B I. \quad (2.127)$$

The complex transmission after a series expansion of the exponential and neglecting higher than linear terms is

$$\tau = e^{i\theta(I)} \approx 1 + i\theta(I). \quad (2.128)$$

The resulting phase transmittance is

$$\tau = e^{i\theta(I)} \approx (1 + i\alpha') + i\beta' t_B (E_P E_P^* + E_R E_R^* + E_P^* E_R + E_P E_R^*) \quad (2.129)$$

analogous to (2.126). For convenience we have set $T = \text{const} = 1$.

The necessary *spatial resolution* of the recording media can be estimated by (2.30). If the angle between reference and object wave is θ , both waves for the moment being assumed as plane waves, the fringe distance is

$$\frac{\pi}{|k''|} = \frac{\lambda}{2 \sin \frac{\theta}{2}}. \quad (2.130)$$

If we assume a wavelength $\lambda = 0.5 \mu\text{m}$, for an angle of $\theta = 1^\circ$ we need a spatial resolution of better than 35 LP/mm (line-pairs per millimeter), for $\theta = 10^\circ$ already more than 350 LP/mm and for 30° more than 1035 LP/mm. As a consequence the spatial resolution puts an upper bound to the angular separation of the object points and thus to the object size, an issue becoming important when using CCD-arrays for recording the holograms (see Section 3.1.1).

2.6.2 Optical Reconstruction of a Wave Field

For optical *reconstruction* of the object wave we illuminate the processed photographic plate, also called a *hologram*, with the reference wave E_R , Fig. 2.22. This results in a modulation of the reference wave by the transmission $\tau(x, y)$.

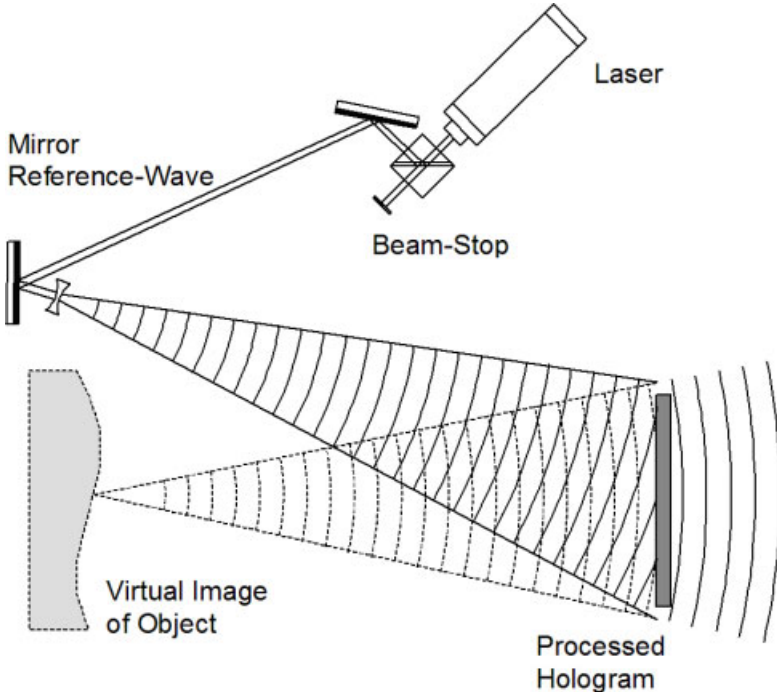


Figure 2.22: Holographic reconstruction.

For an amplitude hologram, directly behind the hologram (2.126) we get the complex amplitude

$$\begin{aligned}
 E_{\text{reconstr}} &= TE_R \\
 &= \alpha E_R - \beta t_B E_R (E_P E_P^* + E_R E_R^* + E_P^* E_R + E_P E_R^*) \\
 &= (\alpha - \beta t_B (|E_R|^2 + |E_P|^2)) E_R \\
 &\quad - \beta t_B E_R^2 E_P^* \\
 &\quad - \beta t_B |E_R|^2 E_P.
 \end{aligned} \tag{2.131}$$

The first term after the last equals sign

$$(\alpha - \beta t_B (|E_R|^2 + |E_P|^2)) E_R = T_0 E_R \tag{2.132}$$

is the zeroth diffraction order, also called dc-term; it is only the reference wave multiplied with the mean transmittance. The second term

$$\beta t_B E_R^2 E_P^* = \beta t_B \frac{E_{0R}^2}{r^2} e^{i2(kr + \psi)} \frac{E_{0P}}{p} e^{-i(kp + \phi)} \tag{2.133}$$

despite the multiplicative factor is a *conjugated image* of the object wave. While the original wavefront was a diverging one from P , the conjugate is a converging wavefront, which

converges to a focus. The *image* is *real* and *pseudoscopic*, the latter describes the property of inverted depths: Parts of the object in the background now appear in the foreground and vice versa, which gives curious parallax effects, difficult to observe. The contrary to pseudoscopic images are called *orthoscopic images*, to them we are used in the real world. The third term

$$\beta t_B |E_R|^2 E_P = \beta t_B \frac{E_{0R}^2}{r^2} \frac{E_{0P}}{p} e^{i(kp + \phi)} \quad (2.134)$$

gives the original wavefront E_P multiplied by a pure intensity term which for a plane reference wave is constant. The reconstructed wavefront produces a *virtual image* of the object which appears to stand at the place it occupied during recording of the hologram. Since the full object wave with amplitude and phase is reconstructed, the holographically recorded and reconstructed scene can be observed three-dimensionally. That means we can observe with varying depth of focus and with varying parallax.

If we reconstruct from a phase hologram (2.129), we get

$$\begin{aligned} E_{\text{restr}} &= \tau E_R \\ &\approx ((1 + i\alpha') + i\beta' t_B (|E_R|^2 + |E_P|^2)) E_R \\ &\quad + i\beta' t_B E_R^2 E_P^* \\ &\quad + i\beta' t_B |E_R|^2 E_P. \end{aligned} \quad (2.135)$$

The three terms consist of the same waves as in (2.131), only the factors before differ.

The *phase conjugated wave* $E_{pc}(z, t)$ belonging to $E(z, t) = E_0 e^{ikz} e^{-i\omega t}$ is

$$E_{pc}(z, t) = E_0 e^{-ikz} e^{-i\omega t}. \quad (2.136)$$

Contrary to $E^*(z, t)$ in $E_{pc}(z, t)$ only the spatial part is conjugated. Physically a phase conjugated wave is the original wave travelling in the opposite direction: instead of being emitted and diverging from a point the phase conjugated wave is converging to this point.

If we have used a plane wave as reference wave, it is easy to produce the phase conjugated one. We only have to turn the hologram by 180° and in the case of an amplitude hologram get

$$\begin{aligned} E_{\text{restr}} &= TE_R^* \\ &= (\alpha - \beta t_B (|E_R|^2 + |E_P|^2)) E_R^* \\ &\quad - \beta t_B |E_R|^2 E_P^* \\ &\quad - \beta t_B E_R^{*2} E_P. \end{aligned} \quad (2.137)$$

Now the second term represents a real orthoscopic image in exactly the position relative to the hologram the object had during the recording.

To get a reconstructed wavefront undistorted by the other reconstructed waves, the reference and object wave have to be separated in space. While Gabor had no sources giving light with sufficient coherence, he had to produce *in-line-holograms* where object and reference waves were travelling the same direction orthogonally to the hologram. Leith and Upatnieks [7–9] were the first who took advantage of the coherence of laser light and who gave the object and the reference beams different directions. In their *off-axis-holograms* all reconstructed waves are well separated.

To find the directions of the reconstructed images, for the moment we assume the object and reference waves as plane waves and calculate the wave in the hologram plane. Without restriction of generality we assume $y = 0$. Furthermore we obey the convention that angles are counted positive in the counterclockwise direction and negative in the clockwise direction.

Let the reference wave E_R illuminate the hologram plate under the angle $-\gamma_1$ and let the object wave E_P impinge under $+\gamma_2$, Fig. 2.23.

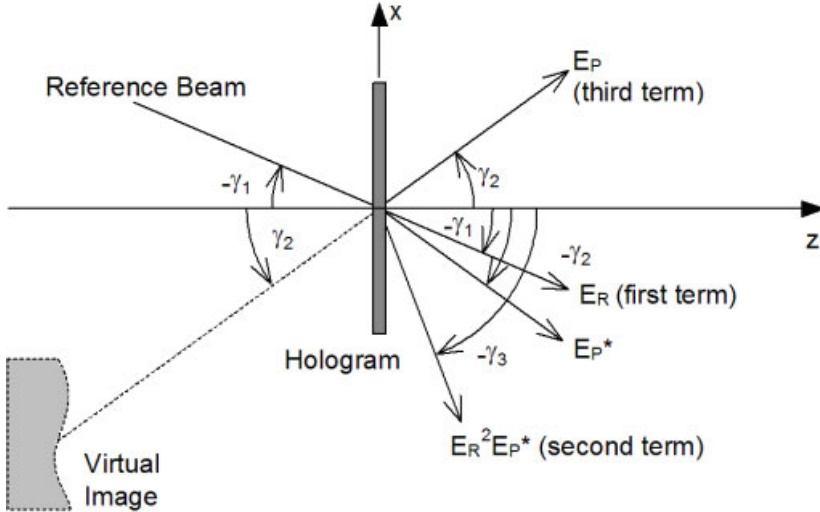


Figure 2.23: Locations of reconstructed images.

Then the broadened reference wave E_R , the first term in (2.131) and (2.135), leaves the hologram plate in direction $-\gamma_1$. To find the second term, we observe that in the hologram plane ($z = 0$) with $E_P(x, 0, 0) = \exp(ikx \sin \gamma_2)$ the conjugate is $E_P^*(x, 0, 0) = \exp(-ikx \sin \gamma_2) = \exp[ikx \sin(-\gamma_2)]$. A conjugate wave would leave the hologram under $-\gamma_2$. The square of $E_R = \exp[ikx \sin(-\gamma_1)]$ is

$$E_R^2(x, 0, 0) = e^{-ikx^2 \sin \gamma_1}. \quad (2.138)$$

Thus the second term in (2.131) and (2.135) is

$$E_R^2 E_P^* = e^{-ikx^2 \sin \gamma_1} e^{-ikx \sin \gamma_2} = e^{ikx \sin(-\gamma_3)}. \quad (2.139)$$

For small γ_1 we observe that $2 \sin \gamma_1 \approx \sin 2\gamma_1$, but always $2 \sin \gamma_1 > \sin 2\gamma_1$. As long as γ_1, γ_2 remain small, we can set $\gamma_3 = 2\gamma_1 + \gamma_2$, but for larger γ_1, γ_2 the image shifts and becomes more and more distorted until it vanishes for

$$2 \sin \gamma_1 + \sin \gamma_2 \geq 0. \quad (2.140)$$

The third term of (2.131) and (2.135) is E_P which leaves the hologram under γ_2 and constitutes the virtual image of the object.

The arrangement simplifies with a reference wave impinging orthogonally onto the hologram plane, then we have $\gamma_1 = 0$.

2.6.3 Holographic Imaging Equations

In Section 2.6.2 we have assumed to reconstruct with exactly the same reference wave of the same wavelength as used for the recording of the hologram. But, for example, a hologram recorded with a pulsed ruby laser of wavelength $\lambda = 0.694 \mu\text{m}$ has to be reconstructed for observation with a continuous laser, normally a He-Ne laser of wavelength $\lambda = 0.633 \mu\text{m}$. Furthermore we are interested in whether the reconstructed image vanishes, if the reconstructing wave is slightly shifted from the recording wave, or what else is happening to the reconstruction [165–169].

The investigations are performed for a single object point $P = (x_P, y_P, z_P)$ and a hologram point $Q = (x, y, 0)$. The hologram is placed in the (x, y) -plane of the Cartesian coordinate system, Fig. 2.24. The reconstructed image of an extended object then can be determined

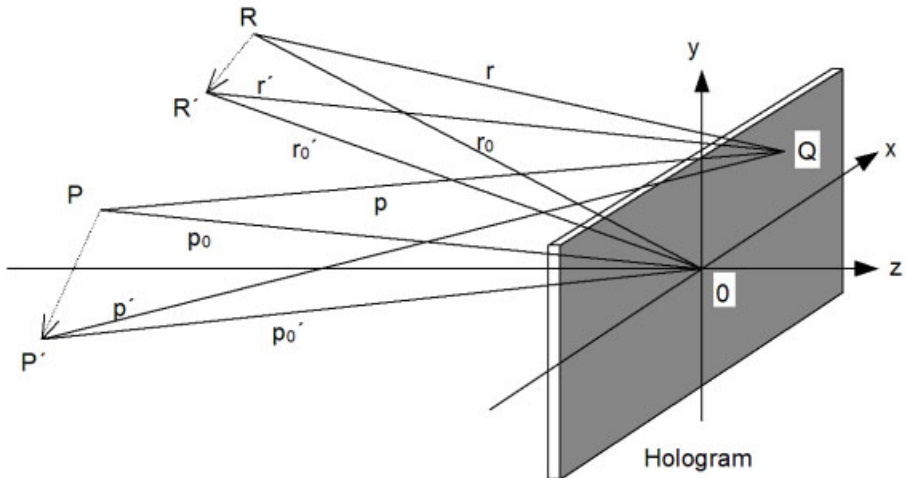


Figure 2.24: Coordinate system for the holographic imaging equations.

by calculating the positions of several of its surface points. The spherical reference wave of wavelength λ during the recording diverges from point R ; during reconstruction it may diverge from R' having wavelength λ' .

Reconstruction with $E_{R'}$ and λ' instead of E_R and λ gives a third term in (2.131) proportional to

$$\begin{aligned} E_P E_{R'} E_R^* &= \frac{E_{0P}}{p} \frac{E_{0R'}}{r'} \frac{E_{0R}}{r} e^{i(kp + \phi)} e^{i(k'r' + \tau)} e^{-i(kr + \psi)} \\ &\sim e^{i(kp + k'r' - kr + \phi + \tau - \psi)} \\ &= e^{i(k'p' + \zeta)} \end{aligned} \tag{2.141}$$

which describes a wave with wave number $k' = 2\pi/\lambda'$ coming from P' to Q . p is the distance from P to Q , r is the distance from R to Q , r' is that from R' to Q and p' is the distance from P' to Q .

We first investigate the distance p

$$\begin{aligned} p &= \sqrt{(x - x_P)^2 + (y - y_P)^2 + z_P^2} \\ &= \sqrt{x^2 + y^2 - 2xx_P - 2yy_P + p_0^2} \end{aligned} \quad (2.142)$$

where p_0 is the distance of P to the origin. We observe that p_0 is large compared to x, y, x_P and y_P , so we can expand p into a power series around p_0 [7–9, 21, 22, 166, 170, 171]

$$p = p_0 + \frac{x^2 + y^2}{2p_0} - \frac{2xx_P + 2yy_P}{2p_0} + \dots \quad (2.143)$$

In the same way we expand r, r' and p'

$$r = r_0 + \frac{x^2 + y^2}{2r_0} - \frac{2xx_R + 2yy_R}{2r_0} + \dots, \quad (2.144)$$

$$r' = r'_0 + \frac{x^2 + y^2}{2r'_0} - \frac{2xx'_R + 2yy'_R}{2r'_0} + \dots, \quad (2.145)$$

$$p' = p'_0 + \frac{x^2 + y^2}{2p'_0} - \frac{2xx'_P + 2yy'_P}{2p'_0} + \dots \quad (2.146)$$

From the definition of p' (2.141) we have

$$k'p' = k(p - r) + k'r'. \quad (2.147)$$

Now we insert the approximations of p, r, r' and p' and observe that (2.147) is valid for all (x, y) , so we equate the coefficients of similar terms and with the definition $\mu = \lambda'/\lambda$ we get

$$\frac{1}{p'_0} = \frac{\mu}{p_0} - \frac{\mu}{r_0} + \frac{1}{r'_0}, \quad (2.148)$$

$$\frac{x'_P}{p'_0} = \frac{\mu x_P}{p_0} - \frac{\mu x_R}{r_0} + \frac{x'_R}{r'_0}, \quad (2.149)$$

$$\frac{y'_P}{p'_0} = \frac{\mu y_P}{p_0} - \frac{\mu y_R}{r_0} + \frac{y'_R}{r'_0}. \quad (2.150)$$

These are the *holographic imaging equations* for the direct image to a first order approximation. In a similar way one can derive the imaging equations of the conjugate image, the second term in (2.131). They have the same form, only the signs preceding μ are interchanged.

In the preceding derivation we have expanded about p_0, p'_0, r_0 and r'_0 [170], which gives a more accurate approximation than the expansion about the z -components z_P, z'_P, z_R, z'_R [172]. This may be performed, if the x - and y -components are negligible compared to the z -components. In that case we would get the imaging equations

$$\frac{1}{z'_P} = \frac{\mu}{z_P} - \frac{\mu}{z_R} + \frac{1}{z'_R}, \quad (2.151)$$

$$\frac{x'_P}{z'_P} = \frac{\mu x_P}{z_P} - \frac{\mu x_R}{z_R} + \frac{x'_R}{z'_R}, \quad (2.152)$$

$$\frac{y'_P}{z'_P} = \frac{\mu y_P}{z_P} - \frac{\mu y_R}{z_R} + \frac{y'_R}{z'_R} \quad (2.153)$$

which can be rearranged to yield the easier to handle and well known form [172, 173]

$$x'_P = \frac{\mu x_P z_R z'_R - \mu x_R z_P z'_R + x'_R z_P z_R}{\mu z_R z'_R - \mu z_P z'_R + z_P z_R}, \quad (2.154)$$

$$y'_P = \frac{\mu y_P z_R z'_R - \mu y_R z_P z'_R + y'_R z_P z_R}{\mu z_R z'_R - \mu z_P z'_R + z_P z_R}, \quad (2.155)$$

$$z'_P = \frac{z'_R z_P z_R}{\mu z_R z'_R - \mu z_P z'_R + z_P z_R}. \quad (2.156)$$

We now consider some special cases. The easiest is the reconstruction with a reference wave identical to the one used for recording, even with the same wavelength. Then we have $p'_0 = p_0$ and $x'_P = x_P$, $y'_P = y_P$ and $z'_P = z_P$, as expected. Next we examine a plane reference wave impinging orthogonally onto the hologram, but during reconstruction with wavelength λ' instead of λ . Then we have $r_0 = z_R \rightarrow \infty$, $r'_0 = z'_R \rightarrow \infty$, $x_R/r_0 = 0$, $y_R/r_0 = 0$, $x'_R/r'_0 = 0$, $y'_R/r'_0 = 0$. From (2.148) we get $\mu p'_0/p_0 = 1$ and together with (2.149) and (2.150) resp.

$$x'_P = x_P, \quad (2.157)$$

$$y'_P = y_P, \quad (2.158)$$

$$z'_P = \frac{1}{\mu} z_P. \quad (2.159)$$

This means the object is shifted and stretched or compressed in the z -direction, but the lateral dimensions remain unaffected.

The *lateral magnification* M_{lat} in the direct image can be defined [172]

$$M_{lat} = \frac{dx'_P}{dx_P} = \frac{dy'_P}{dy_P}. \quad (2.160)$$

It is

$$M_{lat} = \frac{1}{1 + z_P \left(\frac{1}{\mu z'_R} - \frac{1}{z_R} \right)}. \quad (2.161)$$

For the plane wave of the case above due to $z_R \rightarrow \infty$ and $z'_R \rightarrow \infty$ we get $M_{lat} = 1$.

Furthermore we may define the *angular magnification* by [172]

$$M_{ang} = \frac{d(x'_P/z'_P)}{d(x_P/z_P)} = \frac{d(y'_P/z'_P)}{d(y_P/z_P)} \quad (2.162)$$

and calculate $|M_{ang}| = \mu$. For the *longitudinal magnification* M_{long} of the primary image we obtain

$$M_{long} = \frac{dz'_P}{dz_P} = \frac{1}{\mu} M_{lat}^2. \quad (2.163)$$

The different magnifications for the conjugate image are derived analogously.

The holographic imaging equations can be used to compensate the effect of CW-reconstruction with a wavelength differing from that of the pulsed recording by an appropriate reference beam adjustment [143]. If the hologram is shifted during the real-time reconstruction, shearing fringes are produced which modify the deformation fringes in a controlled way [174]. If in the expansion (2.143) we retain higher order terms, we get the *aberrations* like spherical aberration, coma, astigmatism, field curvature and others [165, 166, 172, 175–178]. They give information about the quality of the imaged object, which means how the image of a point is washed out.

2.6.4 Types of Holograms

In Section 2.6.2 we already mentioned the distinction between Gabor's in-line holograms and the Leith-Upatnieks off-axis holograms. The *in-line arrangement* is still used for the analysis of transparent objects, or small particles like droplets, Fig. 2.25a.

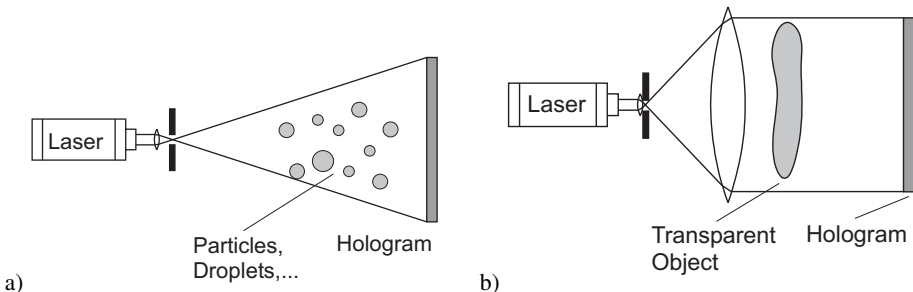


Figure 2.25: In-line holography with divergent (a) and collimated (b) light.

The reference wave is the light passing unaffected by the particles and the object wave is the wave field scattered by the particles. We may use divergent or collimated light, Fig. 2.25b. Reconstruction by the illuminating wave alone without the object gives the virtual image of the particles or the transparent object at its original position as well as the real image on the opposite side of the hologram. There is no beam splitting into reference and object beam, so the method sometimes is called *single beam holography*.

The main disadvantages of in-line holograms are the disturbed reconstruction due to the bright reference beam and the twin images: Virtual and real image are along the same line of sight, so while focusing on one of them we see it overlaid by an out of focus image of the other one. These drawbacks are avoided by the *off-axis arrangement*. Here the laser beam is split by wavefront division, Fig. 2.18, or by amplitude division, Fig. 2.19, into reference and object wave. This approach has been called *split beam holography* or *two beam holography*. If the offset angle between reference and object wave is large enough, we have no overlap between the virtual and the real reconstructed images nor do we stare into the directly transmitted reference beam.

If we have flat or nearly flat objects we may record the Fourier transform of the object and reference waves. Then we speak about *Fourier transform holography*. Imagine an object located in the front focal plane of a lens, Fig. 2.26a, illuminated by coherent light.

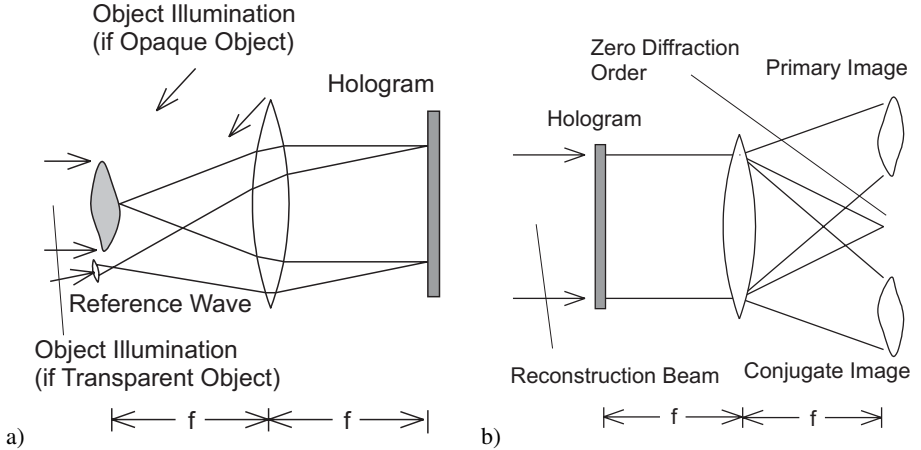


Figure 2.26: Recording (a) and reconstruction (b) of a Fourier transform hologram.

Let the complex amplitude leaving the object plane be $E_P(x, y)$, then the complex amplitude of the wave field at the holographic plate located in the back focal plane of the lens is the Fourier transform of $E_P(x, y)$

$$\mathcal{E}_P(\xi, \eta) = \mathcal{F}\{E_P(x, y)\}. \quad (2.164)$$

The reference wave is a spherical wave emitted from a point source at (x_0, y_0) in the front focal plane. Without loss of generality we can assume unit amplitude, so $E_R(x, y) = \delta(x - x_0, y - y_0)$. $\delta(x, y)$ describes the *Dirac delta impulse*, see (A.6). The complex amplitude of this reference wave in the hologram plane is

$$\mathcal{E}_R(\xi, \eta) = \mathcal{F}\{\delta(x - x_0, y - y_0)\} = e^{-i2\pi(\xi x_0 + \eta y_0)} \quad (2.165)$$

as follows from the shift theorem (A.15) and the forth line of Table A.1. In the hologram plane, the back focal plane of the lens, we obtain a hologram characterized by the transmission

$$\begin{aligned} T(\xi, \eta) &= \alpha - \beta t_B (\mathcal{E}_P + \mathcal{E}_R)(\mathcal{E}_P + \mathcal{E}_R)^* \\ &= \alpha - \beta t_B (\mathcal{E}_R \mathcal{E}_R^* + \mathcal{E}_P \mathcal{E}_P^* + \mathcal{E}_R^* \mathcal{E}_P + \mathcal{E}_R \mathcal{E}_P^*)(\xi, \eta). \end{aligned} \quad (2.166)$$

For reconstruction we illuminate this *Fourier transform hologram* with the plane wave of (2.165) and obtain

$$T\mathcal{E}_R = (\alpha - \beta t_B |\mathcal{E}_R|^2) \mathcal{E}_R - \beta t_B (\mathcal{E}_P \mathcal{E}_P^* \mathcal{E}_R + \mathcal{E}_R \mathcal{E}_R^* \mathcal{E}_P + \mathcal{E}_R \mathcal{E}_R \mathcal{E}_P^*). \quad (2.167)$$

The hologram plane now is the front focal plane of the reconstruction lens, see Fig. 2.26b,

which produces the Fourier transform of $T\mathcal{E}_R$ in its back focal plane, the (x', y') -plane.

$$\begin{aligned}
 & \mathcal{F}\{T(\xi, \eta)\}(x', y') \\
 &= (\alpha - \beta t_B |\mathcal{E}_R|^2) \mathcal{F}\{\mathcal{E}_R\}(x', y') - \beta t_B (\mathcal{F}\{\mathcal{E}_P \mathcal{E}_P^* \mathcal{E}_R\} \\
 &\quad + \mathcal{F}\{\mathcal{E}_R \mathcal{E}_R^* \mathcal{E}_P\} + \mathcal{F}\{\mathcal{E}_R \mathcal{E}_R \mathcal{E}_P^*\})(x', y') \\
 &= \text{const. } \delta(x' + x_0, y' + y_0) - \text{const. } [(E_P \otimes E_P)(x' + x_0, y' + y_0) \\
 &\quad + E_P(-x', -y') + E_P^*(x' + 2x_0, y' + 2y_0)]
 \end{aligned} \tag{2.168}$$

according to the rules for manipulating Fourier transforms. The \otimes denotes correlation and the sign change in the arguments is due to the fact that the lens performs a direct Fourier transform instead of an inverse one. The first term of this reconstructed wave field represents a focus that is the pointwise dc-term. The second term constitutes a halo around this focus. The third term is proportional to the original object wave field but inverted, while the forth term is a conjugate of the original wave shifted by $(-2x_0, -2y_0)$. Both images are real and sharp and can be registered by film or TV camera in the back focal plane. The conjugated image in the registered intensity distribution is identified only by its geometric inversion. The main advantage of such a Fourier hologram is the stationary reconstructed image even when the hologram is translated in its own plane, due to the shift invariance of the Fourier transform intensity (see Appendix A.4). Furthermore the resolution requirements on the recording medium are less.

Collimation by the lens in Fourier transform holography means that the object points and the reference source are at infinity. *Lensless Fourier transform holography* is possible if object point and reference source are at a finite but the same distance from the holographic plate. For proving this statement, let the wave leaving the object be $E_P(x, y)$, Fig. 2.27.

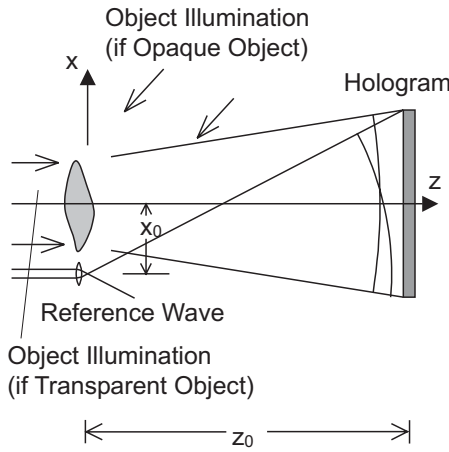


Figure 2.27: Recording of a lensless Fourier transform hologram.

The Fresnel-Kirchhoff integral (2.73) implies that the complex amplitude in the hologram plane is

$$\begin{aligned}\mathcal{E}_P(\xi, \eta) &= \frac{e^{ikz}}{i\lambda z} e^{i\pi z\lambda(\xi^2 + \eta^2)} \\ &\times \int_{-\infty}^{\infty} \int_{-\infty}^{\infty} E_P(x, y) e^{\frac{i\pi}{z\lambda}(x^2 + y^2)} e^{-2i\pi(\xi x + \eta y)} dx dy \\ &= \text{const. } e^{i\pi z\lambda(\xi^2 + \eta^2)} \mathcal{F}\{E_P(x, y) e^{\frac{i\pi}{z\lambda}(x^2 + y^2)}\}(\xi, \eta) \\ &= \text{const. } e^{i\pi z\lambda(\xi^2 + \eta^2)} \mathcal{E}'_P(\xi, \eta)\end{aligned}\quad (2.169)$$

with $\mathcal{E}'_P = \mathcal{F}\{E_P(x, y) e^{\frac{i\pi}{z\lambda}(x^2 + y^2)}\}$. The same formalism holds for the reference wave $E_R(x, y) = \delta(x - x_0, y - y_0)$

$$\begin{aligned}\mathcal{E}_R(\xi, \eta) &= \frac{e^{ikz}}{i\lambda z} e^{i\pi z\lambda(\xi^2 + \eta^2)} \\ &\times \int_{-\infty}^{\infty} \int_{-\infty}^{\infty} \delta(x - x_0, y - y_0) e^{\frac{i\pi}{z\lambda}(x^2 + y^2)} e^{-2i\pi(\xi x + \eta y)} dx dy \\ &= \text{const. } e^{i\pi z\lambda(\xi^2 + \eta^2)} \mathcal{E}'_R(\xi, \eta)\end{aligned}\quad (2.170)$$

with $\mathcal{E}'_R = e^{\frac{i\pi}{z\lambda}(x^2 + y^2)} e^{-2i\pi(\xi x + \eta y)}$. The resulting hologram transmission is

$$\begin{aligned}T &= \alpha - \beta t_B (|\mathcal{E}_R|^2 + |\mathcal{E}_P|^2 + \mathcal{E}_R^* \mathcal{E}_P + \mathcal{E}_R \mathcal{E}_P^*) \\ &= \alpha - \beta t_B (|\mathcal{E}'_R|^2 + |\mathcal{E}'_P|^2 + \mathcal{E}'_R^* \mathcal{E}'_P + \mathcal{E}'_R \mathcal{E}'_P^*)\end{aligned}\quad (2.171)$$

which has the same form as (2.166). The crucial fact is that the z in (2.169) and in (2.170) is the same, so the factors $e^{i\pi z\lambda(\xi^2 + \eta^2)}$ and its conjugate in each term multiply to unity. The effect of the spherical phase factor associated with the near-field Fresnel diffraction pattern here is eliminated by the spherical reference wave with the same curvature.

If the object is focused into the plane of the hologram, Fig. 2.28, we speak of an *image hologram*. Here the real image of the object is recorded instead of the wave field reflected or scattered by the object. The advantage of image holograms is that they can be reconstructed by an incoherent light source of appreciable size and spectral bandwidth and they still produce acceptably sharp images. Also the image luminance is increased. But we have to pay with an observation angle limited by the angular aperture of the used lens [172].

For the above mentioned image hologram the distance between object and hologram appears to be zero. The most general case is the holographic plate in the *near-field* or *Fresnel diffraction region*, Fig. 2.29, then we speak of a *Fresnel hologram*. Fresnel holograms are the most generated in holographic interferometry.

As the distance between object and hologram increases we reach the *far-field* or *Fraunhofer diffraction region* and get a so-called *Fraunhofer hologram*. In this case either the object

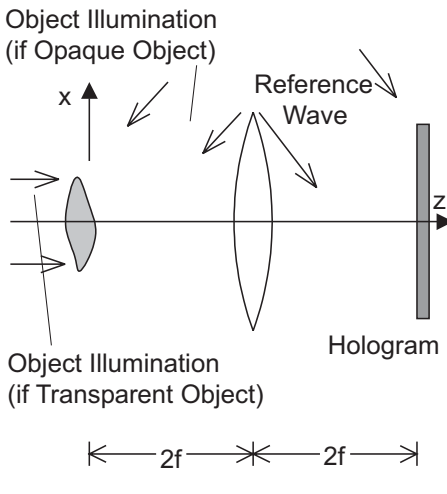


Figure 2.28: Recording of an image hologram.

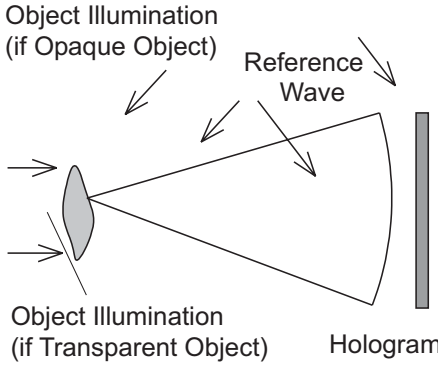


Figure 2.29: Recording of a Fresnel hologram.

has to be small compared to the dimensions of the holographic arrangement

$$z_0 \gg \frac{x_0^2 + y_0^2}{\lambda} \quad (2.172)$$

where x_0 and y_0 are the maximal lateral dimensions of the object, or the object must be in the focus of a lens, Fig. 2.30.

Of course holographers have attempted early to get rid of the coherence requirements, at least in the reconstruction stage. If a usual hologram is illuminated with white light, all the frequencies of the white light are diffracted in different directions. At each point different frequencies stemming from different points in the hologram are superimposed, so normally we will not recognize a reconstruction of an object wave field. The quality may be improved slightly by a color filter, but then the brightness decreases drastically.

The so-called *white light holograms*, which can be reconstructed with white light, use the finite thickness of the photographic emulsion in the hologram [179]. Up to now we have only considered the lateral distribution of the phase or transmittance of the hologram. If the thickness of the sensitive layer is much greater than the distance between adjacent surfaces

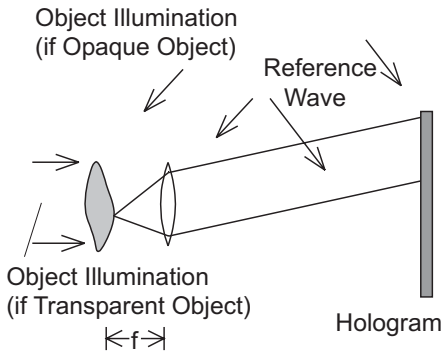


Figure 2.30: Recording of a Fraunhofer hologram.

of the interference maxima, then the hologram should be considered as a *volume* or *three-dimensional hologram*. Generally we may speak of a volume hologram, if the thickness d_H of the layer is

$$d_H > \frac{1.6d^2}{\lambda} \quad (2.173)$$

where d is the distance between adjacent interference planes [180].

If now the coherent object and reference waves impinge onto the hologram from opposite sides we get interference layers nearly parallel to the hologram surface. The distance between subsequent interference layers is $\lambda/(2 \sin \frac{\theta}{2})$ according to (2.30) and Fig. 2.3. For reconstruction this thick hologram is illuminated with white light which is reflected at the layers. Dependent on the wavelength the reflected waves interfere constructively in defined directions, an effect called *Bragg reflection*. Let the distance of the interference layers be d and illuminate by an angle α , then we find the n -th diffraction order for the wavelength λ in the observation direction of angle β

$$d = \frac{n\lambda}{\sin \alpha + \sin \beta}. \quad (2.174)$$

The most intense wave is that in the first diffraction order $n = 1$. So if we look under the angle β onto the hologram illuminated under the angle α , we see a clear image with color corresponding to λ . The parallel layers modulated by the information about the image react like an interference filter for the specific wavelength λ .

An arrangement for recording such a white light hologram is given in Fig. 2.31. The expanded and collimated laser beam is directed through the hologram plate onto the object. The reference wave is given by the light coming directly from the laser, the wave passing through the plate and reflected by the object is the object wave. For good results we need strongly reflecting objects and a hologram plate close to the object.

Another way to prevent the different diffracted colors from overlaying during the reconstruction with white light is the exchange of the variation of the vertical parallax against a variation of the wavelength [159]. For this task first a master hologram of the object is produced as usual, Fig. 2.32a.

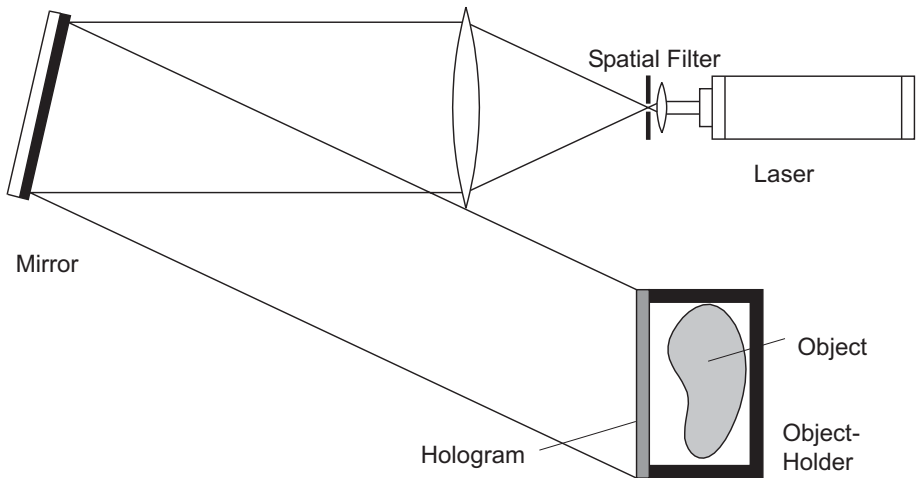


Figure 2.31: Recording of a white light hologram.

By reversing the direction of the reference beam or by turning the hologram by 180° a real pseudoscopic image is reconstructed. In front of the hologram a horizontal slit aperture is now placed and a hologram of the wave field passing through this slit is recorded, Fig. 2.32b. This has the first effect that the vertical parallax is lost, but this is not recognized immediately, as long as the eyes of the observer are horizontally arranged. The second effect is that the different colors reconstructed from the second hologram still overlap in space. But the colors converge to different reconstructed slits. Although neighboring colors are overlayed in the reconstructed slits, the range from blue to red can be stretched over a broad area so that each reconstructed slit produces a sharp image. The eyes of the observer are placed in one reconstructed slit and see the object in one color. If the head is moved in the vertical direction the object is seen in another spectral color than before, Fig. 2.32c. Since in this way the object can be observed in the successive colors of the rainbow, the secondary hologram is called a *rainbow hologram* and we speak of *rainbow holography*.

2.7 Elements of the Holographic Setup

2.7.1 Laser

Optical holography and holographic interferometry in the visible range of the spectrum became possible with the invention of a source radiating coherent light, the *laser*. The basic principle behind the laser is the *stimulated emission* of radiation. Contrary to the ubiquitous *spontaneous emission* here the emission of photons is triggered by an electromagnetic wave. All photons generated this way have the same frequency, polarization, phase, and direction as the stimulating wave.

Normally in a collection of atoms each one tends to hold the lowest energy configuration. Therefore in thermal equilibrium or even when excited the majority of all atoms are in the

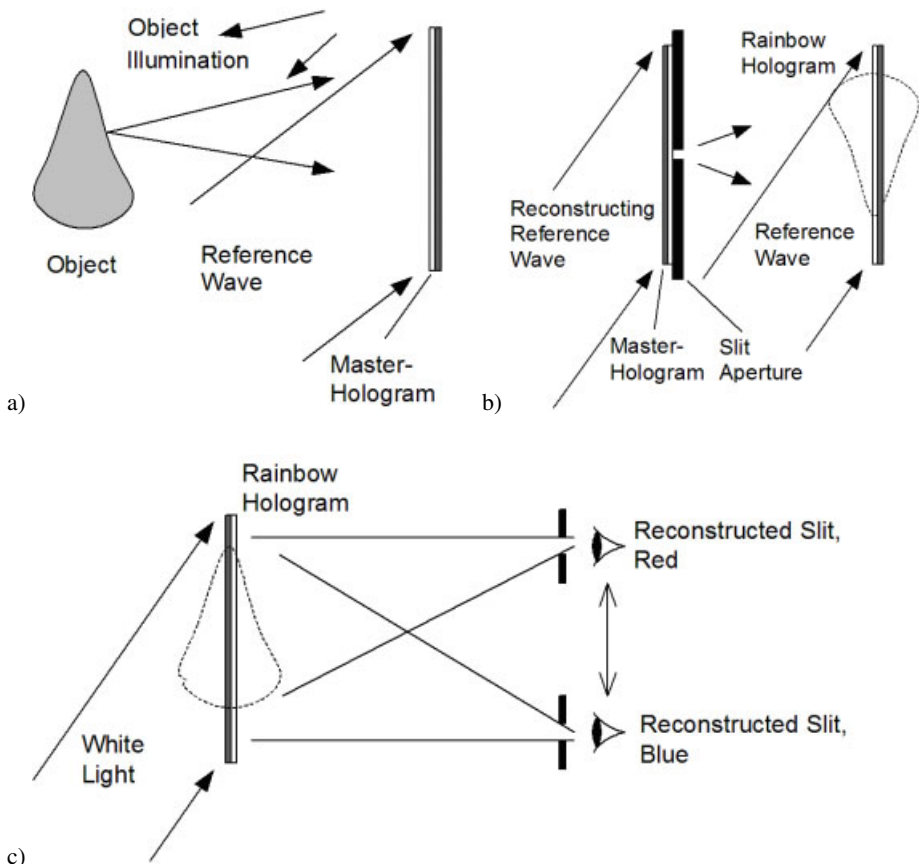


Figure 2.32: Rainbow holography: (a) recording of a master hologram, (b) recording of the rainbow hologram, (c) reconstruction with white light.

ground state. Only if one succeeds in bringing a larger part of the atoms into a higher excited state than remain in a lower state, which may be the ground state or itself an excited state, then an impinging wave can stimulate the emission of an avalanche of waves, all with equal phase and propagating in the same direction. This stimulated emission takes place as long as the *population inversion* between the lower and the higher energy states is maintained. To achieve the inversion, energy must be provided to the system by a process called *pumping*. So the laser can be regarded as an amplifier since an impinging wave generates a manifold of waves of the same direction, frequency, and phase.

To prevent this amplifier from amplifying only noise, a feedback is introduced by installing two mirrors on opposite sides of the active medium. If plane mirrors are adjusted exactly parallel, photons are reflected back and forth, and what we get is an oscillator of high quality. Standing waves will be formed between the two mirrors. If one of the mirrors is semi-transparent, some of the photons can leave the laser as the so called *laser beam* of coherent

radiation. The resonant frequencies possible in a *cavity* of length L , the separation between the mirrors, are

$$\nu_n = \frac{nc}{2L} \quad (2.175)$$

with n an integer and c the speed of light.

Since the active medium possesses a gain curve around a central line, amplification takes place only at those frequencies where the gain is higher than the cavity losses, Fig. 2.33a.

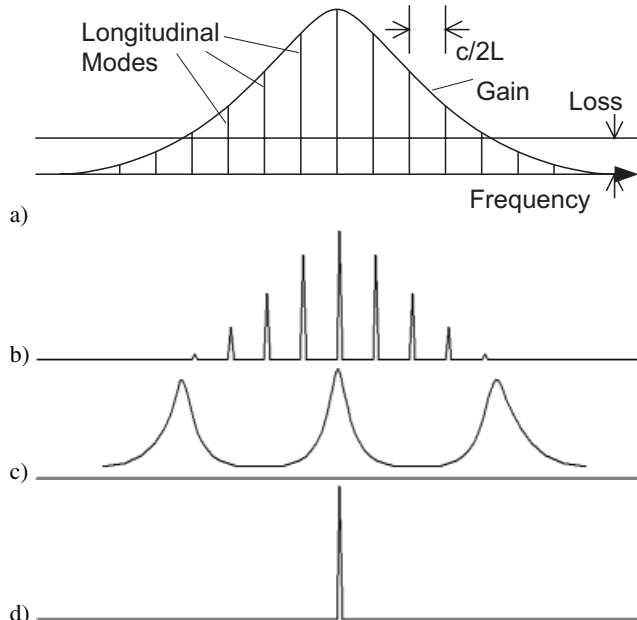


Figure 2.33: Single frequency selection: (a) oscillation frequencies, gain, and loss, (b) multi-frequency output, (c) etalon transmittance, (d) single frequency output.

If the medium allows for several central lines in the spectrum, these are selected by a *wavelength selector prism*, Fig. 2.34.

The existence of several frequencies ν_n under the gain curve – one speaks of the *longitudinal modes* – results in a coherence length too short for most holographic applications. On the other hand short cavities would produce the desired single longitudinal mode under the gain curve, but with extremely low power. The solution to this contradiction is an intracavity *etalon*, Fig. 2.34, which is basically a *Fabry-Perot interferometer*. Only those modes are allowed to oscillate that match into the long laser cavity as well as the short cavity of the etalon. The result is a single frequency radiation of high coherence length, Figs. 2.33c and d.

Although principally a laser may emit in various *transverse modes*, which describe the intensity variation across the diameter of the laser beam, in holography only the TEM_{00} mode, rendering the best spatial coherence, has to be used. This mode is achieved by inserting an aperture of small diameter into the resonator, the pinhole in Fig. 2.35. In the TEM_{00} -mode

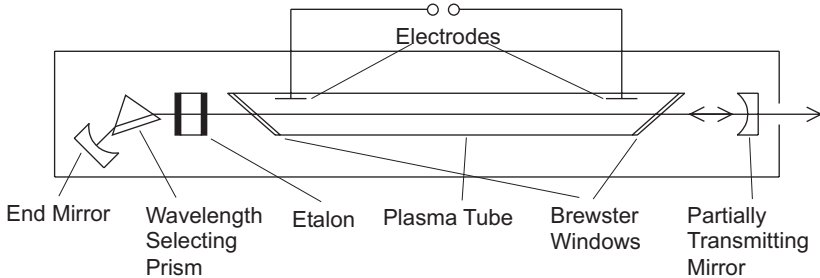


Figure 2.34: Typical gas laser.

the intensity is Gaussian distributed, which constitutes the Gaussian background illumination of most holographic interferograms.

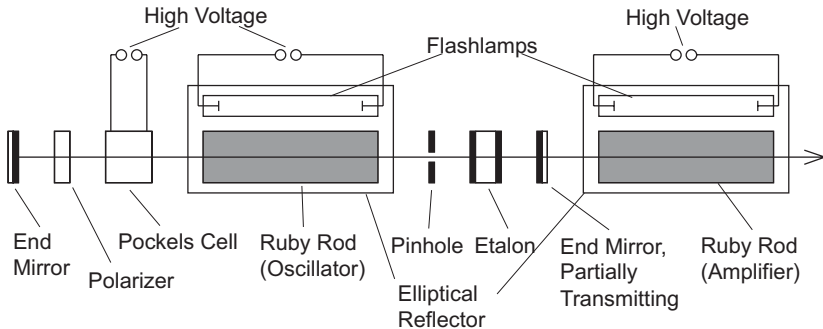


Figure 2.35: Q-switched ruby laser.

There is a vast number of materials showing laser activity, pumped in various ways. But only some of them have gained importance for holographic applications, Table 2.1.

The *ruby laser*, Fig. 2.35, is the most widely used *pulsed laser* in optical holography [181], mainly because of its output energy of up to about 10 J per pulse. Pumping is performed with xenon flashlamps. To achieve a single pulse of short duration an intracavity *Q-switch* is employed. This is a fast-acting optical shutter, normally realized by a *Pockels cell*. The Pockels cell is a crystal showing birefringence when an electric field is applied. If its principal axes are oriented at 45° to the direction of polarization of the laser beam, it produces a mutual phase shift of 90° between the two polarization components when the voltage is applied. A wave transmitted by the activated Pockels cell after reflection at the end mirror is polarized 90° to its original direction and thus blocked by a polarizer. As soon as the flashlamp is fired, the Q-switch is closed. A large population inversion is built up. At the end of the flashlamp pulse, the voltage is switched off, Pockels cell and polarizer transmit freely, and the oscillation can take place. A short pulse, typically of 10 to 20 ns duration, is emitted. The wavelength of the ruby emission is 694 nm, which fits well to the sensitivity of photographic emulsions

Table 2.1: Lasers used in holographic interferometry.

Laser	Wavelength	Pulsed/CW	Typical Power/Energy (single mode)	Excitation
Ruby	694 nm	Pulsed	10 J/pulse	Flash lamp
He-Ne	633 nm	CW	2 mW – 50 mW	Electrical
Ar ⁺	458 nm	CW	200 mW	Electrical
Ar ⁺	488 nm	CW	1000 mW	Electrical
Ar ⁺	514 nm	CW	2000 mW	Electrical
Kr ⁺	647 nm	CW	500 mW	Electrical
He-Cd	325 nm	CW	25 mW	Electrical
He-Cd	442 nm	CW	25 mW	Electrical
Nd ³⁺ :YAG	1060 nm	CW/Pulsed		
	530 nm (Frequency doubled)	CW/Pulsed	400 mW	Diode Laser
Dye	217 nm – 960 nm	CW/Pulsed	100 mW	Optical (Ar ⁺ -Laser)
Laser Diode	670 nm	CW/Pulsed	25 mW	Electrical

used in holography. One or more additional ruby rods normally follow the cavity to boost the output while preserving spatial and temporal coherence, Fig. 2.35.

The most common continuous wave lasers (*CW-lasers*) used for holography for a long time have been the *gas lasers*. For many applications the *helium-neon laser* (He-Ne laser) is the most economical choice. It emits red coherent light of 633 nm, has a long life and needs no water cooling. More power is supplied by the *argon-ion lasers* they are used if large areas have to be illuminated. They can be adjusted to operate in one of several lines, mainly in the blue and green. But now they are replaced by the *neodymium:YAG lasers* which when frequency doubled also give green coherent light, but are compactly build and only need air-cooling, while the argon laser is water-cooled [182, 183]. Frequency doubled Nd:YAG-lasers can be used in pulsed operation. The holograms are reconstructed with the same laser, ensuring identical wavelengths during recording and reconstruction [184]. The *krypton laser* is similar to the argon laser, but emits in the red. The *helium-cadmium laser* has a short wavelength matching the sensitivity of photoresists. *Laser diodes* with good coherence and radiation in the visible are on the market now, and their use in holography is constantly increasing. An interesting feature of the laser diodes is their tunability, in which the wavelength of a single-mode laser can be changed continuously by variation of the injection current and/or the temperature of the active region [185, 186]. The *dye lasers*, although relatively cumbersome to handle, offer the possibility of continuous variation of the wavelength over typically about 50 nm for a single dye. By changing the dyes more than the whole visible spectrum can be covered. Recently also the use of CO₂-lasers emitting at 10.6 μm wavelength in digital holography has been reported. The recording sensor in this case is of a pyroelectric type [92].

2.7.2 Recording Media

Recording materials suitable for holographic interferometry should exhibit a number of properties, like a spectral sensitivity well matched to available laser wavelengths, a linear transfer characteristic, high resolution, and low noise. They should be easy to handle, reusable or at least recyclable, and inexpensive. No material has been found so far that meets all these requirements, so for a special application one has to find the optimal choice. A selection of recording materials is given in Table 2.2 [172].

Table 2.2: Recording materials used in holographic interferometry.

Medium	Hologram Type	Processing	Reusable	Required Exposure [J/m ²]	Spectral Sensitivity [nm]	Resolution [mm ⁻¹]
Silver halides	Ampl./Phase	Wet chemical	No	5×10^{-3} -5×10^{-1}	400–700	1000–10000
Dichr. gelatin	Phase	Wet chemical	No	10^2	350–580	> 10000
Photoresists	Phase	Wet chemical	No	10^2	UV–500	~ 3000
Photopolymers	Phase	Post exposure	No	$10 - 10^4$	UV–650	200–1500
Photochromics	Ampli.	None	Yes	$10^2 - 10^3$	300–700	> 5000
Photothermoplastics	Phase	Charge	Yes	10^{-1}	400–650	500–1200 (bandpass)
LiNbO ₃	Phase	None	Yes	10^4	350–500	> 1500
Bi ₁₂ SiO ₂₀	Phase	None	Yes	$10^1 - 10^2$	350–550	> 10000
CCD	Ampli.	None	Yes	10^{-4} -10^{-3}	400–1000	~ 75

The most widely used recording materials still are the *silver halide photographic emulsions*. These emulsions are commercially available on glass plates or film. They show a high sensitivity as well as a high spatial resolution. The main disadvantages are the wet chemical processing and the single use. Normally an *amplitude hologram* is recorded but by bleaching also a *phase hologram* can be obtained.

Dichromated gelatin for holographic recording is used as a gelatin layer containing a small amount of a dichromate. By a photochemical reaction this medium becomes harder on exposure to light. If the unhardened unexposed gelatin is washed out with warm water, a relief image is formed. If the gelatine film is processed properly, a refractive index modulation is obtained [172].

Photoresists are light-sensitive organic films which yield a relief image after exposure and development. Although they are relatively slow and show nonlinear effects at diffraction efficiencies greater than about 0.05, they have found some use where the possibility of easy replication and the absence of any grain structure are important.

The *photopolymers* are organic materials which can be activated through a photosensitizer to exhibit thickness and refractive index changes due to photopolymerization or cross-linking.

Thick layers can be produced to yield volume phase holograms with high diffraction efficiency and high angular selectivity, which can be viewed immediately after exposure [172].

Photochromics undergo reversible changes in color when exposed to light. While being grain free and offering high resolution, photochromics have limited use due to their low diffraction efficiency and low sensitivity. Dichromated gelatin, photoresists, photopolymers, and photochromics are not available ready to use, but must be prepared by the user before application.

Photothermoplastics before the introduction of CCDs and digital holography have been used widely in holographic interferometry [187], as a reusable recording medium not demanding a wet-chemical processing. The recording unit is a transparent stack of four layers: the glass substrate, a transparent conducting layer acting as a heating element, a photoconductor and the photothermoplastic film itself. A typical cycle of operation consists of five steps [172], Fig. 2.36:

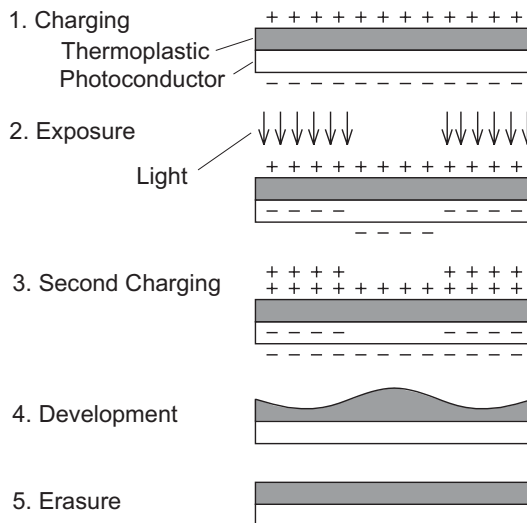


Figure 2.36: Hologram recording on photothermoplastic film.

- **Charging:** A uniform electrical charge is applied in darkness. Positive ions are sprayed onto the top surface, a uniform negative charge is induced in the photoconductor.
- **Exposure:** Charge carriers are produced in the photoconductor where light impinges. The carriers migrate to the oppositely charged surfaces and neutralize part of the charge from the first charging. This reduces the surface potential but does not change the surface charge density and the electric field.
- **Second charging:** By a second charging to a constant potential additional charges are deposited where the exposure caused a migration of charge. The electric field increases in these regions, producing a spatially varying field and hence a latent image.
- **Development:** The thermoplast is heated nearly to its melting point. In regions of high electric field strength the layer gets thinner, these are the illuminated areas. The layer

gets thicker in the unexposed areas. Cooling to room temperature freezes the thickness variation with the result of a phase hologram.

- Erasure: Heating to even higher temperatures than those used for development now smoothes out the thickness variations by surface tension. The hologram is erased, the thermoplastic is ready for a new recording cycle.

In *photorefractive crystals* the dark and the bright zones of the microinterferogram, the hologram, give rise to a charge migration because of the photoconductive effect. The charges are trapped in crystal defects in the dark zones, so that a local charge field is created by which the refractive index is spatially modulated. Thus a phase hologram is generated by the linear electro-optic effect, a dynamic and reversible process [188].

Photorefractive crystals are categorized into two main families. On the one hand there are the ferroelectrics like LiNbO_3 , BaTiO_3 , etc. which in visible light have poor sensitivities but show high diffraction efficiency. Since one records thick phase holograms in the photorefractive crystals, 100% diffraction efficiency can be reached. The second main family consists of the sillenites with its most prominent candidate bismuth silicon oxide $\text{Bi}_{12}\text{SiO}_{20}$ (*BSO*) [189–191]. The sillenites are characterized by better sensitivities but relatively poor diffraction efficiencies [188].

Diffraction efficiency is the ratio between the intensities of the diffracted beam and the readout beam entering the crystal. The sillenites typically have diffraction efficiencies of 10^{-4} to 10^{-3} with the higher values obtained when an external electric field is applied to the crystal. There are ways to enhance the diffraction efficiency, see [188]. The *energy density* is the amount of luminous energy per unit surface necessary to reach the saturation of holographic recording. For BSO crystals without electric field it is in the range of 10 mJ/cm^2 .

The big advantages of photorefractive crystals are their unlimited reusability, their in-situ operation, their high resolution allowing large angles between object and reference beams and their fast response. They respond at least at the nanosecond scale. This makes them applicable with continuous as well as with pulsed lasers. So not only static deformations but also vibrations and transient phenomena can be recorded and analyzed well.

Pyroelectric cameras are to be used when the applied laser light is in the infrared range of the spectrum. Allaria et al. [92] report on the employment of such a camera with light of $10.6 \mu\text{m}$ wavelength. It has an array of only 124×124 elements of LiTaO_3 with a pixel size of $85 \mu\text{m} \times 85 \mu\text{m}$ and $15 \mu\text{m}$ gaps between pixel areas.

Bacteriorhodopsin film is a real-time recording medium that requires no extra processing. Its resolution is about 5000 line-pairs/mm that even exceeds high-resolution holographic film. The object-light recording sensitivity is $50 \mu\text{J}/\text{cm}^2$ which is in the range of holographic emulsions. Bacteriorhodopsin holograms can be produced in large formats, say $100 \text{ mm} \times 100 \text{ mm}$. They can be recycled indefinitely without degradation. Usually they are recorded at green wavelength and erased with blue light between 0.40 and $0.45 \mu\text{m}$, which now does not need to be coherent. At room temperature bacteriorhodopsin films may thermally decay with a half-life of about 100 s, but at 0°C ambient temperature it can be stable for hours. When reconstructed at $0.532 \mu\text{m}$ it works as an absorption hologram with a diffraction efficiency of about 1%. A stronger diffraction is at higher wavelengths, e. g. $0.632 \mu\text{m}$, when it operates as a phase grating. As a special feature bacteriorhodopsin can record and reconstruct the

relative polarization of the object wavefront. Barnhart et al. report on its employment in digital holographic velocimetry [192].

TV camera-tubes and CCD-targets generally do not have the resolution required by off-axis holography. This on the one hand led to the development of the *ESPI methods*, Section 7.2, and on the other hand to *digital holography*, Chapter 3. Digital holography utilizes all the advantages the CCD-targets are offering: Fast acquisition of the primary holograms, rapid digital storage, numerical evaluation instead of optical reconstruction, thus not suffering from optical imperfections or limited diffraction efficiency. Because of their importance for digital holography CCD and CMOS image sensors are treated in more detail in Section 2.8.

2.7.3 Optical Components

Here we have not the room to treat the fundamentals of all optical components used in holographic interferometry; these can be found in every optics textbook [159, 193, 194]. Only some hints and practical considerations are given. To produce good quality holograms, the mechanical and optical components always have to be fixed in a way to prevent spurious motions or vibrations. Sources of vibrations like transformers, ventilators, cooling with streaming water, etc. should be kept away from the holographic arrangement. A mechanical shutter should not be mounted on the same vibration-isolated table as the other components. If motions cannot be avoided, a pulsed laser or one of the methods described in Section 6.1.4 have to be applied.

The quality of the expanded laser beam illuminating the object can be significantly improved by positioning a *pinhole* in the focal point of the magnifying lens. Dust and scratches on optical surfaces produce spatial noise. The pinhole acts as a *spatial filter* that allows to pass only the dc-term of the spectrum. Thus a clean illumination of nearly Gaussian characteristic will result. Magnifying the beam by a positive lens and spatial filtering is not possible when using a pulsed ruby laser. Here the power concentration in the focus would be high enough to ionize the air, the resulting plasma is opaque to light. Therefore with pulsed ruby lasers only negative lenses should be used. Employing adequate optics, objects of varying size and form can be investigated. Even the interior walls of pipes have been holographically analyzed by utilizing panoramic annular lenses [195].

Polarization plays a minor role in holographic interferometry. Of course one has to guarantee that object and reference wave are polarized at identical angles to obtain good contrast holographic fringes. Holographic setups most often have optical axes only in one horizontal plane, vertical deflections are rather rare. It is recommended to use the lasers in such an orientation that the normals to the Brewster windows of the laser are in a vertical plane. This prevents any reflecting mirror from being accidentally positioned at the Brewster angle, thus cutting off the reflection [196].

Optical fibers are a means to conduct the laser light along paths differing from the straight propagation [197, 198]. Thus the laser, the splitting of the primary beam into object and reference beam, as well as parts of the paths of these beams can be decoupled from the rest of the holographic arrangement. Areas which are unaccessible by straight rays become accessible to holographic interferometry if optical fibers are used. Furthermore an optical fiber can be used as a sensor for pressure or temperature, since any expansion of the fiber due to the pressure or temperature variations influences the measurable optical path length.

Generally it can be stated that the influence of optical fibers on the temporal coherence can be neglected. But the spatial coherence is affected significantly if *multimode fibers* are used. Many modes can propagate in the fiber which may interfere and produce speckles. This may be tolerated for object illumination, since the diffusely scattering object also will degrade the spatial coherence. But a good spatial coherence in the reference wave during recording as well as for reconstruction is crucial. *Monomode fibers* with a core diameter less than 50 µm should be employed [199]. Also results are reported on the use of coherent multimode fiber bundles to transmit the image of the test object from the test site to the holographic plate [200].

Optical fibers are already used in holographic interferometry in combination with CW lasers. The use of Q-switched lasers with fibers is under investigation [201]. The problems are that the high energies can destroy the faces of the fiber and may stimulate Brillouin scattering in the fiber volume.

2.7.4 Beam Modulating Components

A number of holographic interferometric methods require the modulation of the laser beam, like the *phase sampling* methods which employ a *phase shifting* device or the *heterodyne methods* which make use of a *frequency shift*. The fast shutter realized by a Pockels cell was already introduced in the context of Q-switched lasers.

A *phase shift* in a beam can be introduced by rotating a half-wave plate, moving a grating or employing an acoustooptical modulator, tilting a glass plate, [94] shifting a mirror [202], or stretching an optical fiber, Fig. 2.37.

The effect of a $\lambda/2$ -plate on circularly polarized light, Fig. 2.37a, is best described in the formalism of *Jones matrices*: Let a left-hand circularly polarized wave E_{circ} be

$$E_{\text{circ}} = \begin{pmatrix} 1/\sqrt{2} \\ i/\sqrt{2} \end{pmatrix} = \frac{1}{\sqrt{2}} \begin{pmatrix} e^{i0} \\ e^{i\frac{\pi}{2}} \end{pmatrix}. \quad (2.176)$$

Ordinary and extraordinary rays are mutually shifted by $\pi/2$. The $\lambda/2$ -plate oriented with the ordinary ray in the x -direction and the extraordinary ray in the y -direction is described by the matrix

$$M_{\lambda/2} = \begin{pmatrix} 1 & 0 \\ 0 & -1 \end{pmatrix} = \begin{pmatrix} e^{i0} & 0 \\ 0 & e^{i\pi} \end{pmatrix}. \quad (2.177)$$

Wave E_{circ} after passing the $\lambda/2$ -plate is

$$M_{\lambda/2} E_{\text{circ}} = \begin{pmatrix} e^{i0} & 0 \\ 0 & e^{i\pi} \end{pmatrix} \frac{1}{\sqrt{2}} \begin{pmatrix} e^{i0} \\ e^{i\frac{\pi}{2}} \end{pmatrix} = \frac{1}{\sqrt{2}} \begin{pmatrix} e^{i0} \\ e^{i\frac{3\pi}{2}} \end{pmatrix}. \quad (2.178)$$

The $\lambda/2$ -plate after undergoing a rotation R_{45} of 45° has the matrix

$$\begin{aligned} R_{45}^{-1} M_{\lambda/2} R_{45} &= \frac{1}{\sqrt{2}} \begin{pmatrix} 1 & -1 \\ 1 & 1 \end{pmatrix} \begin{pmatrix} e^{i0} & 0 \\ 0 & e^{i\pi} \end{pmatrix} \frac{1}{\sqrt{2}} \begin{pmatrix} 1 & 1 \\ -1 & 1 \end{pmatrix} \\ &= \begin{pmatrix} 0 & 1 \\ 1 & 0 \end{pmatrix}. \end{aligned} \quad (2.179)$$

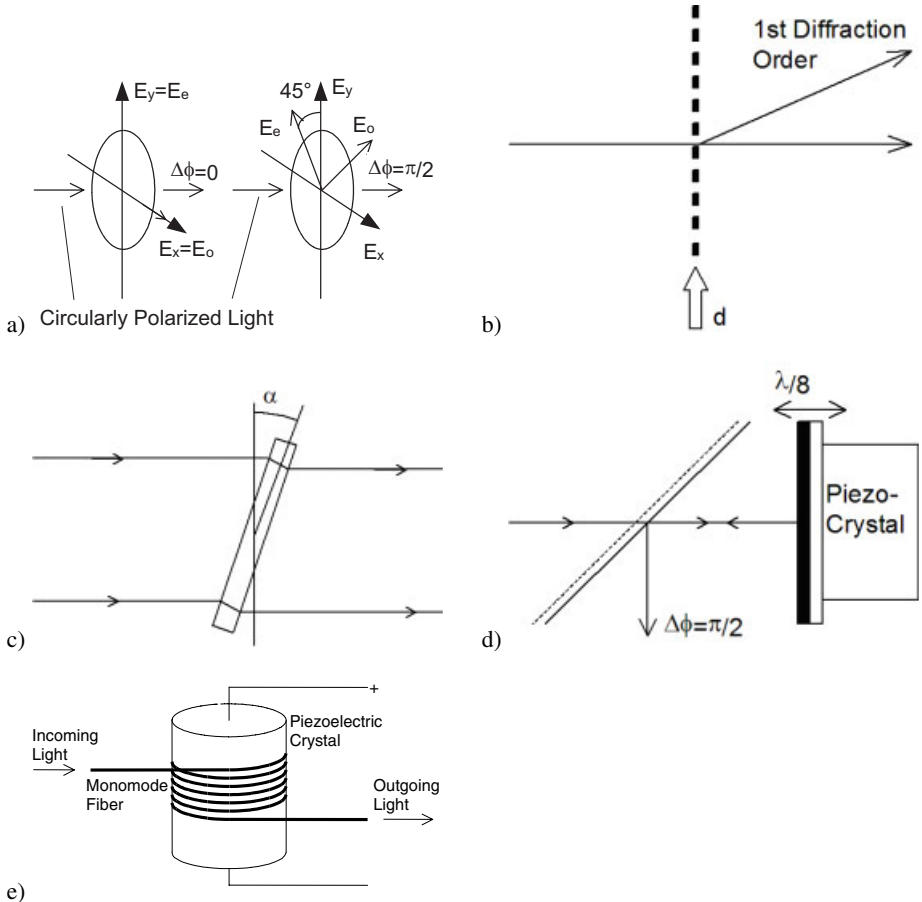


Figure 2.37: Phase shifting by (a) rotating half-wave plate, (b) shifted diffraction grating, (c) tilted glass plate, (d) translated mirror, (e) elongation of fiber.

The wave E_{circ} after passing the rotated half-wave plate is

$$\begin{aligned}
 R_{45}^{-1} M_{\lambda/2} R_{45} E_{\text{circ}} &= \begin{pmatrix} 0 & 1 \\ 1 & 0 \end{pmatrix} \frac{1}{\sqrt{2}} \begin{pmatrix} e^{i0} \\ e^{i\frac{\pi}{2}} \end{pmatrix} = \frac{1}{\sqrt{2}} \begin{pmatrix} e^{i\frac{\pi}{2}} \\ e^{i0} \end{pmatrix} \\
 &= \frac{1}{\sqrt{2}} \begin{pmatrix} e^{i(0 + \frac{\pi}{2})} \\ e^{i(\frac{3\pi}{2} + \frac{\pi}{2})} \end{pmatrix}
 \end{aligned} \tag{2.180}$$

which is the wave after going through the unrotated plate (2.178) but now shifted by $\pi/2$ [203].

In an analogous way e. g. three consecutive phase shifts by $\pi/2$ can be obtained. This is frequently used in phase shifting holographic interferometry, see Section 5.5, or phase shifting digital holography, see Section 3.4.1. The $\lambda/2$ -plate is accompanied by a $\lambda/4$ -plate as shown in Fig. 2.38.

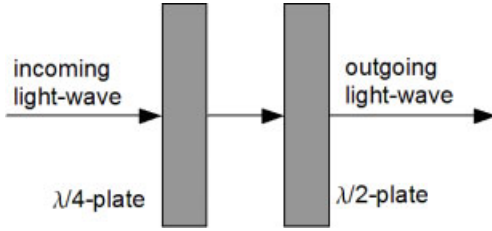


Figure 2.38: Phase shifting using quarter and half wave plate.

The $\lambda/4$ -plate is described by the matrix

$$M_{\lambda/4} = \begin{pmatrix} 1 & 0 \\ 0 & -i \end{pmatrix} = \begin{pmatrix} e^{i0} & 0 \\ 0 & e^{i\frac{\pi}{2}} \end{pmatrix}. \quad (2.181)$$

Take as the incoming wave a linearly polarized wave with polarization direction oriented 45° with respect to the x -axis of a coordinate system in which the ordinary axes of the $\lambda/4$ - and the $\lambda/2$ -plates coincide with the x -axis. This wave of unit amplitude is

$$E_{\text{lin}} = \frac{1}{\sqrt{2}} \begin{pmatrix} e^{i0} \\ e^{i0} \end{pmatrix}. \quad (2.182)$$

After passing through the two plates it is

$$M_{\lambda/2} M_{\lambda/4} E_{\text{lin}} = \begin{pmatrix} 1 & 0 \\ 0 & -1 \end{pmatrix} \begin{pmatrix} 1 & 0 \\ 0 & -i \end{pmatrix} \frac{1}{\sqrt{2}} \begin{pmatrix} e^{i0} \\ e^{i0} \end{pmatrix} = \frac{1}{\sqrt{2}} \begin{pmatrix} e^{i0} \\ e^{i\frac{\pi}{2}} \end{pmatrix} \quad (2.183)$$

which is a left hand circularly polarized wave. Now we rotate the plate by $+45^\circ$ and -45° using the rotation matrices

$$R_{45} = R_{-45}^{-1} = \begin{pmatrix} \frac{1}{\sqrt{2}} & -\frac{1}{\sqrt{2}} \\ \frac{1}{\sqrt{2}} & \frac{1}{\sqrt{2}} \end{pmatrix} \quad \text{and} \quad R_{45}^{-1} = R_{-45} = \begin{pmatrix} \frac{1}{\sqrt{2}} & \frac{1}{\sqrt{2}} \\ -\frac{1}{\sqrt{2}} & \frac{1}{\sqrt{2}} \end{pmatrix}. \quad (2.184)$$

First we rotate both plates by -45°

$$R_{-45}^{-1} M_{\lambda/2} R_{-45} R_{45}^{-1} M_{\lambda/4} R_{-45} E_{\text{lin}} = \frac{1}{\sqrt{2}} \begin{pmatrix} e^{i0} \\ e^{i0} \end{pmatrix}. \quad (2.185)$$

Next both plates are rotated by $+45^\circ$ with respect to the original orientation

$$R_{45}^{-1} M_{\lambda/2} R_{45} R_{45}^{-1} M_{\lambda/4} R_{45} E_{\text{lin}} = \frac{1}{\sqrt{2}} \begin{pmatrix} e^{i\frac{\pi}{2}} \\ e^{i\frac{\pi}{2}} \end{pmatrix}. \quad (2.186)$$

Now we rotate the half wave plate by $+45^\circ$ and the quarter wave plate by -45°

$$\begin{aligned} R_{45}^{-1} M_{\lambda/2} R_{45} R_{-45}^{-1} M_{\lambda/4} R_{-45} E_{\text{lin}} &= \frac{1}{4\sqrt{2}} \begin{pmatrix} 1 & 1 \\ -1 & 1 \end{pmatrix} \begin{pmatrix} 1 & 0 \\ 0 & -1 \end{pmatrix} \begin{pmatrix} 1 & -1 \\ 1 & 1 \end{pmatrix} \begin{pmatrix} 1 & -1 \\ 1 & 1 \end{pmatrix} \begin{pmatrix} 1 & 0 \\ 0 & -i \end{pmatrix} \begin{pmatrix} 1 & 1 \\ -1 & 1 \end{pmatrix} \begin{pmatrix} 1 \\ 1 \end{pmatrix} \\ &= \frac{1}{2\sqrt{2}} \begin{pmatrix} -1-i & -1+i \\ 1+i & -1-i \end{pmatrix} \begin{pmatrix} 1 \\ 1 \end{pmatrix} = \frac{1}{\sqrt{2}} \begin{pmatrix} e^{i\pi} \\ e^{i\pi} \end{pmatrix}. \end{aligned} \quad (2.187)$$

The last rotation is -45° of the $\lambda/2$ -plate and $+45^\circ$ of the $\lambda/4$ -plate

$$\begin{aligned} R_{-45}^{-1} M_{\lambda/2} R_{-45} R_{45}^{-1} M_{\lambda/4} R_{45} E_{\text{lin}} \\ = \frac{1}{4\sqrt{2}} \begin{pmatrix} 1 & -1 \\ 1 & 1 \end{pmatrix} \begin{pmatrix} 1 & 0 \\ 0 & -1 \end{pmatrix} \begin{pmatrix} 1 & 1 \\ -1 & 1 \end{pmatrix} \begin{pmatrix} 1 & 1 \\ -1 & 1 \end{pmatrix} \begin{pmatrix} 1 & 0 \\ 0 & -i \end{pmatrix} \begin{pmatrix} 1 & -1 \\ 1 & 1 \end{pmatrix} \begin{pmatrix} 1 \\ 1 \end{pmatrix} \quad (2.188) \\ = \frac{1}{2\sqrt{2}} \begin{pmatrix} -1-i & 1-i \\ 1-i & -1-i \end{pmatrix} \begin{pmatrix} 1 \\ 1 \end{pmatrix} = \frac{1}{\sqrt{2}} \begin{pmatrix} e^{i\frac{3\pi}{2}} \\ e^{i\frac{3\pi}{2}} \end{pmatrix}. \end{aligned}$$

We see that (2.185), (2.186), (2.187), and (2.188) generate four waves with consecutive mutual phase shifts of $\pi/2$.

A lateral displacement d of a *diffraction grating* [204, 205] shifts the phase of the n -th diffraction order by $\Delta\phi = 2\pi ndf$, where f is the spatial frequency of the grating, Fig. 2.37b. A moving diffraction grating also is realized in an *acoustooptical modulator* (AOM) that can be employed for phase shifting likewise.

If a plane parallel glass plate is tilted, the path through the plate changes and a phase shift is produced that depends on the thickness of the plate, its refractive index, the wavelength and the tilt angle, Fig. 2.37c. Because the exact phase shift is strongly influenced by the quality of the plate, this approach is not frequently used.

Most often the phase is shifted by a reflecting mirror mounted on a *piezoelectric transducer*, Fig. 2.37d. The piezo-crystal can be controlled electrically with high precision. A mirror shift of $\lambda/8$ corresponds to a pathlength change of $2\pi/8$ and due to the double pass results in a phase shift of $\pi/2$ in the reflected wave. If the light for illumination and/or the reference wave is transmitted through optical fibers, a common way to perform the phase shift is to wrap a portion of the fiber firmly around a piezoelectric cylinder that expands when a voltage is applied [206]. The stretching of the fiber results in a phase shift, Fig. 2.37e.

A *frequency shift* in principle can be produced the same way as the phase shift with the only difference that a continuous motion of the phase shifting component is required instead of a single step. Practically the frequency shift is realized by a diffraction grating moving with continuous velocity. This may be achieved by a rotating *radial grating*, or an AOM. An AOM or *Bragg cell* is a quartz material through which an ultrasonic wave propagates. Because this is a longitudinal or compression wave, the index of refraction of the material varies sinusoidally with the same wavelength. Incident light that is diffracted or deflected into the Bragg angle gets a Doppler shift that is equal to the sound frequency. Wavelength shifts also can be induced by applying a ramp current to a laser diode [207].

2.8 CCD- and CMOS-Arrays

Digital holography in the context treated here is based on the digital recording of holograms using CCD-arrays instead of holographic film, photorefractive crystals, photothermoplast, or others. In recent decades the development of CCDs has reached maturity, the arrays needed for our specific purposes now can be ordered off the shelf. CCD-cameras have more and more replaced conventional tube cameras in the vast majority of applications, ranging from entertainment to science and engineering.

In this chapter the fundamental operational principle of CCDs is introduced and the main performance parameters of CCD-arrays are defined. This should help to find the optimally suited CCD for the special application of digital holography. The concept of modulation transfer functions (MTF) is introduced to explain spatial sampling with CCD-arrays. Also CMOS technology and consumer cams, the color still cams, which meanwhile reached a technological standard enabling their use in digital holography, are described.

2.8.1 CCD Concept

The essential idea behind the *charge coupled devices* (CCDs) is the way the image is read off the array. Contrary to their forerunners like the microchannel plate (MCP), where individual narrow electron multiplier tubes are fused together into an imaging array, or the SIDAC using an electron beam to read the image off a photodiode array, CCDs actually transfer stored images through the detector array itself [208].

The basic building block of this technique, first proposed in [209], is the metal-oxide-semiconductor (MOS) capacitor, Fig. 2.39. A MOS capacitor typically consists of an intrinsic silicon substrate with an insulation layer of silicon dioxide on it. A thin metal electrode, called the gate, is deposited on to this layer. Applying a positive voltage across this structure causes the holes in the p-type silicon to move away from the Si-SiO₂ interface below the gate, leaving a region depleted of positive charges. This depletion region, that of course has not the sharp boundaries of Fig. 2.39 but a gradual shape, now can act as a potential energy well for mobile electrons.

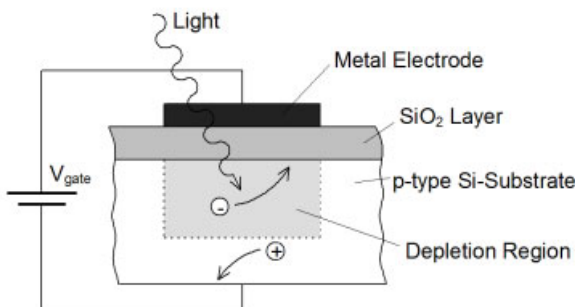


Figure 2.39: MOS capacitor.

The higher the gate voltage, the deeper the potential-energy well. If a photon of sufficient energy is absorbed in the depletion region, while voltage is applied, an electron-hole pair is generated. While the hole moves to the ground electrode the electron stays in the depletion region. The more light is absorbed by the silicon the more electrons are collected in the potential-energy well under the gate electrode. This continues until the well becomes saturated or the voltage is removed. The amount of negative charge, the electrons, that can be collected is proportional to the applied voltage, oxide thickness, and gate electrode area. The total number of electrons that can be stored is called the *well capacity* [210]. A two-dimensional array of such MOS capacitors can therefore store images in the form of trapped charge carriers beneath the gates.

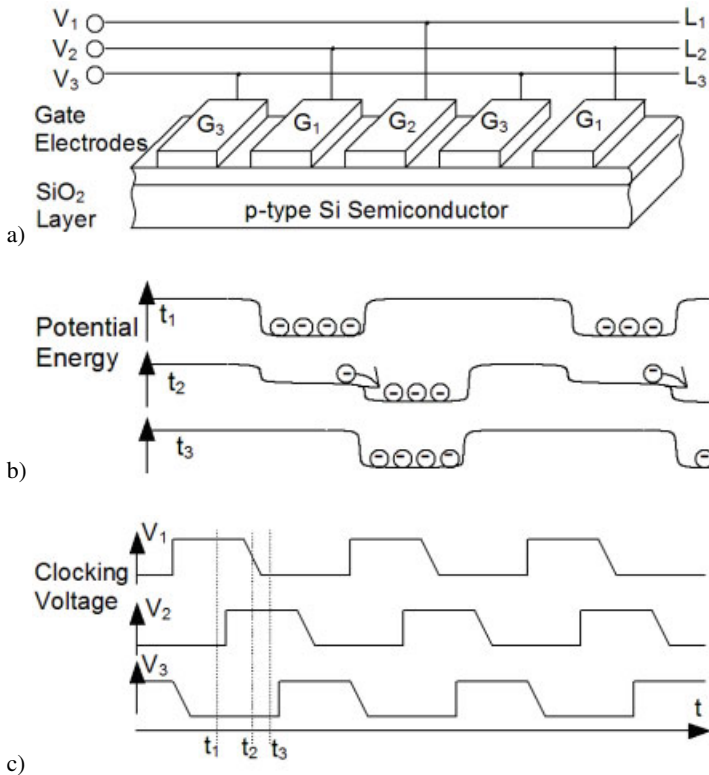


Figure 2.40: Charge transfer in three-phase CCD.

The CCD solution to move the accumulated charges off the array is to adjust the voltages to each gate of the array in a way that transfers the charges from one potential well to the neighboring one. This process is illustrated for three-phase clocking in Fig. 2.40. While a CCD register consists of a series of gates, a CCD array is a series of registers, say column registers. For three-phase clocking the column gates are connected to separate voltage lines L_1 , L_2 , L_3 in contiguous groups of three gates G_1 , G_2 , G_3 , Fig. 2.40a. Initially, say at time instant t_1 , a high voltage V_1 is applied to gate G_1 so that photoelectrons are collected in the wells below all the gates G_1 , Fig. 2.40b. The period with which the high voltage is applied is known as the *integration time*. After integration V_1 is reduced to zero while V_2 is increased. That occurs at time instant t_2 according to Fig. 2.40c. When V_1 drops below V_2 , the G_2 gates will have deeper potential wells, which draws the electrons from the G_1 wells to the G_2 wells. The same voltage sequence is repeated for lines L_2 and L_3 , now the electrons are transferred from all G_2 wells to the G_3 wells. This V_1 , V_2 , V_3 voltage sequence is repeated to move all electrons off the array. They are read out as a serial signal by a linear MOS register called the readout register, Fig. 2.41.

In this method of charge transfer, called *line address transfer*, one row at a time exits the readout register. But whenever the high voltage level is applied to the gate to move the

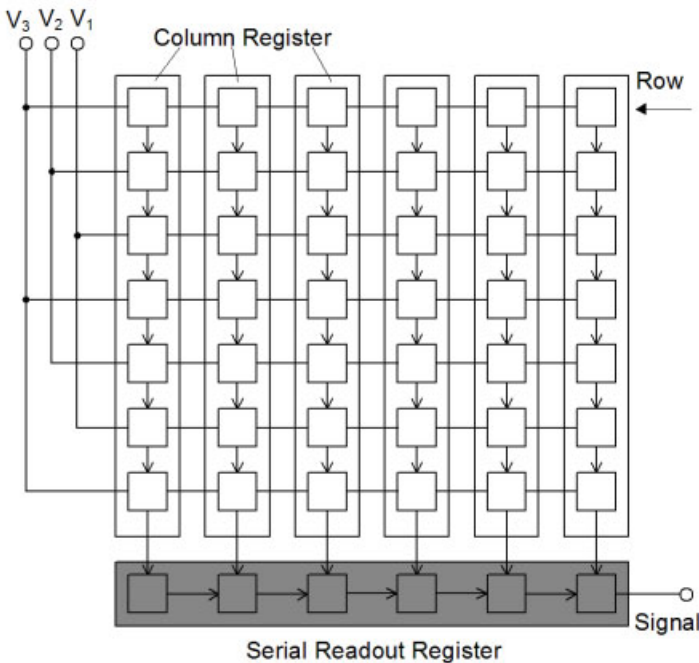


Figure 2.41: Three-phase CCD array, line address transfer.

charges, new charges can be produced by light shining on the array. Existing and new charges accumulate and cause image smearing. A reasonable solution is to mechanically shutter the array between the integration times. A more efficient solution is the *interline transfer* CCD. Here columns of MOS capacitors, the vertical shift registers, are interlaced between the light collecting columns of pixels, Fig. 2.42. These shift registers are covered by opaque metal shields. While the stored charges are transferred off the array over the light protected shift and readout registers, the light sensitive pixels may integrate a new image.

A third charge transfer method is *frame transfer*. Frame transfer CCDs quickly move all the accumulated charges into an adjacent shielded storage array the same size as the light sensitive pixel array, Fig. 2.43. While the pixels integrate the next image, the stored image is clocked off to the readout register.

Frame transfer CCDs as well as the line-address transfer CCDs are slower than interline transfer CCDs. Image smear is least with interline transfer. But the interline transfer concept leaves less room at the array area for active sensors. The shields obscure half the information that is available in the scene. The area fill factor may be as low as 20 percent. In this case the output voltage is only 20 percent of a detector that would completely fill the pixel area. With the help of microlenses concentrating light of a larger area onto the sensitive area, the fill factor may be optically increased [210].

Holography of moving scenes normally demands the employment of pulsed lasers. Traditional camera tubes had a readout time of 19 ms on a total readout cycle of 20 ms according

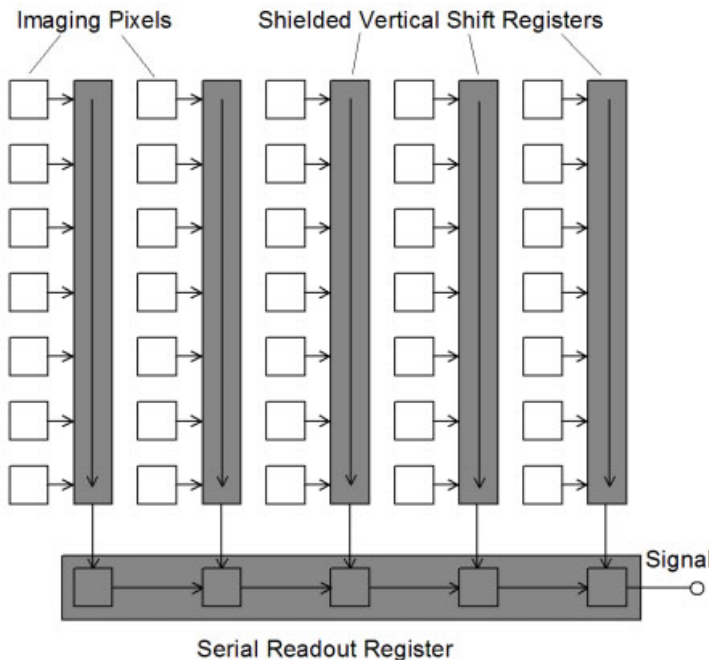


Figure 2.42: Interline transfer CCD array.

to the CCIR standard. So the laser pulses had to be triggered onto the 1 ms blanking period just before the readout of an even field [211]. With CCD arrays the image is read out much faster. In the frame transfer arrays the image is transferred from the photosensitive area to the shielded area in typically 300 μ s. With interline transfer arrays the charge transfer to the shielded shift registers is a single step process and thus even shorter: typically 1 μ s, which makes pulse timing even more flexible. It may be advantageous to reset the array prior to the generation of the laser pulse to get rid of the ghost image problem [211]. A ghost image may occur if some of the incident photons are detected by the supposedly light-shielded shift registers, because of diffraction, refraction, or multiple reflections.

The ghost image problem should not be confused with *blooming*. This effect occurs if very bright parts of scenes, e. g. specular reflections, oversaturate some of the pixels and cause spill-over of charge to neighboring pixels. This results in a local loss of spatial information. Some CCD arrays are equipped with antiblooming drains, where excess carriers produced by local overload are disposed so that the neighboring pixels are not affected by the oversaturation.

Besides the three-phase clocking scheme described here there exist other clocking schemes, like two-phase clocking, four-phase clocking and even more specific schemes which can be used for electronic shuttering, iris control, or image-scanning functions such as interlaced video fields.

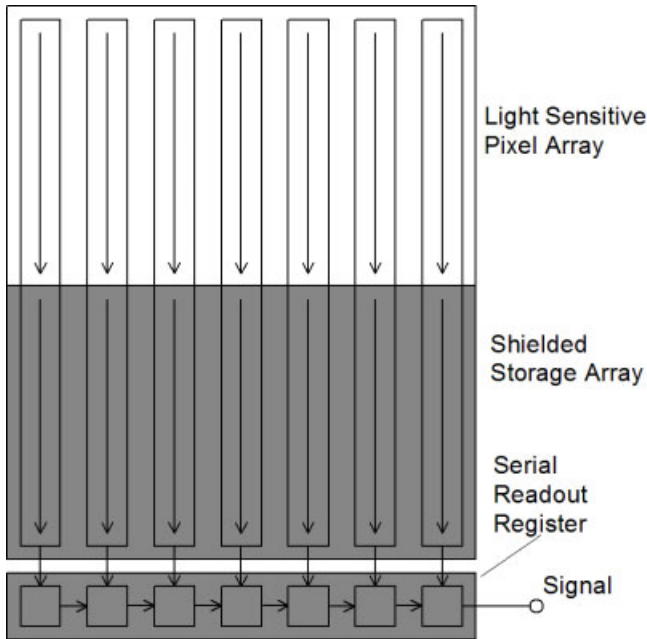


Figure 2.43: Frame transfer CCD array.

CCDs can be illuminated either from the front or the back. In front-illuminated CCDs, Fig. 2.44a, the light enters through the gate electrodes, which must therefore be produced of transparent material such as polysilicon. Back-illuminated CCDs avoid interference and absorption effects caused by the gates but must be thinned for imaging in visible or near-infrared regions of the spectrum, Fig. 2.44b.

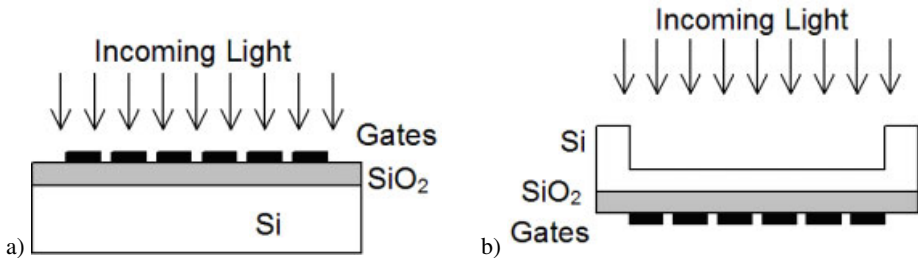


Figure 2.44: Front-illuminated (a) and back-illuminated (b) CCD arrays.

2.8.2 CCD Array Performance Parameters

CCD arrays exhibit a number of features which influence their performance. To select the best array for a specific application, e. g. digital holography, one has to know these features

and their consequences on the application. A number of parameters precisely quantify these features.

The rate of conversion of the incident photons into electrons is the *quantum efficiency*. Assuming an ideal material and a photon energy higher than the semiconductor band gap energy, then each photon would produce one electron-hole pair. We would have a quantum efficiency of one. However, the absorption coefficient is wavelength dependent and decreases with increasing wavelengths. Therefore long wavelength photons may even pass through the CCD without being absorbed. Any photon absorbed within the depletion region will yield a quantum efficiency near unity. For photons absorbed in the bulk material their contribution depends on the diffusion length. A diffusion length of zero implies immediate recombination of electrons created in the bulk material and a quantum efficiency going to zero for these wavelengths. On the other hand for a diffusion length of nearly infinity the electrons eventually reach the charge well and contribute to a quantum efficiency approaching one. Since the quantum efficiency depends upon the gate voltage and material thickness, the *spectral responsivity* differs between front-illuminated and back-illuminated CCD arrays. Typical curves are shown in Fig. 2.45.

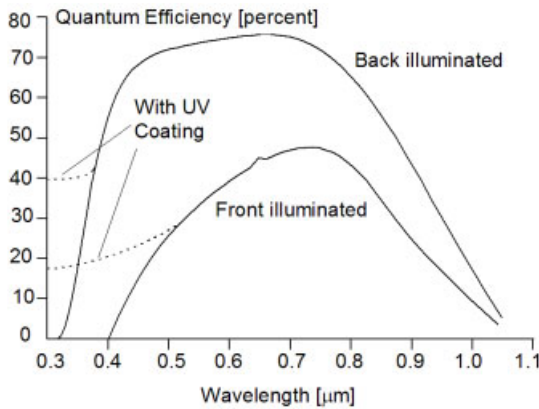


Figure 2.45: Typical spectral response of front- and back-illuminated CCD arrays.

The quantum efficiency of the back-illuminated CCD generally is higher, mainly since the photons do not have to pass the polysilicon gate. The response in the ultraviolet may be enhanced with UV fluorescent phosphors deposited onto the array. When they are excited by light of wavelengths between $0.12 \mu\text{m}$ and $0.45 \mu\text{m}$ these phosphors emit light at approximately $0.54 \mu\text{m}$ to $0.58 \mu\text{m}$, which is efficiently absorbed, .

Ideally the CCD output is proportional to the exposure. But in practice for long exposure times as used for low-light-level operation, the *dark current* may become a problem. Sources of dark current are thermal generation and diffusion of electrons in the neutral bulk material and in the depletion region or due to surface states. Typical dark current densities vary between 0.1 nA/cm^2 and 10 nA/cm^2 in silicon CCDs. As an example, in a pixel of dimension $24 \mu\text{m} \times 24 \mu\text{m}$ a dark current of 1000 pA/cm^2 produces 36,000 electrons/(pixel·sec). If the well capacity is 360,000 electrons, the well fills in 10 seconds [210]. Dark current due to thermally generated electrons can be reduced by cooling the device. Some arrays contain shielded extra pixels at the end of the array. These establish a reference dark current level, that can be subtracted from each active pixel value as a first crude correction.

Besides the dark current there are other noise sources influencing the performance of the CCD array. *Shot noise* is due to the discrete nature of electrons. It always occurs when photoelectrons are created and when dark current electrons are present. Shot noise is a random process that can be modeled by a Poisson distribution. Additional noise is added when reading the charge (*reset noise*) or may be introduced by the amplifier (*1/f noise* and *white noise*). If the output is digitized, *quantization noise* has to be regarded. *Fixed pattern noise* refers to the pixel-to-pixel variation that occurs when the array is in the dark. It is a signal-independent additive noise. On the other hand *photoresponse nonuniformity*, due to differences in the responsivity, is a signal-dependent multiplicative noise. For a more thorough discussion of these noise sources the reader is referred to [210].

The dependence of the output signal voltage on exposure is shown in an idealized sketch in Fig. 2.46. The slope of this transformation in the linear range between dark current and saturation is the average *responsivity* of the array. It has the units of volts/(joule cm²). Cameras intended for consumer video indicate their responsivity normalized to photometric units. The units of radiation are normalized to the spectral sensitivity of the human eye. In this case the responsivity is given in volts/lux.

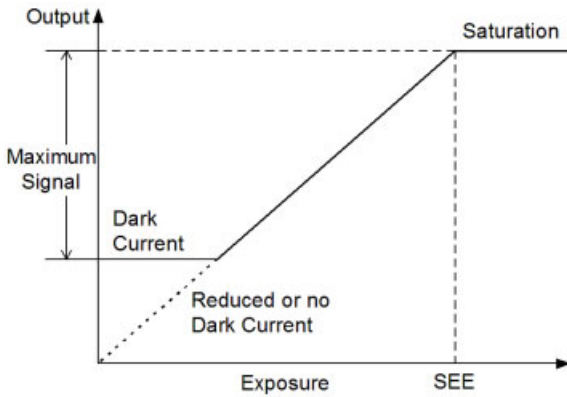


Figure 2.46: Dependence of output voltage on exposure.

The *noise equivalent exposure* (*NEE*) is the exposure that produces a signal-to-noise ratio of one. For CCD arrays, *NEE* is the noise value in rms electrons. The minimum noise level is the noise floor, this value is used most often for the *NEE*. The *saturation equivalent exposure* (*SEE*) is that input that fills the charge wells completely, Fig. 2.46. With these definitions of *NEE* and *SEE* the *dynamic range* *DR* is defined as the maximum signal divided by the rms noise

$$DR = \frac{SEE}{NEE} = \frac{N_{\text{well}}}{\langle n_{\text{sys}} \rangle} = \frac{V_{\max}}{V_{\text{noise}}}. \quad (2.189)$$

Instead of *SEE* and *NEE* we can use the well capacity *N_{well}* in electrons divided by the system noise $\langle n_{\text{sys}} \rangle$ measured in electrons rms or the voltages corresponding to the maximum and the noise signal. With $DR = 20 \log(SEE/NEE)$ dB the dynamic range is expressed in decibels.

The exposure can be varied by changing the integration time, therefore an *integration time control* improves the application of CCDs in many areas. Reduction of the integration time is

interesting when objects are studied with a cw laser under unstable experimental conditions, provided that enough laser intensity is available. When pulsed lasers are applied, shuttering synchronously to the laser pulses is a way to remove background light, which otherwise would destroy the dynamic range for the signal of interest [211].

Both interline transfer and frame transfer CCD cameras are offered with integration times adjustable from about 1/50,000 s to arbitrarily long exposures, while retaining the TV standard readout. The latter is an advantage because standard video equipment then still can be used to transmit and record the camera signal. For extended integration this means that the integration time always is an integer times the standard integration time, empty television frames are presented at the output while integrating [211].

The standard video synchronization pulses from a commercial television camera often are not precisely locked to the pixel clocks, which control the readout of the CCD array. This effect is called *jitter*. Jitter can cause substantial errors when the video signal is being digitized. Especially when two digital holograms have to be compared in holographic interferometry it is extremely important that pixels have the same positions in subsequent digitized frames. This can be ensured by synchronizing the frame grabber to a pixel clock signal from the camera, which is often offered as an option.

A useful measure of performance of CCD arrays, especially if they are compared to hologram recording emulsions, see Section 2.7.2, is the *space-bandwidth product*. According to (A.61) the space-bandwidth product of a CCD device is defined as the product of the dimensions of the device and the pixel frequency. Therefore a conventional hologram with, say, 3000 linepairs/mm and a size of 20 cm² has a space-bandwidth product in the range of 10¹⁰, while CCDs with 1000 – 2000 pixels in each direction and pixel sizes down to 7 µm exhibit a space-bandwidth product in the range of 10⁶ to 10⁷ [212]. The consequences using CCDs as recording media in holography are described in Section 3.1.1.

2.8.3 CMOS Image Sensors

In recent years CMOS image sensors have entered the market. The CMOS (*complementary metal oxide semiconductor*) devices have complementary pairs of p- and n-type transistors. While CCDs are specialized chips, used only for image capture, they are manufactured by only a handful of very specialized fabrication facilities. On the other hand CMOS technology is used in the vast majority of electronic devices. Because CMOS tends to be produced using standard processes in high volume facilities, the economies of scale are such that CMOS image sensors are considerably less expensive to manufacture [213].

In the past CMOS sensors exhibited less light sensitivity than CCDs and significantly more noise. But progress in technology has closed this gap, so now CMOS image sensors have found their way into consumer and professional digital video and still cameras.

At its most basic, an image sensor needs to achieve five key tasks: absorb photons, generate a charge from the photons, collect the charge, transfer the charge, and convert it to a voltage. Both CCD and CMOS sensors perform all five tasks. The first three tasks are performed similarly, but they diverge in their methods of charge transfer and voltage conversion. A key characteristic of CMOS devices is that they consume negligible power when they are doing nothing other than storing a one or zero; significant power consumption is confined to the times when a CMOS is switching from one state to another. CMOS image sensors can have

much more functionality on-chip than CCDs. In addition to converting photons to electrons and transferring them, the CMOS sensor might also perform image processing, edge detection, noise reduction, or analog to digital conversion, to name just a few. This functional integration onto a single chip is the CMOS's main advantage over the CCD. It also reduces the number of external components needed. In addition, because CMOS devices consume less power than CCDs, there is less heat, so thermal noise can be reduced.

As far as digital holograms are recorded, there is no principal difference whether we use a CCD or a CMOS image sensor, so in the following the term CCD chip refers to both CCD and CMOS image sensors.

2.8.4 Spatial Sampling with CCD-Arrays

Spatial resolution describes the ability of an imaging device to resolve image details. The main parameters which determine spatial resolution are *pixel size* and *pixel number*. Normally we have rectangular arrays of light sensitive pixels organized in N lines and M rows. Often $N = M$ holds. The center-to-center spacing of the pixels, the pixel pitch, is $\Delta\xi$ and $\Delta\eta$ in the two orthogonal directions. If there is a gap between consecutive pixels, the effective pixel dimensions are $\alpha\Delta\xi$ and $\beta\Delta\eta$ with $\alpha \leq 1.0$ and $\beta \leq 1.0$ in the two directions, see also Fig. 3.41. The α and β are the *fill-factors* in the ξ - and η -directions. For square pixels $\alpha\Delta\xi = \beta\Delta\eta$ and with identical spacing in vertical and in horizontal directions $\Delta\xi = \Delta\eta$, the fill factor is the square root of the light sensitive detector area divided by the whole array area. According to the sampling theorem the signals can be reproduced faithfully from data recorded by the array up to spatial frequencies

$$f_{N\xi} = \frac{1}{2\Delta\xi} \quad \text{and} \quad f_{N\eta} = \frac{1}{2\Delta\eta} \quad (2.190)$$

the Nyquist frequencies in both directions.

A tool for analyzing the capability of imaging devices to record and reproduce spatially varying signals is the *modulation transfer function* (*MTF*). The *MTF* is defined as the ratio of output and input modulation at each frequency

$$MTF = \frac{M_{\text{output}}}{M_{\text{input}}} \quad (2.191)$$

where the modulation M is given by

$$M = \frac{V_{\max} - V_{\min}}{V_{\max} + V_{\min}} \quad (2.192)$$

with V_{\max} and V_{\min} denoting the maximum and minimum signal levels. This concept is presented in Fig. 2.47 for three input signals [210]. The *MTF* of a system indicates how the various frequencies are affected by the system.

The influence of the spatial integration on the modulation is illustrated in Fig. 2.48. In Fig. 2.48a we have a very small, ideally a pointwise, sampling detector. The maximum and minimum input and output amplitudes agree, and we obtain an $MTF = 1$. Figure 2.48b shows the sampling with a CCD array whose pixel width is one-half of the center-to-center

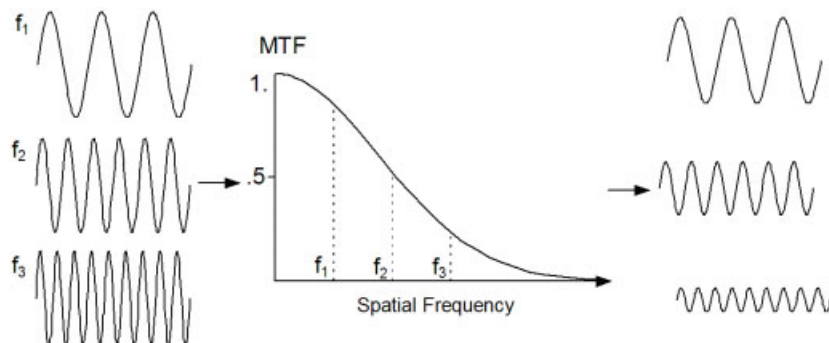


Figure 2.47: Modulation transfer function applied to three frequencies.

spacing. The heavy lines indicate the pixel output. The maximum output amplitude is less than the maximum input, and we have an $MTF < 1$. For an array with a fill-factor of one, Fig. 2.48c, the MTF is even lower. We see that with increasing pixel width Δ the MTF decreases.

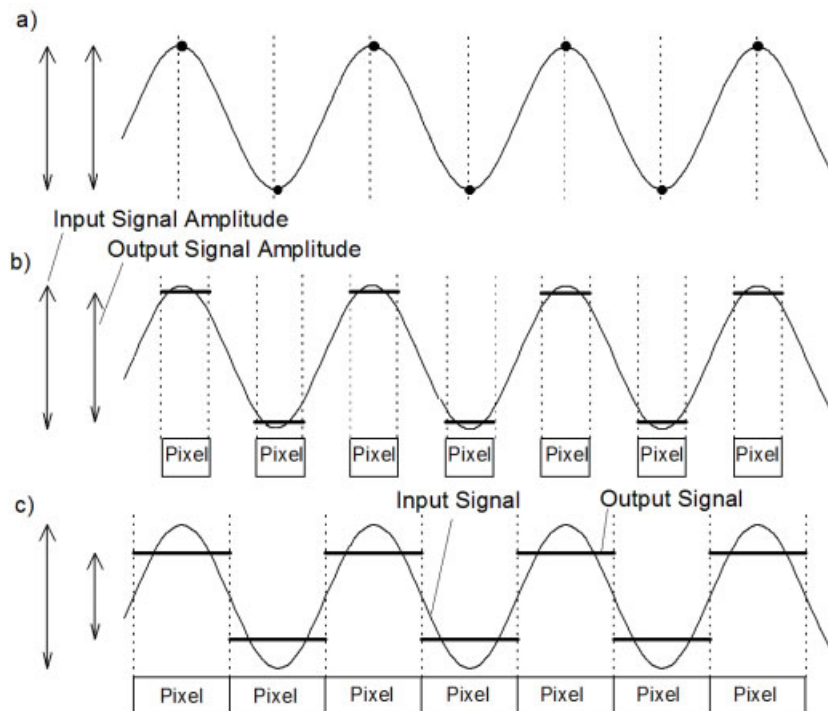


Figure 2.48: Sampling with different spatial integration.

Furthermore each individual pixel has an optical MTF, which in one dimension is [210]

$$MTF_{\text{pixel}}(f) = \frac{\sin(\pi\Delta f)}{\pi\Delta f}. \quad (2.193)$$

This is shown for normalized spatial frequencies Δf in Fig. 2.49. The MTF is zero when $f = k/\Delta$, $k \in \mathbb{N}$. The first zero ($k = 1$) defines the pixel cutoff frequency f_C ; higher frequencies cannot be resolved by such a pixel.

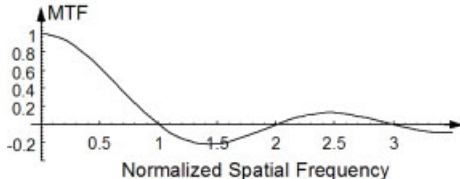


Figure 2.49: Pixel MTF.

A CCD-array will sample with a sampling rate d_{CC} denoting the center-to-center distance between the individual pixels of width Δ . The fill-factor for square detectors with equal spacing in horizontal and vertical directions is $(\Delta/d_{CC})^2$. According to the sampling theorem signals up to the Nyquist frequency $f_N = 1/(2d_{CC})$ can be faithfully reproduced. Figure 2.50 gives a plot of the MTF up to the sampling frequency $f_S = 1/(d_{CC})$ (here normalized to one) which agrees with the pixel cutoff frequency in the case $\Delta = d_{CC}$. For fill-factors less than one the sampling frequency is below the pixel cutoff frequency but still the Nyquist frequency is half the sampling frequency. Summarizing, we can state that in each case the Nyquist frequency defines the upper limit for faithful reconstruction.

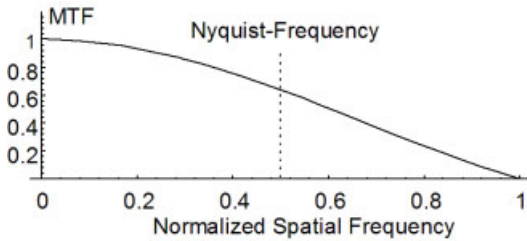


Figure 2.50: MTF for Nyquist and sampling frequencies.

2.8.5 Color Still Cameras

The biggest market for digital image sensors is digital photo-cameras and digital video-cameras. Mass production enables large numbers of items and thus low prices. The sensors needed in this realm generally are *color sensors*. The monochrome sensors, although less complex, have only a limited market, therefore their significantly higher price.

Basically all image sensors are grayscale devices that record the intensity of light from black to white with the appropriate intervening gray. To sensitize the sensors to color, a layer of color filters is bonded to the silicon using a photolithography process to apply color dyes. Image sensors employing micro lenses have the color filter between the micro lens and the photodetector. Some expensive high-end digital cameras use three array image sensors with

the incoming light being split by properly arranged prisms. For this approach it is easy to coat each of the three sensors with a separate color. But nearly all consumer or professional digital still cameras today are single sensor devices, which use a color filter array (CFA).

Theoretically color is described in terms of what are called *tristimulus values* X, Y, Z :

$$\begin{aligned} X &= k \sum \phi(\lambda) \bar{x}(\lambda) \Delta\lambda \\ Y &= k \sum \phi(\lambda) \bar{y}(\lambda) \Delta\lambda \\ Z &= k \sum \phi(\lambda) \bar{z}(\lambda) \Delta\lambda. \end{aligned} \quad (2.194)$$

Here \bar{x} , \bar{y} , and \bar{z} are the *color matching functions*, and they represent the sensitivities of human visual systems' three color channels, Fig. 2.51.

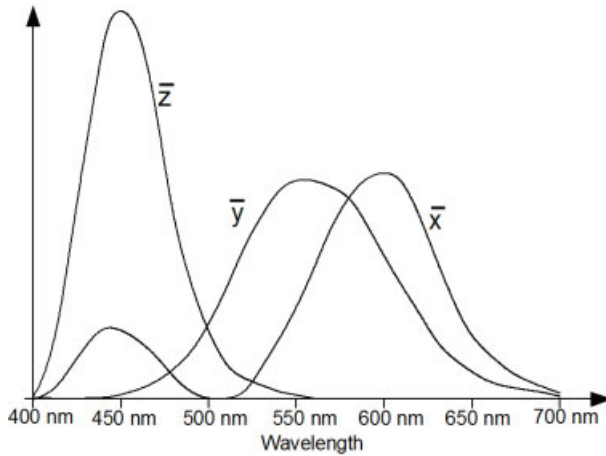


Figure 2.51: Color matching functions.

The term $\phi(\lambda)$ is the stimulus function, which is $\phi(\lambda) = S(\lambda)R(\lambda)$ for opaque objects, $\phi(\lambda) = S(\lambda)T(\lambda)$ for transparent objects, and $\phi(\lambda) = S(\lambda)$ for light sources. In these formulas $S(\lambda)$ is the spectral power distribution of the light source, $R(\lambda)$ is the spectral reflectance of the opaque object, and $T(\lambda)$ is the spectral transmittance of the transparent object. $\Delta\lambda$ is the wavelength resolution of the color-matching and stimulus functions and k is a normalizing constant [214]. In a similar way image detectors sense three primary colors, mostly red, green, and blue (RGB), Fig. 2.52, or yellow, cyan, and magenta (YCM).

There are principally two distinct categories of color filter design: the relatively new *vertical color filter detector* and the *lateral color filter detector* [215]. The vertical color filter detector features three separate layers of photodetectors embedded in silicon, Fig. 2.53a.

Each layer captures a different color, since slab silicon absorbs different colors of light at different depths, Fig. 2.53b. Stacked together, full-color pixels capture red, green, and blue light at every lateral pixel location, Fig. 2.53c. The more conventional lateral color filter detector uses a single layer of photodetectors with the color filters arranged in a tiled mosaic pattern, Fig. 2.54a.

Here each filter lets only one color of light – e. g. red, green, or blue – pass through, allowing the pixel to record only one color, Fig. 2.54b. The most common arrangement of colors in the CFA is that of the *Bayer array* [216]. In the Bayer array the sensor captures a mosaic of

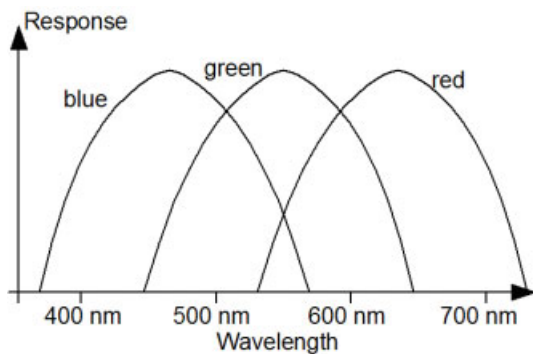


Figure 2.52: Color filter response.

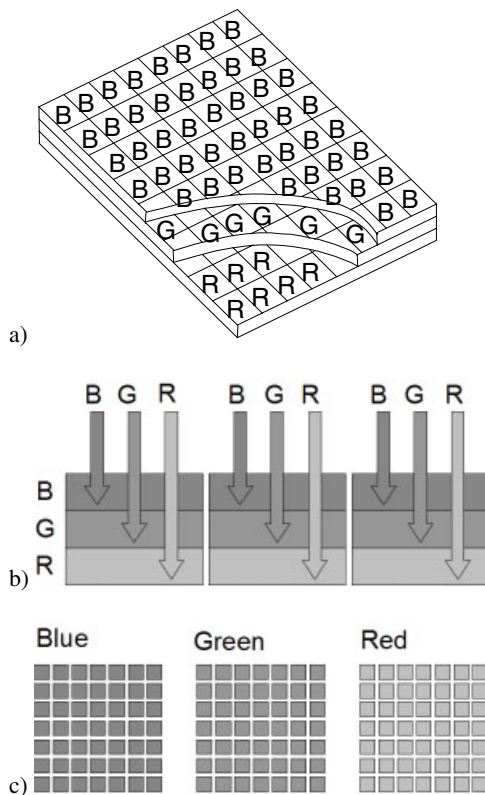


Figure 2.53: Vertical color filter detector.

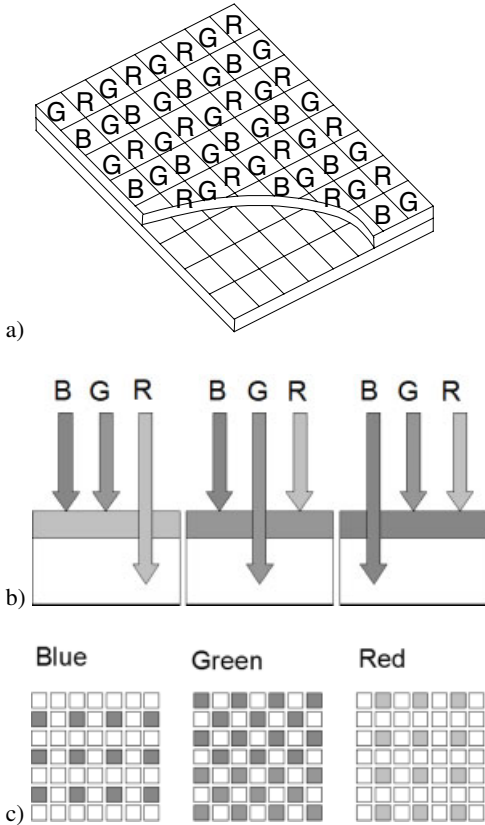


Figure 2.54: Lateral color filter detector.

25% of the red, 25% of the blue, and 50% of the green light, Fig. 2.54 c. This accords with the principle that the luminance channel (here the color green) needs to be sampled at a higher rate than the chrominance channels (red and blue). The choice of green as the representative for the luminance is due to the fact that the luminance response curve of the human eye peaks at around the frequency of green light (around 550 nm) [217]. Generally *luminance* is defined as any positive weighted sum of the primary colors R, G, and B. The weights are chosen so that luminance approximates the photopic function $V(\lambda)$ which represents the human luminosity sensation [216]. The luminance record contains most of the spatial information of the image. On the other hand *chrominance* contains the color information.

Since in single layer sensors with lateral CFAs like the Bayer array at each pixel only one spectral measurement is made, the other colors must be estimated using information from all the color planes in order to obtain a high resolution color image. This process is often referred to as *demosaicking* [217]. Demosaicking algorithms can be categorized into three different groups:

- Simple straightforward interpolation algorithms using surrounding cells of the same color channel, like linear filtering, nearest neighbor interpolation, and median filtering.

- Advanced interpolation algorithms that use surrounding cells of all three channels and take into account spatial information about the image data.
- Reconstruction techniques that use information about the capturing device itself and that make certain assumptions about the captured scene.

The goal of the demosaicking process can be to reconstruct a color image that comes as close as possible to a full resolution image, or aims at maximum perceptual quality [218]. However, in the context of this book, using monochromatic laser light, only luminance is the interesting measure.

3 Digital Recording and Numerical Reconstruction of Wave Fields

Here an introduction to the technique called digital holography is given. In this book the term ‘digital holography’ is understood as the digital recording of the hologram field by CCD- or CMOS-arrays and the numerical reconstruction of the wave fields in a computer. This should not be confused with the computer generation of holograms which then are printed onto physical media and from which the wave fields are reconstructed optically – an approach also called digital holography occasionally [219]. In this chapter the preliminaries as well as the main methods of numerical reconstruction are presented, forming the basis for digital holographic interferometry to be introduced in more detail in Section 5.8.

3.1 Digital Recording of Holograms

This section presents the way to record Fresnel holograms as well as Fraunhofer holograms with common CCD- or CMOS-arrays. In the discussion we will address only CCD-arrays, although also CMOS-arrays are meant. It is the angle between object wave and reference wave that must be controlled carefully in order to produce holograms which can be resolved by a given CCD-array. Optical methods for reducing the wave fields emanating from large objects are described which enable also the recording of such wave fields. A variety of possible reference waves and their numerical description are revealed. Based on the given number and spacing of the pixels of the CCD and based on the size of the object to be recorded, this section supplies the necessary information to design the optical arrangement for recording successfully digital holograms.

3.1.1 CCD Recording and Sampling

The aim of *digital holography* is the employment of CCD-arrays for recording holograms which are then stored in a computer memory and can be reconstructed numerically. As presented in detail in Section 2.6 the hologram is the microscopically fine interference pattern generated by the coherent superposition of an object and a reference wave field. The spatial frequency of this interference pattern is defined mainly by the angle between these two wave fields, (2.30) and (2.32). A typical geometry for recording a digital hologram is shown in Fig. 3.1.

Let the CCD-array have $N \times M$ light sensitive pixels with distances $\Delta\xi$ and $\Delta\eta$ between the pixel centers in the x - and y -directions, respectively. Without restriction of generality we

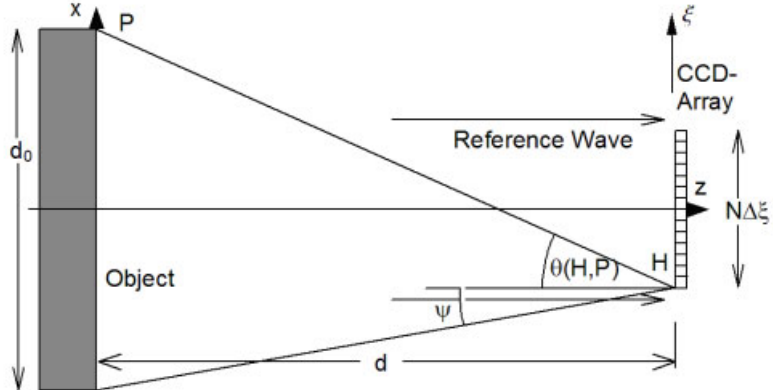


Figure 3.1: Geometry for recording a digital Fresnel hologram.

can assume that $N = M$ and $\Delta\xi = \Delta\eta$. Since the x - and y -directions, and in the same way the ξ - and η -directions, are equivalent, it is sufficient to perform the analysis only in the x - z -plane. For our analysis we assume a plane reference wave impinging normally onto the CCD, which constitutes the most frequently used arrangement, Fig. 3.1. θ is the angle at point H between the reference and object wave emitted from an object point P . The distance p between two consecutive interference fringes forming the hologram at H was seen in (2.30) and (2.32) to be

$$p = \frac{\lambda}{2 \sin(\frac{\theta}{2})}. \quad (3.1)$$

A meaningful sampling of the intensity distribution constituting the hologram is only guaranteed if the *sampling theorem* (A.50) is obeyed. The sampling theorem requires that the period p must be sampled with more than two pixels, implying more than two pixels fitting into the distance p

$$p > 2\Delta\xi. \quad (3.2)$$

If one pleases, this can also be expressed using the spatial frequency f of the holographic fringes

$$f < \frac{1}{2\Delta\xi}. \quad (3.3)$$

In practical applications the CCD-array with parameters N , M , $\Delta\xi$, $\Delta\eta$ is given, so it sets a limit to the angle θ . Because θ in all practical cases remains small, we can use $\sin \theta/2 = \tan \theta/2 = \theta/2$ in the calculations. From (3.1) and (3.2) we obtain an upper limit to the angle θ

$$\theta < \frac{\lambda}{2\Delta\xi} \quad (3.4)$$

or, with the definition $\theta_{\max} = \max\{\theta(H, P) : H, P\}$, see Fig. 3.1

$$f < \frac{2}{\lambda} \sin\left(\frac{\theta_{\max}}{2}\right). \quad (3.5)$$

The following table lists the spatial resolution of some frequently used holographic recording media. These are holofilm on the base of silver halides, photothermoplastic film, and the CCD-arrays of the frequently used videocameras Kodak Megaplus 1.4 and Megaplus 4.2. The maximum angle θ is given for these materials assuming the employment of a helium-neon laser with a wavelength $\lambda = 0.6328 \mu\text{m}$.

Recording material	Resolution	Maximum angle
Holofilm (Silver halide)	up to 7000 line pairs/mm	arbitrary
Photothermoplast	750 – 1250 line pairs/mm	27° to 47°
Megaplus 1.4 ($\Delta\xi = 6.8 \mu\text{m}$)	73 line pairs/mm	2.67°
Megaplus 4.2 ($\Delta\xi = 9.0 \mu\text{m}$)	55 line pairs/mm	2.01°

The conclusion is that we can employ CCD-arrays to record holograms as long as the angle between reference wave and object wave remains small enough so that the sampling theorem is fulfilled. The restricted angles are obtained either by objects of small lateral dimensions or by objects placed far away from the CCD-target. A further solution to this problem is presented in the next section.

For the typical geometry of Fig. 3.1 with the plane object of lateral extension d_0 in the x -direction placed symmetrically to the optical axis, and a plane reference wave travelling along the optical axis and impinging orthogonally onto the CCD, we can calculate the maximum object width d_0 for each distance d . According to Fig. 3.1 we have

$$\tan \theta = \frac{\frac{d_0}{2} + \frac{N\Delta\xi}{2}}{d}. \quad (3.6)$$

Together with the maximum angle of (3.4) we obtain

$$\frac{\frac{d_0}{2} + \frac{N\Delta\xi}{2}}{d} < \frac{\lambda}{2\Delta\xi} \quad (3.7)$$

which is resolved with respect to d_0 to yield the limit to the lateral extension

$$d_0(d) < \frac{\lambda d}{\Delta\xi} - N\Delta\xi. \quad (3.8)$$

In its other form this inequality defines the minimum distance between an object of given lateral width d_0 and the recording target

$$d(d_0) > \frac{(d_0 + N\Delta\xi)\Delta\xi}{\lambda}. \quad (3.9)$$

In this derivation we have claimed that all pixels of the CCD-array together with all object points fulfill the sampling theorem. A weaker requirement is that for each point of the object at least one pixel fulfills the sampling theorem. This leads to the angle ψ , see Fig. 3.1, with

$$\tan \psi = \frac{\frac{d_0}{2} - \frac{N\Delta\xi}{2}}{d} \quad (3.10)$$

and instead of (3.8) to

$$d_0(d) = \frac{\lambda d}{\Delta\xi} + N\Delta\xi \quad (3.11)$$

or conversely

$$d(d_0) > \frac{(d_0 - N\Delta\xi)\Delta\xi}{\lambda}. \quad (3.12)$$

In this case slightly larger objects are admitted. But as a consequence the information about marginal points of the object which make full use of these limits are faithfully stored only in a few hologram points. As a result they appear noisy, with weak contrast, and unreliable in the reconstruction. It must be thought over carefully whether one is willing to pay this price for having an object of 5.3 cm width in 50 cm distance instead of one 4 cm wide (assuming $\lambda = 0.6328 \mu\text{m}$, $N = 1024$, $\Delta\xi = 6.8 \mu\text{m}$) while on the other hand the larger object also can be recorded with full resolution in all pixels if it stands 65 cm apart from the CCD instead of 50 cm. As a rule of thumb the distance between object and CCD must be roughly at least

$$d > d_0 \frac{\Delta\xi}{\lambda}. \quad (3.13)$$

We have seen here that the pixel size $\Delta\xi \times \Delta\eta$ plays a crucial role in determining the maximum allowable angle between object and reference waves and we will see later on that spatial resolution and speckle size also depend on pixel size. Although CCD- or CMOS-arrays with very small pixels – comparable to the resolution of holographic plates – are not offered on the market today, Jacquot et al. [120, 121] have found a technical solution. In the recording plane they position an opaque screen containing an array of 128 transparent apertures each of $2 \mu\text{m} \times 2 \mu\text{m}$ size with a pitch of $8 \mu\text{m}$ in both directions, Fig. 3.2. The light transmitted by the transparent apertures is imaged onto the CCD by a magnification objective. In a sequential acquisition process 4×4 digital holograms are recorded with the mask shifted by a piezo translation stage in $2 \mu\text{m}$ steps in the ξ - and η -direction. The final image is composed from these 16 sub-images and acts like a digital $N\Delta\xi \times M\Delta\eta$ -hologram with $\Delta\xi = \Delta\eta = 2 \mu\text{m}$ and $N = M = 4 \times 128 = 512$.

3.1.2 Reduction of the Imaging Angle

In practical applications of holographic metrology we often have objects with large surfaces. A surface of 50 cm lateral dimension would require a distance of at least 5.4 m between object and CCD if we use $\lambda = 0.6328 \mu\text{m}$, $N = 1024$, $\Delta\xi = 6.8 \mu\text{m}$. This is not a feasible distance to record holograms, since the refractive index of air may vary significantly during recording

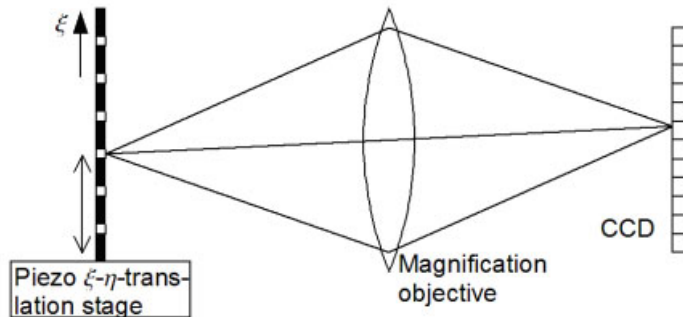


Figure 3.2: Decreasing the pixel size by a mask.

or between the records to be compared interferometrically, vibration isolation may become more difficult, or simply the room in the laboratory is restricted. But in such cases the wave field reflected from the object's surface can be drastically reduced by using a lens [59, 60]. Figure 3.3 displays this for a concave (negative) lens. The object wave field impinging onto

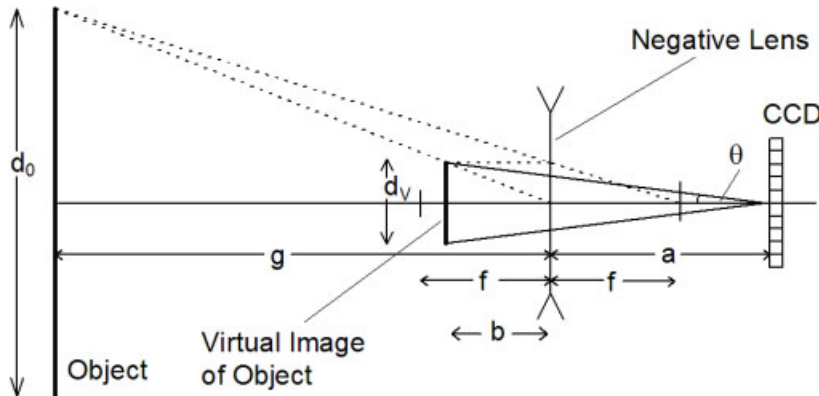


Figure 3.3: Reduction of the imaging angle by a concave lens.

the CCD target seems to come from the small virtual image of the object and not from the large object itself. Although the angle between rays from edge points of the large object and the normally impinging plane reference wave is too large for producing holographic interferences which fulfill the sampling theorem, the angle β between rays coming from the virtual object and the reference wave is much smaller so that it meets requirement (3.4).

In typical applications the object is given; let its lateral dimension in the direction investigated here be d_O . The results in the same way are valid for the other lateral coordinate direction. The CCD-array with its specified pixel distance $\Delta\xi$ and pixel number N together

with the wavelength λ of the available laser defines the angle θ . Furthermore the focal length f of the lens is provided, which is negative for the concave lens. From these quantities we can calculate the distance a the lens must be from the CCD and the distance g of the object from the lens, see Fig. 3.3. The calculation is based on the *lens formula*

$$\frac{1}{f} = \frac{1}{g} - \frac{1}{b} \quad (3.14)$$

where b is the distance of the virtual image from the lens and the *magnification formula*

$$M_T = \frac{d_V}{d_0} = -\frac{f}{g-f}. \quad (3.15)$$

Here M_T denotes the transversal magnification and d_V is the lateral extension of the virtual image. With $\tan \theta = d_V/[2(a+b)]$, $d_V = -d_O f/(g-f)$, and $b = gf/(f-g)$ we obtain

$$a = \frac{-d_0 f}{(g-f)2 \tan \theta} + \frac{fg}{g-f}. \quad (3.16)$$

In the reconstruction stage of digital holograms recorded in this way, of course one has to consider the distance between the CCD-array and the small virtual image of the object which now is

$$d = a + b \quad (3.17)$$

instead of the object's distance $g+a$.

Equation (3.16) shows that different distances g between object and lens correspond to different distances a between lens and CCD. This is illustrated for three object positions in Fig. 3.4. We see that the object size is reduced by the magnification factor M_T but the distances b are not reduced by the same factor. For them the longitudinal magnification factor M_L applies, which is a consequence of the lens formula. We have $M_L = -M_T^2$ [220]. The minus sign accounts for the reversal of the position order. The difference between lateral or transverse magnification and longitudinal magnification is important for holographic contour measurements when the object size is reduced by a lens.

For practical applications we have to fix the arrangement of object, lens, and CCD by selecting an optimal choice of g and z . It is often helpful to calculate some tables. For some available lenses and a given object dimension d_O we list the width of the virtual image d_V and the distance b of the virtual image from the lens in dependence on some typical lens-object distances g . The underlying equations are $d_V = -d_O f/(g-f)$, and $b = gf/(f-g)$.

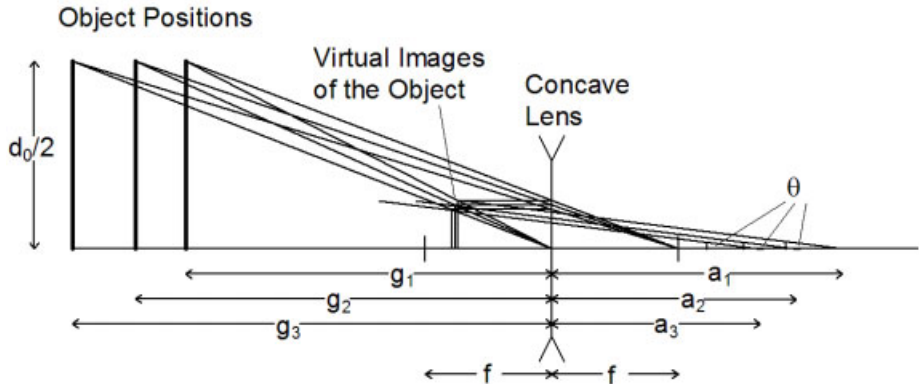


Figure 3.4: Influence of the object distance.

$f = -50 \text{ mm}$ $d_0 = 130 \text{ mm}$			$f = -100 \text{ mm}$ $d_0 = 130 \text{ mm}$			$f = -200 \text{ mm}$ $d_0 = 130 \text{ mm}$		
$g [\text{mm}]$	$d_V [\text{mm}]$	$b [\text{mm}]$	$g [\text{mm}]$	$d_V [\text{mm}]$	$b [\text{mm}]$	$g [\text{mm}]$	$d_V [\text{mm}]$	$b [\text{mm}]$
20	92.9	14.3	20	108.3	16.6	20	118.2	18.2
50	65.0	25.0	50	86.7	33.3	50	104.0	40.0
100	43.3	33.3	100	65.0	50.0	100	86.7	66.7
200	26.0	40.0	200	43.3	66.7	200	65.0	100.0
300	18.6	42.9	300	32.5	75.0	300	52.0	120.0
400	14.4	44.4	400	26.0	80.0	400	43.3	133.3
500	11.8	45.5	500	21.7	83.0	500	37.1	142.9
600			600	18.6	85.7	600	32.5	150
700			700	16.2	87.5	700	28.9	155.6
800			800	14.4	88.9	800	26.0	160.0

Equations (3.8) and (3.11) now are used to calculate $d_V = d_0(d)$ to enter one of these tables. The distance d of the virtual image from the CCD here is composed of the individual distances $d = b + a$.

Instead of a concave lens we also may use a convex lens, Fig. 3.5. Equation (3.16) now changes to

$$a = \frac{+d_0 f}{(g-f)2 \tan \theta} + \frac{f g}{g-f}. \quad (3.18)$$

The focal length f now is positive, the image is real and appears upside down. Generally if we use a concave lens the total length $g + a$ of the arrangement is shorter. Therefore the use of concave lenses for reducing the object wave field is recommended. On the other hand if we have to magnify very small objects in holographic microscopy applications it is recommended to produce a magnified virtual image using a convex lens.

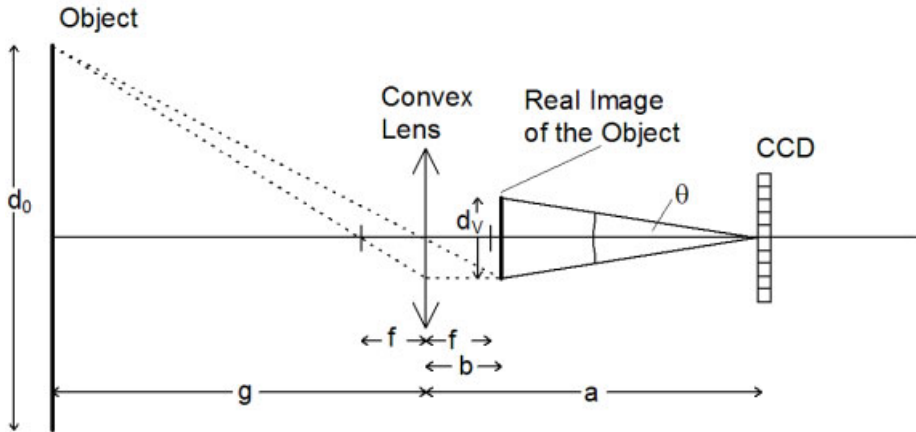


Figure 3.5: Reduction of the imaging angle by a convex lens.

Another way for reducing a large imaging angle caused by extended objects is to introduce an aperture of appropriate dimensions between object and CCD, Fig. 3.6 [221, 222].

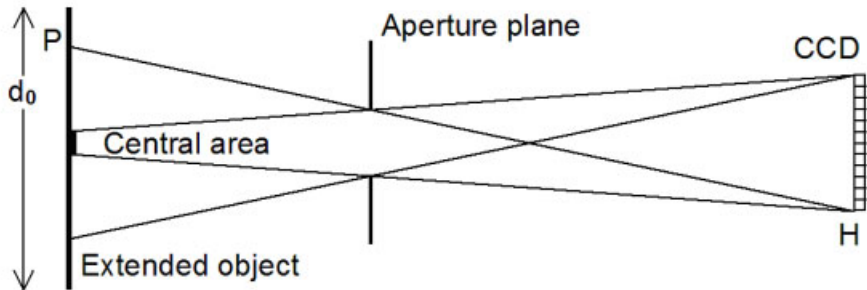


Figure 3.6: Aperture reducing the imaging angle.

This aperture limits the angles of the light rays scattered from the object points to within acceptable values. The aperture, by blocking those ray bundles making relatively large angles with the reference beam, serves to restrict the maximum angle between object and reference beams. A digital hologram of a large object could thus be recorded. But one must notice that not all points of the imaged area of the object surface contribute equally to any CCD-pixel. In Fig. 3.6 we recognize that the central area contributes to all hologram points, while e. g. object point P illuminates only point H of the hologram. Moreover the aperture may cause vignetting with the result that not the whole object wave field is stored in the recorded digital hologram. Multiple recordings with shifted positions of the aperture in its plane and a

mosaic-like combination of the reconstructed fields will become necessary. Moving the CCD array towards or away from the aperture has an effect similar to zooming a lens [223].

3.1.3 Reference Waves

In digital holography the CCD array registers the intensity distribution that is produced by the coherent superposition of a wave field scattered by the object and another wave field, the *reference wave*. For optical holographic reconstruction this hologram that is stored as an amplitude transmission is illuminated by the reference wave. Then by diffraction the wave field consisting of the real and the virtual images together with the zero-order diffracted reference wave arise. On the other hand in digital holography the reconstruction is accomplished by multiplication of the digitally stored intensity distribution with a digital model of the reference wave and subsequent numerical determination of the diffracted field in a defined image plane. Each of a variety of reference wave fields may be used, the most important reference wave fields are presented in the following.

The reference wave most easy to handle in any numerical processing is the plane wave impinging normally onto the CCD-array, Fig. 3.7. In this and all following figures the object

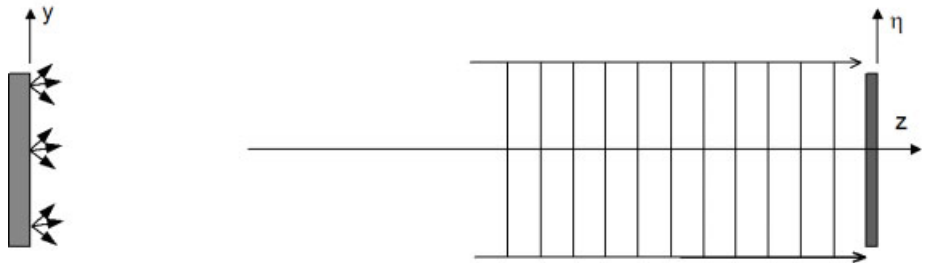


Figure 3.7: Normally impinging plane reference wave.

is placed in the x - y -plane orthogonal to the z -axis at $z = 0$, while the CCD-array is positioned at $z = d$ in the ξ - η -plane. The numerical description of the mentioned plane wave is

$$r(\xi, \eta) = E_r + 0.0i. \quad (3.19)$$

We have a pure real distribution with constant amplitude E_r . Since any constant intensity factor is of no relevance in the numerical evaluation we may neglect it and use only $r(\xi, \eta) = 1.0$ as the reference wave. A multiplication of the hologram with this reference wave does not change the hologram, so the multiplication can be omitted. For this reason the plane normally impinging reference wave is the one used most often in digital holography. Since one can omit the multiplication with such a reference wave, in some publications on digital holography no explicit attention is given to the reference wave at all in the numerical reconstruction stage.

A plane wave tilted in the η - z -plane by the angle θ is shown in Fig. 3.8. The wave vector of such a reference wave is $\mathbf{k} = \frac{2\pi}{\lambda}(0, \sin \theta, \cos \theta)$. At the points $\mathbf{r} = (\xi, \eta, z)$ in the hologram

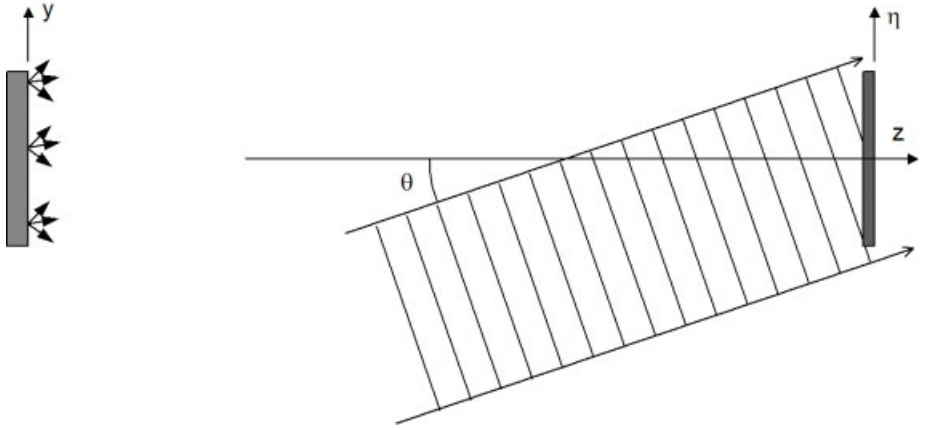


Figure 3.8: Plane reference wave, oblique incidence.

plane we therefore have

$$\begin{aligned}
 r(\xi, \eta) &= E_r e^{i(\mathbf{k} \cdot \mathbf{r} + \phi)} \\
 &= E_r e^{i(\frac{2\pi}{\lambda}\eta \sin \theta + \frac{2\pi}{\lambda}z \cos \theta + \phi)} \\
 &= E_r e^{i(\frac{2\pi}{\lambda}z \cos \theta + \phi)} e^{\frac{2\pi i}{\lambda}\eta \sin \theta}.
 \end{aligned} \tag{3.20}$$

The first of the two exponentials in the last line of (3.20) is a phase factor that is constant over the hologram. Without restriction of generality it can be omitted in any numerical simulation or reconstruction process. Therefore

$$r(\xi, \eta) = E_r e^{\frac{2\pi i}{\lambda}\eta \sin \theta} \tag{3.21}$$

describes the plane reference wave impinging under an oblique angle. However, in this context it must be recognized that a large angle θ will produce dense phase variations which may violate the sampling theorem.

A further important reference wave is the spherical wave that diverges from a source point (x_R, y_R, z_R) , Fig. 3.9.

$$r(\xi, \eta) = E_r e^{i(k \cdot \rho + \phi)} \tag{3.22}$$

with $\rho = \sqrt{(\xi - x_R)^2 + (\eta - y_R)^2 + (d - z_R)^2}$ and $k = 2\pi/\lambda$. Contrary to the case of the plane waves we now can reconstruct with the divergent reference wave (3.22) or the convergent conjugated reference wave

$$r(\xi, \eta) = E_r e^{-i(k \cdot \rho + \phi)}. \tag{3.23}$$

If we multiply the digital hologram with the original divergent reference wave (3.22), the result is a wave field that diverges from the virtual image in the object plane. Multiplication

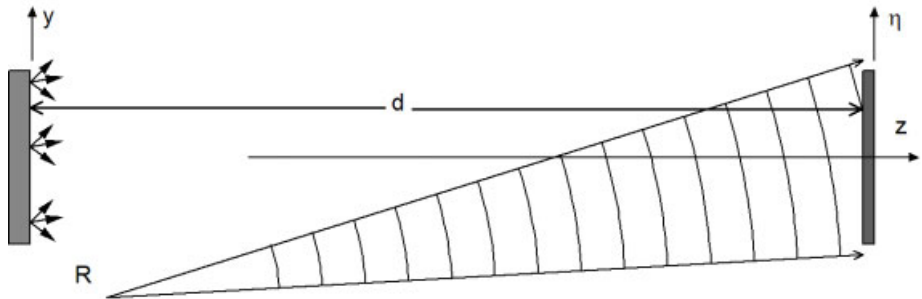


Figure 3.9: Spherical reference wave.

with the conjugated reference wave (3.23) reconstructs a wave field converging to a real image in the image plane. The special case $d = z_R$, that is a reference source point in the plane of the object's surface, corresponds to the so called *lensless Fourier transform holography*, see also Fig. 2.27.

We have seen in Section 3.1.1 that for resolving the holographic micro-interference by a CCD-array reference and object wave fields must impinge nearly colinearly onto the target. In order that the beam forming optics do not obscure the object that has to be recorded holographically, the reference wave can be combined with the object wave and guided to the CCD via a beamsplitter cube, Fig. 3.10, or a doubly refractive prism. Especially if the reference wave is a plane one that has to illuminate the CCD-array in normal or near normal direction, a beam splitter cube is used. This cube significantly changes the optical path length between

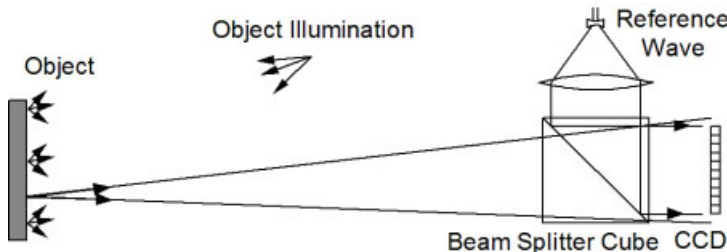


Figure 3.10: Reference wave guided over a beam splitter cube.

object and CCD array [224]. Let the refractive index of the beam splitter be n_t while in the surrounding air we have $n_i = 1$. The side length of the beam splitter cube is l and the distance between CCD and the object, or the virtual image of the object when reduced by a lens, is d . The path of a ray from an object point P to the array point Q is bent at the beam splitter, Fig. 3.11. According to the law of refraction it is

$$\frac{\sin \theta_i}{\sin \theta_t} = n_t \quad (3.24)$$

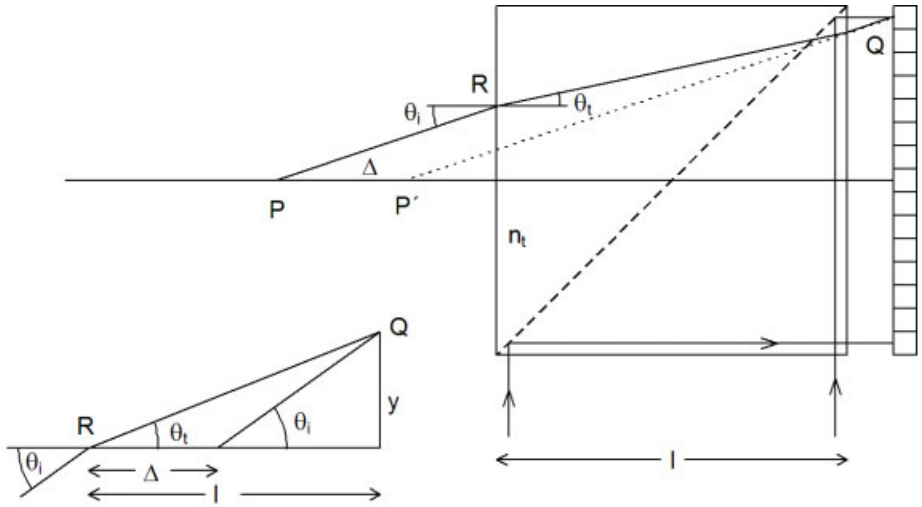


Figure 3.11: Ray bending by the beam splitter cube.

where θ_i is the angle of incidence and θ_r is the refracted angle. After leaving the beam splitter the ray is parallel to its original direction but shifted. It meets the CCD array like a ray coming from P' without passing the beam splitter. P' has the distance $d - \Delta$ from the CCD instead of d . The correction term Δ is calculated from

$$\begin{aligned} y &= l \tan \theta_t \\ y &= (l - \Delta) \tan \theta_i \end{aligned} \quad (3.25)$$

and we obtain

$$\Delta = \frac{l \tan \theta_i - l \tan \theta_t}{\tan \theta_i} = l \left(1 - \frac{\tan \theta_t}{\tan \theta_i} \right) \approx l \left(1 - \frac{1}{n_t} \right). \quad (3.26)$$

Since Δ does not depend on the choice of the ray, this Δ holds for all object points.

A frequently used beam splitter cube has side lengths $l = 4$ cm and consists of a glass with $n_t = 1.5$. The distance d measured with e. g. a yardstick now has to be reduced by $\Delta = l/3 = 1.33$ cm before we use d in the numerical reconstruction.

The working principle of the *doubly refractive prism* (a *Wollaston prism* for instance) is depicted in Fig. 3.12 [225]. Since the wavefronts transmitted by the two axes of the doubly refractive prism are orthogonally polarized upon exit, a polarizer with its polarization axis oriented at an azimuth of 45 degrees is placed between prism and camera target, enabling interference of the two now colinear waves. The longitudinal image shift has to be treated in the same way as with the beam splitter cube.

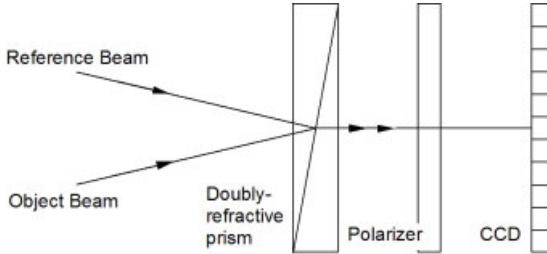


Figure 3.12: Beam combination by doubly refractive prism.

3.2 Numerical Reconstruction by the Fresnel Transform

In this chapter the *numerical reconstruction* of digitally recorded holograms is addressed. Although the captured digital hologram can be fed to a spatial light modulator enabling an optical reconstruction of the recorded wave field [226, 227], here we concentrate on the numerical calculation of the wave field. The general coordinate system for the description of the generation of holograms as well as the reconstruction of the real and virtual images is introduced. The theoretical tool for the numerical reconstruction is the scalar diffraction theory that was already introduced in Section 2.4. In this section we confine ourselves to the Fresnel approximation of the diffraction integral which is feasible due to the sufficient distance between object and CCD-array, and which on the other hand enables one easily to handle reconstruction procedures. The continuous formulas are transferred into finite discrete algorithms which can be implemented in digital image processing systems. The parameters of the resulting numerically expressed wave fields and the corresponding digital images are specified, the roles of the real and virtual images are explained, and the influence of the various possible reference waves is studied. The d.c.-term in the reconstructed image is analyzed and a method to suppress the d.c.-term is presented. At this point we will encounter the concept of negative intensities, which becomes possible numerically, but has no physical counterpart in real-world optics.

3.2.1 Wave Field Reconstruction by the Finite Discrete Fresnel Transform

Let us assume an opaque diffusely reflecting object that is illuminated by a coherent wave field. The object surface contour may be denoted by $F(x, y, z) = 0$, it is illuminated by the wave field $E(x, y, z) = |E(x, y, z)|e^{i\alpha(x, y, z)}$. The reflection of the surface is described by the complex reflection coefficient $b(x, y, z)$

$$b(x, y, z) = |b(x, y, z)|e^{i\beta(x, y, z)} \quad (3.27)$$

where b and β indicate the variation of amplitude and phase by the surface. However, for our purposes it is sufficient to consider the object surface as a self-luminescent object, where each surface point (x, y, z) emits a spherical wavelet $b(x, y, z)$. Since we assumed a diffusely scattering object, the phases $\beta(x, y, z)$ are random; this characteristic is not changed by the

illuminating wave $E(x, y, z)$. Therefore it is sufficient to describe the object surface by the complex amplitude $b(x, y, z)$ of (3.27).

Let the geometry for the numerical description be as in Fig. 3.13. To keep the analysis simple the object surface is approximately flat, that means the z in $b(x, y, z)$ is constant. The microstructure of the rough surface is only contained in the stochastic phase β . A distance d apart from the object surface we have the recording medium, the hologram plate or in the digital case the CCD target. The plane of the recording medium has the coordinates (ξ, η) .

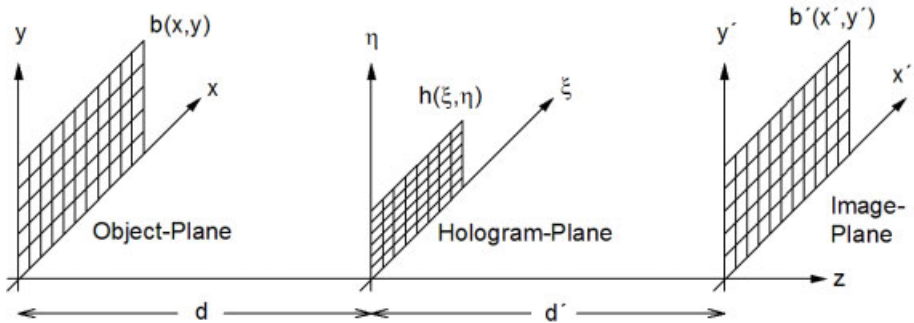


Figure 3.13: Geometry for digital holography.

At distance d' from this hologram plane we have the image plane also named the observation plane where the real image can be reconstructed. The coordinates of this plane are chosen as (x', y') . While the object is denoted by $b(x, y)$, the corresponding field in the hologram plane is $B(\xi, \eta)$. Its superposition with the reference wave field $r(\xi, \eta)$ by interference produces a wave field whose intensity distribution $h(\xi, \eta)$ is recorded by the CCD-array, see (2.122). After recording this real distribution, $h(\xi, \eta)$ is stored in a quantized and digitized form in the computer. Numerical evaluation then produces the complex distribution $b'(x', y')$ which represents the reconstructed image.

Let us start our analysis with the complex amplitude distribution $b(x, y)$ in the object plane. In most holographic applications its distance from the hologram plane is far enough that the Fresnel approximation can be applied. Therefore according to (2.73) in the hologram plane we obtain by diffraction the complex field

$$B(\nu, \mu) = \frac{e^{ikd}}{i\lambda d} e^{i\pi d\lambda(\nu^2 + \mu^2)} \iint b(x, y) e^{\frac{i\pi}{d\lambda}(x^2 + y^2)} e^{-2i\pi(x\nu + y\mu)} dx dy \quad (3.28)$$

with the correspondence

$$\nu = \frac{\xi}{d\lambda} \quad \mu = \frac{\eta}{d\lambda} \quad (3.29)$$

between the coordinates (ξ, η) in the hologram plane and the spatial frequencies (ν, μ) . The constant factor $e^{ikd}/(i\lambda d)$ does not depend on the spatial frequency coordinates nor the special object, so it will be omitted in the following.

In practical applications the pixel numbers N, M and the pixel distances $\Delta\xi, \Delta\eta$ are given by the CCD array at hand. So in the following discussion these are the fundamental parameters to which the others are related. In the hologram plane we have the discrete coordinates

$$\begin{aligned}\xi &= n \Delta\xi & n &= 1, \dots, N \\ \eta &= m \Delta\eta & m &= 1, \dots, M.\end{aligned}\quad (3.30)$$

With the given parameters in the object plane we have the step widths

$$\Delta x = \frac{1}{N\Delta\nu} = \frac{d\lambda}{N\Delta\xi} \quad \Delta y = \frac{1}{M\Delta\mu} = \frac{d\lambda}{M\Delta\eta}. \quad (3.31)$$

In the (ξ, η) -plane the discrete reference wave model $r(n\Delta\xi, m\Delta\eta)$ is superposed, the resulting intensity $h(n\Delta\xi, m\Delta\eta)$ is recorded as the digital hologram

$$h = (B + r)(B + r)^*. \quad (3.32)$$

The reconstruction of the real and virtual images in optics would require the illumination of the hologram by the reference wave. This process now is modeled numerically by a multiplication of the digital hologram h with the reference wave. Since we want to obtain a real image we have to multiply the digital hologram with the conjugate $r^*(\xi, \eta)$ of the reference wave, see (2.137). The real image in the (x', y') -plane is determined by the diffraction formula that is approximated by the inverse Fresnel transform (2.73). To yield a sharp image we must choose $d' = d$. The z of (2.73) is replaced directly by d and not by d' to avoid confusion.

$$\begin{aligned}b'(\delta, \varepsilon) &= e^{\frac{i\pi}{d\lambda}(x'^2 + y'^2)} \iint h(\xi, \eta) r^*(\xi, \eta) e^{\frac{i\pi}{d\lambda}(\xi^2 + \eta^2)} e^{-\frac{2i\pi}{d\lambda}(x'\xi + y'\eta)} d\xi d\eta \\ &= e^{i\pi d\lambda(\delta^2 + \varepsilon^2)} \iint h(\xi, \eta) r^*(\xi, \eta) e^{\frac{i\pi}{d\lambda}(\xi^2 + \eta^2)} e^{-2i\pi(\xi\delta + \eta\varepsilon)} d\xi d\eta\end{aligned}\quad (3.33)$$

where we used the substitutions

$$\delta = \frac{x'}{d\lambda} \quad \varepsilon = \frac{y'}{d\lambda}. \quad (3.34)$$

With these substitutions we can clearly recognize that despite of a phase factor which does not depend on the specific hologram the field is calculated by a Fourier transform of the digital hologram $h(\xi, \eta)$ multiplied with the reference wave $r^*(\xi, \eta)$ and also multiplied with the chirp function $\exp[i\pi(\xi^2 + \eta^2)/(d\lambda)]$.

The discrete version of (3.33) is

$$\begin{aligned}b'(n\Delta\delta, m\Delta\varepsilon) &= e^{i\pi d\lambda(n^2\Delta\delta^2 + m^2\Delta\varepsilon^2)} \\ &\cdot \sum_{k=0}^{N-1} \sum_{l=0}^{M-1} h(k\Delta\xi, l\Delta\eta) r^*(k\Delta\xi, l\Delta\eta) e^{\frac{i\pi}{d\lambda}(k^2\Delta\xi^2 + l^2\Delta\eta^2)} e^{-2i\pi(\frac{kn}{N} + \frac{lm}{M})}.\end{aligned}\quad (3.35)$$

Due to (3.31) and

$$\Delta\delta = \frac{1}{N\Delta\xi} = \frac{\Delta x'}{d\lambda} \quad \Delta\varepsilon = \frac{1}{M\Delta\eta} = \frac{\Delta y'}{d\lambda} \quad (3.36)$$

the pixel spacing in the real image coincides with the pixel spacing in the object plane

$$\Delta x' = \Delta x \quad \text{and} \quad \Delta y' = \Delta y. \quad (3.37)$$

The reconstruction formula (3.35) now expressed with $\Delta\xi$ and $\Delta\eta$, the fundamental parameters, is the *central reconstruction formula of digital holography*

$$b'(n\Delta x', m\Delta y') = e^{i\pi d\lambda(\frac{n^2}{N^2\Delta\xi^2} + \frac{m^2}{M^2\Delta\eta^2})} \cdot \sum_{k=0}^{N-1} \sum_{l=0}^{M-1} h(k\Delta\xi, l\Delta\eta) r^*(k\Delta\xi, l\Delta\eta) e^{\frac{i\pi}{d\lambda}(k^2\Delta\xi^2 + l^2\Delta\eta^2)} e^{-2i\pi(\frac{kn}{N} + \frac{lm}{M})}. \quad (3.38)$$

If the plane normally impinging reference wave field $r(\xi, \eta) = 1.0$ is employed, then the multiplication with $r^*(k\Delta\xi, l\Delta\eta)$ in (3.38) can be omitted.

Formula (3.38) constitutes the practical discrete finite calculation method on the basis of the Fresnel transform for the reconstruction of the wave field coded in a digital hologram. The result $b'(n\Delta x', m\Delta y')$ is a numerical representation of a complex optical wave field from which by

$$I(n\Delta x', m\Delta y') = |b'(n\Delta x', m\Delta y')|^2 \quad (3.39)$$

$$\text{and} \quad \phi(n\Delta x', m\Delta y') = \arctan \frac{\text{Im}\{b'(n\Delta x', m\Delta y')\}}{\text{Re}\{b'(n\Delta x', m\Delta y')\}} \quad (3.40)$$

intensity and phase distributions can be determined. This is a real advantage compared to the optical reconstruction, because in the optical case we only obtain the intensity distribution. In the digital case we also have access to the phase modulo 2π , which at first glance seems to be of no concern, because for rough object surfaces it varies stochastically. But we will see that the phase access makes up a real advantage when we come to applications in digital holographic interferometry [228], see Section 5.8.

From (3.36) we get the pixel size

$$\Delta x' = \frac{d\lambda}{N\Delta\xi} \quad \Delta y' = \frac{d\lambda}{M\Delta\eta}. \quad (3.41)$$

For this special relation it is possible to have the last exponential of (3.35) and (3.38) in the form $\exp\{-2i\pi(kn/N + lm/M)\}$. This form enables the use of the FFT-algorithm. If we want another pixel size we have to use (3.33) and find the discrete version

$$b'(n\Delta\delta, m\Delta\varepsilon) = e^{i\pi d\lambda(n^2\Delta\delta^2 + m^2\Delta\varepsilon^2)} \sum_{k=0}^{N-1} \sum_{l=0}^{M-1} h(k\Delta\xi, l\Delta\eta) r^*(k\Delta\xi, l\Delta\eta) \times e^{\frac{i\pi}{d\lambda}(k^2\Delta\xi^2 + l^2\Delta\eta^2)} e^{-2i\pi(k\Delta\xi n\Delta\delta + l\Delta\eta m\Delta\varepsilon)} \quad (3.42)$$

but now we have to perform all the complex multiplications under the double sum without the effective acceleration by the FFT-algorithm.

The fundamental array parameters N and M , $\Delta\xi$ and $\Delta\eta$ define the number and distances of the pixels in the reconstructed images. The reconstructed image in the case of Fresnel reconstruction displays a field of size

$$N\Delta x \times M\Delta y = \frac{d\lambda}{\Delta\xi} \times \frac{d\lambda}{\Delta\eta}. \quad (3.43)$$

It normally is displayed in the full frame of the monitor of the image processing system.

A remarkable fact is that the pixel distances $\Delta x' = \Delta x$ and $\Delta y' = \Delta y$ depend on the wavelength λ and the reconstruction distance $d' = d$ (3.41), if the Fresnel transform is employed while N , M , $\Delta\xi$, and $\Delta\eta$ are predetermined constants.

An example is given in Fig. 3.14.

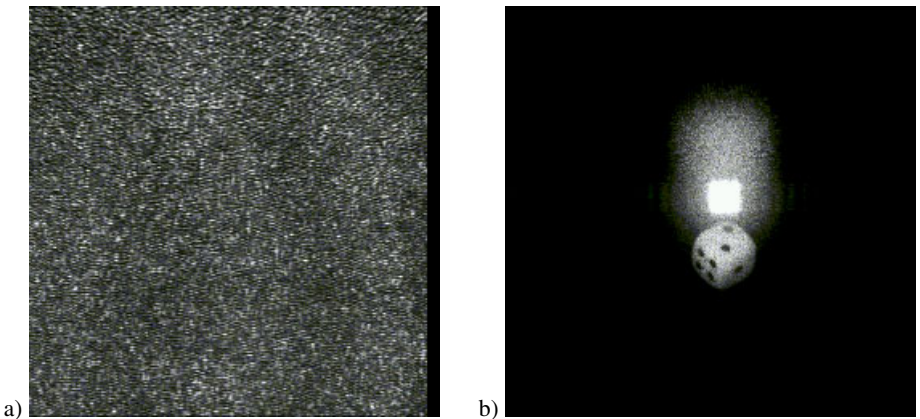


Figure 3.14: Digital Fresnel hologram (a) and numerically reconstructed intensity (b) of a die.

A Kodak Megapixel 1.4 camera was used to record the digital hologram shown in Fig. 3.14a. The lens system of the camera was removed to admit the direct impinging of the wave fields onto the CCD array. The array parameters in this application are $N = M = 1024$, $\Delta\xi = \Delta\eta = 6.8 \mu\text{m}$. The object is $d = 1.054 \text{ m}$ apart from the array and the He-Ne laser used has a wavelength $\lambda = 0.6328 \mu\text{m}$. This results in a reconstructed image field of width $N \times \Delta x' = 1024 \times 95.8 \mu\text{m} = 98 \text{ mm}$ in both directions. The intensity distribution calculated from the $b'(n\Delta x', m\Delta y')$ that was reconstructed using the Fresnel approximation is given in Fig. 3.14b. What we can recognize is the rather sharp real image of the object, a die, the central bright d.c.-term and a cloudlike phenomenon above the center, which is the unsharp virtual image of the object. The calculated intensity values are mapped to the gray values of the image processing system in a way that the structure of the object is clearly detectable. The range between properly chosen upper and lower thresholds to the intensity is mapped linearly to the full range of the display's gray values from black to white.

3.2.2 Real and Virtual Image

The optical reconstruction of the wave fields from the hologram by illumination with the reference wave produces simultaneously a real and a virtual image. The *real image* corresponds

to a wavefront converging to a sharp image, while the *virtual image* belongs to a divergent wavefront that seems to be emitted from the object as it was located during recording of the hologram. Therefore a registration of the virtual image always requires an optical system to transform the divergent wave field into a convergent one. Typical examples for such optical systems are the lens in the observer's eye or the objective of a camera.

In the same way the numerical reconstruction in digital holography by multiplication with the reference wave field produces the converging and the diverging wave fields simultaneously. The reconstruction into the image plane, $d' = d$, yields a sharp real image accompanied by an unsharp virtual image. But also the virtual image can be numerically reconstructed: Imagine a convex lens of focal length f placed directly behind the hologram. According to the lens equation

$$\frac{1}{f} = \frac{1}{d} + \frac{1}{d'} \quad (3.44)$$

with an object distance d and an image distance d' for a magnification of 1 we obtain $d' = d$ and thus $f = d/2$. The phase transformation by this lens is given by (2.85) as

$$t_l(\xi, \eta) = \exp \left[-\frac{i2\pi}{\lambda d} (\xi^2 + \eta^2) \right]. \quad (3.45)$$

We can now calculate the field in the (x', y') -plane by (3.38) considering the field

$$h(\xi, \eta)r^*(\xi, \eta)e^{-\frac{i2\pi}{\lambda d}(\xi^2 + \eta^2)} \quad (3.46)$$

instead of $h(\xi, \eta)r^*(\xi, \eta)$ in the hologram plane as demanded by (2.86). In (3.38) now the exponential terms stemming from the assumed lens and the chirp function can be combined

$$\begin{aligned} h(k\Delta\xi, l\Delta\eta)r^*(k\Delta\xi, l\Delta\eta)e^{-\frac{i2\pi}{\lambda d}(k^2\Delta\xi^2 + l^2\Delta\eta^2)} e^{\frac{i\pi}{d\lambda}(k^2\Delta\xi^2 + l^2\Delta\eta^2)} \\ = h(k\Delta\xi, l\Delta\eta)r(k\Delta\xi, l\Delta\eta)e^{-\frac{i\pi}{\lambda d}(k^2\Delta\xi^2 + l^2\Delta\eta^2)}. \end{aligned} \quad (3.47)$$

We see that we only have to exchange d in the reconstruction by $-d$ under the double sum. The sign of d in the exponential preceding the double sum is not altered, but this would only change the global sign of the phase and does not influence the intensity at all. The reconstruction of the virtual image thus can be interpreted as the numerical calculation of the field in the $(z = -d)$ -plane, which is the object plane according to Fig. 3.13.

The reconstructed intensity fields at different distances, positive and negative, from the hologram are displayed in Fig. 3.15.

The hologram used for these reconstructions is the one shown already in Fig. 3.14a. The real image that is reconstructed at $d = 1.054$ m is given in Fig. 3.15a, the intensity fields corresponding to $d = 0.79$ m in Fig. 3.15b, to $d = 0.527$ m in Fig. 3.15c, $d = -0.527$ m in Fig. 3.15d, $d = -0.79$ m in Fig. 3.15e, and the virtual image at $d = -1.054$ m in Fig. 3.15f. We recognize the sharp real and virtual images in the image and object plane, respectively, and the unsharp images reconstructed in the counterparts of these planes. Since there is no significant difference between real and virtual image besides a 180° rotation, both are often summarized as the *twin images*.

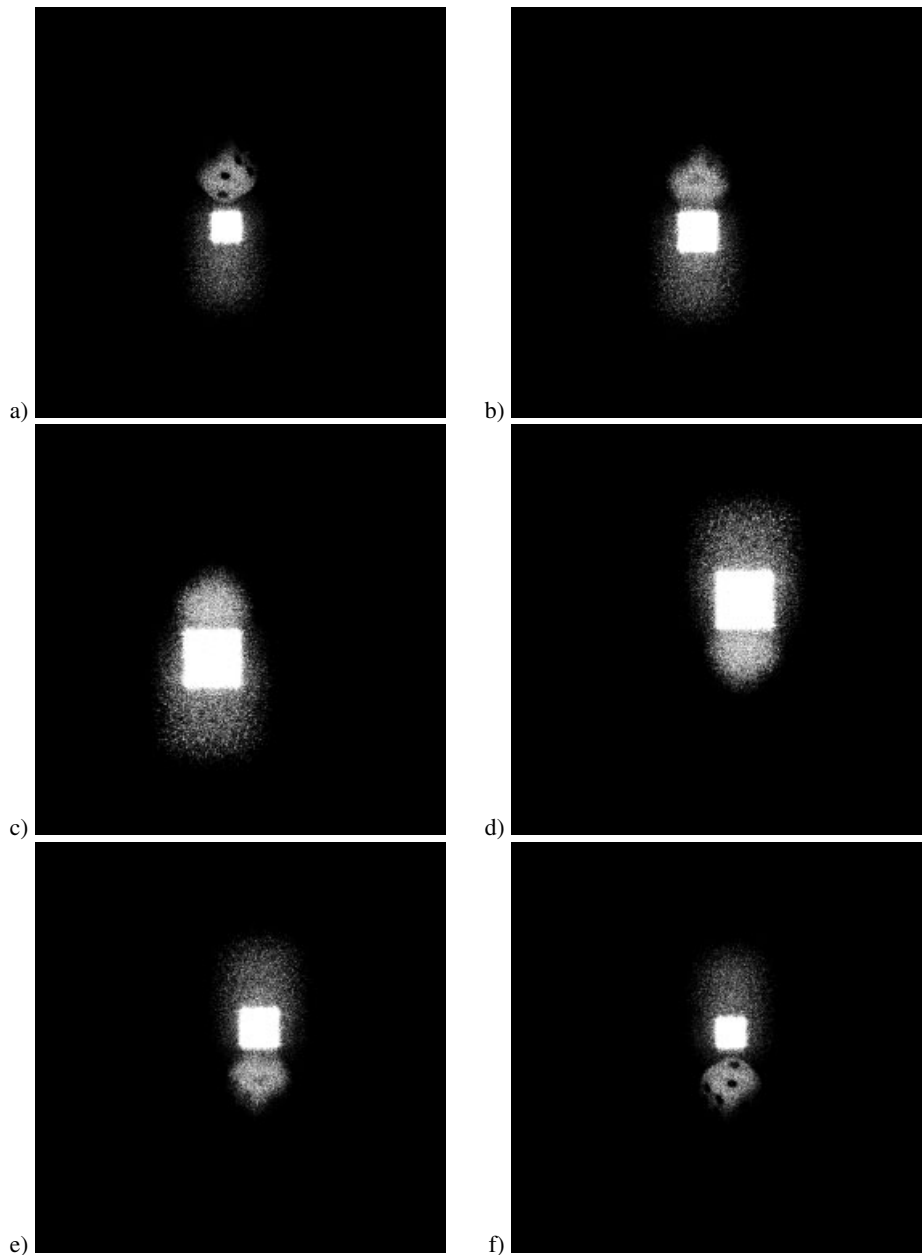


Figure 3.15: Variation of reconstruction distance.

We have seen in Section 3.1.3 that there is a basic difference between using plane and spherical reference waves. When a spherical wave is divergent from a source point placed on

the same side of the hologram as the object, then a multiplication of the digital hologram with the original reference wave yields a divergent wave field emanating from the virtual image in the object plane. This must be reflected in the choice of the reconstruction plane: we must use the $-d$ for the object plane. On the other hand if we calculate the real image at distance $+d$, we must use the conjugate of the original reference wave (3.23). However, this choice is rather arbitrary as we have seen that both reconstructed wave fields are identical up to a 180° -rotation. For the plane wave the distinction between direct and conjugated wave has no meaning, so we do not have to consider it in this case.

If in practical experiments the distance d was not exactly measured when arranging the holographic setup, the distance yielding the sharpest image can be identified in an iterative search. Generally we notice that real and virtual images carry the same information, so in practical measurements one may use either of them.

3.2.3 Digital Fourier Transform Holography

In Section 2.6.4 we met Fourier transform holography and recognized some advantages like the stationary reconstructed image and the weaker resolution requirements imposed on the recording medium. This makes that option interesting for digital holography. The transforming lens can be omitted by placing the source point of the reference wave as in the arrangement for *lensless Fourier transform holography*. So let us use the geometry shown in Fig. 3.16 and assume a spherical reference wave diverging from a point R directly beside the object.

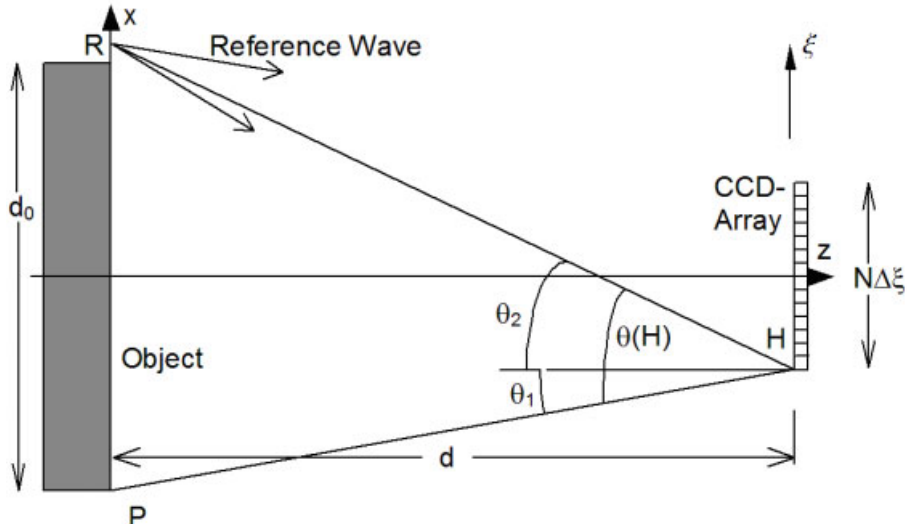


Figure 3.16: Geometry for recording a digital lensless Fourier transform hologram.

We obtain the maximum angle θ at any hologram point H for the object point P furthest away from to the source point R . The angle θ is $\theta = \theta_1 + \theta_2$ with

$$\begin{aligned}\theta_1 \approx \tan \theta_1 &= \frac{\frac{d_0}{2} + \frac{N\Delta\xi}{2}}{d} \\ \theta_2 \approx \tan \theta_2 &= \frac{\frac{d_0}{2} - \frac{N\Delta\xi}{2}}{d}\end{aligned}\quad (3.48)$$

resulting in

$$\theta = \theta_1 + \theta_2 = \frac{d_0}{d}. \quad (3.49)$$

Now the sampling theorem demands

$$\frac{d_0}{d} < \frac{\lambda}{2\Delta\xi} \quad (3.50)$$

which gives a minimum distance d for a given lateral width d_0 of the object

$$d(d_0) > \frac{2d_0\Delta\xi}{\lambda} \quad (3.51)$$

or a maximum width of the object d_0 for a given distance d

$$d_0(d) < \frac{d\lambda}{2\Delta\xi}. \quad (3.52)$$

Now we compare the minimum distance d_N for a normally impinging plane reference wave as given in (3.12) with the minimum distance between object and CCD-array d_{LFTH} in lensless Fourier transform holography, which is given in (3.51). We see that the limit $2d_0\Delta\xi/\lambda$ is less than $(d_0\Delta\xi + N\Delta\xi^2)/\lambda$ if $d_0 < N\Delta\xi$. This means that for objects with lateral dimensions less than those of the CCD-array, a smaller distance between object and CCD-array is allowed in lensless Fourier transform holography. This is particularly important in digital holographic microscopy: While for the plane reference wave the distance is always larger than $N\Delta\xi^2$ for any d_0 , in the case of lensless Fourier transform holography this limit decreases linearly with decreasing object size.

In lensless Fourier transform holography each object point is encoded in a fringe system with a spatial frequency that is proportional to the distance of that point from the reference point [160]. This is shown in Fig. 3.17a: For each point P the angle $\theta(P, H)$ remains nearly constant over the hologram points H . We have seen, Section 2.8.4, that the *MTF* results in an increasing attenuation for increasing spatial frequencies. Therefore now this attenuation will increase for points P further from the reference points, because their $\theta(P, H)$ is larger producing higher spatial frequencies. Thus the *MTF* can be interpreted as an attenuating mask placed over the object, or equivalently over the real and virtual image [160]. The intensity decrease at the borders of the reconstructed picture due to a 100% fill factor of the CCD pixels is analyzed in [229]. Nevertheless a vignetting is not expected, because the Nyquist frequency f_N is always less than the frequency f_{DC} , where the *MTF* falls to zero, see Figs. 3.17a or b.

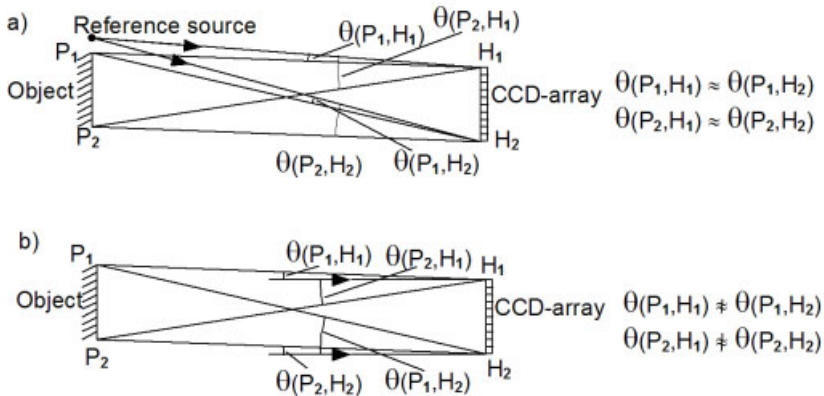


Figure 3.17: Divergent (a) and plane (b) reference waves.

These facts which hold for lensless Fourier transform holography are not valid for collimated reference waves, because there the angle $\theta(P, H)$ for each object point varies significantly with H , Fig. 3.17b. There the influence of the *MTF* on the image cannot be described in an easy fashion. The introduction of an aperture for reducing the imaging angle – see Section 3.1.2 – in lensless digital Fourier transform holography is treated in [221–223].

3.2.4 The D.C.-Term of the Fresnel Transform

In the intensity displays of the holographic reconstructions of Fig. 3.14b and Fig. 3.15 we recognize a bright central square. It is much brighter than the reconstructed real or virtual images, for the display its intensity has been clipped to enhance the eligibility of the overall pattern. The physical meaning of the bright central square is that it represents the zero-order diffraction of the reference wave or equivalently it is the projection of the illuminated CCD array. From the optical point of view it is the undiffracted part of the reconstructing reference wave; from the computational standpoint it is the *d.c.-term* of the Fresnel transform, as can be seen in the following.

If we neglect the factors before the integrals of (3.33) or the sums of (3.38), which only affect the phase in a way independent of the specific hologram, the Fresnel transform is the Fourier transform of a product, the factors being the hologram times the reference wave $h \cdot r^*$ and the chirp function. According to the convolution theorem this gives the same result as the convolution of the Fourier transforms of the individual factors. The Fourier transform H of the hologram multiplied with the reference wave $h(k\Delta\xi, l\Delta\eta) \cdot r^*(k\Delta\xi, l\Delta\eta)$ generally is trimodal with a high-amplitude peak at the spatial frequency $(0, 0)$. This d.c.-term $H(0, 0)$, whose value is calculated by

$$H(0, 0) = \sum_{k=0}^{N-1} \sum_{l=0}^{M-1} h(k\Delta\xi, l\Delta\eta) r^*(k\Delta\xi, l\Delta\eta), \quad (3.53)$$

can be modeled by a Dirac delta function. The d.c.-term of the Fresnel transform now is the d.c.-term of the Fourier transform of the digital hologram multiplied by the reference

wave convolved with the Fourier transform of the two-dimensional chirp function. Since we assume a Dirac delta function for the former, the d.c.-term of the whole Fresnel transform is the Fourier transform of the finite chirp function

$$e^{\frac{i\pi}{\lambda d}(k^2\Delta\xi^2 + l^2\Delta\eta^2)} = e^{\frac{i\pi}{\lambda d}k^2\Delta\xi^2} e^{\frac{i\pi}{\lambda d}l^2\Delta\eta^2} \quad (3.54)$$

restricted to the finite extent of the hologram.

The Fourier transform $G(x')$ of the finite chirp function $g(\xi)$ is investigated in Appendix A.13. Only the coordinates in the results of Appendix A.13 must be modified. For the one-dimensional function $\exp[(i\pi/d\lambda)k^2\Delta\xi^2]$, $k = 0, \dots, N-1$ we translate $\beta = \Delta\xi^2/(d\lambda)$, $\xi = k$, and $2L = N$. Then the d.c.-term has a width of $2\pi N\Delta\xi^2/(d\lambda)$. If we count the spatial frequencies $2\pi n/N$ by the corresponding pixel numbers $n = 0, \dots, N-1$, we obtain the width of the d.c.-term expressed in the experimental parameters extending over $N^2\Delta\xi^2/(d\lambda)$ pixels. In two dimensions this gives the area of the d.c.-term as

$$\frac{N^2\Delta\xi^2}{d\lambda} \times \frac{M^2\Delta\eta^2}{d\lambda} \quad (3.55)$$

with $N^2\Delta\xi^2/(d\lambda)$ being the width in the x' -direction and $M^2\Delta\eta^2/(d\lambda)$ that in the y' -direction. The width of the d.c.-term increases with increasing pixel dimensions and pixel number of the CCD target and it decreases with increasing distance d . This effect can be seen in Fig. 3.15, where different reconstruction distances d have been used. For the limiting case of infinite d we have the d.c.-term of the Fourier transform which covers only a single pixel.

Also in Section A.13 it is investigated how a shift of the finite chirp function influences the location of its Fourier spectrum and thus the d.c.-term. If we reconstruct using (3.38), the hologram is defined in $[0, N\Delta\xi] \times [0, M\Delta\eta]$, so the chirp function $\exp(\frac{i\pi}{d\lambda}k^2\Delta\xi^2) \exp(\frac{i\pi}{d\lambda}l^2\Delta\eta^2)$ carries local frequencies from 0 to $N\Delta\xi/(d\lambda\pi)$ in the ξ -direction and from 0 to $M\Delta\eta/(d\lambda\pi)$ in the η -direction. The square d.c.-term is located totally in the first quadrant starting at $(0, 0)$. The display normally is reordered so that the d.c.-term appears in the center of the pattern as we are used to from optics, e. g. with holographic reconstructions or with Fraunhofer diffraction patterns.

As can be seen in Fig. 3.15 after reordering the edge point of the square d.c.-term coming from $(0, 0)$ is shifted for all reconstruction distances to the central point while the other edge points reflect the varying size of the d.c.-term due to the different d . If we shift the finite chirp function by say $k_0\Delta\xi$ in the ξ -direction and $l_0\Delta\eta$ in the η -direction, we obtain

$$\exp\left[\frac{i\pi}{d\lambda}(k - k_0)^2\Delta\xi^2\right] \exp\left[\frac{i\pi}{d\lambda}(l - l_0)^2\Delta\eta^2\right] \quad (3.56)$$

which carries local frequencies from $-k_0\Delta\xi/(d\lambda\pi)$ to $(N\Delta\xi - k_0\Delta\xi)/(d\lambda\pi)$ and from $-l_0\Delta\eta/(d\lambda\pi)$ to $(M\Delta\eta - l_0\Delta\eta)/(d\lambda\pi)$ in the two directions. If k_0 is between $-N$ and $+N$ (l_0 between $-M$ and $+M$) the d.c.-term in the reconstruction is divided to the four edges of the display before reordering. The location of the d.c.-term is demonstrated in Fig. 3.18.

The real part of the unshifted, $k_0 = l_0 = 0$, chirp function is shown in Fig. 3.18a, the resulting virtual image has a d.c.-term totally in the upper right corner before reordering, Fig. 3.18b. It is in the third quadrant after reordering, Fig. 3.18c. The real part of the shifted chirp function with $k_0 = N/2$, $l_0 = M/2$ is given in Fig. 3.18d. Here the d.c.-term is divided into equally sized parts at all four corners before reordering, Fig. 3.18e. It appears in the center of the image after reordering, Fig. 3.18f.

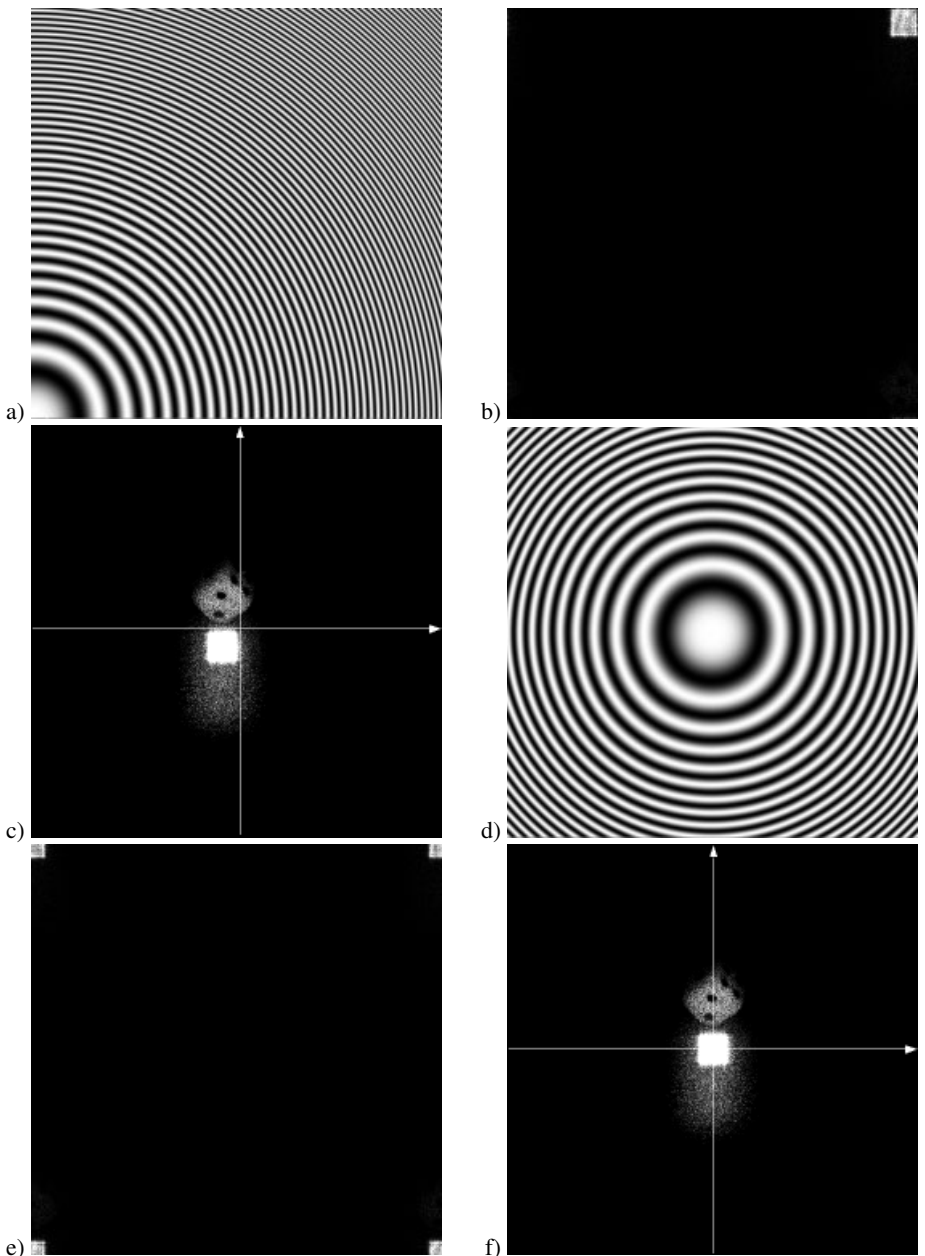


Figure 3.18: Shift of the chirp function and location of the d.c.-term.

3.2.5 Suppression of the D.C.-Term

In digital holography we encounter the same problem as in optical holography: the zero-order image, also called the d.c.-term, and the conjugate image, also known as the twin image. While in the original Gabor in-line geometry these images degrade the true image severely, the off-axis geometry introduced by Leith and Upatnieks separated these three images and made holography and holographic interferometry feasible. Nevertheless the d.c.-term is of no practical use but due to its high intensity compared to the real image it disturbs the reconstructed field by affecting the dynamic range of the display. The twin image also is of no use, but it reduces the size of the real image area in the total reconstructed field. But contrary to the optical case in digital holography there exist some effective numerical methods to eliminate the d.c.-term and the twin image.

A number of procedures for eliminating the two disturbing terms have been suggested: some are purely numerical, some require additional experimental effort, so these latter methods can be interpreted as hybrid methods. In Section 3.4.1 we present phase shifting digital holography. This makes necessary the recording of several phase shifted digital holograms from which the complex distribution in the hologram plane is calculated. When starting with this distribution the real image is determined, no d.c.-term or twin image arise.

The separate recording of the object wave intensity and of the reference wave intensity alone and their subtraction from the recorded digital hologram is described in [101]. The introduction of an additional deterministic phase [101] or a stochastic phase [230] and the subtraction of the digital hologram recorded with this additional phase from that without this phase also leads to a suppression of the unwanted terms. While these hybrid methods require the modification of the holographic arrangement – shutter, phase modulator – as well as the recording of multiple digital holograms of the same scene, the following purely numerical methods only use a single digital hologram.

A digital filtering technique suppressing the d.c.-term and the twin image in digital in-line holography has been presented by Onural [130]. However, this technique can be used only when the object to be reconstructed has a real-valued transmittance function.

In the following we present a method that is a numerical one and can be applied to any type of digital hologram [231]. The numerical treatment of the twin image is postponed to the next section.

Once we have access to the recorded hologram multiplied with the reference wave $h(k\Delta\xi, l\Delta\eta)r^*(k\Delta\xi, l\Delta\eta)$ we can calculate the average intensity

$$h_m = \frac{1}{NM} \sum_{k=0}^{N-1} \sum_{l=0}^{M-1} h(k\Delta\xi, l\Delta\eta)r^*(k\Delta\xi, l\Delta\eta). \quad (3.57)$$

This average intensity we now subtract from each stored hologram intensity value, yielding the modified digital hologram h'

$$\begin{aligned} h'(k\Delta\xi, l\Delta\eta) &= h(k\Delta\xi, l\Delta\eta)r^*(k\Delta\xi, l\Delta\eta) - h_m \\ k &= 0, \dots, N-1; \quad l = 0, \dots, M-1. \end{aligned} \quad (3.58)$$

As a consequence the d.c.-term in the Fourier spectrum of h' calculated by (3.53) is zero. The convolution of a zero d.c.-term with any kernel – here the transform of the finite chirp function

– remains zero. With the modified hologram h' we can determine the real or virtual images as usual but now the d.c.-term is effectively suppressed. Let us for the moment assume the plane normally impinging reference wave $r = 1.0$. While the hologram h has only positive intensities, h' exhibits negative intensities as well. Although optically impossible, numerically this concept is feasible. The relations between the intensities of the individual pixels remain the same, only the whole hologram is downshifted in intensity by performing (3.58).

One may interpret this way of suppressing the d.c.-term as the application of a high-pass filter with a cutoff frequency just equal to the smallest nonzero frequency: Only the spatial frequency $(0, 0)$ is suppressed. Therefore other high-pass filters suppressing the smallest spatial frequencies can be employed to achieve comparable effects. In this way good results have been realized by the high-pass filter that is defined by the subtraction of the averages over each 3×3 pixel neighborhood from the original digital hologram:

$$\begin{aligned} h'(k, l) &= h(k, l) - \frac{1}{9} [h(k-1, l-1) + h(k-1, l) + h(k-1, l+1) \\ &\quad + h(k, l-1) + h(k, l) + h(k, l+1) \\ &\quad + h(k+1, l-1) + h(k+1, l) + h(k+1, l+1)] \\ &\quad k = 2, \dots, N-1; \quad l = 2, \dots, M-1. \end{aligned} \quad (3.59)$$

The factors $\Delta\xi$, $\Delta\eta$ in the pixel arguments have been omitted for convenience.

A special case of a high-pass filter in two dimensions is the Laplacian \mathcal{L} , which resembles the second derivative

$$\mathcal{L}\{f(x, y)\} = \nabla^2 f(x, y) = \frac{\partial^2 f(x, y)}{\partial x^2} + \frac{\partial^2 f(x, y)}{\partial y^2}. \quad (3.60)$$

Its discrete version applied to the digital hologram $h(k, l)$ is calculated by

$$\begin{aligned} \mathcal{L}\{h(k, l)\} &= \frac{1}{\Delta\xi \Delta\eta} [4h(k, l) - h(k+1, l) \\ &\quad - h(k-1, l) - h(k, l+1) - h(k, l-1)]. \end{aligned} \quad (3.61)$$

Liu et al. [81] have shown that the Fourier transform of the modified hologram $h'(k, l) = \mathcal{L}\{h(k, l)\}$ is of the form

$$\mathcal{F}\{h'(k, l)\}(u, v) = 4 \left[\frac{\sin^2(\pi\Delta\xi u)}{\Delta\xi} + \frac{\sin^2(\pi\Delta\eta v)}{\Delta\eta} \right] \mathcal{F}\{h(k, l)\}(u, v) \quad (3.62)$$

if the hologram intensity is written $h(x, y) = I_R + I_0 + \sqrt{I_R I_0} \cos(kr + \tau)$ as in (2.122). The sum of the squared sines is a factor that is zero for zero-frequency and slowly varying, thus suppressing the zero and low-frequency terms but leaving intact the $+1$ and -1 diffraction orders giving the real and virtual images at least if they are separated well from the d.c.-term.

An example demonstrating the effective suppression of the d.c.-term is shown in Fig. 3.19. The reconstructed object in Fig. 3.19a is nearly totally obscured by the d.c.-term, but after suppression of the d.c.-term it is clearly visible in Fig. 3.19b. The advantages of this approach will become even more evident in Section 5.8. The presented procedures for suppressing the d.c.-term are a central option in software packages for performing digital holography, e. g. [232].

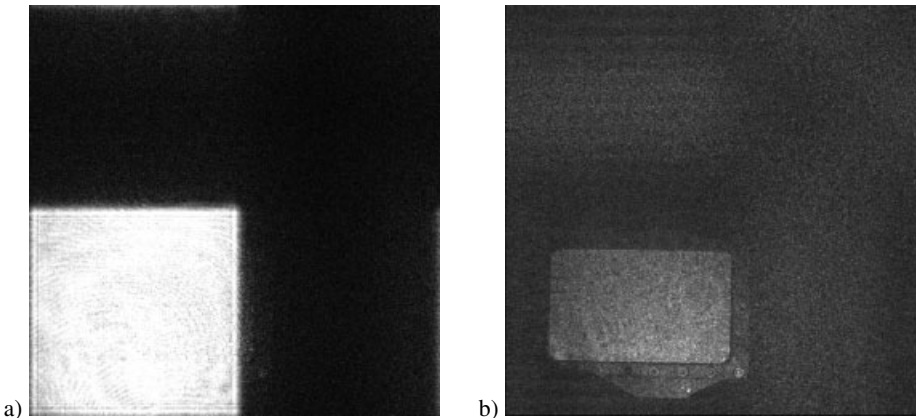


Figure 3.19: Reconstructed real image intensity without (a) and with (b) suppression of the d.c.-term.

3.2.6 Suppression of the Twin Image

We have seen how we can effectively suppress the disturbing d.c.-term by eliminating the zero-frequency or low-frequency spectral components of the digital hologram. This idea in many cases can be extended to eliminate also the disturbing twin image [127]. If the object is placed completely outside the optical axis so that the twin images in the reconstructed frame will not overlap, then the amplitude spectrum of the digital hologram will consist of two symmetrically placed distinct partial spectra [111, 233]. One of these contains the frequencies leading to the real image, the other contains those responsible for the virtual image. So we can set to zero the frequencies of the virtual image, and in the reconstructed frame only the real image remains. Although the digital hologram is real, the filtered hologram now is a complex one. This approach exhibits similarities to the old Fourier transform evaluation of holographic interferograms.

An example of this approach to twin image suppression is given in Fig. 3.20 using the hologram already displayed and reconstructed in Fig. 3.14. In Fig. 3.20a we see the reconstructed image after high-pass filtering using the filter defined in (3.59). We still recognize the unsharp twin image. The complete amplitude spectrum of the filtered hologram is shown in Fig. 3.20b. Due to the high-pass filter applied before the transformation, there is no central zero-frequency peak, also the low frequencies are severely damped. One half of the spectrum is set to zero, leaving only one partial spectrum, Fig. 3.20c. This operation is performed to the complex spectrum, an inverse Fourier transform gives the filtered hologram. The intensity reconstructed from this hologram shows only the real image, Fig. 3.20d.

One must admit that this twin image elimination is of pure cosmetic nature because the twin images must be well separated, but then they do not conflict with each other. The concept is extended further to multiplexed holograms in a later section.

A constrained iterative twin image elimination algorithm for digital in-line holograms also dealing with the noise introduced by inappropriate digitization of the hologram is described in [234]. Other methods for reconstruction without d.c.-term and without twin image are the

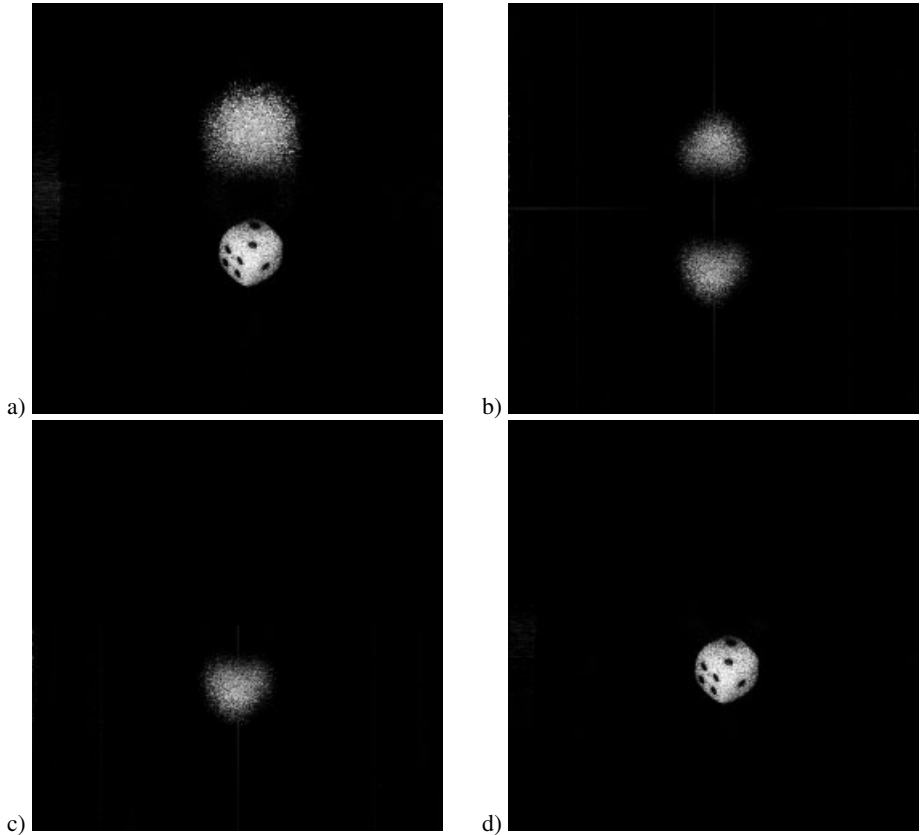


Figure 3.20: Twin image suppression.

hybrid methods [101, 230] already mentioned in the previous section, but there one has to pay with additional experimental effort. An iterative approach for twin image elimination is presented in [130, 131]. Bandpass filtering in the spatial frequency domain for suppressing the d.c.-term and parts of the twin image in digital in-line holographic interferometry is described in [235].

3.2.7 Variation of the Reference Wave

In Section 3.1.3 the most frequently applied reference waves – plane wave and spherical wave – have been introduced. In the reconstruction stage the digital holograms are multiplied with the numerical models of the reference waves before the diffracted field in the image plane is calculated. The effects of using different reference waves in the digital holographic process are shown in Fig. 3.21 with simulated digital holograms. The object consists of black and white rectangles occupying slightly less than half of the object plane. The random phase at the object surface is uniformly distributed between 0 and 2π to simulate diffuse reflection.

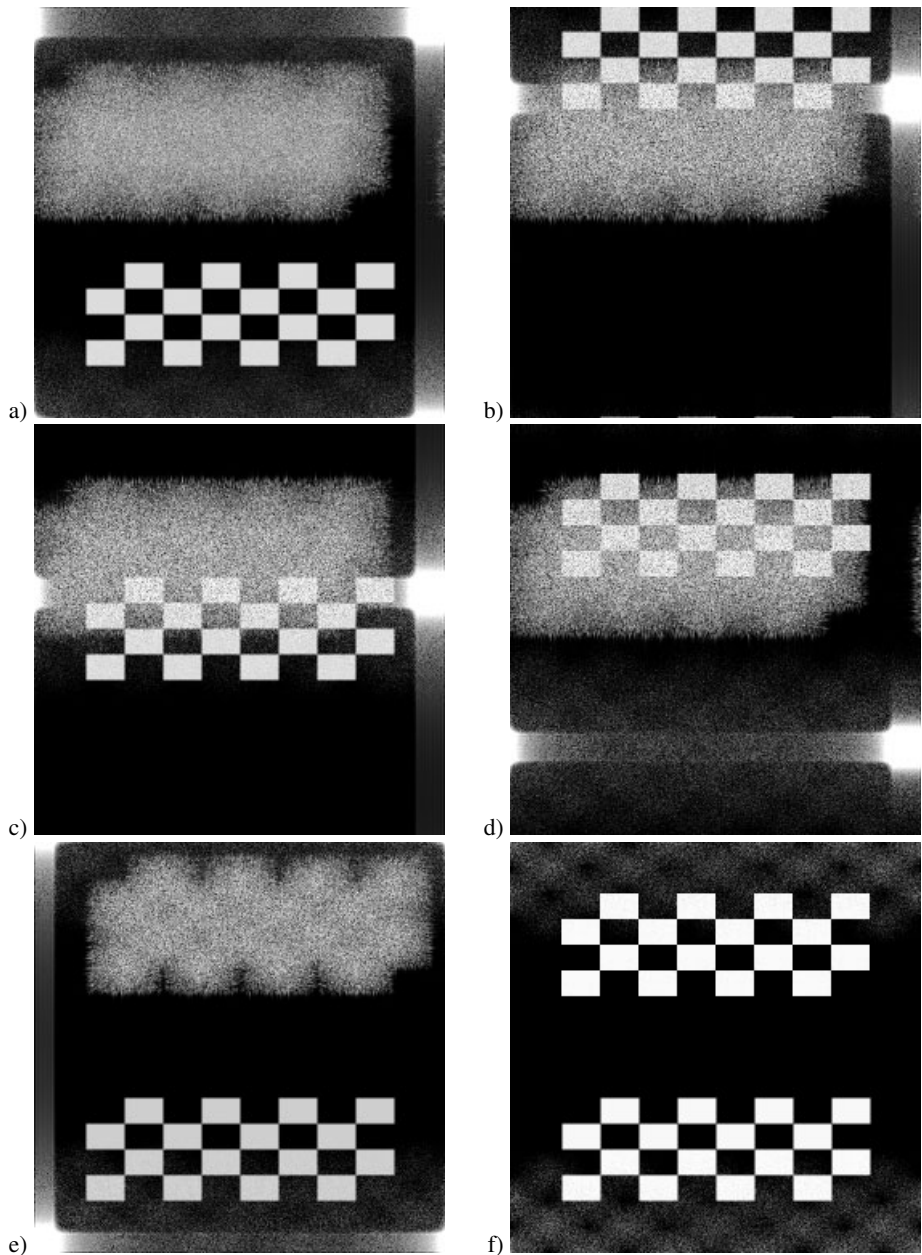


Figure 3.21: Variation of the reference wave.

The displays of the reconstructed fields are not reordered, the d.c.-terms are not suppressed, only the contrast is enhanced adequately. Having in mind the He-Ne laser and the CCD-

arrays often used in practice, the parameters chosen for the simulations are $\lambda = 0.6328 \mu\text{m}$, $\Delta\xi = \Delta\eta = 6.8 \mu\text{m}$, $N = M = 1024$, $d = 1.0 \text{ m}$.

Figure 3.21a shows the reconstructed real image together with the unsharp virtual image when using the up to now frequently mentioned normally impinging plane wave as the reference wave. The total image field (not only the reconstructed image of the object) is $d\lambda/\Delta\xi = 9.3 \text{ cm}$ in both directions. The width of the d.c.-term corresponds to the size of the CCD-array and is $N\Delta\xi = 0.7 \text{ cm}$. It is seen in the upper right corner of Fig. 3.21a. This matches with (3.55) since the 9.3 cm are displayed as the whole $N = 1024$ pixels, while the 0.7 cm correspond to 77 pixels $\approx (N^2\Delta\xi^2)/(d\lambda)$. Figure 3.21b was calculated employing a plane reference wave with oblique incidence in the η -direction using (3.21). The angle of the reference wave with the z -axis was chosen as $\theta = 1^\circ$. The d.c.-term appears shifted by $d \tan \theta$ from the origin, as can easily be derived from the geometric optics analogy of Fig. 3.22a. In Fig. 3.21c we have $\theta = 2^\circ$ and in Fig. 3.21d $\theta = 4^\circ$.

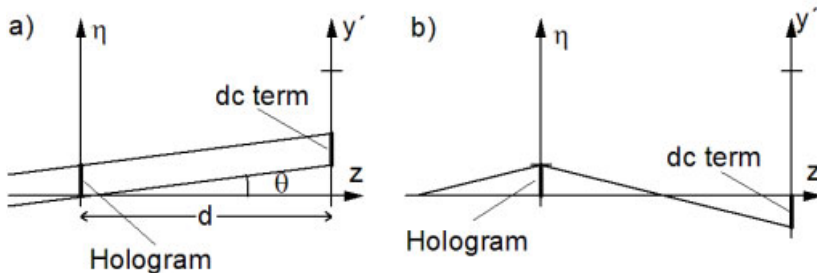


Figure 3.22: Location of d.c.-term in the reconstructed pattern; (a) inclined plane reference wave, (b) spherical reference wave.

The quality of the reconstructed wave fields shown in the intensity display in Figs. 3.21b–d is poorer than that in Fig. 3.21a. The reason is the overlap of the reconstructed image and its corresponding twin image. The twin images are point-symmetrical to the origin and due to the finite character of the discrete transforms (Fourier, Fresnel), parts outside the pattern appear folded inside the pattern from the opposite side. This topic will be treated in more detail in Section 3.3.2.

In Fig. 3.21e a spherical reference wave was used, its source was placed on the z -axis at a distance 0.6 m from the hologram plane. Reconstruction with the conjugated reference wave yielded the result of Fig. 3.21e. The geometric optics argument explains the position of the d.c.-term, Fig. 3.22b. In the last example, Fig. 3.21f, the source of the spherical reference wave was in the object plane. Thus we have the geometry of lensless Fourier transform holography, the reconstruction shows two sharp real images and no discernible d.c.-term which now has collapsed to a single pixel.

Generally any of the reference waves can be employed in digital holography. As long as the sampling theorem is fulfilled they all yield equivalent results. Therefore the normally impinging plane wave should be the first choice due to its computational simplicity. However sometimes in experiments the best is done to arrange such a reference wave, but in reality the reference wave is slightly tilted or it is not a perfect plane one, but a spherical wave.

Nevertheless in the reconstruction the normally impinging plane wave is assumed. In the following we will investigate the influence of these errors and give hints of how to deal in practical evaluations with such cases.

First a plane reference wave that is not normally impinging onto the CCD, but whose direction is inclined in the (z, η) -plane by the angle θ , is considered. The correct evaluation according to (3.38) would be

$$\begin{aligned} b'(n, m) = & e^{i\pi d\lambda(\frac{n^2}{N^2\Delta\xi^2} + \frac{m^2}{M^2\Delta\eta^2})} \\ & \cdot \sum_{k=0}^{N-1} \sum_{l=0}^{M-1} h(k, l) r^*(k, l) e^{\frac{i\pi}{d\lambda}(k^2\Delta\xi^2 + l^2\Delta\eta^2)} e^{-2i\pi(\frac{kn}{N} + \frac{lm}{M})}. \end{aligned} \quad (3.63)$$

The $\Delta\xi$, $\Delta\eta$, $\Delta x'$, $\Delta y'$ in the arguments have been omitted for clarity. The reference wave $r(k, l)$ is from (3.21)

$$r(k, l) = E_r e^{\frac{2i\pi}{\lambda} l \Delta\eta \sin \theta}. \quad (3.64)$$

If we abbreviate the exponential preceding the double sum by $e^{i\alpha}$ we obtain

$$\begin{aligned} b'(n, m) = & E_r e^{i\alpha} \\ & \cdot \sum_{k=0}^{N-1} \sum_{l=0}^{M-1} h(k, l) e^{\frac{i\pi}{d\lambda} k^2 \Delta\xi^2} e^{\frac{i\pi}{d\lambda} (l^2 \Delta\eta^2 - 2dl \Delta\eta \sin \theta)} e^{-2i\pi(\frac{kn}{N} + \frac{lm}{M})} \\ = & E_r e^{i\alpha} e^{-\frac{i\pi d \sin^2 \theta}{\lambda}} \\ & \cdot \sum_{k=0}^{N-1} \sum_{l=0}^{M-1} h(k, l) e^{\frac{i\pi}{d\lambda} k^2 \Delta\xi^2} e^{\frac{i\pi}{d\lambda} (l - \frac{d \sin \theta}{\Delta\eta})^2 \Delta\eta^2} e^{-2i\pi(\frac{kn}{N} + \frac{lm}{M})}. \end{aligned} \quad (3.65)$$

The multiplication of the digital hologram with this specific reference wave $r^*(k, l)$ now has the same effect as a shift of the chirp function as was investigated following (3.56). There we have seen that a shift of the chirp function results in a shift of the reconstructed image. If we omit the multiplication with $r^*(k, l)$, we get an inverse shift of the reconstructed image. This is illustrated in Fig. 3.23.

Figure 3.23a shows the reconstructed real image of the object simulated and evaluated with a normally impinging plane wave. In Fig. 3.23b an obliquely ($\theta = 1^\circ$) incident plane wave was used in the recording and the reconstructing stage, the real image as well as the unsharp virtual image are shifted, the same is true for the d.c.-term. But if we record with the slightly tilted reference wave ($\theta = 1^\circ$) and erroneously reconstruct with the normally impinging reference wave ($\theta = 0^\circ$) we obtain the result displayed in Fig. 3.23c, where the digital hologram of Fig. 3.23b was evaluated using $r = 1$. The d.c.-term appears at the place that is correct with respect to the reconstruction wave, but real and virtual images are shifted compared to Fig. 3.23a.

If in practice this occurs, although the orientation of object and CCD is such that real and virtual images should not overlap or are expected generally at another location, that might be

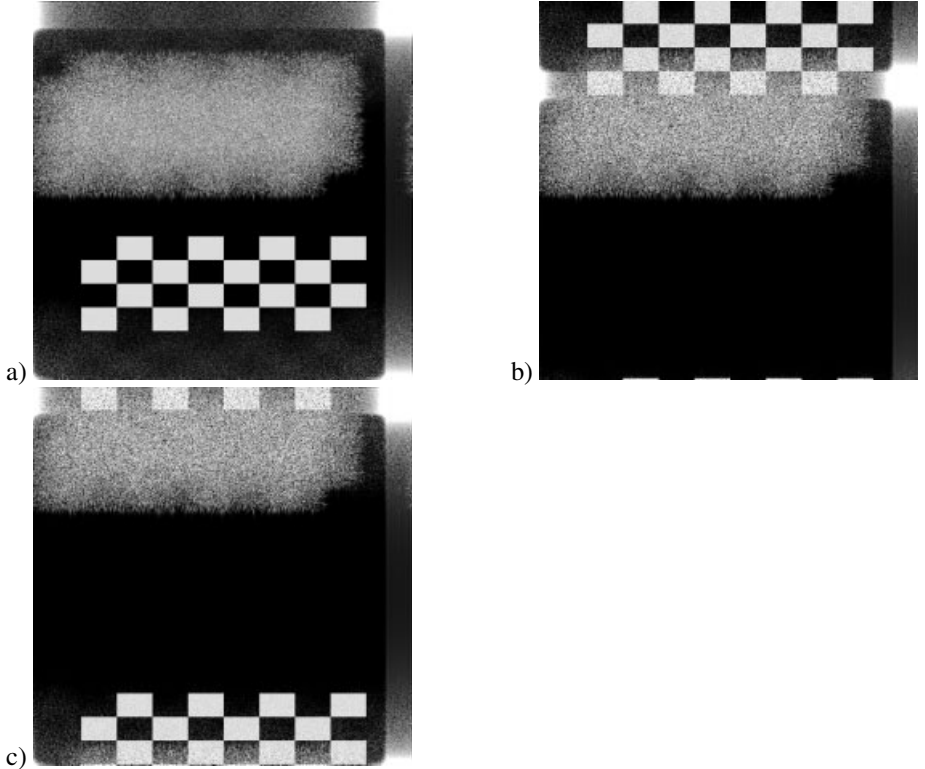


Figure 3.23: Reconstructed real images simulated with normally impinging plane reference wave (a) and tilted plane reference wave (b,c) during recording, reconstructed assuming a normally impinging plane reference wave (a,c) and tilted plane reference wave (b).

a hint for an erroneously tilted reference wave. We further see from Figs. 3.23b and c that the overlap of the twin images is originated already during the recording of the digital hologram. There is no easy way to separate the overlapped images in the reconstruction stage.

The second case to be considered is a spherical wave employed in the recording stage of the digital hologram. The numerical expression for the spherical reference wave according to (3.22) is

$$r(k, l) = E_r e^{\frac{2i\pi}{\lambda} \sqrt{(k\Delta\xi - x_R)^2 + (l\Delta\eta - y_R)^2 + (d - z_R)^2}} \quad (3.66)$$

where (x_R, y_R, z_R) denotes the Cartesian coordinates of the source of the spherical reference wave. The square root is approximated in the well known manner and we obtain

$$r(k, l) = E_r e^{\frac{2i\pi\Delta d}{\lambda} \left[1 + \frac{1}{2} \left(\frac{k\Delta\xi - x_R}{\Delta d} \right)^2 + \frac{1}{2} \left(\frac{l\Delta\eta - y_R}{\Delta d} \right)^2 \right]} \quad (3.67)$$

with $\Delta d = d - z_R$, Fig. 3.24. Without restriction of generality we can assume $x_R = y_R = 0$,

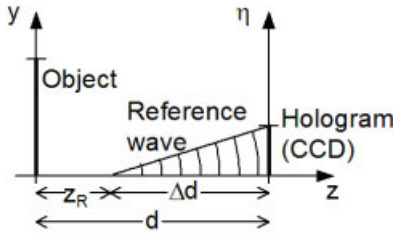


Figure 3.24: Spherical reference wave.

for the influence of any non-vanishing x_R and y_R is analogous to that of the inclined plane reference wave treated above. Thus we have

$$r(k, l) = E_r e^{\frac{2i\pi\Delta d}{\lambda}} e^{\frac{i\pi}{\Delta d \lambda} (k^2 \Delta \xi^2 + l^2 \Delta \eta^2)}. \quad (3.68)$$

With the conjugate of such a reference wave the correct reconstruction would be

$$\begin{aligned} b'(n, m) &= e^{i\alpha} e^{\frac{2i\pi\Delta d}{\lambda}} \sum_{k=0}^{N-1} \sum_{l=0}^{M-1} h(k, l) r^*(k, l) e^{\frac{i\pi}{d\lambda} (k^2 \Delta \xi^2 + l^2 \Delta \eta^2)} e^{-2i\pi(\frac{kn}{N} + \frac{lm}{M})} \\ &= E_r e^{i\beta} \\ &\quad \cdot \sum_{k=0}^{N-1} \sum_{l=0}^{M-1} h(k, l) e^{-\frac{i\pi}{\Delta d \lambda} (k^2 \Delta \xi^2 + l^2 \Delta \eta^2)} e^{\frac{i\pi}{d\lambda} (k^2 \Delta \xi^2 + l^2 \Delta \eta^2)} e^{-2i\pi(\frac{kn}{N} + \frac{lm}{M})} \\ &= E_r e^{i\beta} \\ &\quad \cdot \sum_{k=0}^{N-1} \sum_{l=0}^{M-1} h(k, l) e^{-\frac{i\pi}{\lambda} (\frac{1}{d} - \frac{1}{\Delta d}) (k^2 \Delta \xi^2 + l^2 \Delta \eta^2)} e^{-2i\pi(\frac{kn}{N} + \frac{lm}{M})}. \end{aligned} \quad (3.69)$$

Up to the phase term before the double sum this is the same as a reconstruction with a plane normally impinging reference wave but a reconstruction distance changed from d to d' , which depend on each other by

$$\frac{1}{d'} = \frac{1}{d} - \frac{1}{\Delta d}. \quad (3.70)$$

An experiment where a plane reference wave is assumed but in reality a spherical one is existent will give an unsharp reconstructed intensity distribution when the exact distance d between object surface and CCD array is used, but a sharp reconstruction when one employs the d' of (3.70). On the other hand one may examine different reconstruction distances in conjunction with the plane normally impinging reconstruction wave, the one giving the sharpest result is d' . If d' differs from the measured d , this indicates that a spherical reference wave was arranged for the recording and furthermore informs us about the location of the source point of this wave. The special case $z_R = 0$ implies $\Delta d = d$. So $1/d' = 0$ and we have again the geometry of lensless Fourier transform holography.

In Fig. 3.21e an example was shown of a hologram recorded with a spherical reference wave and reconstructed with a conjugated replica of this wave. The object's distance from the

CCD was $d = 1.0$ m and the z -coordinate of the reference source point was $z_R = 0.4$ m. If we reconstruct with a plane normally impinging reference wave, but retain the distance d , we obtain the unsharp reconstruction of Fig. 3.25a. The reconstruction with $d' = 1.5$ m and a plane reconstruction wave on the other hand yields the intensity distribution of Fig. 3.25b, which agrees with that of Fig. 3.21e.

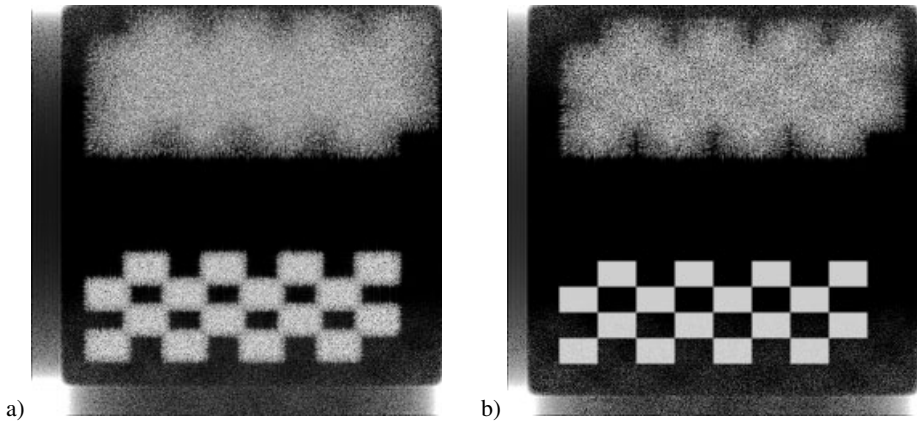


Figure 3.25: Reconstructed intensities from hologram produced with spherical reference wave and plane reconstruction wave, different image distances.

3.2.8 Anamorphic Correction

Digital holography allows the modification of the reconstructed wave field by a variation of the numerical process. We have recognized already the suppression of the d.c.-term, Section 3.2.5, and the suppression of the twin image, Section 3.2.6. In digital holographic microscopy the aberration induced by the magnifying objective is compensated by an additional phase factor introduced into (3.35) during reconstruction. The compensation of spherical aberrations is demonstrated e. g. in [236]. In the same way aberrations which manifest as *anamorphism* or *astigmatism* in the reconstructed image can be compensated [94, 95].

Especially when using a *reflective grating interferometer* [95] strong anamorphism is produced that prevents correct imaging of the object. Without loss of generality let us assume that decorrelation of the reconstructed object field's phase occurs along the horizontal direction without disturbing the field along the vertical direction. It is possible to compensate for this anamorphism by substituting the η in (3.33) by $\eta \cos \alpha$ and the ε by $\varepsilon \cos \alpha$ with a suitable α . In reflective grating interferometry performed by digital holography this α is the angle between the object wave's incidence direction and the grating normal. As a result of this substitution the pixel size in the reconstructed image is differently affected in both directions. While according to (3.34) and (3.36) $\Delta\delta = \Delta x'/(d\lambda) = 1/(N\Delta\xi)$ resp. $\Delta x' = d\lambda/(N\Delta\xi)$ remains unchanged, now $\Delta\varepsilon = \Delta y' \cos \alpha/(d\lambda) = \cos \alpha/(N\Delta\eta)$ giving $\Delta y' = d\lambda \cos \alpha/(N\Delta\eta)$. An originally square object will be reconstructed as a rectangular one but the anamorphism is corrected. Examples of this procedure working with reflective grating interferometry and with phase shifting digital holography can be found in [94, 95].

Astigmatism is a third-order wavefront aberration that results in different focal lengths of the imaging systems for structures oriented in horizontal direction compared to those oriented in vertical direction. Such astigmatism can be compensated by replacing the chirp function $\exp\left\{\frac{i\pi}{d\lambda}(\xi^2 + \eta^2)\right\}$ in (3.33), (3.35), or (3.38) with

$$\exp\left\{\frac{i\pi}{\lambda}\left(\frac{\xi^2}{d_x} + \frac{\eta^2}{d_y}\right)\right\} \quad (3.71)$$

where d_x and d_y are the different distances from hologram plane to the plane of the sharply focused horizontal and vertical object structures.

3.3 Numerical Reconstruction by the Convolution Approach

The numerical reconstruction of digital holograms consists in a multiplication of the stored hologram with a wave field representing the reference wave followed by the calculation of the field diffracted from this product distribution into the image plane. In Section 3.2.1 the diffraction formula used for this calculation was approximated by the Fresnel transform. An effective reconstruction method resulted. However, in Section 2.4.5 we have seen that the diffraction formula is a superposition integral of a linear shift invariant system, so it can be realized as a convolution. In Section A.5 the convolution theorem is introduced which offers an effective way to calculate convolutions. Therefore in this chapter reconstruction procedures based on that concept, which in the following will be called the *convolution approach*, will be introduced, some consequences will be treated and the methods will be compared to reconstruction by the Fresnel transform, because there are more than only conceptual differences between the two approaches.

3.3.1 The Diffraction Integral as a Convolution

As we have seen in Section 2.4.5 the field diffracted at the distribution $h(\xi, \eta) \cdot r^*(\xi, \eta)$ in the hologram plane can be calculated in any (x', y') -plane by the convolution integral

$$b'(x', y') = \iint h(\xi, \eta) \cdot r^*(\xi, \eta) g(x' - \xi, y' - \eta) d\xi d\eta \quad (3.72)$$

where g is the impulse response of free space propagation as introduced in (2.90)

$$g(x' - \xi, y' - \eta) = \frac{i}{\lambda} \frac{e^{ik\sqrt{(x' - \xi)^2 + (y' - \eta)^2 + d^2}}}{\sqrt{(x' - \xi)^2 + (y' - \eta)^2 + d^2}}. \quad (3.73)$$

In short notation (3.72) becomes

$$b'(x', y') = [h(\xi, \eta) \cdot r^*(\xi, \eta)] * g(\xi, \eta) \quad (3.74)$$

where $*$ denotes the convolution operation. The convolution theorem allows us to reduce the computational effort drastically by replacing the convolution in the spatial domain by a

multiplication of the complex spectra in the spatial frequency domain followed by an inverse Fourier transform of this product back into the spatial domain. Now the effective FFT algorithm is repeatedly used to calculate the forward Fourier transform \mathcal{F} as well as the inverse Fourier transform \mathcal{F}^{-1} :

$$b' = \mathcal{F}^{-1} \{ \mathcal{F}\{h \cdot r^*\} \cdot \mathcal{F}\{g\} \}. \quad (3.75)$$

Of these three Fourier transforms one may be saved at least theoretically if we do not define the impulse response g and calculate $G = \mathcal{F}\{g\}$, but directly define the free space transfer function G that was introduced in its continuous form in (2.92).

For the numerical realization of this approach the continuous coordinates (ξ, η) are replaced by the discrete values $k\Delta\xi$ and $l\Delta\eta$, so that the impulse response now reads

$$g(k, l) = \frac{i}{\lambda} \frac{e^{\frac{2\pi i}{\lambda} \sqrt{d^2 + (k-1)^2\Delta\xi^2 + (l-1)^2\Delta\eta^2}}}{\sqrt{d^2 + (k-1)^2\Delta\xi^2 + (l-1)^2\Delta\eta^2}}. \quad (3.76)$$

For programming we use $ie^{i\phi} = -\sin\phi + i\cos\phi$. The discrete impulse response $g(k, l)$; $k = \{1, \dots, N\}$, $l = \{1, \dots, M\}$ now has to be transformed using the FFT algorithm to obtain the discrete finite transfer function G .

The direct calculation of the transfer function G proceeds as in (2.92)

$$G(\nu, \mu) = \begin{cases} \exp \left[-\frac{i2\pi d}{\lambda} \sqrt{1 - (\lambda\nu)^2 - (\lambda\mu)^2} \right] & : (\lambda\nu)^2 + (\lambda\mu)^2 \leq 1 \\ 0 & : \text{otherwise.} \end{cases} \quad (3.77)$$

The discrete values of ν and μ are

$$\nu = \frac{n-1}{N\Delta\xi} \quad \text{and} \quad \mu = \frac{m-1}{M\Delta\eta} \quad n = 1, \dots, N; m = 1, \dots, M \quad (3.78)$$

so that the finite discrete transfer function becomes

$$\begin{aligned} G(n, m) &= e^{\frac{2\pi id}{\lambda} \sqrt{1 - \left(\frac{\lambda(n-1)}{N\Delta\xi} \right)^2 - \left(\frac{\lambda(m-1)}{M\Delta\eta} \right)^2}} \\ &= e^{\frac{2\pi id}{N\Delta\xi} \sqrt{\frac{N^2\Delta\xi^2}{\lambda^2} - (n-1)^2 - (m-1)^2}} \end{aligned} \quad (3.79)$$

where the last expression holds in the frequently occurring case $N = M$ and $\Delta\xi = \Delta\eta$. As soon as the argument under the square root becomes negative we set $G(n, m) = 0$.

If we take a closer look at the Fresnel approximation (2.72) we recognize that it also has the form of a convolution with the convolution kernel

$$g_F(\xi - x, \eta - y) = \frac{e^{ikd}}{i\lambda d} e^{\frac{ik}{2d} [(\xi - x)^2 + (\eta - y)^2]}. \quad (3.80)$$

The finite discrete version is

$$g_F(k, l) = \frac{e^{ikd}}{i\lambda d} e^{\frac{ik}{2d} [(k-1)^2\Delta\xi^2 + (l-1)^2\Delta\eta^2]}. \quad (3.81)$$

The transfer function in Fresnel approximation is

$$G_F(\nu, \mu) = G_{0F} e^{i\pi\lambda d(\nu^2 + \mu^2)} \quad (3.82)$$

with

$$G_{0F} = e^{\frac{-2\pi i d}{\lambda}}. \quad (3.83)$$

The realization of this transfer function in discrete numerics is

$$G_F(n, m) = e^{i\pi d \left(\frac{\lambda[(n-1)^2 + (m-1)^2]}{N^2 \Delta\xi^2} - \frac{2}{\lambda} \right)} \quad (3.84)$$

where we have assumed that $N = M$ and $\Delta\xi = \Delta\eta$.

Altogether we now have four procedures to reconstruct from a digital hologram by the convolution approach: We may define the exact impulse response $g(k, l)$ or its Fresnel approximation $g_F(k, l)$ and calculate $\mathcal{F}\{g\}$ or $\mathcal{F}\{g_F\}$. In the same way we may use directly the exact transfer function $G(n, m)$ or its Fresnel approximation $G_F(n, m)$. With any of these four expressions the reconstruction is performed by (3.75) or $b' = \mathcal{F}^{-1}\{\mathcal{F}\{h\} \cdot G\}$.

3.3.2 Size of the Image Field

The numerical reconstruction of digital holograms by the convolution approach differs principally from that by the Fresnel approach. If we interpret the hologram plane, the (ξ, η) -plane, as the spatial domain and use the Fresnel transform for reconstruction, the result is a Fourier spectrum of a product in the spatial domain, i. e. the result is a spatial frequency spectrum in the spatial frequency domain. This manifests in the existence of a d.c.-term as well as in the achieved resolution. In the spatial domain, the hologram plane, we have a resolution of $\Delta\xi$. To this belongs a resolution of $\Delta x' = d\lambda/(N\Delta\xi)$ in the spatial frequency domain, here the plane of the real image. The same resolution holds for the virtual image.

If on the other hand we evaluate using the convolution approach, we transform the hologram multiplied with the reference wave from the spatial domain into the spatial frequency domain, where we multiply the spectrum with the transfer function. By an inverse Fourier transform this product is transferred back into the spatial domain. The result is a reconstructed image with the same resolution as the original hologram, i. e. N values with spacing $\Delta\xi$. The same is valid for M and $\Delta\eta$. We get a reconstructed image of the same size and the same resolution as the employed CCD array.

As a consequence when using the convolution approach the size of the reconstructed image does not depend on the reconstruction distance d or the wavelength λ as it does with the Fresnel approach. Therefore the convolution approach is especially suited for in-line holography with collimated illumination as shown in Section 3.6.1.

The object field has the width $N\Delta\xi$ of the CCD array, so it will be reconstructed to the full field. On the other hand the application of the Fresnel transform results in an image field of width

$$N\Delta x' = \frac{Nd\lambda}{N\Delta\xi} = \frac{d\lambda}{\Delta\xi}. \quad (3.85)$$

The relevant part of this field in in-line holography covers the ratio

$$\frac{N\Delta\xi}{N\Delta x'} = \frac{N\Delta\xi^2}{d\lambda} \quad (3.86)$$

which exactly corresponds to the width of the d.c.-term (3.55).

The fixed and limited size of the image in the image plane obtained by reconstruction with the convolution approach imposes problems as soon as the objects have larger lateral extent than the CCD-array. A typical example was given in Fig. 3.14b, where we recognize that the object, the die, is larger than the d.c.-term. In fact the hologram can contain information about a larger object, as long as the sampling theorem is fulfilled. These informations are reconstructed and due to the finite discrete nature of the Fourier transforms employed in the reconstruction process, informations from outside the image field appear folded into it from the opposite side. This behavior can be best demonstrated by a simulated experiment for *particle analysis* by digital in-line holography.

Imagine an *in-line arrangement* with a collimated laser beam hitting the CCD-array, Fig. 3.26a. There are no particles inside that part of the beam that corresponds in size to the CCD. But there are opaque particles outside that part, which produce the typical ring structures in the hologram plane. Although the centers of these rings are not on the CCD, information about these particles are in the digital hologram. This is simulated here by calculating a digital hologram of three particles in a 2048×2048 -pixel format, Fig. 3.26b. Then a partial 1024×1024 -pixel hologram is cut out, indicated by the white lines in Fig. 3.26b. The retained partial hologram is displayed in Fig. 3.26c. The numerical reconstruction from this partial hologram by any of the convolution based procedures gives images of particles which appear folded from outside into the formerly particle-free area, Fig. 3.26d. The dark particles here are reconstructed accompanied by bright spots just beside them. These spots are the higher harmonics caused by the sharp horizontal (1 particle) and vertical (2 particles) clipping of the ring structures. The message to the experimenter is that any components reflecting, scattering, or diffracting laser light, which do not belong to the investigated part of the object to be measured, should be carefully avoided, even outside the direct beam path. Any spurious light waves will contribute to the hologram and can be reconstructed as a ghost image. This is overlayed on the desired image and thus degrades it.

3.3.3 Shifting of the Image Field

When using the impulse response (3.73) or the transfer function (3.77) the reconstructed image has the size and the location of the d.c.-term. To reconstruct parts of the image besides the d.c.-term we have to shift the origin of the image plane. The system remains shift-invariant under a shift of the origin, therefore the prerequisite for the application of the convolution theorem still is fulfilled. The shifted version of the impulse response (3.73) is now

$$g_{\alpha,\beta}(x' - \xi, y' - \eta) = \frac{i}{\lambda} \frac{e^{ik\sqrt{(x' - \alpha - \xi)^2 + (y' - \beta - \eta)^2 + d^2}}}{\sqrt{(x' - \alpha - \xi)^2 + (y' - \beta - \eta)^2 + d^2}} \quad (3.87)$$

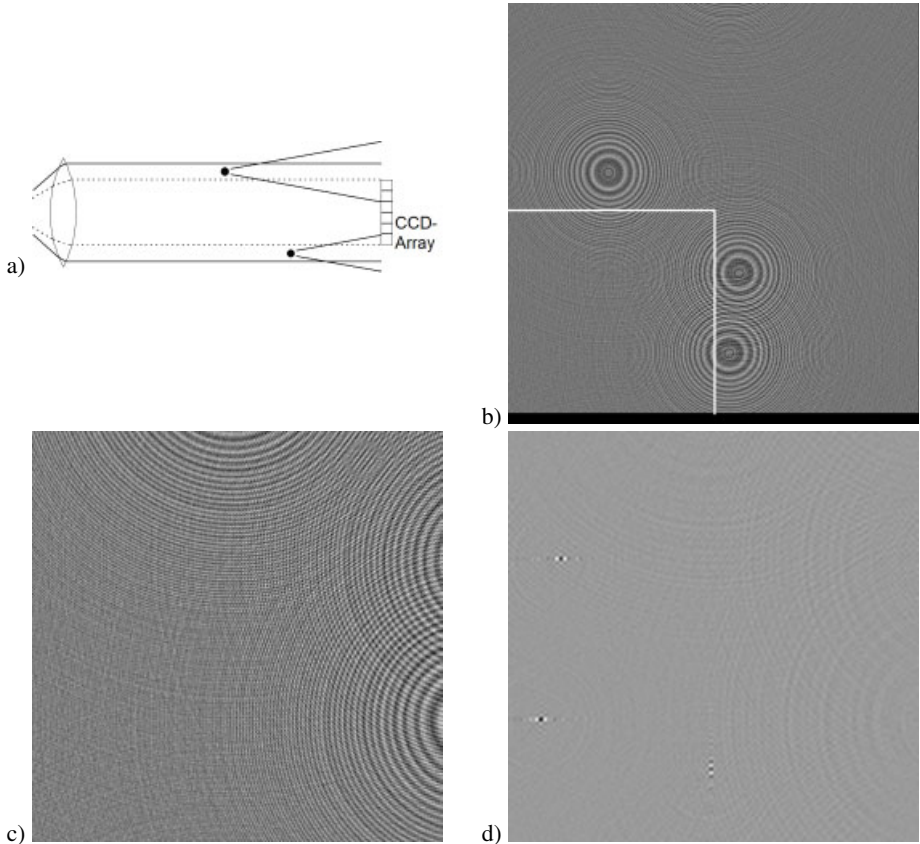


Figure 3.26: Particles in collimated laser beam.

where α denotes the shift in the x' -direction and β gives the shift in the y' -direction. The discrete finite version with the shifts s_k and s_l is

$$g(k + s_k, l + s_l) = \frac{i e^{\frac{2\pi i}{\lambda} \sqrt{d^2 + (k + s_k)^2 \Delta\xi^2 + (l + s_l)^2 \Delta\eta^2}}}{\lambda \sqrt{d^2 + (k + s_k)^2 \Delta\xi^2 + (l + s_l)^2 \Delta\eta^2}}. \quad (3.88)$$

If we reconstruct using this impulse response the resulting field is shifted by $(s_k \Delta\xi, s_l \Delta\eta)$. A limit to possible shifts (s_k, s_l) is only set by the sampling theorem. Several reconstructions with different shifts can be combined like a mosaic to produce a larger image field. An example is shown in Fig. 3.27. Here the impulse response of (3.88) has been used with the shifts (s_k, s_l) taking the values $\{(1536, 1536), (512, 1536), (-512, 1536), (1536, 2560), (512, 2560), (-512, 2560), (1536, 3584), (512, 3584), (-512, 3584)\}$.

The individual reconstructed intensity patterns are of size $N \times N$ with $N = 1024$. The displayed images appear degraded by the overlayed alias information. A way for obtaining

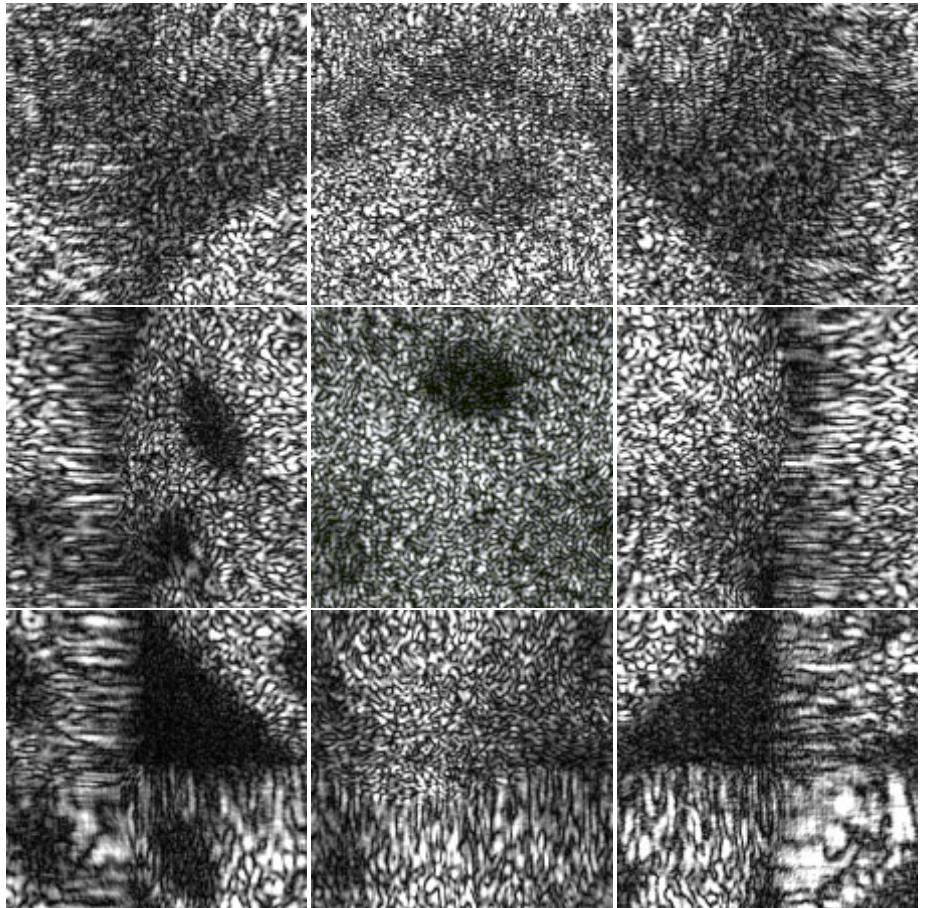


Figure 3.27: Shifted reconstructions of the digital hologram of Fig. 3.14a using the convolution approach.

reconstructions of better quality with the convolution approach for objects larger than the CCD-array will be given in the next section.

3.3.4 Scaling of the Image Field

Up to now we have seen that the size of the reconstructed image field in the case of Fresnel transformation depends on the distance d , the wavelength λ , the pixel size $\Delta\xi \times \Delta\eta$, and the pixel number $N \times M$, while in the case of the convolution approach it coincides with the CCD dimensions $N\Delta\xi \times M\Delta\eta$. The example of the digitally recorded and reconstructed hologram of the die showed an image field much larger than the object when the Fresnel transform was used, but fields covering only a small part of the object when the convolution approach was

applied. It would be advantageous if we could control the size of the reconstructed image field to fit the size of the object.

A variation of d or λ in the Fresnel reconstruction process would only result in unsharp wave fields. If we analyze the Fresnel reconstruction formulas, e. g. (3.38), we recognize that d and λ always appear as a product, therefore a change of one of them has always the same effect as if d was varied away from the optimal distance, so that the reconstructed field only becomes blurred.

Let us now turn to reconstruction by the convolution approach. If we try to rescale the image field without changing the scale of the hologram field, the Fresnel-Kirchhoff formula (2.69) or the related superposition integral (2.88) will exhibit coordinate differences $\xi - ax$ and/or $\eta - by$ with $a \neq 1$ and $b \neq 1$. As a consequence the system characterized by the superposition integral (2.88) is no longer shift-invariant, so the convolution theorem cannot be applied and none of the four methods introduced in Section 3.3.1 works.

The only way out of this dilemma is to rescale the hologram. Consequently the image plane is rescaled simultaneously in the same way. In the following we treat this by doubling the resolution to show the principles in an easy way. Nevertheless we have to keep in mind that factors other than 2 also apply. But the holographer should not be guided into a wrong direction: The way to perform practical measurements should not be to record the hologram with any geometry and to find the best scaling and resolution in the reconstruction stage. It is best practice to carefully plan the experiment and the holographic arrangement's geometry to obtain objects covering nearly the full frame of the reconstructed field without the need for rescaling.

The first way to scale the fields is to expand the $N \times M$ -pixel hologram to, say, a $2N \times 2M$ -pixel hologram. The original $N \times M$ -pixel hologram is surrounded by pixels of intensity 0. Now the pixel numbers in each direction are doubled, $N' = 2N$, $M' = 2M$, the pixel size $\Delta\xi \times \Delta\eta$ remains unchanged. The reconstruction now must proceed with N' and M' and we get a reconstructed image of size $N' \Delta\xi \times M' \Delta\eta = 4NM \Delta\xi \Delta\eta$. In Fig. 3.28a we see the hologram of Fig. 3.14a augmented by black pixels around it. The intensity distribution of

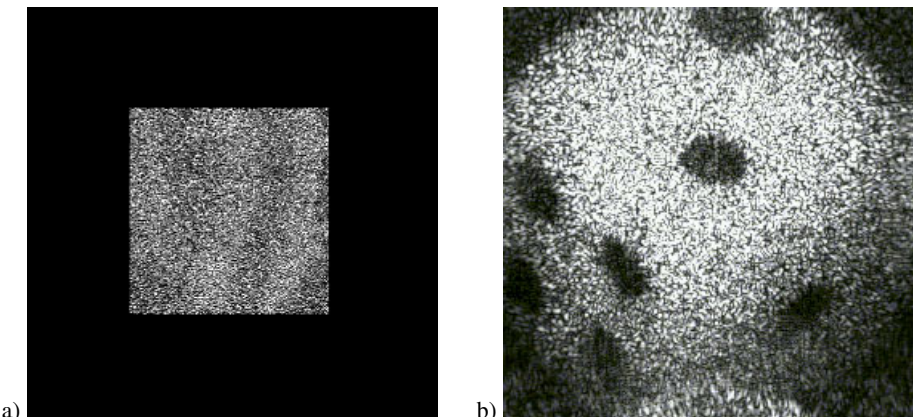


Figure 3.28: Reconstruction after quadrupling the pixel number of the hologram.

the field reconstructed from this augmented hologram is shown in Fig. 3.28b. It consists of 2048×2048 pixels of size $6.8 \times 6.8 \mu\text{m}^2$ each. The degradation of the reconstructed fields by the overlayed information from outside is much less severe than in the 1024×1024 -pixel case, as can be seen by comparing with Fig. 3.27.

If we want to keep the numbers N and M while doubling the image size in each direction, we can average the intensities of all contiguous 2×2 -pixel neighborhoods and in this way build a new hologram of $N/2 \times M/2$ pixels with a pixel size of $\Delta\xi' = 2\Delta\xi$ and $\Delta\eta' = 2\Delta\eta$. This new hologram forms the central part of an $N \times M$ -pixel hologram with black pixels surrounding it as described before. The numerical reconstruction proceeds with $\Delta\xi'$, $\Delta\eta'$, N , M . Again we obtain a field of size $4NM\Delta\xi\Delta\eta = N\Delta\xi' \times M\Delta\eta'$. The differences in the results from those of the aforementioned approach are below the resolution of printing, the results of the experimental example look like Figs. 3.28a and b.

Both approaches to scale the reconstructed image field can be combined: The original $(\Delta\xi, \Delta\eta, N, M)$ -hologram is reduced to a $(2\Delta\xi, 2\Delta\eta, N/2, M/2)$ -hologram, and this new hologram is embedded into surrounding black pixels which fill up to a $(2\Delta\xi, 2\Delta\eta, 2N, 2M)$ -hologram. The result will be a reconstructed image field of size $16NM\Delta\xi\Delta\eta = 2N2\Delta\xi \times 2M2\Delta\eta$. Figure 3.29a displays the averaged and augmented digital hologram now containing

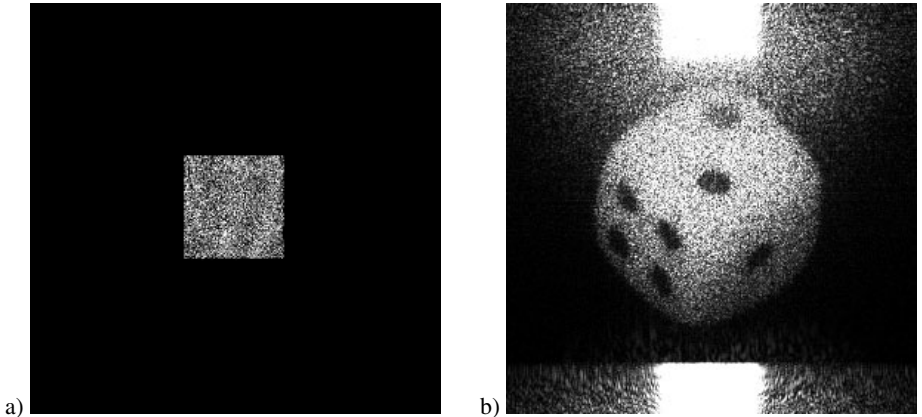


Figure 3.29: Reconstruction after combined quadrupling the pixel number and changing the pixel size of the hologram.

2048×2048 pixels of size $13.6 \times 13.6 \mu\text{m}^2$ each, where only the central 512×512 pixels contain the averaged recorded digital hologram. The intensity distribution of the resulting reconstructed wave field is given in Fig. 3.29b. Factors for scaling other than 2 are feasible as well. If non-integer factors should be used, an interpolation of hologram intensity values may be necessary. Furthermore scaling factors leading to pixel numbers N and M , which are $N \neq 2^n$ and $M \neq 2^m$ require discrete finite Fourier transforms which are generally calculated by (A.45) without the possibility of simplification by the FFT algorithm.

Now let us return to the experiment concerning particle analysis by digital in-line holography. The first results have been illustrated in Fig. 3.26. If we now embed the partial 1024×1024 -pixel hologram into the 2048×2048 -pixel field by augmenting with zero-intensity

pixels, Fig. 3.30a, then the 2048×2048 -pixel reconstruction displays the particles at their correct location, Fig. 3.30b. Here the reconstructed particles can be seen outside the d.c.-term which in size corresponds to the non-vanishing part of the hologram.

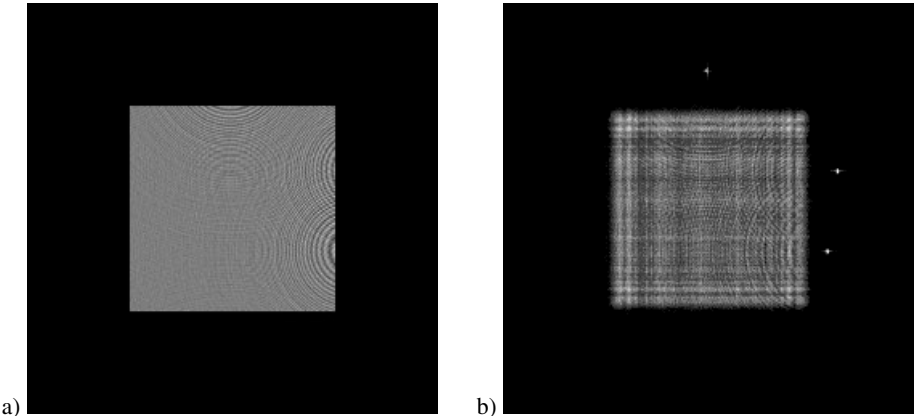


Figure 3.30: Reconstruction from partial hologram.

These facts represent a digital analogy to an effect known from optical holography. If we break a hologram into parts, the whole scene can be reconstructed from each single fragment, only the noise increases when the size of the used hologram decreases.

Another way to rescale the image field is to use a reference wave R' during reconstruction which is different from R , the reference wave employed for recording the digital hologram. We have seen in Section 2.6.3 that a change of the reference wave geometry and a change in reference wave wavelength produces a lateral magnification M_{lat} described in (2.161). The sharp reconstruction of the image in this case is found in a modified distance. This distance change is given in the holographic imaging equations (2.156).

The scaling of the image by reference wave variation will not succeed when using the Fresnel reconstruction. This is easily seen when we check the pixel size. Let the hologram be recorded with a reference wave having a z -coordinate z_R and wavelength λ . The reconstruction is performed with z'_R and wavelength λ' . The object point originally in distance $d = z_P$ now is reconstructed at distance

$$d' = z'_P = \frac{dz'_R z_R}{\mu z_R z'_R - \mu dz'_R + dz_R} \quad (3.89)$$

according to (2.156). The pixel size $d\lambda/(N\Delta\xi)$ if using the original reference wave now is changed to

$$\frac{d' \lambda'}{N\Delta\xi} = \frac{d\lambda}{N\Delta\xi} \left(\frac{\mu z'_R z_R}{\mu z_R z'_R - \mu dz'_R + dz_R} \right). \quad (3.90)$$

On the other hand the lateral magnification resulting from the reference wave variation according to (2.161) is

$$M_{lat} = \frac{1}{1 + d \left(\frac{1}{\mu z'_R} - \frac{1}{\mu z_R} \right)} = \frac{\mu z'_R z_R}{\mu z_R z'_R - \mu d z'_R + d z_R} \quad (3.91)$$

which obviously is the same as the pixel size magnification calculated before. So the reconstructed image appears in the same size as before in the reconstructed frame due to the corresponding pixel size modification.

We have already seen that the pixel size remains constant for any distance or wavelength if we use the convolution approach. And indeed now we can scale the image field to any desired lateral magnification. This is demonstrated again for the well known example of the die: Its digital hologram was recorded with a plane reference wave R assumed to diverge from $(0, 0, \infty) m$. Thus in (2.151) the term μ/z_R vanishes. The distance between the CCD and the die was $d = z_P = 1.054$ m. We now reconstruct with spherical reference waves diverging from $(0, 0, z'_R)$. The distances d' where the images are sharp are given in Table 3.1 together with the resulting lateral magnifications – in our case reductions of the size – and the used wavelengths.

Table 3.1: Data for scaling experiment.

z'_R	λ'	d'	M_{lat}	Display
$\infty = z_R$	$0.6328 \text{ }\mu\text{m} = \lambda$	$1.054 \text{ m} = d$	1	Fig. 3.27
0.2 m	$0.6328 \text{ }\mu\text{m} = \lambda$	0.1681 m	0.16	Fig. 3.31a
0.3 m	$0.6328 \text{ }\mu\text{m} = \lambda$	0.2335 m	0.22	Fig. 3.31b
0.5 m	$0.6328 \text{ }\mu\text{m} = \lambda$	0.339 m	0.32	Fig. 3.31c
0.5 m	$0.3164 \text{ }\mu\text{m} = \lambda$	0.404 m	0.19	Fig. 3.31d

The other parameters are the pixel size $6.8 \text{ }\mu\text{m} \times 6.8 \text{ }\mu\text{m}$ and $(s_K, s_l) = (768, 1536)$. The resulting intensities are shown in Fig. 3.31. So starting with a digital hologram with known recording reference wave and object distance we begin with (2.161) to calculate the plane from where the reconstruction wave has to diverge to obtain a desired image size magnification or reduction. Then we calculate by (2.151) the plane where the image is sharply reconstructed and with these data we perform the reconstruction by convolution. Scaling of the reconstructed image field is a frequent option in digital holography software packages [232].

3.4 Further Numerical Reconstruction Methods

3.4.1 Phase-Shifting Digital Holography

In the preceding sections several methods have been introduced for calculating the object wave field from a single digital hologram. A complex field in the hologram plane was generated

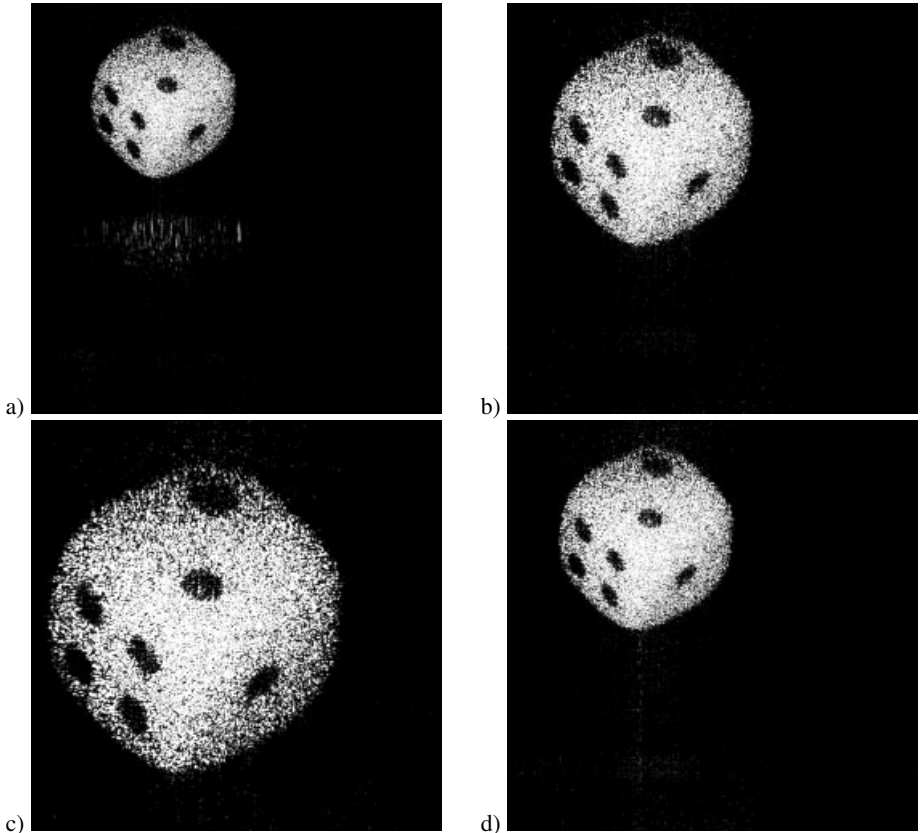


Figure 3.31: Scaled reconstructed images.

by multiplying the digital hologram with the reference wave. Then the field in the image plane was calculated by simulating free-space propagation using the Fresnel transform or the convolution approach. As we have seen (2.131) the multiplication of the real digital hologram with the possibly complex reference wave leads to three components in the reconstructed field, which manifest in the image plane as the d.c.-term, the object field and the conjugated object field, the latter two also called real and virtual images, or the twin images.

Another way to obtain a complex field in the hologram plane was first suggested by Yamaguchi and Zhang [103, 104]. Not a single, but at least three digital holograms are recorded with a mutual phase shift in the reference wave. In Fig. 3.32 a reference mirror mounted on a piezoelectric crystal performs the phase-shift. Other ways of shifting the phase in the reference arm of the holographic interferometer are possible, see Section 2.7.4. Let the object field in the (ξ, η) -plane, the hologram plane, be

$$E_P(\xi, \eta) = \frac{E_{0P}(\xi, \eta)}{p(\xi, \eta)} e^{i\phi(\xi, \eta)} \quad (3.92)$$

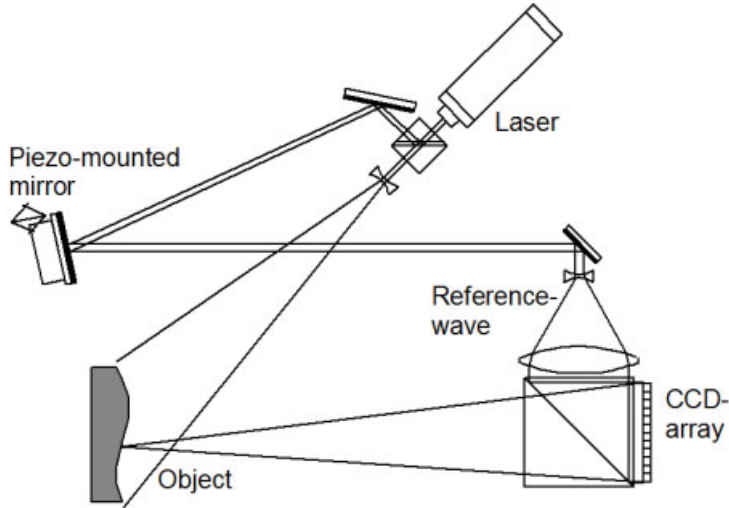


Figure 3.32: Arrangement for phase-shifting digital holography.

and the phase shifted reference wave fields

$$E_{Rn}(\xi, \eta) = \frac{E_{0R}(\xi, \eta)}{r(\xi, \eta)} e^{i\psi_n(\xi, \eta)} \quad n = 1, \dots, L. \quad (3.93)$$

The resulting holograms according to (2.122) are

$$h_n(\xi, \eta) = \left(\frac{E_{0P}}{p} \right)^2 + \left(\frac{E_{0R}}{r} \right)^2 + 2 \left(\frac{E_{0P}}{p} \right) \left(\frac{E_{0R}}{r} \right) \cos(\phi - \psi_n). \quad (3.94)$$

By any of the phase-shift algorithms presented in Section 5.5 the phase ϕ can be calculated [237]. In [103] four intensities with a mutual phase shift of $\pi/2$ were used, so that the algorithm

$$\phi(\xi, \eta) = \arctan \frac{h_4(\xi, \eta) - h_2(\xi, \eta)}{h_1(\xi, \eta) - h_3(\xi, \eta)} \quad (3.95)$$

with $\psi_n = (n - 1)\pi/2$ modulo 2π could be employed. The control of the exact phase shift by an integrated second interferometer with additional CCD and a realtime fringe analyzer is presented in [104, 105]. In a further recording the reference wave field can be blocked so that only the intensity $(E_{0P}/p)^2(\xi, \eta)$ is registered by the CCD array. This gives the real amplitude E_{0P}/p , so that together with (3.95) we have the complex field in the hologram plane. Now again using the Fresnel transform the field in the image plane can be calculated. Since we now have a single complex field in the hologram plane, the field in the image plane does not suffer from a d.c.-term or a twin image. The elimination of phase-shifting error by an iterative algorithm finding the exact phase-shift value is presented in [80].

In [139] only two holograms with a 90° phase shift – the sine and the cosine holograms – are produced by temporal heterodyning, see Section 5.4. Even there an effective zero-order and twin-image elimination is demonstrated. A related approach is demonstrated for incoherent triangular holography of point objects in [238].

Up to now the whole complex field calculated from the phase-shifted digital holograms has been used for reconstruction of the original wave field. However good results in digital as well as in optical reconstruction can be obtained by using only the phase information of the calculated complex field. Matoba et al. [97] propose the use of a phase-only spatial light modulator receiving the digital phase-only wave field $\phi(\xi, \eta)$ for optical reconstruction. Good reconstruction results are obtained, but with only half of the information. Thus storage capacity or transmission time can be saved.

An example of *phase-shifting digital holography* in shape characterization of microelectromechanical systems (MEMS) is shown in Figs. 3.33 and 3.34. Figure 3.33 displays the intensity of the reconstructed field originally reflected from a microaccelerator package [239]. The phase distribution of the reconstructed field is given in Fig. 3.34. Since the height variations are small enough no demodulation is necessary, and the gray scale values are directly related to the heights of the reflecting MEMS surface.

Phase-shifting digital holography can be used for simultaneous three-dimensional particle image velocimetry and temperature measurements [119]. With a recording time $t < 1/1000$ s and a time interval between complete hologram recordings of the order of 0.2 s, Skarman et al. [119] achieved a maximum measurable velocity of $v \approx 10 \text{ mm s}^{-1}$. While this is an issue of holographic imaging, the interferometric comparison of two reconstructed wave fields allows the investigation of the phase variation in a fluid cell, thus giving information on density and temperature distributions, see Section 6.10.

A continuous phase change can be produced by inserting two acoustooptic modulators (AOMs) into the reference beam, see Section 5.4. LeClerc et al. [84–86] employ two AOMs working at $\omega_1/(2\pi) = -80 \text{ MHz}$ and $\omega_2/(2\pi) = +80 \text{ MHz} + 6.25 \text{ Hz}$ which is one quarter of the CCD image frequency $f_{CCD} = 25 \text{ Hz}$. In this way four phase shifted digital holograms are recorded and the usual phase shifting algorithms can be employed. Nevertheless due to the generation of the continuous phase shift the method is called *numerical heterodyne holography*.

It remains an open question in which applications the additional effort of the generation of several phase-shifted digital holograms and the additional reference-free recording is justified. As soon as the object is not stable enough, and especially if we have moving objects, e. g. falling particles, this approach is of no use. On the other hand there exist powerful methods to eliminate the d.c.-term, see Section 3.2.5, and to suppress the twin image, see Section 3.2.6, in the reconstruction from a single digital hologram.

Phase shifting digital holography in its data recording stage differs from phase shifting speckle interferometry, Section 7.3, in recording the Fresnel diffraction field of the object instead of the image of the object focused onto the CCD. A drawback of both techniques is their sensitivity to relative motions between object and reference arm of the interferometer. This sensitivity is drastically reduced by taking a shifted image of the object as reference. The self-reference results in the so-called speckle shearography, Section 7.4, which defines an equal-path interferometer relatively insensitive to motions. Albertazzi and Vieira-Fantin [71, 240] transferred these ideas to digital holography. In a Michelson shearing arrangement, Fig. 3.35,

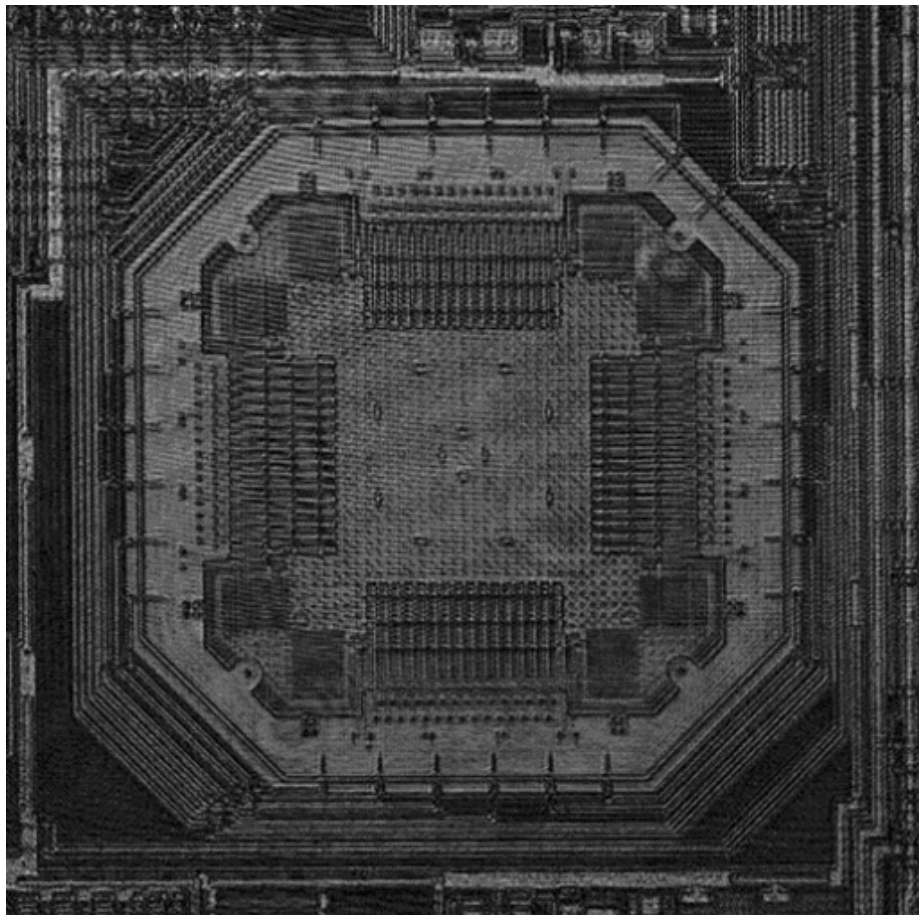


Figure 3.33: Reconstructed intensity of MEMS in phase-shifting digital holography (Courtesy of E. Kolenovic (BIAS) and C. Furlong (WPI)).

they use two mirrors, one performing the phase shifting, the other can be rotated around two axes, managing the x -shear and the y -shear. Now twelve holograms must be recorded: without, with x -shear, and with y -shear and each of these three cases with four relative phase shifts. From the twelve digital holograms the phase differences between adjacent pixels are determined with the accuracy offered by the phase shift method. Imperfection and rotation terms are determined in a calibration step using a plane wave as object wave and can then be eliminated. From the phase differences the phase distribution of the object wave in the CCD-plane is determined in a procedure like path-independent interference phase demodulation, Section 5.9.3. The corresponding intensity distribution can be directly recorded by blocking one of the two mirrors. Details of the numerical process and first experimental results can be found in [71,240]. Simultaneous recording of phase shifted holograms at three wavelengths of

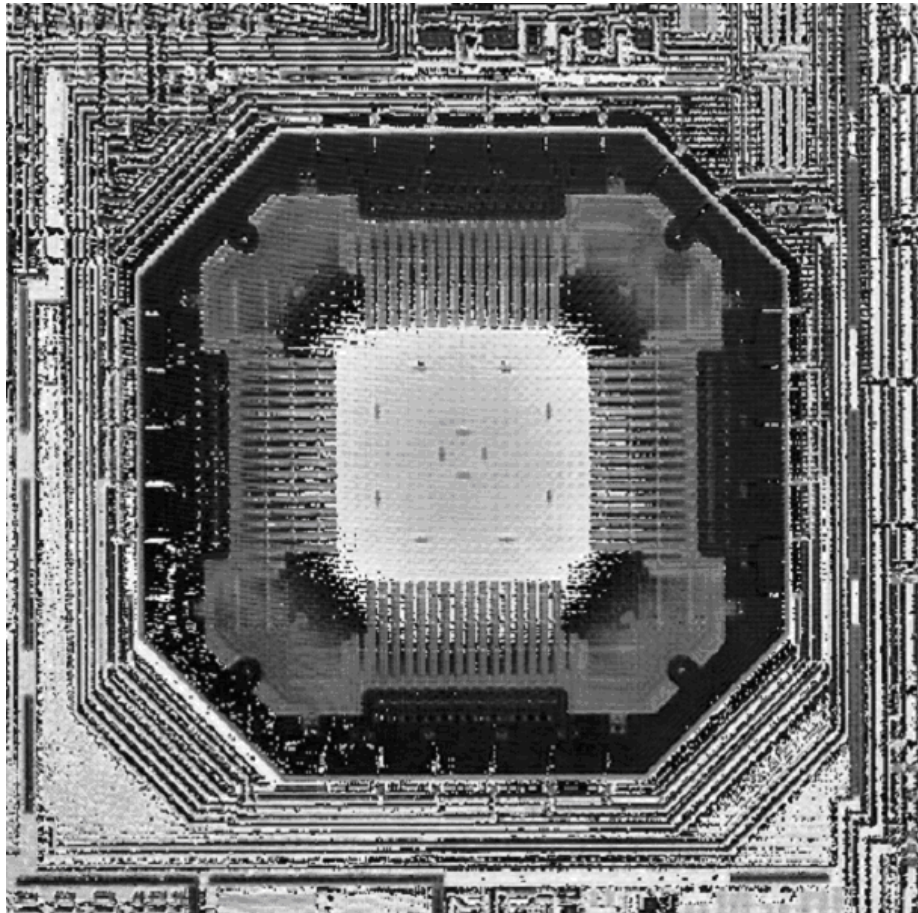


Figure 3.34: Reconstructed phase of MEMS in phase-shifting digital holography (Courtesy of E. Kolenovic (BIAS) and C. Furlong (WPI)).

a He-Cd laser (441.6 nm, 537.8 nm, 636.0 nm) enables the reconstruction of three monochromatic images which can be combined into full-color images in computer [110].

3.4.2 Local Amplitude and Phase Retrieval

Phase shifting digital holography offers the great advantage that in the reconstructed wave field neither zero-order term nor the twin image is present. This is due to the two-step reconstruction process. In a first step the complex wave field in the hologram plane is determined, then in the second step the wave is propagated to the image plane where the complex wave field of the object is reconstructed. While in Section 3.4.1 several phase shifted digital holograms are used to calculate the complex field in the hologram plane, here we present a procedure that uses only one single hologram. For each point in the real hologram a weighted linear set of

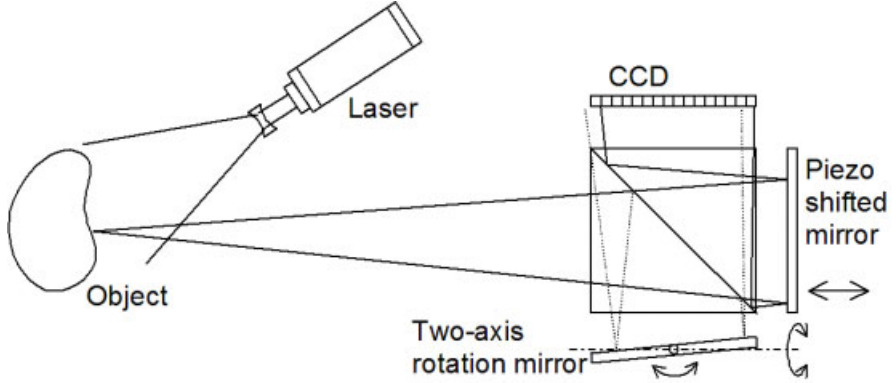


Figure 3.35: Arrangement for shearing digital holography.

equations is solved in the least-squares sense. This yields amplitude and phase with good accuracy under reasonable conditions [241–243].

Let the recorded digital hologram according to (2.122) and (3.32) be

$$H(\xi, \eta) = |E_O(\xi, \eta) + E_R(\xi, \eta)|^2 \quad (3.96)$$

where $E_O(\xi, \eta) = A_O(\xi, \eta) \exp[i\phi_O(\xi, \eta)]$ is the wave field diffracted by the object and the reference is $E_R(\xi, \eta) = A_R(\xi, \eta) \exp[i\phi_R(\xi, \eta)]$. We want to recover the complex $E_O(\xi, \eta)$, but have only one real value $H(\xi, \eta)$ at each (ξ, η) . Normally the reference wave $E_R(\xi, \eta)$ is known. Its phase $\phi_R(\xi, \eta)$ can be modeled with good accuracy, see Section 3.1.3. For computational reasons the amplitude $A_R(\xi, \eta)$ is treated as an additional unknown besides the two unknowns $A_O(\xi, \eta)$ and $\phi_O(\xi, \eta)$. We assume that these three quantities vary slowly with the spatial variable (ξ, η) , whereas $H(\xi, \eta)$ and $\phi_R(\xi, \eta)$ are allowed to move more rapidly. With these hypotheses at each location (ξ, η) a set of M non-linear equations

$$H(\xi_m, \eta_m) = |A_O(\xi, \eta) \exp[i\phi_O(\xi, \eta)] + A_R(\xi, \eta) \exp[i\phi_R(\xi_m, \eta_m)]|^2 \quad (3.97)$$

can be defined. Here the (ξ, η) stand for the central position, while the (ξ_m, η_m) , $m = 1, \dots, M$ denote all pixels in the neighborhood of (ξ, η) . Figure 3.36 shows for example a 3×3 -neighborhood, $M = 9$. Equation (3.97) for any (ξ, η) is rewritten as

$$H_m = A_O^2 + A_R^2 + 2A_O A_R \cos(\phi_O - \phi_{Rm}). \quad (3.98)$$

For finding the least squares solution the functional

$$\begin{aligned} & \sum_m w_m (H_m - [A_O^2 + A_R^2 + 2A_O A_R \cos(\phi_O - \phi_{Rm})])^2 \\ &= \sum_m w_m (H_m - [A_O^2 + A_R^2 + 2A_O A_R \cos \phi_O \cos \phi_{Rm} + 2A_O A_R \sin \phi_O \sin \phi_{Rm}])^2 \end{aligned} \quad (3.99)$$

has to be minimized with respect to A_O , A_R , and ϕ_O . The weights w_m with $\sum_m w_m = 1$ account for the distance of the pixels (ξ_m, η_m) from the central (ξ, η) . Pixels far away get

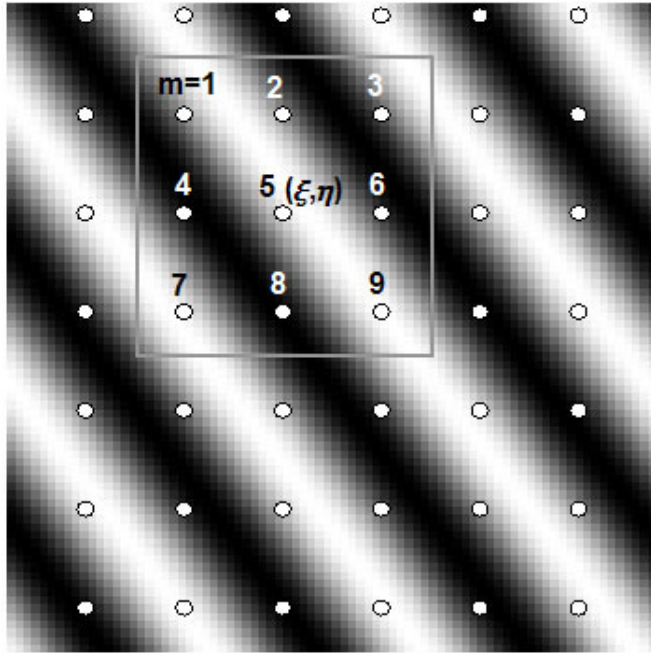


Figure 3.36: Neighborhood of 3×3 pixels.

less weight than those in close vicinity. A normalized two-dimensional Gaussian can do this. The non-linear problem (3.99) is linearized by $u = A_O^2 + A_R^2$, $v = A_O A_R \cos \phi_O$, and $w = A_O A_R \sin \phi_O$. So we obtain the functional

$$\sum_m w_m (H_m - u - 2 \cos \phi_{Rm} v - 2 \sin \phi_{Rm} w)^2. \quad (3.100)$$

Differentiation with respect to u , v , and w after rearrangement gives the set of linear equations

$$\begin{pmatrix} \sum_m w_m H_m \\ \sum_m w_m H_m \cos \phi_{Rm} \\ \sum_m w_m H_m \sin \phi_{Rm} \end{pmatrix} = \begin{pmatrix} u \\ v \\ w \end{pmatrix} \begin{pmatrix} 1 & 2 \sum_m w_m \cos \phi_{Rm} & 2 \sum_m w_m \sin \phi_{Rm} \\ \sum_m w_m \cos \phi_{Rm} & 2 \sum_m w_m \cos^2 \phi_{Rm} & 2 \sum_m w_m \sin \phi_{Rm} \cos \phi_{Rm} \\ \sum_m w_m \sin \phi_{Rm} & 2 \sum_m w_m \sin \phi_{Rm} \cos \phi_{Rm} & 2 \sum_m w_m \sin^2 \phi_{Rm} \end{pmatrix} \quad (3.101)$$

This system is defined and solved for each (ξ, η) , with eventually smaller neighborhoods for positions at the edges of the digital hologram. The original variables we have been looking for are restored by

$$\phi_O = \arctan \frac{w}{v} \quad (3.102)$$

and

$$\{A_O, A_R\} = \sqrt{\frac{u \pm \sqrt{u^2 - 4v^2 - 4w^2}}{2}}. \quad (3.103)$$

The decision as to which of the signs belongs to A_O and which to A_R depends on the prior knowledge about the reference amplitude A_R . This process is repeated for all (ξ, η) and gives the complex diffraction pattern of the object in the CCD-plane, from which by Fresnel transform or by a wavelet approach [241] the object wave field is calculated.

3.4.3 Wavelet Approach to Numerical Reconstruction

The wavelet transform is a relatively new concept for analyzing temporal or spatial signals. A powerful method for signal analysis is the Fourier transform used frequently in this book. Its amplitude spectrum indicates which frequencies are contained in a given signal, but not when or where these frequencies occur. This information is coded in the phase spectrum, but this is a second aspect of the complex spectrum, not easy to interpret. The amplitude spectrum is a good analysis tool for stationary signals, where the frequency content does not change with time or space, but has drawbacks when dealing with non-stationary signals.

These disadvantages led to the development of the *short time Fourier transform*, STFT. Here a sliding window function of finite length $w(x)$ is shifted over the function $f(x)$ to be analyzed yielding

$$\text{STFT}_w\{f(x)\}(x', u) = \int_{-\infty}^{\infty} f(x) w^*(x - x') e^{i2\pi ux} dx. \quad (3.104)$$

For every temporal or spatial coordinate x' and every temporal or spatial frequency u an STFT coefficient is calculated. The STFT analysis of a 1D function thus gives a 2D result indicating not only which frequency components occur, but also where these arise. This concept was suggested for holographic nondestructive testing already in the mid-1980s, see [244]. But now we have a problem known as the uncertainty principle of the STFT, which is basically a resolution problem: If we use narrow window functions, we have a good time (or space) resolution but poor frequency resolution; vice versa if a wide window is employed, we obtain well resolved frequency values, but the time (or spatial) resolution is poor. The *wavelet transform* concept solves this dilemma of resolution to a certain extent. The central idea of the wavelet transform is that the window is changed as the transform is computed for every single spectral component. The continuous wavelet transform (CWT) is defined as

$$\text{CWT}_\psi\{f(x)\}(\tau, s) = \frac{1}{\sqrt{|s|}} \int_{-\infty}^{\infty} f(x) \psi^*\left(\frac{x - \tau}{s}\right) dx. \quad (3.105)$$

Here τ is the *translation parameter* and s is the *scale parameter*. The latter can be interpreted as an inverse frequency. Since the scale parameter s is used in the denominator, scales $s > 1$ dilate the signals whereas scales $s < 1$ compress the signal. $f(x)$ is the signal to be

transformed. The $1/\sqrt{|s|}$ -factor is for energy normalization purposes, so that the transformed signal will have the same energy at every scale. $\psi(x)$ is the so-called *mother wavelet*. Like in the STFT case we obtain a 2D result: an amplitude over translation (in space or time) and scale ($=1/\text{frequency}$). But unlike the STFT which has a constant resolution at all times (or positions) and frequencies, the wavelet transform has good time (space) and poor frequency resolution at high frequencies, and good frequency and poor temporal (spatial) resolution at low frequencies. Often used mother wavelets are the Mexican hat, which is the second derivative of the Gaussian function $(\exp\{-x^2/(2\sigma^2)\})/(\sqrt{2\pi}\sigma)$

$$\psi(x) = \frac{1}{\sqrt{2\pi}\sigma^3} \left[e^{-\frac{x^2}{2\sigma^2}} \left(\frac{x^2}{\sigma^2} - 1 \right) \right] \quad (3.106)$$

or the Morlet wavelet

$$\psi_a(x) = e^{iax} e^{-\frac{x^2}{2\sigma^2}} \quad (3.107)$$

which is basically a harmonic function windowed by a Gaussian bell shaped curve.

The possibilities to work with different user-specified and wavelength independent scales stimulate the interest in a wavelet approach to reconstruction of digital holograms. In digital holography a transformed function is available over a finite support and with a given sampling width, so the Heisenberg-like uncertainty relation, see Section A.13, can yield a bound on the maximal resolution one can expect when reconstructing the original function [129]. The implications of the uncertainty relation (A.117) suggest the use of Gabor-like functions. But unfortunately these functions do not satisfy the partition of unity condition, implying that a representation of a function in terms of shifted elementary functions will not converge to the target function as the sampling step goes to zero [129]. Therefore Liebling et al. employ B-splines as a base for their construction of a class of wavelets, which they call *Fresnelets*. An explicit expression for a *B-spline* of degree n is

$$\beta^n(x) = \begin{cases} \sum_{k=0}^n (-1)^k \binom{n+1}{k} \frac{(\max\{0, x-k\})^n}{n!} & 0 < x < n+1 \\ 0 & \text{otherwise} \end{cases} \quad (3.108)$$

which also can be expressed as the n -fold convolution of the rectangular pulse in the unit interval

$$\beta^n(x) = \underbrace{\beta^0 * \dots * \beta^0}_{n+1 \text{ times}}(x) \quad \text{with } \beta^0(x) = \begin{cases} 1 & 0 < x < 1 \\ 1/2 & x = 0 \text{ or } x = 1 \\ 0 & \text{otherwise.} \end{cases} \quad (3.109)$$

Based on the properties of the B-splines, a family of spline wavelets ψ^n can be constructed by

$$\psi^n\left(\frac{x}{2}\right) = \sum_k g(k) \beta^n(x-k) \quad (3.110)$$

and finally the Fresnelets are defined as the Fresnel transforms of these B-spline wavelets [129]. This allows the definition of the numerical Fresnelet transform based on the Fresnelet

decomposition [129]. The Fresnel transform then can be used for the reconstruction of the original function from its digital hologram. Typically for the wavelet approach we obtain several reconstructed images with different scales. The energy corresponding to the zero order and the twin image terms is concentrated at high frequencies, so it is mainly encoded in the fine scale Fresnel coefficients. Thus coarse scale reconstructions essentially suppress the zero order and twin image terms [245]. The computational effort is comparable to that of the convolution approach, say roughly two 2D-FFTs. Since the Fresnel transform approach provides us with wavelet coefficients, we can apply simple wavelet-domain thresholding techniques to reduce the measurement noise in the reconstructed images [129].

Another application of the wavelet transform in digital holography is in the localization and visualization of glass fibers in a hot and turbulent environment [246, 247]. The random spatial distribution of temperature induces a strong local variation of the refractive index. Consequently, the focusing to a specific plane is not very reliable. Therefore the wavelet representation of the recorded digital in-line hologram is used to recover the 3D location and orientation of the glass fiber. The wavelet transform represents the 2D image in 4D space consisting of two spatial coordinates, one scale parameter and one angle parameter. Using the maximum of the wavelet transform modulus, the 4D representation is reduced to a 2D scale-angle representation. It must be noted that no focusing is necessary in this technique, which would be extremely difficult in the special environment envisaged here [246]. An improvement of the method by using an optical wavelet transform system based on a Vander-Lugt correlator with inclusion of an electrically addressed spatial light modulator is described in [248]. The analysis of typical ring structures in the hologram produced by particles in an in-line holographic setup is based on a wavelet transform and envelope reconstruction in [249]. An in-depth analysis of the potential of a wavelet approach to general diffraction issues is given in [250, 251].

3.4.4 Comparison of Reconstruction Methods

Digital reconstruction of holograms recorded by a CCD array is performed by numerical calculation of the field in the image plane that is diffracted from the hologram illuminated by the reference wave. The diffraction integral may be approximated by the Fresnel transform. Four further methods interpret the diffraction integral as a convolution and offer effective calculation due to the convolution theorem. All five methods employ the efficient FFT algorithm. Thus we have to define the impulse response function of free-space propagation $g(k, l)$, multiply its Fourier transform with the Fourier transform of the hologram times the reference wave and apply the inverse Fourier transform to this product. Instead of calculating the Fourier transform of the impulse response we may directly define the transfer function $G(n, m)$ for free space propagation. If the image plane is far enough from the hologram, the square roots in the definitions of the impulse response or the transfer function can be replaced by the first terms of the series expansion. In this way we get the Fresnel approximations $g_F(k, l)$ and $G_F(n, m)$, respectively. Each of these five reconstruction methods leads to a complex field $b'(k, l)$, from which the intensity and phase distributions can be determined in a pointwise manner. A summary of the five methods [252] is given in Table 3.2.

Some conceptual differences between the Fresnel transform approach and the convolution approach already have been discussed. While the Fresnel transform yields a spectrum in

Table 3.2: Reconstruction methods in digital holography.

- Reconstruction using Fresnel Transform (Chirp Function)

$$z \cdot \mathcal{F}^{-1}\{h \cdot r \cdot w\}$$

$$w(k, l) = \exp \left\{ \frac{i\pi}{d'\lambda} (k^2 \Delta\xi^2 + l^2 \Delta\eta^2) \right\}$$

$$z(n, m) = \exp \left\{ \frac{-i\pi d'\lambda}{N^2} \left(\frac{n^2}{\Delta\xi^2} + \frac{m^2}{\Delta\eta^2} \right) \right\}$$

- Reconstruction using Impulse Response

$$\mathcal{F}^{-1}\{\mathcal{F}\{h \cdot r\} \cdot \mathcal{F}\{g\}\}$$

$$g(k, l) = \frac{1}{i\lambda} \frac{\exp \left\{ \frac{2\pi i}{\lambda} \sqrt{d'^2 + (k - N/2)^2 \Delta\xi^2 + (l - N/2)^2 \Delta\eta^2} \right\}}{\sqrt{d'^2 + (k - N/2)^2 \Delta\xi^2 + (l - N/2)^2 \Delta\eta^2}}$$

- Reconstruction using Transfer Function

$$\mathcal{F}^{-1}\{\mathcal{F}\{h \cdot r\} \cdot G\}$$

$$G(n, m) = \exp \left\{ \frac{2\pi i d'}{\lambda} \sqrt{1 - \frac{\lambda^2 \left(n + \frac{N^2 \Delta\xi^2}{2d'\lambda} \right)^2}{N^2 \Delta\xi^2} - \frac{\lambda^2 \left(m + \frac{N^2 \Delta\eta^2}{2d'\lambda} \right)^2}{N^2 \Delta\eta^2}} \right\}$$

- Reconstruction using Fresnel Approximation of Impulse Response

$$\mathcal{F}^{-1}\{\mathcal{F}\{h \cdot r\} \cdot \mathcal{F}\{g_F\}\}$$

$$g_F(k, l) = \frac{\exp \{id'2\pi/\lambda\}}{i\lambda d'} \exp \left\{ \frac{i\pi}{\lambda d'} [(k - N/2)^2 \Delta\xi^2 + (l - N/2)^2 \Delta\eta^2] \right\}$$

- Reconstruction using Fresnel Approximation of Transfer Function

$$\mathcal{F}^{-1}\{\mathcal{F}\{h \cdot r\} \cdot G_F\}$$

$$G_F(n, m) = \exp \left\{ i\pi d' \left[\frac{2}{\lambda} - \lambda \left(\frac{n}{N\Delta\xi} + \frac{N\Delta\xi}{2d'\lambda} \right)^2 - \lambda \left(\frac{m}{N\Delta\eta} + \frac{N\Delta\eta}{2d'\lambda} \right)^2 \right] \right\}$$

the spatial frequency domain, if the hologram plane is interpreted as the spatial domain, the convolution approach gives a distribution in the spatial domain. The consequences are the different pixel sizes for these two approaches as well as the dependence of the pixel size on reconstruction distance and wavelength only for the Fresnel approach. This would require a size adaptation if reconstructions related to different depths have to be compared, as e. g. in particle analysis using in-line holography. For such applications the convolution procedures are recommended [93].

If small objects have to be investigated, at least theoretically we may work in a region where the Fresnel approximation of the spherical wavefronts by parabolic ones produces reasonable errors. Then again the convolution approach is recommended since it yields an exact solution to the diffraction integral as far as the sampling theorem is not violated.

The digital hologram may be viewed as a diffractive optical element, only that the optical reconstruction is replaced by its numerical counterpart. On this base parameters like speckle size and depth of focus can be calculated [253]. To determine the speckle size in the reconstructed intensity distribution we follow Goodman [254] and Section 2.5.2. The average speckle is the autocorrelation $R(x'_1, y'_1; x'_2, y'_2)$ of the intensity in the image plane

$$R(x'_1, y'_1; x'_2, y'_2) = \langle I(x'_1, y'_1)I(x'_2, y'_2) \rangle. \quad (3.111)$$

The autocorrelation can be expressed by [254]

$$\begin{aligned} R(x'_1 - x'_2, y'_1 - y'_2) \\ = \langle I \rangle^2 \left\{ 1 + \left| \frac{\int_{-\infty}^{\infty} \int_{-\infty}^{\infty} |I(\xi, \eta)|^2 e^{i \frac{2\pi}{\lambda d} (\xi(x'_1 - x'_2) + \eta(y'_1 - y'_2))} d\xi d\eta}{\int_{-\infty}^{\infty} \int_{-\infty}^{\infty} |I(\xi, \eta)|^2 d\xi d\eta} \right|^2 \right\} \end{aligned} \quad (3.112)$$

where $|I(\xi, \eta)|$ is the intensity of the scattering points (ξ, η) in the hologram plane. The important parameters defining the speckle size are the dimensions of the scattering area, but not its gray-value distribution, therefore we can assume

$$|I(\xi, \eta)| = \begin{cases} 1 & \text{for } \xi \in [0, N\Delta\xi], \eta \in [0, M\Delta\eta] \\ 0 & \text{otherwise} \end{cases} \quad (3.113)$$

The resulting autocorrelation then is

$$\begin{aligned} R(x'_1 - x'_2, y'_1 - y'_2) \\ = \langle I \rangle^2 \left\{ 1 + \operatorname{sinc}^2 \left(\frac{N\Delta\xi(x'_1 - x'_2)}{\lambda d} \right) \operatorname{sinc}^2 \left(\frac{M\Delta\eta(y'_1 - y'_2)}{\lambda d} \right) \right\}. \end{aligned} \quad (3.114)$$

The average speckle size s_x in x' -direction now is defined as that value of $x'_1 - x'_2$ where $\operatorname{sinc}^2(N\Delta\xi(x'_1 - x'_2)/(\lambda d))$ for the first time becomes zero, that is $s_x N \Delta \xi / (\lambda d) = \pi/2$ or

$$s_x = \frac{\lambda d \pi}{2 N \Delta \xi} \quad \text{and} \quad s_y = \frac{\lambda d \pi}{2 M \Delta \eta}. \quad (3.115)$$

The speckle size increases with increasing reconstruction distance and with decreasing area of the CCD array.

The interpretation of the reconstructed intensity distributions requires a comparison of the average speckle size s_x (or s_y) to the pixel size $\Delta x'$ (or $\Delta y'$). If we reconstruct using the Fresnel transform, we have $\Delta x' = d\lambda/(N\Delta\xi)$, so the speckle size is in the same range as the pixel size

$$s_x = \frac{\pi}{2} \Delta x', \quad s_y = \frac{\pi}{2} \Delta y'. \quad (3.116)$$

On the other hand if we evaluate by one of the convolution methods, $\Delta x' = \Delta\xi$, $\Delta y' = \Delta\eta$, one speckle is on the average

$$\frac{\lambda d\pi}{2N\Delta\xi^2} \text{ pixel} \quad \text{or} \quad \frac{\lambda d\pi}{2M\Delta\eta^2} \text{ pixel} \quad (3.117)$$

wide. For our frequent example $d = 1.054\text{m}$, $\lambda = 0.6328 \mu\text{m}$, $N = M = 1024$, $\Delta\xi = \Delta\eta = 6.8 \mu\text{m}$ the average speckle size in the horizontal as well as in the vertical direction is 22 pixels for reconstruction with the convolution approach.

Spatial resolution has been seen to depend basically on the number of pixels. Thus an improvement of spatial resolution can be obtained by combining multiple laterally shifted views of the object to produce a large synthetic aperture, a concept successfully applied for a long time in radar, sonar, or astronomy. Different approaches to this concept in digital holography are known: LeClerc et al. [87] move the filter position in a two-lens spatial filtering system where the backtransforming lens and the CCD are fixed to the spatial filter and perform the same motions. Binet et al. [83] use phase shifting digital holography. Their overlapping multiple digital holograms are produced by rotating the object while keeping the illumination and acquisition bench static. The author et al. [255] move the CCD to record non-overlapping multiple holograms. These are embedded into one large synthetic hologram or the individually reconstructed wave fields are superposed coherently.

These concepts enlarge the aperture by increasing the number of pixels while keeping the pixel pitch and the pixel size constant. A different way is adopted by Jacquot et al. [120, 121] who decrease the pixel size and pixel pitch while increasing the pixel number but the aperture size is kept fixed, see Section 3.1.1.

Another option for improvement of the quality of the reconstructed images and reduction of the speckle noise especially in digital holographic interferometry is wavelength scanning [140, 141]. A number of holograms with varied wavelengths coming from a dye laser are recorded, and the resulting reconstructed fields then are combined to yield tomographic images with narrow axial resolution.

Fresnel holography offers the possibility of focusing onto a single plane during reconstruction. This is valid for optical as well as for numerical reconstruction. Therefore it is of special interest which depth of focus we have for a specific choice of experimental parameters.

We have a resolution of pixels with dimension $\Delta x' \times \Delta y'$ in the reconstructed image. Without restriction of generality we can perform a one-dimensional analysis. So we look for the range of d where the circle of confusion will not become larger than a single pixel $\Delta x'$. This is the range from a_v to a_h . Figure 3.37 shows that the furthest point that is sharp within the criterion $\Delta x'$ when reconstructed with distance d is in the range $a_h > d$. From elementary

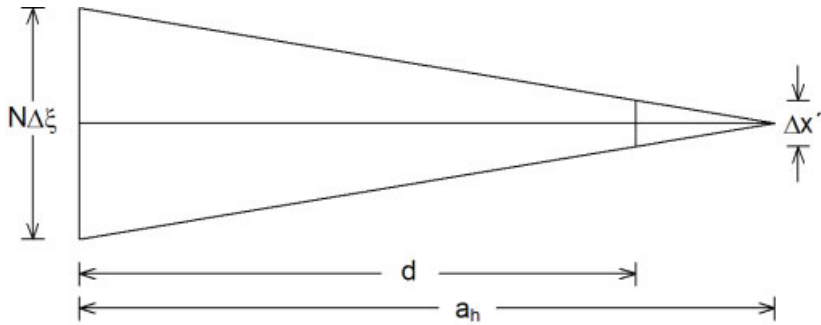


Figure 3.37: Calculation of focal range.

geometry we obtain

$$\frac{\Delta x'}{N\Delta\xi} = \frac{a_h - d}{a_h} \quad \text{or} \quad a_h = \frac{dN\Delta\xi}{N\Delta\xi - \Delta x'}. \quad (3.118)$$

The nearest point that is still focused is at $a_v < d$, Fig. 3.38, and we get

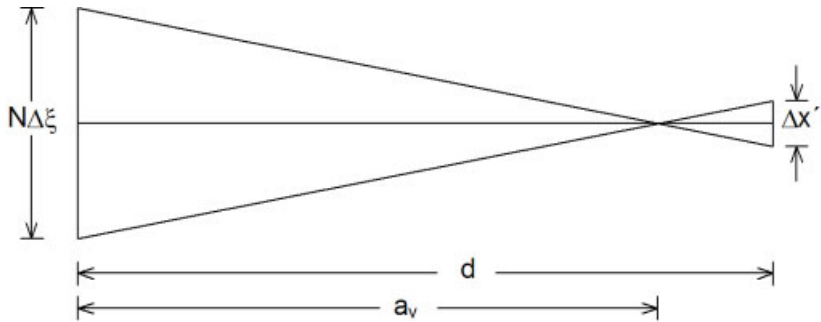


Figure 3.38: Calculation of focal range.

$$\frac{\Delta x'}{N\Delta\xi} = \frac{d - a_v}{a_v} \quad \text{or} \quad a_v = \frac{dN\Delta\xi}{N\Delta\xi + \Delta x'}. \quad (3.119)$$

If we now reconstruct with distance d , all object points placed between a_v and a_h are focused with respect to the resolution of the reconstructed image.

These expressions have to be related to the experimental parameters of the two reconstruction approaches. The Fresnel transform reconstruction implies $\Delta x' = d\lambda/(N\Delta\xi)$ and the focal depth is from

$$a_v = d \left(\frac{1}{1 + \frac{d\lambda}{N^2\Delta\xi^2}} \right) \quad \text{to} \quad a_h = d \left(\frac{1}{1 - \frac{d\lambda}{N^2\Delta\xi^2}} \right). \quad (3.120)$$

Reconstruction by the convolution approach with $\Delta x' = \Delta\xi$ defines a focal depth from

$$a_v = d \frac{N}{N+1} \quad \text{to} \quad a_h = d \frac{N}{N-1}. \quad (3.121)$$

The different depths are elucidated by an example. Let $d = 1$ m, $N = 1024$, $\Delta\xi = 6.8$ μm , and $\lambda = 0.6328$ μm . The reconstruction by one of the convolution methods gives a focal range $[a_v, a_h] = [d - 976$ μm , $d + 978$ $\mu\text{m}]$ while the application of the Fresnel transform defines $[a_v, a_h] = [d - 12.9$ mm, $d + 13.2$ mm]. In the Fresnel case we have a focal range more than 13 times wider than in the convolution case.

If we perform a digital holographic experiment with optical reduction of the object size according to the methods presented in Section 3.1.2, the depth of focus considered above applies to the reduced virtual image of the object. Furthermore in Section 3.1.2 we considered the transverse magnification M_T , while for the depth resolution the longitudinal magnification M_L is valid. It is $M_L = M_T^2$. Since here we have a reduction of the wave field, the depth dimensions of the object are reduced more than the lateral dimensions. Therefore large depth ranges are simultaneously sharp and even for strongly curved object surfaces all surface points can be reconstructed in focus with a single reconstruction distance d .

3.4.5 Hologram Recording Using Consumer Cameras

The rapid progress in the sector of *consumer still cameras* leading to higher pixel numbers and falling prices makes these cameras interesting for digital holography. Investigations on the applicability of common color photo-cameras have been performed by Sekanina and Pospisil [82] (submitted for publication in June 2001) and the author (in 2002).

A necessary condition for a successful application in digital holography is the access of raw-image data, which means the hologram data must not be compressed by a lossy data compression method, e. g. the JPEG format. The TIFF mode provides the uncompressed color data at each pixel after the demosaicking process due to the Bayer array, see Section 2.8.5. It is advantageous if the camera objective is detachable; however this is only the case for some reflex cameras but not an attribute of the most common cheap digital still cameras. For the reflex cameras then it is necessary that the mirror can be manually fixed before recording to prevent minute vibrations.

The experiments presented in [82] employ a camera with a CCD-chip of 2048×1536 pixels having a pixel pitch of 5.51 μm in both directions. Unfortunately this cam has an undetachable objective, therefore an optical arrangement as shown in Fig. 3.39 has been used.

We recognize the point source of a spherical reference wave in the plane of the object, thus here we have lensless Fourier transform holography. The microinterference field present in aperture A_1 is imaged onto the CCD via the lenses L_1 , L_2 , and L_3 . The apertures A_2 and A_3 are the images of A_1 created by L_1 and L_2 , respectively. Lens L_3 is the given objective of the camera.

The experiments performed by the author employed a reflex camera with a 3072×2048 pixel CMOS image sensor. Its pixel pitch is 7.4 μm in each direction. The holograms are recorded with a plane reference wave, and green laser light has been used. The reconstructed field was calculated by the Fresnel transform from the green color TIFF image, which also can be interpreted as the luminance signal. Effective FFT calculation as described in Section A.11

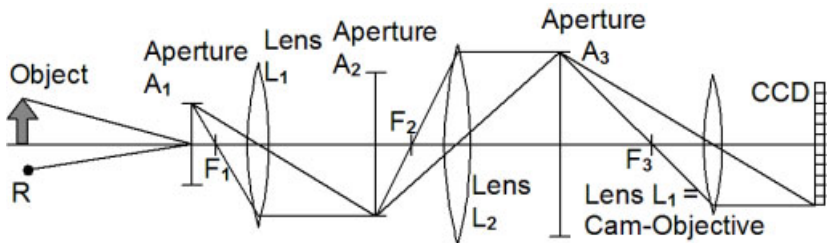


Figure 3.39: Digital holography using a camera with undetachable objective.

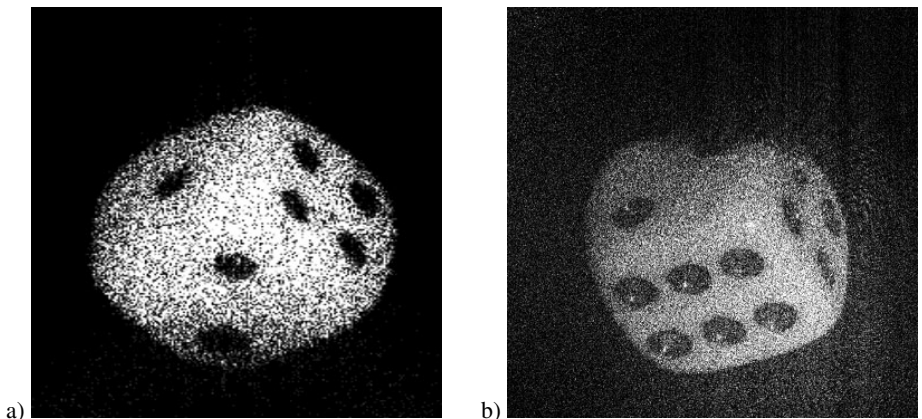


Figure 3.40: Digitally reconstructed intensity of a die. Hologram recorded with (a) 1024×1024 pixels, (b) 3072×2048 pixels.

was performed. The result of one such experiment is given in Fig. 3.40b. For comparison in Fig. 3.40a we have the identical object but whose digital hologram was recorded with a 1024×1024 pixel monochromic CCD array. It is an excerpt from the reconstructed intensity distribution already presented in Fig. 3.14. We recognize the smaller speckles and the better resolution obtained with the 6 times higher pixel number. The applicability of consumer still cams offers to holographers all the advantages of these machines like flexibility, automatic exposure control, in-cam storage of images, and no need for extra frame-grabber cards, and this for a lower price.

3.5 Wave-Optics Analysis of Digital Holography

The process of digital holography from the recording of an optical wave field by a CCD array, storing it in digital form in computer memory, to the numerical reconstruction of the image field can be interpreted as a coherent optical system yielding a complex wave field which is an image of the wave field originally reflected or refracted by an object. Fourier analysis is a powerful tool to describe coherent and incoherent imaging of optical systems [160]. By

its means the *point spread function* (PSF), also called the *impulse response*, of the system is calculated, which characterizes the optical system and specifies the influences of the various parameters.

In this section a Fourier analysis of the digital holography optical system is presented both for the Fresnel reconstruction and for convolution reconstruction [221, 256, 257]. It is shown that the point spread function mainly depends on the CCD aperture. Furthermore the effects of the fill factor of CCD pixels are derived with the help of the point spread function.

3.5.1 Frequency Analysis of Digital Holography with Reconstruction by Fresnel Transform

Digital holography now is interpreted as an optical system imaging an object wave field in the (x, y) -plane to a reconstructed optical field related to the (x', y') -plane, this plane existent only in a computer. To find the impulse response $t(x', y')$ of this imaging system, we follow Goodman [160]. Let the object be a point source characterized by $b(x, y) = \delta(x - x_0, y - y_0)$ in the object plane. Then incident on the CCD-target in the hologram plane, the (ξ, η) -plane, will appear a spherical wave $B(\xi, \eta; x_0, y_0)$ diverging from point (x_0, y_0) . In paraxial approximation this wave is written

$$B(\xi, \eta; x_0, y_0) = \frac{1}{i\lambda d} \exp \left\{ \frac{ik}{2d} [(\xi - x_0)^2 + (\eta - y_0)^2] \right\}. \quad (3.122)$$

A reference wave $r(\xi, \eta) = u_r(\xi, \eta) \exp\{i\phi(\xi, \eta)\}$ is superposed in the hologram plane. Both waves interfere, and the resulting intensity distribution is the hologram $h(\xi, \eta; x_0, y_0)$, which is recorded by the CCD, see (3.32):

$$\begin{aligned} h(\xi, \eta; x_0, y_0) &= |B(\xi, \eta) + r(\xi, \eta)|^2 \\ &= \frac{1}{\lambda^2 d^2} + u_r^2(\xi, \eta) + \frac{2u_r(\xi, \eta)}{\lambda d} \exp \left\{ \frac{ik}{2d} [(\xi - x_0)^2 + (\eta - y_0)^2] - \phi(\xi, \eta) \right\} \\ &\quad - \frac{2u_r(\xi, \eta)}{\lambda d} \exp \left\{ -\frac{ik}{2d} [(\xi - x_0)^2 + (\eta - y_0)^2] - \phi(\xi, \eta) \right\} \\ &= \frac{1}{\lambda^2 d^2} + u_r^2(\xi, \eta) + \frac{2u_r(\xi, \eta)}{\lambda d} \sin \left\{ \frac{k}{2d} [(\xi - x_0)^2 + (\eta - y_0)^2] - \phi(\xi, \eta) \right\}. \end{aligned} \quad (3.123)$$

This continuous real valued hologram is recorded by the CCD array and by this transformed into a two-dimensional array of discrete values, which constitute the digital hologram. The resulting digital hologram h_1 is characterized by

$$\begin{aligned} h_1(\xi, \eta; x_0, y_0) &= h(\xi, \eta; x_0, y_0) \left[\text{rect} \left(\frac{\xi}{\alpha \Delta \xi}, \frac{\eta}{\beta \Delta \eta} \right) * \text{comb} \left(\frac{\xi}{\Delta \xi}, \frac{\eta}{\Delta \eta} \right) \right] \text{rect} \left(\frac{\xi}{N \Delta \xi}, \frac{\eta}{M \Delta \eta} \right). \end{aligned} \quad (3.124)$$

Here $\text{rect}[\xi/(\alpha \Delta \xi), \eta/(\beta \Delta \eta)]$ represents a single two-dimensional pixel of the CCD. The pixel pitch is $\Delta \xi$ in the ξ -direction and $\Delta \eta$ in the η -direction. The fill-factors in these directions are $\alpha, \beta \in [0, 1]$. The periodic appearance of pixels is expressed by the convolution

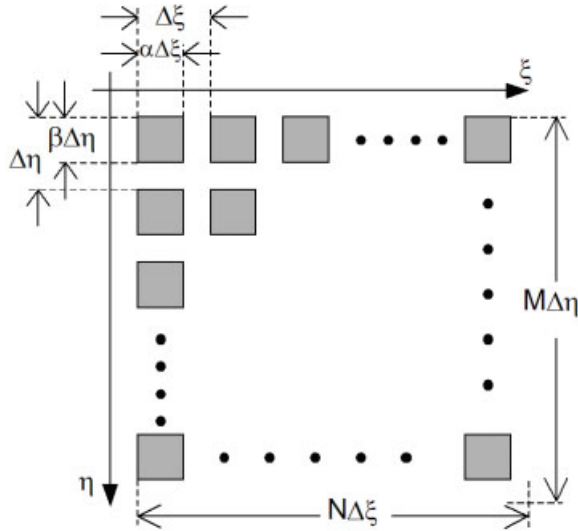


Figure 3.41: Parameters of the CCD-array.

with the comb-function $\text{comb}[\xi/\Delta\xi, \eta/\Delta\eta]$. The whole array has a finite width given by $N\Delta\xi \times M\Delta\eta$ where N and M are the pixel numbers in each direction, Fig. 3.41.

For reconstruction the stored hologram $h_1(\xi, \eta; x_0, y_0)$ is multiplied with the conjugate reference wave r^* and from the resulting product field in the hologram plane the field in the image plane is calculated by the Fresnel diffraction equation which accounts for the propagation over d' , see (3.33).

$$\begin{aligned} b'(x', y'; x_0, y_0) & \quad (3.125) \\ & = \frac{1}{i\lambda d'} \int_{-\infty}^{\infty} \int_{-\infty}^{\infty} h_1(\xi, \eta; x_0, y_0) r^*(\xi, \eta) \exp \left\{ \frac{ik}{2d'} [(x' - \xi)^2 + (y' - \eta)^2] \right\} d\xi d\eta. \end{aligned}$$

After evaluating the squares in the exponential and the coordinate transform $x' / (\lambda d') \rightarrow x'$, $y' / (\lambda d') \rightarrow y'$ this represents the Fourier transform

$$b'(x', y'; x_0, y_0) = \mathcal{F} \left\{ h_1(\xi, \eta; x_0, y_0) r^*(\xi, \eta) \exp \left[\frac{ik}{2d'} (\xi^2 + \eta^2) \right] \right\} (x', y') \quad (3.126)$$

where phase factors which do not depend on the hologram also are omitted.

For the further discussion of the point spread function $b'(x', y'; x_0, y_0)$ as derived in (3.126), several cases will be treated separately. The first case that will be considered in more detail is the one using the most simple reference wave: the plane wave of unit amplitude impinging normally onto the CCD: $u_r(\xi, \eta) \exp\{i\phi(\xi, \eta)\} = 1$. Since now there are no mixed terms xy , $x'y'$ or $\xi\eta$, the equations can be separated for both directions and it is sufficient to

consider only one dimension.

$$\begin{aligned} b'(x'; x_0) &= \mathcal{F} \left\{ h_1(\xi; x_0) \exp \left[\frac{ik}{2d'} \xi^2 \right] \right\} (x') \\ &= \mathcal{F} \left\{ h(\xi; x_0) \left[\text{rect} \left(\frac{\xi}{\alpha \Delta \xi} \right) * \text{comb} \left(\frac{\xi}{\Delta \xi} \right) \right] \text{rect} \left(\frac{\xi}{N \Delta \xi} \right) \exp \left(\frac{ik}{2d'} \xi^2 \right) \right\} (x'). \end{aligned} \quad (3.127)$$

The hologram field, Eq. (3.123), can be expressed in one dimension by

$$h(\xi; x_0) = A + C \exp \left[\frac{ik}{2d} (\xi - x_0)^2 \right] + C^* \exp \left[-\frac{ik}{2d} (\xi - x_0)^2 \right] \quad (3.128)$$

where additive and multiplicative terms are summarized in A and C . This gives

$$\begin{aligned} b'(x'; x_0) &= \mathcal{F} \left\{ \left[\text{rect} \left(\frac{\xi}{\alpha \Delta \xi} \right) * \text{comb} \left(\frac{\xi}{\Delta \xi} \right) \right] \text{rect} \left(\frac{\xi}{N \Delta \xi} \right) \left[A + \frac{C}{2i} \exp \left(\frac{ik}{2d} (\xi - x_0)^2 \right) \right. \right. \\ &\quad \left. \left. - \frac{C}{2i} \exp \left(-\frac{ik}{2d} (\xi - x_0)^2 \right) \right] \exp \left(\frac{ik}{2d'} \xi^2 \right) \right\} (x'). \end{aligned} \quad (3.129)$$

Performing the multiplication of the last term in square brackets with the exponential yields

$$\begin{aligned} &\left[A + \frac{C}{2i} \exp \left(\frac{ik}{2d} (\xi - x_0)^2 \right) - \frac{C}{2i} \exp \left(-\frac{ik}{2d} (\xi - x_0)^2 \right) \right] \exp \left(\frac{ik}{2d'} \xi^2 \right) \\ &= A \exp \left(\frac{ik}{2d'} \xi^2 \right) + \frac{C}{2i} \exp \left[\frac{ik}{2} \left(\frac{\xi^2}{d} + \frac{\xi^2}{d'} - \frac{2x_0 \xi}{d} + \frac{x_0^2}{d} \right) \right] \\ &\quad - \frac{C}{2i} \exp \left[-\frac{ik}{2} \left(\frac{\xi^2}{d} - \frac{\xi^2}{d'} - \frac{2x_0 \xi}{d} + \frac{x_0^2}{d} \right) \right]. \end{aligned} \quad (3.130)$$

The impulse response we are looking for is the Fourier transform of the product resulting when the three terms on the right-hand side of Eq. (3.130) are multiplied with the CCD-term. The presence of a quadratic phase factor in what otherwise would be a Fourier transform relationship will generally have the effect of broadening the impulse response [160]. One has to recognize that only the terms containing the squared variable of integration ξ^2 make trouble, phase factors containing x_0^2 do not affect the Fourier transform. Now the trick is to choose special reconstruction distances d' which make some of these terms identically vanish.

The first term on the right-hand side of Eq. (3.130) corresponds to the d.c.-term. The second term represents the virtual image. It simplifies for $d' = -d$. In the third term, which stands for the real image, the quadratic phase factor is eliminated by the choice $d' = +d$. Let us look at the real image more closely. By choosing $d' = +d$, we obtain a sharp real image without broadening by quadratic exponentials. Nevertheless the d.c.-term remains present and the virtual image is severely broadened so that it appears as a very unsharp cloud in the reconstructed intensity field, see Fig. 3.14b. Now the real image stems from the term $-\frac{C}{2i} \exp \left\{ -\frac{ik}{2d} (-2x_0 \xi + x_0^2) \right\}$ in Eq. (3.130). By application of the convolution theorem

Eq. (3.129) gives

$$\begin{aligned}
b'_{real}(x'; x_0) &= \mathcal{F} \left\{ \left[\text{rect} \left(\frac{\xi}{\alpha \Delta \xi} \right) \star \text{comb} \left(\frac{\xi}{\Delta \xi} \right) \right] \text{rect} \left(\frac{\xi}{N \Delta \xi} \right) \frac{C}{2i} \exp \left[-\frac{ik}{2d} (-2x_0 \xi + x_0^2) \right] \right\} \\
&= \alpha \Delta \xi \text{sinc}(\alpha \Delta \xi x') \text{comb}(\Delta \xi x') \star \mathcal{F} \left\{ \text{rect} \left(\frac{\xi}{N \Delta \xi} \right) \frac{C}{2i} \exp \left[-\frac{ik}{2d} (-2x_0 \xi + x_0^2) \right] \right\}.
\end{aligned} \tag{3.131}$$

Since

$$\mathcal{F} \left\{ \text{rect} \left(\frac{\xi}{N\Delta\xi} \right) \exp \left(\frac{ik}{2d} 2x_0 \xi \right) \right\} = \text{sinc} \left[N\Delta\xi \left(x' - \frac{kx_0}{d} \right) \right] \quad (3.132)$$

we obtain finally

$$b'_{real}(x'; x_0) = D \operatorname{sinc}(\alpha \Delta \xi x') \operatorname{comb}(\Delta \xi x') \star \operatorname{sinc} \left[N \Delta \xi \left(x' - \frac{k x_0}{d} \right) \right] \quad (3.133)$$

where constant intensity and phase factors are contained in D .

Many CCD-arrays have a fill-factor of 100%, meaning $\alpha = \beta = 1$. In this case we use $\text{sinc}(\Delta\xi x')\text{comb}(\Delta\xi x') = \delta(x')$ and Eq. (3.133) simplifies and leads to the compact result

$$b'_{real}(x'; x_0) = D \operatorname{sinc} \left[N \Delta \xi \left(x' - \frac{k x_0}{d} \right) \right]. \quad (3.134)$$

Thus the impulse response of the optical system digital holography producing the real image by using the standard plane reference wave is represented by the shifted Fraunhofer diffraction pattern of the aperture defined by the CCD-dimensions. It is a well known fact that if we sample in the spatial domain with a rate $\Delta\xi$ and N samples, then in the related spatial frequency domain the samples calculated by a discrete finite Fourier transform have the distances $\Delta x' = (N\Delta\xi)^{-1}$. Now let the width of the impulse response be defined by the distance between the first zeros of the sinc-function right and left to the origin, then it has the width of two sample distances in the numerically reconstructed image.

Up to now of the three terms on the right-hand side of (3.130) we have considered in more detail only the one related to the real image. The one related to the virtual image can be treated with the same reasoning. On the other hand in Section 3.2.6, we have seen methods for suppressing this image. The d.c.-term of the complex impulse response is determined from (3.130) as

$$\begin{aligned}
b'_{dc}(x'; x_0) &= \mathcal{F} \left\{ \left[\text{rect} \left(\frac{\xi}{\alpha \Delta \xi} \right) * \text{comb} \left(\frac{\xi}{\Delta \xi} \right) \right] \text{rect} \left(\frac{\xi}{N \Delta \xi} \right) A \exp \left(\frac{ik}{2d'} \xi^2 \right) \right\} \\
&= A \alpha \Delta \xi \text{sinc}(\alpha \Delta \xi x') \text{comb}(\Delta \xi x') * \mathcal{F} \left\{ \text{rect} \left(\frac{\xi}{N \Delta \xi} \right) \exp \left(\frac{ik}{2d'} \xi^2 \right) \right\}.
\end{aligned} \tag{3.135}$$

The Fourier transform on the right-hand side of the convolution is calculated in Section A.13. Therefore the d.c.-term manifests as a bright square of width $2\pi N \Delta\xi^2 / (d' \lambda)$. A minimization of d' is dictated by the required focusing of the real image. Nevertheless the d.c.-term must

have no detrimental effects for there are effective ways to completely eliminate the d.c.-term as introduced in Section 3.2.5.

In the above derivation we have assumed a 100% fill-factor. A large fill-factor results in an averaging of the hologram's intensity distribution in the CCD-plane. A suitable way to analyze the averaging effect of different fill-factors is the sampling of a *chirp function*. Because its frequency increases linearly with the spatial coordinate the influence of the fill-factor to different frequencies can be depicted in a single image. Figure 3.42a displays the real part

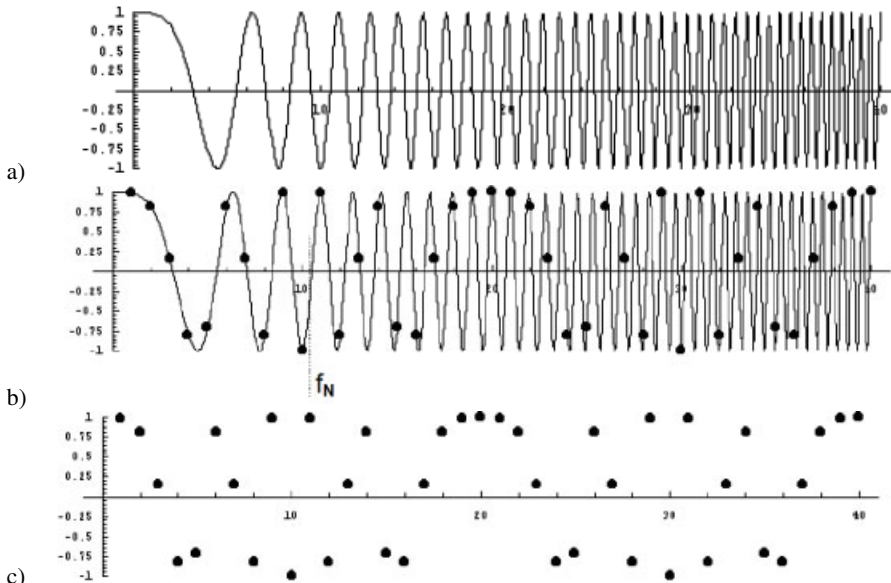


Figure 3.42: Sampling of a chirp function.

of the one-dimensional chirp function $g(\xi) = \exp\{ia\xi^2\}$. The sampling at discrete points, corresponding to a fill-factor approaching zero, is shown in Fig. 3.42b, only the sampled values are shown in Fig. 3.42c. We clearly recognize the Nyquist-limit posted by the sampling theorem at the spatial frequency where one period of the oscillation begins to be sampled by less than two samples. The periodic nature of the samples in Fig. 3.42c stems from the fact that the sampling interval is an integer multiple of a in the formula of $g(\xi)$.

If on the other hand we sample the same chirp function as before with a fill-factor of 100%, we obtain the sampled values of Fig. 3.43a. The continuous chirp function between consecutive sample points is integrated to yield the sampled values. The amplitudes differ from those of Fig. 3.42. While in the foregoing example, Fig. 3.42, the modulus of each sampled complex value was 1, now this modulus varies according to Fig. 3.43b. If we choose a fill-factor of $\alpha = 0.5$ we get the moduli of the sampled complex values as shown in Fig. 3.43c. Figs. 3.43b and 3.43c represent discrete samples of the geometric modulation transfer function (MTF) given in Section 2.8.4 in (2.193). The MTF quantifies the ability of the optical system to transmit spatial frequencies. For fill-factors greater than the zero of pointwise sampling

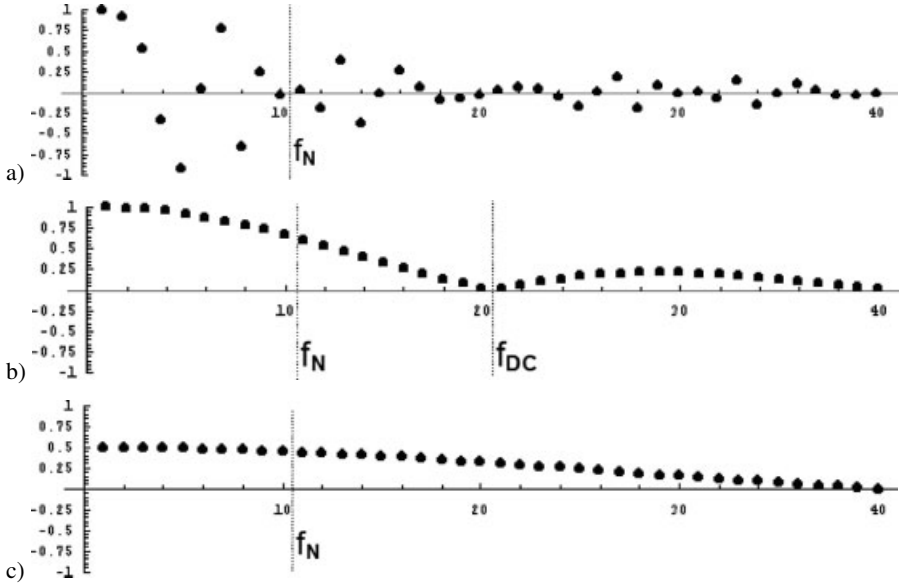


Figure 3.43: Sampling of a chirp function with fill-factors below 100%.

higher frequencies are imaged with less contrast. For a 100% fill-factor, the *MTF* falls to about 64% of the maximum value at the Nyquist frequency f_N .

For fill-factors less than 100% the factor $\text{sinc}(\alpha\Delta\xi x')\text{comb}(\Delta\xi x')$ in (3.133) will not reduce to a simple δ -impulse at zero. Instead the δ -pulses of the comb-function obtain different amplitudes from the sinc-function which now can take on nonzero values at the points sampled by the comb. The convolution in (3.133) then leads to a periodic replication of the impulse response in (3.134). One such period has the width $1/\Delta\xi$. Since we have N samples, the whole reconstructed image has the width $N\Delta x' = 1/\Delta\xi$ according to (3.36), so in fact we reconstruct only one of the replicated images [258]. Therefore in digital holography with numerical reconstruction this special aspect of the fill-factor can be neglected. On the other hand if we reconstruct digital holograms optically by using a suitable spatial light modulator, e. g. a digital micromirror device (DMD) [227, 259] then all replicated reconstructed images are projected.

The periodic nature of the sampled chirp function as seen in Fig. 3.42c leads to the effect that a finite sized object placed in a way that large angles between object wave and reference wave result and thus high spatial frequencies are produced which are severely undersampled, nevertheless the object surface is faithfully reconstructed. However frequencies now must be restricted to an interval $[n2f_N, (n+1)2f_N]$ in the spatial frequency domain, otherwise ambiguities occur. For fill-factors other than 0% (the pointwise sampling of Fig. 3.42) the intensity of the recorded patterns is reduced. Full theoretical support for this behavior is given by Onural in [132].

Up to now we have only investigated the case of a plane normally impinging reference wave. Next let a spherical reference wave diverge from the point (x_R, y_R, z_R) . This wave in

the (ξ, η) -plane is

$$r(\xi, \eta) = u_r(\xi, \eta) \exp \left\{ \frac{ik}{2z_R} [(\xi - x_R)^2 + (\eta - y_R)^2] \right\}. \quad (3.136)$$

The corresponding hologram distribution in analogy to (3.123) has the form

$$\begin{aligned} h(\xi, \eta; x_0, y_0) &= |u_t(\xi, \eta) + r(\xi, \eta)|^2 \\ &= \frac{1}{\lambda^2 d^2} + u_r^2(\xi, \eta) \\ &\quad + \frac{2u_r(\xi, \eta)}{\lambda d} \sin \left\{ \frac{k}{2} \left[\frac{(\xi - x_0)^2}{d} + \frac{(\eta - y_0)^2}{d} - \frac{(\xi - x_R)^2}{z_R} - \frac{(\eta - y_R)^2}{z_R} \right] \right\}. \end{aligned} \quad (3.137)$$

If we restrict ourselves again to one dimension, we can write

$$h(\xi; x_0) = A + C \sin \left\{ \frac{k}{2} \left[\frac{(\xi - x_0)^2}{d} - \frac{(\xi - x_R)^2}{z_R} \right] \right\}. \quad (3.138)$$

In analogy to the way that led to Eq. (3.130) we obtain

$$\begin{aligned} h(\xi; x_0) &\exp \left\{ i \frac{k}{2d'} \xi^2 \right\} \\ &= A \exp \left\{ i \frac{ik}{2d'} \xi^2 \right\} \\ &\quad + \frac{C}{2i} \exp \left\{ \frac{ik}{2} \left(\frac{\xi^2}{d'} + \xi^2 \left(\frac{1}{d} - \frac{1}{z_R} \right) - 2\xi \left(\frac{x_0}{d} - \frac{x_R}{z_R} \right) + \frac{x_0^2}{d} - \frac{x_R^2}{z_R} \right) \right\} \\ &\quad - \frac{C}{2i} \exp \left\{ -\frac{ik}{2} \left(-\frac{\xi^2}{d'} + \xi^2 \left(\frac{1}{d} - \frac{1}{z_R} \right) - 2\xi \left(\frac{x_0}{d} - \frac{x_R}{z_R} \right) + \frac{x_0^2}{d} - \frac{x_R^2}{z_R} \right) \right\} \\ &= A \exp \left\{ i \frac{ik}{2d'} \xi^2 \right\} \\ &\quad + \frac{C}{2i} \exp \left\{ \frac{ik}{2} \left(\frac{\xi^2}{d'} + \frac{\xi^2}{\hat{d}} - \frac{2\xi}{\hat{d}} \left(\frac{x_0 z_R - d x_R}{z_R - d} \right) + \frac{1}{\hat{d}} \left(\frac{x_0^2 z_R - d x_R^2}{z_R - d} \right) \right) \right\} \\ &\quad - \frac{C}{2i} \exp \left\{ -\frac{ik}{2} \left(-\frac{\xi^2}{d'} + \frac{\xi^2}{\hat{d}} - \frac{2\xi}{\hat{d}} \left(\frac{x_0 z_R - d x_R}{z_R - d} \right) + \frac{1}{\hat{d}} \left(\frac{x_0^2 z_R - d x_R^2}{z_R - d} \right) \right) \right\} \end{aligned} \quad (3.139)$$

where in the last two lines we have introduced

$$\hat{d} = \frac{d z_R}{z_R - d}. \quad (3.140)$$

Again we only investigate the last part of (3.139) which is related to the real image and also concentrate only on the terms containing ξ^2 . One way to perform the numerical reconstruction is to multiply the hologram h with the conjugate of the spherical reference wave (3.136). This eliminates the ξ^2 -terms in that part of (3.139) describing the real image and the problem is reduced to the already treated case of a plane reference wave resulting in the same impulse response. Another way to reconstruct is to leave out the multiplication with the conjugate

reference wave and to use instead the reconstruction distance $d' = \hat{d}$, which has the same effect of eliminating the ξ^2 -terms. This approach is recommended since it avoids some complex multiplications with possible rounding errors, especially in the high spatial frequency regions of the digital holograms.

The important case of lensless Fourier transform holography, see Section 3.2.3, is characterized by $z_R = d = d'$. In this case Eq. (3.138) simplifies to

$$h(\xi; x_0) = A + C \sin \left\{ \frac{k}{2} \left[\frac{2\xi(x_R - x_0)}{d} - \frac{x_0^2 - x_R^2}{d} \right] \right\}. \quad (3.141)$$

The multiplication with $\exp\{ik\xi^2/(2d')\}$, e. g. as in Eq. (3.127), is compensated at least in the terms containing ξ^2 by the multiplication with the conjugate of the reference wave. Thus in practice we neither have to multiply with $\exp\{ik\xi^2/(2d')\}$, which is characteristic for the Fresnel transform, nor do we have to carry out the multiplication with the reference wave, we have to perform only the Fourier transform. Equation (3.139) now reduces to

$$\begin{aligned} h(\xi; x_0) = A &+ \frac{C}{2i} \left[\exp \left\{ \frac{ik}{2d} (2\xi(x_R - x_0) + x_0^2 - x_R^2) \right\} \right. \\ &\quad \left. - \exp \left\{ \frac{-ik}{2d} (2\xi(x_R - x_0) + x_0^2 - x_R^2) \right\} \right]. \end{aligned} \quad (3.142)$$

The Fourier transform of this expression represents the reconstructed image of lensless Fourier transform holography. It has a d.c.-term that is not broadened but is restrained to a single pixel. Furthermore the choice $z_R = d = d'$ eliminates all ξ^2 -terms simultaneously in the real and the virtual image, so both images are reconstructed sharply focused, a behavior we already know.

3.5.2 Frequency Analysis of Digital Holography with Reconstruction by Convolution

Besides reconstruction by the Fresnel transform there exist powerful reconstruction methods based on convolution. This approach is introduced in Section 3.3. As in Section 3.5.1 we perform a frequency analysis to find out the point spread function in the case of reconstruction by convolution. Again we start with an idealized point source at coordinates (x_0, y_0) in the object plane producing the field $B(\xi, \eta; x_0, y_0)$ in the hologram plane as given in (3.122). The resulting hologram $h(\xi, \eta; x_0, y_0)$ as well as the sampled, digitized, recorded, and stored hologram $h_1(\xi, \eta; x_0, y_0)$ are the same as in the aforementioned case of reconstruction by the Fresnel transform and given in (3.123) and (3.124) respectively. From the digital hologram $h_1(\xi, \eta; x_0, y_0)$ multiplied with the conjugate of the reference wave $r^*(\xi, \eta)$ the field in the image plane is now calculated by

$$b'(x', y'; x_0, y_0) = \mathcal{F}^{-1} \{ \mathcal{F} \{ h_1(\xi, \eta; x_0, y_0) \cdot r^*(\xi, \eta) \} \cdot \mathcal{F} \{ g(\xi, \eta) \} \}. \quad (3.143)$$

The equivalence of the image plane and the hologram plane in the case of convolution reconstruction has been discussed in Section 3.4.4, so the coordinates (x', y') are chosen for

comparability reasons; (ξ, η) could have been chosen with the same justification. The impulse response $g(\xi, \eta)$ in (3.143) is the one defined in (3.73) or with discrete arguments in (3.76). Its Fourier transform can be replaced by the transfer function G of (3.77) or (3.79) respectively. As in the preceding section we begin with the plane reference wave of unit amplitude impinging normally onto the recording element and furthermore restrict our investigations to one dimension. In one dimension the hologram $h(\xi; x_0)$ is defined as in (3.128). Then the reconstructed field is

$$\begin{aligned}
b'(x'; x_0) &= \mathcal{F}^{-1} \left\{ \mathcal{F} \left\{ \left[\text{rect} \left(\frac{\xi}{\alpha \Delta \xi} \right) \star \text{comb} \left(\frac{\xi}{\Delta \xi} \right) \right] \text{rect} \left(\frac{\xi}{N \Delta \xi} \right) h_1(\xi; x_0) \right\} \cdot \mathcal{F} \{g(\xi)\} \right\} \\
&= \mathcal{F}^{-1} \left\{ \left[\mathcal{F} \left\{ \text{rect} \left(\frac{\xi}{\alpha \Delta \xi} \right) \right\} \cdot \mathcal{F} \left\{ \text{comb} \left(\frac{\xi}{\Delta \xi} \right) \right\} \right. \right. \\
&\quad \left. \left. \star \mathcal{F} \left\{ \text{rect} \left(\frac{\xi}{N \Delta \xi} \right) h_1(\xi; x_0) \right\} \right] \mathcal{F} \{g(\xi)\} \right\} \\
&= \mathcal{F}^{-1} \left\{ [\text{sinc}(\alpha \Delta \xi f_\xi) \text{comb}(\Delta \xi f_\xi) \right. \\
&\quad \left. \star \mathcal{F} \left\{ \text{rect} \left(\frac{\xi}{N \Delta \xi} \right) \exp \left[\frac{-ik}{2d} (\xi - x_0)^2 \right] \right\} \right] \mathcal{F} \{g(\xi)\} \right\}.
\end{aligned} \tag{3.144}$$

Again we have taken only the last term of (3.128), and constant factors have been omitted. The product $\text{sinc}(\alpha \Delta \xi f_\xi) \text{comb}(\Delta \xi f_\xi)$ is a series of Dirac-deltas with unequal amplitudes which have been described in detail in Section 3.5.1. Here we investigate only the central Dirac pulse, so we can replace the last named product by $\delta(f_\xi)$ and obtain

$$b'(x'; x_0) \approx \mathcal{F}^{-1} \left\{ \mathcal{F} \left\{ \text{rect} \left(\frac{\xi}{N\Delta\xi} \right) \exp \left[\frac{-ik}{2d} (\xi - x_0)^2 \right] \right\} \mathcal{F} \{g(\xi)\} \right\}. \quad (3.145)$$

The first of the two Fourier transforms in the product to be inversely transformed is the transform of a shifted chirp function windowed to a finite extent by $\text{rect}(\xi/(N\Delta\xi))$. This windowing cuts off all spatial frequencies other than from $x/(d\lambda) - N\Delta\xi/(2d\lambda)$ to $x/(d\lambda) + N\Delta\xi/(2d\lambda)$. The amplitude spectrum is nearly flat over this range of frequencies and zero outside. Such a spectrum is investigated in more detail in Section A.13. It extends over $N^2\Delta\xi^2/(d\lambda)$ of the N pixels in the f_ξ -space which is shown in Fig. 3.44.

Figure 3.44a displays the digital hologram of a noncentral point ($x_0 \neq 0, y_0 \neq 0$). It looks like the real part or the imaginary part of a displaced 2D windowed chirp function. The amplitude spectrum of its Fourier transform is given in Fig. 3.44b. Since the hologram is real, the spectrum is Hermitean, which manifests in the two parts, mutually symmetric with respect to the origin and overlapping in the present case.

The complex Fourier transform of the hologram still contains the whole information that was existent in the digital hologram. Possibly this information content is decreased when the complex spectrum is multiplied with the transfer function. As an example, if we use the transfer function, whose amplitude is shown in Fig. 3.45a, then the spectrum shown in Fig. 3.44b is truncated to the one displayed in Fig. 3.45b.

Application of the inverse Fourier transform in (3.145) results in the reconstructed real image of the point source, which represents the point spread function of the whole system, Fig. 3.46.

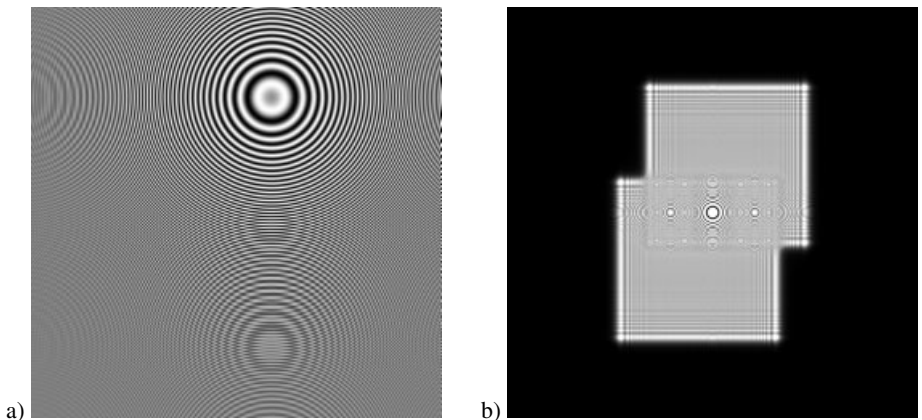


Figure 3.44: Digital hologram of (a) a point source and (b) its Fourier transform.

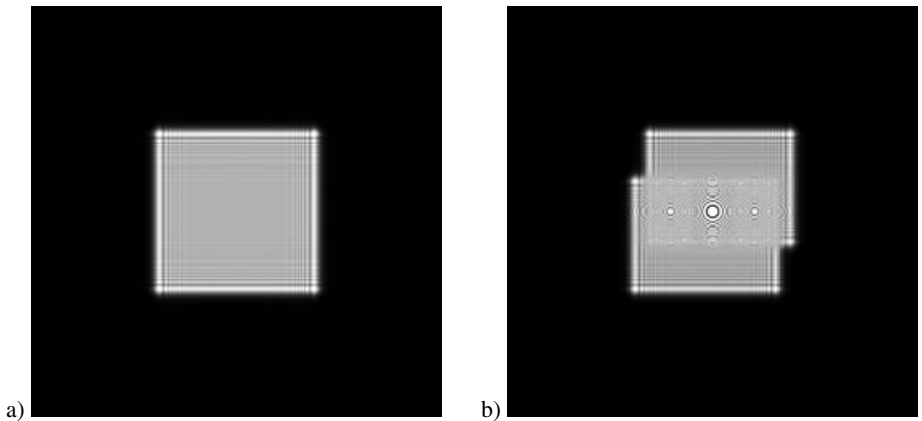


Figure 3.45: Intensity of (a) the transfer function and (b) the ‘filtered’ spectrum.

It is approximately a two-dimensional sinc-function, whose arguments are defined by either the size of the transfer function, or by the size of the transformed hologram, depending on which is the smaller of the two. In the displayed example the transfer function defines the sinc-function characteristics. The non-symmetric appearance of the point spread function evident in Fig. 3.46b is due to the noncentral position of the original point in the object plane. The size of the hologram transform can be modified only in the design stage of the experiment, so in order to obtain the best resolution, the transfer function should be more extended than the hologram transform. Therefore in the next section the transfer function is investigated in more detail, leading to the concept of *cascaded reconstruction*.

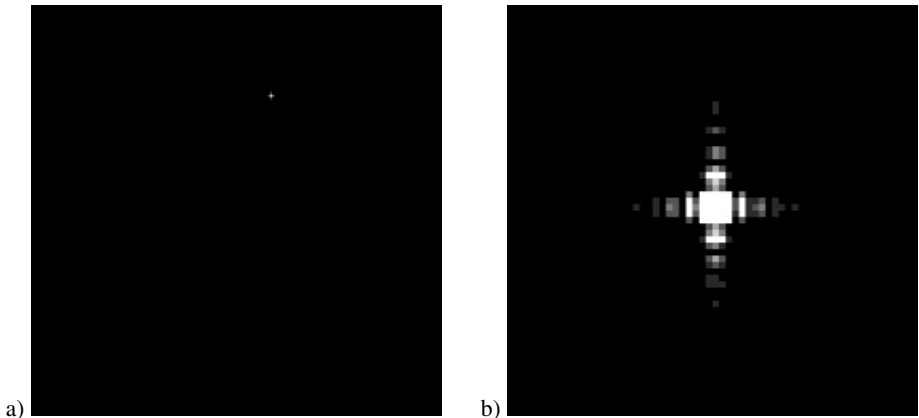


Figure 3.46: Reconstructed image of a point (a) and (b) enlarged part of (a).

3.5.3 The Transfer Function as a Filter

In the following the impulse response functions as well as the transfer functions are investigated in more detail to understand the results of digital holographic reconstruction and to define further options for processing digital holograms. In Fig. 3.47 two impulse responses are compared.

For the fictitious parameters $\lambda = 0.5 \text{ } \mu\text{m}$, $\Delta\xi = \Delta\eta = 10 \text{ } \mu\text{m}$, $N = M = 1024$, and $k_s = l_s = 512$ the impulse response $g_{1.0m}(k, l)$ belonging to a reconstruction distance $d = 1.0 \text{ m}$ and $g_{0.5m}(k, l)$ corresponding to $d = 0.5 \text{ m}$ are presented. The real and imaginary parts together with the phase are displayed. The intensity is not given since it is nearly constant. While the real part is the cosine of the specific argument the imaginary part is the sine of the same argument. Therefore the imaginary part looks like a phase shifted version of the related real part.

The transfer functions belonging to the impulse responses of Fig. 3.47 are given in Fig. 3.48.

In the intensity patterns, Figs. 3.48c and d, we see that only over a finite range the transfer function has values which are significantly distinct from zero. Only in this range does the phase have relevant data, the phases outside are artificial values generated from numerical noise. The reason for the limited domain of the transfer function is the finite impulse response. We see in Section A.13 as well as in Fig. 3.47 that the restriction of the impulse response to a finite rectangular window allows the formation of only a limited band of spatial frequencies. Also we recognize that for a smaller distance d even more spatial frequencies are in the same window. This leads to a larger area of nonzero spatial frequencies in the transfer function, as can be seen in a comparison of Figs. 3.48c and d. The width of the significant part of the transfer function measured in pixels is

$$\frac{N^2 \Delta\xi^2}{d\lambda} \quad (3.146)$$

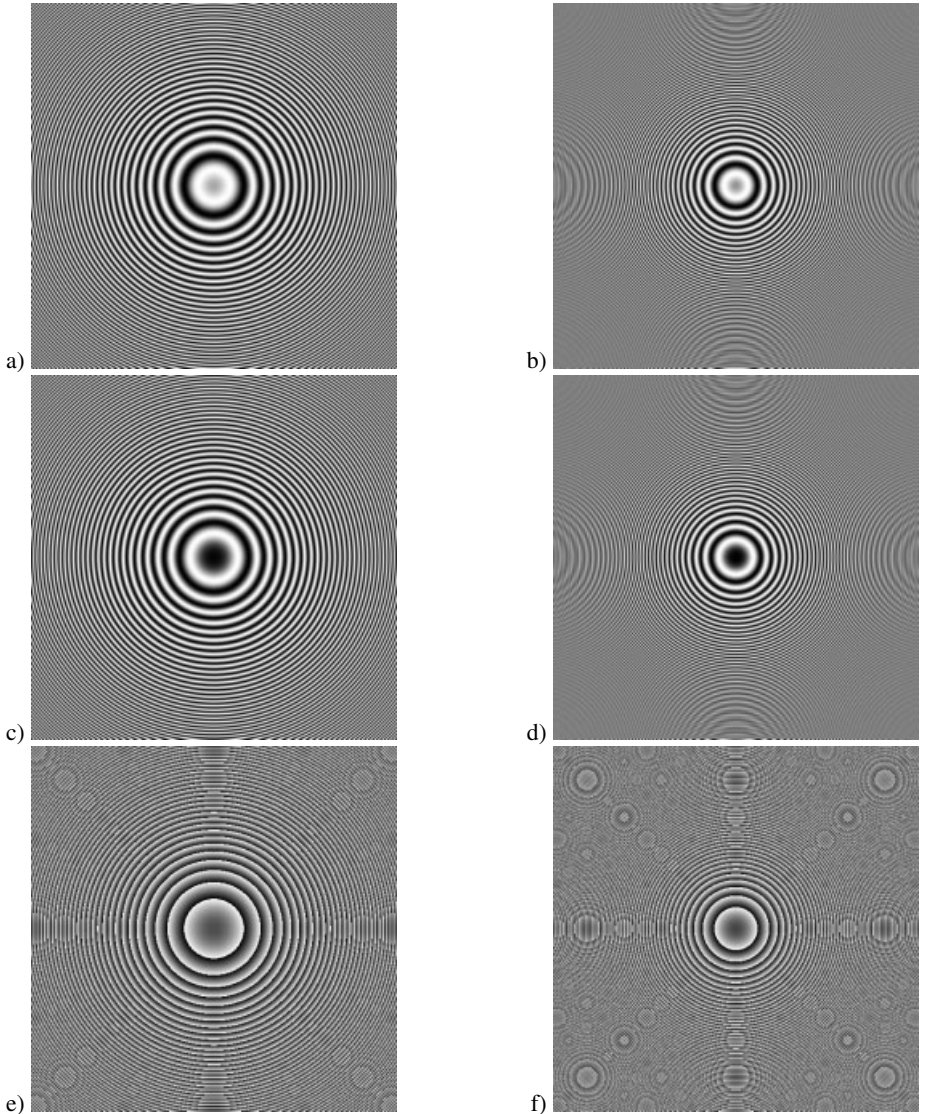


Figure 3.47: Impulse responses: (a) real part of $g_{1.0m}(k, l)$, (b) real part of $g_{0.5m}(k, l)$, (c) imaginary part of $g_{1.0m}(k, l)$, (d) imaginary part of $g_{0.5m}(k, l)$, (e) phase of $g_{1.0m}(k, l)$, (f) phase of $g_{0.5m}(k, l)$.

in the ξ -direction and the same with M and $\Delta\eta$ in the other direction. The maximum width N we have for $d = N\Delta\xi^2/\lambda$. A larger width is impossible; this would belong partially to spatial frequencies which cannot be resolved in the finite discrete impulse response. Two more intensity displays of transfer functions belonging to the same parameters as before are given

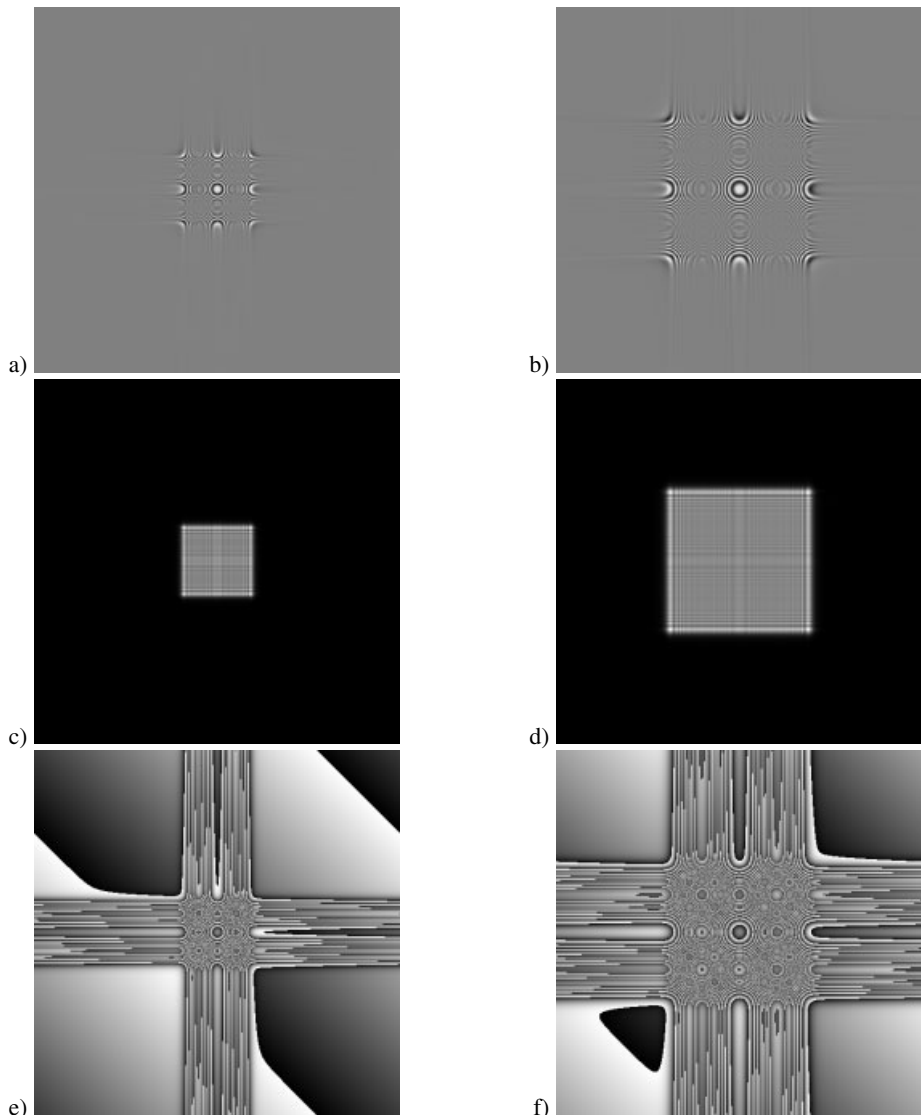


Figure 3.48: Transfer functions: (a) real part of $G_{1.0m}(n, m)$, (b) real part of $G_{0.5m}(n, m)$, (c) intensity of $G_{1.0m}(n, m)$, (d) intensity of $G_{0.5m}(n, m)$, (e) phase of $G_{1.0m}(n, m)$, (f) phase of $G_{0.5m}(n, m)$.

in Fig. 3.49, but now for the distances 0.33 m and 0.2048 that represents the maximum field for the chosen parameters.

The limited domain in the transfer function now has the effect that not all spatial frequencies eventually contained in the product of hologram and reference wave pass through

the multiplication step with the transfer function in the spatial frequency domain. This inherent low-pass filtering eliminates the high frequencies, eventually fine details are averaged out. To avoid this effect a transfer function with positive amplitudes over a rather large frequency band should be chosen for performing the reconstruction. It was already mentioned that the frequency range where the transfer function is non-vanishing increases with decreasing reconstruction distance d . Therefore d should be as small as possible without violating the sampling theorem. This is shown in one dimension in Fig. 3.50. The object consists of bright bars of differing width, Fig. 3.50a. The parameters for the simulation are $\lambda = 0.5 \mu\text{m}$, $\Delta\xi = 5.0 \mu\text{m}$, $N = 1024$. The amplitude of the normally impinging reference wave is 1. The impulse response for $d = 0.4 \text{ m}$ is given in Fig. 3.50b, and Fig. 3.50c shows its Fourier transform amplitude, the amplitude of the transfer function. The reconstructed intensity is shown in Fig. 3.50d with the original intensity inserted for better comparison. Figs. 3.50e to g show the same distributions for $d = 0.2 \text{ m}$ and Figs. 3.50h to j these for $d = 0.1 \text{ m}$. It is obvious how the steepness of the flanks increases with the increasing frequency bands.

The aim to use transfer functions belonging to small reconstruction distances d leads to the concept of cascaded free space propagation. Let us take the transfer function as defined in (3.77) or (3.79). With the properties of the exponential it can easily be shown that

$$G_d(n, m) = \prod_{i=1}^k G_{d_i}(n, m) \quad \text{with} \quad \sum_{i=1}^k d_i = d \quad (3.147)$$

where the subscript d in G_d indicates the distance for which the transfer function is defined. As an example

$$G_d(n, m) = G_{d/2}(n, m)G_{d/2}(n, m) \quad (3.148)$$

which is displayed in Fig. 3.51. Here we see that the diffraction field $b_2(x'', y'')$ can be calculated by free space propagation from the (ξ, η) -plane over the distance d . But alternatively we

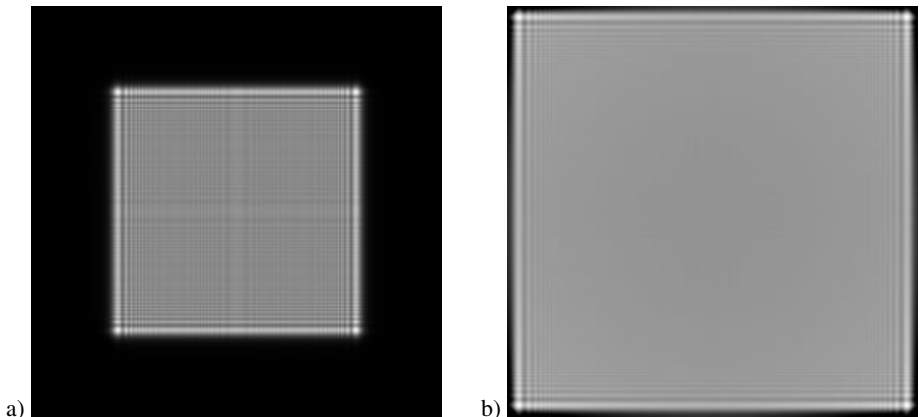


Figure 3.49: Transfer functions: (a) intensity of $G_{0.33m}(n, m)$, (b) intensity of $G_{0.2048m}(n, m)$.

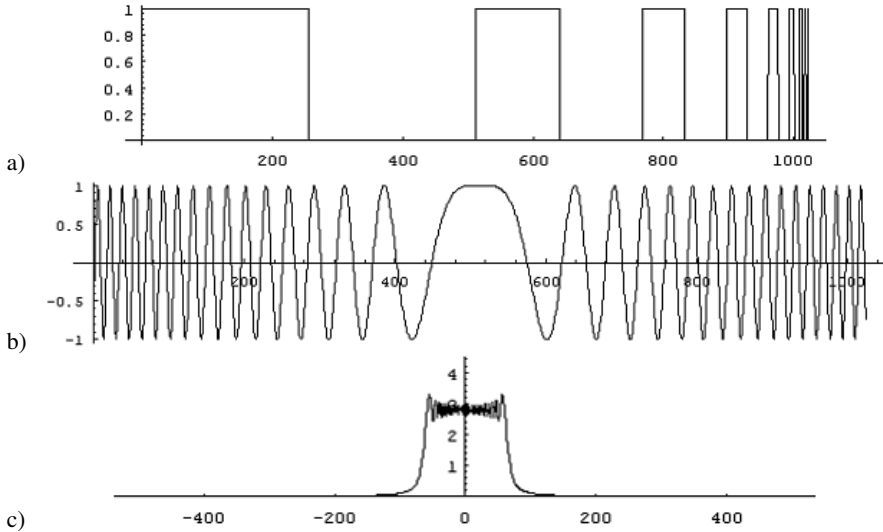


Figure 3.50: Simulated reconstructions of a bar pattern.

can calculate first the field $b_1(x', y')$ by free space propagation over $d/2$ followed by a second propagation over $d/2$ from $b_1(x', y')$ to $b_2(x'', y'')$. The field in the (x', y') -plane is

$$b_1(x', y') = \mathcal{F}^{-1}\{\mathcal{F}\{h \cdot r\} \cdot G_{\frac{d}{s}}\}. \quad (3.149)$$

With this we get

$$\begin{aligned} b_2(x'', y'') &= \mathcal{F}^{-1}\{\mathcal{F}\{b_1(x', y')\} \cdot G_{\frac{d}{s}}\} \\ &= \mathcal{F}^{-1}\{\mathcal{F}\{\mathcal{F}^{-1}\{\mathcal{F}\{h \cdot r\} \cdot G_{\frac{d}{s}}\}\} \cdot G_{\frac{d}{s}}\} \\ &= \mathcal{F}^{-1}\{\mathcal{F}\{h \cdot r\} \cdot G_{\frac{d}{s}} \cdot G_{\frac{d}{s}}\} \end{aligned} \quad (3.150)$$

because $\mathcal{F}\{\mathcal{F}^{-1}\{f\}\} = f$ for any f .

The effect of the cascaded transfer function is shown in an example where the object consists of bright stochastic phase rectangles of different size. These were chosen to demonstrate the fidelity and resolution of the reconstruction, Fig. 3.52a.

The whole object has the size of the d.c.-term, the parameters are $\lambda = 0.5 \mu\text{m}$, $\Delta\xi = \Delta\eta = 10 \mu\text{m}$, $n = m = 1024$, $d = 0.82 \text{ m}$. The Fresnel-reconstructed intensity is given in Fig. 3.52b. The reconstructions using convolutions and the cascaded transfer functions $G_{0.82m}$, $(G_{0.41m})^2$, $(G_{0.273m})^3$, and $(G_{0.205m})^4$ are shown in Figs. 3.52c, d, e, and f. We recognize large speckles of low frequency in Fig. 3.52c where we reconstructed with $G_{0.82m}$. The fine high-frequency structures of the object are blurred. These fine structures are better recognized in Figs. 3.52d and e. The blurring increases again for $(G_{0.0205m})^4$ but now the reason is that we are at the limit of the sampling theorem for this distance and the chosen parameters.

The results of the theoretical investigations on shifted versions of the chirp function in Section A.13 are valid also for the shifted impulse response functions (3.88) since the chirp

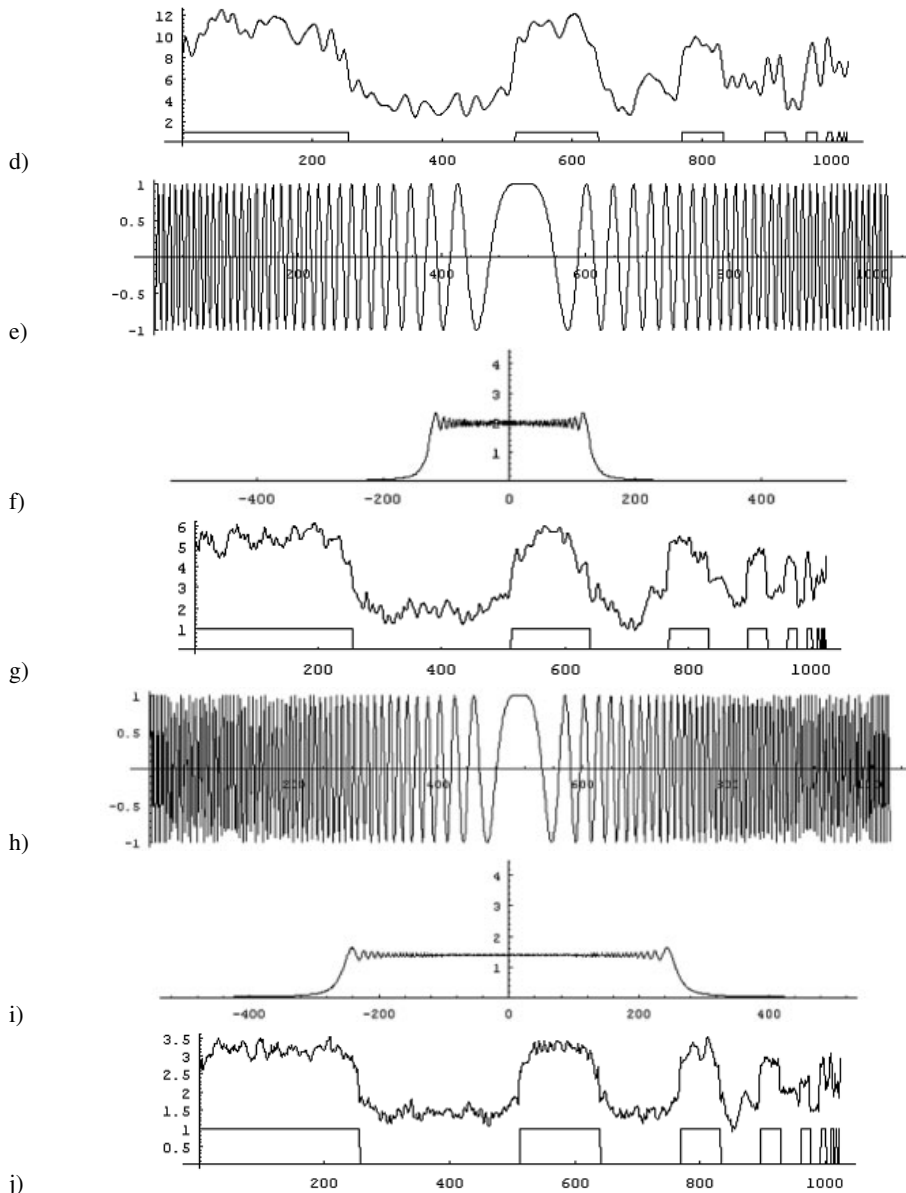


Figure 3.50 (continued): Simulated reconstructions of a bar pattern.

function is an approximation of this impulse response, which is especially evident for the Fresnel approximated version g_F , see (3.80). Shifts (s_k, s_l) move the centers of the ring structures of the impulse responses in the finite rectangular window. It is even possible that the center is far outside the window and only high-frequency partial rings are in the finite field.

This in the spatial frequency domain moves the non-zero part of the transfer function. However, the various reconstructed fields displayed in Fig. 3.27 required different shifts, so the

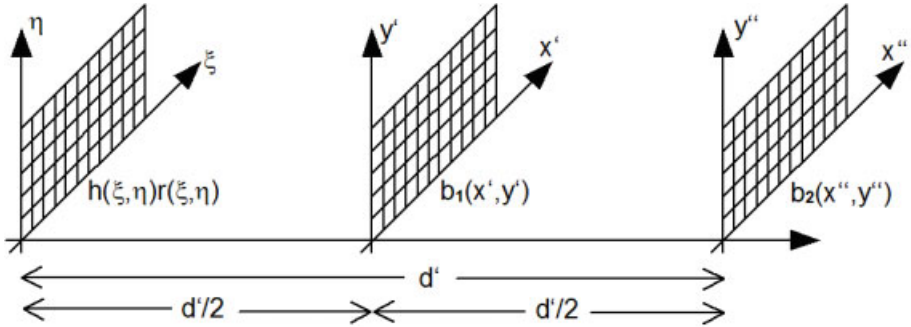


Figure 3.51: Cascaded free space propagation.

transfer functions defined different passbands, nevertheless all nine reconstructed intensities show nearly the same frequency content. For the investigation of this effect we assume an object centered on the optical axis as shown in Fig. 3.53. The object plane is divided into different sections. First we look at section 1 that is reconstructed using the impulse response

$$g(k - N/2, l - M/2) = \frac{i e^{\frac{2\pi i}{\lambda} \sqrt{d^2 + (k - N/2)^2 \Delta \xi^2 + (l - M/2)^2 \Delta \eta^2}}}{\lambda \sqrt{d^2 + (k - N/2)^2 \Delta \xi^2 + (l - M/2)^2 \Delta \eta^2}}. \quad (3.151)$$

The dimensions of this section agree with the dimensions of the CCD array, meaning a length $N \Delta \xi$ in the considered coordinate direction. The spectrum of the impulse response is centered around the zero frequency, thus the transfer function acts like a low-pass filter. The cutoff frequency f_C of this filter is the local frequency at $k = N/2$. Following the definition (A.105) of the local frequency we have to calculate

$$f_{loc}(k) = \frac{1}{2\pi} \frac{\partial}{\partial k \Delta \xi} \left(\frac{2\pi}{\lambda} \sqrt{d^2 + (k - N/2)^2 \Delta \xi^2} \right) \quad (3.152)$$

where we neglect the second coordinate direction and omit the denominator of (3.151) that is only slowly spatially varying. The reconstructed field appears low-pass filtered, no spatial frequencies higher than f_C are present in the image.

For the reconstruction of section 2 that also has the width like the CCD array and that follows section 1 without a gap, we must employ the impulse response that is shifted by $(s_k, s_l) = (N, 0)$ with respect to (3.151)

$$g(k + N/2, l - M/2) = \frac{i e^{\frac{2\pi i}{\lambda} \sqrt{d^2 + (k + N/2)^2 \Delta \xi^2 + (l - M/2)^2 \Delta \eta^2}}}{\lambda \sqrt{d^2 + (k + N/2)^2 \Delta \xi^2 + (l - M/2)^2 \Delta \eta^2}}. \quad (3.153)$$

The spectrum of this impulse response is not centered about zero but defines a bandpass filter with positive low and high cutoff frequencies. Now the agreeing frequency contents in Fig. 3.27 seem to be a contradiction. The resolution of this supposed contradiction lies in the nature of holography, namely the coding of information with the help of a reference wave:

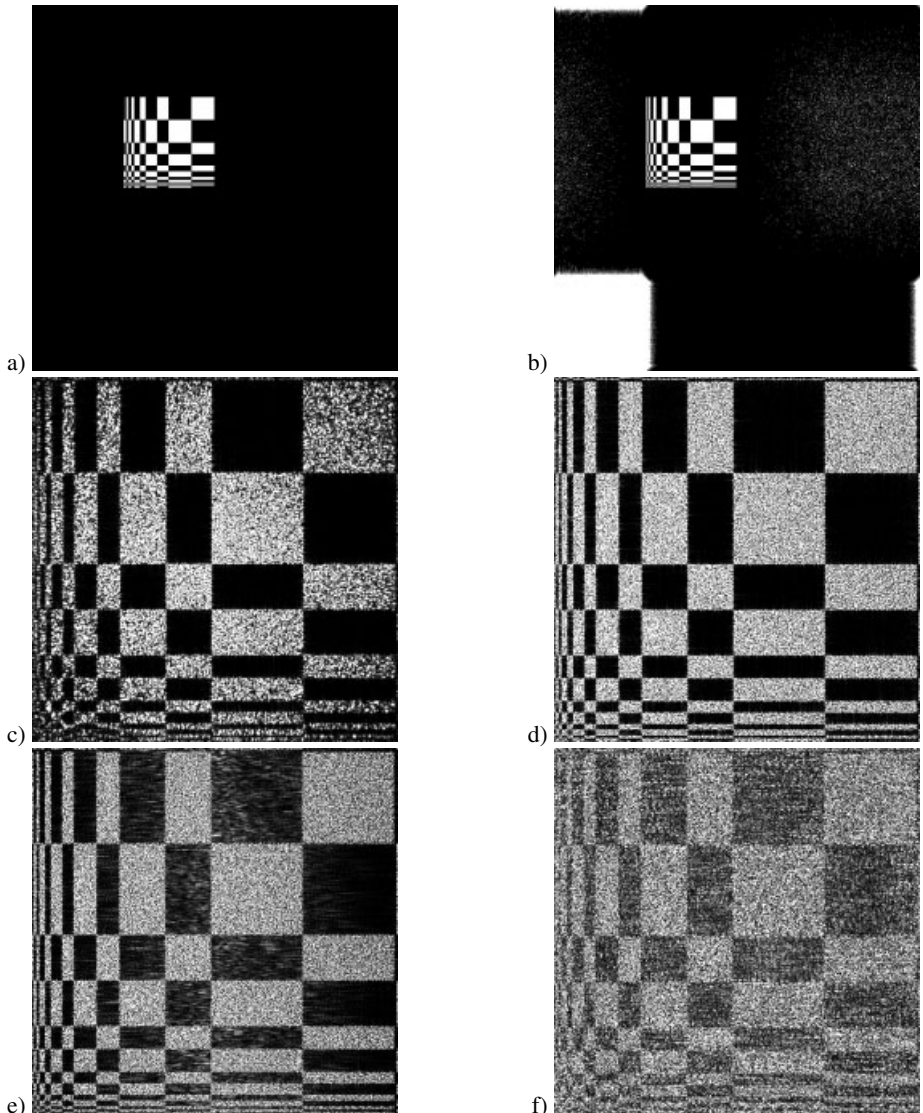


Figure 3.52: Cascaded reconstruction: (a) object, (b) reconstruction with Fresnel transform, (c) reconstruction using $G_{0.82m}$, (d) reconstruction using $(G_{0.41m})^2$, (e) reconstruction using $(G_{0.273m})^3$, (f) reconstruction using $(G_{0.205m})^4$.

All rays coming from points of section 1 form angles with the normally impinging reference wave which are between $-\theta$ and $+\theta$, defined by lines $\overline{x_1\xi_2}$ to $\overline{x_2\xi_1}$, Fig. 3.53. In the hologram they form microinterferences of frequencies $-\frac{2}{\lambda} \sin \frac{\theta}{2}$ to $+\frac{2}{\lambda} \sin \frac{\theta}{2}$. On the other hand the rays emitted from the points of section 2 intersect the reference wave under angles 0 to ψ , defined

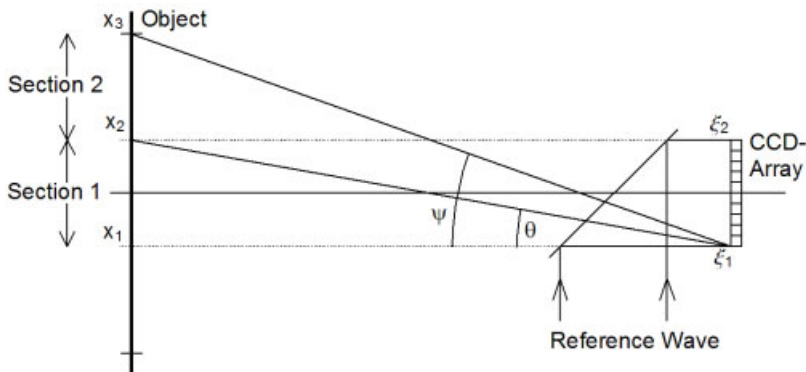


Figure 3.53: Geometry for the investigation of filtering.

by the lines $\overline{x_2\xi_2}$ to $\overline{x_3\xi_1}$, so they produce spatial frequencies from 0 to $+\frac{2}{\lambda} \sin \frac{\psi}{2}$ on the CCD array. It is $\tan \psi = 2 \tan \theta$, but since θ and ψ must remain small due to the sampling theorem, we are allowed to set $\psi = 2\theta$ and $\sin \frac{\psi}{2} = 2 \sin \frac{\theta}{2}$. The points of section 2 thus generate a holographic microinterference pattern that modulates the carrier frequency $\frac{2}{\lambda} \sin \frac{\theta}{2}$. Therefore the corresponding spectrum appears shifted in the spatial frequency domain. We may consider the carrier frequency by shifting the spectrum of the hologram and the transfer function by the amount of the carrier. Then we can argue as for section 1 with regard to the filtering: The low-frequency information about the object is coded into high frequency microinterferences due to the angles with the reference wave. These high frequencies are recognized by the properly placed transfer function that is needed to reconstruct the low frequency object. It must be mentioned that still the sampling theorem is fulfilled, we do not have the case described in Section 3.5.1.

3.6 Non-Interferometric Applications of Digital Holography

The objective of this book is to give a coherent presentation of the many options in holographic interferometry as a metrologic tool. One of the most promising developments in this direction is digital holography which has become possible due to the rapid progress in computer and CCD/CMOS technology. But any description of digital holography remains incomplete, if other non-interferometric applications are not at least very briefly presented. Therefore in this section particle analysis, microscopy, and data encryption by digital holography are introduced. These applications have gained considerable attention and been the subject of research work. On the other hand there are fields where not so many results exist yet, e. g. pattern recognition by digital holography [260]. In the following description an emphasis is given to characteristic techniques, which may influence the further development of digital holographic interferometry. A detailed presentation of the various non-interferometric applications of digital holography is left for another book written by other authors.

3.6.1 Particle Analysis by Digital Holography

Holography is a prominent tool for the investigation of particle fields, especially of moving particles [261, 262]. It permits the recording of particles distributed throughout an appreciable volume. A typical example is the dispersion of droplets in turbulent two-phase flows. If short laser pulses are used, any motion is frozen. The hologram can be evaluated by focusing into different depths, so the 3D information can be revealed. In particular, microscopic moving particles in this way are effectively evaluated, which is not possible with a conventional optical system [172]. An evaluation of the hologram can determine size, position, spatial distribution, velocity etc. of the particles.

The holographic arrangement most common for *particle analysis* is that of Gabor's classic in-line holography, see Section 2.6.4. The in-line hologram captures the coherent superposition of the undiffracted component of an illuminating beam and the component that is diffracted at the particles [150, 261, 263, 264]. Reasonable quality of in-line holograms is obtained if a sufficient amount of light is directly transmitted to serve as the reference wave. As a rough estimate one should have at least 80 percent of the light in the reference wave [172]. The in-line arrangement requires a minimum of optical components, it is extremely robust due to the common path of object and reference wave, and it needs no very great coherence lengths of the laser used. This makes the method well suited for applications in adverse industrial and field environments.

Digital holography offers a new potential to holographic particle analysis. The tedious optical reconstruction of the various planes and scanning by repeated reconstruction through the investigated volume now can be done by computer program and may be performed fully automatically. The small angles between the diffracted field and the undiffracted reference wave immediately fulfill the sampling theorem of digital holography, see Section 3.1.1. An arrangement for particle analysis using digital in-line holography is shown in Fig. 3.54.

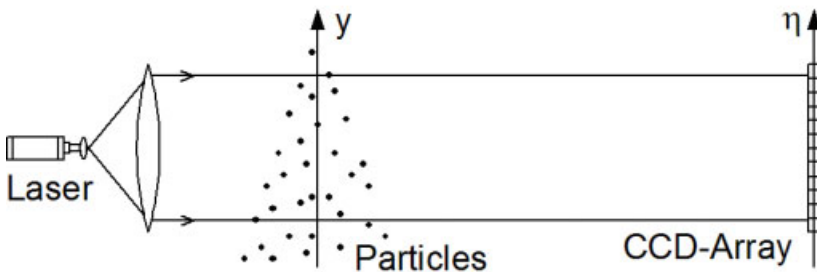


Figure 3.54: Scheme for particle analysis.

The conical form of the particle stream is typical for particles sprayed from a nozzle. A collimated laser beam illuminates the particle stream [265]. A part of the beam is diffracted by the particles, the other part passes the particle zone unaffected and acts as a plane reference wave. A hologram produced in this way is shown in Fig. 3.59a and the reconstructed intensity image in one plane indicating three particles is displayed in Fig. 3.59b. While the lateral position of each particle center can be localized with a resolution given by the pixel size in the reconstructed image, the depth resolution is rather poor. The reason is the depth of

focus that depends on the aperture of the optical system which is given here by the size of the CCD-array, see Section 3.4.4. This limited resolution can be depicted by the so called depth images: In digital holography we cannot only reconstruct in image planes parallel to the hologram plane [90], but also in those orthogonal to that plane, Fig. 3.55. Conventionally

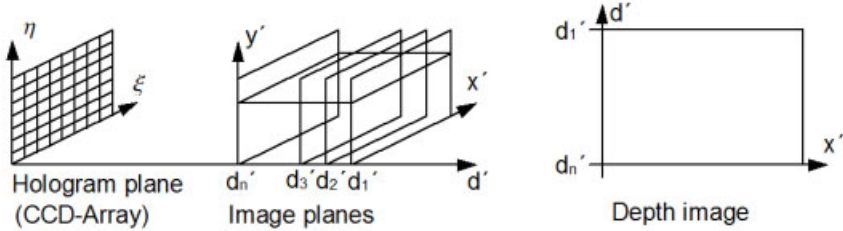


Figure 3.55: Orientation of reconstructed depth image.

we reconstruct in (x', y') -planes for fixed d' , but here we calculate the field in a (x', d') -plane for a fixed y' . Figure 3.56a gives the intensity reconstruction in the (x', y') -plane for three simulated particles at different distances to the CCD, each particle having a size of one pixel. The reconstruction depth d' coincides with the distance of the leftmost particle,

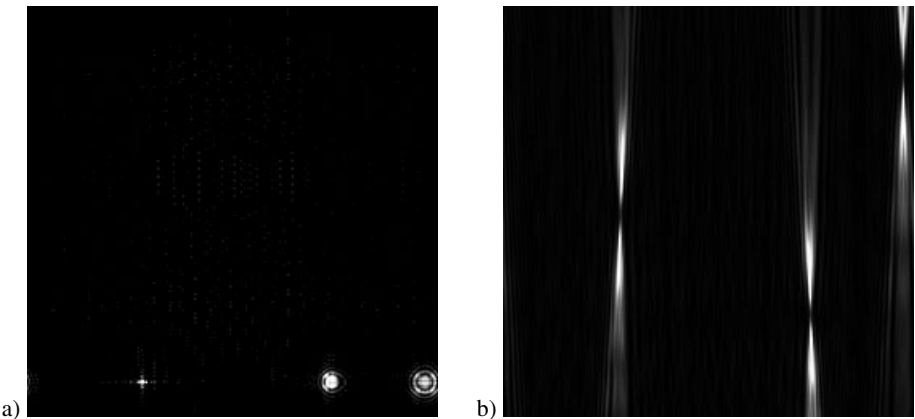


Figure 3.56: Reconstructed particles, image planes oriented parallel (a) and orthogonal (b) to the hologram plane.

therefore the other two particles are unsharp. The corresponding depth image is shown in Fig. 3.56b. The waists of the projected cones roughly indicate the loci of the three particles. Computational time can be saved if not the whole 2D depth image is calculated but only the 1D intensity distribution along a line parallel to the z -axis going through the center of the axisymmetric fringes belonging to a specific particle. The particle is located where this intensity is extremal [96].

A better attempt to determine position and form of the particles in 3D space is by a method related to tomography [253, 265, 266]. Several views of the particle or droplet spray corresponding to different angles of observation have to be recorded simultaneously. This is performed by a multiple pass arrangement. Figure 3.57a shows an arrangement where the collimated laser beam passes the particle stream three times. The deconvoluted light path is depicted in Fig. 3.58. Since in digital holography we can numerically focus to arbitrary distances d' , the images reconstructed for different distances correspond to different angular views of the particles.

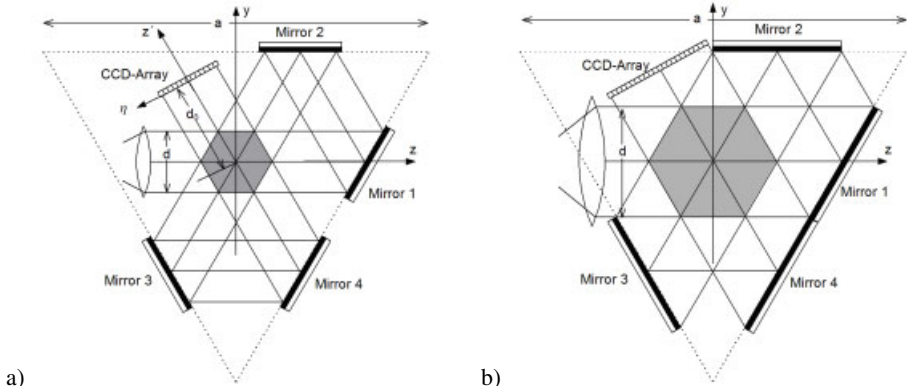


Figure 3.57: Triple pass arrangement for digital holographic particle analysis.

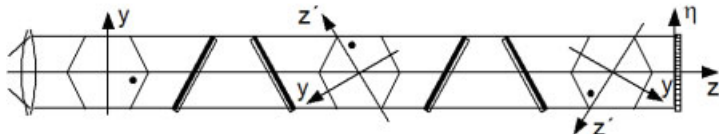


Figure 3.58: Virtual particles in deconvoluted light path.

An analysis of the arrangement of Fig. 3.57a shows that the flat mirrors coincide with the side planes of a prism whose base is an equal-sided triangle. If its sidelength is a then the width d of the collimated laser beam, which also is the width of the measurement volume, has to remain $d \leq a/(2\sqrt{3})$ to prevent shadowing by components. The arrangement with the maximum $d = a/(2\sqrt{3})$ is shown in Fig. 3.57b. For this arrangement the optical path from the origin over two mirrors back to the origin is exactly a , which defines the amount the reconstructed image planes have to be apart.

For the reconstruction the convolution approach instead of the Fresnel transform is now recommended, because all reconstructed images have the same size independent from the individual reconstruction distance. No adaptation of the image coordinates is necessary. An even more refined method for the reconstruction of particle fields in digital holography based on the 2D fractional-order Fourier transformation is presented in [89].

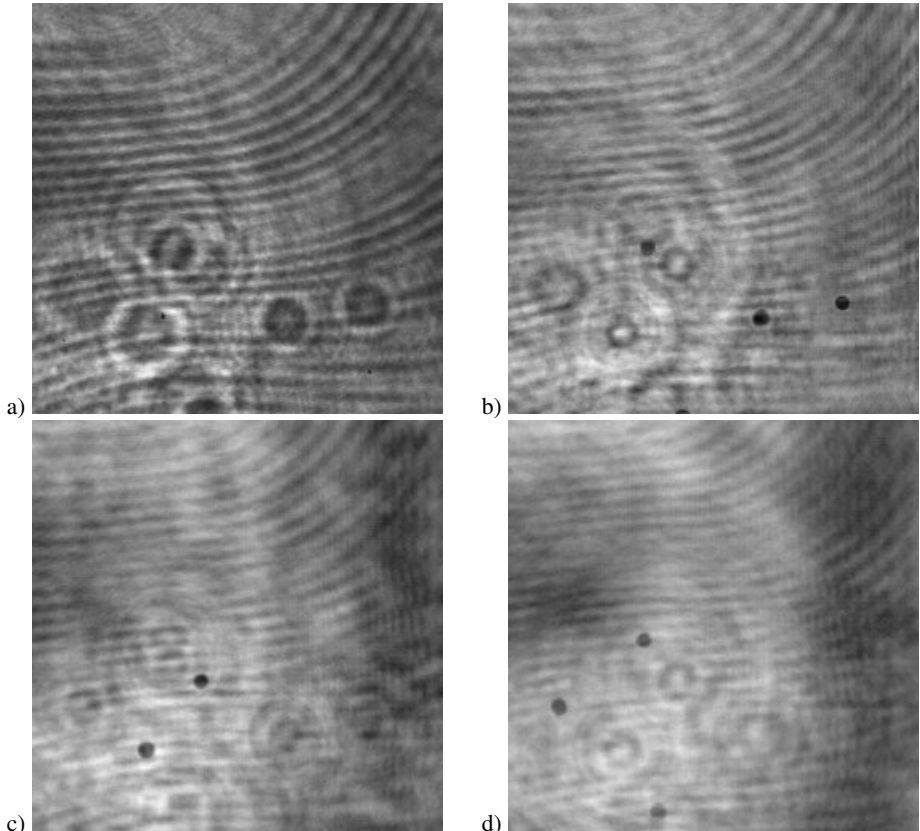


Figure 3.59: Digital hologram of particles (a) and reconstructed intensities for different distances (b), (c), (d).

By numerical focusing onto different distances during reconstruction, the different views of the particle field are gained. Figure 3.59a shows the digital in-line hologram of particles having about 250 μm diameter falling through the collimated beam of a pulsed laser. The CCD-array used in this experiment had 2048×2048 pixels each of size $9 \mu\text{m} \times 9 \mu\text{m}$. The particle fields now are reconstructed from the digital hologram at distances 40 cm, 65.5 cm, and 95.5 cm. The resulting intensity distributions are displayed in Figs. 3.59b, c, and d.

The reconstructed fields now can be evaluated with respect to size and position of the particles. As an intermediate step identical particles in the three reconstructions have to be identified. As long as in a fixed height y_0 there is a single particle image in each reconstruction, these images must stem from the same particle. Ambiguities will occur if there are more than one particle in a certain height y_0 . But since we have three views for determining the two-dimensional position (x_0, z_0) , this overdetermination can be used for particle identification: The positions of a particle in all three reconstructions must be compatible.

A concept related to the evaluation of different angular views of the same scene is *computerized tomography*. The intensity reconstructions along the line of the same height in all views are used for tomographic processing by e. g. the method of *filtered backprojection*. A schematic sketch of the backprojection principle is given in Fig. 3.60a. A result of this

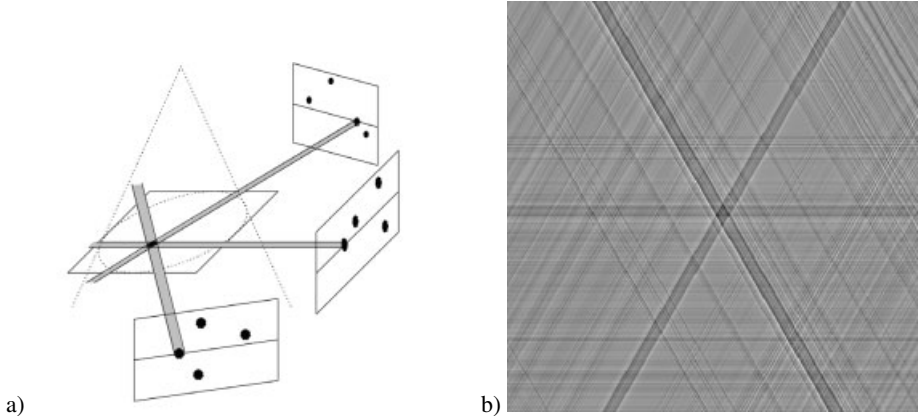


Figure 3.60: Tomographic reconstruction: Principle of filtered backprojection (a), reconstructed plane (b).

approach for the three views of Fig. 3.59 is given in Fig. 3.60b. The particle is located in the cross-section of the three projections visible as the darker streaks. However, the tomographic approach will become feasible if there are much more projections through the particle field than three. Using tomography to detect particle positions from only three views is like taking a sledgehammer to crack a nut. We do not need the ability of tomography to determine continuous transmission values: Our field is binary, the particles are opaque, the space between the particles is transparent.

A straightforward localization of the particles is by measuring their η -coordinate η_i in each view i ($i = 1, 2, 3$) for the investigated intersecting plane and solving the system of equations

$$\begin{aligned} y &= -\sqrt{3}z - 2\eta_3 \\ y &= +\sqrt{3}z - 2\eta_2 \\ y &= \eta_1. \end{aligned} \tag{3.154}$$

The depth coordinate of the particles does not need to be controlled very exactly due to the large depth of focus, nevertheless the lateral η -coordinates are determined very precisely.

The equations (3.154) define three lines whose common intersection gives the position of the particle in the chosen plane through the particle stream, Fig. 3.61a. Since the system is overdetermined, here even two particles in one plane produce no ambiguities but can be located uniquely, Fig. 3.61b.

Another arrangement used in practice also having three angular views is shown in Fig. 3.62. The dashed lines indicate the walls of an octagonal pressure chamber in and out of which the collimated beam is guided through transparent windows. The mirrors, the optics

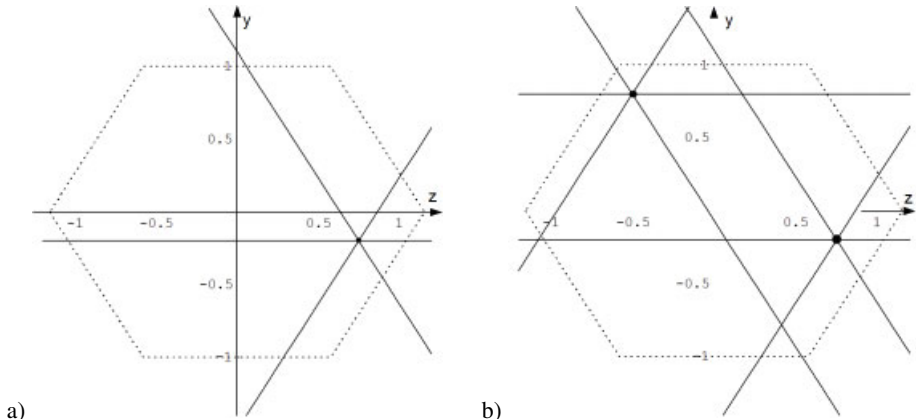


Figure 3.61: Lines indicating particle positions at triple intersection points.

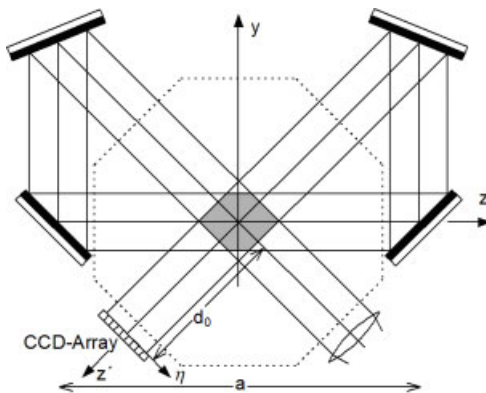


Figure 3.62: Arrangement for particle measurement in an octagonal chamber.

and the CCD-array are outside of the chamber. The related system of equations for this case is

$$\begin{aligned} y &= +z - \sqrt{2}\eta_3 \\ y &= \eta_2 \\ y &= -z - \sqrt{2}\eta_1. \end{aligned} \quad (3.155)$$

More alternatives for multiple pass arrangements are displayed in Fig. 3.63.

The velocity of the particles is obtained by recording digital holograms using double pulsed lasers [261, 265]. Figure 3.64a shows one of the intensity reconstructions of a digital double pulse hologram where the arrangement of Fig. 3.62 was used. Each particle appears twice. From the positions in space and the known pulse delay of 400 μs , a velocity of about 0.6 m s^{-1} was evaluated. The positions of five identified particles determined from several reconstructions are displayed perspectively in Fig. 3.64b. Digital image plane holography as a

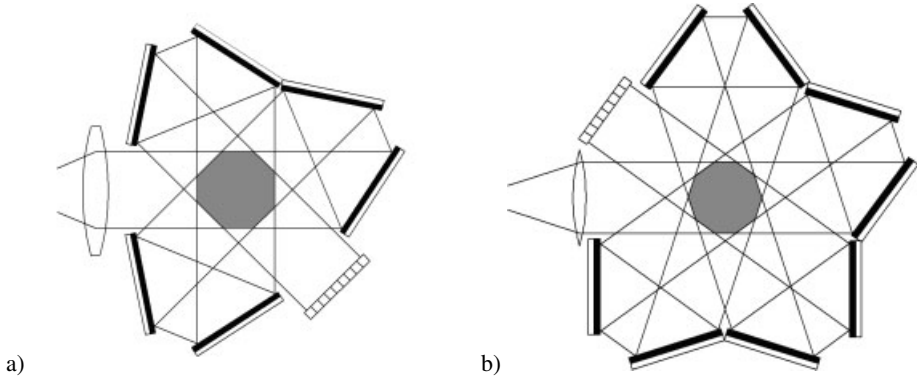


Figure 3.63: Arrangements with four (a) and five (b) passes through the particle stream.

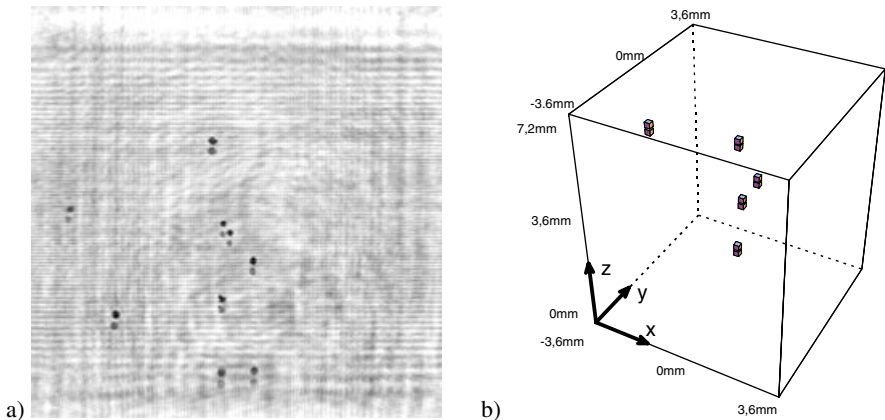


Figure 3.64: Particles reconstructed from digital double exposure hologram (a) and 3D particle distribution (b).

measurement tool for three-dimensional flow velocimetry is presented in [267]. A wavelet approach evaluating digital in-line holograms for multiple plane velocimetry is described in [88].

One may suspect that particles which are positioned one behind the other in the deconvoluted light path would hide each other. This would be so in a purely geometric approach analyzing only the shadow casting. But since the diffracted field of each particle spreads over the whole digital hologram, information from the rear particles is also contained in the hologram. This is demonstrated in the computer simulation shown in Fig. 3.65.

Figure 3.65a gives the digital hologram of particles assumed in three different planes which have the distances 1.0 m, 0.75 m, and 0.5 m from the CCD-array. The positions of the particles in the first plane are in pixel coordinates $\{(600, 300), (500, 800), (100, 900)\}$, in the second plane $\{(600, 300), (500, 800), (800, 400)\}$, and $\{(100, 100), (500, 800), (800, 400)\}$ in the third plane. This means that we have two times two particles one behind the other and once we have three particles lined up. The three intensity reconstructions are displayed in Figs. 3.65b to d, and all particles are uniquely reconstructed.

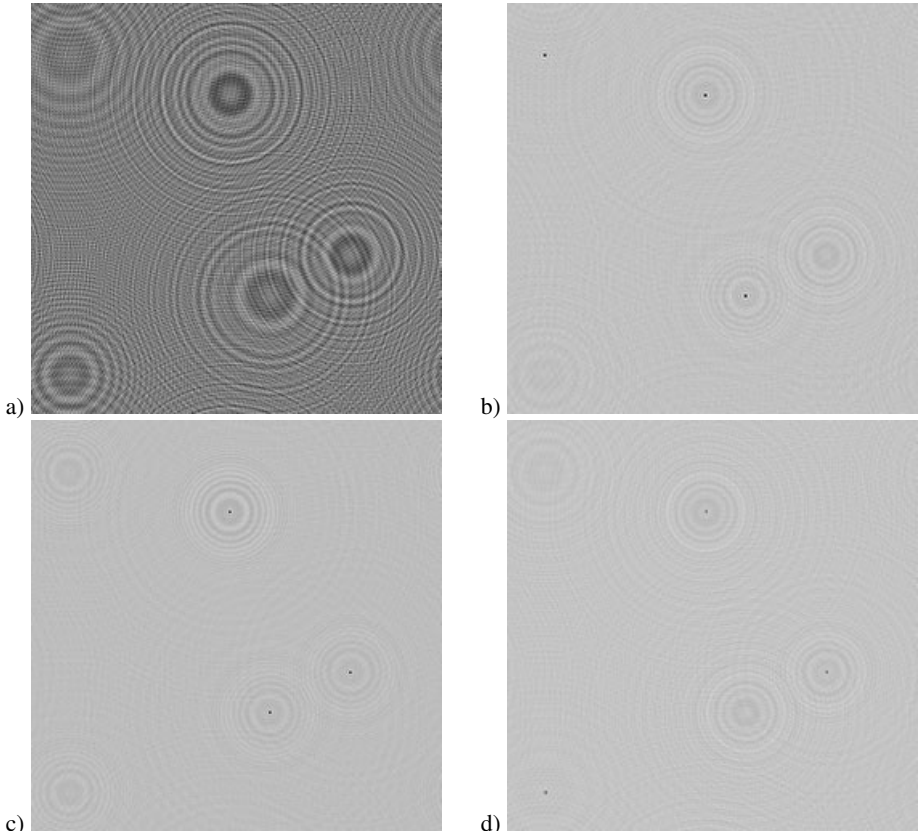


Figure 3.65: Simulated digital hologram and reconstructed particles.

A typical problem in digital in-line holography is the presence of the d.c.-term and the twin image in the reconstructed field, see e. g. Figs. 3.56b, c, and d. While the overall d.c.-term degrades the contrast, the twin images of the particles manifest as unsharp ring structures. Besides the possibilities of d.c.-term suppression of Section 3.2.5 or the employment of phase-shifting digital holography [268], an interesting method for eliminating the twin image in digital in-line holography is proposed by Lai et al. [269]: If not the whole area of the digital hologram is used for numerical reconstruction, but only a non-central part, then for a number of object points in a certain area we have an off-axis geometry with well separated d.c.-term and twin image. By changing the areas of the digital hologram in several reconstruction processes, different areas in the image plane can be reconstructed without a twin image. Finally these undisturbed areas are combined to the total reconstructed field.

A further source for a possible degradation of the reconstructed particle images is the limited size of the CCD array. Consider a single small particle. Its hologram in digital in-line holography consists of infinitely many concentric rings, see e. g. Fig. 3.65a. Due to the limited size of the CCD array only a finite number of such rings fit into the hologram, furthermore

the hologram pattern is rectangularly clipped. The consequences from these two facts are now discussed in more detail.

The finite number of rings leads to a blurring of the reconstructed particle image. The radii and thus the number of rings strongly depend on the distance d between particle and hologram: The further away the particle is from the hologram, the larger the ring radii are and the smaller is the number of rings hitting the CCD array. But the rings far away from the center with small distances between are those carrying the high frequency information. If they are cut away the particle image appears low-pass filtered. On the other hand the reconstructed particle is sharper if the distance d is decreased.

The square contour of the CCD array can be modeled by a two-dimensional rectangular function $\text{rect}(ax) \cdot \text{rect}(ay)$, see (A.6). The infinite hologram is multiplied with this function. Therefore the reconstructed particle appears as convolved with the transform of this function, a two-dimensional sinc-function, see Table A.1. Figure 3.66 illustrates this with a simulation of a single particle at different distances.

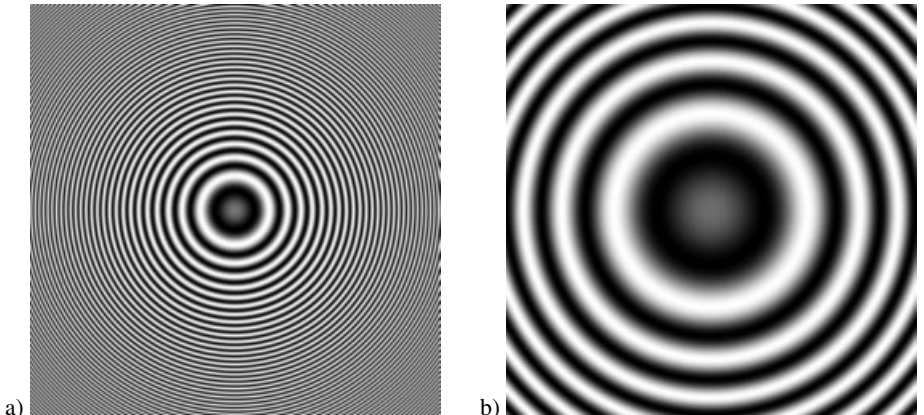


Figure 3.66: Digital holograms of a particle: (a) $d = 1.0$ m, (b) $d = 8.0$ m.

Figure 3.66a shows the hologram of the particle $d = 1.0$ m away from the hologram plane, while Fig. 3.66b displays the hologram for $d = 8.0$ m. The fewer rings in Fig. 3.66b are obvious. Figures 3.66c to f give the magnified central parts of the reconstructed intensity fields. The partial image that has been magnified has the same size in all four displays. The simulations were performed with the distances $d = 1.0$ m (Figs. 3.66a and c), $d = 2.0$ m (Fig. 3.66d), $d = 4.0$ m (Fig. 3.66e), and $d = 8.0$ m (Figs. 3.66b and f). One can recognize the increasing blurring with increasing distance d , also the sinc-function influence. Although the reconstructed patterns here are displayed to the full gray-scale their contrast decreases with increasing d : The contrast $C = (I_{\max} - I_{\min})/(I_{\max} + I_{\min})$ is $C(d = 1.0m) = 0.56$, $C(d = 2.0m) = 0.17$, $C(d = 4.0m) = 0.035$, and $C(d = 8.0m) = 0.0075$. The advice we have to conclude from these facts is that in particle analysis the optical arrangements should be compact to keep the distances d as short as possible.

Applications of digital in-line holography for 3D visualization are numerous. Besides particle tracking, e. g. in the study of erosion processes in sediments [270], there are imaging of

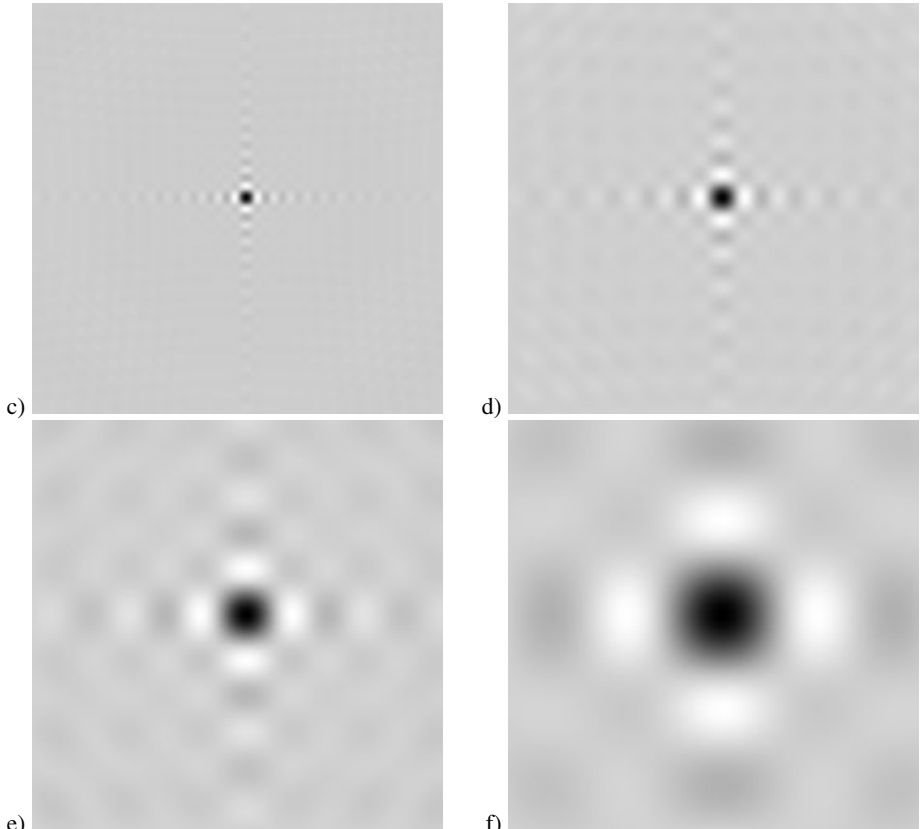


Fig. 3.66 (continued): Reconstructed particle: (c) $d = 1.0$ m, (d) $d = 2.0$ m, (e) $d = 4.0$ m (f) $d = 8.0$ m.

marine micro-organisms [145], micrometer sized latex spheres [78], and biological specimens like diatoms or heads of fruit flies [77] or algae in water [79] to name just a few.

3.6.2 Microscopy by Digital Holography

When Gabor proposed the principle of holography [1, 2] his primary intention was the improvement of electron microscopy. In his original concept, Gabor illuminated the sample by a diverging wave of coherent light and recorded the interference between the waves scattered from the object and the unaffected waves. This so-called in-line arrangement had the disadvantage that during reconstruction the high intensity reference wave overexposed the much weaker object signal. Therefore the method was soon abandoned in favor of off-axis holography where this drawback was eliminated [7, 8].

But nowadays if we perform numerical reconstructions of digitally recorded holograms, a strong background will not disturb as long as it is less varying than the object-related intensity variations. Furthermore there exist powerful numerical methods to eliminate the reference

wave contribution: by high-pass filtering of the digital hologram, see Section 3.2.5, or by subtracting the separately recorded background intensity from the recorded hologram.

Basically, there are two different approaches to *digital holographic microscopy*: One uses a microscope objective which magnifies the wave field to be recorded and reconstructed, and in the second approach the field scattered by the small object is recorded directly without any imaging optics. Let us first turn to the concept of direct recording of the wave field.

The most critical parameter in holographic microscopy is resolution. When light passes through a translucent object or is reflected by an object that contains high-spatial-frequency components, it diffracts at large angles. However if we want to resolve these components we must record those high diffraction orders in the hologram. Therefore an arrangement for digital holographic microscopy as shown in Fig. 3.67 was suggested [100], where the distance

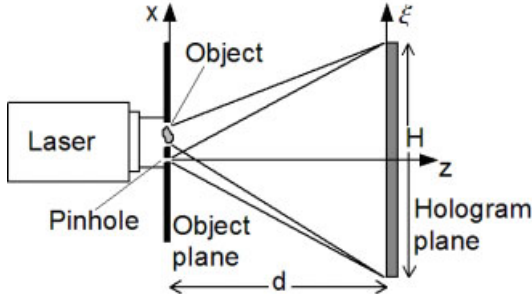


Figure 3.67: Digital holographic microscope.

between object plane and hologram plane is rather short. The arrangement is basically a lensless Fourier transform holography setup. The spherical reference wave with source point near the object increases the pitch of the microinterference in the hologram, thus relaxing the resolution requirements on the CCD sensor.

The first attempt to reconstruct the image of the object is to use the Fresnel transform which in Fourier transform holography is especially simple because the numerical form of the spherical reference wave here cancels out the chirp function, so only a Fourier transform (FFT) of the digital hologram is all that has to be done. This in principle works well, but we have to notice that we will not obtain the required resolution.

We have seen in Section 2.4.3 that the Fresnel approximation is valid when the object extent and the hologram extent as well as the distance d between object plane and hologram plane fulfill the inequality (2.78)

$$\frac{\pi}{4\lambda} [(\xi - x)^2 + (\eta - y)^2]^{1/2} < d^3. \quad (3.156)$$

In the case of holographic microscopy with direct recording we can assume that the hologram dimensions are much larger than those of the object $\xi \gg x, \eta \gg y$. Let the CCD-sensor recording the digital hologram be a square with sidelengths H , then (3.156) especially applies for $\xi = H/2$ and $\eta = H/2$, which gives

$$H < 2 \left(\frac{\lambda d^3}{\pi} \right)^{1/4}. \quad (3.157)$$

Two point resolution is treated in [160] or in [106, 108] for phase-shifting digital holography with the result that the minimum resolvable distance δ in the reconstructed image is proportional to $\lambda d/H$

$$\delta \sim 0.61 \frac{\lambda d}{H}. \quad (3.158)$$

The combination with (3.157) now yields

$$\delta > \frac{0.61\pi^{\frac{1}{4}}}{2} \lambda^{\frac{3}{4}} d^{\frac{1}{4}} = 0.406(\lambda^3 d)^{\frac{1}{4}}. \quad (3.159)$$

This implies that the resolution obtained by the Fresnel approximation is always restricted, high resolution cannot be obtained.

We see that the distance d is not large enough to justify the Fresnel approximation and we have to deal with the obliquity factor in (2.67). While for the plane wave illuminating the object we can set $\cos(\mathbf{r}_{SP}, \mathbf{n}) = 1$, we now must use $\cos(\mathbf{r}_{PB}, \mathbf{n}) = -d/r$. Therefore the complex amplitude distribution $B(\xi, \eta)$ in the hologram plane resulting from the microscopic object with complex amplitude transmittance $b(x, y)$ is given by the Fresnel-Kirchhoff integral in the form

$$B(\xi, \eta) = \frac{i}{\lambda} \iint b(x, y) \frac{e^{ikr}}{r} \left(\frac{1}{2} + \frac{d}{2r} \right) dx dy \quad (3.160)$$

with $r = \sqrt{d^2 + (\xi - x)^2 + (\eta - y)^2}$. Let the spherical reference wave emanate from the origin of the (x, y, z) -coordinate system, Fig. 3.67, so its description is

$$R(\xi, \eta) = \frac{iC}{\lambda} \frac{e^{ikr}}{r} \left(\frac{1}{2} + \frac{d}{2r} \right) \quad (3.161)$$

with $r = \sqrt{d^2 + \xi^2 + \eta^2}$ and a constant C . The intensity distribution captured as the digital hologram h is

$$h(\xi, \eta) = |B(\xi, \eta) + R(\xi, \eta)|^2. \quad (3.162)$$

The reconstruction of the complex field $b'(x', y')$ corresponding to the real image now may be performed by first multiplying a spherical reference wave front to the hologram $h(\xi, \eta)$ and second calculating the diffracted field by the Fresnel-Kirchhoff integral. The disadvantage of this reconstruction method is the considerably long time required for calculating the Fresnel-Kirchhoff integral, because there is no fast algorithm to do this. Takaki and Ohzu [100] proposed an approximation technique reducing drastically the time for calculation of the double integrals. This approximation is based on the observation that in microscopy the light diffracts from a region much smaller than the digital hologram, so for the coordinates we can assume $x, y \ll \xi, \eta, d$. Therefore the optical pathlength r is approximated by

$$\begin{aligned} r &= \sqrt{d^2 + \xi^2 - 2x\xi + x^2 + \eta^2 - 2y\eta + y^2} \\ &\approx \sqrt{d^2 + \xi^2 + \eta^2 - 2x\xi - 2y\eta} \\ &\approx \sqrt{d^2 + \xi^2 + \eta^2} \left[1 - \frac{x\xi + y\eta}{d^2 + \xi^2 + \eta^2} \right]. \end{aligned} \quad (3.163)$$

This approximation now is applied to the Fresnel-Kirchhoff integral (3.160) where the r in the denominator and in the obliquity factor can be replaced by only the first factor of (3.163). In the argument of the complex exponential we must use both factors, see also the argumentation in Section 2.4.2.

$$\begin{aligned}
 B(\xi, \eta) &= \frac{i}{2\lambda} \iint b(x, y) \left(1 + \frac{d}{r}\right) \frac{1}{r} e^{\frac{2\pi i r}{\lambda}} dx dy \\
 &= \frac{i}{2\lambda} \iint b(x, y) \left(1 + \frac{d}{\sqrt{d^2 + \xi^2 + \eta^2}}\right) \frac{1}{\sqrt{d^2 + \xi^2 + \eta^2}} \\
 &\quad \times e^{\frac{2\pi i \sqrt{d^2 + \xi^2 + \eta^2}}{\lambda}} e^{-\frac{2\pi i (x\xi + y\eta)}{\lambda \sqrt{d^2 + \xi^2 + \eta^2}}} dx dy \\
 &= \frac{i}{2\lambda} \left(1 + \frac{d}{\sqrt{d^2 + \xi^2 + \eta^2}}\right) \frac{1}{\sqrt{d^2 + \xi^2 + \eta^2}} e^{\frac{2\pi i \sqrt{d^2 + \xi^2 + \eta^2}}{\lambda}} \\
 &\quad \times \iint b(x, y) e^{-2\pi i (x\nu_x + y\nu_y)} dx dy \\
 &= \frac{i}{2\lambda} \left(1 + \frac{d}{\sqrt{d^2 + \xi^2 + \eta^2}}\right) \frac{1}{\sqrt{d^2 + \xi^2 + \eta^2}} e^{\frac{2\pi i \sqrt{d^2 + \xi^2 + \eta^2}}{\lambda}} \mathcal{F}\{b(x, y)\}
 \end{aligned} \tag{3.164}$$

with the spatial frequencies in the x - and y -directions defined as

$$\nu_x = \frac{\xi}{\lambda \sqrt{d^2 + \xi^2 + \eta^2}} \quad \nu_y = \frac{\eta}{\lambda \sqrt{d^2 + \xi^2 + \eta^2}}. \tag{3.165}$$

In the same way the reference wave is approximated

$$R(\xi, \eta) = \frac{iC}{2\lambda} \left(1 + \frac{d}{\sqrt{d^2 + \xi^2 + \eta^2}}\right) \frac{1}{\sqrt{d^2 + \xi^2 + \eta^2}} e^{\frac{2\pi i \sqrt{d^2 + \xi^2 + \eta^2}}{\lambda}}. \tag{3.166}$$

Now we can express the hologram as

$$\begin{aligned}
 h(\xi, \eta) &= (B(\xi, \eta) + R(\xi, \eta)) (B^*(\xi, \eta) + R^*(\xi, \eta)) \\
 &= \left(\frac{i}{2\lambda \sqrt{d^2 + \xi^2 + \eta^2}} \left(1 + \frac{d}{\sqrt{d^2 + \xi^2 + \eta^2}}\right) e^{\frac{2\pi i \sqrt{d^2 + \xi^2 + \eta^2}}{\lambda}} \right) \\
 &\quad \times (\mathcal{F}\{b(x, y)\} + C) \left(\frac{i}{2\lambda \sqrt{d^2 + \xi^2 + \eta^2}} \left(1 + \frac{d}{\sqrt{d^2 + \xi^2 + \eta^2}}\right) \right. \\
 &\quad \times \left. e^{\frac{2\pi i \sqrt{d^2 + \xi^2 + \eta^2}}{\lambda}} \right) (\mathcal{F}^*\{b(x, y)\} + C^*) \\
 &= \frac{-1}{4\lambda^2(d^2 + \xi^2 + \eta^2)} \left(1 + \frac{d}{\sqrt{d^2 + \xi^2 + \eta^2}}\right)^2 \\
 &\quad \times (|\mathcal{F}\{b(x, y)\}|^2 + |C|^2 + C\mathcal{F}^*\{b(x, y)\} + C^*\mathcal{F}\{b(x, y)\}).
 \end{aligned} \tag{3.167}$$

This indicates that the reconstruction process can be performed by the following steps:

Step 1: The recorded digital hologram $h(\xi, \eta)$ is multiplied by $4\lambda^2(d^2 + \xi^2 + \eta^2)(1 + d/\sqrt{d^2 + \xi^2 + \eta^2})^{-2}$.

Step 2: The coordinate transformation of (3.165) from the hologram plane to the spatial frequency plane is carried out. This transformation is depicted in Fig. 3.68.

Step 3: From the resulting distribution the inverse Fourier transform is calculated.

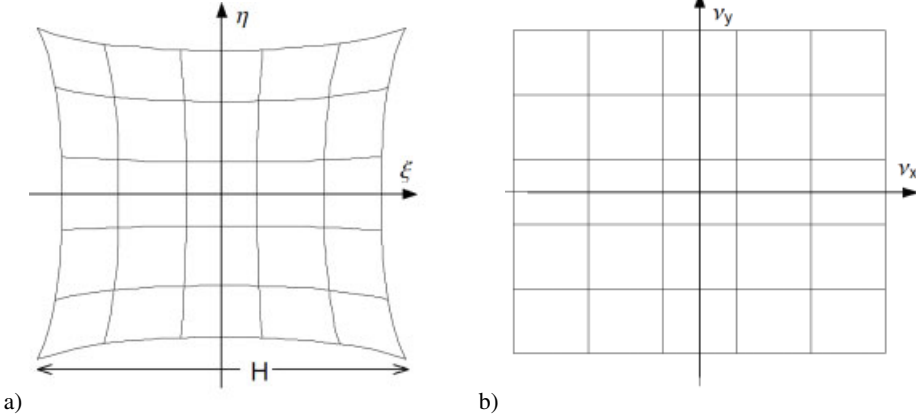


Figure 3.68: Coordinate transformation from the hologram plane (a) to the spatial frequency plane (b).

For the calculation in step 3 the efficient FFT algorithm is employed. Since steps 1 and 2 are pointwise operations, altogether we obtained a fast algorithm for reconstruction. Experimental verifications of this reconstruction method are presented in [100]. The resolvable distance δ obtained by this algorithm can be estimated as follows. Because of $\sqrt{\xi^2 + \eta^2} \leq H/\sqrt{2}$ the highest spatial frequency ν_{\max} is given by (3.165) as

$$\nu_{\max} = \frac{1}{\lambda} \sqrt{2 + 4 \left(\frac{d}{H} \right)^2}. \quad (3.168)$$

Since the resolvable distance δ obeys the relationship $\delta = \frac{1}{2}\nu_{\max}$ we obtain

$$\delta = \lambda \sqrt{\frac{1}{2} + \left(\frac{d}{H} \right)^2}. \quad (3.169)$$

So the resolution increases, which means that the resolvable distance decreases, when the ratio d/H decreases.

It was assumed that the extent of the investigated object is small. With the help of (3.163) we can determine the allowable object extent. The first approximation in (3.163)

$$\begin{aligned} kr &= k\sqrt{d^2 + \xi^2 + \eta^2 - 2x\xi - 2y\eta} \left[1 + \frac{x^2 + y^2}{2(d^2 + \xi^2 + \eta^2 - 2x\xi - 2y\eta)} \right] \\ &\approx k\sqrt{d^2 + \xi^2 + \eta^2 - 2x\xi - 2y\eta} \end{aligned} \quad (3.170)$$

is valid when the term $(x^2 + y^2)/[2(d^2 + \xi^2 + \eta^2 - 2x\xi - 2y\eta)]$ is small. Let it be smaller than π , then no contrast reversal of fringes would appear

$$x^2 + y^2 < \lambda(d^2 + \xi^2 + \eta^2 - 2x\xi - 2y\eta). \quad (3.171)$$

The right-hand side becomes minimal for $x = \xi$ and $y = \eta$ and we get an allowable extent for the object of

$$x^2 + y^2 < \lambda d^2. \quad (3.172)$$

The approximation in the last line of (3.163) holds if

$$(d^2 + \xi^2 + \eta^2)^{\frac{3}{2}} > \frac{(x\xi + y\eta)^2}{\lambda}. \quad (3.173)$$

With Schwartz's inequality we obtain

$$x^2 + y^2 < \frac{\lambda(d^2 + \xi^2 + \eta^2)^{\frac{3}{2}}}{\xi^2 + \eta^2} \quad (3.174)$$

where the right-hand term is minimal for $\xi^2 + \eta^2 = 2d^2$ yielding

$$x^2 + y^2 < \sqrt{\frac{27}{4}}\lambda d \quad (3.175)$$

which is a less stringent condition than (3.172). Therefore the allowable object width w_{obj} is

$$w_{obj} = \sqrt{2\lambda d}. \quad (3.176)$$

With modified coordinate transformations as presented in [271,272] the viewing angles can be changed. This allows a variation of the perspective from which the object is viewed. A related approach for reconstruction of particle fields in tilted planes is described in [273].

A slightly different arrangement for digital holographic microscopy is the in-line holography geometry with a divergent wave as shown in Fig. 3.69. The laser beam is focused by a

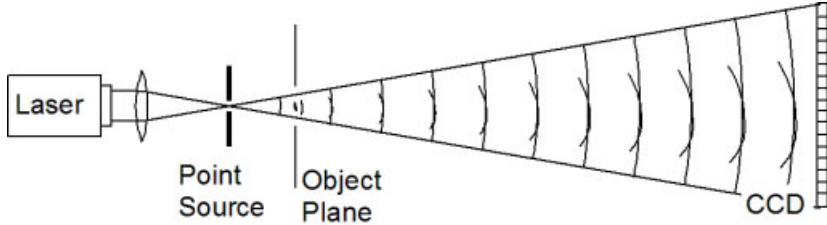


Figure 3.69: Arrangement for point source microscope.

lens with focal length of a few millimeters into a pinhole where the locus of the point source is defined [76]. The object is placed just a few millimeters further along, such that only a

fraction of the incident beam is scattered. The scattered wave interferes with the rest of the spherical wave at the detector, which can be a screen that is recorded by a CCD camera, or which can directly be the CCD array.

The numerical reconstruction of these digital holograms of microscopic scenes was developed and investigated by Kreuzer et al. [72, 73, 75]. The first step proposed by them is to calculate the contrast image. Therefore not only the hologram $h(n, m)$ in the detector plane is recorded but also a background image $h_0(n, m)$, where only the illumination is present but the object is removed. Then the contrast image $h_k(n, m)$ is determined pointwise by

$$h_k(n, m) = \frac{h(n, m) - h_0(n, m)}{\sqrt{h_0(n, m)}}. \quad (3.177)$$

This contrast image hereafter is centered around zero intensity by subtracting the average of all $h_k(n, m)$, see Section 3.2.5, so the results will not suffer from a d.c.-term. The modified contrast image $h_k^*(n, m)$ is used to reconstruct the object wave front by the Kirchhoff-Helmholtz transform

$$K(\mathbf{r}) = \frac{1}{4\pi} \int_S h_k^*(\xi) \exp\{ik\xi \cdot \mathbf{r}/|\xi|\} d\xi \quad (3.178)$$

Here S denotes the screen, which is at a distance D from the source. The screen coordinates are $\xi = (\xi, \eta, D)$, the integration is performed in two dimensions over ξ and η . $K(\mathbf{r})$ is significantly different from zero only in the space region occupied by the object. $K(\mathbf{r})$ is a complex function and usually the object is represented by its magnitude, although phase information can also be obtained. Normally one reconstructs the wavefront on a number of planes at varying distances from the source in the vicinity of the surface until one obtains the sharpest image of the object.

The general criteria are that the image screen must be large enough so that at least two diffraction orders are recorded and that its spatial resolution must be able to define interference patterns of the order of the wavelength when projected from the screen to the image plane [73].

The arrangement of Fig. 3.69 applies for translucent objects or for objects whose contours are of main interest. However the method is also applicable to investigate opaque surface variations in reflection under glancing incidence [73]. The geometry of this simplest realization of off-axis holography is shown in Fig. 3.70. Here the detector is placed perpendicular to the central reflected beam. The numerical reconstruction is performed analogously to the in-line case.

We now come to the more classic concept of using a microscope objective producing a magnified image of the sample. This image field is used as the object for the hologram generation. In a way this is the inverse approach to that presented in Section 3.1.2 where the wave field reflected from a large object was reduced. The procedure to record and reconstruct the magnified object wave field in digital holographic microscopy is straightforward by using the Fresnel or convolution methods for reconstruction. But digital holography enables us not only to reconstruct intensity contrasts, also we can get phase contrast images. To exploit this additional feature of phase contrast microscopy by digital holography we must recognize the phase aberrations associated with the microscope objective. For an interferometric comparison of two reconstructed wave fields carrying the same aberrations, these eliminate each other and

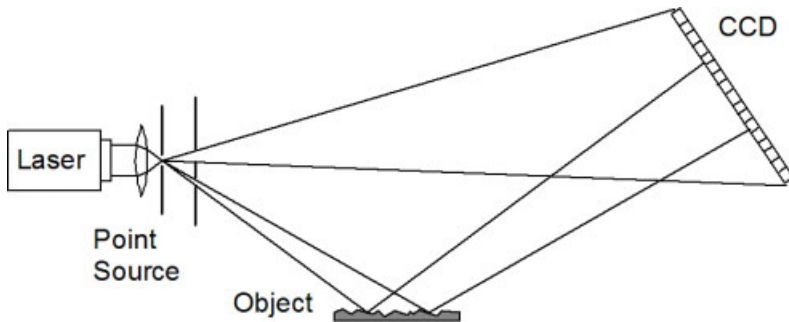


Figure 3.70: Arrangement for point source microscope with glancing incidence.

do not affect the measurement, but in single hologram phase contrast microscopy they matter. However, the phase aberrations can be effectively compensated for by a modification of the digital reconstruction procedure [124].

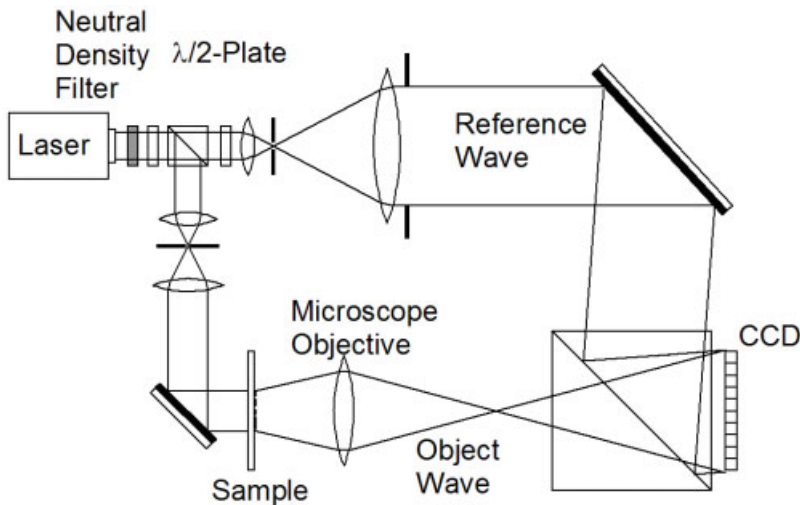


Figure 3.71: Digital holographic microscope, transparent objects.

The arrangement for digital holographic microscopy generally is a Mach-Zehnder interferometer [128]. It can be adapted to measure transparent objects, Fig. 3.71, or can be prepared for reflection imaging, Fig. 3.72. The linearly polarized laser beam passes a neutral density filter and a half-wave plate before it is split into reference and object wave by a polarizing beam splitter. A second half-wave plate is inserted into the reference arm to obtain parallel polarization at the CCD. The reference wave does not hit the CCD in the normal direction, but impinges with a small inclination angle to produce well separated real and virtual images. The transparent sample (or sample holder plus sample) is illuminated by a plane wave, the transmitted light is collected by a microscope objective. For reflection imaging, Fig. 3.72, a

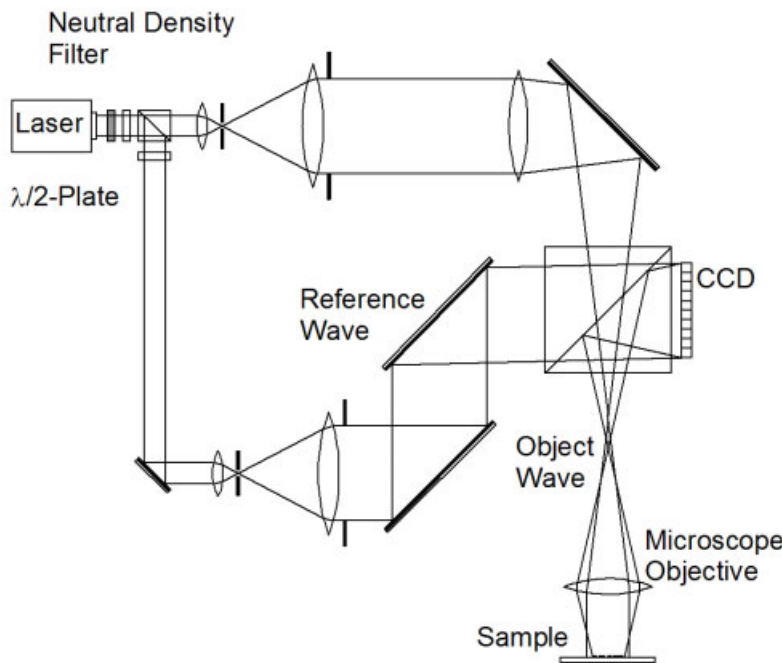


Figure 3.72: Digital holographic microscope, opaque objects.

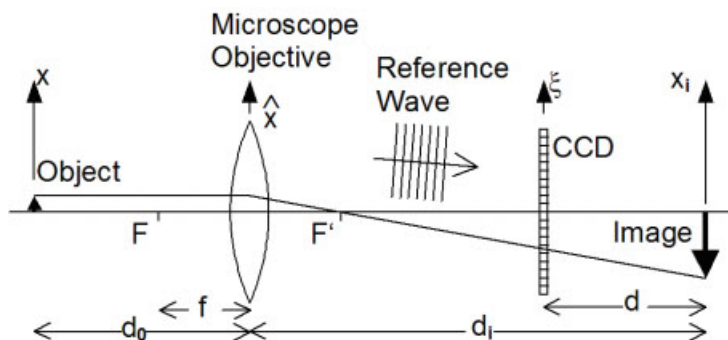


Figure 3.73: Digital holographic microscope, optical configuration.

lens with long focal length is inserted between beam expander and microscope objective. It acts as a condenser, its position is adjusted to illuminate the opaque sample with a collimated beam.

Let us investigate the optical arrangement in the object arm in more detail. It is a single-lens imaging system, Fig. 3.73. The microscope objective produces a magnified image of the object, and the CCD is placed between the objective lens and the image. The distance of

the CCD to the image is d . Two special cases are worth mentioning. If the object–hologram distance is zero, $d = 0$, then the image is focused onto the CCD. This would constitute an ESPI or DSPI configuration, which can be used for interference microscopy where phase-shifting interferometry is applied to obtain phase information. The second special case is the sample located in the object focal plane of the microscope objective. Now the distance d_i between objective and image becomes infinite and the Fresnel transform in the reconstruction stage converts to a pure Fourier transform of the digital hologram.

The reconstruction of the image field from the digitally recorded hologram now can be performed by the Fresnel transform, Eq. (3.38). In the numerical model of the reference wave the oblique incidence must be considered, e. g.

$$r(k\Delta\xi, l\Delta\eta) = E_r \exp \left[\frac{i2\pi}{\lambda} (k_\xi k\Delta\xi + k_\eta k\Delta\eta) \right] \quad (3.179)$$

where k_ξ and k_η are components of the unit vector in the propagation direction of the reference wave [274]. There remains the problem of wavefront deformation by the microscope objective, Fig. 3.74. The resulting phase aberrations are crucial in phase contrast imaging.

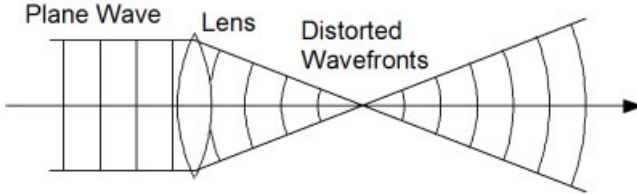


Figure 3.74: Wavefront deformation by the microscope objective.

They can be eliminated by multiplication of the reconstructed field with an appropriate digital phase mask, as derived in [124] or by one of the methods presented in [275].

The relation between the fields $U_0(x, y)$ in the object plane and $U_i(x_i, y_i)$ in the image plane can be described by the superposition integral

$$U_i(x_i, y_i) = \iint h(x_i, y_i; x, y) U_0(x, y) dx dy \quad (3.180)$$

with the point spread function $h(x_i, y_i; x, y)$. For the moment let us restrict the discussion to two dimensions, say the (x, z) -plane and investigate $h(x_i; x)$. The results are then extended in a natural way to three dimensions. According to Fig. 3.73 we have

$$\frac{1}{d_i} + \frac{1}{d_0} = \frac{1}{f} \quad (3.181)$$

and following [160] we obtain

$$h(x_i; x) = C \exp \left(\frac{i\pi}{\lambda d_i} x_i^2 \right) \exp \left(\frac{i\pi}{\lambda d_0} x^2 \right) \int P(\hat{x}) \exp \left[\frac{-i2\pi}{\lambda} \left(\frac{x}{d_0} + \frac{x_i}{d_i} \right) \hat{x} \right] d\hat{x} \quad (3.182)$$

where \hat{x} is the coordinate in the plane of the microscope lens, whose pupil function is $P(\hat{x})$. C is a complex constant. We assume perfect imaging with magnification $M = d_i/d_0$ which maps

$$(x, y) \longmapsto (x_i, y_i) = (-Mx, -My). \quad (3.183)$$

Then the integral in (3.182) can be approximated by a Dirac pulse δ . Furthermore we replace $x = -x_i d_0/d_i$ and obtain in three dimensions

$$h(x_i, y_i; x, y) = C' \exp \left[\frac{i\pi}{\lambda d_i} \left(1 + \frac{d_0}{d_i} \right) (x_i^2 + y_i^2) \right] \delta(x_i + Mx, y_i + My). \quad (3.184)$$

This equation states that the image is a magnified replica of the object field multiplied by a paraboloidal phase term. So the phase aberrations are corrected by multiplication of the reconstructed wavefront with the conjugate of this term. In finite discrete coordinates the resulting phase mask is

$$\Psi(n, m) = \exp \left[\frac{-i\pi}{\lambda D} (n^2 \Delta x'^2 + m^2 \Delta y'^2) \right] \quad (3.185)$$

with

$$\frac{1}{D} = \frac{1}{d_i} \left(1 + \frac{d_0}{d_i} \right). \quad (3.186)$$

Altogether we have to calculate $b'(n, m)$ according to (3.38) and multiply it with $\Psi(n, m)$. Then we can get the amplitude contrast image by $I(n, m) = |b'(n, m)\Psi(n, m)|^2$ and the phase contrast image by $\phi(n, m) = \arctan\{\text{Im}[b'(n, m)\Psi(n, m)]/\text{Re}[b'(n, m)\Psi(n, m)]\}$.

The quality of the reconstructed amplitude and phase maps depends strongly upon the exactness of the parameters d , D , k_ξ , and k_η as has been demonstrated in [124]. These parameters can be measured in the optical arrangement, but this can act only as a first rough estimate. A fine tuning of the values of these parameters is obtained by digital variation in the reconstruction stage and checking areas where no phase variations are expected.

An in-line digital microscopic holography system incorporating a long-distance microscope is proposed by Xu et al. [113, 114, 258, 276]. It fulfills the requirements of imaging microstructures with high resolution at sufficient working distances to permit good illumination of the samples.

Digital holographic microscopy is not restricted to visible wavelengths. In [74] in-line holography with a low energy electron point source is considered.

A heterodyne approach to digital microscopic holography is presented in [137, 138]. The reference wave is reflected from a mirror mounted on a saw-tooth voltage driven piezo-translator providing a temporal frequency difference between the two arms of the interferometer. So each scatterer of a three-dimensional object is encoded as a temporally modulated Fresnel pattern, which is recorded by a CCD. Temporal heterodyning of the signal from each pixel results in a single-sideband, on-line holographic record in digital form. Reconstruction of an image focused on a chosen transverse plane in the 3D object volume is performed by digital correlation with a reconstruction function matched to that plane. The method poses

relaxed demands on the spatial bandwidth of the detector and does not really need spatially coherent illumination. This spatiotemporal digital holography can be used for imaging through scattering media even when using a white-light source for illumination [137].

The reconstruction process in digital holography involves finite discrete Fourier transforms. If especially in microscopy the digital holograms at opposite border points in the horizontal or vertical direction have discontinuous or non-smooth continuation, the aliasing effects produce spurious diffraction-like patterns. A reduction of these effects can be achieved by border processing [69]. By this the digital hologram is extended to a larger size with the additional part filled by values that minimize, according to a numerical criterion, the erroneous spatial frequencies.

A lensless digital holographic microscope discriminating in depth is reported in [277]. Using a short-coherence-length laser holographic information is only captured if the path lengths of reference and object beam are matched within the coherence length. An aberration compensation for this lensless holography by expansion of the hologram with interpolation of the intensity values and simulation of diffraction using the Rayleigh-Sommerfeld propagation theory is given in [278, 279].

3.6.3 Data Encryption with Digital Holography

We have seen, e. g. Fig. 3.14, that a digital hologram of a 2D or 3D scene looks rather stochastic and seems to give no hint on the content of the original scene. So digital holography on first sight offers a means for *data encryption*. Security of data in the sense of prevention from unauthorized knowledge is a key issue when data from diverse fields are to be stored or transmitted. However, directly recorded digital holograms do not constitute a secure tool for encryption. They are highly redundant, as investigations for effective encoding and data compression [280] have shown. A variation of only a few parameters in a trial and error procedure will quickly lead to the original information.

Nevertheless digital holography with some modifications is a proper means for encrypting two- or three-dimensional optical information. The approach to digital holographic encryption presented here is based on phase-shifting digital holography, Section 3.4.1, and a random phase code that constitutes the key for encrypting and decrypting [134, 135, 281].

The optical system for encrypting 2D or 3D information in this way is schematically shown in Fig. 3.75. It is based on a Mach-Zehnder interferometer architecture. In the displayed configuration data diffusely reflected from the surface of a 3D object are recorded. Instead of the 3D object also a 2D object positioned at the same place can be used. If not the reflective mode but the transmission mode is to be employed, the system of Fig. 3.76 has the object at the same place. Now the object may be a transparency, scattering particles, 3D refractive index distributions etc.

Let the opaque 3D object surface in Fig 3.75 be composed of point sources with complex amplitudes $E_O(x, y, z)$. If we admit a varying depth coordinate z , according to (2.72) the field in the hologram plane is in Fresnel approximation

$$\begin{aligned} E_H(\xi, \eta) &= \frac{1}{i\lambda} \iiint E_O(x, y, z) \frac{1}{z} e^{\frac{i2\pi}{\lambda} z} e^{\frac{i\pi}{\lambda z}} [(\xi - x)^2 + (\eta - y)^2] dx dy dz \\ &= A_H(\xi, \eta) e^{i\phi_H(\xi, \eta)}. \end{aligned} \quad (3.187)$$

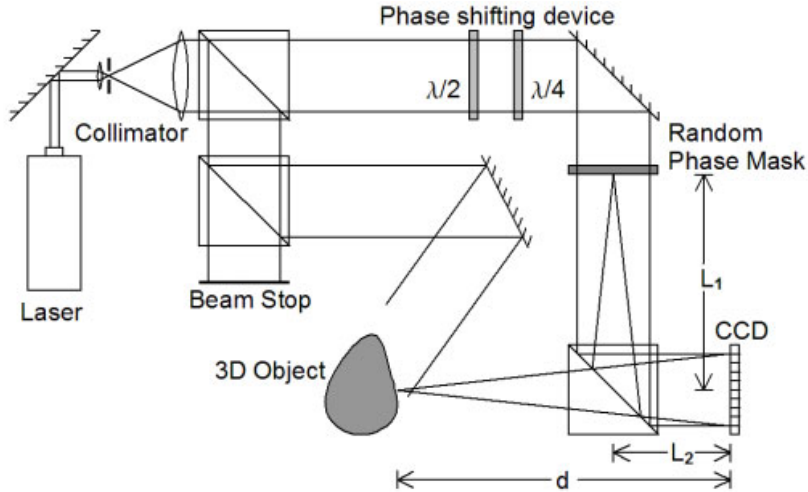


Figure 3.75: Phase shifting digital holographic system for encryption of optical information: Recording 3D object data.

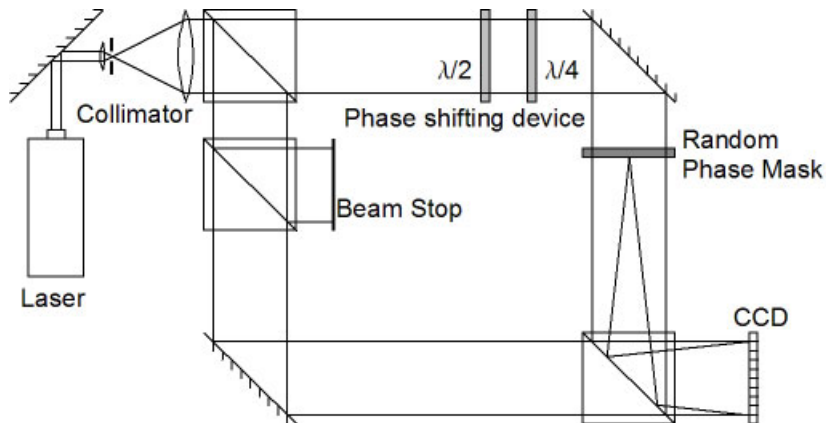


Figure 3.76: Phase shifting digital holographic system for encryption of optical information: Recording the key.

The collimated reference beam travels first through a $\lambda/2$ - and a $\lambda/4$ -plate, which perform phase retardations of $\Delta\phi_1 = 0$, $\Delta\phi_2 = -\pi/2$, $\Delta\phi_3 = -\pi$, $\Delta\phi_4 = -3\pi/2$, see Section 2.7.4, then through a random phase mask. This phase mask is at distance $L = L_1 + L_2$ from the CCD-array. The reference field in the hologram plane now is

$$\begin{aligned} E_R(\xi, \eta; \Delta\phi_p) &= e^{i\Delta\phi_p} e^{i\frac{\pi}{\lambda L}(\xi^2 + \eta^2)} \iint e^{i\phi(x, y)} e^{-i\frac{2\pi}{\lambda L}(\xi x + \eta y)} dx dy \\ &= A_R(\xi, \eta) e^{i[\phi_H(\xi, \eta) + \Delta\phi_p]}. \end{aligned} \quad (3.188)$$

Here $\Delta\phi_p$ is the actual phase shift and $\phi(x, y)$ is the random phase introduced by the mask. The phase shifted holograms recorded by the CCD are the intensity distributions given by the coherent superposition of E_H and E_R

$$\begin{aligned} I_p(\xi, \eta) &= |E_H(\xi, \eta) + E_R(\xi, \eta)|^2 \\ &= A_H^2(\xi, \eta) + A_R^2(\xi, \eta) + 2A_H(\xi, \eta)A_R(\xi, \eta)\cos[\phi_H(\xi, \eta) - \phi_R(\xi, \eta) - \Delta\phi_p]. \end{aligned} \quad (3.189)$$

A set of four phase shifted digital holograms $I_p(\xi, \eta)$, $p = 1, \dots, 4$ are recorded – three or more than four are also possible, see Section 5.5.2. From the recorded holograms the encrypted amplitude $A_E(\xi, \eta)$ and the encrypted phase $\phi_E(\xi, \eta)$ can be calculated. If phase shifts of $\pi/2$ as mentioned above are employed, these are

$$\begin{aligned} A_E(\xi, \eta) &= A_H(\xi, \eta)A_R(\xi, \eta) \\ &= \frac{1}{4}\sqrt{[I_1(\xi, \eta) - I_3(\xi, \eta)]^2 + [I_4(\xi, \eta) - I_2(\xi, \eta)]^2} \end{aligned} \quad (3.190)$$

and

$$\phi_E(\xi, \eta) = \phi_H(\xi, \eta) - \phi_R(\xi, \eta) = \arctan \frac{I_4(\xi, \eta) - I_2(\xi, \eta)}{I_1(\xi, \eta) - I_3(\xi, \eta)}. \quad (3.191)$$

A reconstruction of the object wave field by inverse Fresnel transform from the encrypted hologram field $A_E(\xi, \eta)\exp[i\phi_E(\xi, \eta)]$ is impossible. We need the knowledge of $A_R(\xi, \eta)$ and $\phi_R(\xi, \eta)$ or at least of $\phi(\xi, \eta)$ and L to recover $A_H(\xi, \eta)$ and $\phi_H(\xi, \eta)$ which then enable the reconstruction of the original object wave field. So $A_R(\xi, \eta)$ and $\phi_R(\xi, \eta)$ or at least $\phi(\xi, \eta)$ and L act as the keys for decryption. We obtain the key functions by using the setup of Fig. 3.76. Now four intensities $I'_p(\xi, \eta)$ are recorded from which the key amplitude $A_K(\xi, \eta)$ is calculated by

$$A_K(\xi, \eta) = A_C A_R(\xi, \eta) = \frac{1}{4}\sqrt{[I'_1(\xi, \eta) - I'_3(\xi, \eta)]^2 + [I'_4(\xi, \eta) - I'_2(\xi, \eta)]^2} \quad (3.192)$$

and the key phase by

$$\phi_K(\xi, \eta) = \phi_C + \phi_R(\xi, \eta) = \arctan \frac{I'_4(\xi, \eta) - I'_2(\xi, \eta)}{I'_1(\xi, \eta) - I'_3(\xi, \eta)}. \quad (3.193)$$

Here A_C and ϕ_C are the constant amplitude and phase of the collimated beam which without loss of generality can be set to $A_C = 1$ and $\phi_C = 0$. Now decryption is performed by

$$A_D(\xi, \eta) = \begin{cases} \frac{A_E(\xi, \eta)}{A_K(\xi, \eta)} & \text{if } A_K(\xi, \eta) \neq 0 \\ 0 & \text{if } A_K(\xi, \eta) = 0 \end{cases} \quad (3.194)$$

and $\phi_D(\xi, \eta) = \phi_E(\xi, \eta) - \phi_K(\xi, \eta)$.

$A_D(\xi, \eta)$ and $\phi_D(\xi, \eta)$ are the amplitude and phase of the decrypted Fresnel hologram, from which by inverse Fresnel transform (3.38) the original object wave field can be reconstructed. Experimental results of this technique and a discussion of the different perspectives belonging to different areas in the hologram plane can be found in [134].

Encryption and decryption by phase shifting digital holography is especially useful for secure storage or transmission of optical 2D or 3D information. The random phase mask or its phase shifted holograms act as the keys. In the presented approach in contrast with other phase encryption methods not only the phase but also the amplitude of the diffraction pattern of the object is modified by the random phase. The Fresnel diffraction offers advantages over Fraunhofer diffraction patterns [135]. One is that phase retrieval algorithms are difficult to apply, which increases security; furthermore the intensity distribution of digital Fresnel holograms is better adapted to the dynamic range of the detectors. An improvement in security can be obtained by a second phase mask in the object arm of the interferometer but for the price of additional computational effort in the decryption stage. Contrary to the digital decryption and reconstruction of the object wave field described above the decrypted digital hologram can be fed into a spatial light modulator for optical reconstruction [98, 142]. If the conditions for the validity of the Fresnel approximation are not fulfilled, meaning the object is too close to the CCD, then the *spectrum manipulating method* (SMM) presented in [91] can be employed for encryption and decryption of multidimensional data.

Another issue in securing digital data is the concept of *watermarking*. In digital watermarking a kind of message is hidden in the digital content in a way that prevents this image from being read by unauthorized persons but lets the message be read as needed. A digital holographic technique that hides a digital watermark as a phase modulation whose Fourier-transformed hologram is superposed on a content image is presented in [282]. A watermarking process using double phase encoding to encode hidden images is described in [283].

4 Holographic Interferometry

In Chapter 2 the interference effect was explained which occurs if two mutually coherent waves are superposed. So we have a means to compare two or more wave fields by checking the resulting interference pattern. Furthermore holography was introduced as a method for recording and reconstructing optical wave fields. These concepts now can be put together in the method of holographic interferometry. Holographic recording and reconstruction of a wave field is precise enough that holographically reconstructed fields can be compared interferometrically either with a wave field scattered directly by the object, or with another holographically reconstructed wave field. Accordingly we define *holographic interferometry* as the interferometric comparison of two or more wave fields, at least one of which is holographically reconstructed [170].

As will become clear in the following only slight differences between the wave fields to be compared by holographic interferometry are allowed. This first concerns the objects, we even have to demand the same microstructure, second the geometry which must be the same for all wave fields to be compared, third the wavelength and coherence requirements for the optical laser radiation used, and fourth the change of the object which is to be measured. All these items – microstructure, geometry, wavelength, and the physical quantities of the object – should be changed in such a small range that only the phase of the scattered wave field is varied, but an alteration of the amplitude can be neglected. If furthermore the change of the wave field is spatially homogeneous enough to vary the phase smoothly from object point to object point, we recognize a macroscopic interference pattern which will be referred to as the *holographic interferogram* or *holographic interference pattern*. To prevent confusion between the stationary interference pattern stored as the hologram and the holographic interferogram, the first mentioned is sometimes called the *microscopic interference pattern* in contrast to the observed and evaluated *macroscopic interference pattern* produced by holographic interferometry. Because holographic interferometry can bring to interference two or more wave fields simultaneously which existed at different times, and since it does not require specular reflecting surfaces, this method has found wide applications as a measurement method. In this book we only deal with laser assisted holographic interferometry, which means we stay in the near infrared, visible or near ultraviolet range of the spectrum. Nevertheless it should be mentioned that holographic interferometry can be performed using microwave or ultrasonic radiation [284, 285].

4.1 Generation of Holographic Interference Patterns

4.1.1 Recording and Reconstruction of a Double Exposure Holographic Interferogram

In the *double exposure method* of holographic interferometry two wavefronts scattered by the same object are recorded consecutively onto the same holographic plate [286]. Here we assume recording onto a photographic plate. But the presented theory also applies for other recording media, especially CCD-arrays, as will be shown in detail in Section 5.8. The two wavefronts correspond to different states of the object, one in an initial condition, Fig. 4.1a, and one after the change of a physical parameter, Fig. 4.1b, e. g. by altering the object loading.

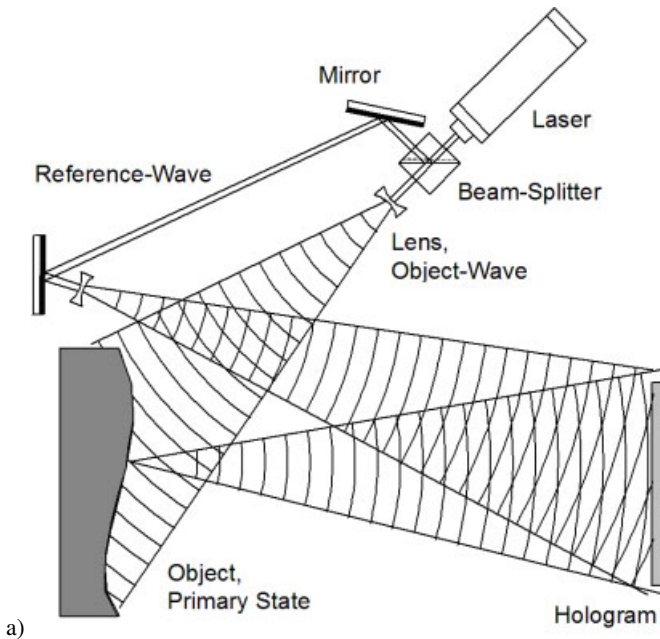


Figure 4.1: Recording (a), (b), and reconstruction (c) of a double exposure holographic interferogram.

Let the complex amplitude of the first wavefront at an object point P be

$$E_1(P) = E_{01}(P) e^{i\phi(P)}. \quad (4.1)$$

which is holographically recorded. E_{01} is the real amplitude and $\phi(P)$ is the phase distribution, (2.15). $\phi(P)$ varies spatially in a random manner due to the microstructure of the diffusely reflecting or refracting object. P identifies an object point. For the moment we do not have to discriminate between points of the object and the corresponding points in the image plane.

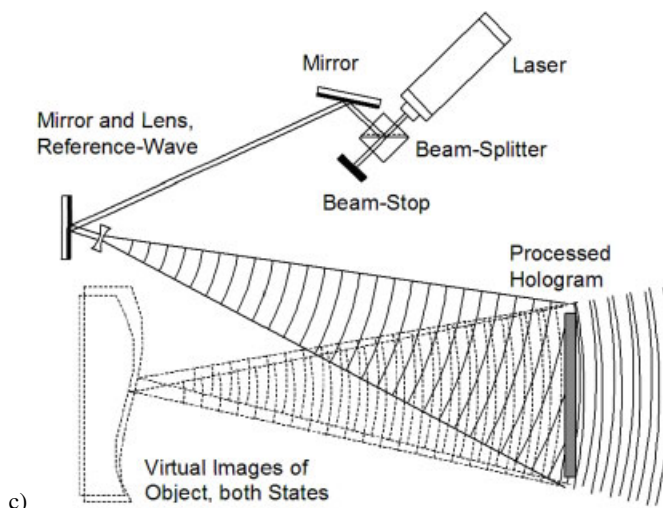
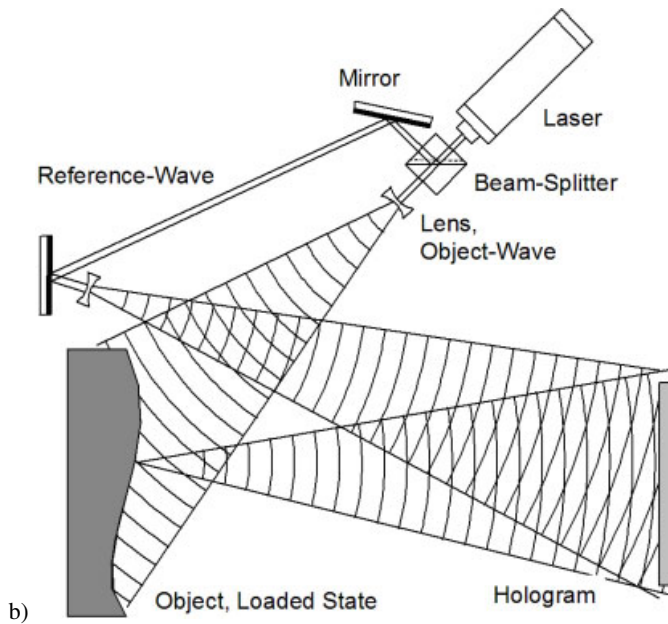


Fig. 4.1: Continued.

The variation of a physical parameter to be measured, e. g. the object shape due to deformation of an opaque object or a change in the refractive index distribution of a transparent object changes the phase distribution at P by $\Delta\phi(P)$. So the complex amplitude of the second

wavefront to be recorded holographically onto the same plate is

$$E_2(P) = E_{02}(P) e^{i(\phi(P) + \Delta\phi(P))} \quad (4.2)$$

After development of the holographic plate both wavefronts are reconstructed simultaneously, Fig. 4.1c. They interfere and give rise to a stationary intensity distribution

$$\begin{aligned} I(P) &= |E_1(P) + E_2(P)|^2 \\ &= (E_{01}(P)e^{i\phi(P)} + E_{02}(P)e^{i(\phi(P)+\Delta\phi(P))})(E_{01}(P)e^{-i\phi(P)} \\ &\quad + E_{02}(P)e^{-i(\phi(P)+\Delta\phi(P))}) \\ &= I_1(P) + I_2(P) + \sqrt{I_1(P)I_2(P)} (e^{-i\Delta\phi(P)} + e^{i\Delta\phi(P)}) \\ &= I_1(P) + I_2(P) + 2\sqrt{I_1(P)I_2(P)} \cos[\Delta\phi(P)]. \end{aligned} \quad (4.3)$$

For identical amplitudes, $E_{01}(P) = E_{02}(P)$, we get

$$I(P) = 2I_1(P)\{1 + \cos[\Delta\phi(P)]\}. \quad (4.4)$$

The change of the phase $\Delta\phi$ is called the *interference phase difference* or shortly *interference phase*. If the spatial variation of the interference phase over the observed reconstructed surface is low, the intensity distribution (4.3) represents the irradiance of the object, modulated by a cosine-shaped fringe pattern. Bright centers of fringes are the contours, where the interference phase is an even integer multiple of π , dark centers of fringes correspond to odd integer multiples of π . Clearly, if the interference phase changes too rapidly from one observable point to the next, say more than π , so that the sampling theorem is violated, we will recognize only a more or less random intensity distribution, which cannot be evaluated any more.

4.1.2 Recording and Reconstruction of a Real-Time Holographic Interferogram

In *real-time holographic interferometry* only one wavefront, belonging to a reference state of the tested object, is holographically recorded, Fig. 4.2a. After processing, the hologram is replaced exactly in its initial recording position. This replacement has to be performed within sub-wavelength precision. During illumination of the hologram with the original reference wave, the reconstructed virtual image wavefront coincides with the wavefront scattered directly by the object which still is in its original position. A change of the object now changes the scattered wavefront and the superposition with the holographically reconstructed original wavefront produces an interference pattern which can be observed in real time, Fig. 4.2b. Dynamic variations of the object lead to simultaneously observable variations of the interference pattern.

In both real-time and double-exposure holographic interferometry, the intensity variation in the fringe pattern has a cosine shape. However while in the double-exposure technique we have bright fringes where the interference phase is an even integer multiple of π , using amplitude holograms in the real-time method we get bright fringes where $\Delta\phi(P)$ is an odd integer

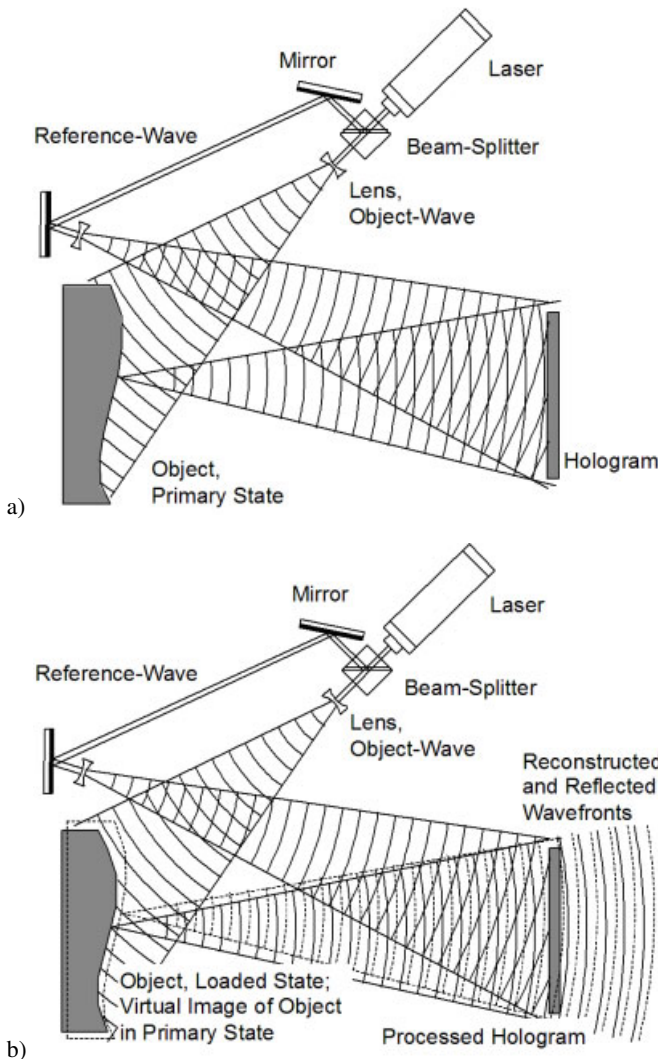


Figure 4.2: Recording (a) and reconstruction (b) of a real-time holographic interferogram.

multiple of π . This is due to the negative sign before the third term of (2.131) which describes the reconstructed virtual image. In the double-exposure technique both reconstructed wavefronts carry the same sign. Using a phase hologram in the real-time technique, we have the same positive sign for the directly scattered and the reconstructed wavefronts, now leading to bright fringes at even integer multiples of π like with the double-exposure technique. As a consequence loci where there is no change, $\Delta\phi(P) = 0$, are the centers of a bright fringe in the double exposure and in the real-time technique with phase holograms, these loci are the centers of a dark fringe for the real-time technique utilizing an amplitude hologram.

4.1.3 Time Average Holography

An in-depth discussion of *holographic vibration analysis* will be given in Section 6.5. Here we only show how fringe characteristics other than the above mentioned cosine shapes arise. One can use the real-time method with a holographically recorded and reconstructed wavefront representing the object in its rest state. Now consider a *harmonic vibration* which gives rise to an interference phase periodically changing in time

$$\Delta\phi(P) \sin(\omega t) \quad (4.5)$$

where ω is the angular frequency of the vibration and $\Delta\phi(P)$ is related to the maximal amplitude of the vibration at object point P . If we assume illumination and observation in normal direction, and the maximal amplitude as $Z(P)$, we get $\Delta\phi(P) = 4\pi Z(P)/\lambda$, since the light has to travel to and from P along $Z(P)$. During vibration the real-time technique at each instant of time t generates a cosine shaped pattern

$$I(P, t) = 2I_1(P)\{1 - \cos[\Delta\phi(P) \sin(\omega t)]\}. \quad (4.6)$$

If the frequency ω is higher than the temporal resolution of the eye (having an assumed average response time of ~ 40 ms) or the applied sensor, a time averaged intensity is seen, which according to (C.2) is

$$\begin{aligned} I(P) &= 2I_1(P) \lim_{T \rightarrow \infty} \frac{1}{T} \int_0^T \{1 - \cos[\Delta\phi(P) \sin(\omega t)]\} dt \\ &= 2I_1(P)\{1 - J_0[\Delta\phi(P)]\}. \end{aligned} \quad (4.7)$$

Here J_0 is the zero-order *Bessel function* of the first kind. These fringes have low contrast, Fig. 4.3. The method can be used for the identification of resonant frequencies by monitoring the fringe pattern while varying the excitation frequency.

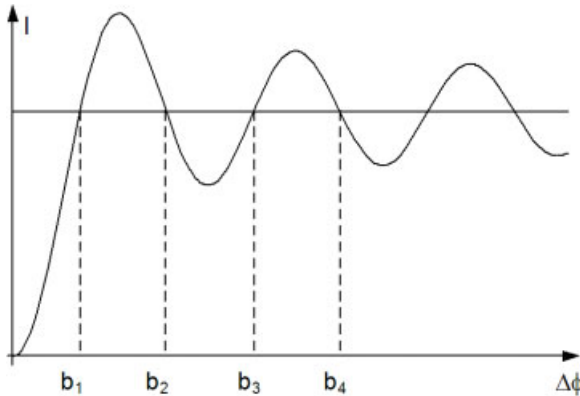


Figure 4.3: Time averaged real-time intensity.

The most frequently applied method for holographic vibration analysis is the *time average method*. Here the vibrating surface is recorded holographically with an exposure time which is long compared with the period of the vibration, $T \gg 2\pi/\omega$. Let us consider again the harmonic vibration as given in (4.5). Then we record and reconstruct holographically a continuum of waves each of the form

$$E_{01}(P)e^{i\Delta\phi(P)} \sin(\omega t). \quad (4.8)$$

This set of wavefronts reconstructed simultaneously will interfere to

$$\begin{aligned} E_{av}(P) &= \lim_{T \rightarrow \infty} \frac{E_{01}(P)}{T} \int_0^T e^{i\Delta\phi(P)} \sin(\omega t) dt \\ &= E_{01}(P) J_0(\Delta\phi(P)). \end{aligned} \quad (4.9)$$

The observable intensity in the reconstructed image then is

$$I(P) = I_1(P) J_0^2(\Delta\phi(P)). \quad (4.10)$$

The fringes now are contours of equal vibration amplitudes of the spatial vibration modes. Maximal intensity belongs to $\Delta\phi(P) = 0$, which occurs at the nodes of the vibration mode. Dark centers of the fringes refer to zeros of the Bessel function J_0 . The contrast of the fringes decreases with increasing order, Fig. 4.4, see also Fig. C.1.

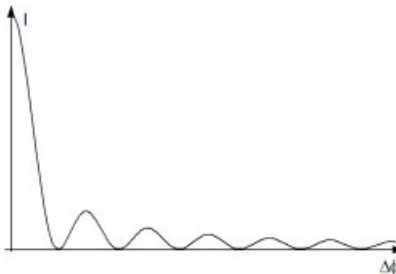


Figure 4.4: Time averaged intensity.

4.1.4 Interference Phase Variation Due to Deformation

In holographic interferometric measurements of the *deformation* of diffusely reflecting opaque object surfaces, the displacement of each surface point P gives rise to an *optical path difference* $\delta(P)$. This is the difference between the paths from the source point S of the illuminating wavefront over the surface point P to the observation point B before and after changing the deformation state [287]. The interference phase $\Delta\phi(P)$ is related to this path difference by

$$\Delta\phi(P) = \frac{2\pi}{\lambda} \delta(P). \quad (4.11)$$

The observed intensity belonging to this interference phase is given in (4.4).

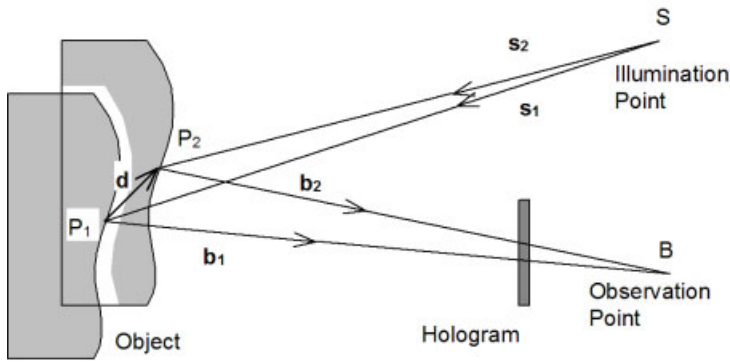


Figure 4.5: Holographic arrangement for measuring the deformation of an opaque surface.

In a holographic arrangement with diverging illumination and converging observation wave fronts, Fig. 4.5, let $S = (x_S, y_S, z_S)$ be the *illumination point* and $B = (x_B, y_B, z_B)$ be the *observation point* given in a Cartesian coordinate system. When the object is deformed, the surface point P moves from $P_1 = (x_{P1}, y_{P1}, z_{P1})$ to the new position $P_2 = (x_{P2}, y_{P2}, z_{P2})$, thus defining the *displacement vector*

$$\mathbf{d}(P) = (d_x(P), d_y(P), d_z(P)) = P_2 - P_1. \quad (4.12)$$

Points P_1 and P_2 are different in a microscopic scale, but macroscopically they can be viewed as the same $P_1 = P_2 = P$. The optical path difference $\delta(P)$ now is expressed as

$$\begin{aligned} \delta(P) &= \overline{SP_1} + \overline{P_1B} - (\overline{SP_2} + \overline{P_2B}) \\ &= \mathbf{s}_1 \cdot \mathbf{SP}_1 + \mathbf{b}_1 \cdot \mathbf{P}_1\mathbf{B} - \mathbf{s}_2 \cdot \mathbf{SP}_2 - \mathbf{b}_2 \cdot \mathbf{P}_2\mathbf{B} \end{aligned} \quad (4.13)$$

where \mathbf{s}_1 and \mathbf{s}_2 are unit vectors in the illumination direction, \mathbf{b}_1 and \mathbf{b}_2 are unit vectors in the observation direction, and \mathbf{SP}_i and $\mathbf{P}_i\mathbf{B}$ are the vectors from S to P_i or P_i to B , respectively. In analogy to Section 2.2.1 let $\mathbf{s}(P_1, P_2)$ be the bisector of the unit vectors \mathbf{s}_1 and \mathbf{s}_2 in illumination direction and $\mathbf{b}(P_1, P_2)$ the bisector of the unit vectors in observation direction. $\Delta\mathbf{s}(P_1, P_2)$ and $\Delta\mathbf{b}(P_1, P_2)$ are the half differences of the unit vectors

$$\begin{aligned} \mathbf{s}(P_1, P_2) &= \frac{1}{2}[\mathbf{s}_1(P_1) + \mathbf{s}_2(P_2)] & \Delta\mathbf{s}(P_1, P_2) &= \frac{1}{2}[\mathbf{s}_1(P_1) - \mathbf{s}_2(P_2)] \\ \mathbf{b}(P_1, P_2) &= \frac{1}{2}[\mathbf{b}_1(P_1) + \mathbf{b}_2(P_2)] & \Delta\mathbf{b}(P_1, P_2) &= \frac{1}{2}[\mathbf{b}_1(P_1) - \mathbf{b}_2(P_2)]. \end{aligned} \quad (4.14)$$

By definition of the displacement vector $\mathbf{d}(P)$ we have

$$\begin{aligned} \mathbf{P}_1\mathbf{B} - \mathbf{P}_2\mathbf{B} &= \mathbf{d}(P) \\ \text{and } \mathbf{SP}_2 - \mathbf{SP}_1 &= \mathbf{d}(P). \end{aligned} \quad (4.15)$$

Inserting this into (4.13) gives

$$\begin{aligned} \delta &= (\mathbf{s} + \Delta\mathbf{s}) \cdot \mathbf{SP}_1 + (\mathbf{b} + \Delta\mathbf{b}) \cdot \mathbf{P}_1\mathbf{B} - (\mathbf{s} - \Delta\mathbf{s}) \cdot \mathbf{SP}_2 - (\mathbf{b} - \Delta\mathbf{b}) \cdot \mathbf{P}_2\mathbf{B} \\ &= \mathbf{b} \cdot \mathbf{d} - \mathbf{s} \cdot \mathbf{d} + \Delta\mathbf{b} \cdot (\mathbf{P}_1\mathbf{B} + \mathbf{P}_2\mathbf{B}) + \Delta\mathbf{s} \cdot (\mathbf{SP}_1 + \mathbf{SP}_2) \end{aligned} \quad (4.16)$$

where the arguments have been omitted for clarity.

Now the displacements are far smaller than the dimensions of the arrangement geometry – $|d(P_1)|$ is in the micrometer range, the $\overline{SP_i}$ and $\overline{P_iB}$ are in the meter range – so the same relation holds between the lengths of Δs and Δb compared to the lengths of the unit vectors s_i and b_i . Furthermore the vector Δs is nearly orthogonal to $SP_1 + SP_2$ and vector Δb is nearly orthogonal to $P_1B + P_2B$, with the consequence that their scalar products are nearly zero. These scalar products can be neglected and we do not have to distinguish between P_1 and P_2 any more. Altogether the following relation holds for the macroscopic point P

$$\delta(P) = d(P) \cdot [b(P) - s(P)]. \quad (4.17)$$

For divergent illumination and observation the unit vectors $s(P)$ and $b(P)$ at surface point P are computed by

$$\begin{aligned} s(P) &= \begin{pmatrix} s_x(P) \\ s_y(P) \\ s_z(P) \end{pmatrix} \\ &= \frac{1}{\sqrt{(x_P - x_S)^2 + (y_P - y_S)^2 + (z_P - z_S)^2}} \begin{pmatrix} x_P - x_S \\ y_P - y_S \\ z_P - z_S \end{pmatrix} \end{aligned} \quad (4.18)$$

and

$$\begin{aligned} b(P) &= \begin{pmatrix} b_x(P) \\ b_y(P) \\ b_z(P) \end{pmatrix} \\ &= \frac{1}{\sqrt{(x_B - x_P)^2 + (y_B - y_P)^2 + (z_B - z_P)^2}} \begin{pmatrix} x_B - x_P \\ y_B - y_P \\ z_B - z_P \end{pmatrix}. \end{aligned} \quad (4.19)$$

These unit vectors together with the factor $2\pi/\lambda$ (4.11) form the so called *sensitivity vector* $e(P)$

$$e(P) = \frac{2\pi}{\lambda} [b(P) - s(P)] \quad (4.20)$$

so that we get

$$\Delta\phi(P) = d(P) \cdot e(P). \quad (4.21)$$

This means that the interference phase at each point is given by the scalar product of the displacement vector and the sensitivity vector. The sensitivity vector is defined only by the geometry of the holographic arrangement. It gives the direction in which the setup has maximal sensitivity. At each point we measure the projection of the displacement vector onto the sensitivity vector. For displacements orthogonal to the sensitivity vector the resulting interference phase is always zero, independent of the magnitude of the displacement.

The above formula (4.21) is the basis of all quantitative measurements of the deformation of opaque bodies by holographic interferometry and will be used frequently in the following

chapters. Throughout this book we assume an illumination point source. For collimated illumination this is infinitely far away, nevertheless there exists a unit vector \mathbf{b} defining the direction of the collimated illumination. Holographic interferometry with diffuse illumination from a circular diffuser is investigated in [288].

4.1.5 Interference Phase Variation Due to Refractive Index Variation

Phase objects are *transparent objects* which do not significantly affect the amplitude of an optical wavefront passing through, but only change the phase of this wavefront. Holographic interferometry has widely replaced Mach-Zehnder interferometry for analyzing phase objects, e. g. in applications like flow visualization, plasma diagnostics, or heat transfer analysis, to name just a few [289]. In the analysis of *transparent media* the optical path difference responsible for the interference fringes is generated by a change in the *refractive index distribution* along the optical path. This change may be due to the absence and presence of a phase object or due to a variation of the phase object under test. As discussed before the double exposure or the real time method can be applied to compare the states before and after the variation of the refractive index field.

If the medium to be tested is held in a transparent container, which is not altered between the recording of the two wavefronts, imperfections in the walls of the container, e. g. fabricated from glass, affect both wavefronts in the same way. But since only the differences between the wavefronts generate the holographic interference pattern, the influence of the wall imperfections is canceled out.

A typical off-axis configuration with collimated beams for holographic interferometric measurements at a phase object is shown in Fig. 4.6. Employing the double exposure method,

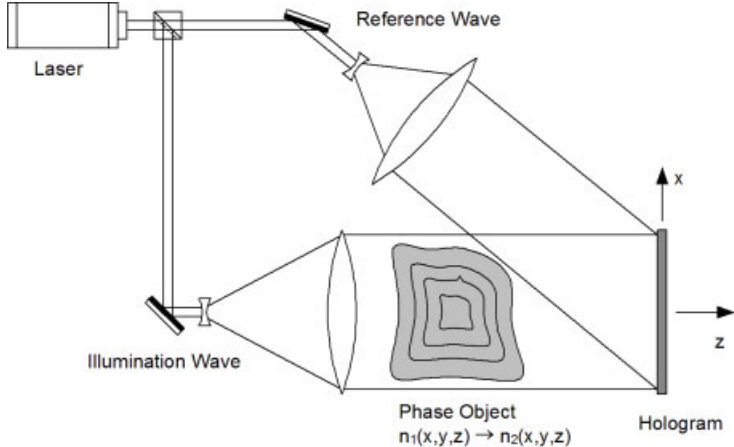


Figure 4.6: Configuration for holographic interferometry at a phase object.

the first recording is done with the refractive index distribution $n_1(x, y, z)$, the second is performed with $n_2(x, y, z)$. Let the rays propagate along straight lines parallel to the z -axis. Then

the interference phase distribution $\Delta\phi(x, y)$ in the plane perpendicular to the z -axis is

$$\Delta\phi(x, y) = \frac{2\pi}{\lambda} \int \Delta n(x, y, z) dz \quad (4.22)$$

with $\Delta n(x, y, z) = n_2(x, y, z) - n_1(x, y, z)$. The resulting intensity distribution in the holographic interferogram is (4.4)

$$\begin{aligned} I(x, y) &= 2I_1(x, y)\{1 + \cos[\Delta\phi(x, y)]\} \\ &= 2I_1(x, y) \left\{ 1 + \cos \left[\frac{2\pi}{\lambda} \int \Delta n(x, y, z) dz \right] \right\}. \end{aligned} \quad (4.23)$$

Equations (4.22) and (4.23) will play the central role in all quantitative measurements of refractive index distributions at phase objects.

Although the configuration of Fig. 4.6 is conceptually easy, the plane waves have several drawbacks [170]: Any dust particle or scratch on optical elements will diffract light into a nearly spherical wave. These unwanted waves then will interfere with the object wavefront and give annoying concentric ring patterns. Direct observation will exhibit a bright spot at the pinhole of the object beam and the field of view is limited to an area having the size of the iris. Hence the fringes have to be projected onto a screen to be observed. All these disadvantages are avoided by using *diffuse illumination holographic interferometry* [19, 20]. A ground glass plate is used to diffusely scatter the object illumination wave, Fig. 4.7. Now

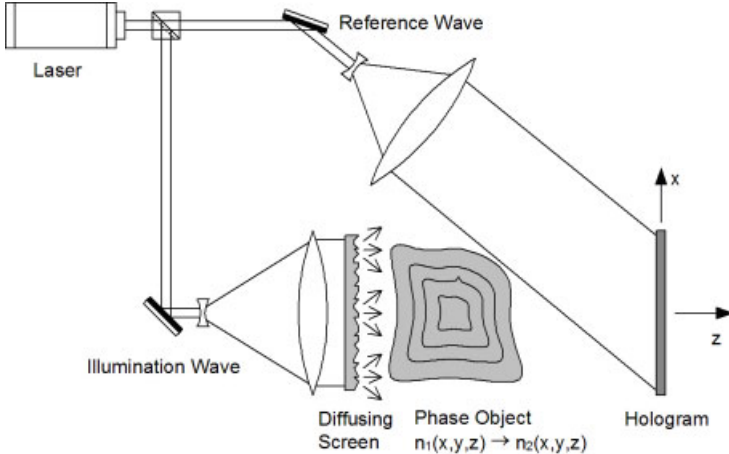


Figure 4.7: Configuration for diffuse illumination holographic interferometry.

the average irradiance is nearly uniform over the hologram, the influence of diffraction rings is minimized, the hologram can be observed with the unaided eye or recorded with a TV camera, and the hologram can be viewed in multiple directions. This last mentioned property will become important for three-dimensional quantitative evaluations, see Section 6.10.

4.1.6 Computer Simulation of Holographic Interference Patterns

Based on the equations (4.3) to (4.23) one can calculate the expected holographic interference pattern for a given setup geometry, including laser wavelength and object shape, as well as the loading applied to the object or the deformation or refractive index distribution [290, 291]. The simulation program basically is a loop over all pixels of the interferogram to be calculated. If we want to calculate an interference pattern of a deformed opaque surface, first each pixel is identified with the Cartesian coordinates of the corresponding point of the surface. With (4.18), (4.19), and (4.20) the sensitivity vectors for these surface points and thus for each pixel are calculated. The scalar multiplication (4.21) with the corresponding displacement vector is performed. The displacement vector has been determined from the loading parameters and the mechanical laws or has been taken from computer memory. While rigid body translations are easiest to handle – the displacement vector remains constant over all surface points – normally we have a combination of a rigid body motion, a deformation, and local deformation variations induced by defects or material inhomogeneities. The cosine (4.4) is applied to the calculated interference phase and gives the intensity distribution. Distortions like Gaussian background or speckle noise also can be taken into account. A Gaussian background may be simulated as an additive term, while the speckles are multiplicative [292]. Their stochastic nature is simulated by a random generator, which mimics the negative exponential probability distribution (2.105).

For the simulation of a real-time or a time average interferogram occurring in vibration analysis, the displacement vector is given by the maximal amplitude at each point, but then the Bessel function (4.7) or the squared Bessel function (4.10) is applied instead of the cosine (4.4). To get a better contrast in the simulated interferogram, the high intensity at the nodal lines, where the interference phase is near at zero, should be truncated, and the remaining intensity is mapped onto the full gray-scale. This results in brighter intensity maxima of higher order. Figure 4.8 shows some simulated holographic interference patterns, where in Fig. 4.8a a rectangular plate was subjected to strain and torsion; the inhomogeneity in the fringe pattern results from an anticipated subsurface void in the plate. Figure 4.8b displays a holographic interferogram of the same kind but with simulated background and speckle noise. Figure 4.8c gives the real-time and Fig. 4.8d the time average interferogram of a vibrating rectangular plate clamped at all four edges.

The simulation of holographic interference patterns is helpful in a number of ways:

- It helps in the planning phase of a holographic interferometric measurement to design optimized holographic arrangements. One can check whether an expected deformation produces fringes of sufficient but not too high a density on the basis of cheap computer experiments instead of expensive practical experiments. The optimal loading amplitudes can be found this way.
- If it is impossible to perform a three-dimensional evaluation with multiple interferograms, one can compare the calculated interferogram of an expected three-dimensional deformation field with the experimentally produced single interference pattern. Although this does not substitute a complete three-dimensional evaluation, it may confirm the results, if also the interferograms of all other possible deformations have been simulated and they differ significantly from the measured one.

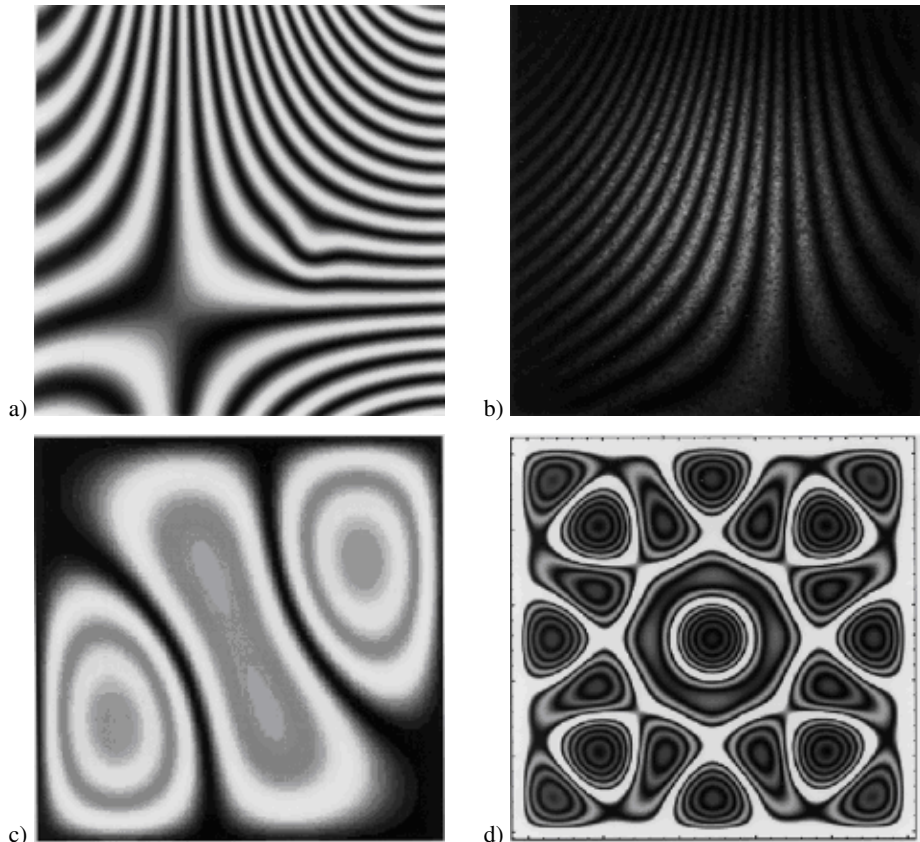


Figure 4.8: Simulated holographic interferograms: (a) double-exposure interferogram, (b) double-exposure interferogram with varying background intensity and speckles, (c) real-time interferogram of a vibrating plate, (d) time average interferogram of a vibrating plate.

- In developing new evaluation methods, e. g. adapted methods for special measurement problems, these methods can be tested first for simulated patterns. Especially the behavior of new methods, when evaluating more or less speckled patterns, can be tested systematically.
- In the application of advanced evaluation methods, e. g. fault detection with neural networks, test data or samples for network training are needed in large numbers and with much diversity [293]. These cannot be all generated experimentally. Based on some experimental examples the vast majority of the training samples are generated by computer simulation.

4.2 Variations of the Sensitivity Vectors

In Section 4.1.4 the foundations for holographic interferometric deformation measurements at diffusely reflecting opaque surfaces have been laid. The displacements of the object surface points together with the fixed sensitivity vectors give rise to the optical path differences which lead to the observable fringe patterns. Since the sensitivity vectors define the directions of the displacement components which are measured with the highest sensitivity, they should be examined in the stage of planning a holographic interferometric measurement experiment. The goal is to find an optimal arrangement that gives maximal accuracy and requires minimum effort for solving a given problem.

Contrary to deformation measurement holographic interferometry can also be applied by leaving the object surface unchanged but altering the sensitivity vectors between the construction of the two wavefronts to be compared interferometrically. This aspect is further addressed in Section 6.6, where it is used for holographic contouring.

4.2.1 Optimization of the Holographic Arrangement

The sensitivity vector is defined by (4.20) where the unit vectors $s(P)$ in illumination direction and $b(P)$ in observation direction are given by (4.18) and (4.19) for the case of divergent illumination and observation beams with a well defined source point S and observation point B . For collimated illumination and observation, Fig. 4.9a, we assume the central points of the collimating lenses as source S and observation point B , and the unit vectors s and b constant over all surface points P . If at least one of the illumination or the observation beam is divergent, then the sensitivity vector varies over the surface, Fig. 4.9b. Only if both the illumination and the observation beam are collimated will the sensitivity vector be the same for all points of the investigated surface, Fig. 4.9a.

The consequences of these two cases can be investigated by looking at the variation of the interference phase (4.21) in e. g. the x -direction

$$\begin{aligned} \frac{\partial}{\partial x} \Delta\phi &= \frac{\partial}{\partial x} [d_x e_x + d_y e_y + d_z e_z] \\ &= \frac{\partial d_x}{\partial x} e_x + d_x \frac{\partial e_x}{\partial x} + \frac{\partial d_y}{\partial x} e_y + d_y \frac{\partial e_y}{\partial x} + \frac{\partial d_z}{\partial x} e_z + d_z \frac{\partial e_z}{\partial x}. \end{aligned} \quad (4.24)$$

The arguments P have been omitted for clarity. We see that a change in the interference phase may stem from a variation of the displacement vector as well as from a variation of the sensitivity vector. For a constant sensitivity vector the interference phase depends solely on the displacement vector variation.

From a theoretical standpoint, only in the case of rigid body translations to be measured does it seem desirable to have varying sensitivity vectors to cover the object with fringes; in all other cases of deformations and rotations the evaluation will become easier with constant sensitivity vectors. But practically this is only possible for objects or illuminated areas on the objects of less than or equal to the collimating lens dimensions. A detailed analysis of sensitivity errors in interferometric deformation metrology, especially for divergent illumination and non-planar objects, is given in [294]. Nevertheless if the illumination and observation points are far away from the examined surface, compared with the surface dimensions, we can

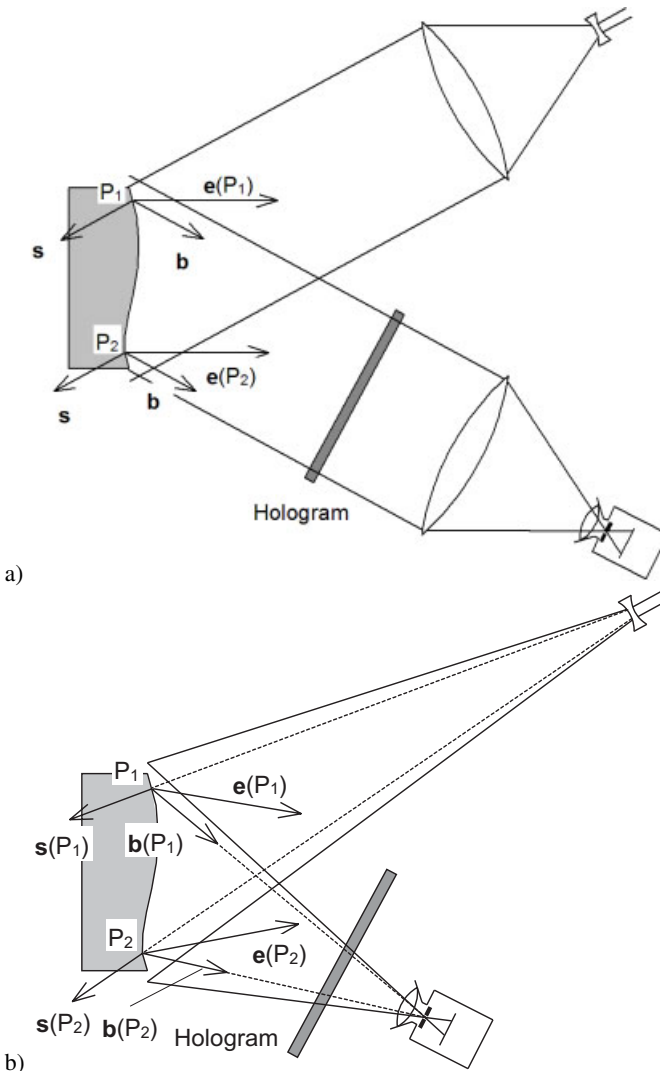


Figure 4.9: Constant (a) and not constant (b) sensitivity vectors.

assume nearly constant sensitivity vectors. The remaining errors may be estimated with the help of (4.24) by taking the maximum anticipated values for all variables and summing the absolute values.

In this way the problem of measuring only the out-of-plane displacements is tackled as follows. The Cartesian coordinate system is defined so that for a central surface point P we have $P = (0, 0, 0)$ and furthermore $y_S = y_B = 0$, $x_S = -x_B$, and $z_S = z_B$. Then the

sensitivity vector at least at P reduces to $e(P) = (0, 0, e_z(P))^T$ with

$$e_z(P) = \frac{2\pi}{\lambda} [z_B(P) - z_S(P)] = \frac{4\pi \cos \Theta}{\lambda} \quad (4.25)$$

where Θ is the angle between the z -axis and the illumination direction which due to the assumptions agrees with the angle between the z -axis and the observation direction. The condition $x_S = -x_B$ and $z_S = z_B$ can be relaxed to only identical angles Θ for both directions. For constant or for nearly constant sensitivity vectors we now can determine the z -component of the displacement with good accuracy by

$$d_z(P) = \frac{\lambda \Delta \phi(P)}{4\pi \cos \Theta}. \quad (4.26)$$

The basic ideas contained in this reduction of complexity can be worked out to a concept of optimizing the holographic setup [295]. In nearly all metrologic problems, we have a lot of previous information, e. g. about the directions of the deformations we expect. Then it is good practice to configure a holographic setup with maximum sensitivity in the expected direction and minimum sensitivity in directions of eventual distortions. As a help for this aim Jüptner et al. [296] have introduced the sensitivity functions and Abramson [297–301] designed the so called *holo-diagram*. A quantification of possible sensitivity errors in interferometric deformation measurements is given by Farrant and Petzing [294].

In [296] a Cartesian coordinate system based on the positions of the illumination source point and the observation point is defined. All lengths are normalized by the distance between these two points. The *sensitivity functions* indicate the sensitivity with respect to the different displacement components. Now if the direction of the object deformation can be anticipated, one has to search for regions where the sensitivity function for this direction varies linearly and the sensitivity functions for the other directions remain as close as possible to zero. It is worth mentioning that in this approach sensitivity is a property varying in space, only depending on the positions of the illumination and observation points, but there is no object already in the holographic arrangement.

The other aid for optimizing the holographic arrangement is the *holo-diagram* [297–301]. This consists of the two-dimensional projection of confocal ellipsoids with the focal points being the point source of illumination S and the point of observation B . By definition the path length from S to B is constant when travelling via any point along one ellipsoid. Adjacent ellipsoids are given path lengths from S to B via this ellipsoid which differ by λ . The distance between adjacent ellipses, the projections of the ellipsoids, varies with the directions to S and B , respectively. But it is constant along arcs of circles, or toroids in the three-dimensional case, known as k-circles. A displacement of an object point P from one ellipse to the next corresponds to one wavelength and thus to one fringe in the interference pattern. Displacements along the ellipses will cause no fringes. On the other hand the required displacement of P for inducing one fringe is minimum when its motion is along the normal to the ellipse. This normal corresponds to the sensitivity vector e . As before the holo-diagram depicts the sensitivity of the holographic setup in space without the presence of an object.

For optimization of the holographic configuration the object has to be positioned in the holo-diagram in an orientation that the main direction of the anticipated displacement becomes

orthogonal to the ellipses. Nevertheless one has to guarantee that the surface under study should not be in shadow and that it should be freely visible from B .

An increase in sensitivity, that is more fringes for the same displacement, can be obtained with the three-step approach described in [302]. A double exposure hologram is recorded, with the illumination beam of the second exposure slightly tilted with respect to the first. The reconstructed image consists of modulated Young's fringes, which are recorded on a photographic plate, that is developed in a nonlinear way. This plate now is a modulated diffraction grating, which is illuminated by two plane waves. By adjusting the angle between the propagation directions of these waves, a $+n$ -order diffracted wave can be made to coincide with a $-m$ -order diffracted wave. These waves are filtered by a pinhole in the Fraunhofer plane. Their interference has an intensity of the form [302]

$$I(P) = I_0(P) + I_1(P) \cos[(n+m)\Delta\phi(P)] \quad (4.27)$$

where the interference phase can be seen to be amplified. The fringe sensitivity increases by $(n+m)$ in comparison with ordinary holographic interferometry (4.4).

When measuring three-dimensional displacement fields, a further optimization criterion is the numerical condition of the system of equations to be solved. This topic is treated in more detail in Section 6.2.3.

4.2.2 Two Reference Beam Holographic Interferometry

In the preceding sections it was shown how the interference phase distribution giving rise to the observable holographic interferometric fringe pattern was affected by changing the optical pathlength. The change of the optical pathlength at each observed object point can be caused by a variation of a physical parameter of the object under test or by a modification of the sensitivity vector. In the next chapter evaluation methods will be introduced which employ an additional variation of the interference phase distribution independent from the interference phase due to the quantity to be measured. The phase of one of the interfering wave fields will be shifted relative to the other. If this shifting is continuously in time, it is equivalent to a frequency shift, and is utilized in the *heterodyne method*. Contrarily, if the shifting is in discrete steps, the many *phase shift* and *phase step methods* build on it.

To have independent access to the two reconstructed wave fields, in order to affect one independently from the other, a holographic setup employing two reference waves is required, Fig. 4.10 [303, 304]. The first exposure of the double exposure method is performed with object state E_1 and reference wave R_1 while R_2 is blocked. The second exposure, now of object state E_2 is done with the help of R_2 with R_1 being blocked. The reconstruction then is accomplished with R_1 and R_2 together to generate the interference between E_1 and E_2 , but now this interference pattern may be modified by varying one of the reference waves while leaving the other one unaffected.

Two reference beam holography requires special attention to the multiplicity of the reconstructed images. Illuminating the hologram with both reference beams R_1 and R_2 together yields not only two, but four reconstructions in the first diffraction order, namely the two desired reconstructions $R_1 R_1^* E_1$ and $R_2 R_2^* E_2$, see (2.131) and (2.134), which give rise to the interference pattern and additionally the two undesired *cross-reconstructions* $R_2 R_1^* E_1$ and

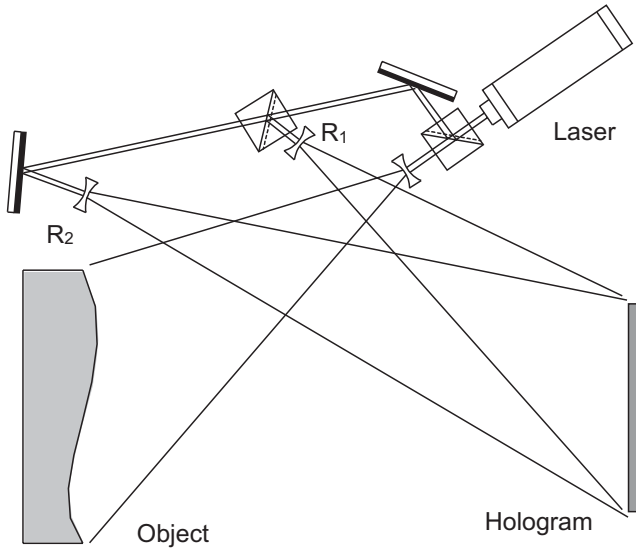


Figure 4.10: Two-reference-beam holographic arrangement with well separated reference sources.

$R_1 R_2^* E_2$. As shown in Section 2.6.3 reconstruction with reference beams other than used during recording will result in shifted and distorted images. Equations (2.154) – (2.156) with $\mu = 1$ may be used to plan a two reference wave arrangement where the cross-reconstructions do not overlap.

As an easy example let an object surface extend along the x -direction from $P_1 = (x_1, 0, z)$ to $P_1 = (x_2, 0, z)$ $x_2 > x_1$, and the reference sources be at $R_1 = (x_R, 0, z)$ and $R_2 = (x'_R, 0, z)$ $x'_R > x_R$. Then (2.154) for P_1 recorded with R_1 and reconstructed with R_2 gives the position $P'_1 = (x_1 + x'_R - x_R, 0, z)$. Non-overlapping here occurs for $x_1 + x'_R - x_R > x_2$. Generally, the two reference sources chosen on the same side of the object must have mutual separation larger than the angular size of the object in the corresponding direction.

However, the consequence of a large separation of the reference sources is high sensitivity to hologram misalignment in the repositioning after development and to changes of the wavelength between hologram recording and reconstruction [143]. The sensitivity of two reference beam holographic interferometry to repositioning and wavelength changes occurs because the propagation of the two reconstructed wave fields are differently affected as can be checked quantitatively with the help of (2.154) – (2.156) using a coordinate system fixed to the hologram plate.

For reference beams assumed as plane waves in the directions \mathbf{k}_1 and \mathbf{k}_2 , the additional phase difference $\Delta\phi$ at a point \mathbf{r}_H in the hologram plane is [304]

$$\Delta\phi(\mathbf{r}_H) = [(\mathbf{k}_1 - \mathbf{k}_2) \times \boldsymbol{\omega}] \cdot \mathbf{r}_H + \frac{\Delta\lambda}{\lambda} (\mathbf{k}_1 - \mathbf{k}_2) \cdot \mathbf{r}_H \quad (4.28)$$

where $\boldsymbol{\omega} = (\Delta\xi, \Delta\eta, \Delta\chi)$ is the rotation vector for small hologram rotations around the x -, y -, and z -axes, respectively, and $\Delta\lambda$ is the change in wavelength. It is seen that both contributions, stemming from small rotations and wavelength shift, depend on the difference vector $\mathbf{k}_1 - \mathbf{k}_2$. So the sensitivity to misalignment or wavelength change is drastically decreased if

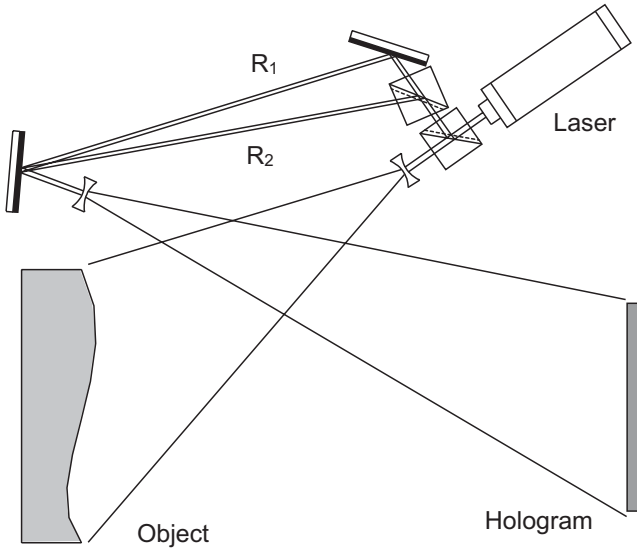


Figure 4.11: Two-reference-beam holographic arrangement with reference sources close together.

the reference sources are close together [305]. In such an arrangement, Fig. 4.11, all reconstructions overlap, but only $R_1 R_1^* E_1$ and $R_2 R_2^* E_2$ will give a stationary interference pattern as long as the cross-reconstructions are shifted laterally by more than the average pixel size. The distortions induced by the cross-reconstructions are merely a tolerable decrease in the contrast of the interference pattern. Wavelength changes between recording and reconstruction cannot be avoided if recording was done with a pulsed laser but reconstruction has to be performed with a continuously emitting laser.

The cross-reconstructed images can be avoided when the holographic patterns belonging to the different – two or more – reference waves are incoherently superposed in the sensor – which may be a hologram plate, or a CCD-array in digital holography. The superposition becomes incoherent if the optical path lengths of the different object and reference wave pairs differ by more than the coherence length of the used laser light. This can be achieved by using fibers of different lengths [306]. The isolation of the different images by a Fourier transform approach is described in [306] for DSPI, see Section 7.3, but can be transferred to holography without posing further problems.

4.3 Fringe Localization

4.3.1 Fringe Formation with Diffusely Scattering Surfaces

In Section 2.5 the speckle effect was introduced which always occurs if rough diffuse scattering surfaces reflect coherent light. In holographic interferometry wave fields interfere, which represent a diffusely reflecting surface in different deformation states. The light from each point of the undeformed surface will interfere with light from each point of the deformed surface. This produces a speckle pattern consisting of random irradiance variations of relatively

high spatial frequency. As outlined in Section 2.5 the speckle pattern primarily is defined by the microscopic contour of the reflecting surface and by the size of the viewing aperture.

But additionally there is a systematic low-frequency variation which constitutes the holographic interferometric fringe patterns conveying information about the displacement and deformation of the object between the exposures. Figure 4.12 shows a rough surface before

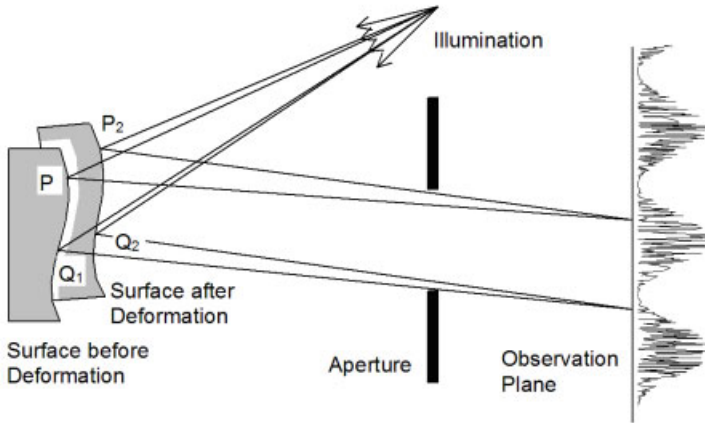


Figure 4.12: Scheme of fringe formation.

and after deformation, where P_1 and P_2 denote the same point of the surface before and after its displacement [170]. The same holds for Q_1 and Q_2 . Light scattered by the surface in the neighborhood of point P_1 gives rise to a complex wave field, the light scattered at a neighborhood of P_2 forms another wave field. The wave fields are nearly identical but are mutually displaced and travel in slightly different directions. The resulting irradiance in an observation plane is shown in Fig. 4.12. The systematic low frequency variation is only induced by interference of light from corresponding points P_1 and P_2 or Q_1 and Q_2 . Noncorresponding point pairs like (P_1, Q_1) , (P_1, Q_2) , (P_2, Q_1) , or (P_2, Q_2) do not contribute to the formation of the holographic interference pattern. This is the concept of *homologous points* or *rays* [307].

These are the same points on the surface before and after deformation. Non-homologous points possess neighborhoods with distinct microstructures which are not correlated, thus not leading to a low-frequency interference fringe pattern but only contributing to the statistical speckle field. Altogether, for computation or for evaluation of fringe patterns, we need to consider only the change in optical pathlength δ of light scattered by homologous points such as P_1 and P_2 . The pathlength δ is the one defined in (4.13).

The simultaneously present wavefronts in holographic interferometry freely propagate in space. They only interfere if they are imaged onto a detector surface, such as a sheet of film, a ground glass screen, a CCD-target or the retina of the eye. If a person looks directly through a double-exposure hologram to see the reconstructed virtual images, or looks through the single exposed hologram and additionally sees the illuminated object for the real-time method, the

optical interference occurs on his or her retina, not at some other location in space. In the terminology of Section 2.5.2, Fig. 4.12 shows the objective fringe formation, while in practice we have the subjective fringe formation.

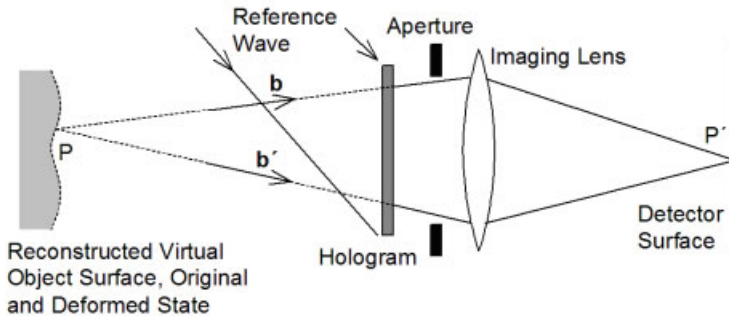


Figure 4.13: Fringe formation in double exposure holographic interferometry, focused on surface.

A simple system for viewing a double exposure hologram is given in Fig. 4.13. The hologram here only acts as a means for delivering the wavefronts simultaneously. Since the optics are focused onto the surface, the image of the composite field at P is formed at P' at the detector. The resulting interference pattern should depend on the optical pathlength δ , (4.17), but now we have a manifold of observation directions, two of them, b and b' , are shown in Fig. 4.13. If the pathlength δ , resulting from all these directions, varies too much, no interference pattern will be observable. Clearly, shutting down the aperture and thus increasing the depth of focus may minimize the b -variation and eventually will produce observable fringes.

Practically it has been found that instead of increasing the focus a shift of the plane, on which it is focused, often exhibits observable fringes. Thus one recognizes that the fringes are not generally fixed to the object surface but may localize in space. This *localization* depends on the type of deformation, the observation direction, and as will be shown in the following, on the illumination direction. As we have seen already, a further important parameter for fringe formation is the aperture.

The focusing onto a fringe localized outside the object surface is shown in Fig. 4.14. The optical pathlength of all rays from Q to Q' and thus the relative phases are equal, independent from the individual b . So the interference pattern at Q' is identical to that which would be formed at Q , if a detector would be placed there. At Q the light is arriving from a ray cone centered on the axis \overline{PQ} . The angular extent of this cone is determined by the aperture of the viewing system. The interference pattern in the neighborhood of Q is the superposition of the interference patterns due to the motion of all surface points P subtended by this cone. If Q is where the fringes are localized, the value of δ (4.17) is nearly constant over the cone. But for arbitrary Q the pathlength δ may vary significantly, so that the many corresponding fringe patterns average out and only the random speckle pattern is observed.

For an analytic description of the fringe localization the point along a given viewing direction is determined, for which the variation of δ over a small cone of observation rays is minimized [308]. Therefore a Cartesian coordinate system fixed to the surface with the x -

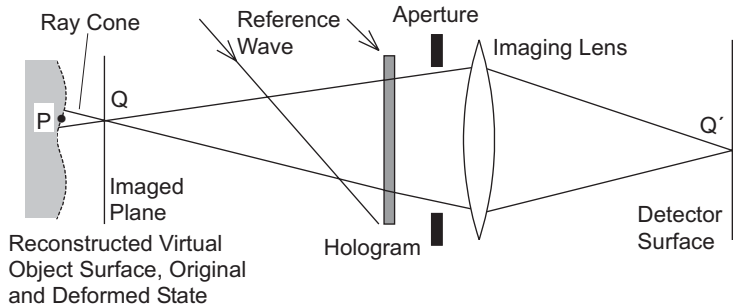


Figure 4.14: Fringe formation in double exposure holographic interferometry, focused on fringe localized outside the surface.

y -plane tangential and the z -axis normal at at least one surface point is defined. Thus the condition for localization of the fringes is that the expression for the optical pathlength δ (4.17) is minimized [170]

$$d\delta = \frac{\partial \delta}{\partial x} dx + \frac{\partial \delta}{\partial y} dy = 0 \quad (4.29)$$

where dx and dy are differential changes in the object point which is viewed from Q . The distance z from the object surface to Q is a parameter in the expression for δ . The values of z for which (4.29) is satisfied define the curve or surface of fringe localization.

It should be mentioned that for this definition of localization the visibility of the holographic fringes defined by

$$V = \frac{\langle I \rangle_{\max} - \langle I \rangle_{\min}}{\langle I \rangle_{\max} + \langle I \rangle_{\min}} \quad (4.30)$$

becomes maximal [309, 310]. Here $\langle \rangle$ describes averaging over an ensemble of surfaces with different microstructures undergoing the same deformations.

4.3.2 Fringe Localization with Collimated Illumination

For small objects or at least for illumination sources sufficiently far from the object surface the curvature of the illumination wavefront at the object surface is quite small [170]. The s (4.18) can be assumed constant, but the b and d of (4.17) are functions of the surface point

$P = (x, y, 0)$ and the observer position $B = (x_B, y_B, z_B)$. Then (4.29) becomes

$$\begin{aligned} & \left(\frac{\partial b_x(P)}{\partial x} d_x(P) + \frac{\partial b_y(P)}{\partial x} d_y(P) + \frac{\partial b_z(P)}{\partial x} d_z(P) + [b_x(P) - s_x(P)] \frac{\partial d_x(P)}{\partial x} \right. \\ & \quad \left. + [b_y(P) - s_y(P)] \frac{\partial d_y(P)}{\partial x} + [b_z(P) - s_z(P)] \frac{\partial d_z(P)}{\partial x} \right) dx \\ & \quad + \left(\frac{\partial b_x(P)}{\partial y} d_x(P) + \frac{\partial b_y(P)}{\partial y} d_y(P) + \frac{\partial b_z(P)}{\partial y} d_z(P) + [b_x(P) - s_x(P)] \frac{\partial d_x(P)}{\partial y} \right. \\ & \quad \left. + [b_y(P) - s_y(P)] \frac{\partial d_y(P)}{\partial y} + [b_z(P) - s_z(P)] \frac{\partial d_z(P)}{\partial y} \right) dy = 0. \quad (4.31) \end{aligned}$$

The vector \mathbf{b} is defined in (4.19), its derivatives with respect to x and y , the corresponding components of P , are easily calculated to be

$$\begin{aligned} \frac{\partial}{\partial x} b_x(P) &= -\frac{b_z(P)}{z_B} (b_y^2(P) + b_z^2(P)) & \frac{\partial}{\partial y} b_x(P) &= \frac{b_z(P)}{z_B} b_x(P) b_y(P) \\ \frac{\partial}{\partial x} b_y(P) &= \frac{b_z(P)}{z_B} b_x(P) b_y(P) & \frac{\partial}{\partial y} b_y(P) &= -\frac{b_z(P)}{z_B} (b_x^2(P) + b_z^2(P)) \\ \frac{\partial}{\partial x} b_z(P) &= \frac{b_z(P)}{z_B} b_x(P) b_z(P) & \frac{\partial}{\partial y} b_z(P) &= \frac{b_z(P)}{z_B} b_y(P) b_z(P). \end{aligned} \quad (4.32)$$

Combination with (4.31) yields

$$\begin{aligned} & \left(\frac{b_z}{z_B} [(b_y^2 + b_z^2)d_x - b_x b_y d_y - b_x b_z d_z] - (b_x - s_x) \frac{\partial d_x}{\partial x} - (b_y - s_y) \frac{\partial d_y}{\partial x} - (b_z - s_z) \frac{\partial d_z}{\partial x} \right) dx \\ & + \left(\frac{b_z}{z_B} [(b_x^2 + b_z^2)d_y - b_x b_y d_x - b_y b_z d_z] - (b_x - s_x) \frac{\partial d_x}{\partial y} - (b_y - s_y) \frac{\partial d_y}{\partial y} - (b_z - s_z) \frac{\partial d_z}{\partial y} \right) dy \\ & = 0. \end{aligned} \quad (4.33)$$

The arguments (P) have been omitted for clarity.

If the viewing aperture is of roughly the same dimension in all directions, as is the case for square or circular apertures, dx and dy can be varied independently, so the factors to dx and dy must each be identically zero, leading to the two conditions

$$z_{B1} = \frac{b_z [(b_y^2 + b_z^2)d_x - b_x b_y d_y - b_x b_z d_z]}{(b_x - s_x) \frac{\partial d_x}{\partial x} + (b_y - s_y) \frac{\partial d_y}{\partial x} + (b_z - s_z) \frac{\partial d_z}{\partial x}} \quad (4.34)$$

$$z_{B2} = \frac{b_z [(b_x^2 + b_z^2)d_y - b_x b_y d_x - b_y b_z d_z]}{(b_x - s_x) \frac{\partial d_x}{\partial y} + (b_y - s_y) \frac{\partial d_y}{\partial y} + (b_z - s_z) \frac{\partial d_z}{\partial y}}. \quad (4.35)$$

Since the observation point B of (4.19) here is equivalent to the point Q in Fig. 4.14, each of these two equations describes a surface $z_{Bi} = z_{Qi} = z_{Qi}(\mathbf{b}, \mathbf{s}, \mathbf{d})$ in space. Both equations must be satisfied, therefore the fringes are generally localized along a curve which is the intersection of these two surfaces. Only in special cases (4.34) and (4.35) define identical surfaces, where then the fringes localize.

In the following the localization is determined for some special displacement fields of the object surface. If the object undergoes a *rigid body translation*, the displacement components d_x , d_y , and d_z are identical at all points of the investigated surface. Their derivatives are identically zero, so (4.34) and (4.35) give a localization at infinity $z_{Bi} = \infty$. Indeed the fringes can be observed with good visibility only at infinity, practically the back focal plane of a lens, Fig. 4.15 [310].

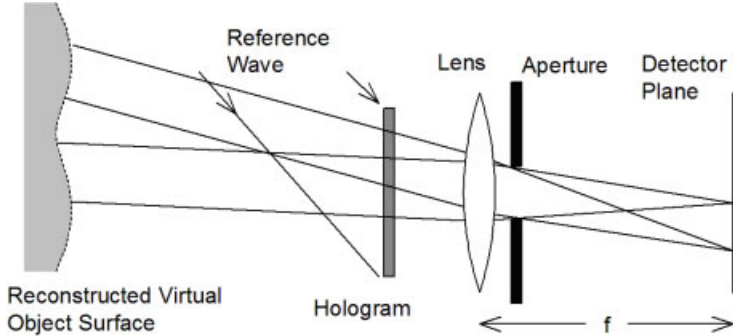


Figure 4.15: Observation of fringes localized at infinity.

For general deformations or *rigid body rotations* not all terms in the denominators of (4.34) and (4.35) vanish, thus giving fringe localization at some finite distance from the surface.

As a first example let the surface rotate by a small angle θ about the y -axis, then

$$\mathbf{d}(x, y, 0) \approx (0, 0, \theta x) \quad (4.36)$$

and (4.34) yields

$$z = -\frac{b_x b_z^2}{b_z - s_z} x. \quad (4.37)$$

This in the following is considered for some representative holographic arrangements, Fig. 4.16. If the observation is along the surface normal, the z -axis, Figs. 4.16a and b, then we have $b_x = 0$, yielding $z_B = 0$, meaning localization in the object surface. If we have an illumination direction inclined 45° to the z -axis and the observation is under -45° with respect to the z -axis, Fig. 4.16c, then $b_x = b_z = -s_x = \sin 45^\circ = \sqrt{2}/2$ and the localization plane is defined by

$$z = -\frac{1}{4} x. \quad (4.38)$$

This defines a plane intersecting the observed surface along the y -axis. For normal illumination, $s_z = 1$, and observation under -45° , Fig. 4.16d, the localization is at

$$z = -\frac{1}{2(1 + \sqrt{2})} x. \quad (4.39)$$

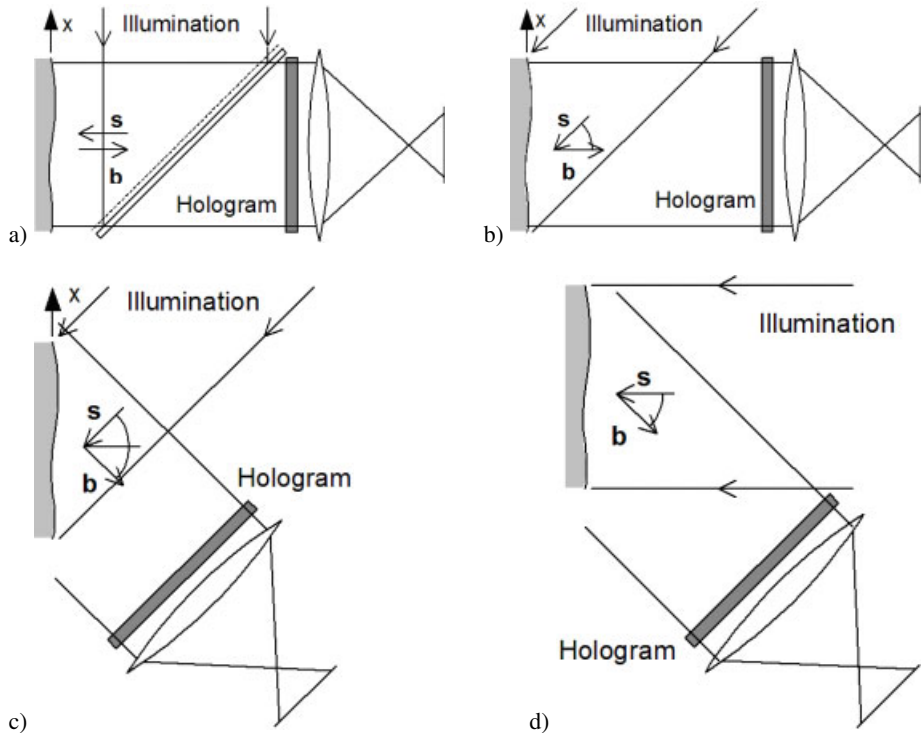


Figure 4.16: Representative holographic configurations for examining fringe localization.

If the object is rotated by an angle θ about an axis parallel to the surface, but not lying in it, the fringes localize off the surface. Let the rotation axis be parallel to the y -axis and lying a distance r behind the surface which is in the x - z -plane, then

$$\mathbf{d}(x, y, 0) \approx (r\theta, 0, -\theta x). \quad (4.40)$$

Let us furthermore for simplicity only consider illumination, observation, and object points in the x - z -plane, then $b_y = s_y = 0$ and from (4.34) we get

$$z = -\frac{b_z[(b_y^2 + b_z^2)r + b_x b_z x]}{(b_z - s_z)} \quad (4.41)$$

which again is a plane like in (4.37). If viewed normally, $b_z = 1$, $b_x = b_y = 0$, Figs. 4.16a and b, the fringes are in a plane parallel to the object surface but behind it, namely by $-r(1 - s_z)$.

A rotation about the z -axis by an angle θ gives

$$\mathbf{d}(x, y, 0) \approx (-\theta y, \theta x, 0) \quad (4.42)$$

and the localization conditions (4.34) and (4.35) are

$$\begin{aligned} z_1 &= -\frac{b_z [(b_y^2 + b_z^2)y + b_x b_y x]}{b_y - s_y} \\ z_2 &= -\frac{b_z [(b_x^2 + b_z^2)x + b_x b_y y]}{b_x - s_x}. \end{aligned} \quad (4.43)$$

If now the object is illuminated and viewed in the normal direction, Fig. 4.16a, the displacement vector is orthogonal to the sensitivity vector, and no fringes are formed at all. For illumination at an angle of 45° and normal observation, Fig. 4.16b, we have $s_x = -s_z = \sqrt{2}/2$, $b_x = b_y = 0$, and $b_z = 1$, now the fringes are localized in the line

$$z = \sqrt{2}x, \quad y = 0 \quad (4.44)$$

The configurations of Figs. 4.16c and d give $z = x/2$ and $z = x$, respectively.

When deformations are involved, the displacement vector \mathbf{d} may be a nonlinear function of the object surface coordinates and the fringes appear to localize along a curve in space, or in a curved surface. An elongation of e. g. a tensile test specimen is described by

$$\mathbf{d}(x, y, 0) \approx (\varepsilon x, 0, 0) \quad (4.45)$$

where ε is the linear strain. For the configurations of Figs. 4.16a and c we will get no fringes, since there is orthogonality between displacement and sensitivity vectors. For the configuration of Fig. 4.16b the localization is at $z = -\sqrt{2}x$

and for Fig. 4.16d at $z = x/2$.

The bending of a cantilever beam of length L fixed at one end is described by

$$\mathbf{d}(x, y, 0) \approx \left(0, 0, \frac{d}{2} \left[3\left(\frac{x}{L}\right)^2 - \left(\frac{x}{L}\right)^3 \right] \right) \quad (4.46)$$

with d the deflection at the loose end. The fringes here are localized in $z = 0$ for arrangements of Figs. 4.16a and b, in

$$z = \frac{L}{6\sqrt{2}} \frac{3\left(\frac{x}{L}\right) - \left(\frac{x}{L}\right)^2}{2 - \left(\frac{x}{L}\right)} \quad (4.47)$$

for Fig. 4.16c and in

$$z = \frac{-L}{6(1 + 1/\sqrt{2})} \frac{3\left(\frac{x}{L}\right) - \left(\frac{x}{L}\right)^2}{2 - \left(\frac{x}{L}\right)} \quad (4.48)$$

for Fig. 4.16d.

Generally it is possible to bring a fringe pattern that is localized far from the object surface to it by tilting the reference beam adequately [311].

4.3.3 Fringe Localization with Spherical Wave Illumination

If the curvature of the illuminating wavefront at the object surface cannot be neglected, differentiation of the sensitivity vectors in (4.29) leads to additional $\partial s_i(P)/\partial x$ - and $\partial s_i(P)/\partial y$ -terms in (4.31). The derivatives of s are calculated analogously to (4.32) and with the abbreviation $R = \sqrt{(x_P - x_S)^2 + (y_P - y_S)^2 + (z_P - z_S)^2}$ as

$$\begin{aligned}\frac{\partial}{\partial x} s_x(P) &= -\frac{s_y^2(P) + s_z^2(P)}{R} & \frac{\partial}{\partial y} s_x(P) &= \frac{s_x(P)s_y(P)}{R} \\ \frac{\partial}{\partial x} s_y(P) &= \frac{s_x(P)s_y(P)}{R} & \frac{\partial}{\partial y} s_y(P) &= -\frac{s_x^2(P) + s_z^2(P)}{R} \\ \frac{\partial}{\partial x} s_z(P) &= \frac{s_x(P)s_z(P)}{R} & \frac{\partial}{\partial y} s_z(P) &= \frac{s_y(P)s_z(P)}{R}\end{aligned}\quad (4.49)$$

and instead of (4.33) now we get

$$\begin{aligned}&\left(\left[\frac{b_z}{z_B} (b_y^2 + b_z^2) - \frac{1}{R} (s_y^2 + s_z^2) \right] d_x - \left[\frac{b_z}{z_B} b_x b_y - \frac{1}{R} s_x s_y \right] d_y - \left[\frac{b_z}{z_B} b_x b_z - \frac{1}{R} s_x s_z \right] d_z \right. \\ &\quad \left. - (b_x - s_x) \frac{\partial d_x}{\partial x} - (b_y - s_y) \frac{\partial d_y}{\partial x} - (b_z - s_z) \frac{\partial d_z}{\partial x} \right) dx \\ &+ \left(\left[\frac{b_z}{z_B} (b_x^2 + b_z^2) - \frac{1}{R} (s_x^2 + s_z^2) \right] d_y - \left[\frac{b_z}{z_B} b_x b_y - \frac{1}{R} s_x s_y \right] d_x - \left[\frac{b_z}{z_B} b_y b_z - \frac{1}{R} s_y s_z \right] d_z \right. \\ &\quad \left. - (b_x - s_x) \frac{\partial d_x}{\partial y} - (b_y - s_y) \frac{\partial d_y}{\partial y} - (b_z - s_z) \frac{\partial d_z}{\partial y} \right) dy = 0 \quad (4.50)\end{aligned}$$

This is the most general condition for fringe localization and can be applied to the different rigid body motions and deformations as well as to the varied holographic configurations in the same manner as (4.33) did. Then one recognizes that the variation in the sensitivity vector introduces curvature into the surface or curve of localization and can lead to localization at finite distances even for rigid body translations. A detailed analysis of this case shows that the fringes now localize in a curved surface near $z = R$.

4.3.4 Fringe Localization with Phase Objects

Using the same approach as in the sections before now we investigate the localization of the holographic interference fringes arising from refractive index changes in phase objects [170]. Here only diffuse illumination holographic interferometry is considered, Fig. 4.7, for it is the practically relevant case. The analysis in the following will employ straight rays, ray bending due to refractive index gradients will be neglected. Figure 4.17 shows the geometry on which the following analysis is based. In front of the illuminated diffuser is a phase object introducing the refractive index variation

$$f(\mathbf{r}) = f(x, y, z) = \frac{2\pi}{\lambda} \Delta n(x, y, z) \quad (4.51)$$

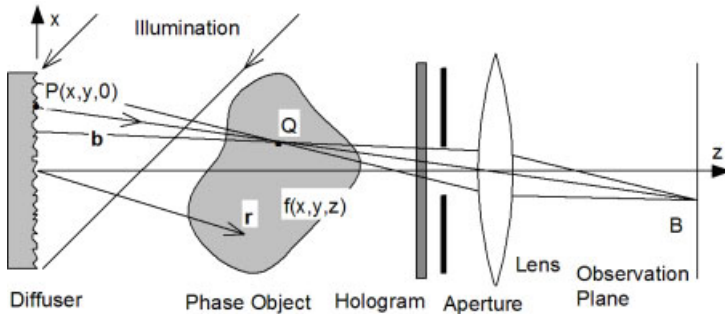


Figure 4.17: Fringe localization of phase objects.

where $\Delta n(x, y, z)$ was already defined in (4.22). Without loss of generality a Cartesian coordinate system is fixed to the diffuser with the x - y -plane tangential and the z -axis normal to the diffuser surface. The viewing system should be focused on a plane containing the point Q . As already seen, the holographic interference fringes are localized at points Q where the phase difference $\Delta\phi$ is nearly constant over the cone of ray pairs passing through Q and imaged onto the observation plane.

In analogy to (4.22) the optical path difference is

$$\Delta\phi = \int_S f(x, y, z) ds \quad (4.52)$$

where s is along the ray of direction b through the phase object. It is assumed that $f(x, y, z) = 0$ outside a finite region S – the intersection of the observation ray with the phase object – and that f exhibits no discontinuities.

The condition for fringe localization is given analogously to (4.29) by

$$d(\Delta\phi) = \frac{\partial\Delta\phi}{\partial x} dx + \frac{\partial\Delta\phi}{\partial y} dy = 0. \quad (4.53)$$

Since the integration limits are fixed, we can interchange the order of integration and differentiation, and with the chain rule we get

$$\frac{\partial\Delta\phi}{\partial x} = \int_S \nabla f \cdot \frac{\partial \mathbf{r}}{\partial x} ds \quad (4.54)$$

with $\nabla f = (\partial f / \partial x, \partial f / \partial y, \partial f / \partial z)^T$. Since

$$\mathbf{r} = \begin{pmatrix} x \\ y \\ 0 \end{pmatrix} + \begin{pmatrix} b_x \\ b_y \\ b_z \end{pmatrix} s \quad (4.55)$$

gives the derivative

$$\frac{\partial \mathbf{r}}{\partial x} = \begin{pmatrix} 1 + \frac{\partial b_x}{\partial x} s \\ \frac{\partial b_y}{\partial x} s \\ \frac{\partial b_z}{\partial x} s \end{pmatrix}, \quad (4.56)$$

(4.54) is written as

$$\frac{\partial \Delta\phi}{\partial x} = \int_S \left[\left(1 + \frac{\partial b_x}{\partial x} s \right) \frac{\partial f}{\partial x} + \frac{\partial b_y}{\partial x} \frac{\partial f}{\partial y} s + \frac{\partial b_z}{\partial x} \frac{\partial f}{\partial z} s \right] ds. \quad (4.57)$$

In the same way the derivative with respect to y is

$$\frac{\partial \Delta\phi}{\partial y} = \int_S \left[\left(1 + \frac{\partial b_y}{\partial y} s \right) \frac{\partial f}{\partial y} + \frac{\partial b_x}{\partial y} \frac{\partial f}{\partial x} s + \frac{\partial b_z}{\partial y} \frac{\partial f}{\partial z} s \right] ds. \quad (4.58)$$

Again Δx and Δy can be varied independently, so each of (4.57) and (4.58) must vanish. With the derivatives of the components of b given in (4.32) we get from (4.57)

$$\int_S \left[\left(1 - \frac{b_z}{z} (b_y^2 + b_z^2) s \right) \frac{\partial f}{\partial x} + \frac{b_z}{z} b_x b_y \frac{\partial f}{\partial y} s + \frac{b_z}{z} b_x b_z \frac{\partial f}{\partial z} s \right] ds = 0 \quad (4.59)$$

and from (4.58)

$$\int_S \left[\left(1 - \frac{b_z}{z} (b_x^2 + b_z^2) s \right) \frac{\partial f}{\partial y} + \frac{b_z}{z} b_x b_y \frac{\partial f}{\partial x} s + \frac{b_z}{z} b_y b_z \frac{\partial f}{\partial z} s \right] ds = 0. \quad (4.60)$$

For the distance s measured from the diffuser we can write $s = z/b_z$. Now splitting the integrals and solving for the z_l where the fringes localize gives the two conditions

$$z_{l1} = \frac{\int_S \left[(b_y^2 + b_z^2) \frac{\partial f}{\partial x} - b_x b_y \frac{\partial f}{\partial y} - b_x b_z \frac{\partial f}{\partial z} \right] z dz}{\int_S \frac{\partial f}{\partial x} dz}, \quad (4.61)$$

$$z_{l2} = \frac{\int_S \left[(b_x^2 + b_z^2) \frac{\partial f}{\partial y} - b_x b_y \frac{\partial f}{\partial x} - b_y b_z \frac{\partial f}{\partial z} \right] z dz}{\int_S \frac{\partial f}{\partial y} dz}. \quad (4.62)$$

Equations (4.61) and (4.62) generally define two surfaces, the interference fringes localize along the intersection of these two surfaces.

For the special case of viewing along the z -axis we have $b_x = b_y = 0$ and $b_z = 1$, then the conditions (4.61) and (4.62) reduce to

$$z_{l1} = \frac{\int_S \frac{\partial f}{\partial x} z dz}{\int_S \frac{\partial f}{\partial x} dz}, \quad (4.63)$$

$$z_{l2} = \frac{\int_S \frac{\partial f}{\partial y} z dz}{\int_S \frac{\partial f}{\partial y} dz}. \quad (4.64)$$

Numerical and experimental examples depicting the localization of fringes due to refractive index variations are given in [170]. For single radially symmetric fields the analysis of (4.63) and (4.64) shows that the fringes localize in the center plane of the object. The plane is normal to the line of sight and contains the axis of symmetry. Looking through two identical radially symmetric objects, one placed behind the other, gives a localization just in the plane midway between the two objects. For more general phase objects the curves of fringe localization become quite convoluted.

4.3.5 Observer Projection Theorem

A concept for considering the effect of variations of the observation vector $\mathbf{b}(P)$ is given by the so called *observer projection theorem*. This theorem is implicit in the geometric optics approach to fringe localization which is followed in this chapter, but can also be derived by wavefront analysis in wave optics [35]. This theorem states that, if the holographic interferometric fringes are localized off the object surface, they can be observed as if projected onto the object surface radially from the center of the aperture of the viewing system.

The theorem is useful when optically reconstructed fringes to be recorded by a CCD-camera are localized well off the object surface, especially if their spatial frequency is high. In order to record the fringes and the object surface simultaneously, the aperture of the camera must be small. But a small aperture will cause unacceptable noise in the form of speckles, as pointed out in Section 2.5. Following the observer projection theorem, however, one may record the fringes while focused with a large aperture in their localization surface. Then the object surface is recorded separately from the same camera position. After appropriate relative magnification these two stored images can be superimposed digitally. Nevertheless this last step can be omitted if the correspondence between the pixel coordinates and the object surface is known and considered in the further processing.

The treatment of localization of holographic interferometric fringes based on geometric optics given here followed closely that of Vest [170]. Its aim was not to give a detailed description of all localization aspects, but to introduce briefly into the problems and possibilities of fringe localization, to present the basic mathematical relations, and to give some easy examples. A more thorough description can be found in [170] in the context of a global description of the fringe patterns. An introduction to localization may further be found in [21, 22]. An exhaustive study of localization was performed by Stetson, presented in a series of pa-

pers [31–35, 312–314]. His treatment is based on wavefront analysis. More facts about localization can be found in [307, 315–319].

4.4 Holographic Interferometric Measurements

4.4.1 Qualitative Evaluation of Holographic Interferograms

Holographic interferometry produces unique two-dimensional patterns of fringes, whose density and form depend on the loading of a tested structure, the structure itself and the geometry of the holographic arrangement. Since even minute loading amplitudes may cause deformation amplitudes that generate observable interference fringes, holographic interferometry is an extraordinary well suited tool for *nondestructive testing (NDT)*: faults and flaws in a technical component like cracks, voids, thin areas, debonds, etc. under proper load induce a characteristic local deformation, which can be detected in the holographic interferogram [320–322]. A defect in a structure may be critical with regard to one loading type or loading direction but not to another, Fig. 4.18. Therefore it is recommended to test a component with the type and

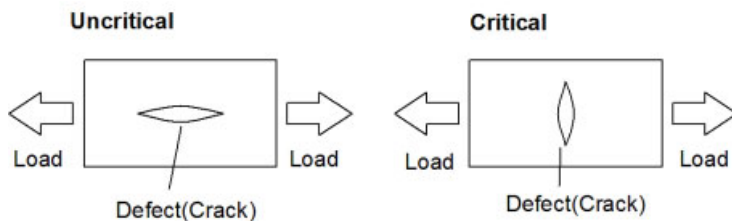


Figure 4.18: Critical and uncritical defects with regard to applied tensile stress.

direction of the intended operational load, but with low loading amplitude just sufficient to produce enough interference fringes to enable a reliable evaluation. This way we get a validation of the tested structure relative to the applied load. The defects are not visualized on their own but their response to the load is registered. The defects may reach the surface, e. g. surface cracks, but also subsurface defects like voids or material inhomogeneities are detectable. All these potentialities and advantages lead to the field of *holographic nondestructive testing (HNNDT)*.

Development and utilization of an HNNDT scheme or device for a particular application involves three interrelated tasks [323]: Selecting a loading – type, direction, and amplitude – which causes a detectable anomaly in the fringe pattern, if a defect is present; designing the optical system – sensitivity vectors in the proper direction –; and interpreting the results. Still for most applications in HNNDT the interferograms are observed and judged by skilled personnel. But there are attempts to perform an automatic computer controlled evaluation in HNNDT, see Section 6.11. Since the interpretation of the interferograms consists only in the detection of typical patterns indicating the existence of a defect, but no quantitative interference phase determination is carried out, one speaks about *qualitative evaluation*.

Application areas for HNNDT are manifold: components like tires or other automotive parts, turbine blades, honeycomb panels, pressure transducers, pressure vessels, aircraft parts,

satellite tanks, musical instruments, artwork, composites, and laminates are tested holographically, to name only a few [324–335]. A 100 percent holographic inspection is performed e. g. on tires for special purposes, like retreaded aircraft tires, or on the nitrogen tanks of European satellites.

4.4.2 Holographically Measurable Physical Quantities

Holographic interferometry measures optical pathlength differences, which affect the interference phase, e. g. according to (4.11) or (4.22), which in turn gives rise to the observable interference pattern, (4.4) or (4.10). There are a number of physical processes where the optical path length is modified by various physical quantities. If the induced modification of the path length can be controlled to change only the phase of the light field and the lateral displacement to stay in the range less than the average speckle diameter, then these physical quantities are measurable by holographic interferometry.

The expression ‘measurable’ here can be understood in a very broad sense. It ranges from the quantitative derivation of the precise values of the physical quantity to a qualitative judgment by trained persons, where by looking at the interferogram areas of inhomogeneous variations of the underlying physical quantity can easily be detected, giving insight into the integrity of the object under test.

In this section only a short glimpse of the many holographically measurable physical quantities are given, the detailed physical laws governing the path length variations and the strategies of how to evaluate them are presented in Chapters 5 and 6.

One class of holographic interferometric measurements concerns the displacements and deformations of diffusely reflecting opaque surfaces, as introduced in Section 4.1.4. Some measurable quantities based on the displacement of surface elements are:

- *One-dimensional displacements* of the surface points in the direction of the sensitivity vector can be measured. If it is known that the displacement of all surface points is in the same direction, as is often the case, an optimized holographic setup as described in Section 4.2.1 should be used. The evaluation then is directed by (4.26).
- The *three-dimensional displacement* vector field of the surface points can be measured. This vector field may be defined by *rigid body translations*, *rigid body rotations*, *general deformations*, or a combination of these. For determining the three-dimensional vectors, a system of at least three linearly independent equations of the form (4.21) has to be solved for each surface point.
- Since holographic interferometry measures with high spatial resolution, numerical differentiation for the derivation of *strains* and *stress* becomes possible. The *in-plane strains* in the case of *plane stress* can be determined [336]. Stresses are then calculated by the related proportionalities. *Bending moments*, *thermal expansion coefficients*, or the *Poisson ratio* have been successfully evaluated. Likewise *surface tensions* of fluids have been measured by holographic interferometry [337].
- Contrary to these *static displacements* also *dynamic displacements* are measured holographically. The motions can be frozen by defined triggering of pulsed illumination for

recording, or the temporally integrated states interfere in the time average method. Motions with constant velocity or with constant acceleration as well as *transient events* as e. g. the propagation of *bending waves* after an impact are amenable to holographic interferometry.

- Mechanical *vibrations* are further dynamic motions to be investigated holographically. The *vibration amplitude* distributions of *harmonic vibrations*, *damped vibrations*, and other *nonlinear vibrations* can be determined. With refined procedures it is even possible to measure *phase relations* of the *vibration modes*.

The second class of holographic interferometric measurements is related to the *refractive index variation of transparent or phase objects*, Section 4.1.5. The refractive index distributions of gases, liquids, solids, or plasmas can be affected by a number of physical quantities which are measured via this effect. Some examples are:

- In *flow diagnostics* holographic interferometry today has widely replaced *Mach-Zehnder interferometry* [338–343]. The *density of a gas* or a mixture of gases is related to the index of refraction by the *Gladstone-Dale equation* [344]. Therefore it is possible to measure holographically the density either in a steady or in a transient state.
- For *flow visualization* in *fluid dynamics* holographic interferometry is a means to depict the *streamlines* in the fluid under test. *Shock waves* [345–350] as well as *crack propagation* in glass [351] are measured. Carrier fringes can be produced by exchanging a liquid for one with another refractive index.
- Combining the Gladstone-Dale relation, which relates the index of refraction to the density of a gas, with the *ideal gas equation* one gets the dependence of the refractive index from the *pressure* and the *temperature* [352], taking additionally into account the molecular weight and the universal gas constant. Thus we have a means to measure the temperature distribution in a gas in *heat transfer* experiments [353].
- For liquids the Gladstone-Dale relation has to be replaced by the *Lorentz-Lorenz equation* which takes into account the specific refractivity of the substance under test.
- In *mass transfer* experiments holographic interferometry can be employed to measure the spatial or temporal distributions of *mass concentrations*. Due to the wavelength dependence of the Gladstone-Dale constant multiple wavelength interferometry is recommended to produce redundant data, especially if multiple parameters like temperature and concentrations are to be measured.
- Since the refractive index of an *electron gas* strongly depends on the *electron density*, this latter quantity can be measured holographically in *plasma diagnostics*. A two-wavelength method for the determination of the electron density is based on the strong *dispersion*, say, the strong dependence of the refractive index of the electron gas on the wavelength.
- The *stresses* in transparent solids can be measured holographically since due to the *stress-optical effect* the refractive index is a function of the model's state of stress. This function

is expressed in the *Maxwell-Neumann stress-optical law* valid for *birefringent* as well as for *optically isotropic materials*.

In a third class of holographic interferometric measurements the object to be measured is not affected, but the holographic arrangement is modified to induce the optical pathlength variation.

- It will be explained in Section 6.6 how the resulting observable interference fringes are related to the *three-dimensional contours* of the object surface shape. Of course by measuring the contour twice, once before and once after a deformation of the object, this is a way to measure deformations also, at least in principle. This procedure may be of interest for large deformations, which would lead to lateral shifts of surface points larger than the average speckle size.
- Illumination of a test object with the reconstructed image of a master object reveals differences in macroscopically identical objects, which nevertheless microscopically differ, which means that there are no homologous points. This is the comparative holographic interferometry introduced in more detail in Section 6.8.

4.4.3 Loading of the Objects

Holographic interferometry can visualize the difference between different deformation states of an opaque surface. To change the deformation state between the generation of the two optical wave fields to be compared, the object must be loaded, or an applied load must be varied. Many measurement problems to be solved holographically are of the following type: Investigate and measure how a given component deforms in reaction to a specific load. The problem of HNDT normally is: Test a component with regard to possible defects. In this latter case one has to decide on the proper loading, which comprises the type, the direction, and the amplitude of the load [354]. Five basic types of loading play a dominant role: direct mechanical load, pressure load, vibrational load, impulse load, and thermal load [323, 355].

Direct *mechanical stressing* is applied by *bending moments*, *tensile stress*, *torsional stress*, *point load*, or *gravity*. If tensile stress should be utilized, one has to examine carefully the test equipment with regard to additional unwanted torsional stress. Since most holographic arrangements are much more sensitive to out-of-plane displacements than to in-plane-displacements, the fringes caused by torsion may dominate the fringe patterns of the in-plane-motions. The direction of direct mechanical stressing must be adapted to the expected flaw orientation in HNDT or to the structural orientation if we have to investigate anisotropic material like fiber-reinforced plastics or wood. Centrifugal forces in rotating components also may be regarded as causing mechanical stresses. Gravitational load can be performed by a 180°-tilt of the whole holographic arrangement contained in a suitable framework including the object.

Pressure loading is produced by internal high or low pressure in hollow components or by placing the test object into a *pressure* or *vacuum chamber*. Cylindrical or spherical pressure vessels as well as whole tube systems are tested by internal pressure. Containers may be filled with water to induce the pressure. Tires are inspected in a differential low pressure to detect ply separations, broken belts, debonds, or voids.

Vibrational load can be excited by the acoustic fields of loudspeakers or by electrodynamic shakers in point contact [356]. This load is used to find out areas of extraordinary sound emission in large structures – e. g. for noise reduction of cars – or to detect debonds, delaminations, or material inhomogeneities. A variation of amplitude, frequency, and sometimes phase of the excitation must be possible, e. g. for the detection of resonant modes. Rayleigh-waves may be excited by ultrasonic transducers [357] or by laser pulses [358]. The vibration mode structure visualized by their holographic interference patterns may disclose manufacturing errors like improper castings or incorrect or uneven wall thickness in a component.

Impulse load by a local impact generates a travelling bending wave that can be recorded by employing a pulsed laser [359]. The impact may be generated by a pendulum or by a modified air-gun. Cracks or debonds obstruct the regular propagation of the bending waves and thus are detected.

There are a number of ways to apply *thermal load*: radiation sources like IR-lamps may heat the tested component – often from the rear side of the inspected surface – hot air jets may be generated by conventional hair-dryers, volatile fluids sprayed on a surface cool it during evaporation, high power DC generates heat in conductive material. Also heat may be brought to a component by induction heating or by microwaves, especially to materials containing water. Due to thermal expansion most materials are deformed when the temperature is changed [360, 361]. Furthermore the thermal conductivity locally varies at voids or debonds. Faulty electronic components have a thermal behavior during operation different from intact components, so they can be identified holographically.

The loads may be categorized into *static loads* and *dynamic loads*. The direct mechanical loads and the pressure loads are static, while thermal load only in the equilibrium state can be viewed as static. The dynamic loads may further be divided into *periodic* and *transient loads*. Vibration loads are periodic while an impact causes a transient effect; thermal loading often must be regarded as transient. While static and periodic loads can be employed in conjunction with CW lasers, the fast transient phenomena require a pulsed laser to be registered holographically.

Contrary to the temporal discrimination of the loads, they can be divided into *point loads* and *distributed loads* due to their spatial characteristics.

5 Quantitative Determination of the Interference Phase

Quantitative evaluation of holographic interference patterns for measurement purposes consists in the pointwise determination of the numerical value of the physical quantity which has produced the optical path length change at each point and thus has given rise to the intensity distribution. The way how the physical quantity to be measured is contained in the observed intensity distribution was shown generally in Chaps. 2 and 4. There the predominant role of the interference phase was discussed.

In the early days of holographic interferometric metrology the fringes in the interferograms, or in photographs of the interferograms, were manually counted to obtain an approximation to the interference phase distribution. Later on the macroscopic interference patterns were recorded by video-cameras – nowadays CCD- or CMOS-cameras – and were stored after digitization and quantization in a computer for further evaluation. In the actual employment of digital holography for interferometric measurement purposes the wave fields are digitally reconstructed from the hologram data – not optically – and the interferograms principally might be generated digitally in computer. But this step normally can be skipped and the interference phase is determined directly from the reconstructed complex wave fields.

A computer aided quantitative evaluation thus is composed of two principal steps: First the interference phase distribution is determined from the recorded holographic interferogram or from the numerically reconstructed phases, see Section 5.8, and second the interference phase is combined with the sensitivity vectors to achieve the spatial distribution of the physical quantity to be measured [325, 362–375]. In this chapter the first of these two steps is addressed and the different methods to perform this task are discussed. The determination of the physical quantities out of the interference phase distribution is discussed in Chapter 6.

Quantitative evaluation stands in contrast to a qualitative evaluation, where not the precise values of the interference phase are interesting, but the global and local shape of the interference pattern. By a qualitative interpretation of the pattern one decides on the existence of areas of extraordinary local deformation in experimental stress analysis or holographic non-destructive testing (HNDT). These issues are discussed in Section 6.11.

5.1 Role of Interference Phase

In (4.4) it was shown how in the double-exposure or in the real-time techniques the intensity distribution $I(x, y)$ of the holographic interference pattern depends on the interference phase distribution $\Delta\phi$ by the cosine-function. There identical amplitudes for all surface points have been assumed. If we want to recognize the more general case of differing amplitudes, Section 2.2.3, and modifications of the intensity by environmental effects, noise, or other distor-

tions, we can write

$$I(x, y) = a(x, y) + b(x, y) \cos [\Delta\phi(x, y)]. \quad (5.1)$$

This is the intensity distribution $I(x, y)$ that is recorded by e. g. a CCD-camera, digitized into an array of $N \times M$ pixels, quantized into L discrete gray-values and in this form stored digitally in the computer memory. The (x, y) denote the pixel coordinates. The mapping of object points to the individual pixel coordinates also is discussed in Chapter 6. The $a(x, y)$ and $b(x, y)$ contain the intensities of the interfering wave fields (2.40) and the various disturbances. Generally one can say that $a(x, y)$ contains all additive contributions and $b(x, y)$ comprises all multiplicative influences.

The objective is to extract the interference phase distribution $\Delta\phi(x, y)$ from the more or less disturbed intensity distribution $I(x, y)$ of (5.1). Constant values of $\Delta\phi$ define fringe loci on the object's surface, therefore $\Delta\phi(x, y)$ is called the *fringe-locus function* by some authors [35, 376].

5.1.1 Sign Ambiguity

When one tries to extract the interference phase $\Delta\phi(x, y)$ out of the intensity distribution $I(x, y)$ by a kind of inversion of (5.1), the problem arises that the cosine is not a one-to-one function, but is even and periodic

$$\cos \Delta\phi = \cos(s\Delta\phi + 2\pi n) \quad s \in \{-1, 1\}, \quad n \in \mathbb{Z}. \quad (5.2)$$

An interference phase distribution determined from a single intensity distribution remains indefinite to an additive integer multiple of 2π and to the sign s .

Each inversion of expressions like (5.1) contains an inverse trigonometric function. All inverse trigonometric functions are expressed by the *arctan-function* like $\arccos(x) = \arctan(\sqrt{1 - x^2}/x)$. The arctan-function of a single variable has its *principal value* in the interval $]-\pi/2, +\pi/2]$. But in most algorithms for quantitative evaluation of holographic interferograms the argument of the arctan-function is accomplished by a quotient, where the numerator characterizes the sine of the argument and the denominator corresponds to the cosine of the same argument. Then it is good practice to consider the signs of the numerator and the denominator separately, as is done by the FORTRAN- or C-function ATAN2(X, Y), for in this case the principal value is determined consistently in the interval $]-\pi, +\pi]$. The four situations of the sine- and cosine signs are shown in Fig. 5.1.

But there still remains a modulo 2π uncertainty as well as the sign ambiguity. Figure 5.2 displays a part of a graph which extends to infinity upward and downward. Each path from the left to the right through this graph represents a one-dimensional interference phase distribution belonging to the intensity distribution given at the bottom of the figure [377, 378].

A practical way to get rid of the *sign ambiguity* is to use side-information about the experimental conditions leading to the measured optical path length changes and so to the interference phase distribution. In many applications one can assume that the measured interference phase distribution is not only continuous but differentiable as well, meaning a smoothly varying function. Depending upon the known direction in which the load acts on the object, e. g.

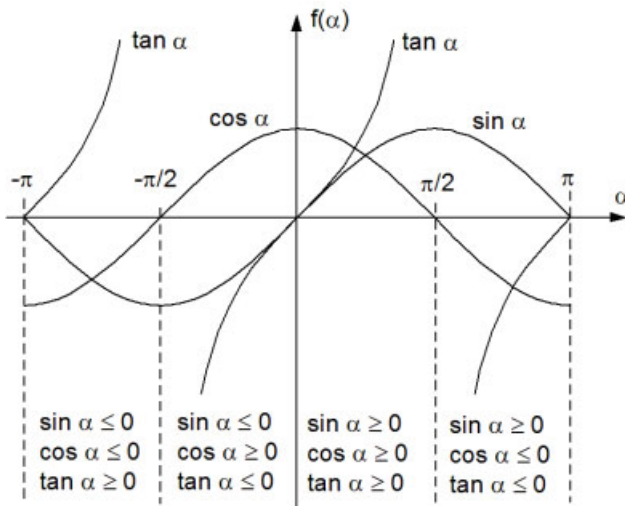


Figure 5.1: Signs of the trigonometric functions in $[-\pi, +\pi]$.

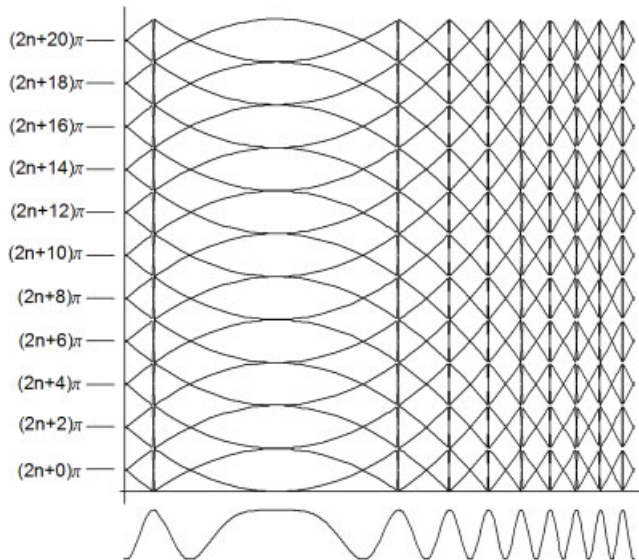


Figure 5.2: Ambiguity of the interference phase.

compressive or tensile, a proper sign distribution assignment norm can be fixed based on the known increase or decrease of the interference phase.

Reliable ways to eliminate the sign ambiguity without using prior knowledge about the underlying experiment consist of either recording multiple phase stepped interferograms or introducing experimentally a linear phase carrier with a positive slope higher than the steepest

descent of the interference phase, thus producing only increasing phase maps [379, 380]. The concepts also are known as *infinite fringes* and *finite fringes*. If for $\Delta\phi(x, y) = 0$ a field of uniform irradiance, that is, an infinitely wide fringe, results, one speaks of an *infinite fringe interferogram*. Since $-\Delta\phi(x, y) = 0$ and $+\Delta\phi(x, y) = 0$ yield the same fringe pattern, there remains a *sign ambiguity*. If reference fringes are introduced by an additional carrier phase gradient of known sign, the resulting interferograms are called *finite fringe interferograms* [170]. It must be mentioned that in digital holography we obtain the interference phase $\Delta\phi(x, y)$ by a subtraction of the calculated phases, as is presented in more detail in Section 5.8. Then we know which is the first and which is the second state – this information is lost in double exposure holography – and no sign ambiguity remains.

5.1.2 Absolute Phase Problem

The 2π *ambiguity* manifests in the evaluated interference phase distributions by wrapping the phase *modulo* 2π . Since only principal values of the arctan-function in the interval $] -\pi, +\pi]$ – or equivalently in $[0, 2\pi]$ – are determined, as soon as an extreme value of the interval is reached, the phase jumps to the other extreme value, although the correct phase proceeds smoothly increasing or decreasing.

The modulo 2π effects are corrected by the processing step called *demodulation, continuation, or phase unwrapping*, see Section 5.9. By addition or subtraction of integer multiples of 2π the phase jumps are eliminated. The correct additive term in some applications can be determined if there is a point P in the pattern where the exact value of the displacement or equivalently the interference phase is known. Preferably this value is $\Delta\phi(P) = 0$. If a continuous variation of the interference phase can be assumed, the 2π -multiples at each point can be determined by counting the 2π -jumps from P to this point along an uninterrupted path. Sometimes an elastic ribbon is tied from one point P on the tested surface to a point in the holographic arrangement which has undergone no displacement but is lying in the observable interference pattern. Then the fringes along this ribbon are counted starting from zero [381].

If one is only interested in the deformation relative to an arbitrary point of the investigated surface but not in any additional rigid body translation, then one might define the interference phase as zero at this starting point. But this is only admissible for constant sensitivity vectors. This approach can be envisaged as evaluating the variation of the displacement from the variation of the interference phase. Now (4.24) shows that the variation of the interference phase in the case of varying sensitivity vectors not only depends on the variation of the displacement vectors but also on the direct values of the displacements. Consequently, if the sensitivity vector varies over the surface, the constant additive term has to be taken into account, meaning that the *absolute phase* including the correct multiples of 2π must be evaluated. Sometimes it may be sufficient to estimate the maximum errors by assuming minimal and maximal multiples of 2π and put them into (4.21) and (4.24) using the extreme sensitivity vectors of the actual holographic setup.

The error of not recognizing the absolute phase is demonstrated in Fig. 5.3 for the example of a cantilever beam clamped at the left end and bent by a point load at the right end. Curve 1 in Fig. 5.3a gives the z -displacement $d_z(x)$ along the x -axis of the cantilever beam of length 100 mm. The z -component of the sensitivity vector is shown in Fig. 5.3b, when the coordinates of the illumination point are $S = (-200, 0, 250)$ mm, and those of the observa-

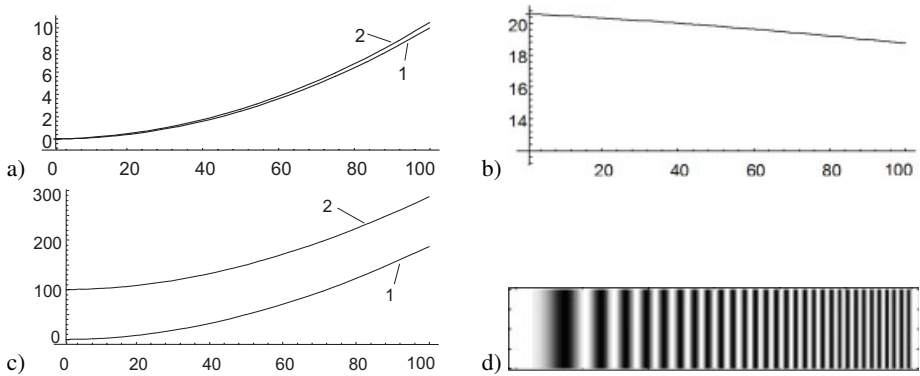


Figure 5.3: Effect of unknown 2π -multiples in the interference phase distribution.

tion point are $B = (50, 0, 250)$ mm. The surface point P varies as $P = (x, 0, 0)$, with x running from $x = 0$ mm to $x = 100$ mm. The wavelength is 514.5 nm. The one-dimensional interference phase distribution corresponding to this deflection and arrangement is shown in curve 1 of Fig. 5.3c. Reflecting the fact that we do not know the additive constant, this interference phase is changed arbitrarily to curve 2 by adding a constant of 32π . The evaluation of this phase distribution gives a $d_z(x)$ which is displayed as curve 2 in Fig. 5.3a, after the evaluated z -displacement at the clamping point is brought to coincidence with the original one by subtraction of the displacement offset. Still there remains a difference at the other end of the cantilever which is of the order of one fringe period. Figure 5.3d shows the expected holographic interference pattern.

5.2 Disturbances of Holographic Interferograms

As already taken into account in (5.1) holographic interferograms besides the ambiguities discussed in Section 5.1 suffer from a number of *distortions* degrading the interference pattern. The methods for computer aided evaluation have to deal with them in order to produce reliable results. A typical intensity distribution at one instant of time is of the form [382]

$$I(x, y) = I_0(x, y)[1 + V(x, y) \cos \Delta\phi(x, y)]R_S(x, y) + R_E(x, y) + R_D(x, y). \quad (5.3)$$

Here $I_0(x, y)$ denotes the low frequency background intensity caused by a varying illumination, e.g. a Gaussian profile of the enlarged laser beam, or a changing object reflectivity. $V(x, y)$ is the fringe visibility influenced mainly by speckle decorrelation and the ratio between the reference and object wave amplitudes. $R_S(x, y)$ describes the contrast variation caused by the speckles, which act as signal dependent coherent noise. $R_E(x, y)$ contains the time-dependent electronic noise due to the electronic components of the image processing equipment and $R_D(x, y)$ describes diffraction patterns of dust particles in the optical paths.

Of these degradations which are summarized in the additive noise $a(x, y)$ and the multiplicative noise $b(x, y)$ of (5.1), the speckles have been treated in Section 2.5, the others are described in the following.

5.2.1 Varying Background Illumination

Reasons for an uneven background illumination in the holographic interference patterns may be

- the beam profile of the illuminating laser beam as modified by the projecting optics, in most cases a Gaussian intensity profile,
- an uneven reflectivity of the object surface caused by spatially varying surface characteristics,
- an uneven sensitivity of the sensor (CCD-target) used for recording the interference pattern,
- additional diffraction patterns and parasitic interferences caused by dust particles in the optical paths.

The varying background illumination influences the maximal intensity which can be reached at a point; this effect is modeled by the multiplicative contrast V as well as it contributes to the additive background I_0 .

The background variations caused by expanded and projected laser beams have a low frequency but those caused by an uneven reflectivity of the object surface or by varying sensor sensitivity may occur with high spatial frequencies.

Spurious diffraction patterns should be avoided in the experimental process, since they lie in the same frequency bands as the desired interference pattern. So they cannot be filtered out easily by a bandpass filter with adapted cutoff frequencies.

5.2.2 Electronic Noise

The *electronic noise* in photodetectors is recognized as a random fluctuation of the measured voltage or current and is caused by the quantum nature of matter. A first category of noise sources is due to the photodetector as an electronic component: noise is generated even without impinging light. Thermal noise, shot noise, generation-recombination noise and the $1/f$ -noise fall into this category. The second category contains the additional noise generated when photons impinge on the detector, especially the photon noise [383].

Electronic noise is a sum of numerous random processes obeying different statistical laws, but the central limit theorem of probability theory states that the overall process will be directed by a Gaussian distribution. This theoretical statement has been confirmed experimentally [384].

Electronic noise is a temporally variant process, so its influence may be diminished by averaging over a sequence of interference patterns recorded at different time instants. The *signal-to-noise ratio* SNR will increase by \sqrt{n} , if n patterns are averaged.

In practical applications of holographic interferometry electronic noise plays a minor role as compared to the speckle noise. So normally no special care is taken regarding electronic noise. In the model describing the content of the interference fringes (5.3) it is recognized in the additive term R_E .

5.2.3 Speckle Decorrelation

Since in holographic interferometry a wavefront change is to be measured, the reconstructing pupil samples slightly different portions of the two wavefronts. Only identical parts interfere, the rest, presenting themselves in the form of noise, leads to a fall in fringe visibility [309]. The random amplitudes of the wavefronts constitute the speckle pattern, see Section 2.5. For generation of a holographic interference pattern only identical speckle fields interfere [310]. So the diminishing of the fringe visibility first is caused by a *speckle decorrelation* due to a variation of the interference phase $\Delta\phi$ across an individual speckle and second by speckle decorrelation due to a displacement of the speckles.

Normally in holographic interferometry the fringe spacing is much greater than the speckle size, meaning approximately constant fringe order or equivalently constant interference phase over one speckle. But it can be proved that the correlation and thus the visibility goes to zero when the fringe spacing approaches the speckle size. So it was shown [310] that the visibility of the fringe pattern is proportional to the correlation coefficient, which in turn is proportional to a quantity Z . For this Z it can be derived that

$$|Z| = \text{sinc}(\pi/N) \quad (5.4)$$

where N is the number of speckles per fringe. Obviously for $N = 1$ we get $|Z| = 0$.

The speckle decorrelation due to an in-plane translation Δx – this motion is the most interesting one in this circumstance – can be determined by considering that the speckle pattern in the image plane moves in the opposite direction in proportion to the magnification of the viewing system. A movement whose amount is small compared with the resolution element size changes the speckle pattern at a given point in the image plane also by a small amount. It can be shown that the speckle pattern at a point is totally decorrelated when the object is translated by an amount Δx equal to the resolution element diameter, namely

$$\Delta x = \frac{1}{m} \frac{f}{a} \lambda \quad (5.5)$$

where m is the magnification, a is the diameter of the viewing lens aperture, and f is its focal length. This shows the larger the magnification of the viewing system, the smaller the in-plane translation which already decorrelates the speckle pattern [310].

The influence of speckle decorrelation is contained in the parameter V standing for the visibility in (5.3).

5.2.4 Digitization and Quantization

Generally for a computer aided quantitative evaluation the optically reconstructed holographic interference pattern is recorded by a CCD-camera and stored in the computer memory in digital format. That means the recorded intensity is digitized into an array of $M \times N$ image points, the so called *pixels*, and quantized into L discrete *gray-values*. The implications of this *digitization* and *quantization* are discussed in the following.

The numbers M and N of digitization set an upper bound to the density of the interference fringes to be recorded. While of course the optical resolution of the imaging system has an influence which can be investigated with the help of the concepts of the *point spread function*

and the *modulation transfer function* [385] which is done in Section 2.8, here however only the role of the *sampling theorem* is discussed. The sampling theorem, Appendix A.7, demands more than two detection points per fringe. But this assumes ideal point detectors while here we are dealing with finite sized detector elements with a fill ratio [386]. Furthermore the effective size of a pixel is not necessarily equal to its spacing, and is usually larger than its physical size. This is most likely due to charge leakage to neighboring elements. So despite of the claims of the sampling theorem one has to supply at least 3 to 5 pixels per fringe period to yield a reliable evaluation. This requirement must be fulfilled particularly in areas where the highest slope of the interference phase in the pattern occurs.

If very dense holographic interference patterns are present, the resolution should be adjusted by zooming into partial patterns and evaluating several of them successively.

In the discussion of resolution and digitization one should always keep in mind that the speckle size must be far less, at least a factor of 10 smaller, than the smallest fringe period. Otherwise the fringes cannot be sampled reliably.

When intensity frames are acquired, the analog video signal is usually converted to a digital signal of discrete levels by an *analog-to-digital converter* (ADC) [387]. In practice quantizations into 8 bits corresponding to 256 gray-values or into 10 bits giving 1024 values are most common. Experience has shown that 8 bits for a reliable evaluation of holographic interference patterns are sufficient. For phase shifting evaluation the resulting error due to quantization into 8 bits was calculated to 3.59×10^{-4} wavelengths [387]. The effect of quantization was first investigated by Freischlad and Koliopoulos [388] for the phase stepping technique using a four-frame (= three-step) algorithm and was then further analyzed by Brophy [389]. Quantization effects for techniques based on Fourier fringe analysis are described in [390].

The quantization error is affected by the modulation depth of the signal. The modulation of the signal times the number of quantization levels yields the effective number of quantization levels. Therefore, the lower the modulation, the fewer the number of quantization levels which span the signal from peak to valley, and the greater the resulting error in the evaluated phase. In order to minimize this effect, the fringe intensity should cover as much of the detector's dynamic range as possible.

5.2.5 Environmental Distortions

Environmental distortions like vibrations, acoustic noise, and air turbulence may cause degradations of the holographic interferograms. Especially if a two reference beam configuration or the real-time method are employed, as necessary for the phase sampling evaluation described in Section 5.5, errors may be generated. So care has to be taken to isolate the holographic arrangement from vibration. This is normally done by vibration isolated tables. Equipment which undergoes any mechanical motion should be removed from the vibration isolated table. If the object is too big to be placed on an optical table, the vibrations may be eliminated by optical compensation with a reference mirror fixed to the object, Section 6.1.4. Acoustic noise of the ambient may be coupled directly or by air into the holographic arrangement, which should be avoided by performing the experiment in a quiet room. Air turbulence may change the refractive index distribution of air and thus the optical path lengths randomly. It should be reduced by covering the optical paths and keeping away air ducts or fans from the setup.

Vibrations, acoustic noise, or air turbulence modify the interference phase distribution to be measured. For long exposure times the fluctuating interference phase is integrated, which leads to a contrast degradation up to a destruction of the interference pattern. This can be avoided by taking short exposures, e. g. with a pulsed laser. Then the instantaneous state of the object is recorded including the influence of the distortions. If these affect different areas of the object surface differently, there is only a rare chance for detecting them.

5.3 Fringe Skeletonizing

The *fringe skeletonizing* methods are computerized forms of the evaluation by manual fringe counting in photographs of the interferograms done at the desktop in the early days of holographic interferometry [38]. These methods assume that the local extrema of the intensity distribution correspond to the maxima and minima of the cosine-function (5.1). In this case the interference phase at pixels, where an intensity maximum or minimum is detected, is an even or odd integer multiple of π .

The methods for fringe skeletonizing can be divided into those based on *fringe tracking*, those related to *segmentation*, and those falling not naturally into one of these two categories. A general processing scheme for an evaluation by skeletonizing of a digitally recorded and stored holographic interference pattern consists of the following steps [382, 391, 392]:

1. Improvement of the signal-to-noise ratio in the interference pattern by spatial and temporal filtering.
2. Specification of the boundary of the fringe pattern to be analyzed in the whole stored frame.
3. Extraction of the raw skeleton by fringe tracking, pattern segmentation, or another method.
4. Enhancement of the skeleton by linking together interrupted lines, by adding missing points, and by removal of artifacts, line crossings or interconnections. This step may be performed interactively.
5. Numbering of the fringes by attaching interference order numbers to them.
6. Interpolation of the interference phase distribution between the skeleton lines.
7. Calculation of the physical values to be measured from the interference phase distribution.

5.3.1 Pattern Preprocessing

Before attempting to extract the skeleton from the stored holographic interference pattern, it is advisable to minimize the disturbances, some of which described in Section 5.2 [393]. Of special importance are the *shading correction* to compensate for an uneven background intensity and the *smoothing* for eliminating the speckle influence.

Smoothing of the speckle noise in the recorded interferogram is mainly done by *linear low-pass filtering*. This process is described by the *convolution* of the intensity pattern $I(x, y)$ with the *impulse response* or *convolution kernel* $h(x, y)$ of the filter.

$$\begin{aligned} I'(x, y) &= I(x, y) * h(x, y) \\ &= \sum_{x'} \sum_{y'} I(x - x', y - y') h(x', y'). \end{aligned} \quad (5.6)$$

Common kernels are 3×3 -kernels, which modify the intensity of each pixel in dependence on its own intensity value and the intensity values of the neighboring pixels. Examples are the averaging filters having the kernels

$$h_1(x, y) = \begin{cases} 1/9 & \text{if } -1 \leq x \leq 1 \text{ and } -1 \leq y \leq 1 \\ 0 & \text{otherwise} \end{cases} \quad (5.7)$$

or

$$h_2(x, y) = \begin{cases} 1/16 & \text{if } (x, y) \in \{(-1, -1), (-1, 1), (1, -1), (1, 1)\} \\ 1/8 & \text{if } (x, y) \in \{(-1, 0), (1, 0), (0, -1), (0, 1)\} \\ 1/4 & \text{if } (x, y) = (0, 0) \\ 0 & \text{otherwise.} \end{cases} \quad (5.8)$$

These kernels are written shortly

$$h_1 = \frac{1}{9} \begin{pmatrix} 1 & 1 & 1 \\ 1 & 1 & 1 \\ 1 & 1 & 1 \end{pmatrix} \quad \text{and} \quad h_2 = \frac{1}{16} \begin{pmatrix} 1 & 2 & 1 \\ 2 & 4 & 2 \\ 1 & 2 & 1 \end{pmatrix}. \quad (5.9)$$

Filters with larger windows than 3×3 are possible. Some of them can also be obtained by repeated application of a 3×3 -filter to the pattern.

The presented linear filters are examples of *nonrecursive* or *finite impulse response filters*, meaning a vanishing impulse response outside a finite interval. No information on the application of *recursive filters* on speckled holographic interferograms has been found in the literature.

The *median filter* is an example of a *nonlinear filter* for speckle suppression. The gray value of each pixel here is replaced by the median of the gray-values of the neighboring pixels. Thus isolated points are removed, but steps or ramps are not blurred as with the spatial averaging filters [394].

Further filter strategies like homomorphic filtering [395–397], geometric filtering [398, 399], or Wiener filtering [400] have been suggested. Nevertheless temporal averaging of multiple frames of the same interference pattern but with varied speckles always is superior to spatial filtering of a single frame [397].

Shading correction is the removal of the low-frequency illumination variation mainly due to the Gaussian intensity distribution of the expanded laser beam. It can be performed by a linear high-pass filter which is accomplished by subtraction of a low-pass filtered version of the pattern from its unfiltered version. It can be done by homomorphic filtering, which means to apply the Fourier transform, then to remove the low frequency components of the spatial frequency spectrum, and finally to transform back into the spatial domain by the inverse

Fourier transform. If it is possible to record the background separately, that is, the illuminated object wavefront before interfering, the pattern can be divided in a pointwise manner by the background intensity [394, 401]. The background intensity distribution also may be obtained by summing two anti-phase reconstructions of the interference pattern [394] or by fitting a Gaussian to the pattern by the method of least squares, with the exponential in the Gaussian being linearized by taking the logarithm.

A histogram modification [393] may compensate detector nonlinearities or may improve the visual appearance of the interferogram, which can be important for interaction by the user, but seems not to be a prerequisite for computerized skeletonizing algorithms.

For the automatic determination of the *boundary of objects* not filling the full frame, common boundary following algorithms will be confused by the dark interference fringes [391]. So one possible approach is to apply heavy low-pass filtering to the pattern, which will blur out the gaps between the bright interference fringes, and then to detect the edge of the blurred object by differentiating the image or simply by applying an appropriate threshold [391]. It would also be possible to use an algorithm for finding the convex hull of a set of points. Both of these approaches will have difficulties with irregular boundaries and with artifacts such as nonuniform illumination. The easiest method is to have the user interactively specifying some sort of simplified boundary [391].

5.3.2 Fringe Skeletonizing by Segmentation

The *segmentation* techniques divide the pixels of the interference pattern into different regions representing bright and dark fringes or representing ridges, valleys, and slopes in the gray-value landscape [382, 402–406]. The extraction of the skeleton based on segmentation mostly consists of the steps:

- Segmentation of intensity into maxima, minima and slopes.
- Enhancement of the regions.
- Production of the fringe skeleton.

A direct approach is the production of a binary pattern by taking the mean intensity as threshold [403]. This requires a good background correction or one has to use an adaptive threshold algorithm. After binarization, the margins of the regions have to be smoothed, normally done by shrinking and expanding operations, also called erosion and dilatation operations. These reduce isolated points, which are remnants of speckles, fill in broken lines or truncate line artifacts. The skeleton then is formed either by finding the centers of the regions corresponding to the dark and bright fringes, which may be performed by thinning the regions to lines of one pixel width [405], or by defining the points of transitions from bright to dark regions and vice versa as skeleton points [403].

Another approach moves a digital filter over the digital pattern, which decides whether a pixel belongs to the center of a bright fringe [406], or classifies the pixels into those belonging to ridges, valleys, slopes, or being undecidable [382, 407]. Again a proper filtering has to be done to improve the skeletons. Anisotropic filters are suitable for this task, they avoid the melting of regions belonging to different fringes [408]. On the other hand interrupted skeleton lines have to be repaired. An algorithm connecting pairs of points with this intent should

recognize the indicators least distance, approximately the same direction, and the absence of line crossings. Some of the steps of an evaluation of a holographic interferogram by skeletonizing based on segmentation are demonstrated in Fig. 5.4. The object is a valve loaded by

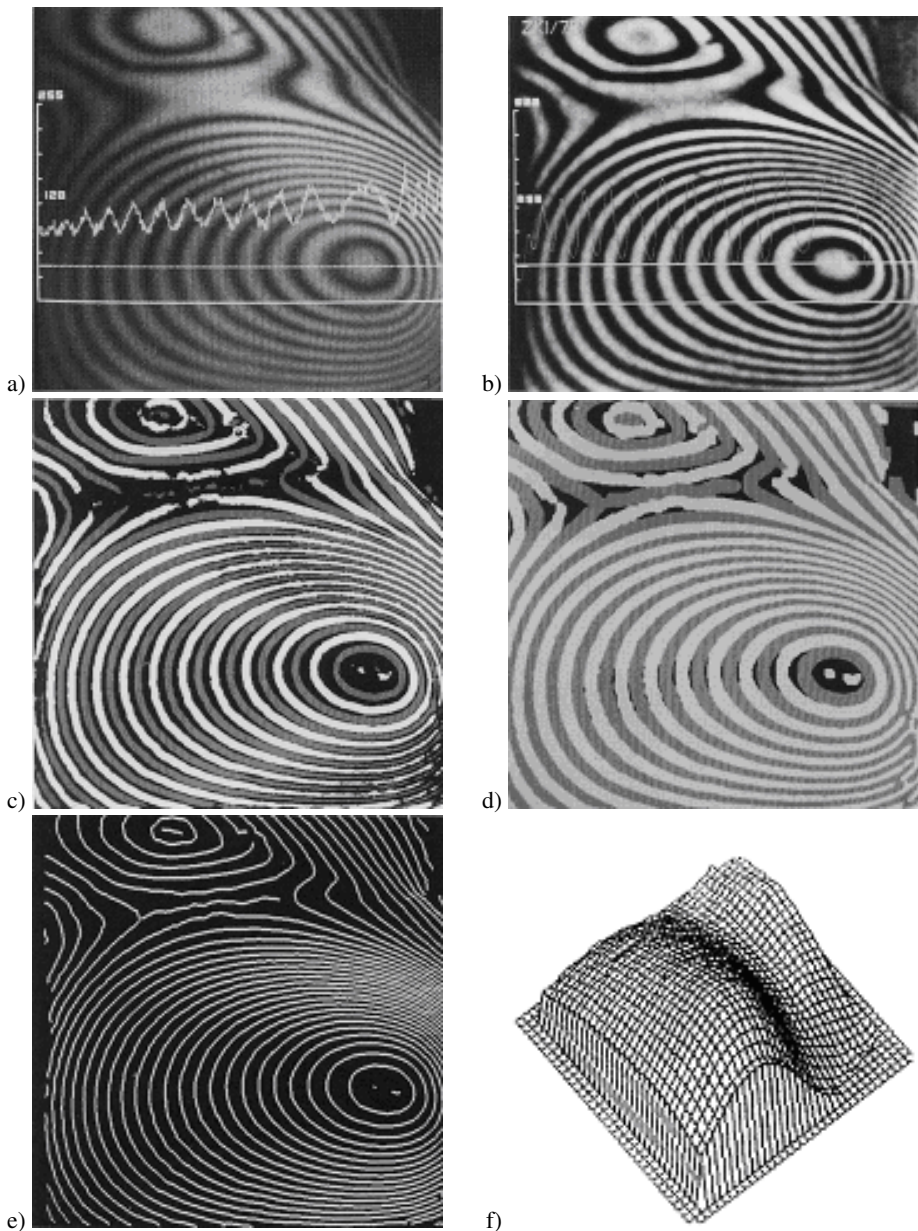


Figure 5.4: Interferogram evaluation by skeletonizing (Courtesy of W. Osten, BIAS).

internal pressure. Figure 5.4a shows the holographic interferogram together with an intensity profile along the dotted horizontal line. The enhanced intensity distribution, after averaging and shading correction, is given in a gray-scale display in Fig. 5.4b. The enhanced intensity is segmented, Fig. 5.4c, where the ridges are white, the valleys are gray, and unidentified pixels are black. This pattern is enhanced by region-growing and binary filtering; the result is given in Fig. 5.4d. These regions are then thinned to a skeleton as shown in Fig. 5.4e. Numbering and interpolation lead to a continuous phase distribution as the one given in Fig. 5.4f.

5.3.3 Skeletonizing by Fringe Tracking

In methods based on fringe tracking, the algorithm looks for neighboring pixels which correspond to local maxima or minima in the gray-value distribution [391, 409–413]. The first step in recognizing the fringes is to locate a starting point on each fringe. Only for a restricted number of interference patterns is it sufficient to traverse a line which is known to cut all fringes, and then to take the maxima on this line as the starting points [391]. Due to the manifold of possible holographic interference patterns usually the starting points are manually defined by the user. If there are locally parallel fringes in the pattern, straight lines of finite length perpendicular to these fringes can be constructed. Along these lines the starting points and the direction of search can be defined [404].

The tracking then either follows the curved ridges characterized by local intensity maxima or traces the boundaries between adjacent fringes by using derivatives of gray levels. Since the starting point is not necessarily at either end of the fringe, the program has to trace in one direction from the starting point and afterwards has to go back to the starting point and trace in the other direction. A search for the next point in the range from -90° to $+90^\circ$ relative to the forward direction or even a smaller range prevents the program from getting caught in small loops around insufficiently filtered speckles [391]. This results in an automatic check of five of the eight nearest neighbors of the current pixel for the maximum intensity.

The tracking procedure stops if a pixel is encountered that is already marked as belonging to a skeleton line. Reaching the starting point either means to have correctly traced a closed fringe, or the process is erroneously caught in a small loop. Another reason for reaching an already marked skeleton point is the attempt to cross another fringe which normally is forbidden. In this case it has to be checked whether a bifurcation of the fringes or hyperbolically formed fringes due to a saddle point in the interference phase distribution have occurred. Most programs at this point require interaction by the user. Also the operator may link data points belonging together, continue if obstacles are met, correct wrong decisions, and finally check that no fringes have been overlooked.

5.3.4 Other Fringe Skeletonizing Methods

The *phase lock method* uses a sinusoidal phase modulation obtained by, for example, a piezoelectrically excited axially oscillating mirror [414]. The resulting intensity is written as

$$I(x, y, t) = a(x, y) + b(x, y) \cos[\Delta\phi(x, y) + L \sin \omega t]. \quad (5.10)$$

$L < \lambda/2$ is the amplitude and $\nu = \omega/2\pi$ the frequency of this oscillation. A bandpass filter, centered on $\sin \omega t$, determines the amplitude $U_\omega = 2b(x, y)J_1(L) \sin \Delta\phi(x, y)$, which

is zero at the points (x, y) , where $\Delta\phi(x, y) = N\pi$. These points can thus be detected and give a skeleton whose lines correspond to the interference phase differences of $\pi/2$.

A special fringe contour detection scheme is proposed in [415]. It only works with interferograms fulfilling the prerequisites: (1) the presence of a dominant *spatial frequency* associated with the fringe pattern, (2) the near invariance of this frequency with position. Then, along lines normal to the fringes, the one-dimensional *Fourier spectrum* is calculated by the *FFT algorithm*. The phase of the dominant spatial frequency computed for each image line is a quantitative measure of fringe displacement at each line.

Skeletonizing methods nowadays are used if there is no way to produce multiple phase shifted interferograms. An alternative in this case is the Fourier transform evaluation, Section 5.6, which in its general form also requires only a single interferogram. From the interference phase distribution determined by the Fourier transform algorithm, (5.51) to (5.53), a skeleton may be produced by taking only those pixels where the 2π -jumps occur. Even further intermediate skeleton lines are possible if the pixels nearest to certain phase values are selected. The evaluation of a single interferogram generally is lacking in the sign, but taking the absolute value circumvents this problem by producing two skeleton lines. As an example let the interference phase distribution $\Delta\phi(x, y)$ modulo 2π be in the interval $]-\pi, +\pi]$. Selecting all points (x, y) with $|\Delta\phi(x, y)| \approx \pi/2$ yields the two skeleton lines belonging to $-\pi/2$ and to $+\pi/2$, but no information as to whether a part of a skeleton line belongs to $-\pi/2$ or to $+\pi/2$.

A rather new approach to skeletonizing uses concepts of *artificial neural networks* [416]. Points of the fringe skeleton are found by Kohonen's *self organizing feature map*. At the beginning a number of points, the *neurons*, are spread randomly over the interference pattern. The processing step consists of a random choice of an interferogram point, searching for the nearest neuron to this point, and moving this neuron towards the selected interferogram point. The amount of this motion is proportional to the distance between the point and the neuron, to the intensity of the interferogram point, and to an actual learning rate. This forces a higher probability for motion towards high intensity fringe centers than towards dark fringe areas. If this step is repeated sufficiently often, all neurons will concentrate at the bright fringe centers. If the number of neurons is high enough, the neurons in each fringe can be automatically connected by a nearest neighbor criterion without ambiguity, thus yielding the skeleton.

5.3.5 Fringe Numbering and Integration

After the skeleton lines are found we have to perform the *fringe numbering*, meaning to define a *fringe order* to each line. The integer fringe orders $n(x, y)$ correspond to the interference phase values $\Delta\phi(x, y)$ via $\Delta\phi(x, y) = 2\pi n(x, y)$. Even if we are not obliged to map the absolute fringe orders to the skeleton lines, see Section 5.1.2, the relations between the fringe orders must be fulfilled. So in particular local fringe order maxima and minima have to be uniquely detected. Generally, if a continuous interference phase distribution can be assumed, neighboring skeleton lines can differ in order only by -1 , 0 , or $+1$, lines of different order must not intersect or merge, lines do not end inside the field of view, and the skeleton line number differences, integrated along any closed line through the interferogram, always yield zero [403]. Automatic fringe numbering algorithms based on these constraints still may re-

quire manual interaction by the user [391, 403, 405, 406, 417]. A graph-theoretic approach to automatic fringe numbering is given in [418].

The problem is made easier if a substantial degree of tilt can be added to the object deformation, leading to essentially parallel fringes with the measurement parameter being encoded as the deviation from straightness of the fringes [393]. The most important fact is that now the interference order behaves monotonically if moving roughly perpendicular to the skeleton lines, enabling an easy fringe numbering.

After assignment of the interference order to each skeleton line, the interference phase values are known along these lines, which represents a rather irregular distribution of points. To determine the values at all points of a regular grid, the interference phase values have to be interpolated for the grid points based on the phase values at the skeleton lines [419]. Three *interpolation* methods are presented in [420]:

- Interpolation based on *one-dimensional splines* fits cubic polynomials to the skeleton points in horizontal and vertical directions through the grid point and gets the phase value for each grid point from the two spline values at this point.
- In another approach at each grid point the four next neighboring skeleton points right and left as well as up and down are taken and from their phase values the interference phase at the grid point is calculated by *bilinear interpolation*.
- Closely related to this scheme is the *interpolation by triangulation*, where the whole skeleton is covered with small triangles. Two vertices of each triangle lie on one skeleton line, the third vertex is on an adjacent skeleton line. The phase at each grid point is found by linear interpolation from the phases at the vertices of the triangle in which it is contained.

A comparison of the resulting accuracy has shown that of these methods the interpolation by triangulation yields the highest accuracy [420].

5.4 Temporal Heterodyning

5.4.1 Principle of Temporal Heterodyning

The basis of *temporal heterodyning* is the interference of two optical waves of different frequencies. As shown in Section 2.2.2, two mutually coherent harmonic waves, differing in frequency by $2\Delta f$, produce an intensity oscillating with the *beat frequency*, which equals the *frequency difference* $2\Delta f$.

To translate this principle into *heterodyne holographic interferometry*, the two interfering wave fields are both holographically reconstructed with different optical frequencies f_1 and f_2 , or the reconstructed wave field has another frequency than the reflected or refracted one [303, 305, 421–424]. Due to the context with the interference phase, more often the angular frequencies $\omega_i = 2\pi f_i$, $i = 1, 2$ are employed in the theoretical description.

The frequency of the holographically reconstructed wave field is defined by the frequency of the reconstructing reference wave. To achieve a frequency shift between the two reconstructed wave fields in the *double exposure method*, they have to be recorded and reconstructed with a *two reference beam holography* arrangement as described in Section 4.2.2.

Now the optical frequency of one of the two reference beams is shifted with respect to the other. This in most cases is done by a pair of *acoustooptical modulators* as is indicated in Fig. 5.5, which shows the typical holographic arrangement with two reference waves for performing the temporal heterodyne method.

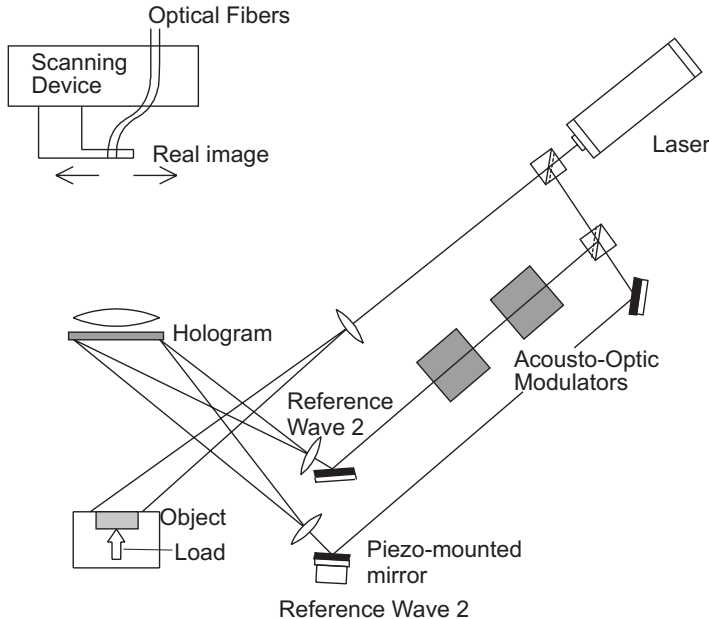


Figure 5.5: Two reference beam arrangement for double exposure temporal heterodyning.

The two reference beam method in conjunction with double exposure holography is the standard for temporal heterodyning. *Real-time holographic interferometry* with a wave field reconstructed by a reference wave having a frequency shift relative to the illuminating wave and being reflected by the object is possible in principle but not feasible, due to the extreme stability requirements and the high sensitivity to distortions from outside.

The holographic interference pattern resulting from reconstruction with two reference waves having a mutual frequency shift of $\Delta\omega = \omega_2 - \omega_1$ is

$$I(x, y, t) = a(x, y) + b(x, y) \cos[\Delta\phi(x, y) + t\Delta\omega] \quad (5.11)$$

where $a(x, y)$ and $b(x, y)$ are the additive and multiplicative distortions and $\Delta\phi(x, y)$ is the interference phase distribution to be determined. If the frequency offset $\Delta\omega/2\pi$ is adjusted low enough to be resolved by opto-electronic sensors, say < 100 MHz, the interference phase can be measured with high accuracy by an electronic phasemeter. One would ideally want a two-dimensional sensor which should simultaneously detect oscillations of some MHz at a high number of pixels. Unfortunately such a sensor does not exist, therefore point-sensors fulfilling the demanded temporal resolution have to be scanned mechanically over the reconstructed real image.

The phase $\Delta\phi(x, y) + t\Delta\omega$ of a single oscillation bears no information, but from the phase difference of the oscillating intensities of two points

$$\Delta\Delta\phi(x_1, y_1; x_2, y_2) = [\Delta\phi(x_1, y_1) + t\Delta\omega] - [\Delta\phi(x_2, y_2) + t\Delta\omega] \quad (5.12)$$

the relative change $\Delta\Delta\phi$ in the interference phase $\Delta\phi$ can be determined. Therefore two detectors have to record the oscillating intensity at different points in the real image and an electronic phasemeter measures the interference phase difference $\Delta\Delta\phi$ modulo 2π between these two points. The interference phase differences can be summed up from point to point to yield the interference phase distribution along a line or across a plane.

5.4.2 Technical Realization of Temporal Heterodyning

Principally there are two ways to perform the temporal heterodyne evaluation. One is to evaluate the interference phase difference by keeping one detector fixed to a reference point whilst the other is scanned. This way one measures the phase difference modulo 2π with respect to the phase occurring at the reference point. The other method is to scan a pair, triple, quadruple, or quintuple of photodetectors over the real image. In this way phase differences $\Delta\Delta\phi_x$ and $\Delta\Delta\phi_y$ between adjacent points with known separations are measured. Of course it is assumed that the x - and y -directions coincide with the scanning directions and the geometric arrangement of the photodetectors. In practice it is not the detectors themselves that are scanned over the real image, but the ends of optical fibers, which transmit the light to photodiodes. The signals of the photodiodes are amplified and after passing a narrowband filter are fed to the phasemeter. A technical realization of a detector with five optical fiber ends about 1 mm apart is shown in Fig. 5.6.

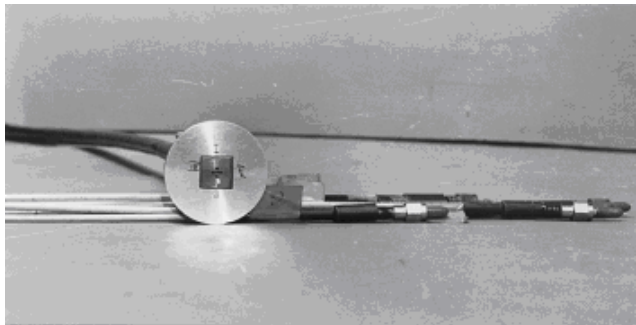


Figure 5.6: Five-fiber detector for temporal heterodyning (Courtesy of R. J. Pryputniewicz, WPI).

The determination of the mutual phase shift between two oscillating signals is done by the simultaneous measurement of the delay Δt between the time instants of the signals passing a *trigger level* in increasing direction and the period T of the oscillation. The phase shift difference $\Delta\Delta\phi$ then is calculated by

$$\Delta\Delta\phi = \frac{\Delta t}{T} 2\pi. \quad (5.13)$$

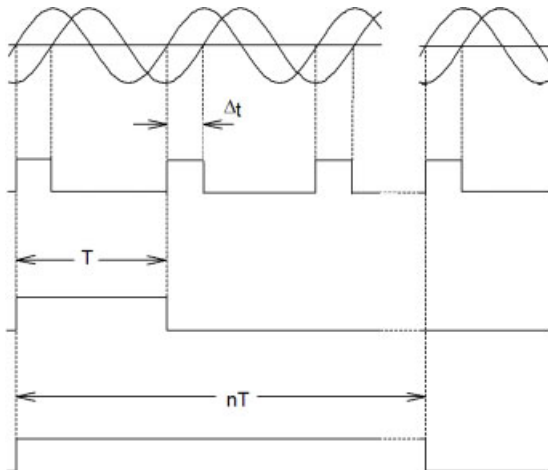


Figure 5.7: Measurement of time delay in temporal heterodyning.

A better accuracy and resolution is achieved by averaging over n periods, Fig. 5.7. Most phasemeters allow a control of the measuring time t_m , then the number n of averaged periods depends on the beat frequency Δf by $n = \Delta f t_m$.

The interference phase distribution determined by temporal heterodyning is correct in the sign as long as the sampling theorem is fulfilled. The solution of the *sign ambiguity* is due to the phasemeter's ability to discriminate positive and negative phase shifts in the interval $] -\pi, \pi]$. The sampling theorem requires that the scanning steps, and the distance of the detectors if detector pairs are scanned, are smaller than half a fringe period. Conversely the fringe density of measurable interference patterns is bounded by the detector separation and the scanning steps.

5.4.3 Errors of Temporal Heterodyning

Temporal heterodyning measures interference phase differences by the phase shift between two signals oscillating with the beat frequency independently of the local mean intensity or local contrast. Electronic phase measurement has a resolution of typically 1/1000 of the full cycle 2π . Thus one may claim a resolution of 1/1000 of a fringe at least theoretically. But a number of systematic and statistical errors make these figures difficult to reach.

Good results presume a proper control of the trigger levels and nearly the same amplitudes of the signals to be compared. The trigger levels of both signals should be equal and near zero. Unequal trigger levels lead to falsely measured intervals $\Delta t'$ instead of the correct Δt , see Fig. 5.8.

Different amplitudes of the signals lead to systematic errors even for identical trigger levels, Fig. 5.9. Due to the hysteresis band a trigger level adjusted to 0 mV can obtain ± 5 mV in reality. This leads to a maximal systematic phase error for sine waves of

$$\arcsin\left(\frac{5 \text{ mV}}{U_{\max 1}}\right) - \arcsin\left(\frac{5 \text{ mV}}{U_{\max 2}}\right) \quad (5.14)$$

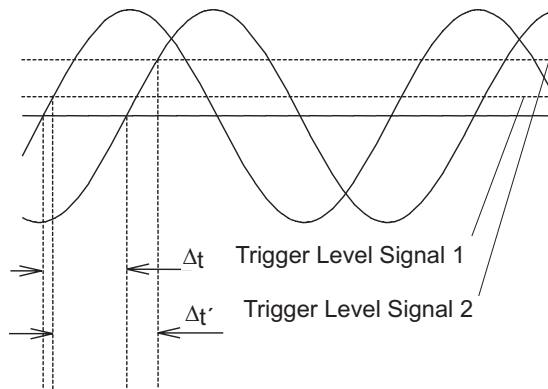


Figure 5.8: Error by unequal trigger levels.

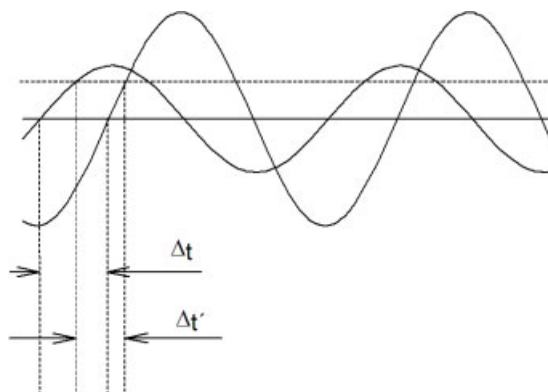


Figure 5.9: Error by unequal amplitudes.

which may induce phase errors up to 1.5° . Unequal intensities between reference point and actually scanned point are always present in holographic interferometry, at least due to speckles or spatially varying reflection.

The influence of a frequency drift during the measuring time caused by improper driving of the frequency shifting components has been tested by numerical simulations [425]. These have shown that the error caused by frequency drift is small compared to the aforementioned errors.

A systematic error can arise with the scanning of detector pairs, if the scanning steps do not agree exactly with the detector spacing. The individual errors depend on the local slope of the interference phase distribution, and they cumulate in the subsequent integration process. If the detector spacing and the scanning steps can be measured exactly, even if they do not agree, the resulting error can be corrected by numerical interpolation [425].

The most critical aspect of temporal heterodyning is the required high mechanical stability during the scanning of the reconstructed interference pattern. On the one hand the mechanical advance of the detectors can be achieved only with limited resolution, while on the other hand scanning the whole pattern, especially along many parallel lines, lasts a long time during which environmental influences like noise, vibrations or temperature changes may falsify the measuring results.

These errors are nearly the same independent of whether the double exposure method with two reference beam holography or the real-time method is employed. In the first case mutual variations of the optical path lengths cause the errors, while in the second case mutual variations between reference wave and reflected object wave are responsible. So after each mechanical scanning step the evaluation process has to wait until the whole arrangement has come to rest. Experiments have shown that the statistical errors occurring during the scanning are the most severe, especially if they go into the integrating process to calculate the overall interference phase distribution from the interference phase differences.

A long-term drift of the interference phase during the scanning process does not affect the result as long as this drift influences all evaluated points in the same way. This is because only interference phase differences are measured. But a temporal change of the interference phase which modifies the evaluation points differently may cause errors. In this regard the method with a fixed reference point is more critical than the method of simultaneously scanning several sensors if the phase difference at points far apart get different amounts of interference phase change. On the other hand measuring phase differences at neighboring points with scanned sensor pairs is much more sensitive to short-time errors, since these accumulate in the subsequent integration process.

5.4.4 Experimental Application of Temporal Heterodyning

Experiments employing temporal heterodyning have been carried out with the two reference beam holographic arrangement, shown schematically in Fig. 5.5 and in a photograph in Fig. 5.10. The arrangement consists of a 35 mW He-Ne laser, whose beam is split into one

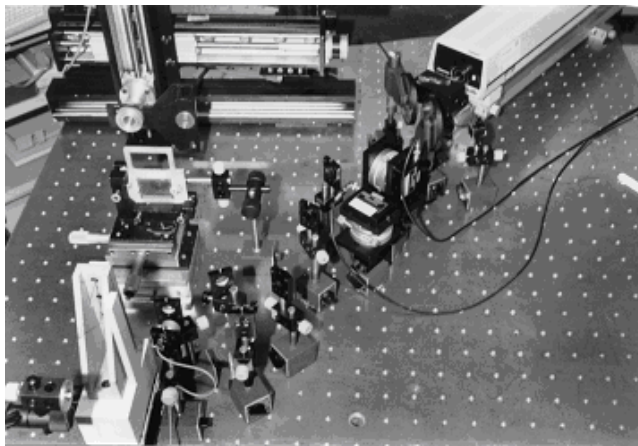


Figure 5.10: Two reference beam arrangement for double exposure temporal heterodyning.

object illumination wave and two reference waves. The two acoustooptical modulators are driven one with 40 MHz, the other with -40.08 MHz, producing a beat frequency of 80 kHz. The negative sign indicates the -1 . diffraction order of the modulators, while the positive sign denotes the $+1$. order. The object is a bent cantilever, Fig. 5.11. The intensities are reg-

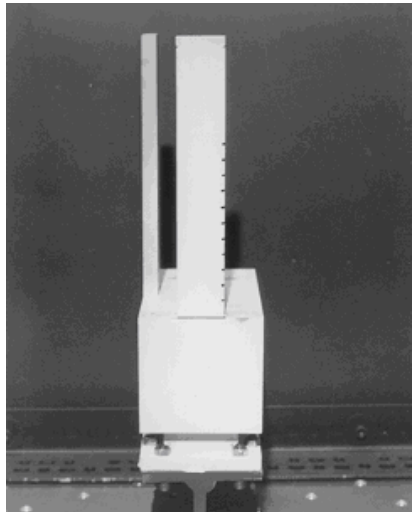


Figure 5.11: Test object.

istered by the ends of two of the five optical fibers, Fig. 5.6, and transmitted to photodiodes. Their signals go via an amplifier and filter to the phasemeter, the evaluated phase difference is transmitted via an IEEE-interface to the computer, which not only collects and evaluates the phase data, but also controls the stepper motors of the scanning device.

In this way 36 interference phase differences of point pairs have been recorded. This number is determined by the length of the object in the real image and the fixed distance of the fiber ends. Integration yields the continuous interference phase distribution which is proportional to the deflection curve of the cantilever beam shown in Fig. 5.12. The small deviations

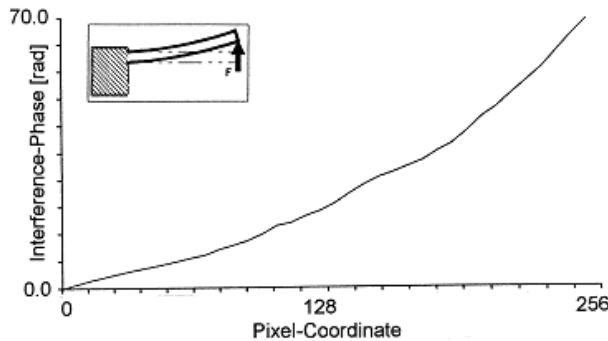


Figure 5.12: Evaluated interference phase by temporal heterodyning.

from the theoretical deflection line are caused by air turbulences during the measuring time. After each scanning step some seconds elapse until all mechanics come to rest. The errors accumulate to about 8% of the whole deflection [426].

5.5 Phase Sampling Evaluation

Although the heterodyne method is the widely used state of the art in interferometric length measurement, in holographic interferometry it has only found limited application. This is mainly due to the necessity of sensors with high temporal bandwidth, which is only accomplished by point detectors. On the other hand the two-dimensional holographic interferograms appeal for image detectors like TV tubes or CCD arrays which do not reach the required bandwidth. A way out of this dilemma is offered by the *phase step* or the *phase shift methods* [202].

The frequency shift in one of the interfering light waves of the heterodyne method can be envisaged as a continuous shift of the mutual phase between the light waves. Now this phase may be varied very slowly, in the extreme case stepwise, so that the intensity can be sampled corresponding to different values of this reference phase. The intensity distributions $I_n(x, y)$ recorded in this way are expressed by the so called *phase sampling equation*

$$I_n(x, y) = a(x, y) + b(x, y) \cos[\Delta\phi(x, y) + \phi_{Rn}] \quad n = 1, \dots, m \quad m \geq 3 \quad (5.15)$$

where $a(x, y)$ and $b(x, y)$ are the additive and multiplicative distortions, $\Delta\phi(x, y)$ is the interference phase distribution to be determined, and ϕ_{Rn} is the shifted reference phase belonging to the n -th intensity distribution $I_n(x, y)$.

The phase step and phase shift methods which record and evaluate a set of intensity distributions (5.15) represent the widely accepted state of the art in the automatic evaluation of interference patterns especially of optically reconstructed holographic interference patterns. Due to the redundant information contained in the I_n 's the interference phase is calculated with high accuracy at all pixels of the interference pattern and without sign ambiguity. The discrete sampling of several phase-shifted digital holograms from the dynamically varying heterodyne signal by a CCD is described in [84]. Due to the above mentioned conceptual relation to heterodyning these methods sometimes are called *quasi heterodyne methods* [305, 427–431].

The different components one can use to perform the phase shifts are described together with the other components of the holographic setup in Section 2.7. A frequently used option is a mirror, which reflects the reference wave, mounted on a piezo-crystal to shift the mirror by fractions of the used wavelength. This is depicted in Figs. 5.13 and 5.14 to indicate any phase shifting component.

Since the holographically reconstructed wave field has an optical phase distribution defined by the phase of the reconstructing reference wave, phase shifting the reference wave during reconstruction of a double exposure hologram would shift both reconstructed images in phase and so no effect on the interference fringes will be seen. Therefore in the *double exposure method* of holographic interferometry the two states have to be recorded with different reference waves and reconstructed by both of them simultaneously, but this approach brings all the problems of *two reference beam holography*, see Section 4.2.2. The phase shift here is introduced by shifting only one of the two reference waves, Fig. 5.13.

The other way is to employ the real-time method, Fig. 5.14. The wave field coming directly from the object is not affected by the phase shift in the reference wave which only modifies the optical phase of the reconstructed wave field. Thus the reference phase ϕ_R in (5.15) can be varied.

In most applications the phase shifted interferograms are recorded subsequently. The simultaneous recording of phase shifted interferograms, e. g. when measuring *transient events*,

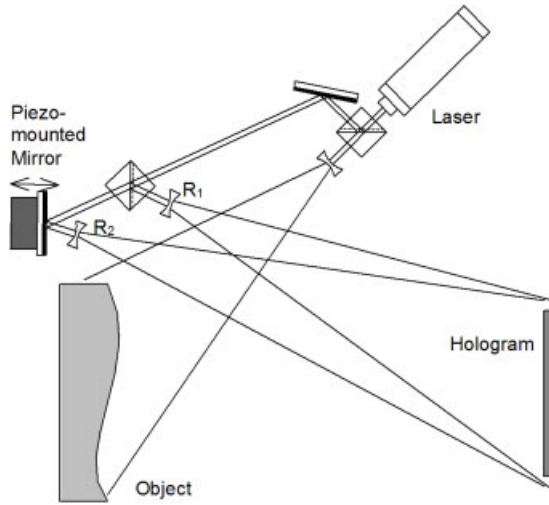


Figure 5.13: Two reference beam arrangement for double exposure phase sampling evaluation.

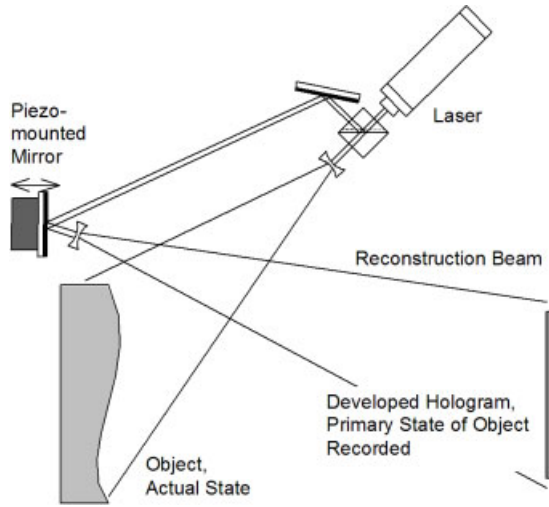


Figure 5.14: Real-time method for phase sampling evaluation.

is enabled by the introduction of a *diffraction grating* in the object beam [205,432]. The fringe patterns are obtained from direct interference of wavefronts propagating in the n -th diffraction order directions behind the grating and the hologram. For phase shifting the grating is shifted transversely between the two exposures of double exposure holography or between recording and reconstruction when employing real-time holographic interferometry, Section 2.7.4.

5.5.1 Phase Shifting and Phase Stepping

Although it is possible to perform arbitrary phase shifts and recognize these in the evaluation, it is recommended to use constant phase steps $\Delta\phi_R = \phi_{Rn+1} - \phi_{Rn}$ to keep the analysis easy. The phase can be shifted linearly in time, Figs. 5.15a and b, or in discrete steps, Figs. 5.15c

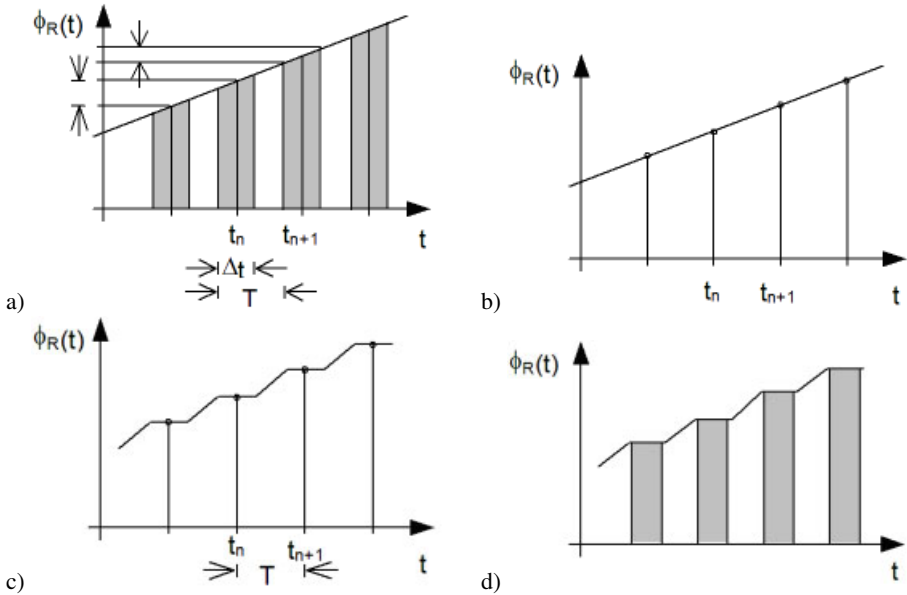


Figure 5.15: Phase shift vs. time: (a) phase shifting, (b)–(d) phase stepping; (a) and (b) linear phase shift, (c) and (d) stepwise phase shift.

and d. In practical applications, the time delay T between the recording of the phase shifted intensities should be as short as possible, e. g. only limited by the video frequency. For short T spurious vibrations induced by the environment have a minimal influence on the interference phase, in a rather worse case they can be modeled as an additional constant phase shift.

Theoretically one may discriminate between *phase shifting*, Fig. 5.15a, where each intensity is integrated over the time interval Δt during which the phase varies linearly, and *phase stepping*, Figs. 5.15b to d, where we have fixed phase values as assumed in (5.15). The result of integration in phase shifting can be calculated:

$$I_n(x, y) = \frac{1}{\Delta t} \int_{t_n - \Delta t/2}^{t_n + \Delta t/2} a(x, y) + b(x, y) \cos[\Delta\phi(x, y) + \phi_R(t)] dt. \quad (5.16)$$

Assuming a linear variation of $\phi_R(t)$ with t , this integral can be evaluated applying a substitution and the formula $\sin(\alpha + \beta) - \sin(\alpha - \beta) = 2 \cos \alpha \sin \beta$ to yield

$$I_n(x, y) = a(x, y) + \text{sinc}\left(\frac{\Delta\phi_R}{2}\right) b(x, y) \cos[\Delta\phi(x, y) + \phi_{Rn}]. \quad (5.17)$$

This expression corresponds to (5.15), only the contrast term $b(x, y)$ is modified by the constant factor $\text{sinc}(\Delta\phi_R/2)$. Here $\Delta\phi_R$ denotes the phase shift during the time interval Δt . In this sense phase shifting is equivalent to phase stepping, both names in the following are used synonymously. One can see that for $\Delta\phi_R = 0$, the phase stepping of Figs. 5.15b to d, the

sinc-function has a value of one. At the other extreme, for sampling over a whole period of $\Delta\phi_R = 2\pi$ the sinc is zero, and we get no intensity modulation at all.

5.5.2 Solution of the Phase Sampling Equations with Known Phase Shifts

If several intensity distributions $I_n(x, y)$ with mutual phase shifts $\Delta\phi_R = \phi_{Rn+1} - \phi_{Rn}$ are recorded, a nonlinear system of equations of the form (5.15) has to be solved for each point (x, y) . As long as the phase shifts are known, there remain three unknowns: $a(x, y)$, $b(x, y)$ and the desired interference phase $\Delta\phi(x, y)$. So at least $m = 3$ equations are necessary, meaning that at least three phase shifted intensities have to be recorded.

For solution of the nonlinear system of equations (5.15) the Gaussian least squares approach is used [433] by introducing

$$u(x, y) = b(x, y) \cos[\Delta\phi(x, y)] \quad \text{and} \quad v(x, y) = -b(x, y) \sin[\Delta\phi(x, y)]. \quad (5.18)$$

Herewith (5.15) is rewritten, with the (x, y) omitted for clarity

$$\begin{aligned} I_n &= a + b \cos[\Delta\phi + \phi_{Rn}] \\ &= a + u \cos \phi_{Rn} + v \sin \phi_{Rn}. \end{aligned} \quad (5.19)$$

The sum of the quadratic errors

$$\sum_{n=1}^m (a + u \cos \phi_{Rn} + v \sin \phi_{Rn} - I_n)^2 \quad (5.20)$$

has to be minimized. Partial differentiation of this functional with respect to a , u , and v and equating the derivatives to zero gives the linear system of three equations with \sum written shortly for $\sum_{n=1}^m$:

$$\begin{pmatrix} m & \sum \cos \phi_{Rn} & \sum \sin \phi_{Rn} \\ \sum \cos \phi_{Rn} & \sum \cos^2 \phi_{Rn} & \sum \sin \phi_{Rn} \cos \phi_{Rn} \\ \sum \sin \phi_{Rn} & \sum \sin \phi_{Rn} \cos \phi_{Rn} & \sum \sin^2 \phi_{Rn} \end{pmatrix} \begin{pmatrix} a \\ u \\ v \end{pmatrix} = \begin{pmatrix} \sum I_n \\ \sum I_n \cos \phi_{Rn} \\ \sum I_n \sin \phi_{Rn} \end{pmatrix}. \quad (5.21)$$

This system has to be solved in a pointwise manner for u and v , while the solution for a may be omitted. Having thus found $u(x, y)$ and $v(x, y)$, the interference phase is determined modulo 2π by

$$\Delta\phi(x, y) = \arctan \frac{-v(x, y)}{u(x, y)}. \quad (5.22)$$

The pointwise solution of system (5.21) requires only a single inversion of the matrix to the left, provided the phase steps $\Delta\phi_R$ are the same for all pixels [203]. Simple solutions of

(5.21) are given for phase steps which are constant and have special values like 30° , 45° , 60° , or 90° because the sines and cosines of these values are easy to handle. The general scheme for deriving the evaluation equation is given in the following for the example for $m = 4$ intensities with constant phase shift $\Delta\phi_R = 90^\circ$ and a starting value of $\phi_{R1} = 0^\circ$. The elements of the matrix in (5.21) are calculated by

n	ϕ_{Rn}	$\sin \phi_{Rn}$	$\cos \phi_{Rn}$	$\sin^2 \phi_{Rn}$	$\cos^2 \phi_{Rn}$	$\sin \phi_{Rn} \cos \phi_{Rn}$
1	0°	0.	1.	0.	1.	0.
2	90°	1.	0.	1.	0.	0.
3	180°	0.	-1.	0.	1.	0.
4	270°	-1.	0.	1.	0.	0.
Σ		0.	0.	2.	2.	0.

The system of equations (5.21) now is

$$\begin{pmatrix} 4 & 0 & 0 \\ 0 & 2 & 0 \\ 0 & 0 & 2 \end{pmatrix} \begin{pmatrix} a \\ u \\ v \end{pmatrix} = \begin{pmatrix} I_1 + I_2 + I_3 + I_4 \\ I_1 - I_3 \\ I_2 - I_4 \end{pmatrix}. \quad (5.23)$$

Its solution $u = (I_1 - I_3)/2$, $v = (I_2 - I_4)/2$ gives the interference phase modulo 2π at each point (x, y) by

$$\Delta\phi(x, y) = \arctan \frac{I_4(x, y) - I_2(x, y)}{I_1(x, y) - I_3(x, y)}. \quad (5.24)$$

More such formulas, all derived by the same scheme, are given in Table 5.1.

The so called *2+1-technique* [434] is contained implicitly in Table 5.1. In this technique the first two intensities $I_1(x, y)$ and $I_2(x, y)$ are taken very quickly with a $\Delta\phi_R = 90^\circ$ phase shift between them. If these two images are taken on either side of the interline transfer in a standard CCD video camera, 1 ms exposures can be taken as quickly as 1 μs apart. This will freeze most vibrations or air turbulence affecting the measurement. The third intensity is the background $I'_3(x, y) = a(x, y)$ which can be acquired at any time, and may be averaged over many noise cycles. Considering $m = 3$, $\phi_{R1} = 0^\circ$, $\Delta\phi_R = 90^\circ$, we have the three intensities

$$\begin{aligned} I_1(x, y) &= a(x, y) + b(x, y) \cos \Delta\phi(x, y) \\ I_2(x, y) &= a(x, y) + b(x, y) \cos[\Delta\phi(x, y) + 90^\circ] \\ I_3(x, y) &= a(x, y) + b(x, y) \cos[\Delta\phi(x, y) + 180^\circ]. \end{aligned} \quad (5.25)$$

Now one observes that $I'_3(x, y) = [I_1(x, y) + I_3(x, y)]/2$, so replacing $I_3(x, y)$ by $2I'_3(x, y) - I_1(x, y)$ in the evaluation formula, Table 5.1, we get

$$\Delta\phi(x, y) = \arctan \frac{I_1 - 2I_2 + I_3}{I_1 - I_3} = \arctan \frac{I'_3 - I_2}{I_1 - I'_3}. \quad (5.26)$$

It is not necessary to take $\Delta\phi_R = 90^\circ$, because for the system of equations

$$\begin{aligned} I_1(x, y) &= a(x, y) + b(x, y) \cos \Delta\phi(x, y) \\ I_2(x, y) &= a(x, y) + b(x, y) \cos[\Delta\phi(x, y) + \Delta\phi_R] \\ I_3(x, y) &= a(x, y) + b(x, y) \cos[\Delta\phi(x, y) + 180^\circ] \end{aligned} \quad (5.27)$$

Table 5.1: Phase shift methods for known phase shifts.

Phase shift	Start	m	Evaluation formula
30°	0°	3	$\Delta\phi = \arctan \frac{(3\sqrt{3}-5)I_1 + (\sqrt{3}-2)I_2 + (7-4\sqrt{3})I_3}{(5-3\sqrt{3})I_1 + (2\sqrt{3}-3)I_2 + (\sqrt{3}-2)I_3}$
30°	-30°	3	$\Delta\phi = \arctan \frac{I_1 - I_3}{(2+\sqrt{3})(-I_1 + 2I_2 - I_3)}$
45°	0°	3	$\Delta\phi = \arctan \frac{(2+\sqrt{2})I_1 - (2+2\sqrt{2})I_2 + \sqrt{2}I_3}{-\sqrt{2}I_1 + (2+2\sqrt{2})I_2 - (2+\sqrt{2})I_3}$
45°	-45°	3	$\Delta\phi = \arctan \frac{\sqrt{2}(I_3 - I_1)}{(2+\sqrt{2})(I_1 - 2I_2 + I_3)}$
60°	0°	3	$\Delta\phi = \arctan \frac{2I_1 - 3I_2 + I_3}{\sqrt{3}(I_2 - I_3)}$
60°	0°	4	$\Delta\phi = \arctan \frac{5(I_1 - I_2 - I_3 + I_4)}{\sqrt{3}(2I_1 + I_2 - I_3 - 2I_4)}$
60°	0°	5	$\Delta\phi = \arctan \frac{\sqrt{3}(2I_1 - 3I_2 - 4I_3 + 5I_5)}{8I_1 + 3I_2 - 4I_3 - 6I_4 - I_5}$
90°	0°	3	$\Delta\phi = \arctan \frac{I_1 - 2I_2 + I_3}{I_1 - I_3}$
90°	45°	3	$\Delta\phi = \arctan \frac{I_3 - I_2}{I_1 - I_2}$
90°	0°	4	$\Delta\phi = \arctan \frac{I_4 - I_2}{I_1 - I_3}$
90°	0°	5	$\Delta\phi = \arctan \frac{7(I_4 - I_2)}{4I_1 - I_2 - 6I_3 - I_4 + 4I_5}$
90°	-180°	5	$\Delta\phi = \arctan \frac{2(I_2 - I_4)}{-I_1 + 2I_3 - I_5}$
120°	0°	3	$\Delta\phi = \arctan \frac{\sqrt{3}(I_3 - I_2)}{2I_1 - I_2 - I_3}$
α	$-\alpha$	3	$\Delta\phi = \arctan \frac{(1 - \cos \alpha)(I_3 - I_1)}{\sin \alpha(I_1 - 2I_2 + I_3)}$
$\frac{2\pi k}{m}$	0°	m	$\Delta\phi = \arctan \frac{-\sum_{i=1}^m I_i \sin[\frac{2\pi k}{m}(i-1)]}{\sum_{i=1}^m I_i \cos[\frac{2\pi k}{m}(i-1)]}$

we have the solution

$$\Delta\phi(x, y) = \arctan \frac{I_1(1 + \cos \Delta\phi_R) - 2I_2 + I_3(1 - \cos \Delta\phi_R)}{(I_1 - I_3) \sin \Delta\phi_R} \quad (5.28)$$

which now is replaced by

$$\Delta\phi(x, y) = \arctan \frac{I_1 \cos \Delta\phi_R - 2I_2 + I'_3(1 - \cos \Delta\phi_R)}{(I_1 - I'_3) \sin \Delta\phi_R}. \quad (5.29)$$

5.5.3 Solution of the Phase Sampling Equations with Unknown Phase Shifts

With an unknown but constant phase shift $\Delta\phi_R$ we have an additional unknown, so that at least $m = 4$ phase shifted intensities have to be recorded [435]. The first case to be treated in the following is for $m = 4$. For ease of computation without loss of generality a starting value of $\phi_{R1} = -3 \Delta\phi_R/2$ is assumed. Then the four equations are

$$\begin{aligned} I_1 &= a + b \cos\left(\Delta\phi - \frac{3\Delta\phi_R}{2}\right) = a + b \cos \Delta\phi \cos \frac{3\Delta\phi_R}{2} + b \sin \Delta\phi \sin \frac{3\Delta\phi_R}{2} \\ I_2 &= a + b \cos\left(\Delta\phi - \frac{\Delta\phi_R}{2}\right) = a + b \cos \Delta\phi \cos \frac{\Delta\phi_R}{2} + b \sin \Delta\phi \sin \frac{\Delta\phi_R}{2} \\ I_3 &= a + b \cos\left(\Delta\phi + \frac{\Delta\phi_R}{2}\right) = a + b \cos \Delta\phi \cos \frac{\Delta\phi_R}{2} - b \sin \Delta\phi \sin \frac{\Delta\phi_R}{2} \\ I_4 &= a + b \cos\left(\Delta\phi + \frac{3\Delta\phi_R}{2}\right) = a + b \cos \Delta\phi \cos \frac{3\Delta\phi_R}{2} - b \sin \Delta\phi \sin \frac{3\Delta\phi_R}{2} \end{aligned} \quad (5.30)$$

With $S_1 = I_1 + I_4$, $S_2 = I_2 + I_3$, $S_3 = I_1 - I_4$, $S_4 = I_2 - I_3$, $u = 2b \cos \Delta\phi$, $v = 2b \sin \Delta\phi$, $w = \cos(\Delta\phi_R/2)$ (5.24) simplifies to

$$\begin{aligned} S_1 &= 2a + u(4w^3 - 3w) \\ S_2 &= 2a + uw \\ S_3 &= v\sqrt{1-w^2}(4w^2 - 1) \\ S_4 &= v\sqrt{1-w^2}. \end{aligned} \quad (5.31)$$

One well known solution to this nonlinear system of equations is the *Carre formula* [39]

$$\Delta\phi = \arctan \frac{v}{u} = \arctan \frac{\sqrt{I_1 + I_2 - I_3 - I_4} \sqrt{3I_2 - 3I_3 - I_1 + I_4}}{I_2 + I_3 - I_1 - I_4}. \quad (5.32)$$

The Carre formula directly calculates $\Delta\phi(x, y)$ from the four recorded intensities. But many experiments have shown that a big advantage lies in a primary pointwise calculation of the unknown phase shift $\Delta\phi_R(x, y)$ [436]. According to the above taken definitions it is $\cos(\Delta\phi_R) = 2w^2 - 1$, and if (5.31) is solved for $2w^2 - 1$ we get for each point

$$\Delta\phi_R(x, y) = \arccos \frac{I_1(x, y) - I_2(x, y) + I_3(x, y) - I_4(x, y)}{2[I_2(x, y) - I_3(x, y)]}. \quad (5.33)$$

By assumption $\overline{\Delta\phi_R}$ has to be constant for all points of the interference pattern, so we can take the average $\overline{\Delta\phi_R}$ over all pixels (x, y) . In this way fluctuations in $\Delta\phi_R(x, y)$, which may have been caused by speckles, are averaged out. Outliers in $\Delta\phi_R(x, y)$ preferably occur where the denominator of (5.33) is zero or near zero, they may be detected by a test for outliers and discarded before the averaging is done.

Having calculated the average phase shift $\overline{\Delta\phi_R}$, now only three unknowns are left and the interference phase can be determined from the first three intensities of (5.24) by

$$\Delta\phi_1(x, y) = \arctan \frac{I_3 - I_2 + (I_1 - I_3) \cos \overline{\Delta\phi_R} + (I_2 - I_1) \cos 2\overline{\Delta\phi_R}}{(I_1 - I_3) \sin \overline{\Delta\phi_R} + (I_2 - I_1) \sin 2\overline{\Delta\phi_R}} + \frac{3\overline{\Delta\phi_R}}{2}. \quad (5.34)$$

In an analogous way the interference phase may be calculated from the last three intensities of (5.24) by

$$\Delta\phi_2(x, y) = \arctan \frac{I_4 - I_3 + (I_2 - I_4) \cos \overline{\Delta\phi_R} + (I_3 - I_2) \cos 2\overline{\Delta\phi_R}}{(I_2 - I_4) \sin \overline{\Delta\phi_R} + (I_3 - I_2) \sin 2\overline{\Delta\phi_R}} + \frac{\overline{\Delta\phi_R}}{2}. \quad (5.35)$$

The arguments (x, y) to the intensities in (5.33) and (5.34) have been omitted for convenience. The 2π -steps of the interference phase distributions $\Delta\phi_1(x, y)$ and $\Delta\phi_2(x, y)$ arise at different points. This additional information can be used in the subsequent demodulation by considering the continuous interference phase variation of the two for the decision of adding or subtracting a further 2π .

The next case to be treated is $m = 5$ recorded intensities with unknown but constant mutual phase shifts. Without loss of generality here the best starting value for easy mathematics is $\phi_{R1} = -2\Delta\phi_R$. The recorded intensities are

$$\begin{aligned} I_1 &= a + b \cos(\Delta\phi - 2\Delta\phi_R) = a + b \cos \Delta\phi \cos 2\Delta\phi_R + b \sin \Delta\phi \sin 2\Delta\phi_R \\ I_2 &= a + b \cos(\Delta\phi - \Delta\phi_R) = a + b \cos \Delta\phi \cos \Delta\phi_R + b \sin \Delta\phi \sin \Delta\phi_R \\ I_3 &= a + b \cos \Delta\phi \\ I_4 &= a + b \cos(\Delta\phi + \Delta\phi_R) = a + b \cos \Delta\phi \cos \Delta\phi_R - b \sin \Delta\phi \sin \Delta\phi_R \\ I_5 &= a + b \cos(\Delta\phi + 2\Delta\phi_R) = a + b \cos \Delta\phi \cos 2\Delta\phi_R - b \sin \Delta\phi \sin 2\Delta\phi_R. \end{aligned} \quad (5.36)$$

Again we define $u = 2b \cos \Delta\phi$ and $v = 2b \sin \Delta\phi$, but now $w = \cos \Delta\phi_R$. This gives the system of equations

$$\begin{aligned} I_1 + I_5 &= 2a + u(2w^2 - 1) \\ I_2 + I_4 &= 2a + uw \\ 2I_3 &= 2a + u \\ I_1 - I_5 &= 2vw\sqrt{1 - w^2} \\ I_2 - I_4 &= v\sqrt{1 - w^2}. \end{aligned} \quad (5.37)$$

A direct solution for the interference phase is

$$\Delta\phi(x, y) = \arctan \frac{v}{u} = \arctan \frac{\sqrt{4(I_2 - I_4)^2 - (I_1 - I_5)^2}}{2I_3 - I_1 - I_5}. \quad (5.38)$$

As with $m = 4$ the intermediate step over the calculation of $\Delta\phi_R(x, y)$ and its averaging is recommended. For the calculation of the phase shift a number of formulas can be derived from (5.37). Perhaps the shortest is

$$\Delta\phi_R(x, y) = \arccos \frac{I_1 - I_5}{2(I_2 - I_4)}. \quad (5.39)$$

More solutions can be designed by convex combinations of two solutions of the $m = 4$ case, e. g. with identical weights

$$\begin{aligned} \Delta\phi_R(x, y) &= \arccos \frac{1}{2} \left[\frac{I_1 - I_2 + I_3 - I_4}{2(I_2 - I_3)} + \frac{I_2 - I_3 + I_4 - I_5}{2(I_3 - I_4)} \right] \\ &= \arccos \frac{I_1(I_3 - I_4) + (I_2 - I_3 + I_4)(I_2 - 2I_3 + I_4) - I_5(I_2 - I_3)}{4(I_2 - I_3)(I_3 - I_4)} \end{aligned} \quad (5.40)$$

A further solution also recognizing all five measured intensities is

$$\Delta\phi_R(x, y) = \arccos \frac{(I_2 - I_4)(I_1 - 2I_2 + 2I_3 - 2I_4 + I_5)}{(I_2 - I_4)(I_1 - 2I_3 + I_5) - (I_1 - I_5)(I_2 - 2I_3 + I_4)}. \quad (5.41)$$

Now after averaging over the $\Delta\phi_R(x, y)$ the interference phase can be determined by any of the formulas

$$\begin{aligned} \Delta\phi(x, y) &= \arctan \frac{I_{i+2} - I_{i+1} + (I_i - I_{i+2}) \cos \overline{\Delta\phi_R} + (I_{i-1} - I_i) \cos 2\overline{\Delta\phi_R}}{(I_i - I_{i+2}) \sin \overline{\Delta\phi_R} + (I_{i+1} - I_i) \sin 2\overline{\Delta\phi_R}} \\ &\quad -(i+1)\overline{\Delta\phi_R} \quad i = 1, 2, 3. \end{aligned} \quad (5.42)$$

A multiple calculation of $\Delta\phi$ again facilitates a noise suppression by averaging and an easier and more reliable demodulation. Alternative formulas for the $m = 5$ case are given in [437].

A further phase shift algorithm may become important for the evaluation of speckle interferograms which are produced by the spatial carrier method employing a tilted reference wave, see Chapter 7. Let us assume an unknown constant phase shift of $\Delta\alpha$ in the horizontal direction and of $\Delta\beta$ in the vertical direction. Then the recorded intensities are

$$\begin{aligned} I_1 &= a + b \cos \Delta\phi \\ I_2 &= a + b \cos(\Delta\phi - \Delta\alpha) \\ I_3 &= a + b \cos(\Delta\phi + \Delta\alpha) \\ I_4 &= a + b \cos(\Delta\phi - \Delta\beta) \\ I_5 &= a + b \cos(\Delta\phi + \Delta\beta). \end{aligned} \quad (5.43)$$

These are the five intensities at least necessary for determining the five unknowns. With the definitions $S_1 = I_2 - I_3$, $S_2 = 2I_1 - I_2 - I_3$, $S_3 = I_4 - I_5$, $S_4 = 2I_1 - I_4 - I_5$, $u = b \cos \Delta\phi$, $v = b \sin \Delta\phi$ we get

$$\left(\frac{v}{u} \right)^2 = \frac{S_1^2 S_4 - S_3^2 S_2}{S_4^2 S_2 - S_2^2 S_4} \quad (5.44)$$

so that one formula for determining the interference phase is

$$\Delta\phi(x, y) = \arctan \frac{\sqrt{(I_2 - I_3)^2(2I_1 - I_4 - I_5) - (I_4 - I_5)^2(2I_1 - I_2 - I_3)}}{\sqrt{(2I_1 - I_2 - I_3)(2I_1 - I_4 - I_5)(I_2 + I_3 - I_4 - I_5)}}. \quad (5.45)$$

If in phase shifting applications with unknown phase shifts even the condition of constant phase shift is not fulfilled, the unknown mutual phase shifts can be determined by the Fourier transform method described in Section 5.6, and the system of equations (5.21) has to be calculated with these determined reference phases. Another approach to automated reduction of phase shifted interferograms involves the recording of the individual wave fields giving rise to the interference. This enables the determination of the noise terms and the subsequent calculation of the phase shifts between two holographic interferograms [438].

5.5.4 Application of Phase Shift Evaluation Methods

The determination of pixels which promise to yield reliable interference phase values proceeds by checking the depth of the *intensity modulation* [439]. This modulation is contained in the $b(x, y)$ of (5.15). It can be calculated from the $u(x, y)$ and $v(x, y)$ of (5.18), which are at hand during the interference phase determination, by

$$b(x, y) = \sqrt{[u(x, y)]^2 + [v(x, y)]^2}. \quad (5.46)$$

Where this $b(x, y)$ is greater than a prescribed threshold, the pixel (x, y) will render a reliable phase value.

For $m = 4$ interferograms and a phase shift roughly in the vicinity of 90° from (5.23) we get the quantity

$$b' = \sqrt{[I_1(x, y) - I_3(x, y)]^2 + [I_4(x, y) - I_2(x, y)]^2} \quad (5.47)$$

to be tested. The factor 2 can be recognized in the threshold. Experiments have shown that nearly the same results for $m = 4$ and $\Delta\phi_R$ near 90° can be achieved even by the simpler quantity

$$b'' = |I_1(x, y) - I_3(x, y)| + |I_4(x, y) - I_2(x, y)|. \quad (5.48)$$

An example is given in Fig. 5.16. Figure 5.16a shows one of the four recorded holographic interference patterns, Fig. 5.16b displays all pixels in white where the quantity of (5.48) exceeds the threshold. By applying a modified digital median filter isolated good pixels may be discarded, the interference phase at bad pixels surrounded by good ones may be determined by taking the average of the phases of the surrounding pixels. In this way sharp borders of the region of reliable pixels can be fixed.

The described method not only fits to find pixels of sufficient contrast but also enables one to detect the borders of the imaged object surface, if the object does not fill the whole frame. Altogether a mask is generated, only in its interior the phase shift evaluation has to be performed.

The big advantage of the methods with unknown constant phase shift and a calculation of this phase shift in a pointwise manner out of the recorded intensities by (5.33), (5.39), (5.40), or (5.41) is the possibility first to check the calculated phase shift distribution for feasibility and second to discard outliers and to gain the most likely phase shift by averaging. Since a constant phase shift is assumed, strong variations would indicate non-constant phase steps. A linear trend along the pixels indicates a systematic error in the phase shifter, e. g. a tilt of the

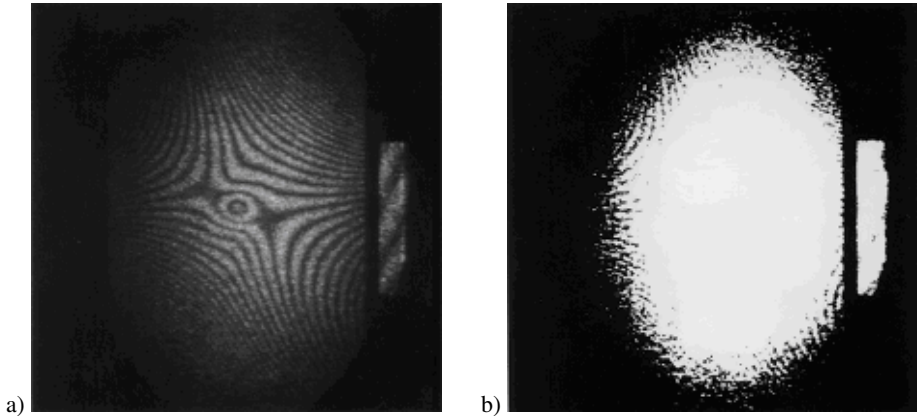


Figure 5.16: Determination of pixels with sufficient intensity modulation.

phase shifting piezo-mounted mirror. Such an error can be compensated by fitting a plane to the phase shift values $\Delta\phi_R(x, y)$ and taking the values of this plane function as the $\Delta\phi_R(x, y)$ in the interference phase calculation by (5.34), (5.35), or (5.42).

Further advantages are offered by the two or more formulas to calculate the interference phase (5.34) and (5.35) or (5.42), which give redundant information, e. g. for the demodulation process. If the interferograms are recorded in sequence with very short time gaps, e. g. with video-frequency, spurious vibrations can be assumed to contribute linearly to the shifted phase and are compensated inherently by the evaluation process.

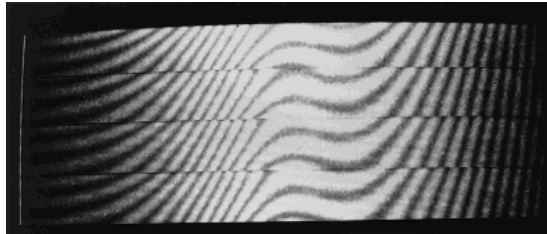


Figure 5.17: Four phase stepped holographic interferograms of tensile test specimen.

A one-dimensional example of phase stepping with unknown but constant phase steps is shown in Figs. 5.17 and 5.18. Figure 5.17 represents the four phase stepped holographic interferograms of a tensile test specimen with an internal crack produced by the real-time method. The evaluation along one line is shown in several steps in Fig. 5.18. The four recorded intensity distributions along the common line are displayed in Figs. 5.18a to d. In Fig. 5.18e the phase step $\Delta\phi_R(x, y)$, calculated by (5.33), is given together with the straight line which corresponds to the averaged $\overline{\Delta\phi_R}$. Figures 5.18f and g display the interference phase distributions modulo 2π determined by (5.34) and (5.35). The continuous interference phase, after unwrapping the 2π -discontinuities, is displayed in Fig. 5.18h. Although a varying background intensity, varying contrast, and even local saturation in the recorded intensities is present, the

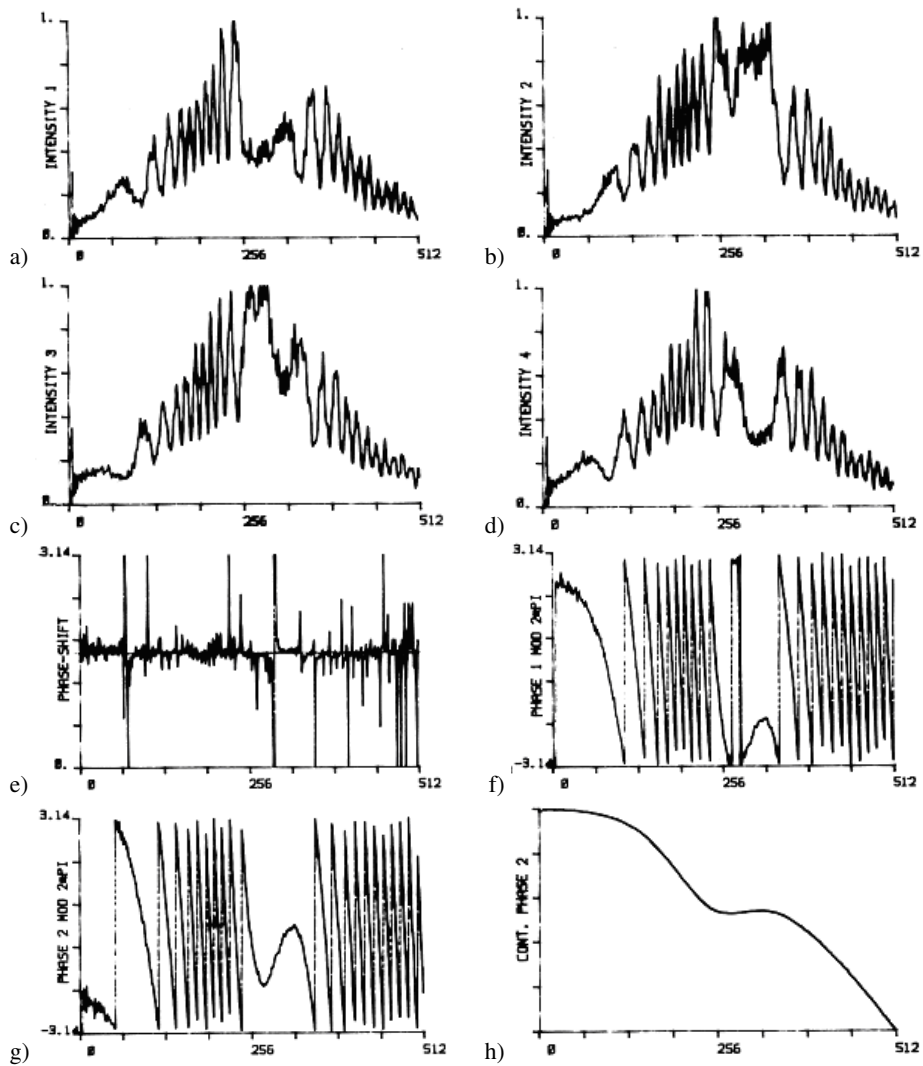


Figure 5.18: Evaluation of phase stepped holographic interferograms along one line: (a – d) intensity distributions; (e) phase shift, (f) interference phase 1, (g) interference phase 2, (h) demodulated interference phase

calculated interference phase distribution is clean and smooth. The changes in slope, decreasing to increasing and vice versa, are uniquely detected.

A two-dimensional evaluation by the same procedure of phase sampling is demonstrated for the example of a thermally loaded panel, consisting of an internal aluminum honeycomb structure with surface layers of carbon fiber reinforced plastic. Figures 5.19a to d exhibit the four phase stepped interferograms arising from a temperature difference of 2°C . The size of

the panel was about 80×80 cm. The resulting interference phase distribution, which can be interpreted as proportional to the normal displacement field due to the optimized sensitivity vectors, is presented in Fig. 5.20. Several debonds of the surface layer from the internal structure are clearly detectable.

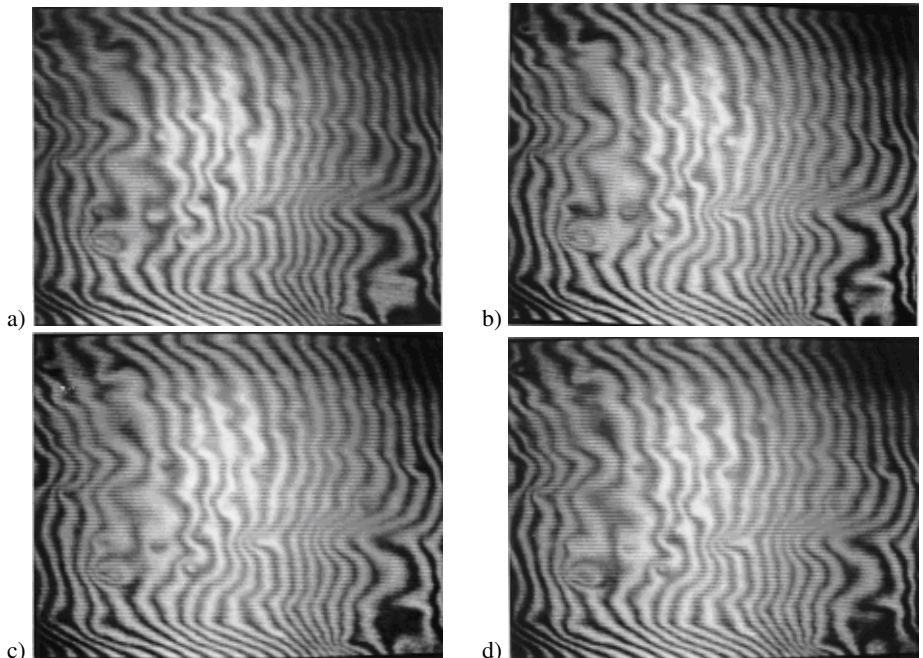


Figure 5.19: Four phase stepped holographic interferograms of a thermally loaded panel.

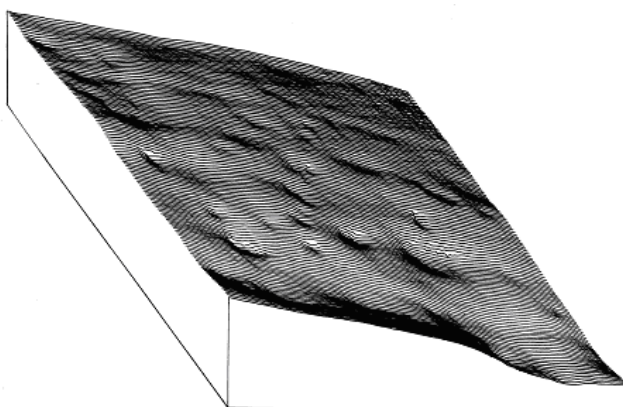


Figure 5.20: Evaluated interference phase distribution.

5.5.5 Discussion of Phase Shift Evaluation Methods

The phase shift methods for determining the interference phase distributions in holographic interferometry offer a number of advantages. The price one has to pay for it is the additional technical effort to perform the phase shifts, the increased requirements necessary for stability as for the *two reference beam holography* with double exposure or for the *real-time method*, as well as the additional storage capacity of the computer, all compared to the recording of a single interference pattern. But the benefits are manifold [440, 441]:

- The evaluation procedure can be fully automated.
- The interference phase is calculated at all pixels, not only at the fringe centers. Thus we get the best *spatial resolution* possible with the available electronics. No interpolation between skeleton lines is necessary.
- Due to the multiple recorded interferograms and the knowledge about their sequential order the *sign ambiguity* is resolved automatically. The evaluated interference phase increases and decreases in the same manner as the original one.
- The additive and multiplicative noise components are inherently recognized and compensated for in the automatic evaluation process.
- There are many different algorithms which fit to different circumstances, e. g. environmental distortions, phase shifter miscalibration, unknown phase shifts, etc.
- The intermediate results of the evaluation procedure allow a detection, whether the whole measurement was erroneous, e. g. zero phase shifts, whether there are points with contrast too low to guarantee a reliable evaluation, or whether there are points where no object surface was existent at all, e. g. at holes or outside the object margins.
- A phase shift which is varying over the pattern can be detected by some algorithms and sometimes can be fitted by a low degree polynomial, especially when the phase of the reference wave is shifted by a piezo-mounted mirror which undergoes an additional tilt.
- The resolution and accuracy of the determined interference phase is better than 1/20 of 2π and with some experimental skill reaches 1/100 of 2π .

Although the evaluation scheme, (5.21) and (5.24), applies for all sets of reference phases ϕ_{Rn} , $n = 1, \dots, m$ which do not produce a singular matrix in (5.21), the best choice for the phase shifts between successive interferograms is between 30° and 150° . This recommendation concerns to the methods with known as well as to those with unknown phase shifts. For the methods with known phase shifts it is not necessary that all phase shifts are constant, but this simplifies the evaluation procedure.

The influence of different error sources on the phase shift methods has been investigated by a large number of researchers [387–389, 442–444]. The results can be summarized by the statement that all these error sources like insufficient quantization, spurious diffraction or reflection patterns, aberrations of the optics, vibrations, air turbulence, inhomogeneity of the reference beam waveform etc., which can be modeled as additive or multiplicative noise degrade the precision and accuracy independently of the choice of the evaluation algorithm.

Exceptions are detector nonlinearities and false phase shifts, e. g. by phase shifter miscalibration, whose consequences depend on the specific evaluation algorithm. Their influence has been tested in a comparison of different algorithms [445].

These tests have shown that a linear phase shift error degrades the calculated interference phase for all algorithms which assume a known constant phase shift. The degradation is reduced with the increase of the number of interferograms, especially for $m = 5$ or $m = 7$, [446–448]. The algorithms which calculate the unknown phase shift from the recorded interference patterns compensate for a linear phase shift error inherently and remain exact.

The same trend holds for nonlinear, quadratic phase shift errors. Although their influence remains present when applying the algorithms with unknown phase shifts, it is least then, compared to the algorithms assuming a known constant phase shift and employing the same number of frames.

A higher number of frames as well as making use of the algorithms with unknown phase shifts also is favorable if detector nonlinearities have to be considered.

5.6 Fourier Transform Evaluation

5.6.1 Principle of the Fourier Transform Evaluation Method

In *Fourier transform evaluation* [43,44,449–455] essentially a linear combination of *harmonic spatial functions* is fitted to the recorded and stored intensity distribution $I(x, y)$, given by (5.1). The admissible spatial frequencies of these harmonic functions are defined by the user via the *cutoff frequencies* of a *bandpass filter* in the spatial frequency domain.

To do this the intensity function is expressed with the help of the complex exponential. Introducing

$$c(x, y) = \frac{1}{2}b(x, y) e^{i\Delta\phi(x, y)} \quad (5.49)$$

the intensity $I(x, y)$ of (5.1) becomes

$$I(x, y) = a(x, y) + c(x, y) + c^*(x, y) \quad (5.50)$$

with $a(x, y)$, $b(x, y)$ as described in Section 5.1, i being the imaginary unit and $*$ denoting complex conjugation. The discrete two-dimensional Fourier transform via the *FFT algorithm* applied to $I(x, y)$ yields

$$\mathcal{I}(u, v) = \mathcal{A}(u, v) + \mathcal{C}(u, v) + \mathcal{C}^*(u, v) \quad (5.51)$$

with (u, v) being the spatial frequency coordinates. Since $I(x, y)$ is a real distribution in the spatial domain, $\mathcal{I}(u, v)$ is a *Hermitean* distribution in the spatial frequency domain, which means

$$\mathcal{I}(u, v) = \mathcal{I}^*(-u, -v). \quad (5.52)$$

The real part of $\mathcal{I}(u, v)$ is even and the imaginary part is odd. The *amplitude spectrum* $|\mathcal{I}(u, v)|$ thus looks point-symmetric with respect to the d.c.-term $\mathcal{I}(0, 0)$. $\mathcal{A}(u, v)$ contains the

zero-peak $\mathcal{I}(0, 0)$ and the low frequency variations of the background. $\mathcal{C}(u, v)$ and $\mathcal{C}^*(u, v)$ carry the same information as evident from (5.52).

By *bandpass filtering* in the *spatial frequency domain*, $\mathcal{A}(u, v)$ and one of the terms $\mathcal{C}(u, v)$ or $\mathcal{C}^*(u, v)$ are eliminated. The remaining spectrum, $\mathcal{C}^*(u, v)$ or $\mathcal{C}(u, v)$, is no longer Hermitean, so the *inverse Fourier transform* applied to, e.g. $\mathcal{C}(u, v)$, gives a complex $c(x, y)$ with non-vanishing real and imaginary parts. The interference phase can be calculated by

$$\Delta\phi(x, y) = \arctan \frac{\text{Im } c(x, y)}{\text{Re } c(x, y)}. \quad (5.53)$$

The inverse transform of $\mathcal{C}^*(u, v)$ instead of $\mathcal{C}(u, v)$ would result in $-\Delta\phi(x, y)$. The uncertainty about which of the symmetric parts of the spectrum belongs to $\mathcal{C}(u, v)$ and which to $\mathcal{C}^*(u, v)$ is a manifestation of the *sign ambiguity*, (5.2).

A one-dimensional example of the Fourier transform evaluation is given in Fig. 5.21. The

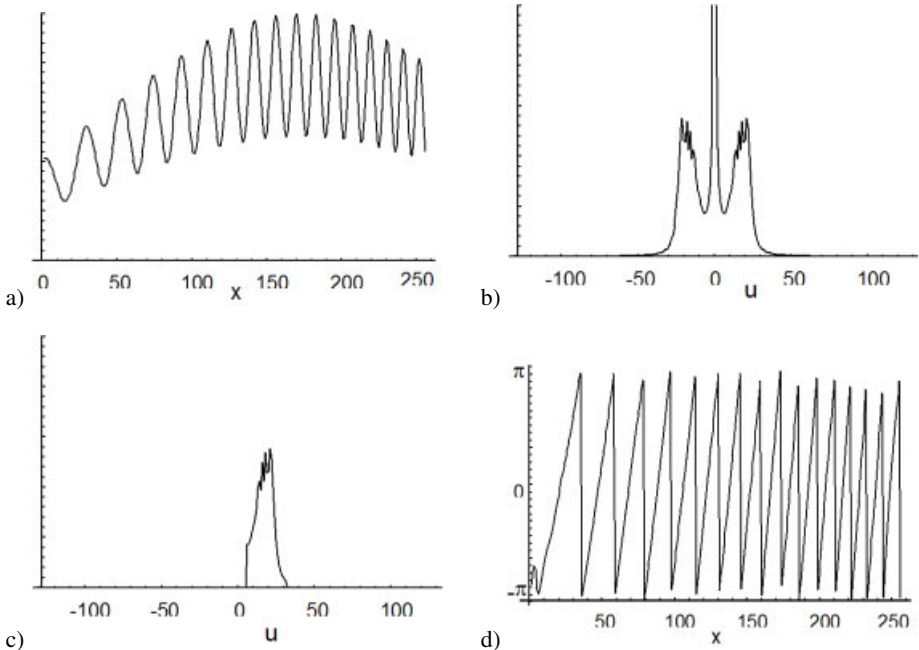


Figure 5.21: Fourier transform evaluation.

intensity distribution with varying contrast and varying background of Fig. 5.21a is Fourier transformed, the amplitude spectrum is shown in Fig. 5.21b. After filtering, the spectrum of which the amplitude is given in Fig. 5.21c remains. The application of the inverse transform and (5.53) result in the phase modulo 2π shown in Fig. 5.21d.

Although the Fourier transform calculated by the FFT algorithm normally has its zero frequency at the left and the two-dimensional Fourier transform has its zero frequency in the upper left corner when displayed, in the examples demonstrated here and in the following, we use the reordered display of the amplitude spectra, as determined by (A.77).

5.6.2 Noise Reduction by Spatial Filtering

The bandpass filtering in the spatial frequency domain not only makes the spectrum non-Hermitean, but also enables a reasonable *image enhancement* [451]. Low frequency *background variations*, e. g. a Gaussian illumination, lead to spectral components centered around the zero-component. Their influence is minimized by a bandpass filter which eliminates all spectral components up to a certain lower *cutoff frequency*. High frequency components, like *speckle noise*, are suppressed to a reasonable amount if the filter stops all frequencies higher than an upper cutoff frequency.

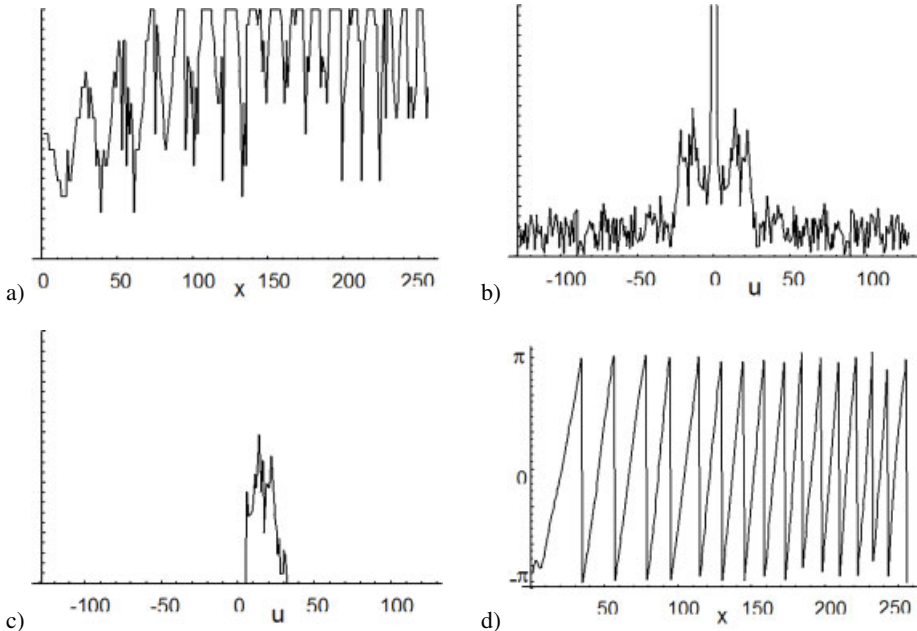


Figure 5.22: Image enhancement by Fourier transform evaluation.

This capability is shown in Fig. 5.22. The intensity, Fig. 5.22a, is degraded by a Gaussian background, varying contrast, speckle noise, reduced *quantization* into 16 gray-levels, and nonlinear response with *saturation*.

We recognize the presence of higher spatial frequencies in the amplitude spectrum, Fig. 5.22b.

Most of them are cut away in the filtered spectrum, Fig. 5.22c, so that the finally evaluated interference phase distribution, Fig. 5.22d, is clean and fully modulated.

In eliminating high frequencies, one has to consider the fact that the *finite discrete Fourier transform* assumes a periodic input signal, whereas, in practice, data consist of one non-periodic stretch of finite length. The discontinuities from the right to the left or from the lower to the upper edge of the image lead to high frequency components in the spectrum. If these are filtered away, the resulting phase distribution suffers from a *wrap-around pollution* by a forced smooth continuation at the edges of the frame. Thus the marginal pixels at the edges

of the frame get no reliable phase values; the number of these pixels depend on the choice of the upper cutoff frequency. The run-out at the left edge in Fig. 5.22d is caused by this effect.

Making the spectrum non-Hermitean means setting to zero one of the spectral values at each spatial frequency or at its symmetric counterpart. Since there is no general way to decide whether $\mathcal{I}(u, v)$ at a certain (u, v) belongs to $\mathcal{C}(u, v)$ or to $\mathcal{C}^*(u, v)$, or is a combination of contributions belonging to both of them, the easiest way is to eliminate one halfplane of the spatial frequency plane. Some of these halfplanes are displayed in Fig. 5.23. In Fig. 5.23a

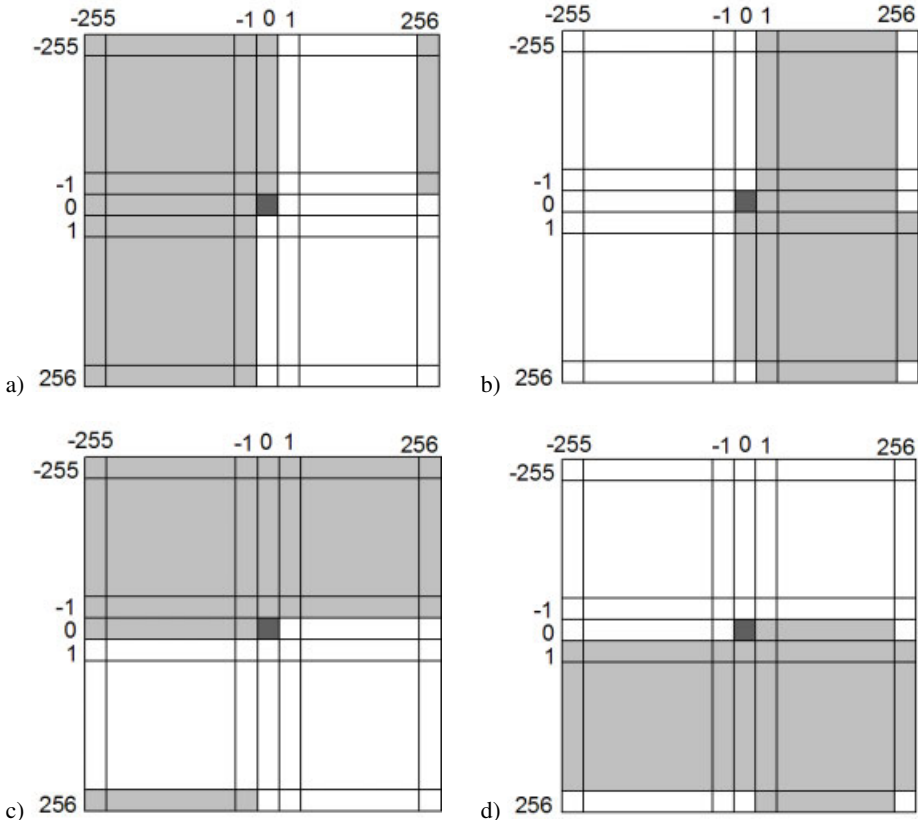


Figure 5.23: Halfplanes for filtering in the spatial frequency domain, reordered display.

the passband is the $+u$ -halfplane, displayed in white, and the shaded region is the stopband. In Fig. 5.23b the passband is the $-u$ -halfplane, in Fig. 5.23c the passband is the $+v$ -halfplane and in Fig. 5.23d we have the passband in the $-v$ -halfplane. For Fourier transform evaluation the component at spatial frequency $(0, 0)$ is always set to zero. Filters which destroy the Hermitean property and eliminate low-frequency background as well as high-frequency speckle noise have the form shown in Fig. 5.24, with a passband in one halfplane and with defined lower and upper cutoff frequencies.

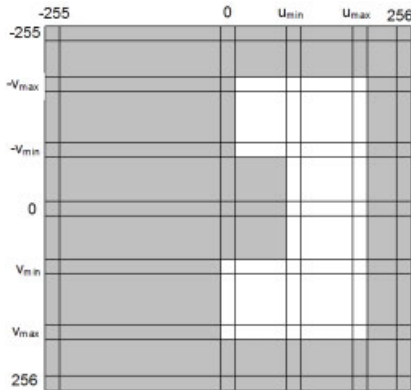


Figure 5.24: Bandpass filter, reordered display.

In many holographic applications it is possible to record and store the illuminated surface before the interference pattern is produced [450, 456]. So in *real-time holographic interferometry* one may:

- Record the object surface illuminated only by the object wave with the reference wave blocked. The hologram plate may be present or absent.
- Record a holographic reconstruction of the object with the object wave blocked. Only the reference wave illuminates the hologram plate.
- Record the zero interference pattern, still without fringes, before starting the loading.

Let this recorded background be $a'(x, y)$ and its Fourier transform be $\mathcal{A}'(u, v)$. A normalized version of $\mathcal{A}'(u, v)$ is then subtracted from $\mathcal{I}(u, v)$

$$\mathcal{I}'(u, v) = \mathcal{I}(u, v) - \frac{\operatorname{Re} \mathcal{I}(0, 0)}{\mathcal{A}'(0, 0)} \mathcal{A}'(u, v). \quad (5.54)$$

Since the imaginary part of the d.c.-term of a Fourier transform is always zero, we have zeroed the d.c.-term and eliminated the background. Now from $\mathcal{I}'(u, v)$ one halfplane is eliminated and after the inverse transform has been obtained the interference phase is calculated as described above. This procedure is recommended if the interference pattern or the object does not cover the whole frame or if we have complicated background variations in the frequency range of the interference pattern.

5.6.3 Spatial Filtering and Sign Ambiguity

The filter of Fig. 5.23a, where only positive *spatial frequencies* in the horizontal, the u -direction, and both positive and negative frequencies in the vertical, the v -direction, can pass, gives an interference phase distribution with an increasing interference phase in the horizontal direction, but increasing and decreasing interference phase in the vertical direction. For a passband in the $-u$ -halfplane the phases are decreasing in the horizontal direction, Fig. 5.23b. In the cases of Figs. 5.23c and d, the roles of the directions interchange with respect to Figs. 5.23a and b.

These facts can be used for the detection of sign changes: two phase distributions determined from the same pattern, but with orthogonally oriented passbands are compared to resolve a local sign ambiguity. Only the global sign is left indefinite, this has to be decided from knowledge about the specific experiment. From a computational view the elimination of a halfplane oriented parallel to the u - or v -axes would look to be the easiest way to render the spectrum non-Hermitean. Other orientations of halfplanes, or even other filter strategies destroying the Hermitean property, are also feasible.

The Fourier transform evaluation of the holographically measured deformation of a plate thermally loaded in a microwave oven is shown in Fig. 5.25.

Overlayed on the interference pattern we see the metallic grid in the window protecting the environment from microwave radiation, Fig. 5.25a. The bright spot in the lower left is a lens in the oven's door transmitting the illumination wave. The amplitude spectrum of this pattern is displayed in Fig. 5.25b in a logarithmic gray-scale to compress the high dynamic range, especially that of the zero-peak. Two mutually orthogonally oriented bandpass filters with lower cutoff frequencies $u_{\min} = v_{\min} = 2$ and upper cutoff frequencies $u_{\max} = 18$, $v_{\max} = 34$ in both cases, are applied. The units are cycles per 512 pixels. The upper cutoff frequencies are chosen lower than the least frequency of the grid pattern. Therefore only fringe periods greater than the grid spacing can be evaluated.

The resulting interference phase distributions modulo 2π are given in gray-scale display in Figs. 5.25c and d. The phase $\Delta\phi_1$ of Fig. 5.25c is produced with the filter in the $+u$ -halfplane, while the phase $\Delta\phi_2$ of Fig. 5.25d stems from the filter in the $+v$ -halfplane. Artificial phases are given by the numerical process to pixels where no interference was present and these regions are masked out during further processing [457].

For the subsequent interactive sign correction, all pixels, where the two phase distributions differ less than a threshold, here chosen as 0.1, are marked:

$$||\Delta\phi_1(x, y)| - |\Delta\phi_2(x, y)|| < 0.1. \quad (5.55)$$

The borders of these regions are defined only along those lines, Fig. 5.25e, at which the phase takes the values $+\Delta\phi_1$, $-\Delta\phi_1$, $+\Delta\phi_2$, and $-\Delta\phi_2$. In this way a sufficiently continuous crossing of the borders is provided. The regions are shown in Fig. 5.25f, and the sign-corrected interference phase distribution modulo 2π is displayed in Fig. 5.25g. The demodulation, see Section 5.9, now leads to the continuous phase distribution of Fig. 5.25h, which as a pseudo-3D-display is shown in Fig. 5.25i.

5.6.4 Fourier Transform Evaluation of Phase Shifted Interferograms

Sign ambiguity is always present in the case of the evaluation of a single interferogram. After interactive sign correction, as demonstrated above, there remains at least a global sign ambiguity, which means the correct sign is assigned to all phase values or the wrong sign is given to all phases. An exact determination of the sign distribution is obtained if an additional phase stepped interferogram is produced with a mutual phase step ϕ_R [44, 458, 459]. Theoretically, ϕ_R must be in the range $0 < \phi_R < \pi$ but, in practice, values $\pi/3 < \phi_R < 2\pi/3$ are recommended. If this condition is fulfilled, the exact value of ϕ_R does not need to be known [44, 452].

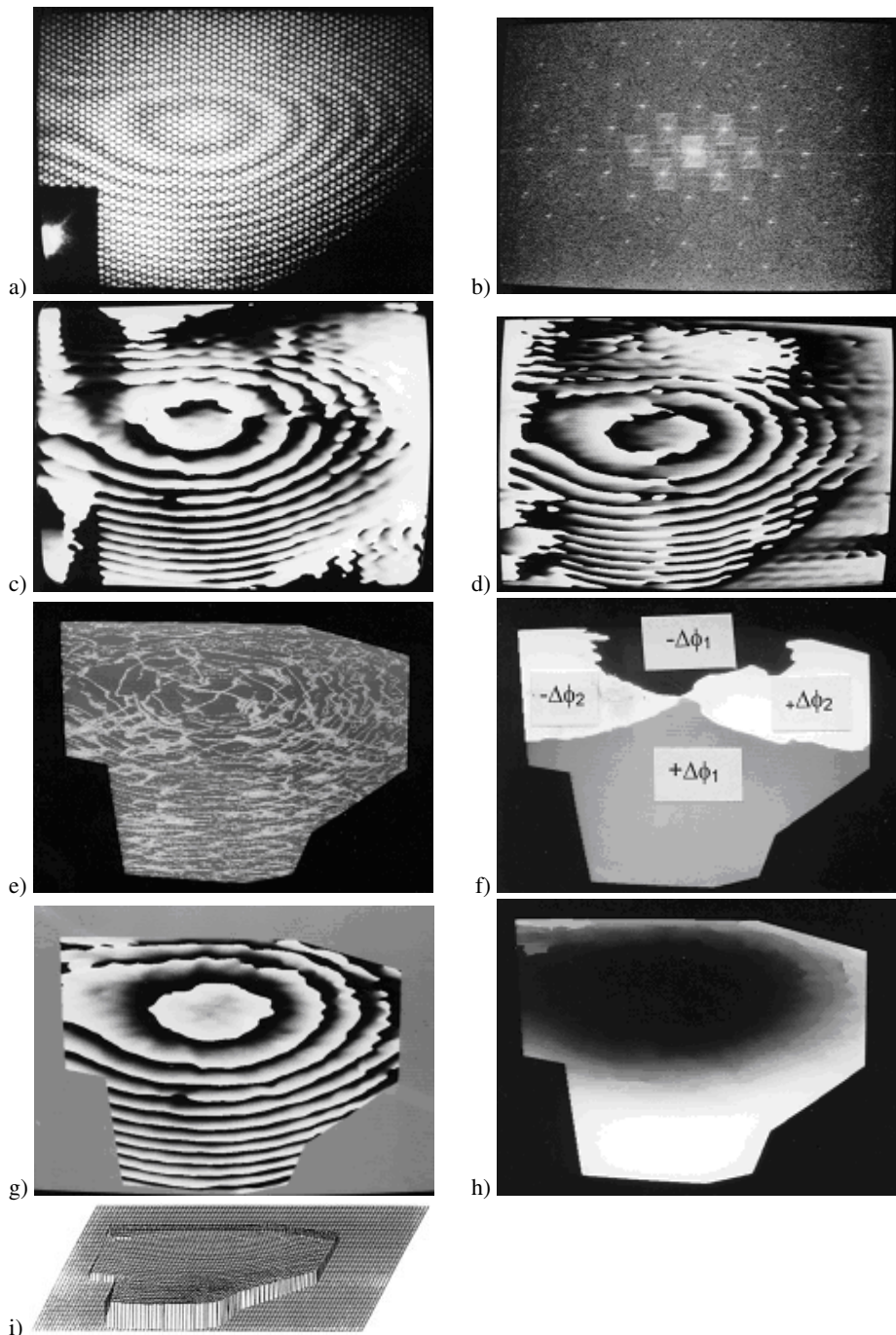


Figure 5.25: Fourier transform evaluation of thermally loaded plate.

The single phase stepping complicates the experimental procedure, but less than with the phase step methods, where several constant phase steps have to be provided. Let us now write the two intensity distributions

$$\begin{aligned} I_1(x, y) &= a(x, y) + b(x, y) \cos [\Delta\phi(x, y)] \\ I_2(x, y) &= a(x, y) + b(x, y) \cos [\Delta\phi(x, y) + \phi_R]. \end{aligned} \quad (5.56)$$

Fourier transform processing of each intensity with the same bandpass filter parameters yields

$$\begin{aligned} c_1(x, y) &= \frac{1}{2} b(x, y) \exp[i\Delta\phi(x, y)] \\ c_2(x, y) &= \frac{1}{2} b(x, y) \exp[i\Delta\phi(x, y) + i\phi_R(x, y)]. \end{aligned} \quad (5.57)$$

From (5.57) $\phi_R(x, y)$ is computed pointwise as

$$\phi_R(x, y) = \arctan \frac{\operatorname{Re} c_1(x, y) \operatorname{Im} c_2(x, y) - \operatorname{Im} c_1(x, y) \operatorname{Re} c_2(x, y)}{\operatorname{Re} c_1(x, y) \operatorname{Re} c_2(x, y) + \operatorname{Im} c_1(x, y) \operatorname{Im} c_2(x, y)}. \quad (5.58)$$

The knowledge of $\phi_R(x, y)$ is used for determination of the sign-corrected interference phase distribution via

$$\Delta\phi(x, y) = \operatorname{sign}[\phi_R(x, y)] \arctan \frac{\operatorname{Im} c_1(x, y)}{\operatorname{Re} c_1(x, y)}. \quad (5.59)$$

Figures 5.26a and b show two phase stepped holographic interferograms. The sign of $\phi_R(x, y)$ as calculated by (5.58) is shown in Fig. 5.26c. Figure 5.26d displays the phase distribution modulo 2π and Fig. 5.26e shows the sign-corrected phase distribution modulo 2π , calculated by (5.59). The demodulated interference phase distribution in a 3D display is shown in Fig. 5.26f.

The Fourier transform calculation of the phase step by (5.58) allows a generalization of the phase step method of Section 5.5. Having recorded three or more phase stepped interference patterns with arbitrary phase steps, provided that these are $< \pi$, the phase steps ϕ_{Rn} can be evaluated by the Fourier transform procedure described above [460]. Taking the average of the absolute values $|\phi_{Rn}|$, we get the phase steps which are used to set up a system of equations similar to (5.21). This system is solved and the interference phase calculated by (5.22). This *generalized phase shifting interferometry*, using additional parallel Fizeau fringes which are evaluated by the Fourier transform method with spatial carrier, is presented in [142].

5.6.5 Spatial Heterodyning

In *spatial heterodyning* an additional *carrier frequency* is added to the interference pattern [43, 461–473]. A common way of generating the spatial carrier frequency in interferometry is to give a relatively large tilt to the reference mirror [470]. To produce linear fringes in holographic interferometry, the object beam may be swung between the two exposures [474], the object may be tilted [475], or in a two reference wave arrangement the hologram position or the reference wave angles during reconstruction are properly controlled [476]. Great care must be taken to have a sensitivity vector not varying too much, to get equidistant carrier fringes. To

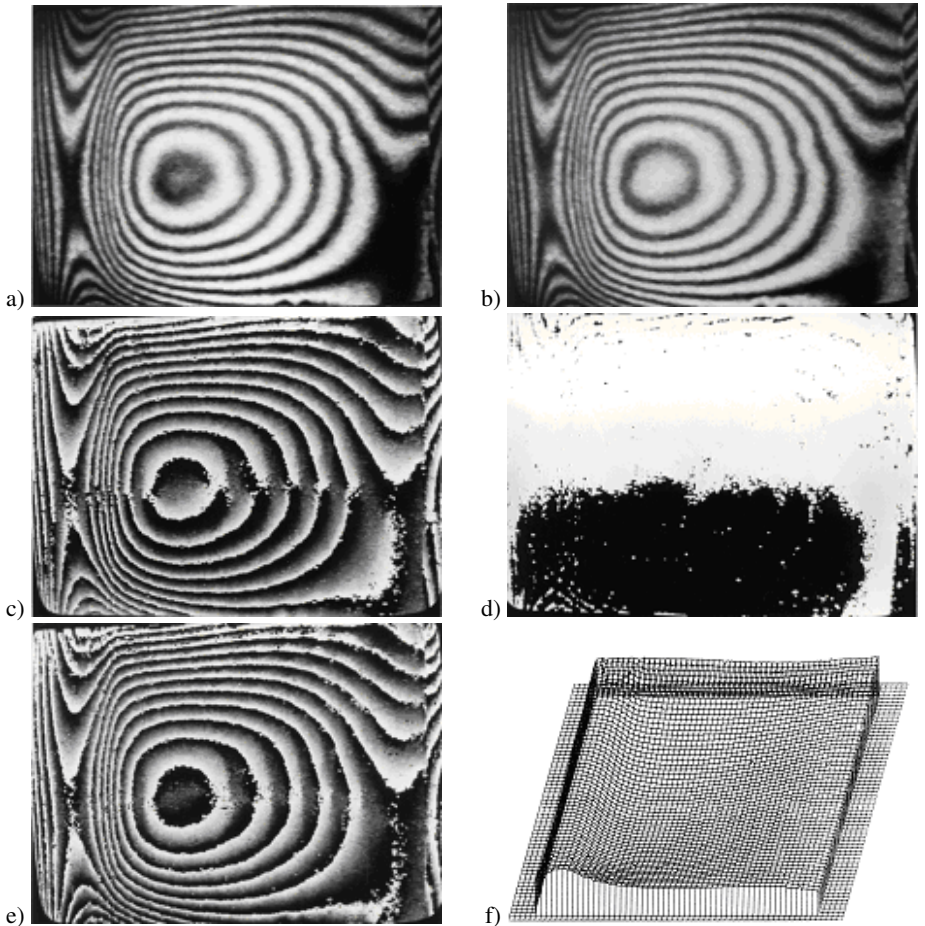


Figure 5.26: Fourier transform evaluation of phase shifted interferograms.

fulfill the sampling theorem the employed detector array must have a spatial resolution high enough to resolve the spatial carrier and the spatial distribution of the detector sensitivity must be uniform over the array. For holographic measurements of phase objects, in [477] the use of Young's fringes as carriers, produced by a laterally shifted diffuser, is suggested. Cylindrical fringe carriers are treated in [478].

Now let us assume that the spatial carrier has the fixed frequency f_0 . Without loss of generality we further assume that the carrier fringes are parallel to the y -axis, meaning the carrier frequency has only an x -component. The recorded intensity pattern then is

$$I(x, y) = a(x, y) + b(x, y) \cos[\Delta\phi(x, y) + 2\pi f_0 x]. \quad (5.60)$$

The formal analogy of (5.60) to temporal heterodyning (5.11) should be noticed. As for the

Fourier transform evaluation now using (5.49) this intensity is written

$$I(x, y) = a(x, y) + c(x, y) \exp(2\pi i f_0 x) + c^*(x, y) \exp(-2\pi i f_0 x). \quad (5.61)$$

The Fourier transform of the intensity with respect to x then yields [479]

$$\mathcal{I}(u, y) = \mathcal{A}(u, y) + \mathcal{C}(u - f_0, y) + \mathcal{C}^*(u + f_0, y). \quad (5.62)$$

Since the chosen spatial carrier frequency f_0 is higher than the spatial variations of $a(x, y)$, $b(x, y)$, and $\Delta\phi(x, y)$, the partial spectra \mathcal{A} , \mathcal{C} , and \mathcal{C}^* are well separated. \mathcal{A} is concentrated around the d.c.-term at $u = 0$ and carries the low frequency background illumination. \mathcal{C} and \mathcal{C}^* are placed symmetrically to the d.c.-term and are centered around $u = f_0$ and $u = -f_0$. If by an adequate bandpass filter first \mathcal{A} and \mathcal{C}^* are eliminated, and then $\mathcal{C}(u - f_0, y)$ is shifted by f_0 toward the origin, the carrier is removed and we obtain $\mathcal{C}(u, y)$. Taking the inverse Fourier transform of $\mathcal{C}(u, y)$ with respect to u yields $c(x, y)$ defined by (5.49). From this $c(x, y)$ the interference phase is calculated by (5.53) with phase values lying between $-\pi$ and $+\pi$. An alternative to the Fourier transform evaluation is the fitting of modified sinusoids to the carrier fringes [480].

A combination of spatial and temporal heterodyning is used for the simultaneous recording of multiple phase objects on a single *space-time interferogram* [207]. Although the method was proposed originally for Michelson- and Mach-Zehnder-type interferometers, it may be used in holographic interferometry as well. An interferogram of the form

$$I(x, y, t) = a(x, y, t) + b(x, y, t) \cos[\Delta\phi(x, y, t) + 2\pi(f_{0X}x + f_{0Y}y + f_{0T}t)] \quad (5.63)$$

with the spatial carrier frequencies (f_{0X}, f_{0Y}) and the temporal carrier frequency f_{0T} can be evaluated by the three-dimensional form of the above evaluation scheme. Now phase variations with wider spatio-temporal bandwidths can be determined than would be possible by using only a single carrier frequency. Partial spectra $c_n(u, v, \omega)$ not separated by using either one of the carrier frequencies are separable when using both spatial and temporal carrier frequencies. Furthermore the spatio-temporal frequency bandwidth available for the system can be effectively utilized. Several images having bandwidths less than the image detection system can be recorded multiplexed on a single interferogram.

5.6.6 Spatial Synchronous Detection

Spatial heterodyning consists of filtering and shifting of frequency components in the spatial frequency domain. The analogue in the spatial domain is the *spatial synchronous detection* method of [481, 482]. This method assumes a holographic interference pattern with a spatial carrier as described by (5.60). The spatial carrier may be artificially introduced by tilting one of the interfering wavefronts or is a constituent of the interference pattern.

In spatial synchronous detection the recorded and stored intensity, (5.60), is multiplied by R_1 and R_2 given by

$$\begin{aligned} R_1(x, y) &= \cos 2\pi f_0 x \\ R_2(x, y) &= \sin 2\pi f_0 x. \end{aligned} \quad (5.64)$$

The multiplication results in

$$\begin{aligned} I(x, y)R_1(x, y) \\ = [a(x, y) + b(x, y) \cos(\Delta\phi(x, y) + 2\pi f_0 x)] [\cos 2\pi f_0 x] \\ = a(x, y) \cos 2\pi f_0 x + \frac{b(x, y)}{2} \cos(\Delta\phi(x, y) + 4\pi f_0 x) + \frac{b(x, y)}{2} \cos(\Delta\phi(x, y)). \end{aligned} \quad (5.65)$$

and

$$\begin{aligned} I(x, y)R_2(x, y) \\ = [a(x, y) + b(x, y) \cos(\Delta\phi(x, y) + 2\pi f_0 x)] [\sin 2\pi f_0 x] \\ = a(x, y) \sin 2\pi f_0 x + \frac{b(x, y)}{2} \sin(\Delta\phi(x, y) + 4\pi f_0 x) - \frac{b(x, y)}{2} \sin(\Delta\phi(x, y)) \end{aligned} \quad (5.66)$$

Of the three terms in (5.65) and (5.66) the first is of high frequency, just the carrier frequency. The second term has an even higher frequency, but the third term represents a low spatial frequency component which can be separated from the remaining terms by low-pass filtering. Afterwards the interference phase is calculated from the isolated cosine- and sine-terms by (5.53).

The filtering in the spatial domain, intended to extract the third terms, is done by convolving the products IR_1 and IR_2 with a window function, which must be several fringe periods wide. This window function may be a rectangular window, or with better results, a Hanning window or one of the numerous others.

5.7 Dynamic Evaluation

Up to now in this chapter we have considered methods evaluating the interference fringes which appear superimposed over the reconstructed virtual image of the object. The fringes are observed from a fixed point of observation. These approaches to the evaluation of holographic interference patterns can be summarized as the *static evaluation methods* [483].

On the other hand the holographic interference fringes are generally localized in space, Section 4.3, so different observation points generate different interference patterns. A continuous variation of the observation point thus will induce a continuous change of the observed interferogram during reconstruction. This is the basic idea behind the so called *dynamic evaluation methods*, which were proposed very early after the invention of holographic interferometry [37, 287, 484]. But despite some conceptual advantages the dynamic methods have not found the as widespread applications as like the static methods.

5.7.1 Principles of Dynamic Evaluation

In the dynamic evaluation methods the interference orders are counted which are moving over a single observed object point while the observation point is continuously changed. Let us consider the case of a deformation of an opaque surface. An arbitrary point P of the surface may be displaced by the vector $\mathbf{d}(P)$ between the two exposures of a *double exposure hologram*, Fig. 5.27. Let this point be observed from an observation point which continuously moves from B_1 to B_2 , then according to (4.20) and (4.21) the interference phase changes from

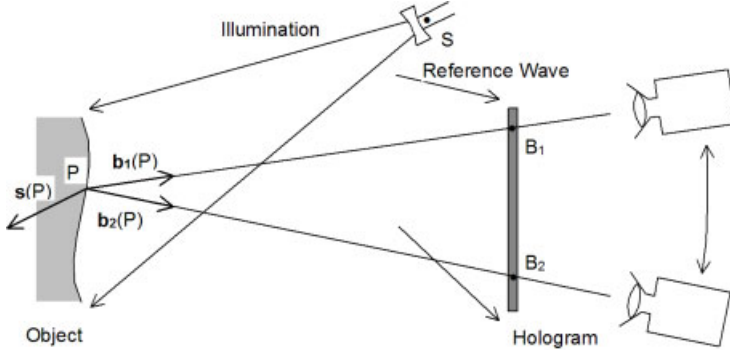


Figure 5.27: Geometry for dynamic evaluation.

$\Delta\phi_1(P) = \frac{2\pi}{\lambda} \mathbf{d}(P) \cdot [\mathbf{b}_1(P) - \mathbf{s}(P)]$ to $\Delta\phi_2(P) = \frac{2\pi}{\lambda} \mathbf{d}(P) \cdot [\mathbf{b}_2(P) - \mathbf{s}(P)]$. What has to be measured is the interference phase difference $\Delta\Delta\phi_{1,2}(P)$ between the two observation points B_1 and B_2 , which is

$$\begin{aligned}\Delta\Delta\phi_{1,2}(P) &= \Delta\phi_2(P) - \Delta\phi_1(P) \\ &= \frac{2\pi}{\lambda} \mathbf{d}(P) \cdot [\mathbf{b}_2(P) - \mathbf{b}_1(P)].\end{aligned}\quad (5.67)$$

This is the central equation for the dynamic evaluation methods.

Two advantages of the dynamic methods now become obvious: (1) the interference phase difference does not depend on the illumination vector $\mathbf{s}(P)$, and (2) there is no absolute phase problem, since the additive phase term which is identical in $\Delta\phi_1(P)$ and $\Delta\phi_2(P)$, is canceled in the subtraction leading to $\Delta\Delta\phi_{1,2}(P)$. What remains is the necessity to determine $\Delta\Delta\phi_{1,2}(P)$ with the proper sign distribution; especially sign changes which may occur for complicated curves of localization must be recognized exactly.

The main sensitivity of the dynamic evaluation methods is in direction $\mathbf{b}_2(P) - \mathbf{b}_1(P)$, which is roughly parallel to the hologram plane and thus in most applications nearly tangential to the object surface. This complements the static methods, where the main sensitivity is for displacements in direction $\mathbf{b}(P) - \mathbf{s}(P)$, which is nearly normal to the surface.

If a one-dimensional displacement parallel to the hologram plane has to be evaluated, a single measurement of $\Delta\Delta\phi_{1,2}(P)$ suffices and a scalar form of (5.67) has to be solved for $d(P)$. For a two-dimensional displacement two measurements $\Delta\Delta\phi_{1,2}(P)$ and $\Delta\Delta\phi_{3,4}(P)$ are required, which may be evaluated from a single hologram if both displacement components are parallel to the hologram. In the general three-dimensional case three observations are necessary and the three-dimensional system of equations (5.67) has to be solved. The three observations can be taken through two holograms whose normals should form a significantly large angle, $> 30^\circ$, to the best a 90° angle. An alternative to the second hologram can be a mirror close to the object, so that the investigated object point can be observed in two directions employing a single hologram [37].

5.7.2 Dynamic Evaluation by a Scanning Reference Beam

A straightforward approach to dynamic evaluation is to record many static reconstructions during a shift of the camera whose optical axis is kept intersecting a fixed object surface point in the virtual image. The angular separation between the frames must be small enough that the fringe count cannot be lost during data analysis. In [483] this was performed with 39 data frames, which were recorded and evaluated with the image processing facilities of those days. The experimental error could be restricted to about 5 %.

A more direct fringe counting is possible if the reconstruction of the holographic interferogram is performed by a thin reconstruction beam conjugate to the original reference beam [485, 486]. In this way, a real object image is obtained at the position of the original object, Fig. 5.28. The position of the reconstruction beam on the hologram plate defines the actual observation point. When the position of the reconstruction beam on the hologram is changed, the projected fringes move across the real image of the object surface. The varying intensity is recorded by a photodetector placed at the object point whose displacement is to be evaluated. To get the displacements at many points the detector position must be scanned over the real image, the same way as in temporal heterodyning, Section 5.4.

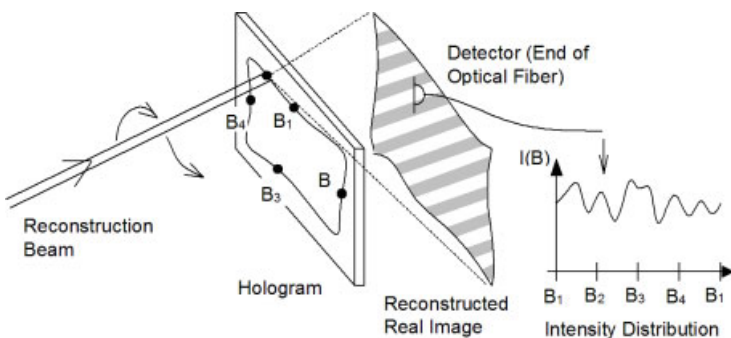


Figure 5.28: Dynamic evaluation by a scanning reconstruction beam.

Due to the small beam diameter, the aperture at the hologram is low and thus fulfills the requirements of the *observer projection theorem*, Section 4.3.5. That means the fringes are projected onto the real image plane independently of the localization in space.

The hologram may be scanned along several lines by a conjugate reference beam, which is produced by a spherical mirror or a converging lens corrected for spherical aberrations. Since more than three measurements now are taken, (5.67) is evaluated by the least squares method [486].

A thin conjugate reference beam can scan along closed loops. A repeated closed loop scan may filter temporal fluctuations by averaging. Arbitrary pairs of observation points B_i now can be chosen from the loop, Fig. 5.28 [485, 487–489].

Nothing is found in the literature about how the fringes, especially fractions of the fringes, are counted, or about the translation of the recorded intensity to interference phase. A change from increasing to decreasing interference order, or vice versa, must be detected. In this context the closed loop scanning offers some advantages: The phase difference along one whole

turnaround must be zero. If the interference phase is calculated by one-dimensional Fourier transform evaluation, Section 5.6, due to the continuous junction at the ends of a whole-turn sample, there is no wrap-around error. Turning points of the fringe order, which must be existent, should be easily detected in the primarily monotonic phase distribution after Fourier transform evaluation. On the other hand phase shifting combined with dynamic evaluation should be in principle feasible.

A major drawback of the dynamic evaluation is the existence of moving parts in the evaluation configuration and the necessary scanning of the real image, comparable to temporal heterodyning.

5.8 Digital Holographic Interferometry

In this section the advantages of digital holography as the base of holographic interferometry will be presented. Up to now single digital holograms and the related reconstructed wave fields have been treated. In this section it will be shown that instead of a digital reconstruction of a double exposure hologram and evaluation of the resulting intensity field the reconstructed phase fields can be directly compared [56, 490]. The cumbersome and error prone computer-aided evaluation methods for determination of the interference phase distribution from intensity patterns now become obsolete. It will be demonstrated that sign-correct interference phases are obtained with minimum noise, high resolution, and an experimental effort which is significantly less than e. g. with any phase step methods. Additional possibilities offered by digital holography will be introduced. These are related to the recording of a series of digital holograms for different loading and thus deformation states, where the decision as to which holograms are compared interferometrically is drawn later in the reconstruction stage. A further aspect is the subtraction of fixed phase distributions to extract hidden structures in the interference phase map, a method which can be compared to the optical sandwich holography technique. If we are interested in the 3D deformation field, several digital holograms from the same surface, but illuminated from different directions, have to be taken. Here some realizations and the related results are presented.

5.8.1 Digital Phase Subtraction

As a first attempt at digital holographic interferometric measurement the already known double exposure technique, Section 4.1.1, should be digitally realized. For this purpose the two digital holograms representing two deformation states of the object surface are recorded and stored and then summed to mimic the optical double exposure onto one holographic plate. The digital sum-hologram now can be numerically reconstructed by application of the Fresnel transform or the convolution approach. From the resulting complex wave field the intensity distribution is calculated which corresponds to the interference pattern of conventional optical holographic interferometry. One of the phase evaluation methods introduced earlier in the chapter, like fringe tracking or Fourier transform evaluation, now can be employed for the determination of the interference phase distribution from this intensity pattern.

An example of this digital counterpart to the double exposure method is shown in Fig. 5.29. The experiment is the same as the one leading to Fig. 3.19. The parameters are

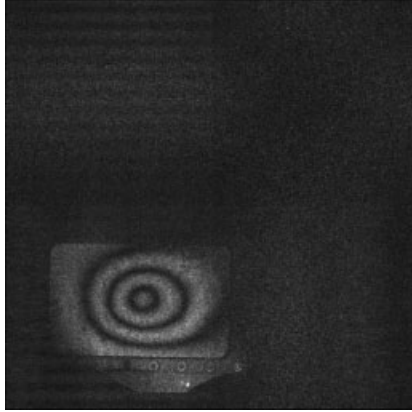


Figure 5.29: Intensity reconstructed from a sum-hologram.

$N = M = 2048$, $\lambda = 0.6328 \mu\text{m}$, $\Delta\xi = \Delta\eta = 9.0 \mu\text{m}$. The two digital holograms recorded before and after a central pressure loading from the back side of an aluminum plate have been added. The sum-hologram then was high-pass filtered according to (3.59) to eliminate the d.c.-term. Figure 5.29 gives the intensity of the reconstructed wave field which is the same as the optically reconstructed intensities used in the past.

But the full advantages of digital holography in interferometric metrology only become apparent if we make use of the capability to reconstruct full complex wave fields instead of just intensities: In digital holography we have numerical access to the phase distributions of the wave fields without the need of complicated techniques like phase shifting.

If the two digital holograms are individually reconstructed and their phase distributions are calculated, then the interference phase can be determined in a pointwise manner by a modulo 2π subtraction. This is the right branch in the diagram of Fig. 5.30. There both possible evaluation procedures in digital holographic interferometry are shown.

While in the left branch we have the digital simulation of the double exposure method, on the right we have

$$\begin{aligned} b_1'(n, m) &= b_{r1}'(n, m) + ib_{i1}'(n, m) \\ \text{and } b_2'(n, m) &= b_{r2}'(n, m) + ib_{i2}'(n, m) \end{aligned} \quad (5.68)$$

the two reconstructed wave fields corresponding to the two object states to be compared interferometrically. The subscripts r and i denote the real and the imaginary parts.

Then the two phase distributions

$$\begin{aligned} \phi_1(n, m) &= \arctan \frac{\text{Im}\{b_1'(n, m)\}}{\text{Re}\{b_1'(n, m)\}} = \arctan \frac{b_{i1}'(n, m)}{b_{r1}'(n, m)} \\ \phi_2(n, m) &= \arctan \frac{\text{Im}\{b_2'(n, m)\}}{\text{Re}\{b_2'(n, m)\}} = \arctan \frac{b_{i2}'(n, m)}{b_{r2}'(n, m)} \end{aligned} \quad (5.69)$$

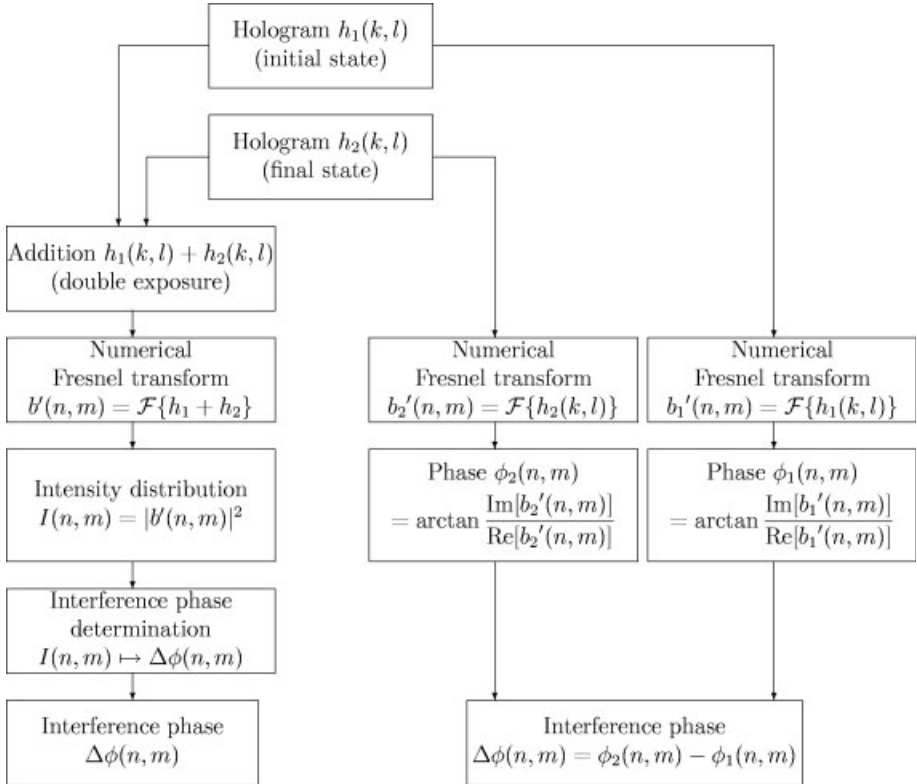


Figure 5.30: Alternative evaluation procedures in digital holographic interferometry.

are determined from which by

$$\Delta\phi(n,m) = \begin{cases} \phi_2(n,m) - \phi_1(n,m) + 2\pi & \text{if } \phi_2(n,m) - \phi_1(n,m) < -\pi \\ \phi_2(n,m) - \phi_1(n,m) - 2\pi & \text{if } \phi_2(n,m) - \phi_1(n,m) \geq +\pi \\ \phi_2(n,m) - \phi_1(n,m) + 2\pi & \text{otherwise} \end{cases} \quad (5.70)$$

the interference phase modulo 2π can be calculated. Here we have assumed that the calculations of (5.69) yield values in the range $]-\pi, +\pi]$.

A more direct calculation of the phase difference $\Delta\phi(n,m)$ without the need for discriminating the cases as in (5.70) is

$$\begin{aligned} \Delta\phi(n,m) &= \arctan \frac{b_{r1}'(n,m)b_{i2}'(n,m) - b_{r2}'(n,m)b_{i1}'(n,m)}{b_{r1}'(n,m)b_{r2}'(n,m) + b_{i1}'(n,m)b_{i2}'(n,m)} \\ &= \arctan \frac{\text{Im}\{b_2'(n,m)b_1'^*(n,m)\}}{\text{Re}\{b_2'(n,m)b_1'^*(n,m)\}}. \end{aligned} \quad (5.71)$$

Without the detour over the intensity, which destroys the sign information due to $\cos(-\phi) = \cos(\phi)$, here the calculated interference phase distribution is sign-correct. Increasing as well as

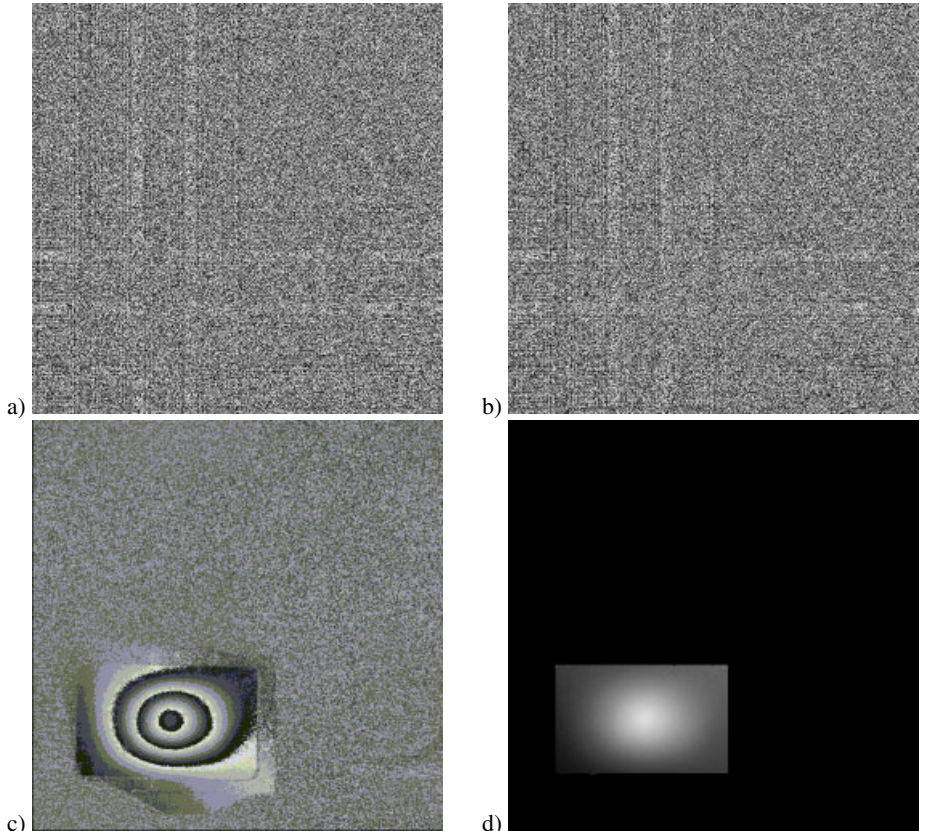


Figure 5.31: Reconstructed phases (a) and (b), phase difference modulo 2π (c), demodulated phase difference (d).

decreasing phases in any direction are correctly detected. An evaluation according to the right branch in this flow-graph is recommended in every application. The digital holograms of the experiment leading to Figs. 3.19 and 5.29 after individual reconstruction yield the two phase distributions $\phi_1(n, m)$ and $\phi_2(n, m)$ shown in Figs. 5.31a and b. They look rather random, no significant information can be recognized. But the subtraction of the two phases produces the phase difference modulo 2π given in Fig. 5.31c. No flipping of the phase variation direction is present like in Fourier transform evaluation, the result is sign-correct. The high resolution allows the direct application of a phase unwrapping procedure to produce the demodulated phase variation, Fig. 5.31d.

The benefits of d.c.-term suppression in digital holographic interferometry are evident. Figure 5.32a displays the phase difference determined in the same way as that of Fig. 5.31c but here without high-pass filtering of the two digital holograms to suppress the d.c.-term.

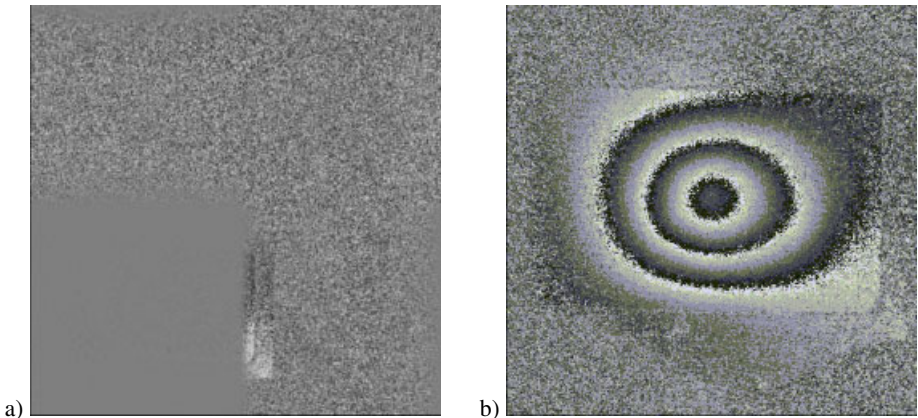


Figure 5.32: Phase difference without d.c.-term suppression (a) and after reconstruction by convolution (b).

The reconstructions leading to the results in Fig. 5.31 were performed by the Fresnel transform. A reconstruction by the convolution approach and the same phase subtraction as before gives the interference phase distribution of Fig. 5.32b. Despite the different pixel sizes and thus the other format of the object in the reconstructed image we have the same resolution of the measured interference phase values. The sharper appearance of the smaller object in Fig. 5.31c is only due to the pixel size. If we average the phase values over several pixels in the distribution of Fig. 5.32b to obtain pixels of the same size as in Fig. 5.31c we will get an identical image.

5.8.2 Enhancement of Interference Phase Images by Digital Filtering

The interference phase distributions generated by digital holographic interferometry as introduced in 5.8.1 exhibit already low noise. The signal-to-noise ratio is typically in the same range as that of phase differences determined by one of the phase shift methods. However, in the sawtooth-like display of the modulo 2π distributions even low-amplitude distortions appear visually annoying, since any single correct value below π that is slightly shifted above π occurs as an isolated black point in a neighborhood of bright points. In the same way a value that is erroneously below $-\pi$ although it correctly must be slightly above $-\pi$, will establish a bright pixel surrounded by dark ones. Therefore to produce a visually attractive interference phase image and to enable a reliable phase unwrapping, a smoothing of the interference phase by digital filtering should be performed.

A simple low-pass filtering, e. g. by replacing each pixel value by the average value of all neighboring pixel values, only is feasible when applied to already demodulated interference phase distributions. If applied to phase differences modulo 2π it will grind down the sharp edges at the 2π -jumps, thus introducing additional errors in the subsequent demodulation process.

It is well known that median filters behave similarly to low-pass filters. They effectively eliminate erroneous isolated points, but only to a certain degree they are edge-preserving. *Median filters* replace the value of each pixel by the median of the values of all pixels in a neighborhood of this pixel. The median of a finite set of values is that value for which there exist the same number of higher values as lower values in the set. The main parameter is the cardinality of the set, here the size of the neighborhoods. Frequently used square neighborhoods have 3×3 , 5×5 , or 7×7 pixels. The higher the pixel number of the used neighborhoods, the smoother the filtered phase distribution will look, but simultaneously the trend to round out the 2π -jumps also increases. This is demonstrated by an example in Fig. 5.33 where an

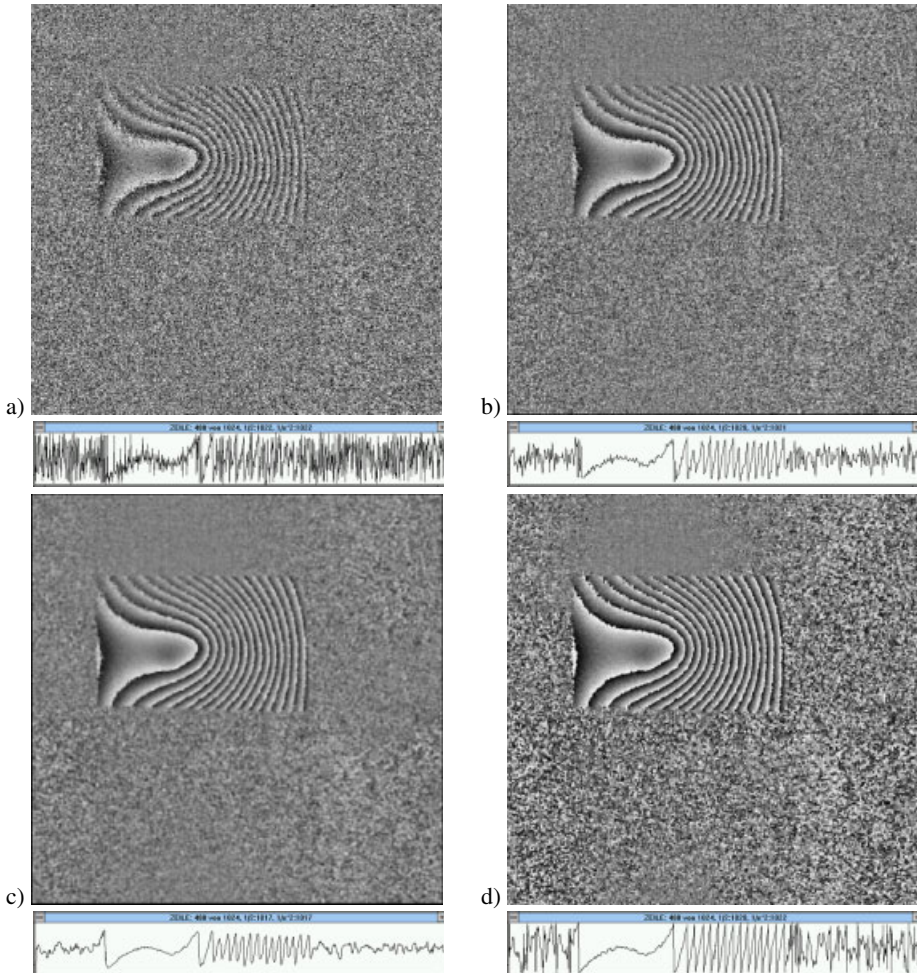


Figure 5.33: Filtering of interference phase distributions.

aluminum plate clamped at the edges was shifted horizontally and centrally pressed from the back side. A negative lens formed a small virtual image of the large object as described in

Section 3.1.2. A normally impinging plane reference wave was used. The interference phase distribution modulo 2π obtained by reconstruction with elimination of the d.c.-term and by subtracting the phases is shown in Fig. 5.33a. Figure 5.33b gives the result after application of a median filter that uses 3×3 -neighborhoods, Fig. 5.33c displays the same for a median filter considering 7×7 -pixel neighborhoods. The effects of the smoother phase variation, but also the amplitude decrease at the 2π -jumps, are obvious.

However, there is a filter that performs even better in smoothing the phase while keeping the 2π -jumps at full amplitude. For this filter first the distributions $s(n, m)$ and $c(n, m)$ are calculated by

$$\begin{aligned} s(n, m) &= \sin[\Delta\phi(n, m)] \\ c(n, m) &= \cos[\Delta\phi(n, m)]. \end{aligned} \quad (5.72)$$

Although $\Delta\phi(n, m)$ is modulo 2π , $s(n, m)$ and $c(n, m)$ show no 2π -discontinuities. They are both smoothed by a conventional low-pass filter, e. g. one replacing each value by the average value over square $k \times k$ -pixel neighborhoods. After this filtering of $s(n, m)$ and $c(n, m)$ the filtered version of $\Delta\phi(n, m)$ is determined by

$$\Delta\phi_f(n, m) = \arctan \frac{s_f(n, m)}{c_f(n, m)}. \quad (5.73)$$

The subscript f denotes the low-pass filtered versions of the corresponding distributions. The result of such a filter applied to the interference phase distribution of Fig. 5.33a is given in Fig. 5.33d. Here 5×5 -pixel neighborhoods have been used.

A low-pass filtering of the numerator and denominator of (5.71) individually will not succeed, since their amplitudes vary from pixel to pixel. The procedure via (5.71) and (5.72) leads to normalized amplitudes.

Normalized $s(n, m)$ and $c(n, m)$ can be determined by

$$\begin{aligned} s(n, m) &= \frac{b_{r1}'(n, m)b_{i2}'(n, m) - b_{r2}'(n, m)b_{i1}'(n, m)}{\sqrt{[b_{r1}'^2(n, m) + b_{i1}'^2(n, m)][b_{r2}'^2(n, m) + b_{i2}'^2(n, m)]}} \\ c(n, m) &= \frac{b_{r1}'(n, m)b_{r2}'(n, m) + b_{i1}'(n, m)b_{i2}'(n, m)}{\sqrt{[b_{r1}'^2(n, m) + b_{i1}'^2(n, m)][b_{r2}'^2(n, m) + b_{i2}'^2(n, m)]}}. \end{aligned} \quad (5.74)$$

These relations also result if $\sin(\arctan x) = x/\sqrt{1+x^2}$ and $\cos(\arctan x) = 1/\sqrt{1+x^2}$ are applied to (5.71).

5.8.3 Evaluation of Series of Holograms

The availability of the individual reconstructed phase distributions in digital holographic interferometry offers flexible metrologic applications. Thus one may record a series of digital holograms with gradually increased load amplitude. In the evaluation stage the convenient states can be interferometrically compared. The best combination of reconstructed phase distributions from all holograms is selected. A criterion for this selection can be the detectability of the interference orders in the resulting phase difference images. An analogous approach in

optical holographic interferometry is known as *sandwich holography*: The states to be combined are recorded onto individual hologram plates, which are combined to a sandwich in the evaluation stage. This sandwich is reconstructed like a double-exposure hologram.

In the following a typical experiment of this kind is presented. The object is an aluminum plate clamped at its edges and positioned on a micro-stage. The reduced virtual image of the plate's surface is at a distance $d = 0.254$ m from the CCD array. This has $N \times M = 1024 \times 1024$ pixels of dimensions $\Delta\xi = \Delta\eta = 6.8$ μm . The laser wavelength is $\lambda = 0.6328$ μm , a normally impinging plane reference wave is guided to the CCD over a beam splitter cube. The refractive index of this cube is already recognized in the distance d . Two different displacements of the surface are possible:

- a deformation by a central pointwise pressure load from the back side of the aluminum plate, and
- a horizontal in-plane rigid body shift of the plate.

Eight digital holograms have been recorded with the displacements applied in accordance to the scheme shown in Fig. 5.34.

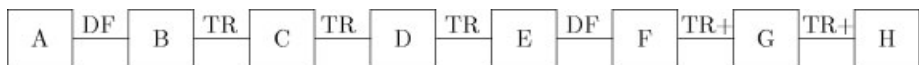


Figure 5.34: Scheme of the displacements and recordings of holograms.

The single capitals denote the recorded digital holograms while the terms between the boxes characterize the motions: DF denotes the deformations and TR stands for a translation. TR+ indicates a translation of higher amplitude than TR.

After reconstruction and calculation of the phase distributions of all digital holograms A to H combinations of phase distributions have been used for subtraction. Figure 5.35 shows some of the resulting interference phase distributions modulo 2π . The combination of holograms A and B displays the typical pattern of a bump produced by a pointwise pressure load. The comparison of holograms B and C exhibit the vertical fringes characteristic for the horizontal in-plane translation. The combination of these two motions leads to the pattern resulting from subtraction of the phases of holograms A and C. The high amplitude translation between holograms G and H leads to high density fringes which are just detectable, on the other hand the even higher amplitude translation between F and G lets the fringes disappear in noise.

In quantitative holographic interferometry it is generally not possible to determine multi-dimensional displacement vectors from a single interference pattern. One needs several interferograms, recorded with various sensitivity vectors, to obtain the data to define a multidimensional system of equations, which has to be solved. However, if the displacement is composed of elementary motions, e. g. rigid body translations, and if we have the ability to perform these motions separately with recording of the digital holograms between the single motions, then we can separate the motions numerically as is demonstrated for holograms A, B, and C of the aforementioned example.

On the object surface we fix three evaluation points P_l , P_c , and P_r , where the subscripts stand for left, center, and right. The angles between the optical axis and all lines between object points and CCD array points remain small, so the unit vector in the observation direction

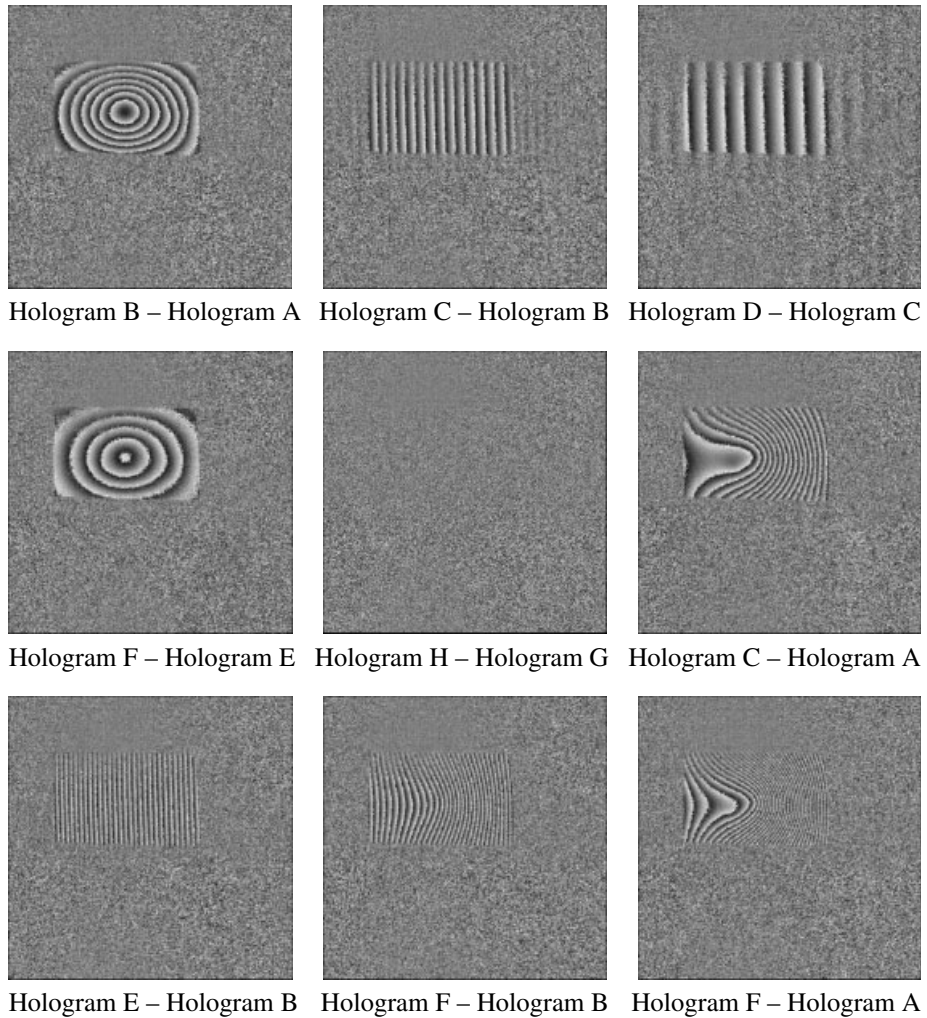


Figure 5.35: Evaluation of a series of digital holograms: interference phase distributions of various combinations.

can be set $\mathbf{b} = (0, 0, 1)$ for all three points. The illumination poses no special conditions on the angles. From the geometry of the holographic arrangement we get the unit vectors in the illumination direction $\mathbf{s}_l = (0.38, 0, -0.93)$, $\mathbf{s}_c = (0.49, 0, -0.87)$, and $\mathbf{s}_r = (0.58, 0, -0.82)$. The differences of the unit vectors are $\mathbf{e}_l = (-0.38, 0, 1.93)$, $\mathbf{e}_c = (-0.49, 0, 1.87)$, and $\mathbf{e}_r = (-0.58, 0, 1.82)$. The interference pattern resulting from comparison of holograms A and B describes a continuous deformation that has only a component in the z -direction. Due to the clamping the interference orders at the left and the right edges are $n = 0$, to the center we count $n = 6.5$. According to $n\lambda = \mathbf{d} \cdot \mathbf{e} = d_z \cdot e_z$ we obtain the z -displacement at the central point caused by the load from the back $d_{zc} = 6.5 \times 0.6328 \mu\text{m}/1.87 = 2.2 \mu\text{m}$. From the

interferogram stemming from holograms B and C we detect an interference order at the right edge that is 15 periods less than that at the left edge, i. e. $n_r = n_l - 15$. The absolute fringe order is unknown, but along the whole surface we must have a constant translation d_x . From the two equations $n_l = d_x \cdot e_{xl}/0.6328 \mu\text{m}$ and $n_l - 15 = d_x \cdot e_{xr}/0.6328 \mu\text{m}$ we obtain the translation $d_x = 47.5 \mu\text{m}$ as a solution. Now we can conclude on the interference orders in the interference pattern of the combined holograms A and C. The displacement vectors to the left, in the center, and to the right are $\mathbf{d}_l = (47.5, 0, 0)$, $\mathbf{d}_c = (47.5, 0, 2.2)$ and $\mathbf{d}_r = (47.5, 0, 0)$. From this the absolute interference orders $\mathbf{d}_l \cdot \mathbf{e}_l/\lambda = -28.52$, $\mathbf{d}_m \cdot \mathbf{e}_m/\lambda = -30.28$, and $\mathbf{d}_r \cdot \mathbf{e}_r/\lambda = -43.54$ result. Between the left edge and the center we have a difference of the interference orders of 1.76, between the center and the right edge this difference is 13.26. This can be controlled visually at the corresponding interferogram in Fig. 5.35. It is not possible to extract the absolute interference orders from only this single interferogram.

5.8.4 Compensation of Motion Components

In digital holographic interferometry the individual phase distributions are available numerically, therefore one may attempt to compensate motion components which lead to high fringe densities.

To make things not too complicated only rigid body translations in the plane of a plane surface should be investigated and we restrict the theoretical treatment to one dimension. A first attempt tries to shift one of the two holograms before the reconstruction process. But this does not lead to success, as can be proven theoretically with the help of the Fresnel approximation.

We have seen that if we shift a distribution $b(x)$ by a to $b(x-a)$ then the Fresnel transform $\mathcal{FR}\{b(x-a)\}$ is the Fresnel transform of $b(x)$ that is shifted by α and multiplied by a phase-factor β

$$\mathcal{FR}\{b(x-a)\} = e^{-i\pi\beta} B(\nu - \alpha) \quad (5.75)$$

where $B(\nu) = \mathcal{FR}\{b(x)\}$, $\alpha = 2\pi a/(d\lambda)$, and $\beta = 2a\nu - a^2/(d\lambda)$.

Let $R(\nu)$ be a reference wave for recording the hologram. Now we will show that even if α and β are known we cannot determine $h_1 = |R(\nu) + B(\nu)|^2$ from $H_2 = |R(\nu) + e^{-i\pi\beta} B(\nu - \alpha)|^2$. It is

$$\begin{aligned} h_1 &= (R_r + iR_i + B_r + iB_i)(R_r - iR_i + B_r - iB_i) \\ &= R_r^2(\nu) + R_i^2(\nu) + B_r^2(\nu) + B_i^2(\nu) + 2R_r B_r(\nu) + 2R_i B_i(\nu). \end{aligned} \quad (5.76)$$

On the other hand

$$\begin{aligned} h_2 &= (R_r + iR_i + \cos \pi\beta B_r + \sin \pi\beta B_i + i \cos \pi\beta B_i - i \sin \pi\beta B_r) \\ &\quad \times (R_r + iR_i + \cos \pi\beta B_r + \sin \pi\beta B_i - i \cos \pi\beta B_i + i \sin \pi\beta B_r) \\ &= R_r^2(\nu) + R_i^2(\nu) + B_r^2(\nu - \alpha) + B_i^2(\nu - \alpha) + 2 \cos \pi\beta R_r(\nu) B_r(\nu - \alpha) \\ &\quad + 2 \cos \pi\beta R_i(\nu) B_i(\nu - \alpha) + 2 \sin \pi\beta R_r(\nu) B_i(\nu - \alpha) - 2 \sin \pi\beta R_i(\nu) B_r(\nu - \alpha). \end{aligned} \quad (5.77)$$

In (5.77) we have dependencies on the arguments ν as well as on $\nu - \alpha$, which shows that in this general case a shift is not possible.

The ν -dependency in (5.77) only concerns the reference wave, therefore the special case of the normally impinging plane reference wave $R_r(\nu) = 1$, $R_i(\nu) = 0$ is considered because this reference wave does not depend on ν . We get

$$h_1 = 1 + B_r^2(\nu) + B_i^2(\nu) + 2B_r(\nu) \quad (5.78)$$

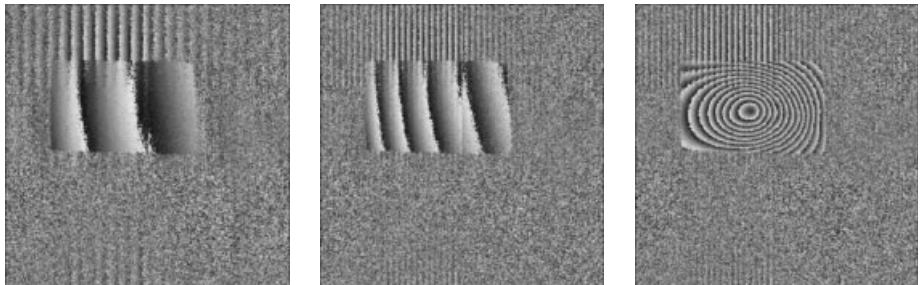
and

$$h_2 = 1 + B_r^2(\nu - \alpha) + B_i^2(\nu - \alpha) + 2 \cos \pi \beta B_r(\nu - \alpha) + 2 \sin \pi \beta B_i(\nu - \alpha). \quad (5.79)$$

A transformation of h_2 into h_1 for all ν by a shift would imply $\cos \pi \beta = 1$ and $\sin \pi \beta = 0$. By definition of β this is only possible for $a = 0$, which is a contradiction to the assumed non-vanishing shift. Altogether it is proven that by a mere shift of the digital hologram we cannot compensate any motion components.

However, a feasible approach is first to reconstruct the phase distributions from the holograms and to add or subtract a certain phase to one of the two or equivalently to the phase difference [491, 492]. This additional phase can be a linearly varying phase distribution. Although we will get no additional information by this procedure, sometimes fine details in the display of the interference phase distribution are better recognized.

This is shown in three examples in Fig. 5.36. Some phase distributions of the holograms leading to Fig. 5.35 have been used for this purpose. The reconstructed phases of holograms B and C have been compared with a phase subtracted that increases linearly from the left to the right. At the left edge of the reconstructed pattern this phase is 0 rad, it increases to the right edge by 150 rad $\approx 24 \times 2\pi$. The second example is with holograms B and E, the



Hologram C – Hologram B Hologram E – Hologram B Hologram F – Hologram A

Figure 5.36: Compensation of motion components by subtraction of linearly varying phases.

third one uses the holograms A and F. In both these cases the linear phase increase is 300 rad $\approx 48 \times 2\pi$. The density of the fringes on the reconstructed surface is significantly reduced. In the remaining low-density fringes now we see a tilt, which is not recognized before the compensation, Fig. 5.35. The reason for this inclination of the fringes is a spatial variation of the sensitivity vector. In the last of the three examples we had a combination of a rigid body translation and a bump. Of these the translation has been nearly completely eliminated.

One may notice interference fringes in the area of the suppressed d.c.-term. This pattern corresponds to the phase distribution of the subtracted linearly increasing phase. A similar approach as presented in this section is used by Gombkötö et al. [493].

5.8.5 Multiplexed Holograms Discriminated in Depth

In most practical applications of holographic interferometric deformation measurement one is only interested in the one-dimensional displacement distribution in the normal direction. This measurement is performed by using a sensitivity vector (4.20) normally oriented to the object's surface and varying as little as possible. Ideally one uses a collimated expanded object illumination beam. However, in various applications the whole three-dimensional displacement vector field has to be determined. Then several holographic interferograms belonging to different sensitivity vectors have to be produced and evaluated. The result of the evaluation of three interferograms is a set of three interference phase distributions $\Delta\phi_i(P)$, $i = 1, 2, 3$, which allow a solution of the system of equations (4.21)

$$\begin{pmatrix} \Delta\phi_1(P) \\ \Delta\phi_2(P) \\ \Delta\phi_3(P) \end{pmatrix} = \begin{pmatrix} d_x(P) \\ d_y(P) \\ d_z(P) \end{pmatrix} \begin{pmatrix} e_{1x}(P) & e_{1y}(P) & e_{1z}(P) \\ e_{2x}(P) & e_{2y}(P) & e_{2z}(P) \\ e_{3x}(P) & e_{3y}(P) & e_{3z}(P) \end{pmatrix}. \quad (5.80)$$

Different sensitivity vectors can be obtained by manifold ways: one can vary the illumination direction, one can vary the observation direction, or both simultaneously. A cheap, robust and reliable method is the recording of different views of the object's surface, corresponding to different observation directions, onto one hologram. The different views come from appropriately placed mirrors, a procedure already suggested by Schönebeck [494, 495].

This approach now should be transferred to digital holography. One has to be careful not to obtain too large angles between object and reference waves, see Section 3.1.1, therefore an arrangement as shown in Fig. 5.37 is suggested. It allows the simultaneous recording of the

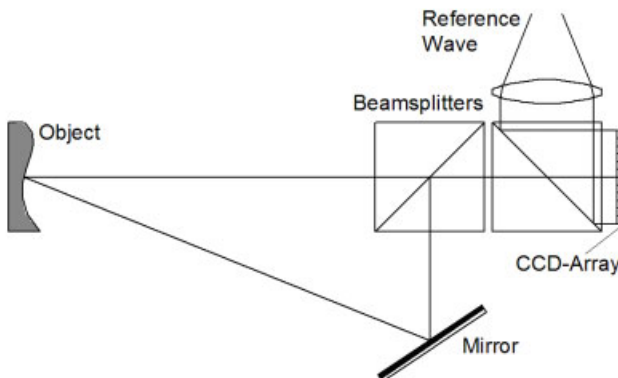


Figure 5.37: Arrangement for multiplexed digital holography.

wave field coming directly from the object and the one coming over the mirror. A third observation direction can be designed with a third beamsplitter and a further mirror, both oriented 90° to the drawing plane of Fig. 5.37. The hologram now contains the information about several angular views of the object, hence we can call it a *multiplexed hologram*. There is

no extra problem with the object's stability since all recordings from different angles are performed simultaneously. The individual interference patterns can be separated by their different distances from the hologram plane. For the geometry of Fig. 5.37 with the two observation directions separated by angle β , the distances d_1 and d_2 as indicated in Fig. 5.38 are given by

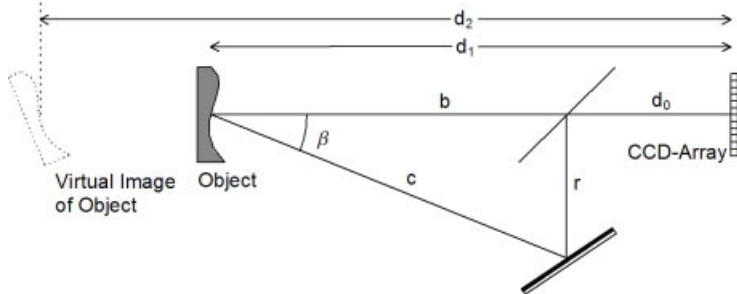


Figure 5.38: Geometry of multiplexed digital holography.

$$\begin{aligned} d_1 &= d_0 + b \\ d_2 &= d_0 + r + c \\ &= d_0 + b \left(\tan \beta + \frac{1}{\cos \beta} \right). \end{aligned} \quad (5.81)$$

Experiments have shown that it is advantageous to have large $|d_2 - d_1|$. If the reconstructed objects are too close together they will disturb each other. This is shown in Fig. 5.39. The two

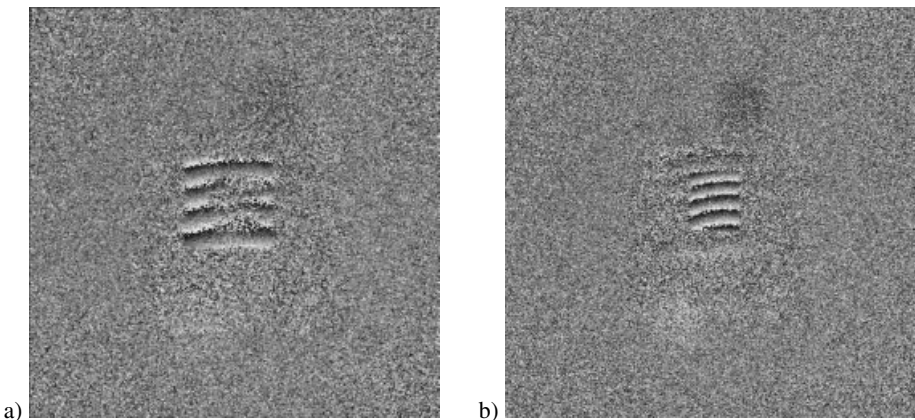


Figure 5.39: Interference phase distributions reconstructed from multiplexed digital hologram at 50 cm (a) and 75 cm (b) distance.

interference phase distributions are reconstructed from a single multiplexed digital hologram. The different sizes of the reconstructed surface are caused by the Fresnel transform (3.43). The distances in this experiment were $d_1 = 50$ cm and $d_2 = 75$ cm. We can recognize in

Fig. 5.39a the disturbance in the center of the interference phase distribution reconstructed for the distance $d_1 = 50$ cm that was caused by the other reconstruction. An alternative way instead of large $|d_2 - d_1|$ is a slight tilt of the mirror so that the reconstructed sharp and unsharp object wave fields do not overlap. The interference phase distributions resulting from such an experiment are given in Fig. 5.40.

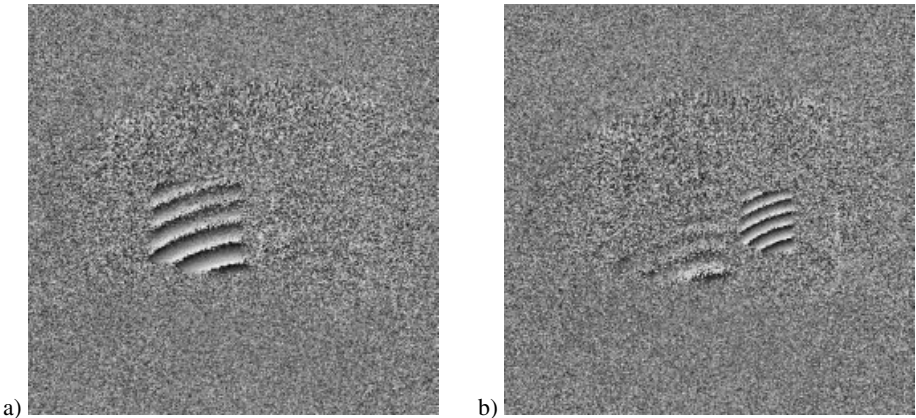


Figure 5.40: Interference phase distributions reconstructed from multiplexed digital hologram at 50 cm (a) and 75 cm (b) distance, tilted mirror.

5.8.6 Multiplexed Holograms with Discrimination by Partial Spectra

We have seen in Sections 3.2.5 and 3.2.6 that in the computer we have access to the frequency spectrum of the digital hologram, which can be manipulated to influence the reconstructed image in a desired way. There the suppression of the d.c.-term as well as the twin image by filtering in the spatial frequency plane was demonstrated. This approach also is feasible for recording simultaneously multiple holograms onto the CCD which can then be discriminated by filtering in the spatial frequency domain. Therefore the multiplexed holograms must exhibit different spatial frequencies. This can be obtained by using different reference waves for the generation of the single holograms. To guarantee that only the corresponding waves interfere and the resulting holograms superpose incoherently avoiding any unwanted cross-interferences, we have basically two possibilities:

- Two single holograms are separated by polarization: one pair of corresponding reference and object waves is linearly polarized in a certain direction, the other wave-pair is linearly polarized in the orthogonal direction [496, 497].
- The light paths are of different lengths, which can be achieved by delay lines, eventually by using optical fibers. The length differences then have to be larger than the coherence length of the used laser light [62, 306]. This option allows even more than two incoherently overlayed holograms.

If we arrange the source points of the divergent spherical reference waves in such a manner that the resulting partial spectra do not overlap, then we can extract the partial spectra by simple band-pass filtering in the spatial frequency domain and reconstruct from the individually filtered digital hologram [498]. So we only have to find the source points of the reference waves enabling this.

The first fact we have to recognize in doing this is the nature of the digital hologram as an intensity distribution described by real numbers. For this reason the spectrum of the hologram as well as the spectrum of each partial hologram is Hermitean, which means it consists of two parts placed symmetrically with respect to the zero frequency. In order to put a certain number of spectra non-overlapping into the spectral range, the size of each partial spectrum is restricted. Therefore first we have to choose an object-to-CCD distance which on the one hand fulfills the sampling theorem, and on the other hand produces holographic structures which have a spectrum smaller than the predetermined partial spectrum size. For an initial test hologram we employ an arbitrary divergent reference wave, which only has its source point in the plane where the source points of the desired reference waves are positioned. This plane should be parallel to the CCD-array, so that for the reference wave source points $(x_R^{(i)}, y_R^{(i)}, z_R^{(i)})$ we have $z_R^{(i)} = z_R$ for all i . The i term numbers the partial holograms and thus the different reference waves. To find proper $(x_R^{(i)}, y_R^{(i)})$, we shift the individual partial spectra in the spatial frequency domain, which means we investigate and manipulate the Fourier transform of the digital hologram. Now we remember that the Fresnel transform reconstruction in the case of lensless Fourier-transform holography reduces to a mere numerical Fourier transform, and the reference wave is a divergent one with its source point in the plane of the object surface. We can assume $(x'_R, y'_R, z'_R) = (0., 0., d)$ as such a reference wave with d the object-to-CCD distance. The choice $x'_R = y'_R = 0.$ can be done without restriction of generality, other values lead to phase factors which do not shift geometrically the reconstructed image.

In the wave field reconstructed with $R' = (0., 0., d)$, which is an unsharp replica of the object wave field recorded with the help of $(x_R^{(i)}, y_R^{(i)}, z_R)$, we now define a point $P = (x_P, y_P, z_P)$ which should be shifted to $P' = (x'_P, y'_P, z_P)$. These data are put into the holographic imaging equations (2.154), (2.155), and (2.156), which describe the shift of points in the reconstructed image if the reference wave source is shifted. The solution of the imaging equations is

$$\begin{aligned} x_R &= x_P \frac{z_R}{z_P} + x'_P \left(1 - \frac{z_R}{z_P} - \frac{z_R}{z'_R} \right) \\ y_R &= y_P \frac{z_R}{z_P} + y'_P \left(1 - \frac{z_R}{z_P} - \frac{z_R}{z'_R} \right) \\ z_R &= \text{predetermined.} \end{aligned} \quad (5.82)$$

This procedure is carried out for all desired spectra and we obtain the reference wave source points. The x_P, y_P, x'_P, y'_P can be expressed in pixel coordinates $n, m; n = 1, \dots, N; m = 1, \dots, M$ or in real lengths $n\Delta x', m\Delta y'$.

The whole process now is demonstrated in a simulated example of black and white rectangles as object. The object has size 256×256 pixels in a 1024×1024 -pixel field. The other parameters are $d = 2.0$ m, $\lambda = 0.6328$ μm , $\Delta\xi = \Delta\eta = 6.8$ μm . The hologram is recorded

with the help of a spherical reference wave emitted from $R = (0.01, 0.02, 0.5)$ m. The hologram is displayed in Fig. 5.41a, the reconstructed intensity image is shown in Fig. 5.41b. The spectrum of this hologram is given in Fig. 5.41c. It is an image reconstructed using the reference wave $\hat{R} = (0., 0., 2.)$ m. In the plane $d = -1.0$ m this reference wave reconstructs sharply, the intensity display in this plane we see in Fig. 5.41d.

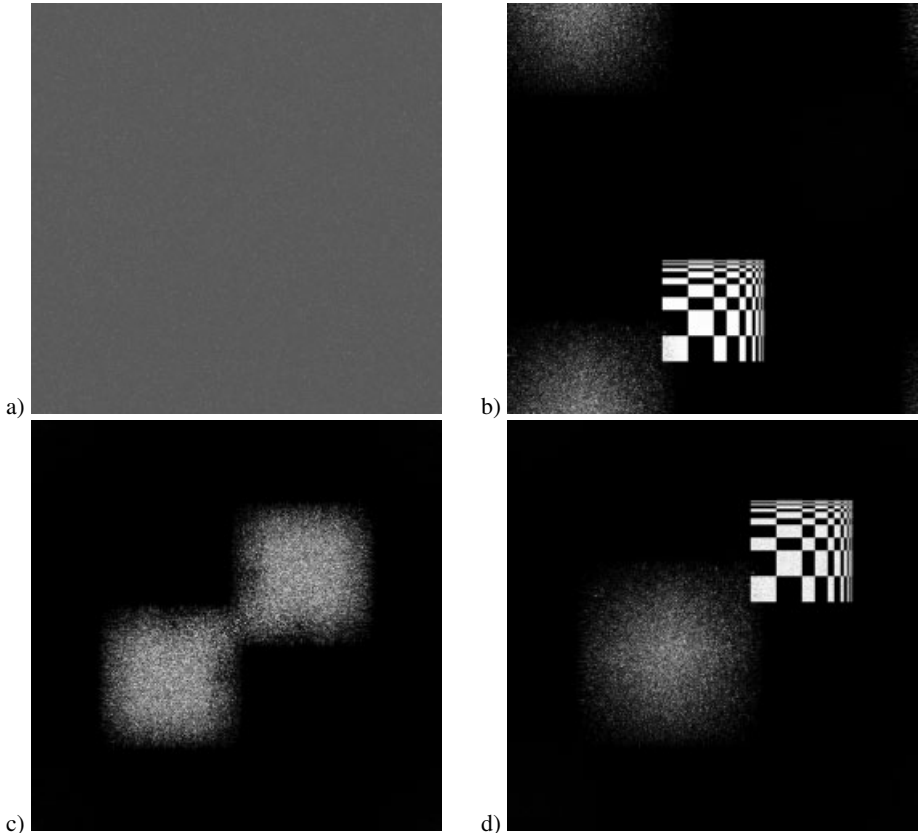


Figure 5.41: Simulated digital hologram (a), reconstructed image (b), spectrum of the hologram (c), reconstructed image in the plane $d = -1.0$ m (d).

Now the two modes of the spectrum of Fig. 5.41c should be taken apart along the diagonal, furthermore a second spectrum along the other diagonal should be generated from the same object. To solve the first of these two tasks we note that the upper right edge of the object is at the pixel coordinates (860, 199), which corresponds to $P = (78.155, 18.085, -1000.)$ mm in real world dimensions, since the pixel size in this plane is $\Delta x = \Delta y = 1 \text{ m} \cdot 0.6328 \mu\text{m}/(1024 \cdot 6.8 \mu\text{m}) = 90.88 \mu\text{m}$. This P should be shifted to $P' = (93.053, 0.091, -1000.)$ mm which corresponds to (1024, 1) in pixel coordinates. But P itself is a shifted point, because the hologram was generated using $R = (0.01, 0.02, 0.5)$ m,

and P was reconstructed by $\hat{R} = (0., 0., 2.)$ m. We have

$$\begin{aligned} 0.078155 \text{ m} &= x_P = \frac{\hat{x}_P z_R \hat{z}_R - x_R z_P \hat{z}_R}{z_R \hat{z}_R - z_P \hat{z}_R + z_P z_R} = \frac{\hat{x}_P - 0.01 \cdot 2 \cdot 2 \cdot \text{m}^3}{1. - 4. + 1. \cdot \text{m}^2} \\ &= \left(\frac{0.04}{2} - \frac{\hat{x}_P}{2} \right) \text{ m} \\ \hat{x}_P &= 0.04 \text{ m} - 2 \cdot 0.078155 \text{ m} = -0.116 \text{ m}. \end{aligned} \quad (5.83)$$

In the same way we calculate

$$\begin{aligned} 0.018085 \text{ m} &= y_P = \frac{\hat{y}_P z_R \hat{z}_R - y_R z_P \hat{z}_R}{z_R \hat{z}_R - z_P \hat{z}_R + z_P z_R} = \left(\frac{\hat{y}_P}{2} - \frac{0.02 \cdot 4}{2} \right) \text{ m} \\ \hat{y}_P &= 0.08 \text{ m} + 2 \cdot 0.018085 \text{ m} = +0.116 \text{ m}. \end{aligned} \quad (5.84)$$

This point $\hat{P} = (-0.116, 0.116, -1.0)$ m now is shifted to P' by the reference wave $R' = (x'_R, y'_R, 0.5 \text{ m})$. The expression $0.093 \text{ m} = (-0.116 \text{ m} - 4x'_R) / -2$ is solved by $x'_R = 0.0175 \text{ m}$ and $0.000091 \text{ m} = (0.116 \text{ m} - 4y'_R) / -2$ is solved by $y'_R = 0.029 \text{ m}$. Thus the desired first reference wave is $R' = (0.0175, 0.029, 0.5) \text{ m}$.

The second reference wave R'' shifts \hat{P} to $P'' = (0.093, 0.070, -1.0 \text{ m})$. As in the preceding case we get $x''_R = 0.0175 \text{ m}$, but now we obtain $0.07 \text{ m} = (0.116 \text{ m} - 4y''_R) / -2$, which is solved by $y''_R = -0.006 \text{ m}$. So we have $R'' = (0.0175, -0.006, 0.5) \text{ m}$. The hologram recorded with R' and reconstructed with \hat{R} gives the sharp image shown in Fig. 5.42a, the hologram recorded with R'' and reconstructed likewise with \hat{R} leads to the image given in Fig. 5.42b.

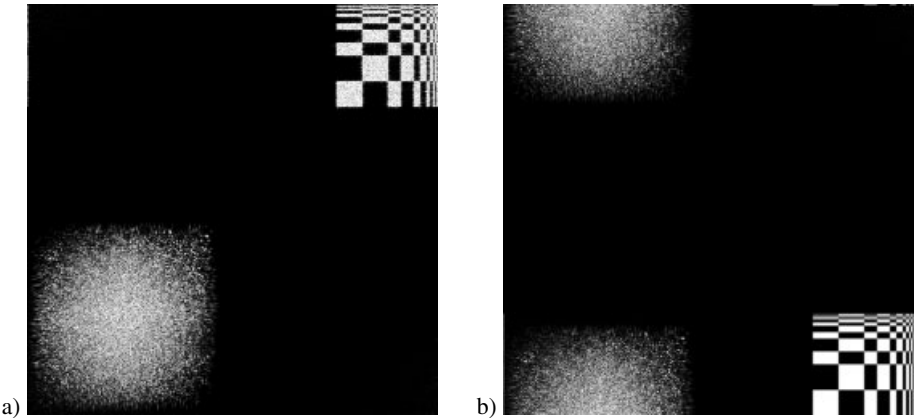


Figure 5.42: Images in the plane $d = -1.0 \text{ m}$, both reconstructed using \hat{R} , but (a) recorded with R' and (b) with R'' .

Now we record two holograms of the object, one with the reference wave $R' = (0.0175, 0.029, 0.5) \text{ m}$, one by using $R'' = (0.0175, -0.006, 0.5) \text{ m}$. The holograms are summed incoherently. The spectrum of this sum-hologram is displayed in Fig. 5.43a. If we reconstruct from the unfiltered sum-hologram using reference wave $R' = (0.0175, 0.029, 0.5) \text{ m}$, we obtain an image which contains the object twice, Fig. 5.43b. But if we filter the sum-

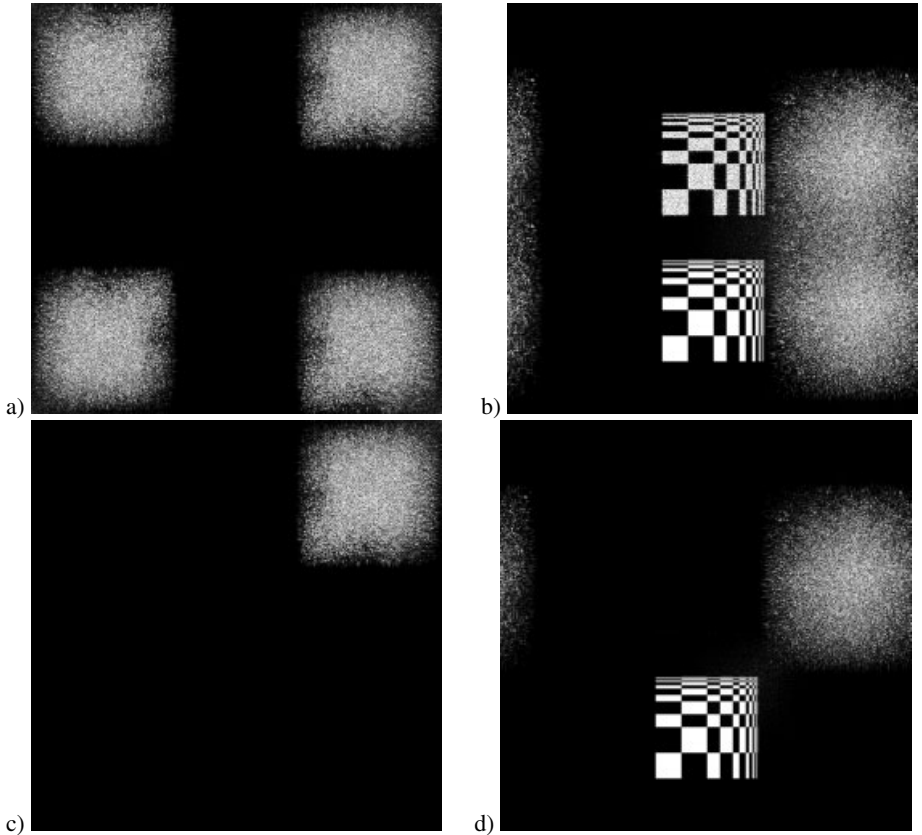


Figure 5.43: Spectrum of sum-hologram (a), reconstructed intensity from sum-hologram (b), filtered spectrum (c), reconstructed intensity from filtered hologram (d).

hologram in such a way that only the spectrum of Fig. 5.43c remains, after reconstruction with $R' = (0.0175, 0.029, 0.5)$ m we get the image of Fig. 5.43d. After the application of a band-pass filter leaving only the spectrum of Fig. 5.43e the reconstruction using the corresponding reference wave $R'' = (0.0175, -0.006, 0.5)$ m gives the field shown in Fig. 5.43f. Because in both cases we used the corresponding reference waves, the image of the object is at the same place in each reconstructed field.

Spectral multiplexing of digital holograms is a way to record fast events on a CCD target. Liu et al. [144] report on the recording of three frames of a fast event in a single CCD frame. The resolution of a single shot was 5.9 ns, defined by the pulsed laser used, the frame interval was 12 ns, generated by a specially designed multiple pulse-generation cavity. The holograms of the three states of the event are well separated in the spatial frequency domain.

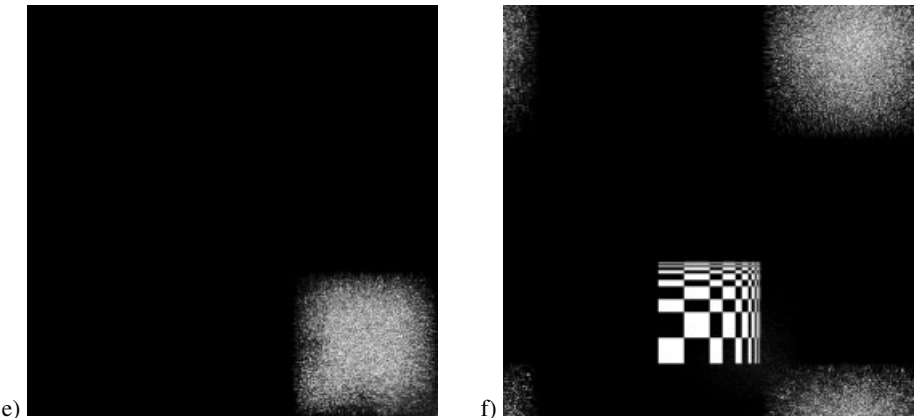


Figure 5.43 (continued): (e) filtered spectrum, (f) reconstructed intensity from filtered hologram.

5.9 Interference Phase Demodulation

As outlined in Section 5.1.1, the evaluated interference phase distributions are ambiguous in having only values between $-\pi$ and $+\pi$. They are said to be wrapped modulo 2π [499, 500]. Although in most practical applications a continuous interference phase distribution is expected, we get a sawtooth-like phase as the one shown in Fig. 5.44a. The process of resolving the 2π -discontinuities by adding a step function consisting only of 2π -steps, Fig. 5.44b, is called *continuation, phase unwrapping* or *demodulation*.

5.9.1 Prerequisites for Interference Phase Demodulation

There are a number of requirements to be fulfilled in order for a reliable demodulation. The first is that continuous phase data are adequately sampled. Each demodulation procedure checks interference phase differences of neighboring pixels. If due to a violation of the sampling theorem this difference exceeds π , the demodulation must fail because of the introduction of unnecessary phase jumps. On the other hand undersampled high frequency fringe data may result in small phase differences between two pixels but in reality a phase jump between these pixels is missed. Nevertheless an approach to phase recovery from undersampled interferograms is suggested by Munoz et al. [501, 502].

Statistical noise like speckle noise is a common cause for false identification of phase jumps. As soon as the amplitude of the noise approaches π , the actual phase jumps become obscured. A low pass filter for smoothing the interference phase data is not recommendable, since it will wash out the sharp 2π -steps. Instead median filtering is a good choice, since it is 2π -step preserving [394], and a still better choice is the sin-cos-filter of Section 5.8.2.

Each demodulation procedure assumes a continuous interference phase distribution which is wrapped into an interval of width 2π . So discontinuities resulting from large height steps or holes or edges of objects not filling the full frame have to be avoided. The region in which the demodulation should be performed has to be defined by masking. If the region for de-

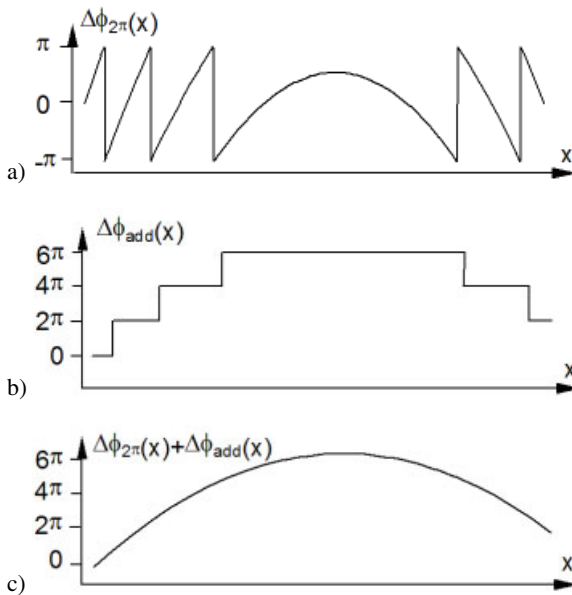


Figure 5.44: Demodulation: (a) interference phase modulo 2π , (b) step function to be added, (c) unwrapped interference phase distribution.

modulation is not topologically connected, then no correct relations of the interference phase in the unconnected parts can be derived without additional side information, e. g. particular points in each part where the exact displacement is known. An approach to automatic phase unwrapping in the presence of surface discontinuities is described in [503].

Especially if the interference phase distribution has been determined by the Fourier transform method without additionally introduced carrier fringes, Section 5.6, then sign-errors may occur. The sign-error must be corrected, e. g. as described in Section 5.6.3, before demodulation. Each demodulation requires sign-correct interference phase distributions modulo 2π [504], only a global sign-change may be tolerable, leading to a global sign-change in the unwrapped continuous phase.

The demodulation procedures can roughly be categorized into *path dependent demodulation* techniques, where the order in which the pixels are investigated and unwrapped is predetermined by the process, and into *path independent demodulation* techniques. In this latter case the order of investigated pixels is determined by the phase values at the pixels.

5.9.2 Path-Dependent Interference Phase Demodulation

A straightforward attempt to demodulate a one-dimensional interference phase distribution $\Delta\phi(x)$ is done by checking the phase differences of adjacent pixels $\Delta\phi(x+1) - \Delta\phi(x)$. If this difference is less than $-\pi$, an additional 2π is added to $\Delta\phi$ from $x+1$ onwards; if the difference is greater than $+\pi$, one more 2π is subtracted from $\Delta\phi$ starting at pixel $x+1$.

Several of these 2π -terms may accumulate, Fig. 5.44b, so that at each pixel an integer multiple of 2π , $\phi_{add}(x) = 2\pi n(x)$ with $n(x) \in \{\dots, -1, 0, 1, \dots\}$ must be added for unwrapping. The starting point need not necessarily lie at the leftmost pixel $x = 1$. If a central starting pixel x_0 is chosen, differences to the right $\Delta\phi(x+1) - \Delta\phi(x)$ and to the left $\Delta\phi(x-1) - \Delta\phi(x)$ have to be calculated.

Demodulation algorithms based on this approach can be elegantly defined [505, 506], but these algorithms strongly depend on numerical differentiation, which will amplify the influence of noise in the phase data. If, due to noise, a wrong difference occurs, leading to an erroneous 2π -term added or subtracted or missing a necessary 2π -term, the resulting phase error spreads up to the outmost pixel (if it is not neutralized by another error with opposite sign). In many practical applications an object is illuminated by an expanded Gaussian laser beam. Then at the margins of the recorded interference pattern the contrast decreases, resulting in a higher probability for erroneous interference phase values and thus false phase differences between adjacent pixels. Therefore a central starting point in the pattern is most often recommendable.

A final check for plausibility of the unwrapped interference phase distribution may be performed by fitting a line through several adjacent pixels of the unwrapped phase and comparing the phase values of the next pixels to this line. This may detect false 2π -steps due to noise, as long as a sufficiently smooth phase distribution can be assumed.

The described one-dimensional demodulation procedure can be transferred to two dimensions along rows and columns of pixels. Let us start, for example, with one row. Once this row is demodulated, the pixels of this row act as starting pixels for column demodulation. There are some trivial variations of this scheme: One may process one row, then go down one pixel, process the next row in reverse direction and so on. The two-dimensional phase data are now treated like a folded one-dimensional data set [507]. Or each row is unwrapped independently from the other rows and then the rows are adjusted by scanning through a center column [508] or by comparing the phase differences averaged along each row.

Another approach makes use of the two dimensions [509]. At each pixel the phase differences to the pixel above in the previous row and the one to the left in the same row are checked. If both differences indicate the same $n(x)$, this is taken for unwrapping. If the differences differ, the pixel is masked and its unwrapping is postponed until more neighbors of it are unwrapped. This concept may be improved to spiral scanning with starting at a central pixel [510]. Instead of checking the pixels above and to the left, by application of a spin filter the direction of the highest slope of the phase distribution can be calculated, and the pixels in this direction are tested for unwrapping [511].

Demodulation along predetermined paths encounters difficulties if coming to a masked region, e. g. at holes in the surface. The spiral scanning then can be modified to scan along the boundaries of the masked area [510].

5.9.3 Path-Independent Interference Phase Demodulation

To avoid the difficulties with a possible spreading of erroneous phase, or a failing at holes, *path independent demodulation* procedures are recommended [452, 512–517]. The following algorithm interprets the interference phase distribution modulo 2π as a graph, where the points are the nodes, and the arcs are the connections between neighboring points. 4-neighborhoods

or 8-neighborhoods may be used. With each arc a value $d_{2\pi}(\Delta\phi_1, \Delta\phi_2)$ is associated, defined by the phase values $\Delta\phi_1$ and $\Delta\phi_2$ of the two points it connects:

$$d_{2\pi}(\Delta\phi_1, \Delta\phi_2) = \min\{|\Delta\phi_1 - \Delta\phi_2|, |\Delta\phi_1 - \Delta\phi_2 + 2\pi|, |\Delta\phi_1 - \Delta\phi_2 - 2\pi|\}. \quad (5.85)$$

The values $d_{2\pi}$ may be interpreted as a distance modulo 2π .

The demodulation now proceeds along paths where these distances are least. Along these paths the probability of an erroneous demodulation is least. Points with wrong phase are surrounded this way and the same is true for regions without interference phase at all, indicated by a mask. If a point possesses an erroneous phase that cannot be reached correctly along any path, the incorrectly demodulated point in the vast majority of cases remains isolated in the finally resulting interference phase distribution.

The algorithm proceeds as follows:

1. For a starting point all emanating free arcs are recorded in a list together with their values $d_{2\pi}$.
2. The minimal value in the list is searched for. The demodulation term 0, -2π , or $+2\pi$ for this arc is stored in an extra file. The arc, together with its value, is discarded from the list and marked to avoid repeated consideration.
3. The final node of the just considered arc acts as a new starting point in step 1. Only those arcs which have not been stored formerly in the extra file in step 2 are considered as free. If no free arcs emanate from this node, one proceeds to step 2 directly.
4. If the capacity of the list is exhausted, the list is checked for arcs which may have already entered the extra file along another path. These arcs are deleted.
5. Steps 1 to 4 are repeated until all points have been an end node of an arc in the extra file.
6. The interference phase distribution is demodulated by using the values in the extra file. There is one and only one path to each point. The -2π - or $+2\pi$ -terms of course may accumulate along these paths.

The demodulation of step 6 may be performed during step 2 in an extra image of already demodulated points. Another modification of this algorithm, which shortens the computational effort, allows only arcs with values less than a prescribed threshold to be recorded in the list. In this way the number of comparisons for searching the minimum in step 2 can be drastically reduced.

This demodulating algorithm is demonstrated by the numerical example of Fig. 5.45a. Figure 5.45b shows how the algorithm detects the best track and circumvents the one bad spot. Figure 5.45c displays the resulting unwrapped phase distributions after demodulation along predetermined horizontal paths and after path-independent phase demodulation. The interference phase distributions of Figs. 5.25h and i, and 5.26f are unwrapped by this path-independent algorithm.

A demodulation algorithm which is claimed to be noise-immune [518,519] first checks the interference phase distribution for inconsistent points. This check, which is described in more detail in Section 5.9.4, is based on the observation that for a continuous phase distribution the

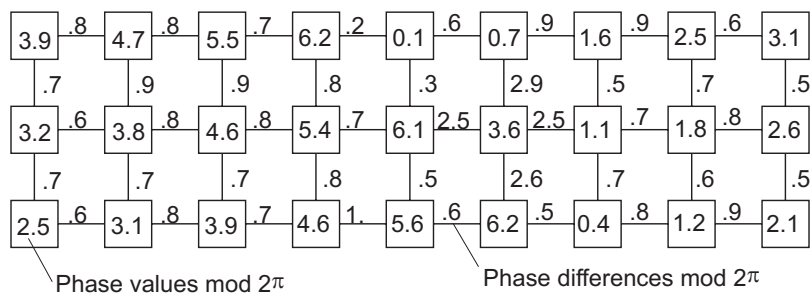


Figure 5.45: (a) Path independent interference phase demodulation, interference phase values.

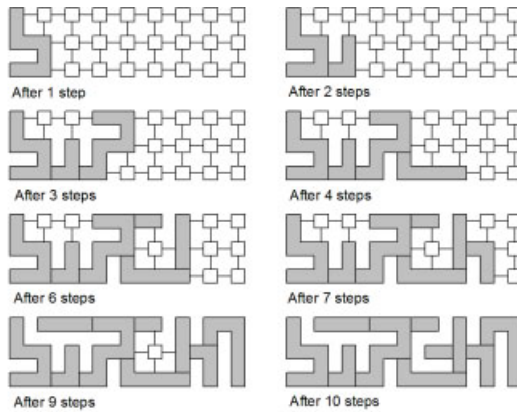


Figure 5.45: (b) Path independent interference phase demodulation, demodulation steps.

3.9	4.7	5.5	6.2	6.4	7.0	7.9	8.8	9.4
3.2	3.8	4.6	5.4	6.1	3.6	1.1	1.8	2.6
2.5	3.1	3.9	4.6	5.6	6.2	6.7	7.5	8.4

Path-dependent demodulation (horizontal direction)

3.9	4.7	5.5	6.2	6.4	7.0	7.9	8.8	9.4
3.2	3.8	4.6	5.4	6.1	9.9	7.4	8.1	8.9
2.5	3.1	3.9	4.6	5.6	6.2	6.7	7.5	8.4

Path-independent demodulation

Figure 5.45: (c) Path independent interference phase demodulation, comparison of results.

integral along any closed loop must be zero. In the discrete case this integral is calculated by the sum of the differences between the phases of all adjacent pixels along the loop. By testing the 4-point loops in all 2×2 -arrays, inconsistent points which act as sources for discontinuities in the unwrapping, are identified. Each such source is paired with a source of opposite sign or with the boundary of the phase-map by the shortest possible cut-line. The unwrapping process then will not cross these cut-lines but follows the pixels neighboring the cut-line. A similar approach but based on an identification of probable discontinuities by searching for regions in which the phase curvature exceeds some threshold is presented in [504]. For that purpose second derivatives of the phase data are calculated and investigated.

A *regional processing* algorithm where the phase map modulo 2π first is segmented into regions containing no phase ambiguities, is described in [520–522]. After the demodulation is completed in these regions, adjacent edges of the regions are investigated for discontinuities. The regions then are mutually phase shifted in order to reduce the discontinuities between them. Now the regions can merge until at the end one region fills the whole data array.

A combination of the concepts of regional processing, pixel processing along predetermined paths, and processing in order of minimal likelihood for erroneous demodulation is known as *tile processing* [523–525]. The whole data array is divided into rectangular sub-arrays, the tiles. In each tile the interference phase is unwrapped by a path-dependent method. Then the phase data at the edges of adjacent tiles are compared and the phase is adjusted by the same 2π -multiple for the whole tile to fit to the adjacent tile. Tiles with a large percentage of edge pixels agreeing to the edge pixels of adjacent formerly processed tiles get a high degree of confidence and thus are preferred in the order of processing. Any discontinuity will be restricted to a region within one tile. The main parameter affecting this method is the size of the tiles which should be chosen such that on the average there are one or two fringes crossing each tile [507]. A path-independent unwrapping algorithm working even with subsampled phase-shifted interferograms is given in [501].

A region growing demodulation by iteratively merging and shifting of continuous areas until a single region is built or no further moves are possible is proposed by Baldi [526].

5.9.4 Interference Phase Demodulation by Cellular Automata

The use of *cellular automata* for interference phase demodulation has first been proposed in [527]. A modification of the algorithm of [527] is given in [528]. Cellular automata are simple, discrete mathematical systems, whose global behavior results from collective effects of a large number of cells. The state of each cell evolves in discrete time steps according to rather simple local neighborhood rules.

For phase unwrapping the decision at each pixel as to whether 2π are added or subtracted or not depends on the phase differences to the neighboring points. In [527] these are the four nearest neighbors in horizontal and vertical direction, in [528] all eight neighbors to the central point of a 3×3 -neighborhood are considered. Each phase difference of the investigated pixel to one of its neighbors gives a vote for addition of 2π if the difference is greater than π , a vote for subtraction of 2π if it is less than $-\pi$, and no vote if the absolute difference is less than π . Then 2π are added or subtracted according to the majority of votes. In the case of a tie, addition or subtraction is chosen arbitrarily, only if no vote at all was given is the actual value retained. This procedure applied to all pixels is called a *local iteration*.

After a number of local iterations – a number, that mainly depends on the maximum distance of 2π -steps in the original phase-map – oscillation between successive patterns occurs. When this oscillatory state is reached, the arithmetic average of the two states is computed at each pixel and the process starts anew. The averaging is called *global iteration*. If a steady state is reached after global iteration, the process stops.

The process of cellular automata demodulation is shown in Fig. 5.46 for the example of a simulated 32×32 -pixel interference phase modulo 2π , Fig. 5.46a. The first oscillation takes place after 6 local iterations, Fig. 5.46d. After 3 global iterations, the phase is successfully demodulated, Fig. 5.46i.

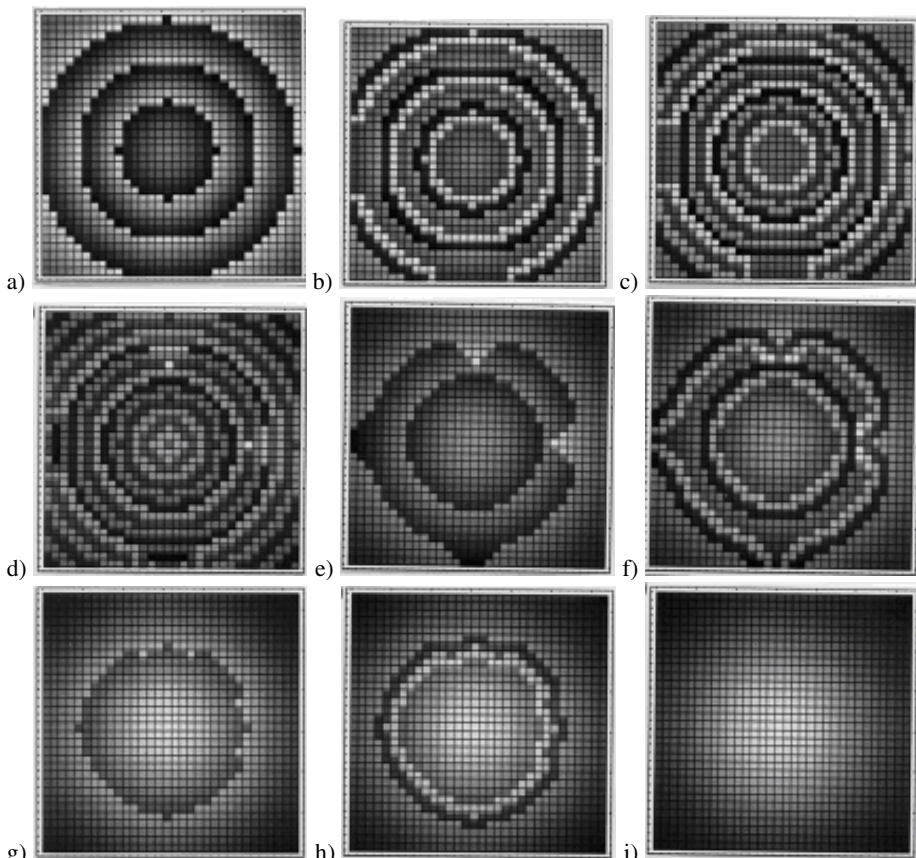


Figure 5.46: Cellular automata demodulation: (a) interference phase modulo 2π , (b) phase after 1 local iteration, (c) phase after 2 local iterations, (d) phase after 6 local iterations, (e) phase after 1 global iteration, (f) phase after 1 global and 1 local iterations, (g) phase after 2 global iterations, (h) phase after 2 global and 1 local iterations, (i) phase after 3 global iterations.

The algorithm is robust against distortions and noise, but there are possible points or regions that would lead to new 2π -discontinuities after each global iteration, so that the algo-

rithm would never terminate. Therefore a *check for consistency* has to be performed. This consists of summing the four phase differences along the closed path connecting the four pixels of a 2×2 -neighborhood. Here each phase difference is taken modulo 2π . If the sum is zero, the neighborhood is said to be consistent, otherwise it is interpreted as being inconsistent. Figure 5.47a gives a consistent 2×2 -array, since $[-2.77 - 2.67] + [-2.04 +$

a)	<table border="1"><tr><td>2.67</td><td>1.94</td></tr><tr><td>-2.77</td><td>-2.04</td></tr></table>	2.67	1.94	-2.77	-2.04	b)	<table border="1"><tr><td>2.45</td><td>1.08</td></tr><tr><td>-2.53</td><td>-1.15</td></tr></table>	2.45	1.08	-2.53	-1.15
2.67	1.94										
-2.77	-2.04										
2.45	1.08										
-2.53	-1.15										

Figure 5.47: Consistent (a) and inconsistent (b) 2×2 -arrays of interference phase values modulo 2π .

$2.77] + [1.94 + 2.04] + [2.67 - 1.94] = 0.84 + 0.73 - 2.30 + 0.73 = 0$. Here $[.]$ denotes the value modulo 2π in $]-\pi, \pi]$. Figure 5.47b is an example of an inconsistent array, for $[-2.53 - 2.45] + [-1.15 + 2.53] + [1.08 + 1.15] + [2.45 - 1.08] = 1.30 + 1.38 + 2.23 + 1.37 = 6.28$. The inconsistent regions are masked and discarded from being tested in the local iterations. The inconsistency test may be performed once before the first local iteration [527] or additionally after each global iteration [528]. Nevertheless there remain the problems that the inconsistency check does not guarantee convergence to the steady state for all possible phase-maps, especially those with phase dislocations induced by aliasing [527], or that the inconsistency regions will increase in size [528].

5.9.5 Further Approaches to Interference Phase Demodulation

The demodulated interference phase distribution is assumed to have no sharp discontinuities which would give rise to high frequency components in the Fourier spectrum. A check of the bandwidth of a one-dimensional phase distribution by the Fourier transform is the base for the *bandlimit demodulation* [529, 530]. Here all possible step functions with one $+2\pi$ - or -2π -step are tested, the step function that minimizes the bandwidth is selected as one that unwraps at one position. This process is repeated until no further reduction of the bandwidth is obtained. The method has been shown to be robust in the presence of signal-independent random additive noise, provided that the correct interference phase function is slowly varying. The method will fail if the number of phase steps increases. The extension of the bandlimit approach to two-dimensional phase-maps on a more effective basis than mere repeated row or column processing has still to be done.

An actual approach to demodulation is the application of a *neural network* of the Hopfield type [531, 532]. In *Hopfield networks* all possible connections between all neurons are existent. The synaptic weights only take on the inhibitory value 0 or the excitatory value 1. Hopfield networks are used to minimize a so-called Hopfield energy function. For demodulation purposes with each pixel a number of neurons is associated. A merit function $E(\phi_{add})$ is defined, which measures the deviation from smoothness of the phase distribution unwrapped by ϕ_{add} . The $n(x)$ in $\phi_{add}(x) = 2\pi n(x)$ is represented by the number of the excited neu-

rones of all those associated with pixel x . This merit function is related to the Hopfield energy function in a discrete-time Hopfield network. According to the equations of the network dynamics, the neurons change their states in such a manner that the value of the energy function decreases with the temporal evolution of the network until a stable state is reached.

As with the cellular automata approach in defining the merit function here we may use 4- or 8-pixel neighborhoods. Furthermore inconsistencies have to be excluded. This is done as described for the cellular automata demodulation, Section 5.9.4. But now no cut-lines as in [519] are defined, instead the synaptic connections across the cut-lines are prohibited.

All demodulation techniques presented so far spatially unwrap a single interference phase distribution. In *temporal phase unwrapping* as proposed in [533, 534] a number of measurements with increasing load is recorded, where the time increments are chosen small enough to fulfill the sampling theorem requirements. Now unwrapping is performed along the time axis for each pixel independently from its neighboring pixels. So objects not filling the full frame, unconnected regions, or regions with poor signal-to-noise ratios will not corrupt the demodulation of good data points. The requirement of sign-correct phase data is fulfilled by using the phase shift method with four interferograms and a mutual phase shift of 90° , see (5.24). By a proper combination of the equation for phase shift evaluation (5.24) and the calculation of the phase difference between successive time instants, this temporal phase difference can be calculated with values in $] -\pi, +\pi]$, as long as the sampling theorem is fulfilled. The overall interference phase without any 2π -discontinuity then for each time instant is determined by summation of the temporal phase differences. Temporal phase unwrapping can be used not only for interference phase distributions but also for the phase maps of complex wave fields in digital image plane holography [535].

A demodulation by two-dimensional fitting of unwrapped phase maps in a least squares sense is proposed in [513]. The problem of two-dimensional *least squares phase unwrapping* is shown to be equivalent to the solution of Poisson's equation on a discrete rectangular grid with Neumann boundary conditions. It is solved by application of a fast discrete cosine transform [536]. If less reliable pixels or regions are known, resulting from regionally varying noise, aliasing, phase inconsistencies, measurement errors, shadows, or no phase data at all, these parts of the pattern can be appropriately weighted. Weighting may be binary into 0 and 1 or continuously inverse proportional to the probability of noise or error. An algorithm based on Picard iteration is given for weighted least squares phase unwrapping. Another algorithm which provides faster convergence is developed on the basis of the method of preconditioned conjugate gradients. Several examples in [513] show how phase noise, data inconsistencies and other degradations are automatically accommodated by this least squares approach. A least-squares modal estimation of wrapped phases by an algorithm specially designed to be used as part of an iterative algorithm can be found in [537].

6 Processing of the Interference Phase

The calculation of the interference phase distribution as described in Chapter 5 normally is not the final goal of a quantitative evaluation of holographic interference patterns, but an intermediate step in the determination of the physical quantity of interest: components of the displacement vector field, strains, stresses, vibration amplitudes, contours, refractive index distributions etc. In Chapter 4 the formation of holographic interference patterns dependent on the geometry of the holographic arrangement and a given change of the optical wave field has been described. Based on these foundations in this chapter the inverse problem is treated, namely to conclude from an already evaluated holographic interference phase distribution and a given geometry of the holographic arrangement the values and directions of the parameters describing the underlying physical process. The basics of computer-aided methods determining a variety of different physical quantities are presented. Since the topics considered in this chapter are under current research, there still remain some open problems which should be identified here and which may be solved in the near future.

6.1 Displacement Determination

In order to determine the components of a *displacement vector field* from the already evaluated interference phase distribution some assumptions have to be made. First a continuous displacement variation at least in defined areas of the interferogram is assumed, and second there should only remain a global uncertainty about the sign. These assumptions allow a continuous counting of the interference order along uninterrupted paths through the interferogram. Normally these assumptions are used in the demodulation of the interference phase, Section 5.9, to obtain a continuous phase distribution. Nevertheless there remains the problem of the overall sign ambiguity, Section 5.1.1, and the absolute phase problem, Section 5.1.2. There are applications, where the displacement at a reference point in the interferogram is known, so one can calculate the absolute phase at this point. This case needs a separate treatment different from the case where no zero order or reference displacement is known. Moreover we have to discriminate between a sensitivity vector that varies over the interferogram and on the contrary a constant sensitivity vector, as was pointed out in Section 5.1.2.

6.1.1 Displacement Determination with Known Reference Displacement

The basis of the displacement determination is (4.21):

$$\Delta\phi(P) = \mathbf{d}(P) \cdot \mathbf{e}(P). \quad (6.1)$$

We assume that we have evaluated the interference phase distribution $\Delta\phi(P)$ without sign ambiguity by e. g. a phase shift method of Section 5.5 or digital holographic interferometry of Section 5.8. With a *known reference displacement* $\mathbf{d}(P_0)$ at a point P_0 the interference phase $\Delta\phi(P)$ at P_0 and at all P which are accessible by an uninterrupted path from P_0 can be calculated. The sensitivity vector for each P of interest has to be calculated according to (4.18) – (4.20), which has to be performed once for a representative P , if the sensitivity vector is constant, or separately for each P , if it is not constant. Then the displacement is determined by inversion of (6.1).

The easiest case is the measurement of only the normal component using an arrangement with a constant sensitivity vector $\mathbf{e}(P)$ having a non-zero component only in the normal direction. Then $d_z(P)$ is determined by

$$d_z(P) = \frac{\Delta\phi(P)}{e_z(P)} \quad (6.2)$$

as outlined in (4.25) and (4.26).

For a varying sensitivity vector this approach is only feasible if it is guaranteed that $d_x(P) = d_y(P) = 0$ for all P . Otherwise errors may occur, since the components $e_x(P)$ or $e_y(P)$ do not vanish for all P . Sometimes this error can be estimated by assuming upper and lower bounds for $d_x(P)$ and $d_z(P)$, taking the extremal $e_x(P)$ and $e_y(P)$ for the given geometry, and putting these values into (6.1). If the error remains small, especially for an optimized holographic arrangement, Section 4.2.1, one can accept it.

If all three components of the displacement vector have to be determined, one has to solve the whole three-dimensional *system of equations* defined by (6.1). Therefore three measurements have to be performed to achieve the phase values $\Delta\phi^1(P)$, $\Delta\phi^2(P)$ and $\Delta\phi^3(P)$ for each point P . These interference phase values correspond to the same object point and thus to the same displacement vector, but to different sensitivity vectors [538]. The sensitivity vectors must be linearly independent, i. e. they should span a three-dimensional vector space, Section 6.2.3. The three interference patterns leading to the three phases may be recorded from the same observation direction, but with different illumination directions. This allows an easy identification of corresponding pixels in each recorded pattern, but requires repeatable or at least stable loading of the object to obtain the multiple holograms, each after switching between the illumination directions. Simultaneous recording on a single plate is possible with three object and three reference beams. Crosstalk then is avoided by noncorrelation between beams not belonging together, which is realized by optical path length differences exceeding the coherence length of the laser used [539]. If the fringes are moving, as is often the case with thermal loading, one has to trigger a simultaneous recording of the patterns along different observation directions [540]. But then the interferograms suffer under different *perspective distortion*, corresponding points P have to be identified, Section 6.2.2.

Let the three sensitivity vectors at P be $\mathbf{e}^1(P)$, $\mathbf{e}^2(P)$ and $\mathbf{e}^3(P)$, respectively. In the following superscript indices denote different sensitivity vectors while subscript indices stand for different object points. The subscript indices x , y , z denote the Cartesian coordinates. Then at each point P we have to solve the system of linear equations

$$\begin{pmatrix} \Delta\phi^1(P) \\ \Delta\phi^2(P) \\ \Delta\phi^3(P) \end{pmatrix} = \begin{pmatrix} e_x^1(P) & e_y^1(P) & e_z^1(P) \\ e_x^2(P) & e_y^2(P) & e_z^2(P) \\ e_x^3(P) & e_y^3(P) & e_z^3(P) \end{pmatrix} \begin{pmatrix} d_x(P) \\ d_y(P) \\ d_z(P) \end{pmatrix} \quad (6.3)$$

to obtain $\mathbf{d}(P)$. This may be written in vector notation by $\Delta\phi(P) = \mathbf{E}(P) \cdot \mathbf{d}(P)$ with $\mathbf{E}(P)$ representing the so called *sensitivity matrix*. The solution is

$$\mathbf{d}(P) = \mathbf{E}^{-1}(P) \cdot \Delta\phi(P). \quad (6.4)$$

If more than three interferograms with more than three sensitivity vectors are recorded and the corresponding interference phases $\Delta\phi^1(P), \dots, \Delta\phi^n(P)$ have been evaluated, the solution is found according to the *least squares method* by

$$\mathbf{d}(P) = (\mathbf{E}^T(P)\mathbf{E}(P))^{-1} (\mathbf{E}^T(P) \cdot \Delta\phi(P)) \quad (6.5)$$

where $\mathbf{E}(P)$ now is the corresponding $n \times 3$ matrix of the n sensitivity vectors [381, 541]. But still it is required that these n sensitivity vectors span a three-dimensional vector space.

6.1.2 Displacement Determination with Unknown Reference Displacement

For a displacement determination with *unknown reference displacement* let us first assume that the *sensitivity vector* is constant across the investigated surface of the object. The evaluated interference phase has the general form

$$\Delta\phi(P) = \mathbf{d}(P) \cdot \mathbf{e}(P) + \phi_0(P) \quad (6.6)$$

where ϕ_0 is an unknown constant. If we consider a point P_0 on the object as a reference, we can count the phase to each other point P_1 by

$$\begin{aligned} \Delta'\phi(P_1) &= \Delta\phi(P_1) - \Delta\phi(P_0) \\ &= [\mathbf{d}(P_1) - \mathbf{d}(P_0)] \cdot \mathbf{e}(P_1) = \Delta\mathbf{d}(P_1) \cdot \mathbf{e}(P_1). \end{aligned} \quad (6.7)$$

Now we can proceed as in Section 6.1.1 with the only restriction that not the absolute displacement but the displacement $\Delta\mathbf{d}$ relative to the reference point P_0 is measured.

Relaxing now the assumption that the sensitivity vector is constant across the surface, we may write $\mathbf{e}(P_1) = \mathbf{e}(P_0) + \Delta\mathbf{e}(P_1)$. Then (6.7) becomes

$$\begin{aligned} \Delta'\phi(P_1) &= \mathbf{d}(P_1) \cdot \mathbf{e}(P_1) - \mathbf{d}(P_0) \cdot \mathbf{e}(P_0) \\ &= \mathbf{d}(P_1) \cdot [\mathbf{e}(P_0) + \Delta\mathbf{e}(P_1)] - \mathbf{d}(P_0) \cdot [\mathbf{e}(P_0) + \Delta\mathbf{e}(P_1)] + \mathbf{d}(P_0) \cdot \Delta\mathbf{e}(P_1) \\ &= \Delta\mathbf{d}(P_1) \cdot \mathbf{e}(P_1) - \mathbf{d}(P_0) \cdot \Delta\mathbf{e}(P_1). \end{aligned} \quad (6.8)$$

Now it is no longer possible to eliminate the displacement $\mathbf{d}(P_0)$ of the reference point because of the variation Δe of the sensitivity vector [542], as shown already in the example in Section 5.1.2, Fig. 5.3.

Equations (6.7) and (6.8) allow the following interpretation. A *rigid body translation*, which implies a constant displacement vector \mathbf{d} for all P will yield a constant interference phase if also the sensitivity vector is constant, (6.7), thus no fringes can be observed. On the other hand for a varying sensitivity vector the term $\mathbf{d}(P_0) \cdot \Delta e(P_1)$ in (6.8) will not vanish for all P_1 and fringes are produced although $\mathbf{d}(P_1)$ is constant over all P_1 . This observation gives rise to a method for measuring absolute vectorial displacements from fringe patterns produced with the help of *varying sensitivity vectors* [542].

Let us assume that interference phase values $\Delta\phi_m^n$ are determined at M points P_m for N sensitivity vectors e^n :

$$\Delta\phi_m^n = \mathbf{d}(P_m) \cdot \mathbf{e}^n(P_m) + \phi_0^n(P_1) \quad n = 1, \dots, N; m = 1, \dots, M. \quad (6.9)$$

Since the phase is assumed to be continuously counted between the P_m , there are only N unknown constants $\phi_0^n(P_1)$, namely one for each sensitivity vector, but for a single arbitrary reference point, here chosen as P_1 . Altogether we have NM equations with $3M + N$ unknowns. This system of equations may be solved only if $NM \geq 3M + N$. One sees that no solutions exist for $N \leq 3$ or $M = 1$. $N = 4$ implies $M \geq 4$, $N = 5$ requires $M \geq 3$, and all $N \geq 6$ yield solutions provided that $M \geq 2$. We recognize that we need at least $N = 4$ sensitivity vectors, which means at least four holographic recordings with different illumination directions and/or observation directions.

The case $N = M = 4$ should be considered in more detail. The 16 equations (6.9) are organized into the matrix equation

$$\begin{pmatrix} \Delta\phi_1^1 \\ \Delta\phi_1^2 \\ \Delta\phi_1^3 \\ \Delta\phi_1^4 \\ \Delta\phi_2^1 \\ \Delta\phi_2^2 \\ \Delta\phi_2^3 \\ \Delta\phi_2^4 \\ \Delta\phi_3^1 \\ \Delta\phi_3^2 \\ \Delta\phi_3^3 \\ \Delta\phi_3^4 \\ \Delta\phi_4^1 \\ \Delta\phi_4^2 \\ \Delta\phi_4^3 \\ \Delta\phi_4^4 \end{pmatrix} = \begin{pmatrix} e_{x1}^1 & e_{y1}^1 & e_{z1}^1 & 0 & 0 & 0 & 0 & 0 & 0 & 0 & 0 & 0 & 0 & 1 & 0 & 0 & 0 \\ e_{x1}^2 & e_{y1}^2 & e_{z1}^2 & 0 & 0 & 0 & 0 & 0 & 0 & 0 & 0 & 0 & 0 & 0 & 0 & 1 & 0 & 0 \\ e_{x1}^3 & e_{y1}^3 & e_{z1}^3 & 0 & 0 & 0 & 0 & 0 & 0 & 0 & 0 & 0 & 0 & 0 & 0 & 0 & 1 & 0 \\ e_{x1}^4 & e_{y1}^4 & e_{z1}^4 & 0 & 0 & 0 & 0 & 0 & 0 & 0 & 0 & 0 & 0 & 0 & 0 & 0 & 0 & 1 \\ 0 & 0 & 0 & e_{x2}^1 & e_{y2}^1 & e_{z2}^1 & 0 & 0 & 0 & 0 & 0 & 0 & 0 & 0 & 1 & 0 & 0 & 0 \\ 0 & 0 & 0 & e_{x2}^2 & e_{y2}^2 & e_{z2}^2 & 0 & 0 & 0 & 0 & 0 & 0 & 0 & 0 & 0 & 1 & 0 & 0 \\ 0 & 0 & 0 & e_{x2}^3 & e_{y2}^3 & e_{z2}^3 & 0 & 0 & 0 & 0 & 0 & 0 & 0 & 0 & 0 & 0 & 1 & 0 \\ 0 & 0 & 0 & e_{x2}^4 & e_{y2}^4 & e_{z2}^4 & 0 & 0 & 0 & 0 & 0 & 0 & 0 & 0 & 0 & 0 & 0 & 1 \\ 0 & 0 & 0 & 0 & 0 & 0 & e_{x3}^1 & e_{y3}^1 & e_{z3}^1 & 0 & 0 & 0 & 0 & 1 & 0 & 0 & 0 & 0 \\ 0 & 0 & 0 & 0 & 0 & 0 & e_{x3}^2 & e_{y3}^2 & e_{z3}^2 & 0 & 0 & 0 & 0 & 0 & 0 & 1 & 0 & 0 \\ 0 & 0 & 0 & 0 & 0 & 0 & e_{x3}^3 & e_{y3}^3 & e_{z3}^3 & 0 & 0 & 0 & 0 & 0 & 0 & 0 & 0 & 1 \\ 0 & 0 & 0 & 0 & 0 & 0 & e_{x3}^4 & e_{y3}^4 & e_{z3}^4 & 0 & 0 & 0 & 0 & 0 & 0 & 0 & 0 & 1 \\ 0 & 0 & 0 & 0 & 0 & 0 & 0 & 0 & 0 & e_{x4}^1 & e_{y4}^1 & e_{z4}^1 & 1 & 0 & 0 & 0 & 0 & 0 \\ 0 & 0 & 0 & 0 & 0 & 0 & 0 & 0 & 0 & e_{x4}^2 & e_{y4}^2 & e_{z4}^2 & 0 & 1 & 0 & 0 & 0 & 0 \\ 0 & 0 & 0 & 0 & 0 & 0 & 0 & 0 & 0 & e_{x4}^3 & e_{y4}^3 & e_{z4}^3 & 0 & 0 & 1 & 0 & 0 & 0 \\ 0 & 0 & 0 & 0 & 0 & 0 & 0 & 0 & 0 & e_{x4}^4 & e_{y4}^4 & e_{z4}^4 & 0 & 0 & 0 & 1 & 0 & 0 \end{pmatrix} \begin{pmatrix} d_{x1} \\ d_{y1} \\ d_{z1} \\ d_{x2} \\ d_{y2} \\ d_{z2} \\ d_{x3} \\ d_{y3} \\ d_{z3} \\ d_{x4} \\ d_{y4} \\ d_{z4} \\ \phi_01 \\ \phi_02 \\ \phi_03 \\ \phi_04 \end{pmatrix} \quad (6.10)$$

which again is written shortly as $\Delta\phi = \mathbf{E} \cdot \mathbf{d}$. The solution is found analogously to (6.4) or (6.5). It is easily shown that the matrix \mathbf{E} becomes singular when there is no variation of the sensitivity vectors across the surface of the object. As soon as the displacements have been calculated for four points by the presented method, the absolute phase can be determined for all points and the displacement of other object points now may be calculated by the methods of Section 6.1.1. The above mentioned method is equivalent to the method presented in [543–

545], which also uses four sensitivity vectors and four object points but reduces the rank of the matrix to 12 by employing fringe order differences corresponding to interference phase differences. Therefore only displacements relative to a reference point are calculated in this latter case.

If the interference phase differences are determined by one of the *dynamic evaluation* methods of Section 5.7, also no reference displacement has to be known. For a three-dimensional evaluation of the displacement vector field at each object point of interest P a system of at least three equations of the form of (5.67) has to be solved. Let three interference phase differences $\Delta\Delta\phi^{1,2}(P)$, $\Delta\Delta\phi^{3,4}(P)$ and $\Delta\Delta\phi^{5,6}(P)$ be evaluated at P , then from (5.67) we get

$$\begin{aligned} & \begin{pmatrix} \Delta\Delta\phi^{1,2}(P) \\ \Delta\Delta\phi^{3,4}(P) \\ \Delta\Delta\phi^{5,6}(P) \end{pmatrix} \\ &= \frac{2\pi}{\lambda} \begin{pmatrix} b_x^2(P) - b_x^1(P) & b_y^2(P) - b_y^1(P) & b_z^2(P) - b_z^1(P) \\ b_x^4(P) - b_x^3(P) & b_y^4(P) - b_y^3(P) & b_z^4(P) - b_z^3(P) \\ b_x^6(P) - b_x^5(P) & b_y^6(P) - b_y^5(P) & b_z^6(P) - b_z^5(P) \end{pmatrix} \begin{pmatrix} d_x(P) \\ d_y(P) \\ d_z(P) \end{pmatrix} \quad (6.11) \end{aligned}$$

which has to be inverted. For more than three measurements the corresponding least squares system analogous to (6.5) has to be solved.

The two-dimensional case [287], when one component of the displacement vector is known, may lead to matrices of lower rank. But it is not treated separately here since the underlying theory is equivalent to the three-dimensional case.

It must be noted that the matrices employed in the evaluation methods of this section are prone to bad condition. So they have to be checked by a measure of condition as will be introduced in Section 6.2.3.

6.1.3 Elimination of Overall Displacement

In a number of applications the interesting displacement field is overlayed by another displacement, e. g. a defect induced deformation is embedded in rigid body motions and homogeneous deformations. To validate the risk by this defect it may be helpful to discriminate the defect induced deformation from the overall displacement field. This can be done quantitatively in the displacement domain after the determination of the displacement field. But for a number of problems it is sufficient to consider the interference phase distribution to achieve good qualitative statements.

The overall displacement field is determined by the method of *Gaussian least squares*, which in the following is demonstrated for the interference phase distribution of a tensile test specimen with an internal crack [546, 547]. Experimental observations and theoretical considerations show that the deformation is a combination of

- a constant translation t_x in longitudinal direction,
- a linearly increasing translation $\varepsilon(x - x_0)$, caused by the strain ε ,
- a constant transversal translation t_z ,

- linearly increasing translation in transversal direction $\tan \gamma(x - x_0)$ due to a tilt γ ,
- the displacement $d_z(x)$ created by the defect.

If an arrangement with no sensitivity in the y -direction is used, the interference phase outside the defect range can be written according to (6.1) as

$$\begin{aligned}\Delta\phi(x) &= d_x(x)e_x(x) + d_z(x)e_z(x) \\ &= t_x e_x(x) + \varepsilon(x - x_0)e_x(x) + t_z e_z(x) + \tan \gamma(x - x_0)e_z(x).\end{aligned}\quad (6.12)$$

The parameters t_x , t_z , ε , and $\tan \gamma$ are now determined by the least squares method from the measured interference phase values $\Delta\phi(x_i)$ outside the defect area. The system of equations to be solved is

$$\begin{pmatrix} \sum e_{xi}^2 & \sum (x_i - x_0)e_{xi}^2 & \sum e_{xi}e_{zi} & \sum (x_i - x_0)e_{xi}e_{zi} \\ \sum (x_i - x_0)e_{xi}^2 & \sum (x_i - x_0)^2 e_{xi}^2 & \sum (x_i - x_0)e_{xi}e_{zi} & \sum (x_i - x_0)^2 e_{xi}e_{zi} \\ \sum e_{xi}e_{zi} & \sum (x_i - x_0)e_{xi}e_{zi} & \sum e_{zi}^2 & \sum (x_i - x_0)e_{zi}^2 \\ \sum (x_i - x_0)e_{xi}e_{zi} & \sum (x_i - x_0)^2 e_{xi}e_{zi} & \sum (x_i - x_0)e_{zi}^2 & \sum (x_i - x_0)^2 e_{zi}^2 \end{pmatrix} \begin{pmatrix} t_x \\ \varepsilon \\ t_z \\ \tan \gamma \end{pmatrix} = \begin{pmatrix} \sum \Delta\phi_i e_{xi} \\ \sum \Delta\phi_i (x_i - x_0)e_{xi} \\ \sum \Delta\phi_i e_{zi} \\ \sum \Delta\phi_i (x_i - x_0)e_{zi} \end{pmatrix} \quad (6.13)$$

where $e_{xi} = e_x(x_i)$, $e_{zi} = e_z(x_i)$, $\Delta\phi_i = \Delta\phi(x_i)$. $e_x(x_i)$, $e_z(x_i)$ and the coordinate of the clamping x_0 are determined from the holographic arrangement. After solving (6.13), the normal displacement $d_z(x)$ in the defect range can be expressed as

$$d_z(x) = \frac{\Delta\phi(x)}{e_z(x)} - [t_x + \varepsilon(x - x_0)] \frac{e_x(x)}{e_z(x)} - t_z - \tan \gamma(x - x_0). \quad (6.14)$$

Figure 6.1a shows an evaluated interference phase distribution and Fig. 6.1b displays the deformation induced by the defect alone.

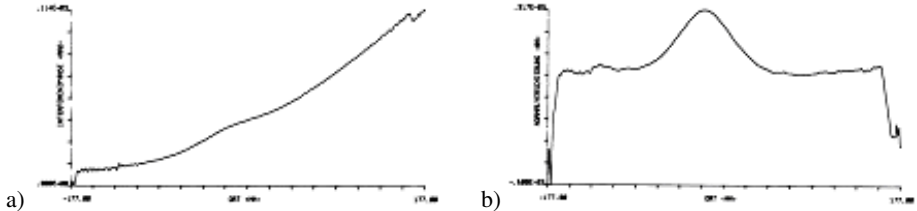


Figure 6.1: Defect induced deformation.

The same method applied in two dimensions is presented in Fig. 6.2. Figures 6.2a to d show four phase stepped holographic interferograms of a pressurized vessel. The interference phase, Fig. 6.2e, is determined by phase sampling evaluation. The surface deformation caused by the internal defect is given in Fig. 6.2f. The displayed distribution is proportional to a normal displacement with a peak to valley difference of about 700 nm.

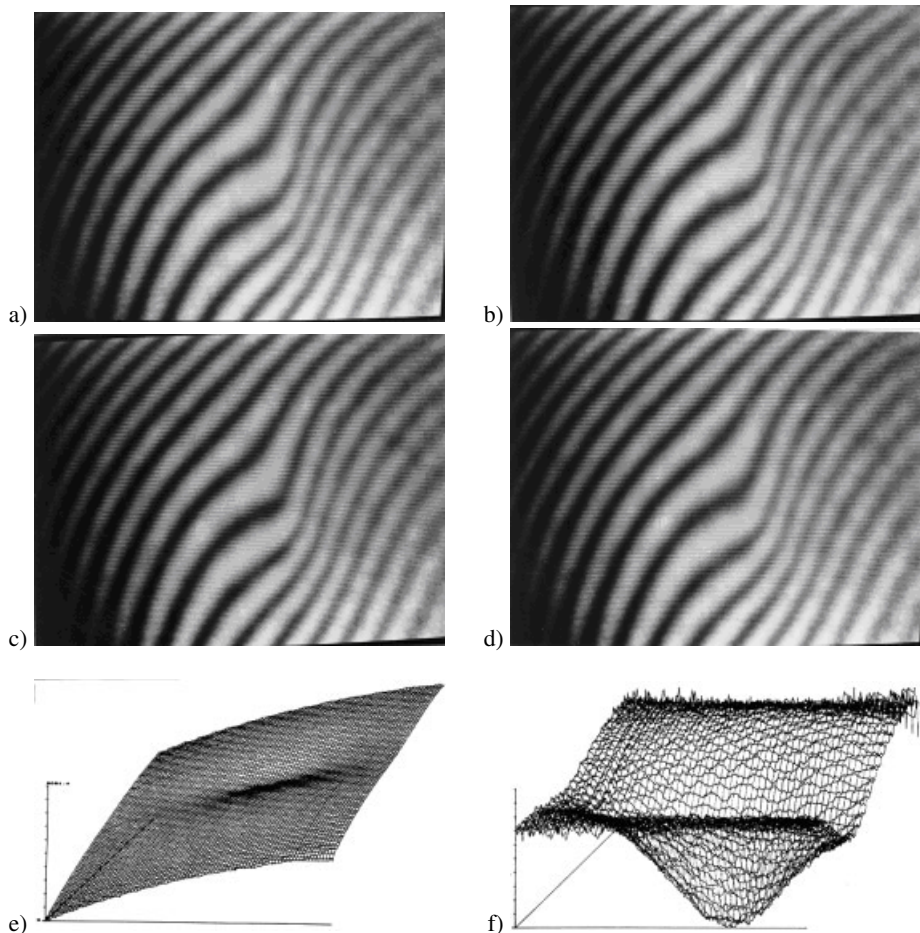


Figure 6.2: (a – d) Phase shifted holographic interference patterns, (e) evaluated interference phase, (f) defect induced deformation.

The fitting of quadratic forms to the interference phase is described in [548], while fitting of polynomials is presented in [481]. Of special interest here is the use of *Zernike polynomials* which generally describe wavefronts in optical testing. Mader [355] reports on a nonlinear least squares fitting program to model the intensity of the holographic interferogram.

6.1.4 Non-Vibration Isolated Objects

In *holographic interferometric metrology* and in *holographic nondestructive testing* the displacement of a surface relative to the illumination source and to the observer is measured. Spurious motions of the object may corrupt the measurement result and thus have to be avoided. The common method is to place all optical components as well as the object onto a vibra-

tion isolated table in a laboratory environment. But especially when dealing with large scale technical objects in industrial environments it is not generally possible to avoid stochastic vibrations of the object and the holographic arrangement. Stochastic motions and vibrations of the object during and between the two recordings of a double-exposure hologram normally destroy any stationary wave field, thus no hologram or interference pattern will be gained. In the following some approaches to circumvent these problems are reported.

To avoid the smearing of the microinterference due to motion during the exposure it must be guaranteed that no significant relative motion between the components occurs. Generally the tendency to unwanted motions can be diminished by keeping the holographic arrangement compact, and by avoiding complicated folded beam paths with many mirrors or beam splitters. If object motions cannot be avoided, *pulsed lasers* instead of *CW lasers* have to be employed [549]. Although good quality holograms of *non-vibration isolated objects* can be generated with a pulsed laser, there remains the uncertainty about parasitic object motion between the two exposures of a double exposure holographic interferogram.

The problem can be solved by the *object related triggering* of the laser [550]. This is accomplished by a CW laser with an intra-cavity *acoustooptic modulator*. External modulation with a Pockels cell is principally possible but the acoustooptic modulator offers the advantage that the laser loses no energy during the closing time of the modulator. The modulator is controlled by the motion of the object, which is measured at one surface point. This measurement can be performed optically or mechanically by a contacting method. In [550] an acceleration detector, amplifier, and comparator is used. A temporal modulation of the laser is realized, exposing the hologram plate only when the chosen object point passes an interval of about $\lambda/10$ around its resting position. The method can be viewed as the transient counterpart of *stroboscopic holography* applied to periodically vibrating structures.

Another way to stabilize the microinterference pattern is the shifting of one of the interfering waves, normally the reference wave, by *feedback control* [551]. The feedback system consists of a phase detector, the electronics, which yield the control signal and an optical phase modulator. The phase detector for generating the electrical signal proportional to the relative phase of the interfering beams may consist of a magnifying microscope objective, a slit and a photomultiplier [551]. The phase modulator driven by the control signal for changing the relative phase of the two wave fields is a mirror fixed on a piezoelectric crystal. Using such a feedback control not only compensates for spurious motions of the object itself which may be caused by acoustic noise, but also for stochastic variations in the interfering wave fields caused by e. g. thermal drift or air turbulence [551]. A refined version of this approach is used for the detection and compensation of misalignments caused by thermally induced deformations in space-borne interferometers [552].

A fringe stabilization method related to both the aforementioned methods is the stabilization by *frequency modulation*, where laser frequency shifts are generated by changing the laser cavity length [553]. The holographic interferometer in this case has different optical pathlengths for object and reference wave. Because of the difference in transit times of beams traversing the unequal paths, a shift in laser frequency results in a relative phase shift of the interfering waves and thus in a lateral shift of the generated fringes at the recording medium. The control signal generated by the photomultiplier and the electronics like in the aforementioned method now is applied to a piezoelectric transducer upon which one of the laser cavity reflec-

tors is mounted. With such a system undesired fringe motion is compensated for, whether due to laser frequency drift or interferometer path difference perturbations [553].

The easiest way to perform a compensation of unwanted object motions by modulating the phase of the reference wave is to direct the reference beam over a small mirror fixed to the object [554–556]. The reference wave thus is reflected out of the object illumination wave by wavefront division. The mirror undergoes the same motions as the point of the object to which it is fixed. A mathematical analysis is based on the fact that the mirror is specularly reflecting while the object surface is diffusely reflecting [554]. The analysis shows that with such a reference mirror not only the rigid body motions of the object are compensated but additionally we have one point in the fringe pattern where the interference order is known to be zero, namely the point of the mirror reflecting the illumination source point to the observation point.

The consequent continuation of these ideas leads to the fixation of the whole holographic arrangement onto the object whose surface deformations instead of the rigid body motions should be measured. Especially for large scale objects this is feasible. In such a way the deformation of a 4.5 m high *pressure vessel* with steel walls of 45 mm thickness has been measured holographically [546]. Some interferograms produced in this experiment have been shown in Fig. 6.2. The whole holographic arrangement including the laser was attached to the vessel by magnetic feet. Moreover, good results have been obtained, if the object is sprayed with a retroreflective paint and only the hologram plate is rigidly attached to it [557].

Although there exist effective methods to stabilize the microinterference fringes to be recorded in the hologram there still may remain an unknown rigid body motion between the two exposures of a double-exposure hologram. A compensation for this motion is possible during the reconstruction when the holographic interference pattern is generated. If the two states are recorded on separate hologram plates, these two plates after development may be tilted and shifted in the reference wave, a procedure called *sandwich hologram interferometry* [558–565]. The relative motion of the plates leads to a relative motion of the reconstructed wave fields, with the consequence that an object translation can be compensated. It is helpful if an area on the object, on the frame, or else in the arrangement, is visible through the holograms, where it is known that no displacement must have occurred. While in sandwich holography the two plates are close together in a common reference wave – thus the name of the method – the two plates can be fully separated with individual reference waves acting on them [566, 567]. Then one of the two plates is fixed to a hologram holder that has all degrees of freedom to move with a precision better than 1 μm . This method is suitable for compensating stress-induced translations in non-destructive testing leading to defect fringes on an infinite fringe background [568]. A detailed theoretical analysis of fringe modifications in the holographic interferometric measurement of large deformations is given in [569, 570].

In holographic measurements of phase objects the idea of dividing the reference wave out of the object wave can be realized not only by using a reference mirror at or near the object but also by extracting the zero frequency out of the whole field in the focal plane of a lens, while the object wave is contained in the first diffraction order [571]. The phase object for this approach is illuminated by a plane wave that has passed a Ronchi grating. To separate the reference and the object wave a spatial filter with two holes must be placed in the focal plane of a lens. A second lens images these two fields onto a plane where they interfere. Since object

beam and reference beam take a common path, this interferometer is proof against external vibrations.

6.2 The Sensitivity Matrix

In the preceding section it has been shown how the displacement vectors are determined from the evaluated interference phase distributions. Connecting elements are the sensitivity vectors which in all evaluations of more than one dimension are combined in the *sensitivity matrix*. This section now will discuss how to obtain the components of the sensitivity matrix and how its condition can be quantified, which is the main property defining the achievable accuracy of the measurement results.

6.2.1 Determination of the Sensitivity Vectors

The *sensitivity vectors* $e(P)$ are calculated by (4.20) with the help of the unit vectors $s(P)$ in the illumination direction and $b(P)$ in the observation direction as defined in (4.18) and (4.19). To find out the sensitivity vectors of a specific experiment in an arbitrary but fixed Cartesian coordinate system one needs the coordinates of the *illumination point S*, which is the focal point of the optics used for expanding the illuminating laser beam, the coordinates of the *observation point B*, which is the center of the entrance pupil of the observing optical system, and the coordinates of the object points P of interest. For collimated illumination or observation the unit vectors are colinear with the illumination or observation directions and are identical for all object surface points.

Although the choice of the origin of the coordinate system is arbitrary, two options yield easier mathematics, since some components then will be zero. First, if the surface to be measured is plane, an origin at the surface with two axes lying in the surface plane should be chosen; second, for arbitrarily shaped object surfaces, a coordinate system with one axis colinear to the line connecting the illumination with the observation point and the origin halfway between these points is advantageous. Nevertheless the determination of the sensitivity vectors remains involved, especially for objects of complicated three-dimensional shape, for wide-angle or multiple illumination directions, or when mirrors are used for back or side views of the tested objects.

The straightforward approach is to make simple yardstick measurements between representative points of the holographic arrangement and then to calculate the necessary coordinates. Often the geometry or the contour of the object surface is given by design data, otherwise it has to be measured. There are optical methods for *contour measurement*, like triangulation, projected fringe, moiré, or holographic methods, which may be applied [164, 572]. In the following only the holographic interferometric methods of these will be discussed.

In the preceding section methods were treated as to how to determine the unknown displacement vectors of surface points from known sensitivity vectors and measured interference phase values. The methods for the determination of the sensitivity vectors to be presented here employ known displacements or known rotations together with measured phases to determine the a priori unknown sensitivity vectors [573].

Consider three separate double exposure holograms of the object undergoing three different, but known, *rigid body displacements* \mathbf{d}^1 , \mathbf{d}^2 , and \mathbf{d}^3 , which must not be effected in coplanar directions. Assume the same recording and observation geometry for the three holograms with respect to the object. This ensures an invariant sensitivity vector from one recording to the other. Now evaluate the interference phases $\Delta\phi^1(P)$, $\Delta\phi^2(P)$, and $\Delta\phi^3(P)$ corresponding to the three displacements and the sensitivity vector $\mathbf{e}(P)$ is obtained as the solution of

$$\begin{pmatrix} \Delta\phi_1(P) \\ \Delta\phi_2(P) \\ \Delta\phi_3(P) \end{pmatrix} = \begin{pmatrix} d_x^1 & d_y^1 & d_z^1 \\ d_x^2 & d_y^2 & d_z^2 \\ d_x^3 & d_y^3 & d_z^3 \end{pmatrix} \begin{pmatrix} e_x(P) \\ e_y(P) \\ e_z(P) \end{pmatrix}. \quad (6.15)$$

The alternative approach is to use three rigid body rotations. Let the rotation vectors defining direction and rotation angles be $\boldsymbol{\theta}^1$, $\boldsymbol{\theta}^2$, and $\boldsymbol{\theta}^3$. We employ the so called *fringe-vector* $\mathbf{K}_f(P)$, whose magnitude is inversely proportional to the normal distance between the spatial fringe shells intersecting the object surface and whose direction coincides with the direction of this normal pointing to the fringe shell of higher interference order. The fringe vector for rotations is given by

$$\mathbf{K}_f(P) = -\boldsymbol{\theta} \times \mathbf{e}(P) \quad (6.16)$$

where \times here denotes the vectorial product. The threefold evaluation of $\mathbf{K}_f(P)$ for each P of interest with $\boldsymbol{\theta}^1$, $\boldsymbol{\theta}^2$, and $\boldsymbol{\theta}^3$ and the identical sensitivity vectors enables one to set up the system of equations

$$\begin{pmatrix} K_{fx}^1(P) & K_{fy}^1(P) & K_{ fz}^1(P) \\ K_{fx}^2(P) & K_{fy}^2(P) & K_{ fz}^2(P) \\ K_{fx}^3(P) & K_{fy}^3(P) & K_{ fz}^3(P) \end{pmatrix} = \begin{pmatrix} \theta_x^1 & \theta_y^1 & \theta_z^1 \\ \theta_x^2 & \theta_y^2 & \theta_z^2 \\ \theta_x^3 & \theta_y^3 & \theta_z^3 \end{pmatrix} \begin{pmatrix} 0 & e_z(P) & -e_y(P) \\ -e_z(P) & 0 & e_x(P) \\ e_y(P) & -e_x(P) & 0 \end{pmatrix} \quad (6.17)$$

which is then solved to obtain $\mathbf{e}(P)$ for each P . With these methods the problem of the determination of the geometry data is transferred to the task of performing precisely the necessary displacements or rotations and to evaluate the interference phase or fringe-vector unambiguously [574].

Another holographic approach is proposed in [575], where the object contours are measured by the holographic contouring using displaced illumination points, see Section 6.6.3. The main advantages are that the fringe pattern now is located on the surface and shows good visibility even for large illumination point displacements, and that the method works contactless with respect to the object.

6.2.2 Correction of Perspective Distortion

The determination of more than one component of the displacement vector necessitates the generation of several interference patterns which in turn are produced with different configuration geometries. If the observation direction varies between the recordings, the fringe patterns

suffer from different *perspective distortions*. Especially when measuring at non-plane objects, errors induced by defocusing of the object surface and distortion due to perspective have to be taken into account [576]. For an oblique sight of the inspected surface, this surface appears deformed in the recorded image and often does not fill the full frame. A *spatial transform* has to map the pixels of the recorded interferogram to new pixels in an output interferogram, such that identical points of the object surface, which are imaged to different pixels in the various recorded images, are mapped to identical pixels in all output images.

In the following, an algorithm is given for the spatial transform which corrects perspective distortion in the case of plane surfaces. Without loss of generality, we assume a rectangular surface area to be evaluated, which by perspective distortion is deformed to an arbitrary convex quadrangle, Fig. 6.3. The spatial transform is performed by a *bilinear interpolation*, which

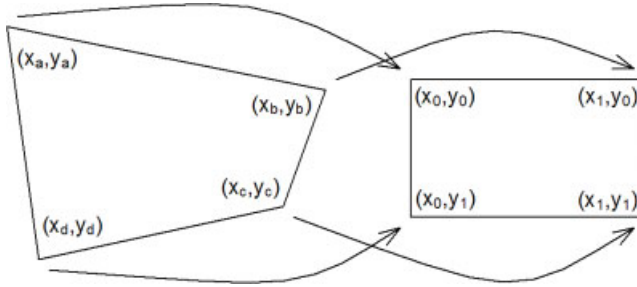


Figure 6.3: Bilinear mapping of a quadrangle onto a rectangle.

on the one hand is fast and computationally simple, and on the other hand produces a smooth mapping that preserves continuity and connectivity.

Let $I(x, y)$ be the recorded and stored perspectively distorted interferogram with pixel coordinates (x, y) . Then the corrected interference pattern is $I'(x, y)$:

$$I'(x, y) = I(x', y') = I(ax + by + cxy + d, ex + fy + gxy + h). \quad (6.18)$$

This bilinear transformation is defined by the values of the eight coefficients a through h . By specifying the mapping of the four vertices (x_a, y_a) , (x_b, y_b) , (x_c, y_c) , (x_d, y_d) of the quadrangle to the four vertices (x_0, y_0) , (x_1, y_0) , (x_1, y_1) , (x_0, y_1) of the output rectangle, we create a system of four equations

$$\begin{pmatrix} x_a \\ x_b \\ x_c \\ x_d \end{pmatrix} = \begin{pmatrix} x_0 & y_0 & x_0y_0 & 1 \\ x_1 & y_0 & x_1y_0 & 1 \\ x_1 & y_1 & x_1y_1 & 1 \\ x_0 & y_1 & x_0y_1 & 1 \end{pmatrix} \begin{pmatrix} a \\ b \\ c \\ d \end{pmatrix}. \quad (6.19)$$

After inversion of the matrix we get the four coefficients a , b , c , and d as

$$\begin{pmatrix} a \\ b \\ c \\ d \end{pmatrix} = \frac{1}{(x_0 - x_1)(y_1 - y_0)} \begin{pmatrix} y_1 & -y_1 & y_0 & -y_0 \\ x_1 & -x_0 & x_0 & -x_1 \\ -1 & 1 & -1 & 1 \\ -x_1y_1 & x_0y_1 & -x_0y_0 & x_1y_0 \end{pmatrix} \begin{pmatrix} x_a \\ x_b \\ x_c \\ x_d \end{pmatrix}. \quad (6.20)$$

The y_a through y_d are given by a system of equations similar to (6.19)

$$\begin{pmatrix} y_a \\ y_b \\ y_c \\ y_d \end{pmatrix} = \begin{pmatrix} x_0 & y_0 & x_0y_0 & 1 \\ x_1 & y_0 & x_1y_0 & 1 \\ x_1 & y_1 & x_1y_1 & 1 \\ x_0 & y_1 & x_0y_1 & 1 \end{pmatrix} \begin{pmatrix} e \\ f \\ g \\ h \end{pmatrix} \quad (6.21)$$

where the four coefficients e , f , g , and h are given by

$$\begin{pmatrix} e \\ f \\ g \\ h \end{pmatrix} = \frac{1}{(x_0 - x_1)(y_1 - y_0)} \begin{pmatrix} y_1 & -y_1 & y_0 & -y_0 \\ x_1 & -x_0 & x_0 & -x_1 \\ -1 & 1 & -1 & 1 \\ -x_1y_1 & x_0y_1 & -x_0y_0 & x_1y_0 \end{pmatrix} \begin{pmatrix} y_a \\ y_b \\ y_c \\ y_d \end{pmatrix}. \quad (6.22)$$

Thus the coefficients of the bilinear transform are defined. The transform can be implemented by (6.18), but a computationally more efficient algorithm is based on a line by line processing of the output image. Each new pixel coordinate is calculated by an increment from the foregoing one. The increments are constant along one line and are raised by a constant increment from line to line.

The spatial transform for each pixel calculates the original position of this pixel in the input image. In most cases it stems from a fractional position in the input pattern, meaning that its origin is between four adjacent pixels. So an interpolation is necessary to determine the gray level of the output pixel. The simplest interpolation is the nearest neighbor interpolation. A better solution, especially if significant gray level changes occur over one unit of pixel spacing, consists of applying the *bilinear interpolation*. Let us look for the intensity $I(n + x, m + y)$ at the fractional position $(n + x, m + y)$ with integers n and m and $x, y \in (0, 1)$, Fig. 6.4.

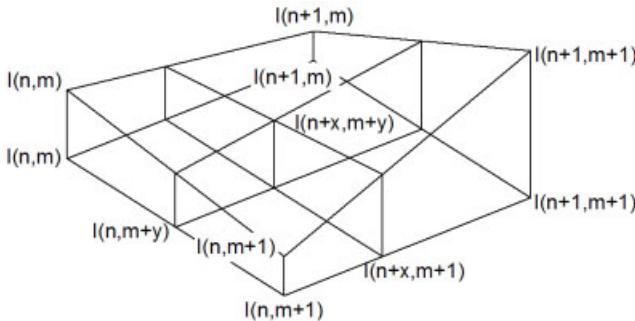


Figure 6.4: Bilinear mapping of the intensity.

The bilinear interpolation then gives

$$\begin{aligned} I(n + x, m + y) = & I(n, m) + [I(n + 1, m) - I(n, m)]x \\ & + [I(n, m + 1) - I(n, m)]y \\ & + [I(n + 1, m + 1) + I(n, m) - I(n, m + 1) - I(n + 1, m)]xy \end{aligned} \quad (6.23)$$

An example of a correction of perspective distortion of a holographic interference pattern of a plane rectangular plate under deformation is given in Fig. 6.5.

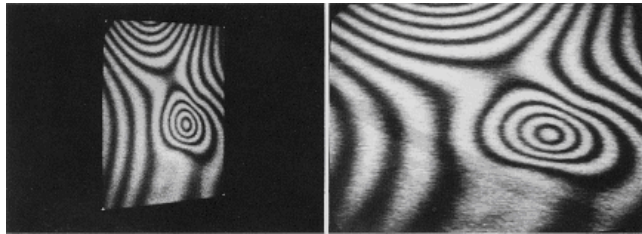


Figure 6.5: Correction of perspective distortion.

6.2.3 Condition of the Sensitivity Matrix

The determination of three-dimensional displacement fields requires the solution of linear systems of equations, as e. g. given in (6.3), (6.10), or (6.11). It is well known that if the equations are linearly dependent, leading to a *singular matrix* whose determinant is zero, the system is not solvable. However, even if the matrices on the right-hand side of (6.3), (6.10), or (6.11) are not singular, the solutions may show errors of up to some 100 percent in magnitude and direction if we have an *ill-conditioned matrix*. Therefore a holographic arrangement with sensitivity vectors oriented in a way yielding a well-conditioned matrix must be striven for.

A figure to measure the *condition of a system of linear equations*, or equivalently that of the matrix \mathbf{E} of this system, is the *Hadamard condition number* $K_H(\mathbf{E})$ defined as

$$K_H(\mathbf{E}) = \frac{|\det \mathbf{E}|}{\prod_{i=1}^n \alpha_i} \quad (6.24)$$

with

$$\alpha_i = \sqrt{\sum_{k=1}^n e_{ik}^2} \quad (6.25)$$

where n is the rank of matrix \mathbf{E} , whose elements are given by e_{ik} ; \det denotes the determinant. The system is ill-conditioned if $K_H(\mathbf{E}) \ll 1.0$, and is optimum for $K_H(\mathbf{E}) = 1.0$. A condition number of $K_H(\mathbf{E}) > 0.1$ is considered to be desirable.

The elements of the matrix are the components of the sensitivity vectors, these are derived from measurements of the geometry of the holographic arrangement. A good condition means that the directions of the sensitivity vectors are linearly independent and as different as possible. As a rule of thumb the sensitivity vectors should have as different directions in the three dimensions as possible.

Of course, the geometry has to be measured precisely. The precision of the geometry data influences the achievable accuracy of the measurement. However, even more important than a precise measurement of the geometry is a proper separation of the sensitivity vectors. With an ill-conditioned system even the smallest errors in the geometry values would cause severe measurement errors. The use of an overdetermined system of equations, which is solved by Gaussian least squares, yields on principle a higher accuracy due to the averaging

property [577–580], but it will cause nearly the same errors if the sensitivity vectors are not separated far enough.

6.3 Holographic Strain and Stress Analysis

In experimental mechanics the deformation of test objects in response to a mechanical or thermal load is studied in order to determine strains, stresses, or bending moments. These quantities are of interest because they affect the strength, safety, and lifetime of mechanical structures or components [170, 336]. A structure most likely will fail where the strain or stress is maximal.

Microstructures such as *microelectromechanical systems (MEMS)* have found numerous applications [239]. The reliability of these structures is determined by the assessment of the micromachining processes in realizing MEMS with the geometry and mechanical properties as required by the proper design. Since MEMS fabrication needs different materials and technological processes involving high temperature treatments, residual stresses can affect the final shape of the MEMS appearing in the form of undesired out-of-plane deformations. Thus it is instrumental for fabricating reliable MEMS to measure the effect of residual stress on the deformation of the single microstructures [113, 114, 239, 581, 582].

In this section the derivation of strains, stresses, and bending moments from holographically measured displacements of objects with opaque diffusely reflecting surfaces will be discussed. After the fundamental definitions, the most common structures, namely beams and plates, are treated in more detail, followed by a more general approach using the fringe-vector theory.

6.3.1 Definition of Elastomechanical Parameters

Let $P = (x_P, y_P, z_P)$ be the Cartesian coordinate description of a point of a solid object which is displaced by $\mathbf{d}(P) = (d_x(P), d_y(P), d_z(P))$. This notation is preferred here for reasons of consistency, while in the standard literature the components of the displacement vector often are written $(u, v, w) = (d_x, d_y, d_z)$. If there is no confusion, the argument P will be omitted in the following.

Strain generally is a tensor completely specified by nine components, of which six are independent [170, 583]. At any point in a solid body the three components of *normal strain* are

$$\varepsilon_x = \frac{\partial d_x}{\partial x}, \quad \varepsilon_y = \frac{\partial d_y}{\partial y}, \quad \varepsilon_z = \frac{\partial d_z}{\partial z} \quad (6.26)$$

and the three independent *shear strains* are

$$\gamma_{xy} = \frac{\partial d_x}{\partial y} + \frac{\partial d_y}{\partial x}, \quad \gamma_{yz} = \frac{\partial d_y}{\partial z} + \frac{\partial d_z}{\partial y}, \quad \gamma_{zx} = \frac{\partial d_z}{\partial x} + \frac{\partial d_x}{\partial z}. \quad (6.27)$$

While the normal strains describe the change of length per unit length in each coordinate direction, the shear strains measure the decrease in the angle between two line segments initially orthogonal and parallel to the coordinate axes. This is depicted in two dimensions for a small

rectangle with sidelengths Δx and Δy in Fig. 6.6. Since the angles are assumed to be only small, the arctangent in the exact definition of the shear strain is approximated by its argument in the above definition.

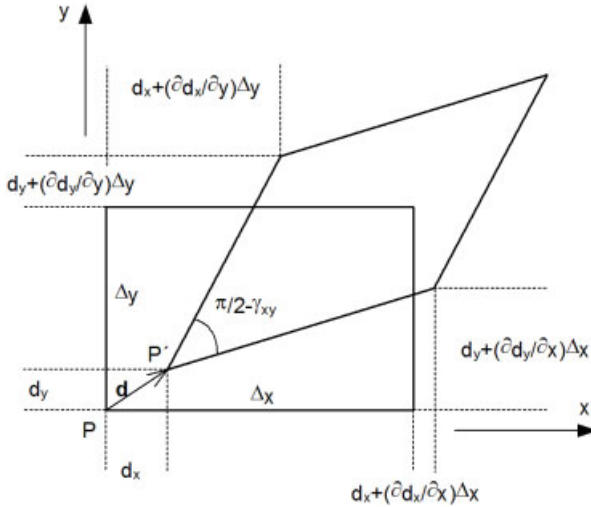


Figure 6.6: Elastic deformation of a small solid rectangle.

The strains are expressed as derivatives of the displacement components. Also the *rotations* of an object can be written by these derivatives: The components ω_x , ω_y , and ω_z describing the rotations about the x -, y -, and z -axes, respectively, are

$$\omega_x = \frac{1}{2} \left(\frac{\partial d_z}{\partial y} - \frac{\partial d_y}{\partial z} \right), \quad \omega_y = \frac{1}{2} \left(\frac{\partial d_x}{\partial z} - \frac{\partial d_z}{\partial x} \right), \quad \omega_z = \frac{1}{2} \left(\frac{\partial d_y}{\partial x} - \frac{\partial d_x}{\partial y} \right). \quad (6.28)$$

If external forces or moments affect a solid body, internal reactive forces maintain the equilibrium. As long as the masses are homogeneously distributed in the body, the reactive forces are distributed in planes. At each point of the solid an arbitrary cut dA can be defined. The *force* \mathbf{F} related to the unit plane element dA is the *stress* s

$$s = \frac{d\mathbf{F}}{dA} \quad (6.29)$$

which is composed of the *normal stress* $\sigma = dF_n/dA$ and the *tangential* or *shear stress* $\tau = dF_t/dA$, Fig. 6.7. The description of the complete stress state at a point requires three planes or equivalently a cubic element to define the *stress tensor*, Fig. 6.8.

$$\mathbf{S} = \begin{pmatrix} \sigma_{xx} & \tau_{xy} & \tau_{xz} \\ \tau_{yx} & \sigma_{yy} & \tau_{yz} \\ \tau_{zx} & \tau_{zy} & \sigma_{zz} \end{pmatrix}. \quad (6.30)$$

Since $\tau_{xy} = \tau_{yx}$, $\tau_{xz} = \tau_{zx}$, and $\tau_{yz} = \tau_{zy}$, we need three normal stresses and three shear stresses to describe the stress state of a point of a solid body. Some relations between strains and stresses for special cases will be discussed in the next subsection.

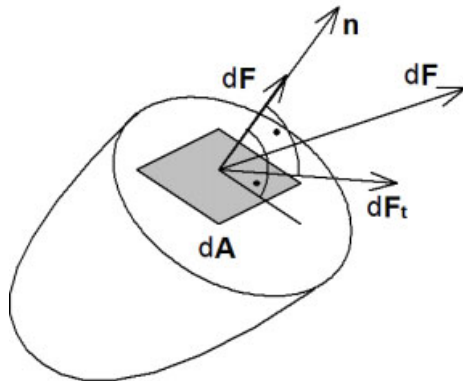


Figure 6.7: Normal and shear stress.

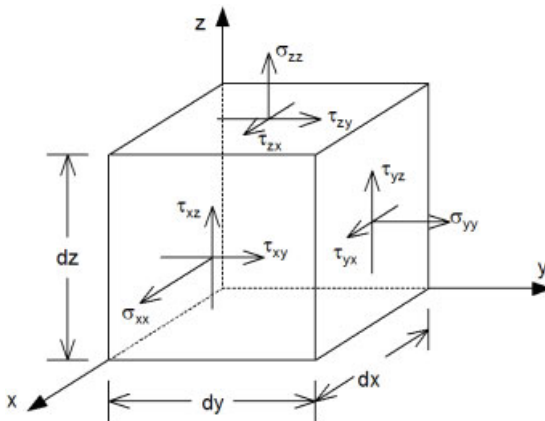


Figure 6.8: Elements of the stress tensor.

The aim of holographic strain and stress analysis is the determination of the strain or stress state of a tested component, which normally is done by measuring the displacement vector field and then calculating the strains and stresses according to the above introduced equations. But holographic interferometry does not provide sufficient information to process all the derivatives of (6.26) to (6.28). In particular the displacement derivatives in the direction normal to the surface of the opaque body cannot be evaluated. By applying the methods of Section 6.1 for a plane surface in the x - y -plane we may evaluate the displacement vector components $d_x(x, y)$, $d_y(x, y)$, $d_z(x, y)$ or precisely $d_x(x, y, z = 0)$, $d_y(x, y, z = 0)$, $d_z(x, y, z = 0)$, but we have no access to the general $d_x(x, y, z)$, $d_y(x, y, z)$, $d_z(x, y, z)$ in the interior $z \neq 0$ of the body.

Nevertheless what we have is sufficient to calculate the in-plane strains ε_x , ε_y and γ_{xy} in the plane surface as well as the in-plane rotation ω_z about an axis normal to the surface. We notice that the rotation components (6.28) are arithmetic averages of the rotations of two orthogonal faces of a cubic element, but this averaging is not required to evaluate the out-of-plane rotation of object surface points, $z = 0$ [170]. So the out of plane rotations at the surface

are

$$\omega_x = \frac{\partial d_z}{\partial y} \quad \omega_y = \frac{\partial d_z}{\partial x}. \quad (6.31)$$

A classic method for determining stresses in models of the interesting component fabricated from birefringent material or in other birefringent media, e. g. biological objects is *polarization imaging*. Polarization sensitive digital holography is presented in [122, 125]. A hologram of a specimen is created by the interference between object wave and two reference waves that have perpendicular polarization states. The reconstruction of such a hologram produces two wavefronts, one for each perpendicular polarization state. While this method takes advantage of only the reconstructed amplitude distributions, also the phase information is reconstructed in the approach published in [123].

6.3.2 Beams and Plates

The holographically measurable displacements $d(x, y, z = 0)$ are sufficient to describe the strains in the case of *plane stress*. We speak of a state of plane stress if a thin flat specimen is affected only by stresses parallel to its surface. Typical examples are the stretching of thin sheets or membranes and the tearing of flat tensile specimens commonly used to measure the mechanical properties of materials [170]. The in-plane strains for these objects are calculated from the measured $d_x(x, y)$ - and $d_y(x, y)$ -components of the displacement vector field.

The strains in another class of objects like beams, plates, or shells are determined from the measured displacement component $d_z(x, y)$ normal to the object surface.

A *beam* is a long slim solid component with a constant cross section subjected to transverse point loads, distributed or area loads, axial loads, and bending moments, Fig. 6.9. The length L of a beam generally is large compared with the width l and the thickness h : $L \gg l, L \gg h$. A beam is a common model for a number of technical components, like supporting beams, shafts, connecting rods, or turbine blades to name only a few.

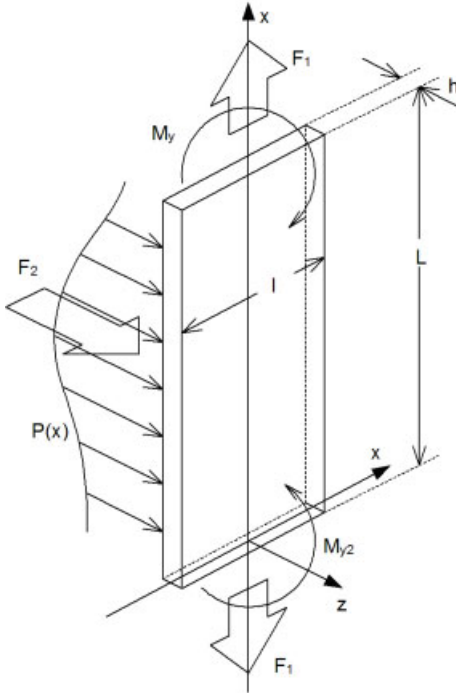
A popular test object among holographers is the *cantilever beam* showing only deflections $d_z(x)$ in the z -direction. The reasons for the popularity are that these deflections are easy to measure holographically – they are in the direction of highest sensitivity – most often we have $d_z = 0$ at the base of the beam thus avoiding the absolute phase problem. Furthermore the theory of these beams is simple and well elaborated to allow a comparison of experimental and theoretical results.

If the beam consists of a material which behaves elastically for the applied load amplitudes, which means stress and strain are proportional, then for example in the x -direction we have

$$\sigma_{xx} = E\varepsilon_x \quad (6.32)$$

where E is the *modulus of elasticity*. Also the shear stresses and the shear strains are proportional

$$\tau_{zx} = G\gamma_{zx} \quad (6.33)$$

**Figure 6.9:** Elastic beam.

with G the *shear modulus of elasticity*. G and E are connected via

$$G = \frac{E}{2(1 + \nu)} \quad (6.34)$$

where ν is the *Poisson ratio*, which in a specimen subjected to tensile or compressive load in the x -direction describes the constant ratio of lateral strain to longitudinal strain

$$\varepsilon_z = \nu \varepsilon_x. \quad (6.35)$$

E , G , and ν all are properties of the material of which the beam is fabricated.

If the beam of Fig. 6.9 is deflected responding to the transverse point load F_z , the distributed area-load $P_z(x)$, longitudinal forces F_x and bending moments M_{y1} , M_{y2} about axes parallel to the y -axis, the longitudinal strain at the observable surface is [170]

$$\varepsilon_x = \frac{\partial d_{x0}(x)}{\partial x} - \frac{1}{2}h \left(\frac{\partial^2 d_z(x)}{\partial x^2} \right). \quad (6.36)$$

Here $d_{x0}(x)$ is the displacement in the x -direction of the central plane at $z = 0$ of the beam due to the longitudinal forces F_x and h denotes the beam thickness. The longitudinal stress σ_{xx} at the surface of the beam then is

$$\sigma_{xx} = E \left[\frac{\partial d_{x0}(x)}{\partial x} - \frac{1}{2}h \left(\frac{\partial^2 d_z(x)}{\partial x^2} \right) \right]. \quad (6.37)$$

As long as the deflections remain small the bending moment at any x is

$$M_y = -\frac{Eh^3}{12} \left(\frac{\partial^2 d_z(x)}{\partial x^2} \right). \quad (6.38)$$

A *plate* is a component where the width l is in the same range as the length L , $l \approx L$, but the constant thickness h is small compared to L and l : $h \ll l, h \ll L$, Fig. 6.10. The plate is

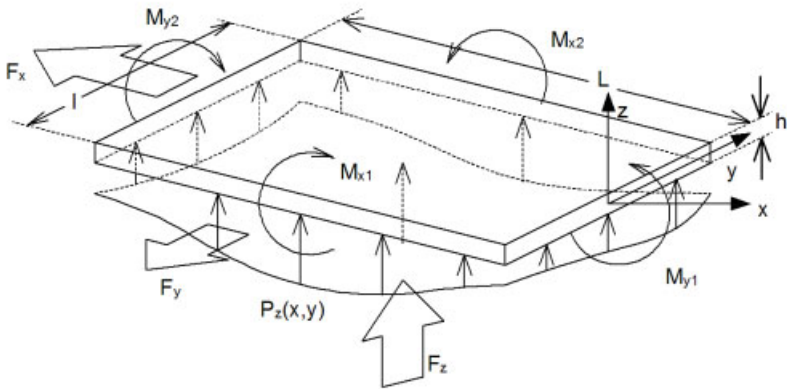


Figure 6.10: Elastic plate.

deformed e. g. by a distributed area-load $P_z(x, y)$, transverse forces F_z , axial forces F_x, F_y applied at its edges, as well as moments, M_x and M_y , acting at the edges. Then the strains at the observable surface are

$$\begin{aligned} \varepsilon_x &= \frac{\partial d_{x0}(x, y)}{\partial x} - \frac{1}{2}h \left(\frac{\partial^2 d_z(x, y)}{\partial x^2} \right) \\ \varepsilon_y &= \frac{\partial d_{y0}(x, y)}{\partial y} - \frac{1}{2}h \left(\frac{\partial^2 d_z(x, y)}{\partial y^2} \right) \\ \gamma_{xy} &= \left(\frac{\partial d_{x0}(x, y)}{\partial x} + \frac{\partial d_{y0}(x, y)}{\partial y} \right) - h \left(\frac{\partial^2 d_z(x, y)}{\partial x \partial y} \right) \end{aligned} \quad (6.39)$$

where $d_{x0}(x, y)$ and $d_{y0}(x, y)$ are the components of the in-plane translation of the central plane at $z = 0$ of the plate due to the axial forces F_x or F_y . The corresponding stresses are again $\sigma_{xx} = E\varepsilon_x, \sigma_{yy} = E\varepsilon_y, \tau_{xy} = G\gamma_{xy}$ and the bending moments per unit length are

$$\begin{aligned} M_x &= -D \left(\frac{\partial^2 d_z(x, y)}{\partial x^2} + \nu \frac{\partial^2 d_z(x, y)}{\partial y^2} \right) \\ M_y &= -D \left(\frac{\partial^2 d_z(x, y)}{\partial y^2} + \nu \frac{\partial^2 d_z(x, y)}{\partial x^2} \right) \\ M_{xy} &= D(1 - \nu) \frac{\partial^2 d_z(x, y)}{\partial x \partial y} \end{aligned} \quad (6.40)$$

with $D = Eh^2/[12(1 - \nu^2)]$ being the *flexural rigidity* of the plate.

In many applications the beams and plates are only affected by bending stresses, then $\partial d_{x0}/\partial x$ and $\partial d_{y0}/\partial y$ are negligible. For these cases the in-plane surface strains and stresses as well as the bending moments can be calculated from only the distribution of the normal displacement $d_z(x, y)$, which for most holographic arrangements is the component to be measured with the highest accuracy [494, 495]. A computer-based technique for direct determination of bending strains in beam and plate structures using digital holography is described in [584].

6.3.3 Numerical Differentiation

The determination of strains, stresses, and bending moments requires a *numerical differentiation* of the measured displacement data [126, 336, 585–587]. It is a well known fact that noise in the data is severely amplified by differentiation. Therefore we need highly accurate measured values at a large number of surface points for calculating the derivatives.

The direct approach to numerical differentiation is to compute *finite differences*. The differential quotient is approximated by a difference quotient, e. g.

$$\left(\frac{\partial d_z(x)}{\partial x} \right)_{x_i} \approx \frac{d_z(x_{i+1}) - d_z(x_i)}{x_{i+1} - x_i} \quad (6.41)$$

or

$$\left(\frac{\partial d_z(x)}{\partial x} \right)_{x_i} \approx \frac{d_z(x_{i-1}) - d_z(x_i)}{x_{i-1} - x_i}. \quad (6.42)$$

or

$$\left(\frac{\partial d_z(x)}{\partial x} \right)_{x_i} \approx \frac{d_z(x_{i+1}) - d_z(x_{i-1})}{x_{i+1} - x_{i-1}} \quad (6.43)$$

For symmetry reasons the central difference approximation (6.43) is recommended, while at the edges of the evaluated data sets the forward (6.41) and the backward (6.42) differences have to be applied. At this stage the advantages of modern evaluation methods like phase stepping or Fourier transform evaluation as well as digital holography compared to fringe counting or skeletonizing become obvious: displacement data now are determined directly at a rectangular dense grid of surface points giving constant denominators in (6.41) to (6.43) and thus constant accuracy. If on the other hand we have only access to the displacements at the fringe centers we get irregularly spaced points and a varying accuracy.

The *second derivative* at x_i we get by the finite difference of the forward and backward differences taken at the average positions between x_{i+1} and x_i and between x_i and x_{i-1} , respectively. The approximation is

$$\left(\frac{\partial^2 d_z(x)}{\partial x^2} \right)_{x_i} \approx 2 \frac{(x_i - x_{i-1})d_z(x_{i+1}) - (x_{i+1} - x_{i-1})d_z(x_i) + (x_{i+1} - x_i)d_z(x_{i-1})}{(x_i - x_{i-1})(x_{i+1} - x_{i-1})(x_{i+1} - x_i)}. \quad (6.44)$$

For evenly spaced points having the constant distance $h = x_{i+1} - x_i$ this takes on the simple form

$$\left(\frac{\partial^2 d_z(x)}{\partial x^2} \right)_{x_i} \approx \frac{d_z(x_{i+1}) - 2d_z(x_i) + d_z(x_{i-1})}{h^2}. \quad (6.45)$$

If in an actual experiment the data points are unevenly spaced or if they still contain some noise although being evenly distributed, it is good practice to fit a smooth curve to the displacement distribution before performing the numerical differentiation. If there are accurate displacement values but we have to interpolate between the points, cubic spline functions are an appropriate choice [170]. Cubic splines interpolate by third order polynomials in adjacent intervals with continuous second derivatives at the points where two intervals meet.

A smoothing of data distributions containing stochastic noise also may be accomplished by appropriate low-pass filtering or by fitting Bezier polynomials or other smooth curves by least squares methods.

6.3.4 Fringe Vector Theory

For the description of strain and rotation under more general circumstances we adopt the notation of the fringe locus function and fringe vectors of [35, 124, 312, 313, 588–590]. Suppose that an object undergoes a sufficiently small rigid body translation plus a *homogeneous deformation*. In homogeneous deformations the deformation of each object element is identical, e. g. a sphere deformed to an ellipsoid, or a cube deformed into a rectangular or trapezoidal parallelepiped. Prismatic bars subjected to simple tension or compression, or the expanding solids under uniform heating undergo homogeneous deformations. Generally the interference phase at each point P is given by (4.21)

$$\Delta\phi(P) = \mathbf{d}(P) \cdot \mathbf{e}(P). \quad (6.46)$$

This equation can be interpreted as a *fringe locus function* because constant values of $\Delta\phi(P)$ define fringe loci on the object surface. The observed fringes are interpreted as the intersections of fringe laminae in space with the object surface. If we investigate only small segments where the sensitivity vector $\mathbf{e}(P)$ can be regarded as constant, the fringes will be seen as equidistant straight lines on a flat object surface, indicating that the fringe laminae are equidistant planes. Let \mathbf{r} be the space vector from an arbitrary origin of the coordinate system to the point P : $\mathbf{r} = (x_P, y_P, z_P)$, then we may write the fringe locus function $\Delta\phi(\mathbf{r})$ as a scalar product

$$\Delta\phi(\mathbf{r}) = \mathbf{K}_f \cdot \mathbf{r}. \quad (6.47)$$

The vector \mathbf{K}_f is the *fringe-vector* whose magnitude is inversely proportional to the spacing between the fringe laminae and whose direction is normal to them.

Let us assume a known value $\Delta\phi(\mathbf{r})$ of the fringe locus function at P having the space vector \mathbf{r} . Then the fringe locus function at a nearby point Q , described by the space vector $\mathbf{r} + \Delta\mathbf{r}_{PQ}$ is expressed by a Taylor series expansion as [376]

$$\Delta\phi(\mathbf{r} + \Delta\mathbf{r}_{PQ}) = \Delta\phi(\mathbf{r}) + \Delta\mathbf{r}_{PQ}^T \cdot \mathbf{K}_f + \frac{1}{2} \Delta\mathbf{r}_{PQ}^T \mathbf{T}_f \Delta\mathbf{r}_{PQ}. \quad (6.48)$$

The second term on the right-hand side is the scalar product of the difference vector of positions and the fringe-vector which has to be the gradient of $\Delta\phi(\mathbf{r})$. \mathbf{T}_f is the *fringe tensor* representing linear variations of \mathbf{K}_f , its consideration is only necessary when dealing also with inhomogeneous deformations and strains.

Calculating \mathbf{K}_f by differentiating the fringe locus function

$$\Delta\phi = d_x e_x + d_y e_y + d_z e_z, \quad (6.49)$$

which contains three products, we see that by applying the product rule of differentiation and this with respect to three coordinates we obtain eighteen terms which are written as the sum of two vector-matrix products

$$\mathbf{K}_f = \mathbf{F} \cdot \mathbf{e} + \mathbf{G} \cdot \mathbf{d}. \quad (6.50)$$

While \mathbf{e} and \mathbf{d} are the sensitivity and displacement vectors, the matrix \mathbf{G} accounts for the perspective variations of the sensitivity vector and \mathbf{F} is the *deformation gradient matrix* which contains the derivatives of the displacement vector:

$$\mathbf{F} = \begin{pmatrix} \frac{\partial d_x}{\partial x} & \frac{\partial d_x}{\partial y} & \frac{\partial d_x}{\partial z} \\ \frac{\partial d_y}{\partial x} & \frac{\partial d_y}{\partial y} & \frac{\partial d_y}{\partial z} \\ \frac{\partial d_z}{\partial x} & \frac{\partial d_z}{\partial y} & \frac{\partial d_z}{\partial z} \end{pmatrix}. \quad (6.51)$$

We recognize that \mathbf{F} is composed of

$$\mathbf{F} = \mathcal{E} + \Theta \quad (6.52)$$

where \mathcal{E} is the symmetric matrix of strains and shears

$$\mathcal{E} = \begin{pmatrix} \varepsilon_x & \frac{1}{2}\gamma_{xy} & \frac{1}{2}\gamma_{zx} \\ \frac{1}{2}\gamma_{xy} & \varepsilon_y & \frac{1}{2}\gamma_{yz} \\ \frac{1}{2}\gamma_{zx} & \frac{1}{2}\gamma_{yz} & \varepsilon_z \end{pmatrix} \quad (6.53)$$

and Θ is the antisymmetric matrix of rotations

$$\Theta = \begin{pmatrix} 0 & -\omega_z & \omega_y \\ \omega_z & 0 & -\omega_x \\ -\omega_y & \omega_x & 0 \end{pmatrix}. \quad (6.54)$$

\mathbf{F} can be decomposed into its symmetric part \mathcal{E} and the antisymmetric part Θ by

$$\mathcal{E} = \frac{1}{2}[\mathbf{F} + \mathbf{F}^T] \quad (6.55)$$

$$\Theta = \frac{1}{2}[\mathbf{F} - \mathbf{F}^T]. \quad (6.56)$$

With this we have a method to obtain the strains, shears, and rotations provided we have determined \mathbf{F} by holographic measurement.

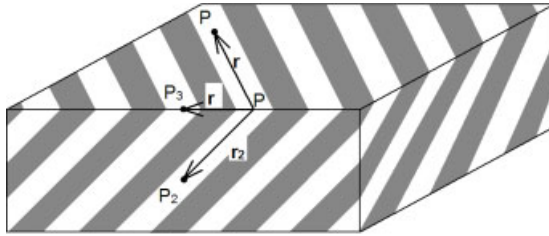


Figure 6.11: Straight fringes due to homogeneous deformation of the object.

If the object's geometry is known, we can assign coordinates to the points of intersection of the object surface with the fringe laminae. In Fig. 6.11 let P , P_1 , and P_2 be points on a common fringe, P_3 a point on an adjacent fringe. The vectors \mathbf{r}_1 , \mathbf{r}_2 , and \mathbf{r}_3 are the vectors from P to P_1 , P_2 , and P_3 . The direction of the fringe vector \mathbf{K}_f then is given by the unit vector \mathbf{k}_f

$$\mathbf{k}_f = \frac{\mathbf{r}_1 \times \mathbf{r}_2}{|\mathbf{r}_1 \times \mathbf{r}_2|} \quad (6.57)$$

and its magnitude $|\mathbf{K}_f|$ is

$$|\mathbf{K}_f| = \frac{\pi}{\mathbf{k}_f \cdot \mathbf{r}_3} \quad (6.58)$$

if the fringe at P_3 has higher interference order than that at P , otherwise we take $-\pi$ in the numerator.

To solve (6.50) for the deformation gradient matrix \mathbf{F} we need three observations with different non-coplanar sensitivity vectors or even more observations and then solving by least squares. For each sensitivity vector we have to determine the corresponding fringe vector. As long as it is assumed that the sensitivity vectors do not vary, \mathbf{G} may be neglected and \mathbf{F} is obtained by inversion of (6.50).

If there is a substantial sensitivity vector variation, the displacements \mathbf{d} have to be evaluated and \mathbf{G} must be calculated from the known sensitivity vectors. Now we are able to correct \mathbf{K}_f for perspective by

$$\mathbf{K}_{fc} = \mathbf{K}_f - \mathbf{G} \cdot \mathbf{d} \quad (6.59)$$

and \mathbf{F} is determined by

$$\mathbf{F} = (\mathbf{e}^T \mathbf{e})^{-1} (\mathbf{e}^T \mathbf{K}_{fc}). \quad (6.60)$$

If we do not have a three-dimensional object but a single plane surface in, say, the x - y -plane, only the x - and y -components of \mathbf{K}_f contribute to the value of the fringe locus function. Therefore only the first two columns of \mathbf{F} can be determined and in consequence only rotations about surface normals and the in-surface strains are processed. Three views, however, are still required in this case.

6.4 Hybrid Methods

The accurate measurement of displacements by holographic interferometry and computer-aided quantitative evaluation allows a subsequent numerical differentiation or other processing steps [325]. Thus these measurements can be combined with structural analysis methods like the finite element methods, boundary-element methods, or the techniques known under the heading of fracture mechanics. The refined analysis methods resulting from such combinations may be categorized as *hybrid methods*. As an example in car production one is highly interested in the behavior of brakes, especially in their noise and vibration. Therefore the results of various metrologies such as CW and pulsed laser holographic interferometry, speckle methods, and laser Doppler vibrometry are combined to identify the root causes of brake concerns and verify engineering solutions [325, 591, 592].

6.4.1 Finite Element Methods and Holographic Interferometry

The *finite element method* is a structural analysis method, where a technical structure is divided into a number of discrete elements which have a simple geometry. All these elements are connected via the nodes by which they are defined. The mechanical behavior in each element can be calculated due to its simple geometry, then the program produces an overall solution that is compatible to all the nodes. Thus displacements, strains and stresses or the thermal behavior of a structure under mechanical and/or thermal load can be approximated with good accuracy.

Holographic deformation analysis [592–596] or holographic vibration analysis [597] and finite element calculations can effectively be combined to reach a number of goals. One of the most important is the holographic verification of the finite element model [598, 599]. Especially for complex shaped or composite structures it is not an easy task to find a proper discretization and to choose the right material parameters. A comparison of the measured displacements with the calculated displacements can confirm the finite element model, which can then be used for, say, strain and stress calculations.

This strategy has been successfully followed in the investigation of vibration modes [600, 601] or stress distributions [547]. For the analysis of *adhesive bondings* it has been determined to what proportions the metal layers and the adhesive layers contribute to the deformation of the specimen [602]. A complete representation of the strain and stress conditions within the specimen has been obtained. The combination of an electro-optic holographic microscope measuring displacements of vibrating microbeams and FEM to describe the behavior of microelectromechanical systems (MEMS) is employed by Brown and Pryputniewicz [603].

The temperature distribution and the deformation of a thermally loaded overlap adhesive bond with a local void in the adhesive layer was calculated by the finite element method and measured by holographic interferometry [604]. The combined evaluations have shown that the characteristic surface deformation above the defect in the internal adhesive layer is not caused by thermal expansion of the enclosed gas. The inhomogeneities in the surface deformation arise from the disturbed heat transfer in the defect area. So in this region we get locally higher temperature differences, which in consequence leads to locally different thermal deformations. These results explain the relevance of *thermal load* for *defect detection* in holographic non-destructive testing.

The combination of holographic interferometry and finite element methods not only enables a defect detection but also a *defect validation*. In systematic calculations a catalog of surface deformations in the region of internal cracks and voids in, say, steel with variations of defect type, length, orientation, volume or position, is compiled. For a given holographically measured displacement field above a defect, one starts with the best fitting displacement field from this catalog. In an iterative process in a finite element model, the parameters of the simulated defect are varied. The displacement field is calculated over and over again with varied defects until the agreement with the measured displacement field is sufficiently good [547].

Of course, the calculation of a displacement field for a given discrete structure and loading by the finite element method is not a one-to-one mapping. Thus the inverse process of determining the discrete structure from the loading and the measured displacement field is not possible. Nevertheless, with the iterative method we get a defect which is representative of the equivalent class of all defects producing the same deformation under the specific applied load.

6.4.2 Boundary Element Methods and Holographic Interferometry

In the finite element method, the whole body to be tested is discretized into finite volumes connected at the nodes. Continuity of parameters which are not explicit variables is only warranted at the nodes and not at the borders between the elements. If we have other functions which fulfill exactly the differential equation in the whole region, we have no discretization errors in the interior of the body. Since only the boundary conditions have to be satisfied, the requirement that the boundary is discretized is in itself sufficient. The relating methods are called *boundary element methods*.

The boundary element methods can be combined advantageously with experimental methods like holography. Especially, if in practical applications the boundary conditions are too complicated to be described theoretically, they have to be measured. Having measured the displacements by, e.g., holographic interferometry, the boundary of two- or three-dimensional regions is then divided into segments on which the displacements and strains are approximated by polynomials of the first degree. The stress components at prescribed internal points of the region are then calculated by means of the boundary element method.

In [605] this method is applied to transparent models manufactured from PMMA with roughened faces. The in-plane components of the displacement vectors are measured by double exposure double aperture speckle interferometry. The objects considered are a three-point loaded beam with an edge crack and a model of a large slab wall stiffened by a frame. Based on the measurements, exact values of stresses σ_x , σ_y , and σ_{xy} in the neighborhood of the crack tip are determined. In another application, the friction between the wall and its base is measured by applying the hybrid evaluation method of coherent optical measurement combined with the boundary element method.

6.4.3 Fracture Mechanics

In linear elastic *fracture mechanics* the influence of a *crack* or another defect on the damage of a technical structure is estimated. An important figure is the *stress intensity factor* K_I and its critical value K_{Ic} , the *fracture toughness*, which is a material property. The K_I -value can be

determined holographically by first measuring the deformation field of the structure exhibiting a crack [606] followed by the determination of the boundary of the *plastic zone* arising above the crack during *tensile loading*. This is functionally related to the K_I -value [607–609]. Another method is based on the integration of the strain equations of Sneddon or Williams-Irwin. This method only requires a displacement measurement along a line perpendicular to the crack propagation direction [610]. In conjunction with these methods holographic interferometry has been used to determine the K_I -value for a CT 500 specimen with high accuracy and without any previous knowledge of the specific defect properties like its size and location.

A further criterion for *crack propagation* is the so-called *J-integral*, which is a figure independent of the path of integration. Crack propagation occurs if the J-integral exceeds a critical material parameter [609]. In [611], the determination of the J-integral is based on measurements of the displacement field by holographic interferometry. Power series estimations up to quadratic terms fulfilling the Lame-Navier equations are set up for the three displacement components. From the coefficients of the power series the integration can then be performed along a rectangular path to yield the J-integral.

6.5 Vibration Analysis

The measurement of vibrations is an important task in engineering, on the one hand to ascertain the operation of components, which should vibrate, like loudspeakers, ultrasonic transducers etc., and on the other hand to check the behavior of components, which have natural frequencies of response within the range of frequencies excited by the operation of an engine of which the component may be part. The aims can be the prevention of fatigue failure or the detection of noise-generating parts or areas, to name just two [591]. Of course non-contacting measurement methods which do not affect and bias the vibration are recommended. Since furthermore the amplitudes to be measured normally are in the range of the wavelengths of laser light, and since one is interested in the simultaneous measurement at a manifold of points, holographic interferometry is a suitable tool for analyzing vibrations [612, 613]. It is worth noting that the first holographic interferograms were made of diffusely reflecting surfaces under vibration [16].

6.5.1 Surface Vibrations

The fundamental surface vibration is the *sinusoidal vibration* also called *harmonic vibration*. Here the displacement of each point of the vibrating surface is

$$\mathbf{d}(P, t) = \mathbf{d}(P) \sin \omega t \quad (6.61)$$

where $\mathbf{d}(P)$ is the vector amplitude and ω the circular frequency of the vibration. The vibrations of continua are described by partial differential equations. Generally the boundary conditions yield transcendental equations for the eigenvalues. Approximate solutions use the Rayleigh quotients or the Ritz method. For some special cases like vibrating cantilever beams, circular or rectangular shells or plates, closed solutions are known.

The solutions differ in the distribution of $d(P)$ over the points P , which defines the *mode-shapes* of the specific vibration. This can be explained with the example of a vibrating rectangular plate being jointed at the edges. The differential equation is

$$\frac{\partial^2 d_z}{\partial t^2} = -\frac{N}{\rho h} \left(\frac{\partial^4 d_z}{\partial x^4} + 2 \frac{\partial^4 d_z}{\partial x^2 \partial y^2} + \frac{\partial^4 d_z}{\partial y^4} \right) \quad (6.62)$$

with the stiffness of the plate $N = Eh^3/[12(1 - \nu^2)]$, the thickness h , and the specific mass ρ . If the sidelengths are a and b , solutions are given by

$$d_z(x, y, t) = d_{max} \sin(\omega t + \phi_0) \sin\left(\frac{j\pi x}{a}\right) \sin\left(\frac{k\pi y}{b}\right) \quad (6.63)$$

with the eigenvalues $\omega_{jk} = (j^2/a^2 + k^2/b^2)\pi^2\sqrt{N/(\rho h)}$ for $j, k = 1, 2, \dots$. The two extreme deformation states of a plate vibrating in the $(j = 2, k = 2)$ -mode is shown in Fig. 6.12. The

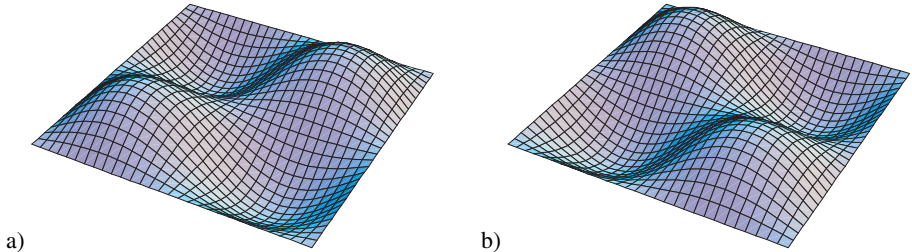


Figure 6.12: Vibrating rectangular plate.

maximum amplitude at each point (x, y) is $|d_{max} \sin(j\pi x/a) \sin(k\pi y/b)|$. The loci where the maximum amplitude is zero all the time are the *nodes*, on the other hand the loci of local extrema of the amplitude are called *antinodes*. In Fig. 6.12 we have two nodal lines parallel to the edges and intersecting in the center of the plate. It is one task of holographic vibration analysis to identify the *mode-shape* (j, k) and the maximum amplitude of the amplitude distribution of a vibration.

In Fig. 6.12 all points vibrate in-phase, there is no phase shift between the oscillations of each point, except that when one antinode reaches its positive maximum another takes its negative maximum, which may be interpreted as a phase shift by π . The phase relation between the vibrating points is another item to be analyzed holographically. Figure 6.13 shows some oscillatory states of a vibrating circular disc where the phase varies over 6π around the circumference. The phase is constant along each radius, while each radius of constant phase is continuously rotating. Figure 6.13a – d indicate how a, say, phase maximum moves around the circumference of the disc. There is only one nodal point in the center of the disc.

The sinusoidal vibration of (6.61) is an example for a separable object motion. *Separable object motions* are such motions which can be separated into a product of a displacement vector $d(P)$ and a real temporal function $f(t)$. This $f(t)$ is $\sin(\omega t)$ in (6.61). Here the point P moves along a line defined by $d(P)$. If the point moves along an arc, this motion can be described by the sum of two or three separable motions. Besides the sinusoidal vibration, $f(t)$ may represent damped harmonic vibrations [614] or other nonlinear vibrations [615–617].

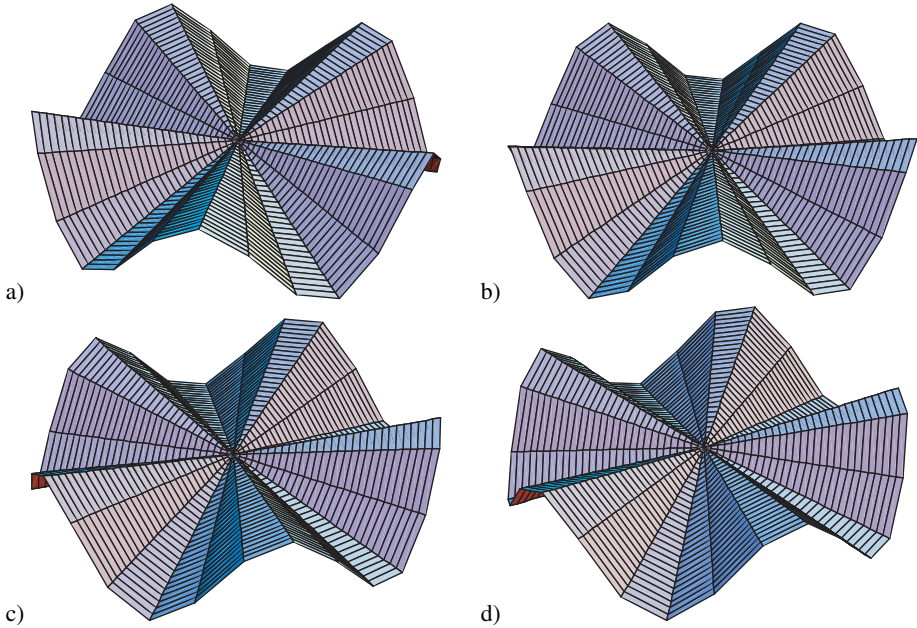


Figure 6.13: Vibrating circular disc.

In many applications the object surface executes a combination of N individual separable motions, e. g. a plate vibrating simultaneously in the $N = 2$ modes

$$d_z(P, t) = d_1(P) \sin(\omega_1 t + \phi_{01}) + d_2(P) \sin(\omega_2 t + \phi_{02}). \quad (6.64)$$

Even if the frequencies agree, $\omega_1 = \omega_2$, the combining modes may differ in mode shape, amplitude and phase. We speak of *dependent object motions* if ω_1/ω_2 is the ratio of two small integers; the motions are *independent* if there is no such ratio.

6.5.2 Stroboscopic and Real-Time Holographic Interferometry

Stroboscopic holographic interferometry consists of recording a hologram by using a sequence of short laser pulses which are synchronized with the vibrating object [618]. One can record a reference state of the object at rest and then illuminate with short pulses all the time the object is in the same position, preferably when the antinodes undergo the maximum displacement. But in most applications the pulses are fired when the object is in its maximum positive displacement and again when it is at its maximum negative displacement. If the motion is $d(P) \sin \omega t$, pulses should be at $\omega t = \pi/2$ and $\omega t = 3\pi/2$, and the same after periods of 2π until the total required exposure is reached. If the pulses are short enough, the result is the same as with double exposure holographic interferometry, that means we get cos-type fringes (4.4) and (4.21)

$$I(P) = 2I_1(P)\{1 + \cos[\mathbf{d}(P) \cdot \mathbf{e}(P)]\} \quad (6.65)$$

with stationary reference state or

$$I(P) = 2I_1(P)\{1 + \cos[2\mathbf{d}(P) \cdot \mathbf{e}(P)]\} \quad (6.66)$$

if the extreme positions are compared. For a sensitivity vector perpendicular to the surface the fringes indicate loci of constant amplitude of the vibration modes. There are two main drawbacks of this approach: First the vibration has to be monitored for the synchronization of the laser pulses, e. g. by a Michelson interferometer or a Doppler velocimeter measuring in one point of the surface, thus increasing the experimental complexity; second if the pulses are short, many are needed for exposure, thus a high mechanical stability is required. On the other hand if the pulse duration is increased, the cosine-type fringes are modulated by a sinc-function with the result that the visibility decreases [619]. An advantage of the stroboscopic method is the cosine-shaped fringes with constant contrast over all fringe orders. Furthermore they allow the introduction of phase shifting for an automatic evaluation of the interference phase with subfringe accuracy [620]. A vibration analysis by stroboscopic *heterodyne holographic interferometry* employing a two reference beam arrangement is presented in [621, 622].

The investigation of the object as it responds to different exciting frequencies is best done by *real-time holographic interferometry*. Hereby a reference state of the object at rest is recorded holographically and the processed hologram plate is exactly repositioned. During object vibration optical wave fields of the reconstructed reference state and of the actual state interfere and for sufficiently high vibration frequency ω the resulting interference pattern is of the form (4.7) according to (C.2)

$$I(P) = 2I_1(P)\{1 - J_0[\mathbf{d}(P) \cdot \mathbf{e}(P)]\} \quad (6.67)$$

where J_0 is the zero-order *Bessel function* of the first kind. The nodal points are the darkest in the pattern, local intensity minima and maxima occur in turn between the zeros of J_0 , Fig. 4.3. Because of the nature of $J_0(\mathbf{d} \cdot \mathbf{e})$ the fringes exhibit low contrast, an effect that is further increased if we have not the same irradiance or polarization state between the two interfering wave fields. But the method is suitable for the quick identification of resonant frequencies by monitoring the fringe pattern while sweeping the excitation frequency continuously through the frequency range of interest.

A modification of the real-time method is the holographic subtraction [623]. A first exposure is made of an object at rest, the second during vibration while an additional phase shift π is introduced. The resulting interference pattern is

$$I(P) = 2I_1(P)\{1 - J_0[\mathbf{d}(P) \cdot \mathbf{e}(P)]\}^2 \quad (6.68)$$

which exhibits the same number and positions of the fringes as in the real-time method but due to the square with higher visibility.

6.5.3 Time Average Holographic Interferometry

The experimentally easiest and most often applied holographic method for vibration analysis is the *time average holographic interferometry* [16, 112, 624–626]. The object is recorded

holographically with a single exposure, employing a CW laser using an exposure time T , which is long compared with the period of the vibration, e. g. for harmonic vibrations $T \gg 2\pi/\omega$. The exact exposure time is only directed by the emulsion of the hologram plate. The resulting intensity in the reconstructed image is according to (4.10) and (C.2)

$$I(P) = I_0(P) J_0^2[\mathbf{d}(P) \cdot \mathbf{e}(P)]. \quad (6.69)$$

At the nodes of the vibration modes we have the maximal intensity, $J_0(0) = 1$, and there are dark fringes where $\mathbf{d}(P) \cdot \mathbf{e}(P)$ equals the arguments of the zeros of the zero-order Bessel function of the first kind, Table C.1. The bright fringes between these zeros which do not correspond to nodal lines exhibit less intensity compared with the zero fringe. Thus the nodal lines can easily be identified. As an example consider a plane vibrating surface and a holographic arrangement with illumination and observation normal to the surface. If each point can be assumed to oscillate only in the normal direction $\mathbf{d}(P) = (0, 0, d_z(P))$, then $\mathbf{e}(P) = 4\pi/\lambda$ according to (4.20) and the amplitudes at the centers of dark fringes are easily calculated by

$$d_z(P) = b_m \frac{\lambda}{4\pi} \quad (6.70)$$

where b_m is the m -th zero of J_0 , Table C.1. The order of the fringe is determined by starting the counting with $m = 1$ for the dark fringe adjacent to the zero fringe, the nodal line.

For thin plates or shells the vibration vector can be assumed to be perpendicular to the surface, any in-plane components can be neglected. Then the time average fringes are interpreted as contour lines of the vibration modes. If for more general objects the direction of the vibration amplitude vector is not known a priori, at least three holographic observations with different sensitivity vectors have to be performed and a system of three linear equations or a least squares system has to be solved, see Section 6.1.

The interpretation of the brightest fringe as a nodal line nevertheless can be erroneous for more complex structures. Consider the pure torsional vibration of a cylinder. For illumination and observation directions parallel to the optical axis, which intersects the hologram, the surface line facing the hologram appears as the brightest fringe. But this is because at these points the vibration vector is orthogonal to the sensitivity vector [627].

Typical holographic interference patterns have been recorded using the time average method, Fig. 6.14. The object here is a square plate rigidly clamped at all edges and excited acoustically by a loudspeaker, driven by various frequencies. This results in the (0,0)-vibration mode in Fig. 6.14a, the (0,2)-mode in Fig. 6.14b, and the (2,2)- and (3,2)-modes in Figs. 6.14c and d, respectively.

6.5.4 Temporally Modulated Reference Wave

In stroboscopic holographic interferometry, Section 6.5.2, the object and the reference wave fields have been modulated by temporal functions $f_{obj}(t)$ and $f_{ref}(t)$, which depend on the object vibration frequency and phase. This constituted a special case of the more general and powerful concept of temporal modulation of the wave fields. It is not necessary to have $f_{obj}(t) = f_{ref}(t)$ as in the stroboscopic method. In most applications it is only the reference wave which is modulated, this is considered in the following.

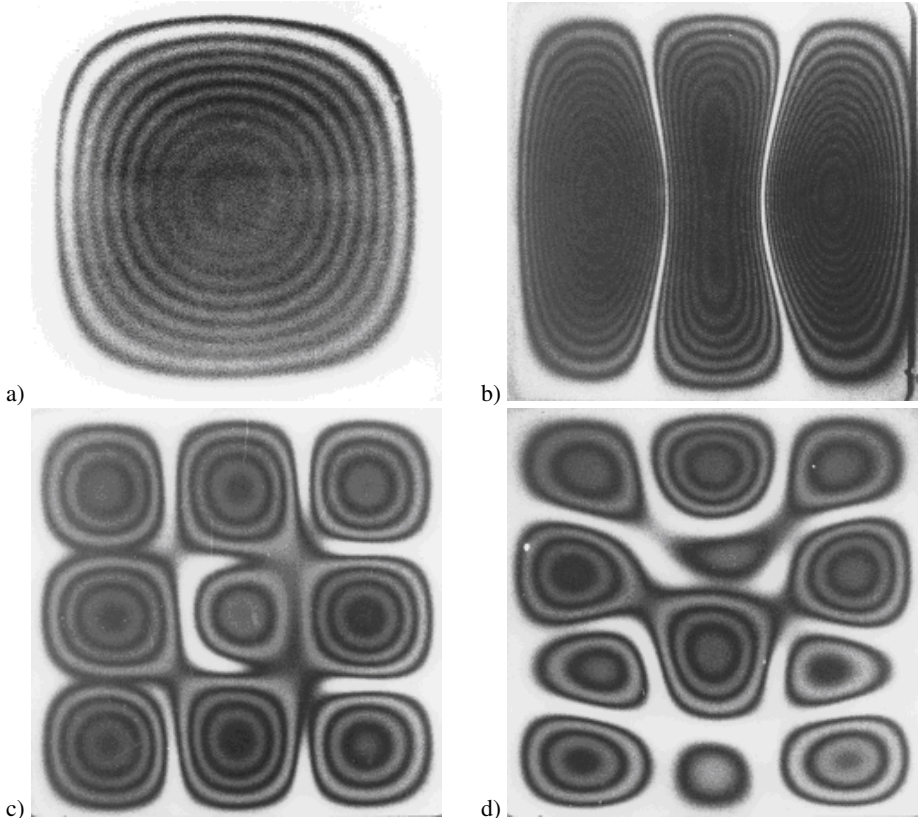


Figure 6.14: Time average holographic interferograms of a square plate clamped at the edges.

There are several ways to modulate the reference wave during the recording of the hologram, offering a number of benefits: increased sensitivity for small vibration amplitudes, detection of the relative phase between the oscillating points across the surface, compensation for extraneous object motion, etc.

If the object wave E_P and the reference wave E_R are modulated by $f_{obj}(t)$ and $f_{ref}(t)$, respectively, the resulting intensity in the hologram plane at time t is according to (2.122) proportional to

$$I(t) = |f_{obj}(t)E_P + f_{ref}(t)E_R|^2. \quad (6.71)$$

Assuming linear recording, the amplitude transmittance of the hologram is, see (2.125)

$$T = \alpha - \beta \int_0^T |f_{obj}(t)E_P + f_{ref}(t)E_R|^2 dt. \quad (6.72)$$

For reconstruction the hologram is illuminated with the continuous unmodulated reference wave E_R , see (2.131). The interesting third term of (2.131) describes the complex amplitude

of a wave field proportional to

$$M_T = \frac{1}{T} \int_0^T f_{obj}(t) E_P f_{ref}^*(t) dt. \quad (6.73)$$

The expression M_T often is called the *characteristic function* [170, 172, 376, 628], but the concept of characteristic functions will not be stressed extensively in this book. The resulting intensity is $I = |M_T|^2$. The M_T for some ways of modulating the reference wave now should be investigated in more detail.

Let the object surface vibrate harmonically with frequency ω , then the object wave is proportional to $\exp[i\mathbf{d}(P) \cdot \mathbf{e}(P) \sin \omega t]$, while $f_{obj}(t) = 1$. In *frequency translated holography* the frequency of the reference wave is modulated by an integer multiple $n\omega$ of the object vibration frequency ω

$$f_{ref}(t) = \exp(in\omega t). \quad (6.74)$$

The resulting characteristic function is proportional to

$$M_T = \frac{1}{T} \int_0^T \exp[i\mathbf{d}(P) \cdot \mathbf{e}(P) \sin \omega t] \exp(-in\omega t) dt. \quad (6.75)$$

Using the identity (C.4) and reversing the order of integration and summation we get

$$\begin{aligned} M_T &= \frac{1}{T} \int_0^T \sum_{m=-\infty}^{\infty} J_m[\mathbf{d}(P) \cdot \mathbf{e}(P)] \exp(im\omega t) \exp(-in\omega t) dt \\ &= \sum_{m=-\infty}^{\infty} J_m[\mathbf{d}(P) \cdot \mathbf{e}(P)] \frac{1}{T} \int_0^T \exp[i(m-n)\omega t] dt. \end{aligned} \quad (6.76)$$

If the exposure time is long compared with the object vibration period, $T \gg 2\pi/\omega$, the integral vanishes for all m except for $m = n$, so that

$$M_T = J_n[\mathbf{d}(P) \cdot \mathbf{e}(P)] \quad (6.77)$$

or

$$I(P) = J_n^2[\mathbf{d}(P) \cdot \mathbf{e}(P)]. \quad (6.78)$$

This result is consistent with the unmodulated time average case having $n = 0$, see (6.69). Proportionality factors influencing only the overall brightness have been omitted for convenience.

Frequency translated holography is used to increase the sensitivity for vibrations with small as well as with large amplitudes: Small amplitudes here are such that the interference phase $\Delta\phi(P) = \mathbf{d}(P) \cdot \mathbf{e}(P)$ remains small, $\Delta\phi(P) \ll 1$. In time average holography with

no modulation $J_0^2(0)$ is unity and has slope zero. So no significant intensity variation in the bright field will result. On the other hand $J_1^2(0)$ has a positive slope in the dark field, see Fig. C.1, yielding visible intensity variations even for small amplitudes. The smallest detectable amplitude was estimated as $2.7 \times 10^{-4}\lambda$ [629]. In the case of large vibration amplitudes we take advantage of the fact that the locations of the zeros of the Bessel functions are spread apart for increasing order n , Fig. C.1. This results in a decreasing number of fringes for the same amplitudes with increasing n , meaning too high fringe densities can be effectively avoided [630].

A general temporally periodic object wave may be considered as composed of its Fourier series terms, having frequencies $\omega_0 + m\omega$, $m = 0, \pm 1, \pm 2, \dots$ with ω_0 the frequency of the used laser light. The reference wave in frequency translated holography has the frequency $\omega_0 + n\omega$. So only the frequency component with $m = n$ will produce a time average hologram, because only this one is coherent with the reference wave. Thus we have a method for temporal filtering by selecting single frequency components from a periodic object motion [170, 630, 631].

In *amplitude modulation holography* the amplitude of the reference wave is modulated with the same frequency as the object vibrates, but with a controllable phase difference ψ with respect to the vibration of a selected object point P , $f_{ref}(t) = \cos(\omega t - \psi)$. In this case the n of (6.74) is 1. The resulting intensity is proportional to

$$I(P) = J_1^2[\mathbf{d}(P) \cdot \mathbf{e}(P)] \cos^2 \psi. \quad (6.79)$$

A sequence of holograms, recorded with amplitude modulation at varied phase ψ , will display contours of constant relative phase [99].

A further method to obtain phase information about the object vibration is *phase modulation holography*. The phase of the reference beam is modulated at the frequency ω of the vibrating object with a modulation depth of Ω_R . The modulation function is

$$f_{ref}(t) = \exp(i\Omega_R \sin \omega t) \quad (6.80)$$

which gives the characteristic function [170]

$$\begin{aligned} M_T &= \frac{1}{T} \int_0^T \exp[i\mathbf{d}(P) \cdot \mathbf{e}(P) \sin(\omega t - \phi_0)] \exp(-i\Omega_R \sin \omega t) dt \\ &= J_0\{[(\mathbf{d}(P) \cdot \mathbf{e}(P))^2 + \Omega_R^2 - 2\mathbf{d}(P) \cdot \mathbf{e}(P)\Omega_R \cos \phi_0]^{1/2}\}. \end{aligned} \quad (6.81)$$

The implication of this characteristic function is that the relative phase ϕ_0 of the vibration at each point is encoded in the fringe pattern. Relative phases [632] as well as amplitudes [633] are measured based on this principle. For simplicity of discussion assume $\phi_0 = 0$. Then we have an intensity

$$I(P) = |M_T(P)|^2 = J_0^2(\mathbf{d}(P) \cdot \mathbf{e}(P) - \Omega_R). \quad (6.82)$$

Now the loci of bright zero fringes are controllable by the user, since they appear where $\mathbf{d}(P) \cdot \mathbf{e}(P) = \Omega_R$. Further insight is gained when the modulation (6.80) includes a phase term ϕ_R . The dark fringes in the interferogram then are characterized by

$$b_m^2 = \mathbf{d}(P) \cdot \mathbf{e}(P) + \Omega_R^2 - 2\mathbf{d}(P) \cdot \mathbf{e}(P)\Omega_R \cos(\phi_0 - \phi_R) \quad (6.83)$$

where b_m denotes the m -th zero of J_0 [634]. If two holographic interferograms are produced in this way with phases ϕ_{R1} and ϕ_{R2} , they may be superimposed. At the intersections of fringes of equal order m we have

$$\phi_0 = \frac{\phi_{R1} + \phi_{R2}}{2} \pm m\pi. \quad (6.84)$$

Using this approach one gets phase contours by simple visual inspection. This work has been extended [635] to bright fringes so that also bright-bright and bright-dark combinations can be used. Hereby phases intermediate to those of (6.84) can be inspected. Objects excited with swept sinusoidal vibration or randomly have been investigated by time average holography with a mechanically excited reference beam. Modes and amplitudes of randomly excited objects were analyzed by a method called *spectroscopic holography* [636].

The holographic interferometry using phase modulation described by (6.82) is closely related to general motion compensation by reference waves modulated by the object motion [554, 556]. If the vibration amplitudes in the vicinity of a point P are large, a reference wave modulated by a mirror fixed at P and undergoing the same motions will yield a vibration measurement relative to this point.

6.5.5 Numerical Analysis of Time Average Holograms

Numerical analysis of cosine fringes by phase shifting or Fourier transform methods allows the determination of interference phases even between the fringe intensity maxima and minima with high accuracy. While a lot of research has been performed to automate the evaluation of cosine fringes, not a great deal has been done to automate Bessel-type fringe interpretation.

One approach is to convert J_0 -fringes into sinusoidal fringes by stroboscopic techniques, and to apply heterodyning [621] or phase stepping [637]. The real-time method of vibration analysis was combined with heterodyne [622] and phase step evaluation [638]. In those methods vibration amplitudes must still be interpolated from integer fringe orders. The direct numerical extraction of vibration amplitudes from time average interference patterns as presented in [639] is given in the following.

The intensity of a time average hologram is (4.10)

$$I(x, y) = I_0(x, y) J_0^2(\Delta\phi(x, y)) \quad (6.85)$$

where $I_0(x, y)$ is the irradiance of the object surface. The interference phase is $\Delta\phi(x, y) = \mathbf{d}(x, y) \cdot \mathbf{e}(x, y)$ with $\mathbf{d}(x, y)$ the vectorial displacement and $\mathbf{e}(x, y)$ the sensitivity vector in (x, y) . As we have seen in Section 6.5.4, the J_0 -fringes can be shifted by modulating the phase of either the object or the reference beam sinusoidally at the same frequency as the object vibration. This adds a phasor bias Ω_R to the argument of the Bessel function. If the object is vibrating in only one vibration mode and if the phase of the sinusoidal beam modulation is adjusted to coincide with that of the object vibration the phasor bias becomes an additive term and the irradiance of a time average hologram reconstruction together with the unavoidable distortions is (6.82)

$$I(x, y) = a(x, y) + b(x, y) J_0^2(\Delta\phi(x, y) - \Omega_R) \quad (6.86)$$

with $a(x, y)$ containing the background irradiance and $b(x, y)$ the multiplicative object surface irradiance. Equation (6.86) has a form analogous to the phase sampling equation (5.15) for cosine fringes. Unfortunately the Bessel function of a sum cannot be expressed as a sum of terms as done in (5.19) for the cosine, so straightforward solutions are not possible. An iterative process for calculation of the phase $\Delta\phi$ of each (x, y) is outlined in [639], but this requires quite lengthy calculations.

A solution that makes use of the nearly periodic nature of the J_0 -function employs the formula

$$\Delta\phi^* = \arctan \frac{(1 - \cos \Omega_R)(I_3 - I_1)}{\sin \Omega_R(I_1 - 2I_2 + I_3)}. \quad (6.87)$$

see Table 5.1, where we use three reconstructions with the bias terms $-\Omega_R$, 0 , $+\Omega_R$ having known values. The interference phase $\Delta\phi^*$ computed by (6.87) differs from the correct argument of the J_0^2 -function. Due to the approximating function $J_0^*(x)$, see (C.6), this error approaches $\pi/4$ for large arguments. The error can be computed for any phase angle $\Delta\phi$ and any value of Ω_R to create a lookup table to convert the incorrect answers obtained from the use of (6.87) into the correct phase values. In practice, since the influence of $a(x, y)$ and $b(x, y)$ is eliminated inherently in the evaluation by (6.87), we can proceed with $a = 0$ and $b = 1$ when compiling the lookup table. For each specific Ω_R the intensities I_1 , I_2 , and I_3 corresponding to $-\Omega_R$, 0 , and $+\Omega_R$ are computed by (6.86) for the desired values of $\Delta\phi$. Then (6.87) is solved for these I_1 , I_2 , I_3 , resulting in a false interference phase $\Delta\phi^*$. These $\Delta\phi^*$ are tabulated with the corresponding correct values of $\Delta\phi$.

The phase data obtained by evaluation using (6.87) with subsequent correction employing the lookup table still have to be demodulated. The one pattern with no bias vibration now is used to identify the loci of the zero-order fringes. These are recognized by their high brightness relative to the rest of the fringes. So when working with time average hologram data we even have access to the absolute fringe order.

Difficulties still occur when two or more vibration modes lie sufficiently close in frequency so that both are excited at the same time. It seems reasonable to suppose, that data recorded with the bias phase at a number of phase angles could be used to extract both the amplitude and the phase of the vibration [639]. In this direction work still has to be done.

6.5.6 Vibration Analysis by Digital Holography

The first experiments in which holographic interference was observed were in holographic vibration measurement [17], and still today holography is a frequently used tool for displaying and evaluating two-dimensional vibration modes [237]. The digital approach to holography also can be employed in vibration analysis. The simplest way is the use of a pulsed laser triggered to a time instant when the modes have maximum amplitude [65]. The reconstructed phase then is compared to the evaluated phase distribution related to a hologram of the object at rest with no vibration. This method does not differ from the digital holographic interferometric measurements of surface deformations already treated in Chapter 5.8.

The use of an image-intensifier system is reported in [640]. The advantage of the image-intensifier is that it can be gated, meaning the electronic shutter action produced by controlling its photocathode voltage. This allows one to record holograms with short exposure times.

Transient vibrations can be measured with multipulse digital holography [641]. Hereby a ruby laser producing four pulses is used, the corresponding digital holograms are captured with three different CCD sensors.

But also the *time average method* for holographic vibration analysis can be performed in the digital mode. Now the CCD-array integrates over a time interval T which is long compared to the period of the vibration, $T \gg 2\pi/\omega$. The intensity of the wave field reconstructed from such a time average hologram obeys a squared Bessel function as is explained in Section 6.5.3.

An example for the digital realization of the time average method in holographic vibration analysis is shown in Fig. 6.15. Here a piezo-membrane as is used in micro-pumps was excited to vibration [262]. The size of the membrane was 12 mm \times 12 mm. We observe the fundamental mode with increasing amplitude over the six intensity reconstructions. The membrane is clamped at the four edges where we have maximum brightness. The higher order bright fringes are much darker than the zero order fringe, as is predicted by the squared Bessel function J_0^2 .

6.6 Holographic Contouring

The holographic interference pattern arises from the superposition of at least two states of a reflected or refracted wave field. In holographic deformation measurements the phase differences between the two states are given by the scalar product of the displacement vector field and the sensitivity vectors, (4.21). While the displacement vectors describe the variation of the surface point positions between the interferometrically measured states, the sensitivity vectors, which are given by the used laser wavelength, the directions of illumination and observation, and the geometry of the measured surface, remain constant.

This concept is inverted for *holographic contouring*. Contouring in general means the modulation of the image of a three-dimensional object by fringes corresponding to contours of constant elevation with respect to a reference plane [386, 642, 643]. For holographic contouring the object is not displaced, but the two states which by superposition form the fringe pattern are produced by variation of other factors in (4.13) and (4.20), respectively.

6.6.1 Contouring by Wavelength Differences

The length of the sensitivity vector depends on the wavelength λ , see (4.20). Of course a change in the wavelength varies the sensitivity vector and thus the optical path length. The wavelength can be changed in predetermined discrete steps with e. g. an argon-ion laser or continuously with a dye laser. A further method is the quick variation of the etalon in a pulsed ruby laser by altering the distance between the etalon's plates. One plate of the etalon may be mounted on a vibrating piezoelectric element [644]. For contouring by the *two-wavelength method* [23–26, 28, 645–647] the optical arrangement shown in Fig. 6.16 is employed. It uses plane illumination and reference waves, and a telecentric viewing system with an image plane hologram.

Let λ be the wavelength utilized in recording of the hologram and then apply the real-time method with wavelength λ' . The points P' of the reconstructed image are shifted relative to the really existing point P according to (2.151) – (2.153). The lateral displacements of the

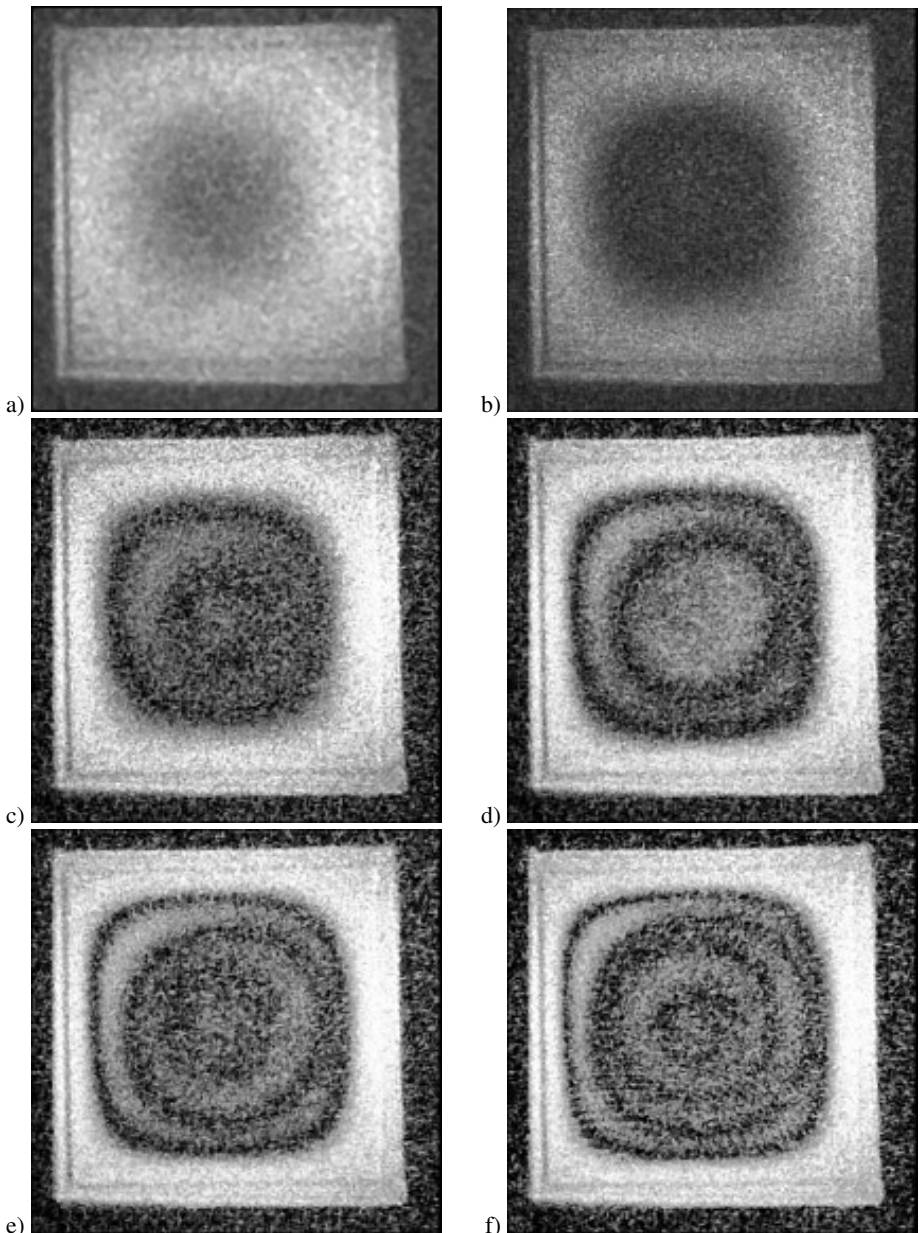


Figure 6.15: Reconstructed intensities in digital time-average holographic interferometry, vibration amplitudes increasing from (a) to (f) (Courtesy of S. Seebacher, BIAS).

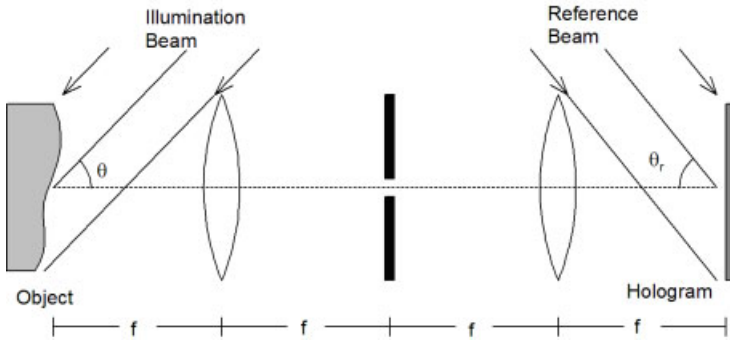


Figure 6.16: Arrangement for wavelength-difference contouring.

points can be eliminated by means of plane recording and reconstructing reference beams and shifting back the reconstructed image by tilting the reference beam by an appropriate amount such that the condition

$$\lambda \sin \Theta'_r = \lambda' \sin \Theta_r, \quad (6.88)$$

is satisfied [309]. Θ_r and Θ'_r represent the initial and final angular positions of the reference beam. Another way of eliminating the lateral shift requires the object to be brought very close to the hologram plate, meaning to record an image plane hologram of the object, Fig. 6.16. Under these assumptions we have the situation of (2.157) – (2.159), so that there is a fictitious displacement vector

$$\mathbf{d} = P' - P = \begin{pmatrix} x'_P - x_P \\ y'_P - y_P \\ z'_P - z_P \end{pmatrix} = \begin{pmatrix} 0 \\ 0 \\ \frac{1}{\mu}z_P - z_P \end{pmatrix} \quad (6.89)$$

with $\mu = \lambda'/\lambda$. By the special choice of the configuration the observation unit vector is $\mathbf{b}(P) = (0, 0, 1)^T$ and the illumination unit vector is $\mathbf{s}(P) = (-\sin \Theta, 0, -\cos \Theta)^T$, Fig. 6.16. Thus the sensitivity vector is

$$\mathbf{e}(P) = \frac{2\pi}{\lambda}(\sin \Theta, 0, 1 + \cos \Theta)^T \quad (6.90)$$

and the resulting phase difference, (4.21), is

$$\begin{aligned} \Delta\phi(P) &= \mathbf{d}(P) \cdot \mathbf{e}(P) \\ &= \frac{2\pi}{\lambda} \left(\frac{1}{\mu}z_P - z_P \right) (1 + \cos \Theta) \\ &= 2\pi \frac{\lambda - \lambda'}{\lambda \lambda'} (1 + \cos \Theta) z_P. \end{aligned} \quad (6.91)$$

The two wavefronts interfere and produce fringes corresponding to *contours* of constant altitude. The fringe planes intersect the object in a direction parallel to the hologram plane. The

contour sensitivity is given by the depth difference Δz

$$\Delta z = \frac{\lambda\lambda'}{(\lambda - \lambda')(1 + \cos \Theta)} \quad (6.92)$$

which induces a change of 2π in the phase difference $\Delta\phi$.

As an example, Fig. 6.17 shows a statuette that was contoured by the wavelength difference method using a dye laser.

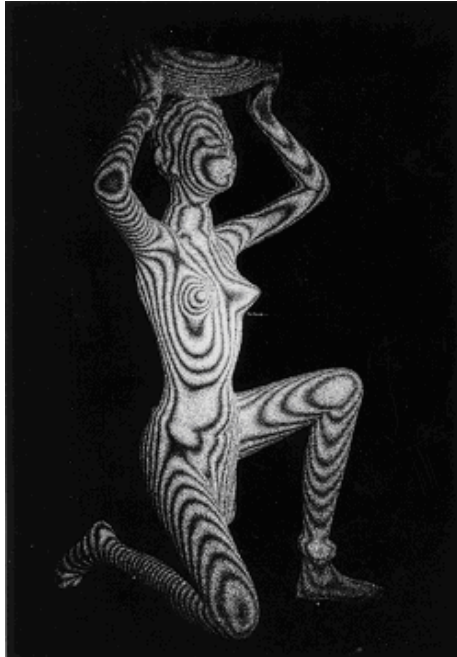


Figure 6.17: Wavelength difference contouring.

6.6.2 Contouring by Refractive Index Variation

A method closely related to the two-wavelength method is the *contouring by refractive index variation*, also called the *immersion method* [27, 309, 648]. Here the wavelength is not modified by changing the frequency of the laser, but by a change in the speed of light according to

$$\nu\lambda = nc \quad (6.93)$$

where n is the refractive index of a transparent material the light is passing through. Equation (2.10) is the special case for vacuum, $n = 1$. The schematic of the immersion method is illustrated in Fig. 6.18. The object is placed in a glass tank filled with a transparent gas or liquid having refractive index n . While the first recording of the object is performed with the medium at refractive index n , the second exposure of the double exposure method is taken when the medium is replaced by another having refractive index n' . In the real-time method during reconstruction of the first holographically stored wave field the object rests in

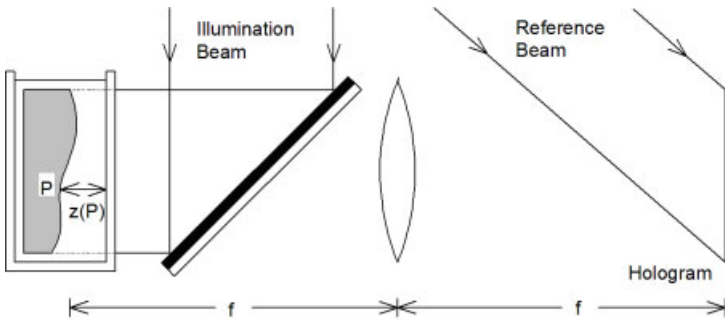


Figure 6.18: Arrangement for contouring by the immersion method.

the medium of refractive index n' . In both methods the produced interference fringes depend on the difference of the refractive indices and the distance $z(P)$ between the object surface and the tank wall.

The object is assumed to be illuminated by a plane wave in a direction perpendicular to the glass plane. Observation is carried out using a telecentric imaging system. Thus different deflections of the rays by the different refractive indices are avoided. The optical phase difference giving rise to fringe formation is

$$\Delta\phi(P) = \frac{4\pi}{\lambda}(n - n')z(P). \quad (6.94)$$

The contour interval Δz producing a change in the phase difference $\Delta\Delta\phi = 2\pi$ is

$$\Delta z = \frac{\lambda}{2(n - n')}. \quad (6.95)$$

If the liquid is a mixture of water and alcohol, and the refractive index is adjusted by the mixture ratio, the method is called the *grog method* [196].

6.6.3 Contouring by Varied Illumination Direction

In the preceding subsections the sensitivity vector between the two interfering states was changed by a variation of the wavelength. Of course the sensitivity vector can be changed by altering the directions of illumination or observation.

If the illumination point S is changed to S' between the two exposures of the double exposure method, the resulting optical path length change δ and the interference phase $\Delta\phi$ can be calculated analogously to (4.13) – (4.21). For $\mathbf{d}_S(S) = S' - S$, we get

$$\Delta\phi(P) = -\frac{2\pi}{\lambda}\mathbf{d}_S(S) \cdot \mathbf{s}(P). \quad (6.96)$$

This means that the object is intersected by fringe surfaces which consist of a set of rotationally symmetric hyperboloids, their common foci being the two points of illumination. The fringe pattern is independent of the point of observation. The longer the distance between object and

illumination sources the flatter are the intersecting surfaces that are approximately parallel to the illuminating beams. Collimated beams produce equidistant parallel flat surfaces. The distance Δh of two such surfaces is

$$\Delta h = -\frac{\lambda}{2 \sin \frac{\Theta}{2}} \quad (6.97)$$

where Θ is the angle between the two illumination directions. The analogy to the results of Section 2.2.1, (2.130), is obvious. Exactly the same result would be produced if holography was not used at all, but rather the object illuminated from the two points simultaneously, this procedure being called *projected fringe contouring*.

If the angle of illumination is changed by translating the object between the two exposures in the proper direction, contouring surfaces of nearly any orientation can be produced [649, 650]. This approach may be combined with a variation of the illumination direction [651–653].

Theoretically the double exposure method with two observation points might be performed by moving the hologram slightly between the two exposures. But since the intersecting surfaces now are parallel to the line of sight, this attempt is useless for contouring purposes. However, if the two states are recorded on different holograms in *sandwich hologram interferometry*, contour lines can be obtained by mutually shifting the plates [654].

6.6.4 Contouring by Light-in-Flight recording

A conceptually different approach to contouring of three-dimensional objects is provided by the holographic *light-in-flight recording* and reconstruction [655–661]. The idea behind holographic light-in-flight recording is the equivalence of a short temporal coherence and a fictitious extremely fast shutter or short light-pulse to produce a motion picture of a propagating optical wavefront. In each small region of a hologram only those parts of an object will be recorded for which the path length from the laser to this small region via the object does not differ from the path length of the reference beam by more than the temporal coherence length of the laser light used for the recording [655, 662].

If the coherence length is short, only those parts of a large object are recorded and appear brightly reconstructed for which a near-zero path difference holds. The object surface seems to be intersected by imaginary interference surfaces in the form of ellipsoids. One focus of these ellipsoids is the source point of the illuminating spherical wave, point A in Fig. 6.19, the other focus is the point in the holographic plate used for observation, point H in Fig. 6.19. To each observation point in the hologram plate there corresponds an ellipsoid representing zero path length difference between object and reference beams, namely $\overline{AP} + \overline{PH} = \overline{AM_1} + \overline{M_1M_2} + \overline{M_2H}$ in Fig. 6.19.

When the point of observation H is moved along the holographic plate, the bright fringe of zero path length can move across the object. Only if H is varied in a way that does not change the zero path length for a specific object point P , this P remains stable. Thus to each object point P there exists a hyperboloid in space representing this zero path length. The two foci of these hyperboloids are the studied object point P and the virtual point source A' of the reference beam. By moving the observation point along the hologram in a way that it crosses

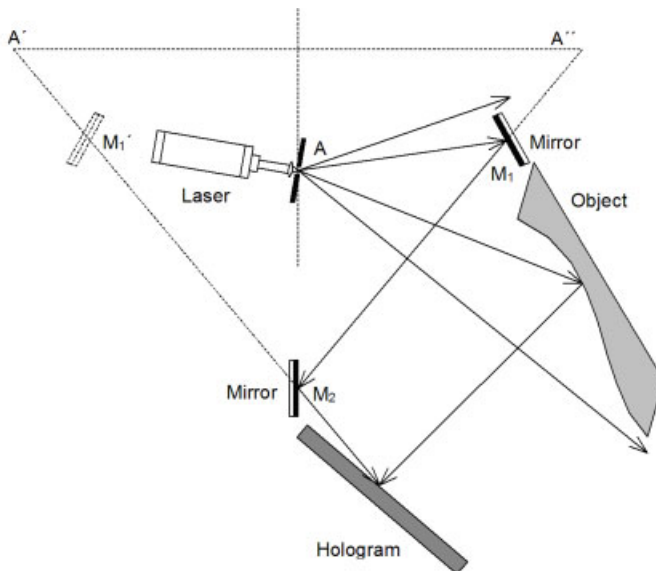


Figure 6.19: Arrangement for holographic light-in-flight recording.

a number of hyperboloids, one sees the fringe intersecting different parts of the object surface as a continuous high-speed motion picture displayed at arbitrary low speeds.

For *contouring* by holographic light-in-flight recording the geometry of the holographic setup has to be optimized in such a way that the ellipsoids in the volume of the three-dimensional object can be approximated by flat surfaces, Fig. 6.20. The object is seen intersected by one flat interference surface S , whose depth position is varied during reconstruction as the observation point is shifted, Fig. 6.20. Here when looking from H_i , one only sees fringes corresponding to the intersection of surface S_i with the object.

The method seems especially suited for a computer-aided evaluation. There is just a single fringe corresponding to one ellipsoid, no zero-order-fringe problem arises. The depth resolution can be controlled by the shift of the observation point during reconstruction. The residual deviations from flatness of the ellipsoids can be taken into account numerically. An evaluation of the contouring lines of light-in-flight holography utilizing an image processing system is described in [117]. Holographic light-in-flight methods also can be used advantageously for visualization and velocimetry in three-dimensional flows [663].

6.7 Contour Measurement by Digital Holography

In Section 6.6 it was shown how holographic interference patterns can be produced, whose local interference phase depends uniquely on the coordinates of the object's surface. These methods can be combined with digital holography, as will be shown. Moreover, the digital approach offers some important advantages over conventional holographic contouring. Because

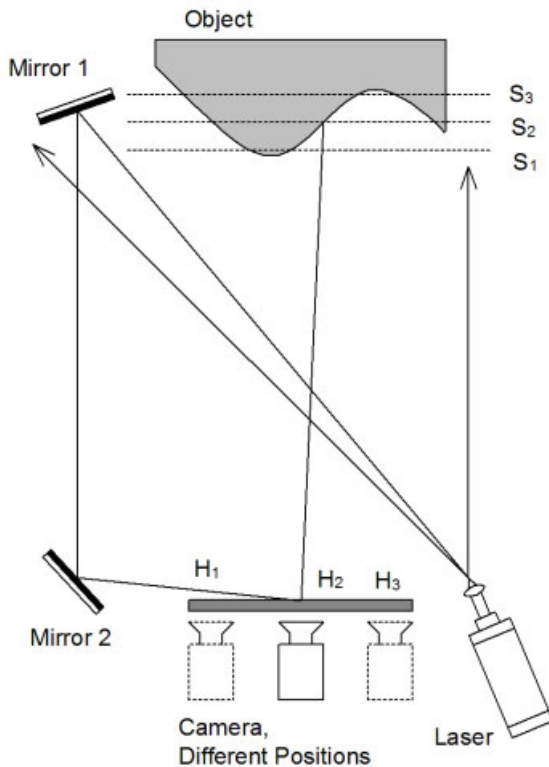


Figure 6.20: Contouring by holographic light-in-flight recording and reconstruction.

now the interference phases are compared numerically they do not have to be reconstructed with the same wavelength as in the optical interferometric comparison. This section presents the methods of Section 6.6 in their digital form.

A special aspect of *digital holographic contouring* is the potential of integrating deformation and contour measurement in a common holographic setup, performing both measurements simultaneously and having an integrated software with common formats [664].

The application of ultrashort laser pulses or laser light beams with only short coherence length enables holographic reconstructions of only those parts of the object which are intersected by specific curves in space.

The presented computer simulations use an object which consists of a rectangular plane plate with a central cap of a sphere [490]. The sphere has a radius of 25 mm, the largest height of the cap over the plane is 5 mm.

6.7.1 Contouring by Digital Holographic Interferometry

If the wavelength between the two recordings is varied, the interference fringes can be interpreted as intersections of the object's surface with a set of ellipsoids. Figure 6.21a shows

this intersection of the plane and the spherical cap with the ellipsoids in the (x, z) -plane. The resulting contour lines in the (x, y) -plane are given in Fig. 6.21b. The interference phase distribution modulo 2π after reconstruction and phase subtraction of the digital holograms is displayed in Fig. 6.22. The parameters used in this example are $N \times M = 1024 \times 1024$ pixel and a pixel center to center distance $\Delta\xi = \Delta\eta = 6.8 \mu\text{m}$. The point source of the divergent illumination is at $S = (0.0, 0.0, 0.4) \text{ m}$. The distance from the flat part of the object to the CCD array is 0.8 m and the two wavelengths used here are $\lambda_1 = 0.6328 \mu\text{m}$ and $\lambda_2 = 0.6338 \mu\text{m}$. The reconstruction is performed with the Fresnel transform and suppression of the d.c.-term.

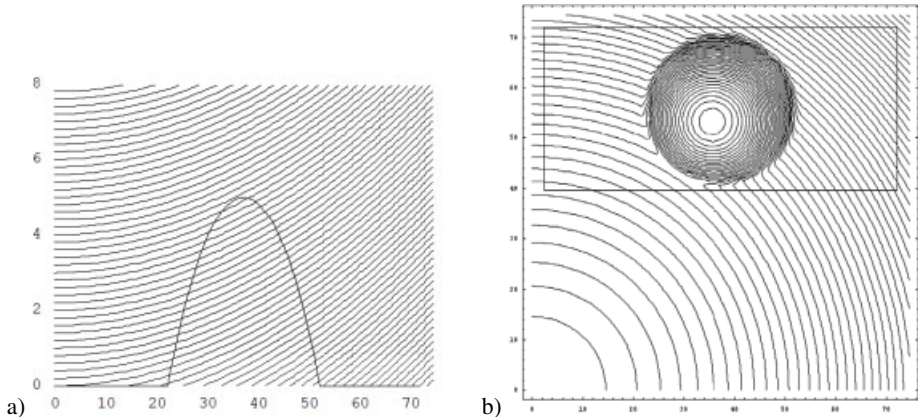


Figure 6.21: Intersection of object with set of ellipsoids.

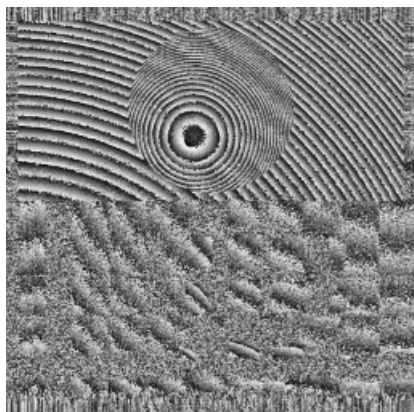


Figure 6.22: Interference phase distribution modulo 2π with two-wavelength method.

This first example demonstrates clearly an important advantage of digital over optical holography: In optics it is not possible to reconstruct the two holograms simultaneously with their related exact wavelengths. Due to heterodyning the interference pattern would oscillate with the beat frequency. Therefore at least one of the holograms must be reconstructed with a wavelength other than the one it had during recording. This in turn would result in at least one distorted reconstructed wave field. However, this distortion can be compensated for by

a special optical arrangement and a shift of the reconstructing reference wave relative to that during recording [237].

On the other hand in digital holography each phase distribution is separately reconstructed with its exact wavelength. Both reconstructed phases then belong to undistorted wave fields representing the object's surface. The subsequent subtraction of the phases is independent from any wavelengths. No compensation of any distortion is necessary, the full freedom of choosing the optical arrangement is maintained.

The next method for generating contour fringes described in Section 6.6 was the two-illumination-points method. Here the surface seems intersected with a set of hyperboloids. This intersection of the plane surface with the cap can be seen for the (x, z) -plane in Fig. 6.23a.

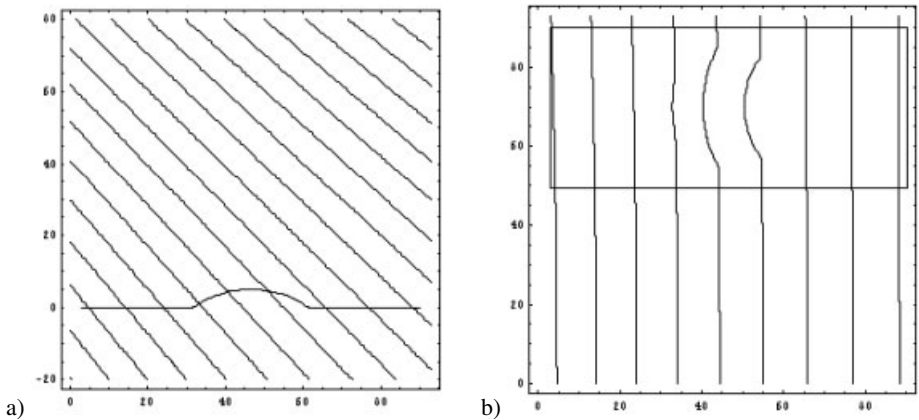


Figure 6.23: Holographic contour lines resulting from two illumination points, intersection with the hyperboloids in (x, z) -plane (a) and (x, y) -plane (b).

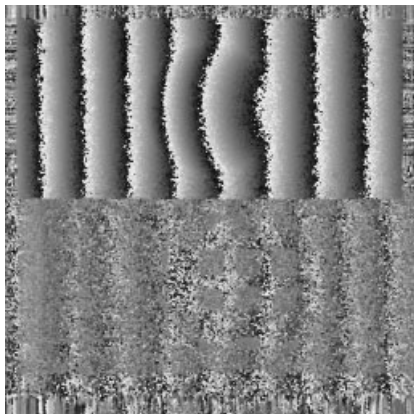


Figure 6.24: Interference phase distribution modulo 2π for the two-illumination method.

The contour lines in the (x, y) -plane are given in Fig. 6.23b. Figure 6.24 shows the interference phase modulo 2π reconstructed from two digital holograms. The illumination source

point is changed from $S_1 = (-300.0, 0.0, 400.0)$ mm to $S_2 = (-299.97, 0.0, 400.03)$ mm. This oblique illumination is better suited for our purpose than the arrangement of the former experiment, since for an illumination wave falling nearly orthogonally onto the object also the hyperboloids intersect the surface nearly orthogonally. Therefore the height variation of the spherical cap would lead to no local lateral shift of the interference fringes. The use of phase-shifting digital holography for measuring surface shape and deformation with the same holographic setup is described in [109, 665]. There the object illumination beam can be tilted due to reflection at a rotatable mirror. The choice of the tilt angle determines the density of the contour fringes [107].

The third holographic contouring method of Section 6.6 is the immersion method. The digital holography example for this method uses a liquid whose refractive index changes from 1.330 to 1.331. The plane wall of the glass container for the liquid and the object is 20 mm in front of the parallel plane part of the object's surface. The resulting curves in space indicating constant phases and their intersection with the surface in the (x, z) -plane are depicted in Fig. 6.25a, the expected contour lines calculated for the (x, y) -plane can be seen in Fig. 6.25b. Figure 6.26 again shows the interference phase distribution modulo 2π resulting from Fresnel reconstruction of the digital holograms.

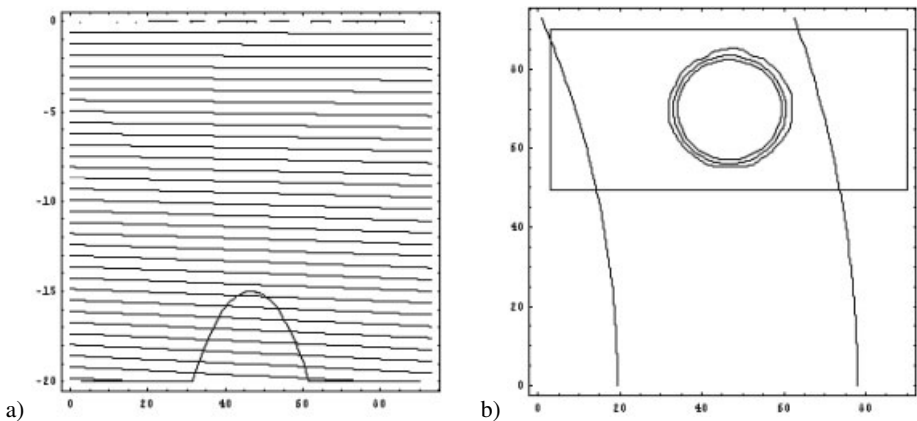


Figure 6.25: Holographic contour lines for the immersion method, intersections in the (x, z) -plane (a) and the (x, y) -plane (b).

6.7.2 Contouring by Digital Multi-Wavelength Holography

The two-wavelength method described in the preceding section can be extended to multiple wavelengths. The various wavelength differences correspond to different synthetic wavelengths [666]. Especially if we measure a discontinuously shaped surface, i. e. one with steps, then the use of more than one synthetic wavelength offers advantages, since steps now can be uniquely detected. Digital multi-wavelength holography also is a useful tool to produce redundant interference phase data enabling the proper demodulation even in the presence of shape discontinuities and height steps [667].

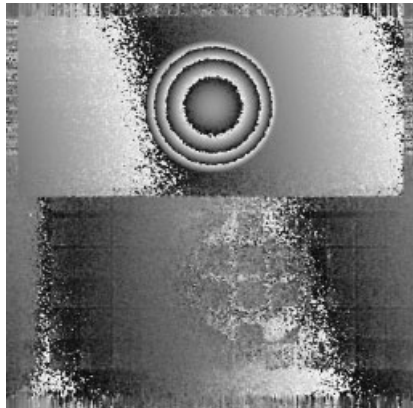


Figure 6.26: Interference phase distribution modulo 2π resulting from the immersion method.

We present an example where the form of a resistor has been measured, Fig. 6.27, using an arrangement according to lensless Fourier transform holography. The source of the spherical illumination wave was slightly above the CCD array to avoid shadows on this severely curved object.

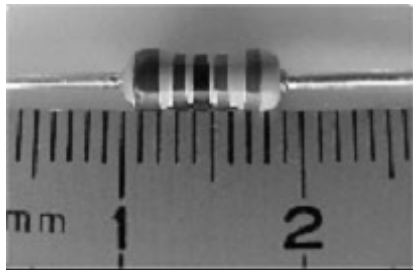


Figure 6.27: Object: resistor.

The first digital hologram was recorded with a wavelength $\lambda_0 = 591.01$ nm. The phase distribution reconstructed from this hologram acted as a reference for the following interferometric comparisons. The wavelength was increased stepwise. Table 6.1 indicates the wavelength differences relative to λ_0 and the related synthetic wavelengths.

Wavelength-difference $\Delta\lambda$	Synthetic wavelength
0.03 nm	5.83 mm
0.08 nm	2.19 mm
0.20 nm	0.88 mm
0.49 nm	0.36 mm
1.02 nm	0.17 mm
2.04 nm	0.086 mm

Table 6.1: Wavelength differences and corresponding synthetic wavelengths.

The interference phase distributions modulo 2π , Fig. 6.28, show precisely, how the interference fringe density increases with decreasing synthetic wavelength. From the phase

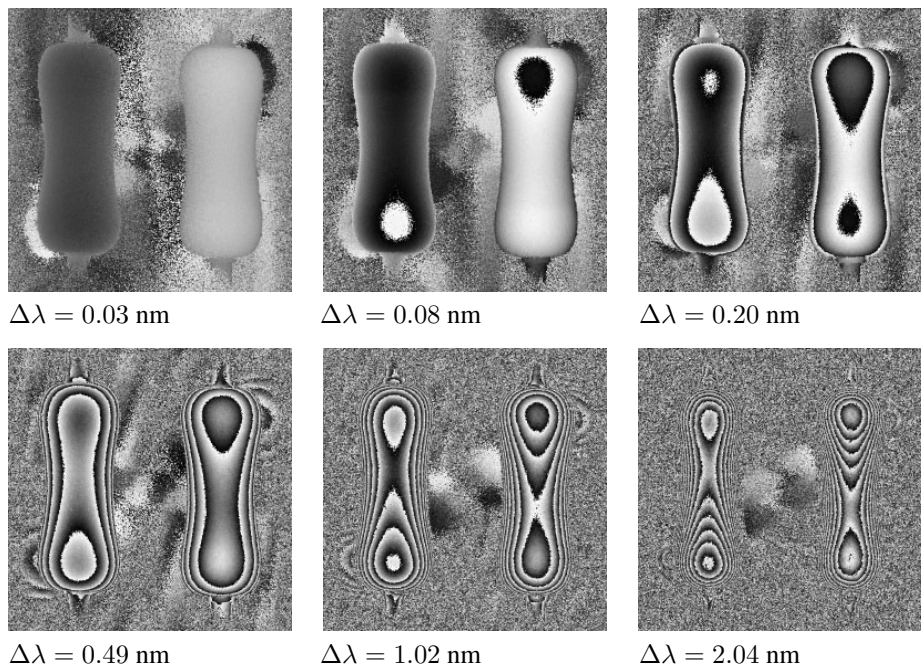


Figure 6.28: Interference phase distributions modulo 2π resulting from digital multi-wavelength holography.

distributions the contours are calculated with high precision, Fig. 6.29, if we demodulate and take into account the variation of the sensitivity vector.

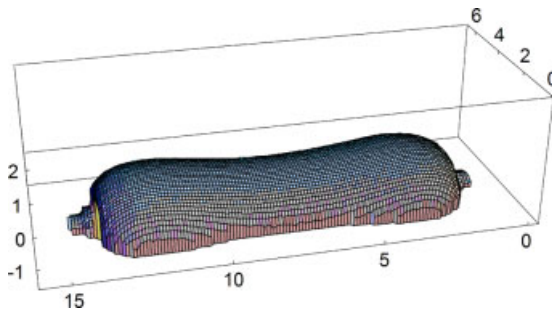


Figure 6.29: Measured contour of the resistor.

6.7.3 Holographic Contouring by Digital Light-in-Flight Measurement

Holographic light-in-flight measurement as a contouring method was already introduced in 6.6.4. It is ideally suited to be combined with digital holography. The main problem in adapting digital holography to this concept is the oblique incidence of the reference wave

onto the hologram. The large angle to the object wave direction produces high frequency holographic structures, higher than can be resolved by a CCD array.

The first attempt to solve this problem was the installation of delay plates in the passage of the plane reference wave impinging normally onto the CCD array, Fig. 6.30. Behind the delay

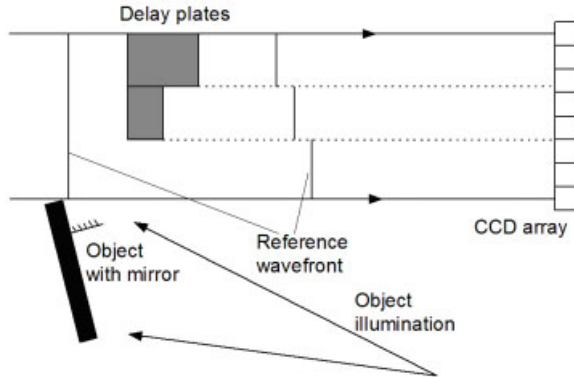


Figure 6.30: Light-in-flight arrangement with delay plates.

plates the wavefront was delayed according to a step function [668]. In this experiment three different light paths over the object to the CCD are recorded. Reconstructions are performed from small stripes in the digital hologram. The laser used in this experiment is an Ar-ion laser pumped CW dye laser with no frequency selecting elements. The resulting coherence length was about 2.3 mm.

A significant progress over the delay of the reference wave with only a few discrete steps was achieved by Carlsson and Nilsson [115, 116, 118, 669]. They use a blazed reflection grating in a Littrow configuration that introduces a continuous linear delay to the reference beam across its diameter while still having constant phase, Fig. 6.31. The resulting reference

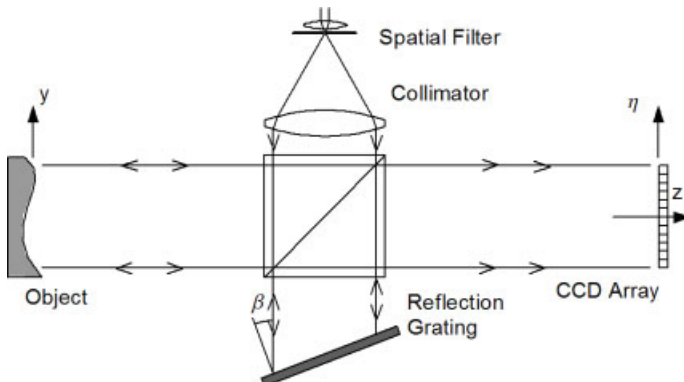


Figure 6.31: Littrow setup for light-in-flight contouring.

field in the hologram plane, the (ξ, η) -plane of the CCD array, can be described by

$$r(\xi, \eta) = \gamma \left(\frac{2\pi}{\lambda} \rho_r - \omega t \right) E_r e^{i(\phi - \omega t)}. \quad (6.98)$$

Here $\gamma \left(\frac{2\pi}{\lambda} \rho_r - \omega t \right)$ describes the properties of the short laser pulse of duration τ_C or short coherence length L_C . We still have a plane wave, therefore $\phi(\xi, \eta) = \phi$ is constant, and the varying delay of the reference wave is contained in $\rho_r(\xi, \eta)$, the path length of the reference wave. It can be expressed by

$$\rho_r(\xi, \eta) = 2\eta \tan \beta + 2z_r \quad (6.99)$$

with z_r the distance between grating and CCD along the z -axis and β the grating angle. The factor 2 comes from the reference wave's double pass to and from the grating. With this reference wave the hologram

$$\begin{aligned} h(\xi, \eta) &= \iiint E_r e^{-i(\phi - \omega t)} \gamma(k\rho_r - \omega t) \frac{E_O}{\rho_O} \gamma(k\rho_O - \omega t) e^{i(k\rho_O - \omega t)} dx dy dt \\ &= \iint \frac{E_r e^{-i\phi}}{\rho_O} \Gamma(\Delta\rho) E_O e^{ik\rho_O} dx dy \end{aligned} \quad (6.100)$$

results. The time integration here is over the pulse length τ_C . The ρ_O is the distance between the object points and the hologram points

$$\rho_O(x, y, \xi, \eta) = \sqrt{d^2 + (x - \xi)^2 + (y - \eta)^2}, \quad (6.101)$$

and $\Gamma(\Delta\rho)$ is the coherence function, i. e. the autocorrelation of $\gamma(k\rho - \omega t)$. It represents the overlapping between the pulses, depending on the path difference $\Delta\rho = \rho_r - \rho_O$.

The reconstruction of the whole object wave field now can be done by using the normally impinging plane wave of unit intensity in the usual way, but then the depth information is lost. Instead one should employ the reconstruction beam

$$r_E(\eta, \eta_0) = \exp \left[-\frac{(\eta - \eta_0)^2}{2\Lambda^2} \right]. \quad (6.102)$$

This constitutes a Gaussian formed strip centered on the line $\eta = \eta_0$ where $\Lambda = L_C/(2 \tan \beta)$ represents the η -width of coherence length L_C in the CCD array. The center η_0 is varied between the reconstructions to permit evaluations of different depths.

Since $\Gamma(\Delta\rho)$ is an autocorrelation, its maximum is $\Gamma(\Delta\rho) = \Gamma(0)$. The maximum intensities in the reconstructed field therefore are at object points for which $\Delta\rho = \rho_r - \rho_O = 0$ is fulfilled. Thus

$$\rho_O = 2\eta_0 \tan \beta + 2z_r. \quad (6.103)$$

It was shown [115] that the curves for equal optical path length form paraboloids in space. There remains an ambiguity in the second, the ξ -coordinate. This can be resolved by use of two exposures with rotated reference gratings.

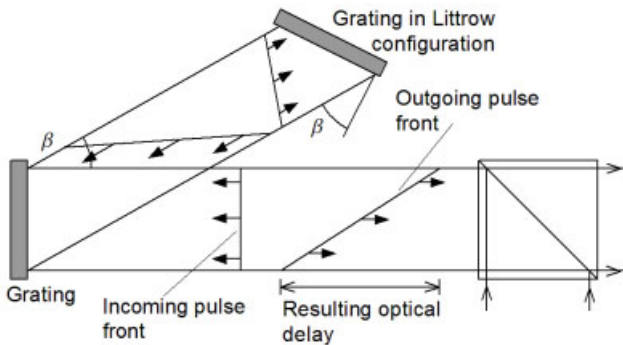


Figure 6.32: Increase of optical delay by gratings in series.

An improvement of the depth measurement range and resolution can be obtained by using larger grating angles. One way to increase the resulting optical delay is to put two gratings in series [118], Fig. 6.32. Up to now only a single digital hologram has been recorded. By recording two pulsed holograms the method can be combined with digital holographic interferometry to allow the simultaneous measurement of shape and deformation.

The concept of holographic light-in-flight contouring also can be realized by using ultra-short pulse lasers [262]. In an arrangement related to a Michelson interferometer, Fig. 6.33, only wave fronts reflected from those parts of the object form holographic structures on the CCD, where their light-paths are of the same length as the path over the piezo-mirror. The agreement must be in the range of the way the wave front travels during this pulse.

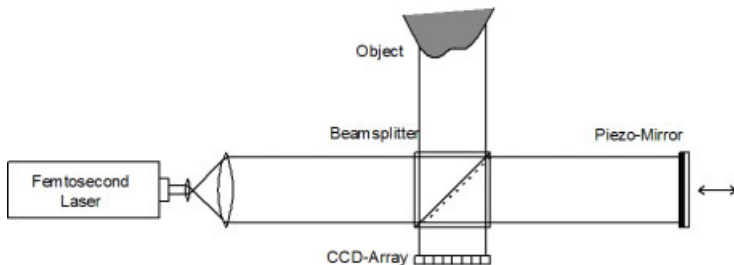


Figure 6.33: Arrangement for contouring using a femtosecond laser.

In the experiments described in the following a Ti:sapphire laser with pulses of 80 fs has been used, this corresponds to a layer of a thickness of about 24 μm the object is intersected by. In a measurement of the contour the optical path length difference is changed in constant steps by the piezo-mirror. Intersections of different depth are recorded and reconstructed by digital holography. There is an advantage of this method over the use of continuously emitting short-coherence lasers, because now the whole CCD records each hologram and not only narrow strips. This improves the quality of the reconstructed images.

The object in the experiments was a stepped cone with steps of $30\text{ }\mu\text{m}$, Fig. 6.34. Between each two recordings of the individual digital holograms the path length difference was increased by $30\text{ }\mu\text{m}$. The reconstructed intensities of these digital holograms are given in Fig. 6.35.

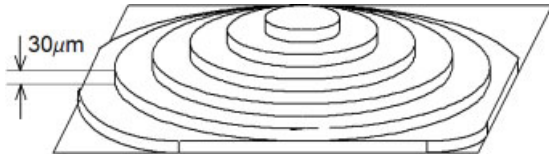


Figure 6.34: Stepped cone.

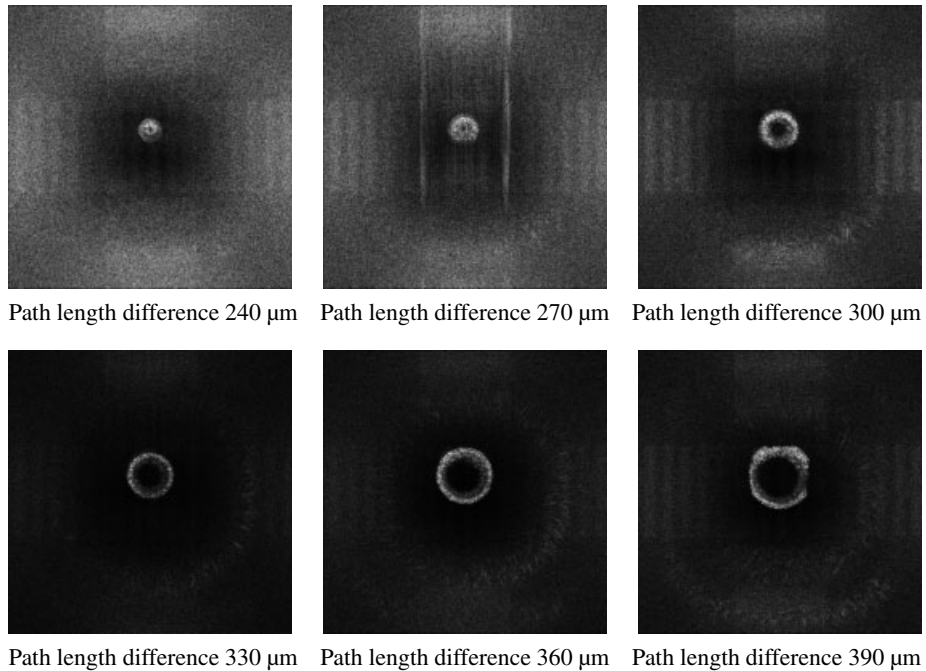


Figure 6.35: Reconstructed intensities from digital holograms recorded with different path length differences (Courtesy of V. Kebbel, BIAS).

6.8 Comparative Holographic Interferometry

6.8.1 Principles of Comparative Holographic Interferometry

One big advantage of holographic interferometry over conventional interferometry is its capability to compare the deformation states of rough diffusely reflecting surfaces as classic interferometry. The technique is not restricted to specularly reflecting surfaces. But with the methods outlined so far it is only possible to compare states of one and the same surface:

apart from the changes to be measured, the microstructure must remain identical. Different objects, although having the same macroscopic geometry, thus cannot be compared by these holographic techniques in a straightforward way.

In non-destructive testing a common problem is to compare a number of produced components against a master object which is guaranteed to have no defect. *Comparative holographic interferometry* now is a technique to compare the deformations of two specimens with respect to the same load or to compare the shapes of two specimens [544, 670–672]. These two specimens are macroscopically identical but have different microstructures. The price one has to pay for this extra potential is the increased experimental effort and complexity.

In *difference holographic interferometry* two holograms are recorded of a master object, normally on separate hologram plates. The two holograms are taken, one in the unloaded and one in the loaded state, Fig. 6.36a. Then a double-exposure holographic interferogram of the object to be tested is produced. While illuminating its surface in the unloaded state by the real reconstruction of the unloaded master object, the loaded test object is illuminated by the reconstructed real image of the loaded master object. The real images of the master object in both states are produced by illuminating the repositioned developed holograms with the conjugate of the reference wave, Fig. 6.36b [544, 670, 673–675].

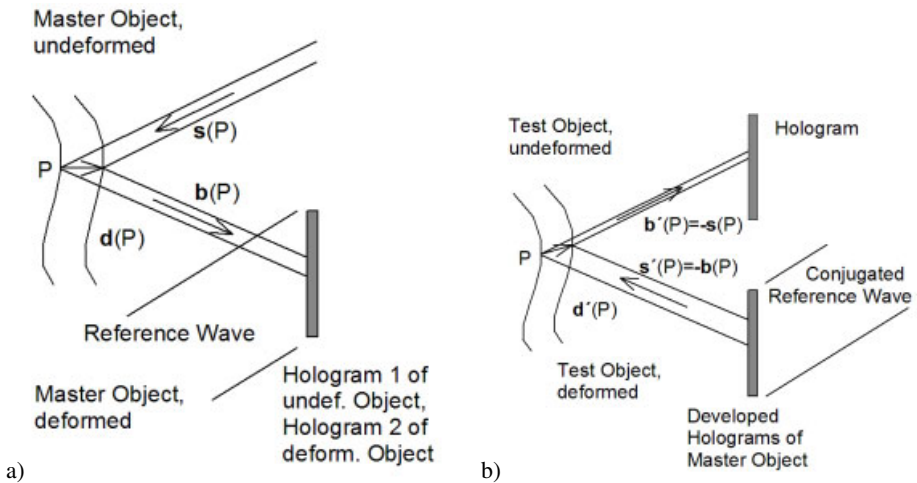


Figure 6.36: Difference holographic interferometry: (a) recording the master holograms, (b) recording the double-exposure test hologram.

For a quantitative description let $E_{1m}(P)$ be the wave field reflected from point P of the surface of the unloaded master object, recorded on hologram 1

$$E_{1m}(P) = E_{01m}(P) e^{i\phi(P)}. \quad (6.104)$$

The wave reflected from the master object in the loaded state, stored in hologram 2, is

$$E_{2m}(P) = E_{02m}(P) e^{i(\phi(P) + \Delta\phi(P))}. \quad (6.105)$$

Reconstruction with E_R^* instead of E_R yields $-\beta t_B |E_R|^2 E_P^*$ in (2.131), that means we illuminate the test object in its initial state with $E_{1m}^*(P) = E_{01m}(P) e^{-i\phi(P)}$ and in the loaded state with $E_{2m}^*(P) = E_{02m}(P) e^{-i(\phi(P) + \Delta\phi(P))}$. The reconstruction of the double exposed hologram of the test object gives the two waves

$$E'_1(P) = E'_{01}(P) e^{-i(\phi(P) - \phi'(P))} \quad (6.106)$$

and

$$E'_2(P) = E'_{02}(P) e^{-i(\phi(P) + \Delta\phi(P) - \phi'(P) - \Delta\phi'(P))} \quad (6.107)$$

which in analogy to (4.3) produce the interference pattern

$$I(P) = I_1(P) + I_2(P) + 2\sqrt{I_1(P)I_2(P)} \cos[\Delta\phi(P) - \Delta\phi'(P)]. \quad (6.108)$$

Here $\Delta\phi(P)$ is the phase difference generated by loading the master object, $\Delta\phi'(P)$ that of loading the test object. According to (4.21) the phase difference $\Delta\phi(P)$ is given by $\Delta\phi(P) = \mathbf{d}(P) \cdot [\mathbf{b}(P) - \mathbf{s}(P)]$, Fig. 6.36a. The illumination direction $\mathbf{s}'(P)$ used to record the test object holographically is the reverse of the observation of the master object $\mathbf{s}'(P) = -\mathbf{b}(P)$ and if furthermore the interferogram is observed along the former illumination direction, $\mathbf{b}'(P) = -\mathbf{s}(P)$, Fig. 6.36b, then we have

$$\begin{aligned} \Delta\phi'(P) &= \mathbf{d}'(P) \cdot \frac{2\pi}{\lambda} [\mathbf{b}'(P) - \mathbf{s}'(P)] \\ &= \mathbf{d}'(P) \cdot \frac{2\pi}{\lambda} [-\mathbf{s}(P) + \mathbf{b}(P)]. \end{aligned} \quad (6.109)$$

Altogether the resulting interferogram shows an intensity distribution belonging to the phase difference

$$\Delta\phi(P) - \Delta\phi'(P) = [\mathbf{d}(P) - \mathbf{d}'(P)] \cdot \frac{2\pi}{\lambda} [\mathbf{b}(P) - \mathbf{s}(P)]. \quad (6.110)$$

This holographic interferogram displays the difference of the displacement vectors between master and test object. As long as the load of the master object can be reproduced exactly for the test object and the holograms can be repositioned precisely, possibly existing component defects lead to differing deformations which are reliably detected in the holographic difference interferogram.

So far the two exposures of the difference hologram have been taken on two separate holograms belonging to the two states of the master object. It is possible to record both states in a single hologram with separate reference waves, see Section 4.2.2. During reconstruction the related conjugate reference waves are employed. Also both master wavefronts may be recorded on a single plate with a single reference beam [544], but the resulting difference interference pattern becomes more complicated. Nevertheless the difference fringes can be resolved [676]. Besides measuring displacement differences this method also can be applied to detect small differences in the shapes of two objects [309, 677, 678], or in the context of measurements at phase objects [679].

Apart from the requirements of recording three separate holograms and repositioning the developed master holograms, difference holographic interferometry is principally a double-exposure method. The real-time comparison of the behavior of two distinct surfaces is possible with the method of *comparative holographic moiré interferometry* [680–682]. To perform this method the images of master and test object are incoherently superimposed by an optical device. In the holographic setup sketched in Fig. 6.37 this is carried out by a Michelson type

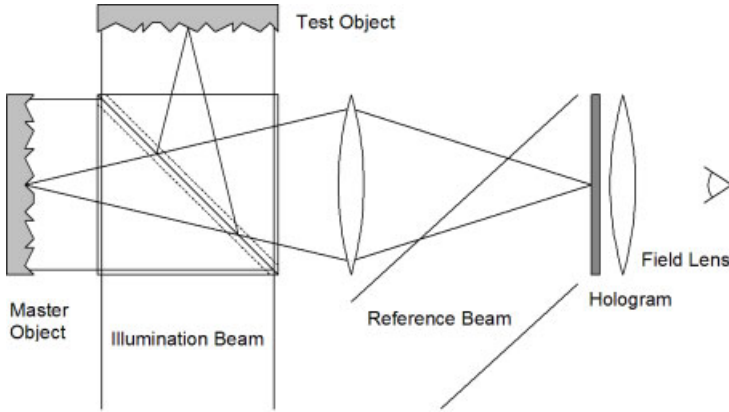


Figure 6.37: Arrangement for comparative holographic moiré interferometry.

of arrangement using a beam splitter. The superposition of unloaded master and unloaded test object is recorded holographically. The reconstructed superposed wave fields then are compared in real-time with the superposition of the wave fields reflected from the loaded master and the loaded test object. The live character of the resulting fringes enables one to follow the evolution of the pattern with increasing load and to compensate for eventually unequal load or rigid body motions.

For a numerical description of comparative holographic moiré interferometry let E_{1m} , E_{2m} , E_{1t} , E_{2t} be the wave fields scattered from the unloaded master, the loaded master, the unloaded test, and the loaded test object, respectively. Without restriction of generality we can assume equal reflectivities and thus equal real amplitudes, see Section 2.2.3:

$$\begin{aligned} E_{1m} &= E_{01}(P) e^{i\phi(P)} \\ E_{2m} &= E_{01}(P) e^{i(\phi(P) + \Delta\phi(P))} \\ E_{1t} &= E_{01}(P) e^{i\phi'(P)} \\ E_{2t} &= E_{01}(P) e^{i(\phi'(P) + \Delta\phi'(P))}. \end{aligned} \quad (6.111)$$

Since master and test do not have microscopically identical surfaces, their wave fields are uncorrelated, which means

$$\begin{aligned} 0 &= \langle E_{1m} E_{1t}^* \rangle = \langle E_{1m} E_{2t}^* \rangle = \langle E_{2m} E_{1t}^* \rangle = \langle E_{2m} E_{2t}^* \rangle \\ &= \langle E_{1t} E_{1m}^* \rangle = \langle E_{1t} E_{2m}^* \rangle = \langle E_{2t} E_{1m}^* \rangle = \langle E_{2t} E_{2m}^* \rangle. \end{aligned} \quad (6.112)$$

Only E_{1m} and E_{2m} as well as E_{1t} and E_{2t} are correlated and can interfere.

The intensity $I(P)$ observed at any point in the image plane during observation of the reconstructed wave fields E_{1m} and E_{1t} together with the scattered fields E_{2m} and E_{2t} is

$$\begin{aligned} I(P) &= \langle |E_{1m}(P) + E_{2m}(P) + E_{1t}(P) + E_{2t}(P)|^2 \rangle \\ &= \langle |E_{1m}|^2 + |E_{2m}|^2 + |E_{1t}|^2 + |E_{2t}|^2 + E_{01}^2 e^{-i\Delta\phi(P)} + E_{01}^2 e^{i\Delta\phi(P)} \\ &\quad + E_{01}^2 e^{-i\Delta\phi'(P)} + E_{01}^2 e^{i\Delta\phi'(P)} \rangle \\ &= 4I_1(P) + 2I_1(P) \cos \Delta\phi(P) + 2I_1(P) \cos \Delta\phi'(P) \\ &= 4I_1(P) \left(1 + \cos \frac{\Delta\phi(P) + \Delta\phi'(P)}{2} \cos \frac{\Delta\phi(P) - \Delta\phi'(P)}{2} \right). \end{aligned} \quad (6.113)$$

The last line is the expression for an additive moiré. The high frequency fringes described by the cosine of the sum of the interference phases are modulated by the low frequency difference phase $\Delta\phi(P) - \Delta\phi'(P)$. For identical mechanical behavior, $\Delta\phi(P) = \Delta\phi'(P)$, the resulting intensity is

$$I(P) = 4I_1(P)(1 + \cos \Delta\phi(P)). \quad (6.114)$$

No moiré fringes are recognized in this case.

Generally the master and test surfaces are illuminated from different directions, s and s' , but observed in common direction b . That means

$$\begin{aligned} \Delta\phi(P) &= \mathbf{d}(P) \cdot \frac{2\pi}{\lambda} [\mathbf{b}(P) - \mathbf{s}(P)] \\ \Delta\phi'(P) &= \mathbf{d}'(P) \cdot \frac{2\pi}{\lambda} [\mathbf{b}(P) - \mathbf{s}'(P)] \end{aligned} \quad (6.115)$$

and thus

$$\Delta\phi(P) - \Delta\phi'(P) = \frac{2\pi}{\lambda} \{ [\mathbf{d}(P) - \mathbf{d}'(P)] \cdot [\mathbf{b}(P) - \mathbf{s}(P)] - \mathbf{d}'(P) \cdot [\mathbf{s}(P) - \mathbf{s}'(P)] \}. \quad (6.116)$$

In practice it is advantageous to have common illumination directions s and s' , as in Fig. 6.37, then the second term in the right-hand side of (6.116) vanishes. The resulting moiré fringe pattern provides information about the difference of the displacement vectors along the direction of the sensitivity vector $\mathbf{b}(P) - \mathbf{s}(P)$ [680].

Comparative holographic interferometry and comparative holographic moiré interferometry enable the measurement of displacement differences or contour differences of distinct objects. This meets many requirements of holographic non-destructive testing. An improvement of the precision of quantitative evaluation and of the quality of the fringe patterns can be achieved by employing phase shifting techniques [683, 684] or Fourier transform evaluation [685] in these techniques.

6.8.2 Digital Comparative Holography

We have seen the various advantages of digital holography, Chapter 3 and Section 5.8, so this approach seems promising when used with the comparative holographic interferometry concept. Now the difference phases (6.110) can be calculated in a computer. However the

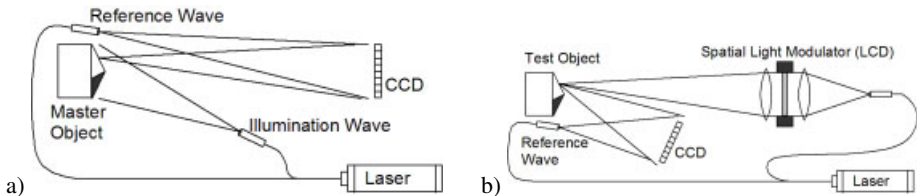


Figure 6.38: Digital comparative holography, a) Recording of coherent mask, b) Coherent illumination of test object.

comparison of the intermediate states is only possible optically. Hereby a spatial light modulator is used to reconstruct the conjugated wavefront of the master object. The arrangements of the optical components for digital comparative holography are shown in Fig. 6.38. The digital holograms of the undeformed and the deformed master object are recorded with the setup of Fig. 6.38a. For comparison purposes then the test object is replaced into the same or an identical arrangement according to Fig. 6.38b which enables the illumination of the test object with the reconstructed conjugated wavefront of the master object. Therefore in the experiment described here a liquid crystal display (LCD) is controlled by the stored digital hologram and optically generates the desired wavefronts [212, 667]. These wavefronts now act as an adaptive illumination of the test object. For a complete cancellation of the fringes, the sensitivity vectors of the master recording arrangement and that of the test arrangement must be the same except for the sign. In the optical realization of comparative holography, Section 6.8.1, we had to record undeformed and deformed states of the objects onto individual hologram plates or we had to separate by different reference waves. In *digital comparative holography* the separate recording and storing of all holograms is delivered automatically, so no additional reference waves are necessary. Thus the whole process is simplified significantly.

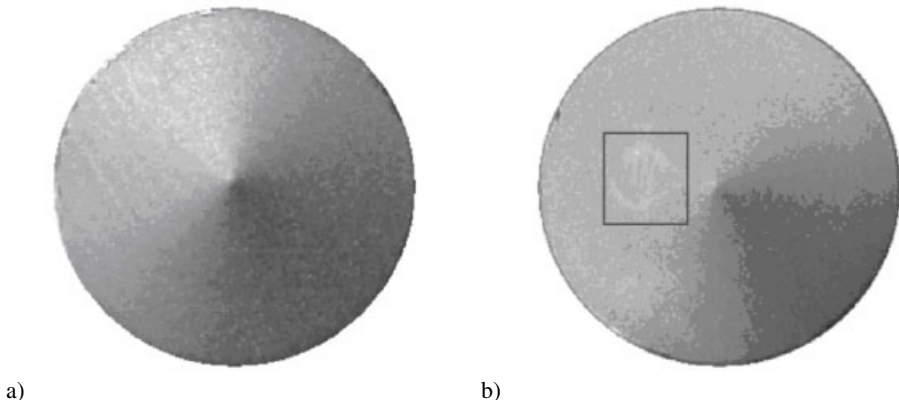


Figure 6.39: Master object (a) and test object with defect in indicated area (b) (Courtesy of T. Baumbach, BIAS).

On the other hand also a digital comparison of phase distributions as in comparative holographic moiré interferometry is possible. The incoherent superposition of intensity recon-

structions of the optical realization is now replaced by the subtraction of the two interference phase distributions calculated by computer.

Digital comparative holography is demonstrated in the following using two macroscopically identical aluminum cylinders with a cone at their upper end, Fig. 6.39. One of the two cylinders has a dent of some micrometers depth in its cone, Fig. 6.39b. In a preliminary test both objects are measured in the same holographic arrangement by holographic contouring using the wavelength difference method of Secs. 6.6.1 and 6.7.2. The wavelengths in the experiment are $\lambda_1 = 746.898$ nm and $\lambda_2 = 749.459$ nm, so the synthetic wavelength of (6.121) is $\lambda_{eq} = 0.218$ mm. The test object's interference phase distribution according to (6.91) is displayed in Fig. 6.40a. The difference of the related interference phase distributions of mas-

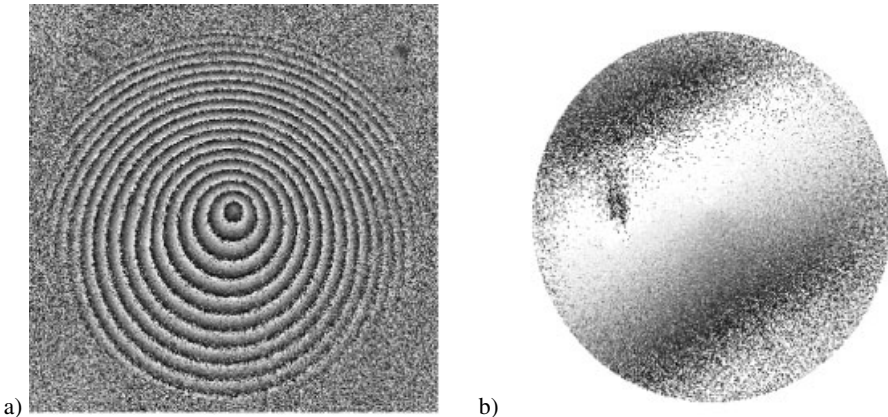


Figure 6.40: Interference phase modulo 2π (contour lines) (a) and result of comparison of interference phases of master and test object (b) (Courtesy of T. Baumbach, BIAS).

ter and test object is given in Fig. 6.40b. While in the difference image, Fig. 6.40b, the dent is clearly visible, in the phase distribution of Fig. 6.40a the dent is hardly recognizable. The remaining two fringes in Fig. 6.40b result from repositioning errors.

The experiments in digital comparative holography on the basis of coherent adaptive illumination presented in Figs. 6.41 and 6.42 use no deformation of the objects, but instead a contouring with the two-wavelength method. The recorded digital holograms have been adjusted to the pixel size of the LCD and were fed into the LCD. The experimental setup of the lensless Fourier transform type, schematically shown in Figs. 6.38a and b is given in Fig. 6.41. The LCD has 1024×768 pixels of size $18 \mu\text{m} \times 18 \mu\text{m}$. Now the master object is the cone with the dent, and the test object is the same cylinder rotated by 180° around the cylinder's axis. The rotated cone is illuminated by the reconstructed real image of the cone in the unrotated state. The resulting digital holograms are recorded and the phase distributions belonging to the different wavelengths used for recording are calculated. The differences of these phase distributions are displayed in Figs. 6.42a and b, first for a synthetic wavelength of $\lambda_{eq} = 0.330$ mm, second with $\lambda_{eq} = 0.254$ mm. We see that the smaller wavelength exhibits a higher noise level but a better recognition of the dents. Further experiments have demon-

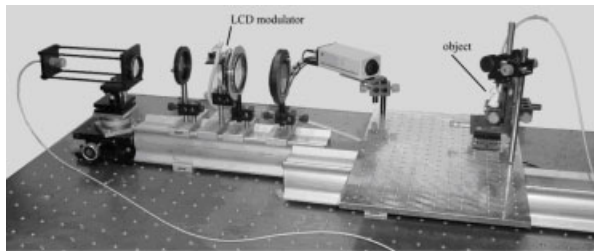


Figure 6.41: Experimental setup for digital comparative holography (Courtesy of T. Baumbach, BIAS).

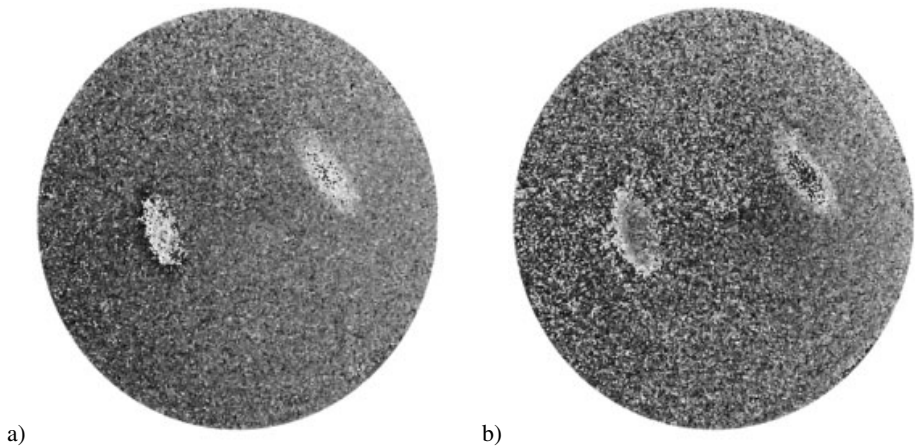


Figure 6.42: Resulting phase differences obtained with coherent illumination using synthetic wavelengths of (a) 0.330 mm, (b) 0.254 mm (Courtesy of T. Baumbach, BIAS).

strated that the noise is diminished and the detection quality is increased by using LCDs with a higher space bandwidth product [212].

The digital approach to comparative holography offers a lot of advantages and benefits: Misalignment between master and sample can be compensated numerically [212,686], there is no cross reconstruction problem with the second wavelengths in the two-wavelength method, and the double exposures are performed in the computer using the individually recorded digital holograms. If master and test object are at different places, the data about the holographic setup and the digital holograms can be easily transmitted using modern communication channels like the internet [687].

6.9 Measurement Range Extension

There are metrologic problems to be solved by holographic interferometry, where the methods introduced so far exhibit some drawbacks. The lack of the correct sign and the absolute

phase, see Section 5.1, may be such a disadvantage. One would wish to measure with a wavelength much larger than the common laser wavelengths to overcome these deficiencies. In other applications one is interested only in the in-plane displacements, while the main sensitivity of the measurement is for out-of-plane displacements. The object may be loaded by centrifugal forces during rotation, for holographic interferometric measurements the interfering wavefronts must be steady. Since in holography only points of a rough surface interfere whose microstructures are identical in a small neighborhood, with conventional holographic interferometry different objects of the same macrostructure cannot be compared.

Solutions to these problems exist as we have seen in the last section. The price one has to pay is generally a more complicated technical and optical arrangement and procedure to be used for the experimental measurements. But these efforts enable a substantial extension of the measuring range of holographic interferometry.

6.9.1 Two-Wavelength Holographic Interferometry

The holographic interferometric measurement of large deformations often leads to high fringe densities which cannot be resolved any more. A longer wavelength, e. g. by a factor 10 to 100, would be desirable. Another effect of a long wavelength would be that it partially solves the absolute phase problem, at least as long as the maximal displacement remains less than this wavelength. But a long wavelength, e. g. the $10.6 \mu\text{m}$ of a CO₂ laser, would cause experimental difficulties since ordinary optical elements are no longer transparent, hologram plates have no sensitivity in this range and the observation requires additional experimental efforts [92]. On the other hand these problems can be circumvented by using two-wavelength holography [688].

In *two-wavelength holographic interferometry* two double-exposure interferograms of the same object undergoing the same deformation are taken with different wavelengths, say λ_1 and λ_2 . In a first approach [688], which is recommended if high fringe densities are expected, the fringe pattern belonging to λ_1 is photographed, the developed transparency is replaced into the holographic arrangement and is illuminated by the interference pattern resulting from λ_2 . A moiré pattern will be obtained, which we get by multiplication of the two overlayed and filtered intensities.

Let the displacement lead to a phase difference $\Delta\phi(x, y)$, then the complex amplitudes are

$$E_j(x, y) = e^{i\frac{2\pi}{\lambda_j}\phi(x, y)} + e^{i\frac{2\pi}{\lambda_j}[\phi(x, y) + \Delta\phi(x, y)]} \quad j = 1, 2 \quad (6.117)$$

and the intensities are

$$I_j(x, y) = E_j(x, y)E_j^*(x, y) = 2 + e^{i\frac{2\pi}{\lambda_j}\Delta\phi(x, y)} + e^{-i\frac{2\pi}{\lambda_j}\Delta\phi(x, y)} \quad j = 1, 2 \quad (6.118)$$

where unit amplitudes were assumed. The moiré is

$$\begin{aligned} I_1(x, y)I_2(x, y) &= 4 + 2e^{i\frac{2\pi}{\lambda_1}\Delta\phi(x, y)} + 2e^{-i\frac{2\pi}{\lambda_1}\Delta\phi(x, y)} + 2e^{i\frac{2\pi}{\lambda_2}\Delta\phi(x, y)} \\ &+ 2e^{-i\frac{2\pi}{\lambda_2}\Delta\phi(x, y)} + e^{i2\pi(\frac{1}{\lambda_1} + \frac{1}{\lambda_2})\Delta\phi(x, y)} \\ &+ e^{-i2\pi(\frac{1}{\lambda_1} + \frac{1}{\lambda_2})\Delta\phi(x, y)} + e^{i2\pi(\frac{1}{\lambda_1} - \frac{1}{\lambda_2})\Delta\phi(x, y)} \\ &+ e^{-i2\pi(\frac{1}{\lambda_1} - \frac{1}{\lambda_2})\Delta\phi(x, y)}. \end{aligned} \quad (6.119)$$

Besides the d.c.- and the high-frequency terms the last two terms lead to an intensity proportional to

$$\cos \left[2\pi \left(\frac{1}{\lambda_1} - \frac{1}{\lambda_2} \right) \Delta\phi(x, y) \right] \quad (6.120)$$

which would have resulted if only the wavelength

$$\lambda_{eq} = \frac{\lambda_1 \lambda_2}{|\lambda_1 - \lambda_2|} \quad (6.121)$$

had been used. This wavelength is called *equivalent wavelength* [688,689] or *synthetic wavelength* [690–692]. As an example, for the two lines of an Ar laser of $\lambda_1 = 0.5145 \mu\text{m}$ and $\lambda_2 = 0.4880 \mu\text{m}$ the equivalent wavelength is $\lambda_{eq} = 9.4746 \mu\text{m}$.

To avoid difficulties in the exact adjusting of the same deformation twice or to avoid spurious interference by air turbulence, the two interferograms can be recorded simultaneously on the same hologram plate. Two separated reference waves, one for each wavelength, are recommended to avoid the disturbing cross-reconstructions [693], see also Section 4.2.2. Then the interferograms are reconstructed and evaluated separately for the two wavelengths. According to (4.20) and (4.21) we have

$$\Delta\phi_j(P) = \frac{2\pi}{\lambda_j} \mathbf{d}(P) \cdot [\mathbf{b}(P) - \mathbf{s}(P)] \quad j = 1, 2. \quad (6.122)$$

The difference of the two evaluated interference phase distributions is

$$\begin{aligned} \Delta\phi_1(P) - \Delta\phi_2(P) &= 2\pi \left(\frac{1}{\lambda_1} - \frac{1}{\lambda_2} \right) \mathbf{d}(P) \cdot [\mathbf{b}(P) - \mathbf{s}(P)] \\ &= \frac{2\pi}{\lambda_{eq}} \mathbf{d}(P) \cdot [\mathbf{b}(P) - \mathbf{s}(P)]. \end{aligned} \quad (6.123)$$

Thus we have a means to extend the range of unambiguity [694] or to reduce the sensitivity. Simultaneous recording avoids the influence of air turbulence, the remaining effect due to the different wavelengths can be neglected since air dispersion is small. Also chromatic aberration can be neglected, for only small wavelength differences are used. Theoretically the method can be expanded to multiple wavelengths yielding still larger equivalent wavelengths.

6.9.2 Holographic Moiré

The main sensitivity of holographic interferometry is in the direction of the bisector between the illumination and the observation direction, described by the sensitivity vector, Section 4.2,

and thus for out-of-plane displacements. For measurement of the in-plane components without multiple observation from different directions and subsequent numerical analysis of the resulting interferograms one can employ the *holographic moiré* method [124, 309, 695, 696]. Here the object is illuminated by collimated waves along two directions which are mutually coherent and symmetric to the surface normal, Fig. 6.43.

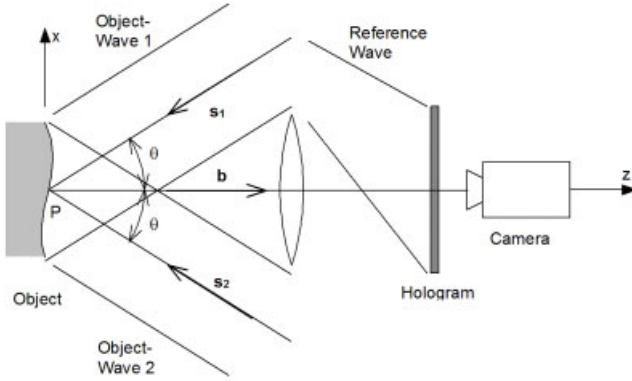


Figure 6.43: Arrangement for holographic moiré.

Let the directions of the two object illumination waves in object point P be described by the unit vectors $\mathbf{s}_1(P) = (-\sin \theta, 0, \cos \theta)$ and $\mathbf{s}_2(P) = (\sin \theta, 0, \cos \theta)$. The observation direction is $\mathbf{b}(P) = (0, 0, 1)$. The complex amplitudes of the two illuminating object waves at P are A_1 and A_2 before the deformation and A'_1 and A'_2 after P has undergone the displacement $\mathbf{d}(P) = (d_x(P), d_y(P), d_z(P))$. This displacement causes the phase differences (4.20) and (4.20)

$$\begin{aligned}\Delta\phi_1(P) &= \frac{2\pi}{\lambda} \mathbf{d}(P) \cdot [\mathbf{b}(P) - \mathbf{s}_1(P)] \\ \Delta\phi_2(P) &= \frac{2\pi}{\lambda} \mathbf{d}(P) \cdot [\mathbf{b}(P) - \mathbf{s}_2(P)]\end{aligned}\quad (6.124)$$

so that $A'_1(P) = A_1(P)e^{i\Delta\phi_1(P)}$ and $A'_2(P) = A_2(P)e^{i\Delta\phi_2(P)}$. The intensity observed at point P when using the real-time method is [309]

$$\langle I(P) \rangle = \langle |e^{i\pi} A_1 + e^{i\pi} A_2 + A'_1 + A'_2|^2 \rangle. \quad (6.125)$$

The reflected wave fields of the two illumination waves are uncorrelated, meaning $\langle A_i A_j^* \rangle = \langle A'_i A'_j \rangle = \langle A_i A_j^* \rangle = \langle A'_i A_j^* \rangle = 0$ for $i \neq j$. Without restriction of generality we can assume equal real amplitudes $\langle |A_i|^2 \rangle = \langle |A'_i|^2 \rangle = \langle I_1 \rangle$ for $i = 1, 2$. Then (6.125) reduces to

$$\langle I(P) \rangle = 4\langle I_1(P) \rangle - 2\langle I_1(P) \rangle (\cos \Delta\phi_1(P) + \cos \Delta\phi_2(P)). \quad (6.126)$$

Introducing $\Phi(P) = (\Delta\phi_1(P) - \Delta\phi_2(P))/2$ and $\Psi(P) = (\Delta\phi_1(P) + \Delta\phi_2(P))/2$ we obtain

$$\langle I \rangle = 4\langle I_1 \rangle (1 - \cos \Phi \cos \Psi). \quad (6.127)$$

The argument (P) is omitted for clarity. From (6.124) it follows that

$$\begin{aligned} \Phi(P) &= \frac{2\pi}{\lambda} d_x(P) \sin \theta \\ \Psi(P) &= \frac{2\pi}{\lambda} d_z(P)(1 + \cos \theta). \end{aligned} \quad (6.128)$$

The loci of the moiré fringes resulting from the multiplication of the two patterns in (6.127) represent contour lines of the projection of the displacement vector $\mathbf{d}(P)$ onto the object plane in the direction containing the two beams [309]. The spacing of the fringes corresponds to an incremental displacement of $\lambda/(2 \sin \theta)$.

To get clearly visible moiré patterns, generally the two multiplied patterns must have high density and have to be oriented in nearly the same direction. Their planes of maximum contrast must match. In practice these requirements can be fulfilled by the introduction of additional phase differences much larger than those generated by the object deformation to be measured. To obtain parallel equidistant fringes of high density localized on the object surface one may rotate the holographic plate around an axis parallel to its plane [697, 698], translate the hologram plate in its plane [699], rotate the reference beam accompanied by a translation of the hologram [670], or rotate the reference beam only [699–701].

Although the auxiliary fringes are necessary to generate the holographic moiré at all, they disturb the visual appearance of the moiré fringes. Therefore an optical or digital low-pass filter eliminating the high-frequency carrier fringes and passing only the low-frequency moiré fringes is applied in the preprocessing step of the evaluation. After this the fringe pattern can be evaluated by one of the diverse quantitative evaluation methods. An interesting combination of numerical preprocessing and quantitative evaluation by Fourier transform fringe pattern analysis which determines instantaneously both phase functions of the pattern is presented in [685].

Another option is phase shifting holographic moiré [696] where the reference beam is directed over a mirror that is mounted on a piezoelectric transducer. From several phase shifted moiré holograms, recorded before and after deformation, the phase difference $\Phi(P)$ is calculated, from which $d_x(P)$ is determined using (6.128).

6.9.3 Holographic Interferometry at Rotating Objects

The *vibration modes* of spinning components excited by *centrifugal forces* generally are different from those of stationary objects excited conventionally. Wheels, propellers, or turbine blades are just a few engineering components where the knowledge of the actual dynamic behavior under real operating conditions helps to optimize the design and performance. Although the circumferential speed often reaches more than 100 m s^{-1} , holographic interferometry can be adapted to measure the deformation and vibration of such *rotating objects* [702–705].

Consequently the holographic recording of moving objects, especially rotating objects, normally requires the use of a pulsed laser. To produce time-resolved holographic interferograms, Carlsson et al. [706] describe a system consisting of a multiple-pulsed Q-switched

ruby laser and a rotating disk having radial slits with a constant angular separation. The disk is used to scan the reference beam along the holographic plate, thereby achieving spatial multiplexing. This system is a tool for full-field dynamic measurements.

If we intend to measure the displacements and deformations excited by the rotation, e. g. by centrifugal forces, or if we want to use a CW laser, e. g. for time average vibration analysis, we need a recording configuration which is insensitive to the rotational motion but sensitive to radial and normal displacements. Such an arrangement must have its illumination point as well as the observation point on the axis of rotation, Fig. 6.44, which here is the z -axis.

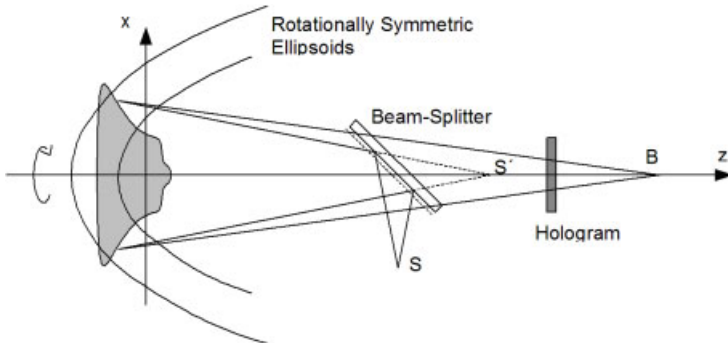


Figure 6.44: Holographic arrangement insensitive to in-plane rotations.

Rotationally symmetric ellipsoids with illumination point S' and observation point B as focal points define the loci of constant optical path length. Since object surface points undergoing only the in-plane rotation do not change the optical path lengths they do not contribute to the generation of the interference pattern. If furthermore the (virtual) illumination point S' and the observation point B coincide, the sensitivity vectors $e(P)$ for all surface points P are parallel to the rotation axis, see (4.20), and in this case the arrangement is insensitive to all in-plane displacements, even to radial displacements. For an arrangement optimized in the described way the maximum rotation speed is only restricted by motion blur and resolution. That means the lateral movement in the image plane is limited to about half a speckle size, (2.117) and (2.118), to obtain an acceptable visibility.

A common method to keep the unwanted contributions of the rotational motions to the interferogram small is the *object related triggering* of the double pulse laser [707]. By encoder disks or other non-contacting optical measurements the angular position of the object during the first of a double pulse is registered. The second pulse is triggered so that the object is in the same angular position, although during a different revolution, as with the first exposure. Pulse separation with this method must be rather high, i. e. some milliseconds, compared to conventional double pulse techniques. This object related triggering was successfully applied to measure forced vibrations of a rotating turbine blade model with maximum circumferential speed at the blade tip of 235 m s^{-1} . The measured deflection behavior was compared to numerical results [708].

A holographic interferometer spinning synchronously with the object is shown in Fig. 6.45. In this *rotating interferometer* two holograms and two reference waves are employed to achieve a better mechanical balance [707]. The object illumination comes from the

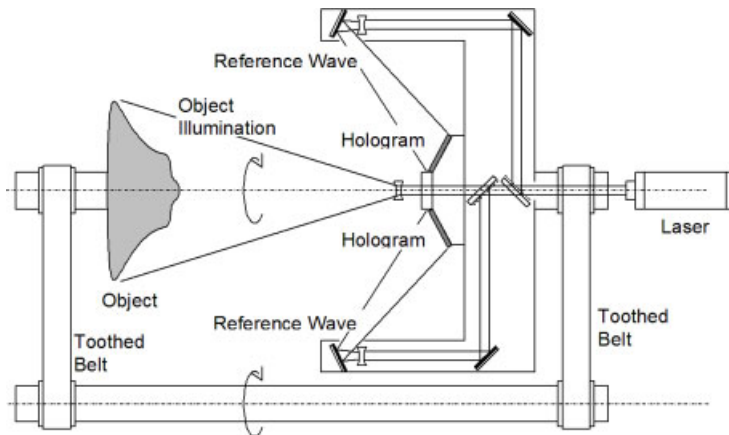


Figure 6.45: Rotating holographic interferometer.

laser beam passing through the hollow shaft of the interferometer. The axes of rotation of the object as well as of the holographic setup must be colinearly aligned. The synchronous rotation is achieved by mechanical coupling via toothed belts, Fig. 6.45, or electrooptical registration of the object rotation and electronic control of the interferometer rotation. A rotating interferometer as described allows one to record double exposure holograms in any angular position in contrast to the stroboscopic technique of the object related triggering method.

An approach to produce a stationary wave field reflected from the rotating object is the compensation of the rotation by an *image derotator* [352, 709, 710]. Its principle is shown in Fig. 6.46. If one observes an image reflected from a roof edge prism, this image appears to

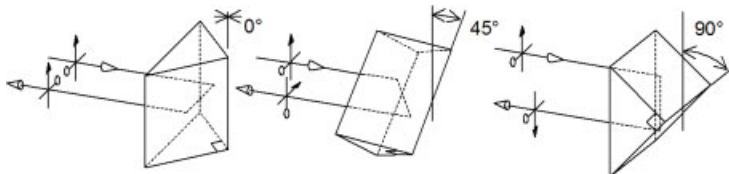


Figure 6.46: Image derotation by a roof edge prism.

rotate as soon as the prism is turned around its optical axis. The image rotates in reverse order to the prism but at twice the angular velocity of the prism rotation. So if the prism is rotating with half the number of revolutions and in the same direction as the rotating object then the reflected image appears stationary to an observer [711]. Of course the axes of rotation must be colinearly aligned. A holographic arrangement with an image derotator operating according to this principle is displayed in Fig. 6.47. The object is illuminated by a divergent wave field coming from a virtual point source located at the common axis of rotation. An encoder may be mounted on the shaft of the rotating component, or the object's rotational speed is recorded by a photocell detector or a tachogenerator to adapt the speeds of the object and the derotator prism. This prism is driven by a servo-controlled motor; if the object rotates with n revolutions

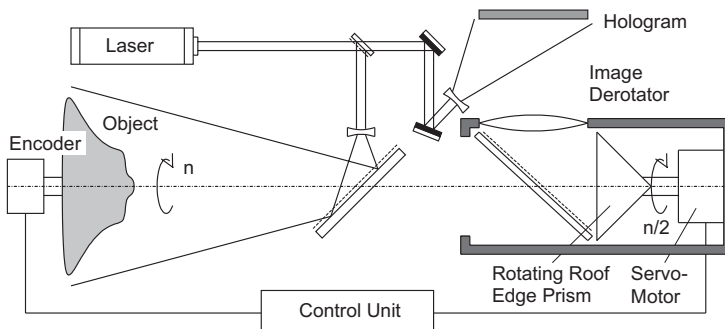


Figure 6.47: Holographic interferometric arrangement with image derotator.

per minute then the prism has to rotate with $n/2$ revolutions per minute. A fixed beamsplitter allows unhindered observation of the derotated image as well as the recording of holograms with double pulsed or continuous exposures. Using the image derotator, the rotating object can be viewed continuously in arbitrary angular positions: we have a non-stroboscopic system for freezing the wave field [712].

One application of holographic interferometry with rotation compensation by an image derotator was the investigation of the blade vibrations of the impeller of a radial compressor [713]. The radial impeller of 290 mm diameter consisted of 20 blades with every second blade cut back at the impeller inlet. Therefore 10 blades are observed along the rotational axis. The double exposure holographic interferogram of Fig. 6.48a was recorded at a rotational speed

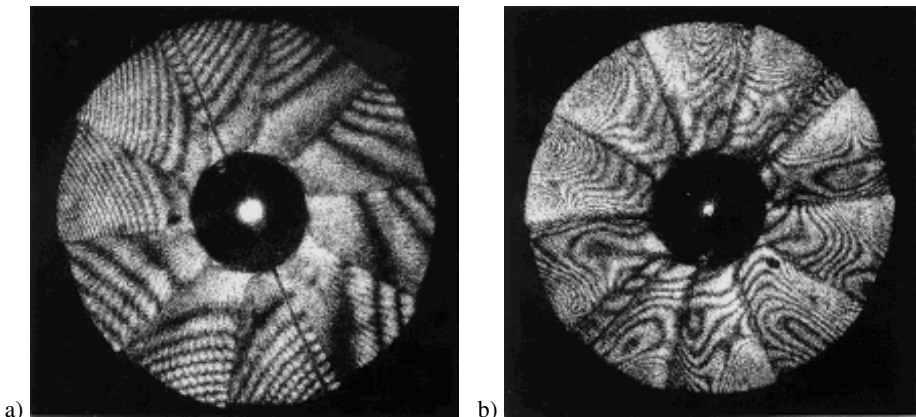


Figure 6.48: Holographic interferograms of a rotating radial impeller (a) at 2,935 rpm, (b) at 13,450 rpm (Courtesy of J. Geldmacher, BIAS).

of 2,935 rpm, and the one of Fig. 6.48b at 13,450 rpm. The resulting circumferential speed in this example reaches 204 m s^{-1} . The interferogram taken at 2,935 rpm was recorded with open compressor inlet. All blades vibrate in the first bending mode. At higher speeds, as in Fig. 6.48b, a closed compressor inlet had to be used. So the derotator was placed outside

the inlet tube, the impeller was viewed via a deflection mirror installed inside the tube. The resulting interferogram displays a superposition of different vibration modes.

The aforementioned experiments still used holographic plates. Nowadays more flexibility is offered by digital holography. So pulsed digital holographic interferometry using a derotator for measuring dynamic deformations of rotating discs is described in [714]. Three-dimensional measurements of all displacement components of a rotating disc combining information from three different illumination directions are presented in [715]. Here pulsed digital holography without image derotator, but synchronized recording is employed.

6.9.4 Endoscopic Holographic Interferometry

Holographic interferometric measurement of form, deformation, vibration, etc. combined with endoscopy enhances the versatility of these methods by giving access to regions which are optically not accessible in the direct easy way. Thus hidden parts or cavities with only small access apertures like body cavities in medicine or the inside of machine components can be measured. Development of *endoscopic holographic interferometry* started with holographic film [716] but nowadays improved solutions using digital holographic interferometry are state of the art [717–720]. Different kinds of endoscopes enabling holographic interferometry are principally possible. So one can discriminate between rigid and flexible endoscopes. Modern rigid endoscopes are equipped with rod lens systems, so in a way a rigid endoscope can be viewed as a long objective. The flexible endoscopes on the other hand employ glass fibers for guiding the light. A further categorization can be introduced by dividing into the class of endoscopes with external interferometer head and the class where the interferometer is at the tip of the endoscope inside the cavity. While in the first named class the reflected wave field is guided over a bundle of fibers, e. g. 10,000 up to 50,000 fibers [718], in the second class illumination and reference light is transmitted over monomode fibers, and the interference between reflected object wave and the reference wave takes place on the 2D detector inside the cavity, so only the electronic data have to be transmitted to the outside world [717, 720].

The concept of an endoscope capable of full three-dimensional measurement of form and deformation by digital holographic interferometry is described in [717]. There reference wave and object illumination wave are guided into the sensor head by monomode glass fibers. Figure 6.49 shows only one object illumination arm although the real sensor has three arms. To

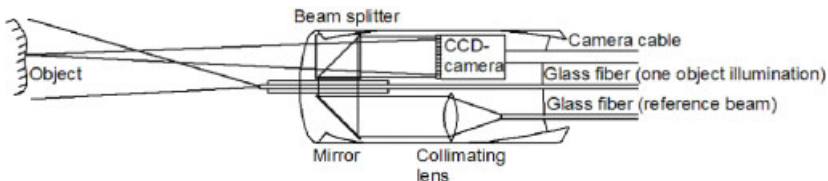


Figure 6.49: Sensor head of holographic endoscope.

obtain three significantly different sensitivity vectors, see Section 6.2, the illuminating fibers are within arms which are folded into the endoscope during induction into the cavity, but unfolded inside the cavity. The three unfolded arms are seen in the photograph of the holographic endoscope in Fig. 6.50. The beam splitter, Fig. 6.49, guides the collimated reference wave as

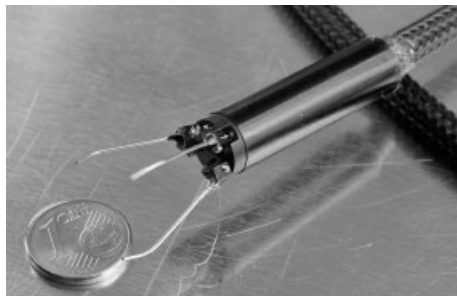


Figure 6.50: Photograph of holographic endoscope sensor head.

well as the reflected object wave to the miniature camera which has a 1/6-inch CCD array. The whole sensor body with folded illumination arms has a diameter of 9.75 mm and a length of 35 mm. The external devices are shown in Fig. 6.51. The piezomechanical light switch splits

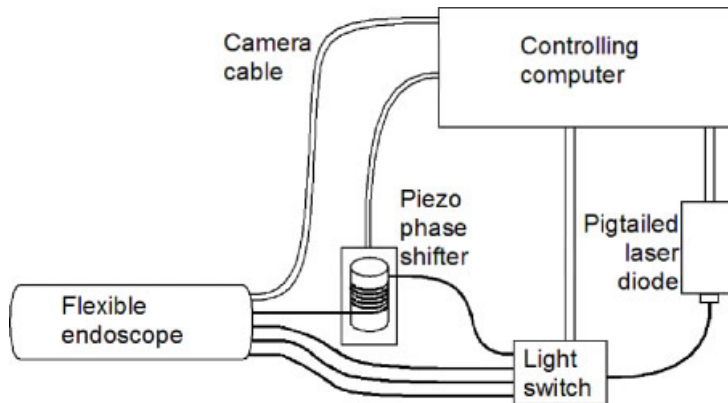


Figure 6.51: Schematic of holographic endoscope with its external devices.

the light into the reference and one of three illumination beams. The reference wave is led over a piezo-based fiber phase-shifter to enable phase shifting digital holography. By this the whole space-bandwidth product of the CCD-sensor is exploited, see Section 3.4.1. With the described endoscopic sensor three-dimensional shape measurements by two-wavelength contouring, see Section 6.7.2, and 3D deformation measurements have been carried out. Due to the fast acquisition of digital holograms during the deformation process, a temporal unwrapping enables the determination of absolute interference orders. Details of the measurement results can be found in [717].

6.9.5 Desensitized Holographic Interferometer

Flatness deviations normally are measured by Fizeau interferometers [196,443]. For measurement of flatness deviations ranging from several to some 100 µm in a *desensitized holographic interferometer* using a custom made holographic optical element is presented in [721]. The key optical component of this interferometer is the *diffractive optical element* which is recorded

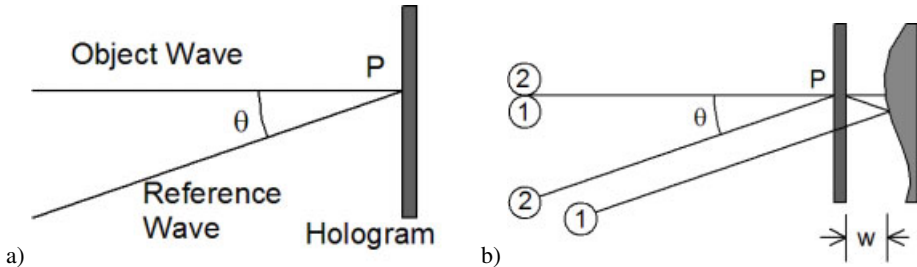


Figure 6.52: Desensitized holographic interferometer: (a) recording of the DOE, (b) testing of a surface.

by two waves intersecting by the angle θ , Fig. 6.52a. At the reconstruction stage, the mirrored surface to be tested is placed just behind this hologram. Two ray paths merit attention, Fig. 6.52b. Ray path 1 is transmitted in the zero diffraction order through the hologram, is reflected by the surface, and finally emerges back from the hologram through diffraction in order +1. Ray path 2 is first diffracted in the +1 order and after reflection by the object surface is transmitted through the hologram in the zero order. The optical path difference $\delta(P)$ between these two rays leaving the hologram in parallel is dependent on the width $w(P)$ of the air gap between hologram and surface

$$\delta(P) = 2w(P)(1 - \cos \theta). \quad (6.129)$$

The interference gives rise to fringes of equal thickness $w(P)$ between hologram and surface

$$w(P) = \frac{n\lambda}{2(1 - \cos \theta)}. \quad (6.130)$$

For small angles θ the desensitization factor can approach values of about 100.

The analysis in [721] shows that as long as the mirrored surface lies close to the hologram and since the hologram itself performs a chromatic filtering, good contrast fringes are obtained even when the reconstruction is carried out in white light. Contrary to reconstruction with laser light, the final image is free from coherent noise arising from dust as well as from the roughness of the tested object. If the holographic plate is mounted on a holder that can be accurately translated normally to the object surface, the resulting fringes can be phase shifted, thus enabling the use of the phase shifting methods for quantitative evaluation.

6.10 Refractive Index Fields in Transparent Media

6.10.1 Refraction of Phase Objects

In a transparent nonpolar dielectric medium the speed of light primarily depends on the density of the medium and the wavelength of the light. The density is described by the *refractive index* n , which is the ratio between the *speed of light* in vacuum c_0 , see (2.3), and the speed of light c in the medium

$$n = \frac{c_0}{c}. \quad (6.131)$$

The refractive index may be spatially constant in the medium, then we speak of a *homogeneous medium*, or n varies from point to point, then we have a *nonhomogeneous medium*. In a non-homogeneous medium there are regions with lower n , where light travels more rapidly than in regions of higher n , so wavefronts get distorted when propagating through this medium. The equation of a ray propagating through a medium with the spatial refractive index distribution $n(x, y, z)$ is

$$\frac{d}{ds} \left(n(x, y, z) \frac{d\mathbf{r}}{ds} \right) = \nabla n(x, y, z) \quad (6.132)$$

where $\mathbf{r} = (x, y, z)$ is the vector of point (x, y, z) on the ray, s is the length coordinate along the ray and ∇ is the *gradient operator*:

$$\nabla = \left(\frac{\partial}{\partial x}, \frac{\partial}{\partial y}, \frac{\partial}{\partial z} \right). \quad (6.133)$$

For a homogeneous medium the *ray equation* (6.132) reduces to $d^2\mathbf{r}/ds^2 = 0$, whose solution is a straight line $\mathbf{r} = \mathbf{c}_0 s + \mathbf{c}_1$ with constant vectors \mathbf{c}_0 and \mathbf{c}_1 . Consequently in a nonhomogeneous medium the rays are curves, some of such curved rays are shown in Fig. 6.53 together with two wavefronts.

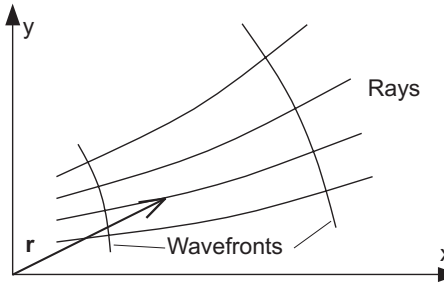


Figure 6.53: Curved rays and wavefronts in a nonhomogeneous medium.

The path of a ray transmitted through a homogeneous transparent body embedded in another homogeneous medium – often this second medium is free space with the refractive index of air approximated by $n \approx 1$ – is governed by *Snell's law*

$$n_1 \sin \theta_1 = n_2 \sin \theta_2 \quad (6.134)$$

which describes the slopes of the path at the boundary between the media. n_1 and n_2 are the refractive indices in the two media, θ_1 and θ_2 are the angles between the normal to the interface and the rays in medium 1 and medium 2, respectively.

Things become more complicated when the refractive index field varies spatially. As a first example [170] assume a refractive index which varies only in one direction perpendicular to the incoming ray, say

$$n(x, y, z) = n(y). \quad (6.135)$$

Let the ray propagate in direction z and enter the volume of refractive index $n(y)$ at y_0 , Fig. 6.54. The two vector components of (6.132) which are not identically zero now are

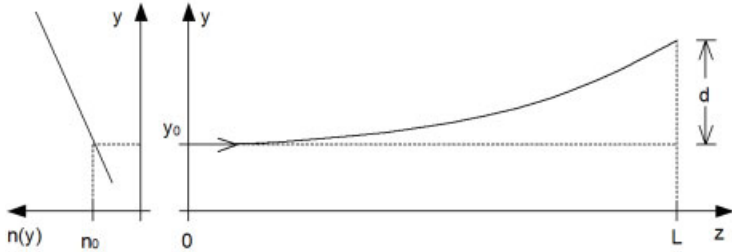


Figure 6.54: Ray propagating through a medium with $n = n(y)$.

$$\frac{d}{ds} \left(n(y) \frac{dy}{ds} \right) = \frac{d}{dy} n(y) \quad \text{and} \quad \frac{d}{ds} \left(n(y) \frac{dz}{ds} \right) = 0. \quad (6.136)$$

The differential line element is $ds = \sqrt{1 + (dy/dz)^2} dz$, so we combine (6.136) to

$$\frac{dn(y)}{dy} = n(y) \frac{y''}{1 + (y')^2} \quad (6.137)$$

with the prime here denoting differentiation with respect to z . By assumption $y(0) = y_0$, $y'(0) = 0$, $n(0) = n_0$, so that the integration of (6.137) yields

$$1 + (y')^2 = \left(\frac{n}{n_0} \right)^2. \quad (6.138)$$

If the variation of n is linear, Fig. 6.54, $n(y) = n_0 + m(y - y_0)$, then we get the solution

$$y - y_0 = \frac{1}{2} \left(\frac{m}{n_0} \right) z^2 \quad (6.139)$$

where the first-order approximation $(y')^2 = 2(m/n_0)(y - y_0)$ is used. This means that the ray entering a linearly stratified medium will travel along a parabolic path. After leaving the test volume of length L the deflection d of the ray is

$$d = \frac{1}{2} \left(\frac{m}{n_0} \right) L^2 \quad (6.140)$$

and its slope is

$$y'(L) = \frac{m}{n_0} L. \quad (6.141)$$

The optical pathlength δ of this ray in the test volume is

$$\delta = \int_0^L n(y) \sqrt{1 + (dy/dz)^2} dz. \quad (6.142)$$

which is approximated by

$$\delta = n_0 L \left(1 + \frac{1}{3} \left(\frac{m}{n_0} \right)^2 L^2 \right) \quad (6.143)$$

Even this simple example exhibits the bending of the rays when a spatial variation of the refractive index is present. This possibility has to be envisaged in the interpretation and evaluation of holographic interferograms which should measure refractive index variations of transparent media.

As mentioned before, each interpretation or evaluation of an interference pattern requires an imaging system to form a real image, at least the lens of the observer's eye. The imaging system is represented by a single thin lens in Fig. 6.55. The refractive index field acting

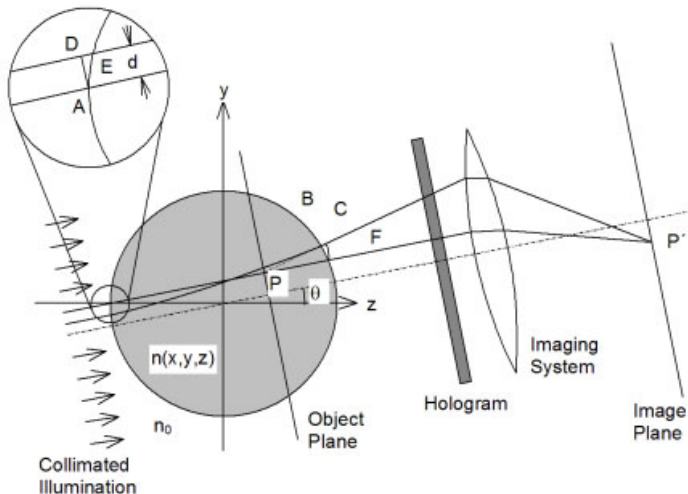


Figure 6.55: Imaging of a refractive index field.

as the object to be measured is assumed to be contained in a circular region as proposed in Appendix B. A ray parallel to the optical axis enters the refracting region in point *A*, is bent and leaves the region at *B*, it passes through the surrounding homogeneous medium of refractive index n_0 , meets the thin lens and is imaged onto point P' in the image plane. In double exposure holographic interferometry of course this role is played by the holographic reconstruction of the ray belonging to the exposure during the presence of the refracting object. At P' the ray interferes with another holographically reconstructed ray, this second one stemming from the exposure when no refracting object was present. To find the corresponding point P in the object plane, we can trace back with the common thin lens techniques. Another way is to extend the first ray from the refracting medium to the lens further along a straight line to the object plane [722], Fig. 6.55. This straight ray enters the refracting region at *E* and leaves it at *F*. These two rays of the collimated illumination are separated by the distance d .

To find the optical path length changes δ , or equivalently the optical phase difference $\Delta\phi$ between the rays interfering at P' , we notice that no relative changes occur left of points A and D or to the right of points C and F . D is the intersection of the straight ray with the perpendicular to the first ray through A . C is at the same distance from P as F , Fig. 6.55. The optical pathlength difference $\Delta\delta$ therefore is

$$\Delta\delta = \int_A^B n(x, y, z) ds + n_0(\overline{BC} - \overline{DE} - \overline{EF}). \quad (6.144)$$

While the first term of (6.144) is the integral of the refractive index along the curved path \widetilde{AB} , the second term accounts for the different path length in the surrounding with refractive index n_0 . For each viewing direction, defined by the angle θ to the arbitrary reference direction z , $\Delta\delta(\rho, \theta)$ or $\Delta\phi(\rho, \theta) = \Delta\delta(\rho, \theta) \cdot 2\pi/\lambda$ can be measured holographically. The ray equation (6.132) and the integral (6.144) together define the so called *path length transform*, which is a nonlinear integral transform of $n(x, y, z)$ and n_0 . If the refractive index variation is sufficiently small the curved ray \widetilde{AB} coincides with the straight line \overline{EF} , so that (6.144) reduces to

$$\Delta\delta = \int_E^F (n(x, y, z) - n_0) dl \quad (6.145)$$

with dl denoting the differential distance along line \overline{EF} . The *line integral transform* defined by (6.132) and (6.145) is mathematically equivalent to the *Radon transform* (B.2), see Appendix B.

6.10.2 Physical Quantities Affecting the Refractive Index Field

In most applications of holographic interferometry for measurements at transparent media it is not the refractive index distribution, Table 6.2, which is of main concern, but another physical quantity. The value of this physical quantity is determined by the effect it has on the refractive index field. So in the following some relations between such physical quantities and the refractive index are given [170].

In *aerodynamics* and *flow visualization* the flow of compressible gases is studied, e. g. in wind tunnels or shock tubes. The quantity of interest is the density ρ in a gas, the mass per unit volume. Its relation to refractive index n is given by the *Gladstone-Dale equation*

$$n - 1 = K\rho \quad (6.146)$$

with the *Gladstone-Dale constant* K , which is a property of the gas. The Gladstone-Dale constant is nearly independent of temperature and pressure under moderate physical conditions and it is a weak function of wavelength [170]. Some values are given in Table 6.3 [170]. The Gladstone-Dale constant of a mixture of gases can be calculated as the mass-weighted average of the values for the component gases

$$K = \sum_i a_i K_i \quad (6.147)$$

Table 6.2: Index of refraction of various optical materials (at yellow) [220].

Material	Index of Refraction	Material	Index of Refraction
Air	1.0003	Sodium chloride	1.54
Water	1.33	Light flint glass	1.57
Methanol	1.33	Carbon disulfide	1.62
Ethanol	1.36	Medium flint glass	1.63
Magnesium fluoride	1.38	Dense flint glass	1.66
Fused quartz	1.46	Extra-dense flint glass	1.73
Pyrex glass	1.47	Sapphire	1.77
Benzene	1.50	Heaviest flint glass	1.89
Xylene	1.50	Zinc sulfide (thin film)	2.3
Crown glass	1.52	Titanium dioxide (thin film)	2.4–2.9
Canada balsam (cement)	1.53		

Table 6.3: Gladstone-Dale constants of gases.

Gas	K (m^3/kg)	
	at $\lambda = 0.5145 \mu\text{m}$	at $\lambda = 0.6328 \mu\text{m}$
Ar	0.175×10^{-3}	0.175×10^{-3}
O ₂	0.191×10^{-3}	0.189×10^{-3}
He	0.196×10^{-3}	0.195×10^{-3}
CO ₂	0.229×10^{-3}	0.227×10^{-3}
N ₂	0.240×10^{-3}	0.238×10^{-3}

with the mass fraction a_i and Gladstone-Dale constant K_i of the i -th component.

The density ρ of a gas in most cases of interest can be calculated from the pressure P , the molecular weight M and the absolute temperature T via the *ideal gas equation*

$$\rho = \frac{MP}{RT} \quad (6.148)$$

with the universal gas constant $R = 8.3143 \text{ J}/(\text{mol K})$. The combination with (6.146) yields

$$n - 1 = \frac{KMP}{RT}. \quad (6.149)$$

This can be used for holographic *temperature measurements*. If the temperature changes remain small, a linear relation between the change of the refractive index and the change of the temperature can be adopted. As an example for air at 288° K and 0.1013 MPa the Gladstone-Dale constant at $\lambda = 0.6328 \mu\text{m}$ is $0.226 \times 10^{-3} \text{ m}^3/\text{kg}$ and the molecular weight is 28.97.

This results in

$$\frac{dn}{dT} = -0.9617 \times 10^{-6} \text{ K}^{-1}. \quad (6.150)$$

With even more precision the dependence of the refractive index of air from temperature at $\lambda = 0.6328 \mu\text{m}$ is [170]

$$n = 1 + \frac{0.292015 \times 10^{-3}}{1 + 0.368184 \times 10^{-2}T} \quad (6.151)$$

and at $\lambda = 0.5145 \mu\text{m}$

$$n = 1 + \frac{0.294036 \times 10^{-3}}{1 + 0.369203 \times 10^{-2}T} \quad (6.152)$$

with T in degrees Celsius.

In liquids the refractive index is related to density ρ by the *Lorentz-Lorenz equation*

$$\frac{n^2 - 1}{\rho(n^2 + 2)} = \bar{r}(\lambda) \quad (6.153)$$

where $\bar{r}(\lambda)$ is the *specific refractivity*, which depends on the substance and the wavelength of light. There is no direct analog to the ideal gas equation (6.148) in the case of liquids, instead empirical relations between refractive index and temperature must be used. Some are given in Table 6.4 [170, 723].

Table 6.4: Dependence of refractive index on temperature in liquids.

Liquid	$-dn/dT (\text{K}^{-1})$ at $\lambda = 0.5461 \mu\text{m}$	$-dn/dT (\text{K}^{-1})$ at $\lambda = 0.6328 \mu\text{m}$
Water	1.00×10^{-4}	0.985×10^{-4}
Methyl alcohol	4.05×10^{-4}	4.0×10^{-4}
Ethyl alcohol	4.05×10^{-4}	4.0×10^{-4}
Isopropyl alcohol	4.15×10^{-4}	4.15×10^{-4}
Benzene	6.42×10^{-4}	6.40×10^{-4}
Toluene	5.55×10^{-4}	5.55×10^{-4}
Nitrobenzene	4.68×10^{-4}	4.68×10^{-4}
c-Hexane	5.46×10^{-4}	5.43×10^{-4}
Acetone	5.31×10^{-4}	5.31×10^{-4}
Chloroform	5.98×10^{-4}	5.98×10^{-4}
Carbon tetrachloride	5.99×10^{-4}	5.98×10^{-4}
Carbon disulfide	7.96×10^{-4}	7.96×10^{-4}

Quite accurate equations for water are

$$n = 1.3331733 - (1.936 T + 0.1699 T^2) \times 10^{-5} \quad (6.154)$$

for $\lambda = 0.6328 \text{ } \mu\text{m}$ and

$$n = 1.337253 - (2.8767 T + 0.14825 T^2) \times 10^{-5} \quad (6.155)$$

for $\lambda = 0.5145 \text{ } \mu\text{m}$ where T again is measured in degrees Celsius.

In transparent solids the refractive index depends on the state of stress, which is termed the *stress-optical effect*. Furthermore the thickness of a component is changed when it is stressed. Both effects together allow a determination of strains and stresses of transparent solid objects or models, as is done in the field of photoelasticity.

Let a thin plane specimen of thickness h be subjected to a tensile force F . Since all stresses lie in the x - y -plane, the specimen is in the state of plane stress. Due to the transverse contraction the material undergoes a strain ε_z in the z -direction

$$\varepsilon_z = \frac{\Delta h}{h} \quad (6.156)$$

where Δh is the change in thickness. This transverse strain in an elastic material is related to the stress field by the *Poisson ratio* ν and the *modulus of elasticity* E

$$\varepsilon_z = \frac{-\nu}{E}(\sigma_1 + \sigma_2) \quad (6.157)$$

where σ_1 and σ_2 are the principal stresses. The principal stresses are mutually orthogonal and lie in the x - y -plane. If the state before stressing the specimen and the one during stressing are holographically recorded and reconstructed, the optical pathlength difference $\Delta\delta$ yielding the interference is

$$\Delta\delta = n(h + \Delta h) - n_0 h - \Delta h. \quad (6.158)$$

Here the term $n(h + \Delta h)$ is due to the refractive index n of the stressed material, in the second term n_0 is the refractive index of the material in its unstressed state, and the third term is the pathlength Δh during the first exposure multiplied by 1, the refractive index of the surrounding air.

The refractive index n is related to the state of stress by the two-dimensional *Maxwell-Neumann stress-optical law*

$$\begin{aligned} n_1 - n_0 &= A\sigma_1 + B\sigma_2 \\ n_2 - n_0 &= B\sigma_1 + A\sigma_2. \end{aligned} \quad (6.159)$$

Here A and B are the *stress-optical coefficients* of the material, and n_i are the refractive indices for light polarized in the direction of σ_i , $i = 1, 2$. For materials of low stress-optical sensitivity we have $A \approx B$ and $n_1 \approx n_2 = n$, so that for an optically isotropic material (6.159) reduces to

$$n - n_0 = A(\sigma_1 + \sigma_2). \quad (6.160)$$

With this and (6.157) the optical pathlength difference is

$$\begin{aligned} \Delta\delta &= [\varepsilon_z(n_0 - 1 + A(\sigma_1 + \sigma_2)) + A(\sigma_1 + \sigma_2)]h \\ &= \left[\varepsilon_z \left(n_0 - 1 - \frac{AE}{\nu} \varepsilon_z \right) - \frac{AE}{\nu} \varepsilon_z \right] h. \end{aligned} \quad (6.161)$$

Neglecting the small term $(AEh/\nu)\varepsilon_z^2$, we obtain

$$\Delta\delta = (n_0 - AE/\nu - 1)h\varepsilon_z. \quad (6.162)$$

The quantity $n_0 - AE/\nu$ can be considered to be the *effective refractive index* of the material.

In *plasma diagnostics* one deals with a plasma, a collection of atoms, ions, and electrons. In plasmas a number of electrons is separated from the nucleus. The refractive index of a plasma is the sum of the refractive indices of the atoms, ions, and electrons weighted by their number densities. The refractive indices of atoms and ions are described by the Gladstone-Dale equation and are of the same order. They are only weakly dependent on the wavelength of the probing light. On the other hand the refractive index n_e of the electron gas is

$$n_e = \sqrt{1 - \frac{N_e e^2 \lambda^2}{4\pi^2 \varepsilon_0 m_e c^2}}. \quad (6.163)$$

Here N_e is the number density of electrons, namely the number of electrons per unit volume, e is the electron charge, m_e is the mass of an electron, ε_0 is the electric field constant, and c is the speed of light. Evaluation of the constants gives

$$n_e = \sqrt{1 - (8.97 \times 10^{-14} \text{ cm})\lambda^2 N_e} \quad (6.164)$$

or approximated to the first order

$$n_e - 1 = (-4.486 \times 10^{-14} \text{ cm})\lambda^2 N_e \quad (6.165)$$

with λ in centimeters and N_e in cm^{-3} [170].

These equations show that the electron gas is very dispersive. Furthermore the contribution to the refractive index of a plasma per electron is an order of magnitude greater than that per atom and is of opposite sign. Therefore the electron gas dominates the refractive index in moderately as well as in highly ionized plasmas.

6.10.3 Two-Dimensional Refractive Index Fields

In holographic interferometric measurements at transparent media the evaluation consists first in extracting the interference phase distribution $\Delta\phi(x, y)$ as given in (4.22) by any of the methods presented in Chapter 5 [724]. For the discussion here we assume a propagation of light in the z -direction, Fig. 4.6.

The easiest case is an object with a refractive index varying in only one, say the y -direction, which is orthogonal to the z -direction, see Section 6.10.1. A typical application is the measurement of thermal boundary layers [391]. Let the object have length l in the z -direction and by assumption a constant refractive index along l . Then the pathlength difference is simply

$$\begin{aligned} \Delta\delta(x, y) &= \int (n(x, y, z) - n_0) dz \\ &= (n(y) - n_0)l \end{aligned} \quad (6.166)$$

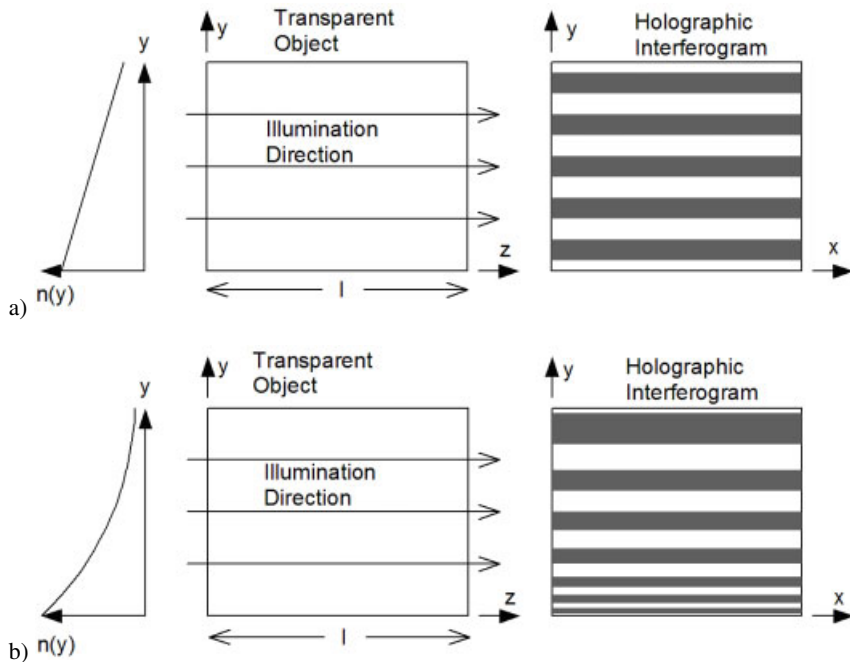


Figure 6.56: Linearly (a) and nonlinearly (b) varying refractive index fields (in y -direction) and resulting holographic interferograms.

or

$$\Delta\phi(y) = \frac{2\pi}{\lambda} [n(y) - n_0]l. \quad (6.167)$$

The fringe spacing is determined by the gradient of n . If the refractive index varies linearly

$$n(y) = n_0 + my \quad (6.168)$$

we get equally spaced parallel fringes, Fig. 6.56a, at

$$y = \frac{N\lambda}{ml} \quad N = 0, 1, 2, \dots \quad (6.169)$$

with N denoting the fringe order.

For a nonlinear refractive index distribution, e. g. the exponential one

$$n(y) = n_0 + me^{-ay} \quad (6.170)$$

we get parallel straight fringes with large spacing in regions of a small gradient and small spacing in regions of a high gradient of the refractive index, Fig. 6.56b.

6.10.4 Holographic Interferometry of Circular Symmetric Refractive Index Fields

In *circular symmetric phase objects* the refractive index is a function of the radius r only [725]. Typical objects are flows around cones, jets, thermal plumes, flames, or plasmas. Their form may be cylindrical or spherical. According to Fig. 6.57 it is

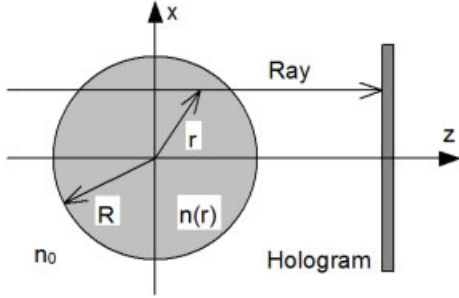


Figure 6.57: Geometry of a circular symmetric phase object.

$$dz = \frac{r dr}{\sqrt{r^2 - x^2}} \quad (6.171)$$

so the optical pathlength difference $\Delta\delta$ is

$$\Delta\delta(x) = 2 \int_x^R \frac{[n(r) - n_0]r}{\sqrt{r^2 - x^2}} dr \quad (6.172)$$

with $n(r)$ the refractive index inside the object of radius R , and n_0 outside. For phase objects whose refractive index decays smoothly to the ambient n_0 the object radius can be taken as $R \rightarrow \infty$. So for the interference phase then we have with $f(r) = n(r) - n_0$

$$\frac{\Delta\phi(x)}{2\pi} \lambda = 2 \int_x^\infty \frac{f(r)r}{\sqrt{r^2 - x^2}} dr. \quad (6.173)$$

The right-hand side of this equation is the *Abel transform* of $f(r)$. Its inversion formula is

$$f(r) = \frac{\lambda}{2\pi^2} \int_r^\infty \frac{d\Delta\phi(x)}{dx} \frac{1}{\sqrt{r^2 - x^2}} dx. \quad (6.174)$$

The problem now is to find an effective way to perform this inversion on the interference phase values measured at discrete locations.

A first simple approach divides the object into discrete annular elements of constant width Δr and assumes a uniform refractive index in each element [170]. This leads to a set of simultaneous linear algebraic equations which are solved by the common methods of matrix inversion [723]. More refined methods use refractive indices which vary linearly with r in

each annular element [726] or employ representations of $f(r)$ by sampling series [727, 728]. Methods based on the inversion of formula (6.174) use interpolated phase data and numerical differentiation.

A fast and efficient method utilizes a Fourier decomposition of the interference phase and calculates the Abel inversion of each spatial frequency component [729]. The Fourier coefficients are obtained from an FFT-routine, Appendix A.10.

6.10.5 Multidirectional Recording of Asymmetric Refractive Index Fields

The determination of *asymmetric refractive index fields* requires the analysis of a large number of holographic interferograms by methods of *computer aided tomography*, see Appendix B. Each of the reconstructed holographic interference patterns has to correspond to a different viewing direction [198]. Therefore holographic interferometry is ideally suited for rendering tomographic data, since just a single hologram allows the realization of a number of viewing directions. Thus although many interferograms are required, the number of necessary holograms remains limited. Some arrangements to record multiple holograms for subsequent tomographic reconstruction are proposed in Fig. 6.58 [730]. Figure 6.58a shows the diffuse illumination via a diffuser of e. g. ground glass. The range of viewing directions is only limited by the size of the diffuser and the aperture of the holograms. But speckles may become a problem due to complicated localization of the fringes as soon as the interferograms have to be observed with a small aperture, see Section 4.3. This possible disadvantage is circumvented by using a phase grating, Fig. 6.58b, which diffracts several plane waves out of the impinging plane wave. In Fig. 6.58c the individual plane waves are produced separately. A fixed plane object wave and a rotating object field are used in the arrangement of Fig. 6.58d. In all cases one has to consider whether a transient or a steady or at least repeatable refractive index distribution is present. The arrangements of Figs. 6.58a, b, and c allow a simultaneous recording of all holograms; the holograms in Fig. 6.58d are recorded sequentially. The system of Fig. 6.58c also enables a sequential registration.

Quite another way of registration of the refractive index variation may be taken by using the holographic *light-in-flight recording* and reconstruction of optical wavefronts, see Section 6.6.4. With this method wavefronts can be visualized as they pass a transparent object [655]. The spatial distortion of a plane or spherical wavefront induced by the refractive index field can be measured this way, Fig. 6.59.

In the treatment of reconstruction of asymmetric refractive index fields we have to consider two cases. The first is when ray bending due to refraction is minor and can be neglected. Then the integral defining the pathlength difference

$$\delta(x, y) = \int_s f(x, y, z) ds \quad (6.175)$$

with $f(x, y, z) = n(x, y, z) - n_0$ can be evaluated along straight lines s . We speak of the *refractionless limit*. The second case is when we have to take into account ray bending by strongly refracting fields.

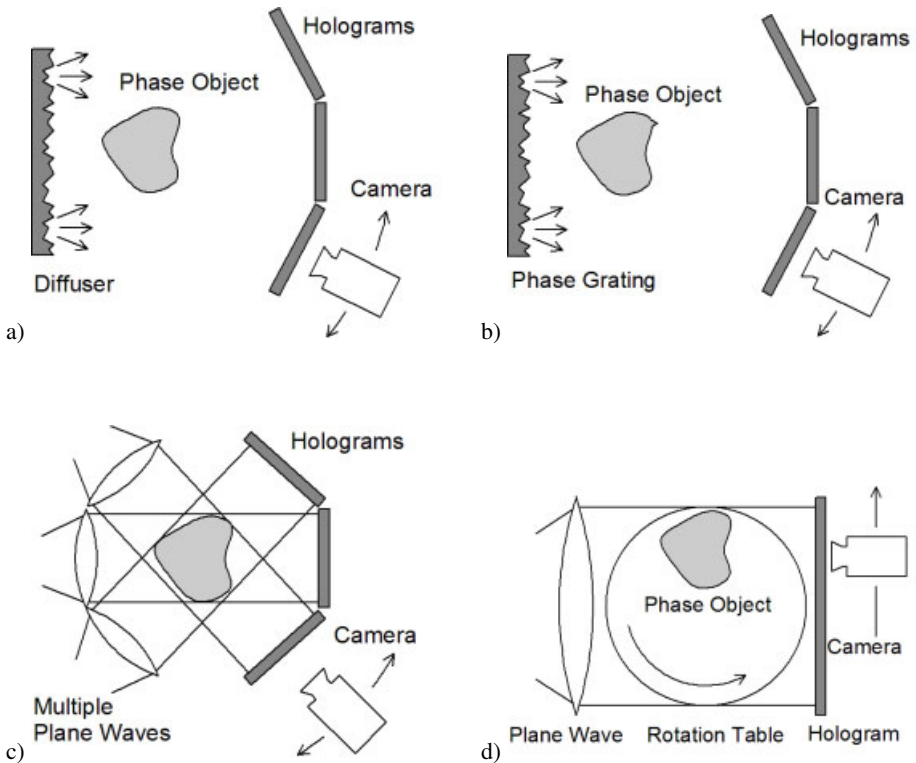


Figure 6.58: Arrangements for recording multiple views of phase objects (reference waves omitted for clarity).

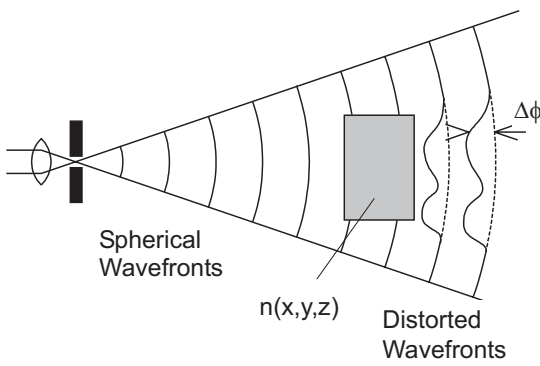


Figure 6.59: Registration of wavefront distortion by light-in-flight recording.

6.10.6 Tomographic Reconstruction in the Refractionless Limit

Reconstructions for both aforementioned cases are based on the tomographic methods introduced in Appendix B [731]. While most of the methods work well with multidirectional data collected along views subtending the whole angle of 180°, in holographic interferometry the

angular range is often less than 180° . The angle of view is restricted by the aperture of the hologram, the angular aperture of the illuminated diffuser, and the extent of the transparent object, Fig. 6.58.

Several reconstruction procedures have been introduced and compared with regard to their capability to work with restricted angles of view in [30, 732]. The first approach in [30] is the *Fourier synthesis*, which fills the spatial frequency plane with values along lines through the origin, as they are given by the *Fourier slice theorem*, (B.7). But this method suffers from the necessity of interpolation when in practice data are collected only for a finite number of views and positions, as pointed out in Appendix B.2.

The problem of the values not uniformly distributed in the frequency plane are avoided by the *direct inversion* of (6.175) as introduced by [733, 734] and adopted by [30]. This approach is equivalent to the one introduced in Appendix B.3. Its practical implementation, when discrete data are at hand, corresponds to the methods of Appendix B.4.

These two methods require optical pathlength data collected over the whole 180° angle of view. The methods described next can be applied even when data are available only for viewing angles less than 180° . A number of such methods represent the $f(x, y)$ of (6.175) in each plane $z = \text{const}$ by a series expansion

$$f_e(x, y) = \sum_{m=0}^{M-1} \sum_{n=0}^{N-1} a_{mn} H_{mn}(x, y). \quad (6.176)$$

Together with (6.175) we get after interchanging the order of integration and summation

$$\delta(x, y) = \sum_{m=0}^{M-1} \sum_{n=0}^{N-1} a_{mn} \int_s H_{mn}(x, y) ds. \quad (6.177)$$

This shows that it is advantageous to choose generating functions $H_{mn}(x, y)$ which are easily integrated along arbitrary straight lines.

A convenient series expansion is directed by the Whittaker-Shannon *sampling theorem*, which states that a properly sampled band-limited function can be exactly represented by a linear combination of sinc-functions, see Appendix A.7

$$f_e(x, y) = \sum_{l=-\infty}^{\infty} \sum_{k=-\infty}^{\infty} f\left(\frac{l}{2B_x}, \frac{k}{2B_y}\right) \text{sinc}\left[2B_x\left(x - \frac{l}{2B_x}\right)\right] \text{sinc}\left[2B_y\left(y - \frac{k}{2B_y}\right)\right] \quad (6.178)$$

where $\text{sinc}(x) = [\sin(\pi x)]/(\pi x)$ and B_x, B_y are the bandwidths in the x - and y -direction. The sinc-function approach leads to a set of algebraic equations [30]

$$\delta(\rho_i, \theta_j) = \sum_{m=0}^{M-1} \sum_{n=0}^{N-1} W_{mn}(\rho_i, \theta_j) f_e(\Delta x m, \Delta y n) \quad (6.179)$$

where the $W_{mn}(\rho_i, \theta_j)$ are defined by

$$W_{mn}(\rho_i, \theta_j) = \begin{cases} \sqrt{1 + \tan^2 \theta_j} \Delta x \text{sinc}[(\rho_i \sec \theta_j + \Delta xm \tan \theta_j - \Delta yn)/\Delta y] \\ \quad \text{for } 0 \leq |\tan \theta_j| \leq \Delta y/\Delta x \\ \sqrt{1 + \tan^2 \theta_j} \frac{\Delta y}{\tan \theta_j} \text{sinc}[(\rho_i \sec \theta_j + \Delta xm \tan \theta_j - \Delta yn)/(\Delta y \tan \theta_j)] \\ \quad \text{for } \Delta y/\Delta x < |\tan \theta_j| < \infty \\ \Delta y \text{sinc}[(\rho_i + \Delta xm)/\Delta x] \quad \text{for } |\tan \theta_j| = \infty \end{cases} \quad (6.180)$$

The θ_j represent the different angular views, the ρ_i the pathlength values in each projection. Δx and Δy denote the spacing of the pathlength values in each direction. The system of equations (6.179) can be solved if at least $M \times N$ pathlength data are measured. Tests have shown that reliable results are obtained when redundant data are used, meaning much more than $M \times N$ values of $\delta(\rho_i, \theta_j)$ are present. This is particularly true if only restricted angles of view are possible. The overdetermined system of linear equations then is solved by the method of Gaussian least squares.

The next method investigated in [30], the so called *grid method*, uses a set of rectangular elements, with constant refractive index in each element. A similar approach is described in Section B.5. As with the sinc-method, we get a set of algebraic equations whose solution represents an approximation to the actual $f(x, y)$.

A Fourier transform approach to reconstruction from data over a restricted angular view is given by the *frequency plane restoration*. If multidirectional data are given only for directions between $-\gamma$ and $+\gamma$, Fig. 6.60a, the resulting frequency samples also are only within an angular range of 2γ , the shaded region in Fig. 6.60b. The determination of the Fourier

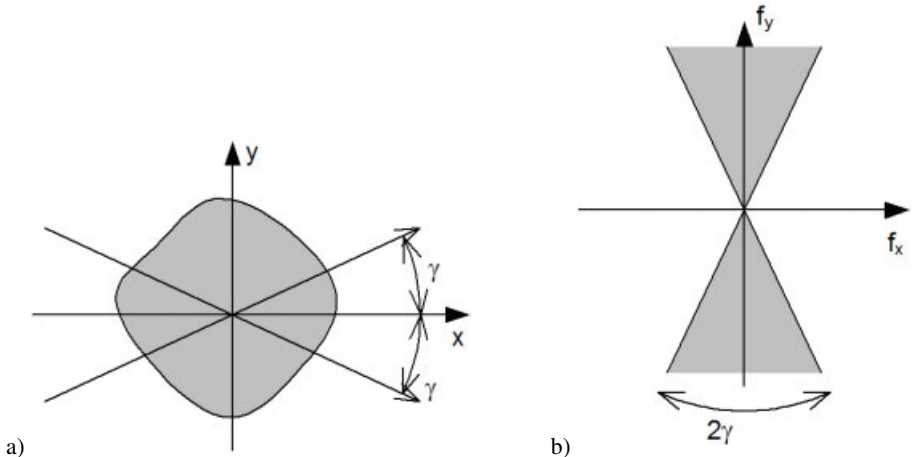


Figure 6.60: Restricted angular views, (a) spatial domain, (b) frequency domain.

transform values outside of this known region is based on the fact that the Fourier transform of a continuous, bounded, and spatially limited function is analytic. If the Fourier transform can be uniquely determined over any finite domain, the entire transform can be determined using analytic continuation [30]. Therefore a truncated summation over sampling functions in the frequency domain is defined with the frequency values of the whole frequency plane as coefficients. This leads to a set of algebraic equations, which can be solved for the unknown coefficients.

The last reconstruction method addressed in [30] is an iterative method for solution of an underdetermined system of linear equations. Of the manifold of possible solutions the one with minimum variance is chosen. Nevertheless the method is also feasible for overdetermined systems of equations.

The six reconstruction techniques mentioned above have been compared with simulated data as they may arise in fluid temperature measurements [30]. These comparisons have given the following results. If a 180° angle of view is available, all techniques produce good reconstructions. Especially the sinc-method, the direct inversion and the frequency restoration achieve a good accuracy, while direct inversion requires the least computer time. If the angle of view is less than 180° , e. g. 45° , the frequency plane restoration provides the most accurate reconstruction. It has been observed that if the angle of view is decreased, the degree of redundancy necessary for a reliable reconstruction increases. On the other hand if in an experiment the amount of data is fixed, this relation limits the number of degrees of freedom, and therefore the achievable resolution.

Independent from the specific technique used for the reconstruction one has to reflect upon the data sampling rates. Theoretically only band-limited functions can be reconstructed exactly, although in practice we have spatially limited refractive index fields which therefore are not band-limited. But if the Fourier components of this field are sufficiently small outside some finite region in the frequency plane, an *effective bandwidth* B can be defined. The sampling theorem now guarantees a reliable reconstruction, if the spacing between consecutive ρ_i is less than $1/(2B)$ in the corresponding θ_j direction. In defining the angular separation $\Delta\theta$ between the views one has to consider that the evaluated points in the frequency plane are lying along radial lines, so they have maximum separation at the effective band limits. If we consider two adjacent radial lines oriented near $\pi/2$ and data should be sampled at the Nyquist rate corresponding to the effective band limit B_y , we meet the condition

$$B_y \tan(\Delta\theta) \leq 1/L_x \quad (6.181)$$

where L_x is the object's extent in the x -direction. The angular spacing between views near $\pi/2$ must obey

$$\Delta\theta \leq \arctan\left(\frac{1}{B_y L_x}\right) \quad (6.182)$$

and similarly for the other direction. In the vicinity of $\pi/2$ the tan-function is steepest, so this is a conservative estimate.

Samples are more close near the origin of the frequency plane than near the band limits. So if the views are chosen to satisfy (6.182) the data will be oversampled. Altogether approximately $8B_x B_y L_x L_y$ samples will be used. Compared to the space-bandwidth product of the

representation of the refractive index distribution, which is $4B_x B_y L_x L_y$, we determine a data redundancy of about 2 [30]. The space-bandwidth product is a measure of the total number of degrees of freedom, and is invariant under Fourier transformation.

6.10.7 Tomographic Reconstruction of Strongly Refracting Fields

In tomography codes have been designed to perform an inversion in the case of the refractionless limit. If these codes are applied to pathlength transforms of *strongly refracting refractive index fields* appreciable errors may result. Although an analytical solution for radially symmetric strongly refracting fields exists, Section 6.10.4, there is no analytical solution for the general asymmetric case. Therefore in the following an iterative algorithm for reconstruction in this instance is presented [722].

Let $\tilde{\delta}(\rho, \theta)$ be the pathlength difference along the ray bent by refraction as given in (6.144). Correspondingly let $\bar{\delta}(\rho, \theta)$ be the pathlength along the straight ray of (6.145). θ is the angle of the projection and ρ the coordinate along the projection, Fig. 6.55. Let the operator \bar{P} express the straight line integral transform and \tilde{P} the bent line integral transform which maps $n(r, \phi) - n_0$ onto $\bar{\delta}(\rho, \theta)$ and $\tilde{\delta}(\rho, \theta)$, resp. The iterative method is based on successive estimation of the deviation $D(\rho, \theta)$ between the straight ray and bended ray pathlength transforms

$$D(\rho, \theta) = \tilde{\delta}(\rho, \theta) - \bar{\delta}(\rho, \theta). \quad (6.183)$$

It is assumed that $\bar{\delta}(\rho, \theta)$ and $\tilde{\delta}(\rho, \theta)$ are defined in the same domain [722]. The iterative algorithm begins with (1) setting an initial estimate of the deviation $D_0(\rho, \theta)$. Then (2) the estimate of the refractionless path length transform $\bar{\delta}(\rho, \theta)$ is calculated from the measured pathlength differences $\tilde{\delta}(\rho, \theta)$ and the assumed deviation

$$\bar{\delta}_i(\rho, \theta) = \tilde{\delta}(\rho, \theta) - D_i(\rho, \theta). \quad (6.184)$$

The corresponding refractive index field $n_i(r, \phi) - n_0$ is (3) reconstructed by a numerical inverse line integral transformation

$$n_i(r, \phi) - n_0 = \bar{P}^{-1}[\bar{\delta}_i(\rho, \theta)]. \quad (6.185)$$

Using computational ray tracing (4), according to (6.132) the pathlength transform of the estimated field is calculated

$$\tilde{\delta}_i(\rho, \theta) = \tilde{P}[n_i(r, \phi) - n_0]. \quad (6.186)$$

A new estimate of the deviation is calculated (5) by

$$D_i(\rho, \theta) = \tilde{\delta}_i(\rho, \theta) - \bar{\delta}_i(\rho, \theta) \quad (6.187)$$

and the algorithm proceeds at step (2). This iterative procedure continues until the change in $D_i(\rho, \theta)$ or the difference between two successive reconstructed fields is smaller than a predetermined value.

The line integral transform to be inverted in step (3) is expressed as a Fourier series within a circular domain of radius R , $\rho/R \leq 1$

$$\overline{\delta_i}(\rho, \theta) = \sum_{m=0}^{M-1} \sum_{n=0}^{N-1} A_{mn} g_{mn}(\rho) e^{im\theta}. \quad (6.188)$$

A finite number of coefficients A_{mn} are found by inverting an overdetermined system of algebraic equations of the form (6.188) with discrete ρ_j and θ_j by a least squares method. Once the coefficients A_{mn} have been calculated, the reconstructed $f(r, \phi) = n(r, \phi) - n_0$ can be presented as a Fourier series within the circular domain $r/R \leq 1$

$$f(r, \phi) = \sum_{m=0}^{M-1} \sum_{n=0}^{N-1} A_{mn} f_{mn}(r) e^{im\theta}. \quad (6.189)$$

Appropriate functions $g_{mn}(\rho)$ and $f_{mn}(r)$, which are line-integral transform pairs are discussed in [722].

The iterative algorithm was applied to numerically simulated data as well as tested in experiments measuring strongly refracting boundary layers. Refractive index fields with multiple maxima and quite steep gradients have been successfully reconstructed, even when refraction was strong enough to bend some rays by as much as 27° . Nevertheless operator interaction was needed to detect computational ray crossing [170]. Path length data contaminated by this effect were eliminated [735].

The iterative algorithm for correction of errors caused by ray bending also is employed in [736], where optical tomography for flow visualization of the density field around a revolving helicopter rotor blade is investigated. The tomographic reconstruction there is based on the convolution backprojection employing a Shepp-Logan-kernel for filtering, see Appendix B.3.

Further approaches to reconstruction of asymmetric refractive index fields which bend rays are the application of perturbation analysis [737], which is feasible for mildly refracting objects or the approach via inverse scattering: If diffraction is mild, the Rytov or Born approximations to the wave equation can be used [738, 739].

More problems encountered in tomographic reconstruction of refractive index fields are caused by limited interferometric data. Physical constraints such as test section enclosures may restrict the angular views to less than the desired 180° , and/or a portion of the probing rays may be blocked [736]. Limited data reconstructions are sensitive to noise and produce geometric distortions with various artifacts. An approach to reconstruct under such circumstances is published in [740]: The so called complementary field method is an iterative one and incorporates a priori information effectively. Another problem occurs when an opaque object is present within the field under study, e. g. the test model around which flow is being studied in aerodynamic testing. A solution by illuminating the embedded objects and holographic recording of the wave field scattered by the object's surface is presented in [741]. By this technique furthermore the fringe localization surface is compressed as well as displaced and the number of fringes is doubled. The compression of the localization surface enables the observer to use a larger numerical aperture than would be possible otherwise, see Section 4.3.5.

To summarize, it can be stated that the approaches to reconstruction of refractive index distributions with ray bending, published up to now, seem to be designed for specialized cases with no guarantee to work under general conditions. Much more needs to be done in the future in this important, challenging, and interesting field [724, 735].

6.10.8 Analysis of Transparent Media with Digital Holography

In the preceding sections the applications of digital holography were in measuring at opaque rough surfaces or in detecting particles. However as with ordinary optical holography and holographic interferometry digital holography also can be used for measuring refractive index distributions in transparent media. A typical application is the measurement of gas flow in front of a nozzle [102] or combustion experiments [151]. In Fig. 6.61 the modified Mach-Zehnder interferometer performing this task by digital holographic interferometry is shown. While the gas flow is injected into the probe arm, the reference beam is focused by a lens to form a point source. When viewed from the CCD-array through the beam splitter the reference point source seems to be at a location which is optically coplanar to the location of the gas flow, depicted as the virtual source of the reference wave in Fig. 6.61. Two digital holograms are recorded with and without the gas flow injection.

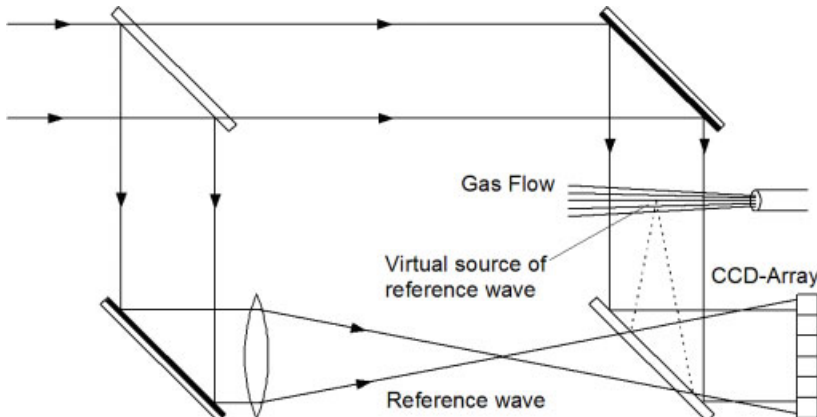


Figure 6.61: Modified Mach-Zehnder interferometer for digital recording of lensless Fourier transform holograms.

This lensless Fourier transform geometry adopted by Takeda et al. [102] has the main advantage that we do not need knowledge about the exact distance d between object and CCD-array in the hologram plane. While in the Fresnel case, d determines the plane of focusing, any error in the measurement of d will cause defocusing and may distort the phase distribution in the observation plane. Alternatively in the Fourier case the error in d influences only the spatial scale factor and not the relative phase of the reconstructed optical fields. A further but minor advantage is the possible saving in computation time and storage requirement: If we Fourier transform the real function $h(\xi, \eta)$ rather than the complex function $h(\xi, \eta)r(\xi, \eta)\exp\{\frac{\pi i}{\lambda d}(\xi^2 + \eta^2)\}$ we need essentially half the number of operations than re-

quired for the complex function. This saving is due to the Hermitean property, see Table A.2. Consequently we can replace the Fourier transform of the real function $h(\xi, \eta)$ by the separable Hartley transform [102], see Appendix A.12. Now all computations are performed for real values. Analogous to the FFT algorithm efficient algorithms are available for the computation of the two-dimensional discrete Hartley transform [742].

Digital holographic interferometry for two- and three-dimensional refractive index measurements as well as particle velocimetry is performed in the Fluid Science Laboratory (FSL) on board the International Space Station (ISS). An integrated optical setup performing holographic as well as other optical measurements in the FSL facility is described in [68].

A portable digital holographic monitor system suitable for characterization of transparent samples is presented in [146, 147]. The system has been applied successfully in microgravity materials and life science research. A comparison of double exposure digital holographic interferometry and a Shack-Hartmann sensor is given in [148].

The characterization of micro-optics like microlens arrays and gradient index lenses by digital holographic interferometry is the topic of [552, 743]. In [552] the convolution approach is combined with a filtering technique for suppression of the twin image.

The density field in two-phase liquids (toluene-water/acetone) is measured by digital holographic interferometry in [744]. There the concentration gradient induced by the mass transfer of acetone into the toluene droplet in a microgravity environment is determined.

If digital holograms are recorded with multiple wavelengths corresponding to different colors, even colored interference patterns can be produced. In this manner Demoli et al. [745] produced a color digital holographic interferometry movie of convective flows induced by thermal dissipation in a tank filled with oil. The wavelengths they used were 476 nm, 532 nm, and 647 nm. As a special feature they applied the option of subtraction digital holography consisting in the subtraction of stochastically changed speckle primary fringe patterns [230] and thus effectively suppressed the zero-order disturbances.

6.10.9 Resonance Holographic Interferometry

The *refractive index* n as well as the *absorption coefficient* κ of gases show a characteristic dependence on the wavelength near the *resonances* of the molecules, Fig. 6.62, an effect often

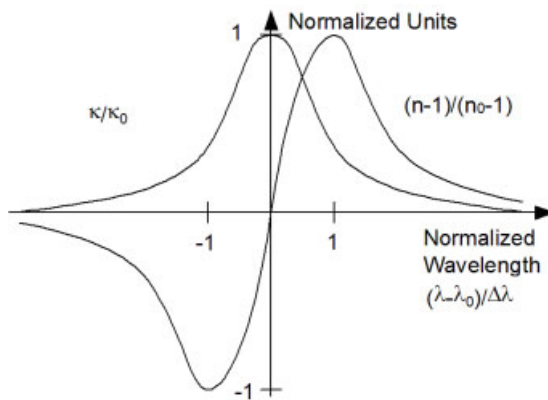


Figure 6.62: Refractive index n and absorption coefficient κ near spectral line; n_0 and κ_0 at resonant wavelength.

termed *abnormal dispersion*. This can be used for holographic interferometric measurement of *species concentrations*, e. g. in combustion research [746]. The experiments are performed with two dye lasers, driven by the same pump laser. They generate two beams, one with wavelength λ_0 on resonance and the other, λ , slightly off resonance, Fig. 6.63. Optimal tuning

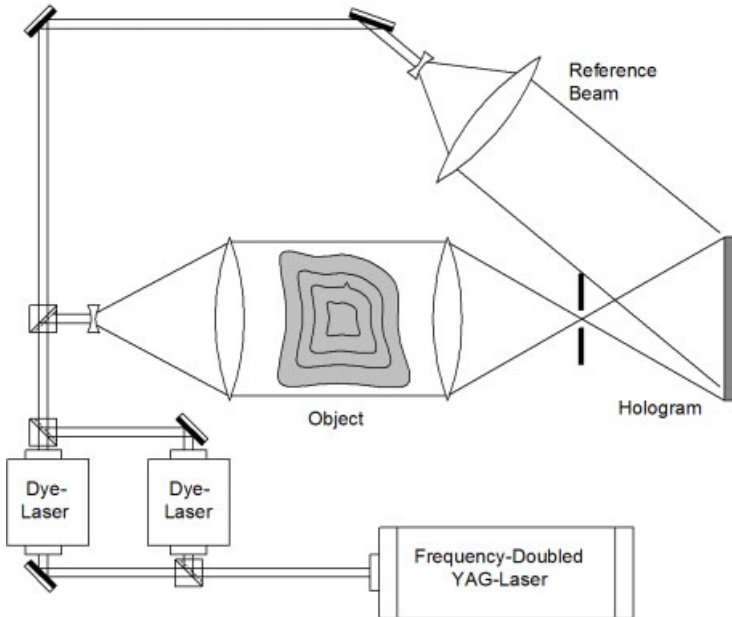


Figure 6.63: Resonance holographic interferometric spectrometer.

is one beam to the minimum and the other to the maximum of n . The beams are combined to produce a single beam of both wavelengths. This beam is divided into object and reference beam with the expanded object beam passing the transparent object. The refractive indices of all species except the resonant species are essentially identical at the two wavelengths. So only the species showing resonance at the used wavelength is characterized by this method. The conversion from refractive index to species concentration N_i is given by [180, 746]

$$N_i = \frac{(n - 1)[(\lambda - \lambda_0)^2 + \Delta\lambda^2]}{Kf\lambda_0^3(\lambda - \lambda_0)} \quad (6.190)$$

where $K = e^2/4\pi mc^2 = 2.24 \times 10^{-14}$ cm is a constant, f is the oscillator strength for the line, and $\Delta\lambda$ is the half-width of the absorption line at half maximum. A further advantage of resonance holographic interferometry is that the effects of turbulence or gradients in a flow are effectively eliminated.

6.11 Defect Detection by Holographic Non-Destructive Testing

In *holographic nondestructive testing* (HNDT) the inspected sample is loaded and the resulting deformations are made visible as fringe patterns. Local faults, like voids, cracks or other defects, lead to typical local deformations which deviate from the global deformation, schematically shown in Fig. 6.64. Thus the faults are detected by their characteristic local

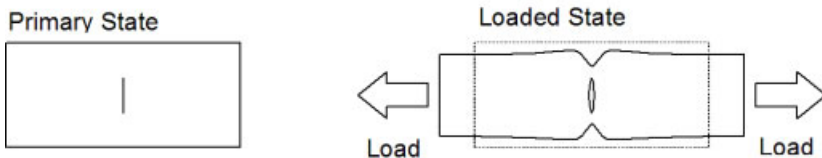


Figure 6.64: Deformation above internal defect (schematically).

interference patterns [747]. HNDT is not restricted to the testing of engineering components but is also successfully employed in biology or medicine [423, 748, 749]. While HNDT has a long tradition using optical reconstruction, nowadays digital holography with numerical reconstruction is becoming more and more prevalent [750].

While a lot has been done in computerized quantitative evaluation of holographic interferograms, little is reported on automatic computer aided detection of local fringe patterns characterizing material defects. The main reasons are the manifold possible global fringe patterns, the variety of local patterns typical of the defects, and the difficulty to translate into computer software the knowledge of the experienced personnel judging the interferograms.

The few known approaches for automatic qualitative evaluation are based on dividing the whole pattern into a number of sections and comparing the fringe densities in these sections. Actual approaches to computerized fault detection in HNDT use modern software concepts, like knowledge based expert systems [667] and artificial neural networks [293]. The basics of all these attempts are outlined in the following.

6.11.1 Classification of Defects

The approaches to automatic HNDT try to detect faults and flaws by their characteristic partial patterns directly in the holographic interferogram, but not by performing a quantitative evaluation and then investigating the deformation field. Therefore it is primarily of interest to know what the special interference patterns indicating defects look like. Some typical interference patterns caused by defects are shown schematically in Fig. 6.65 [667].

The compression of fringes shown in Fig. 6.65a manifests in a locally higher fringe density. It may be caused by weak points or areas, subsurface voids or separation of layers in compound materials. The bending of the fringes in Fig. 6.65b exhibits a noncontinuous change in the fringe direction although the fringes themselves are continuous. The reason may be a bending or buckling of the structure, local debonds, or the abrupt change of material properties along a line. The interference fringes have no continuous paths in Fig. 6.65c, they are displaced or broken. This normally indicates a crack reaching up to the inspected surface.

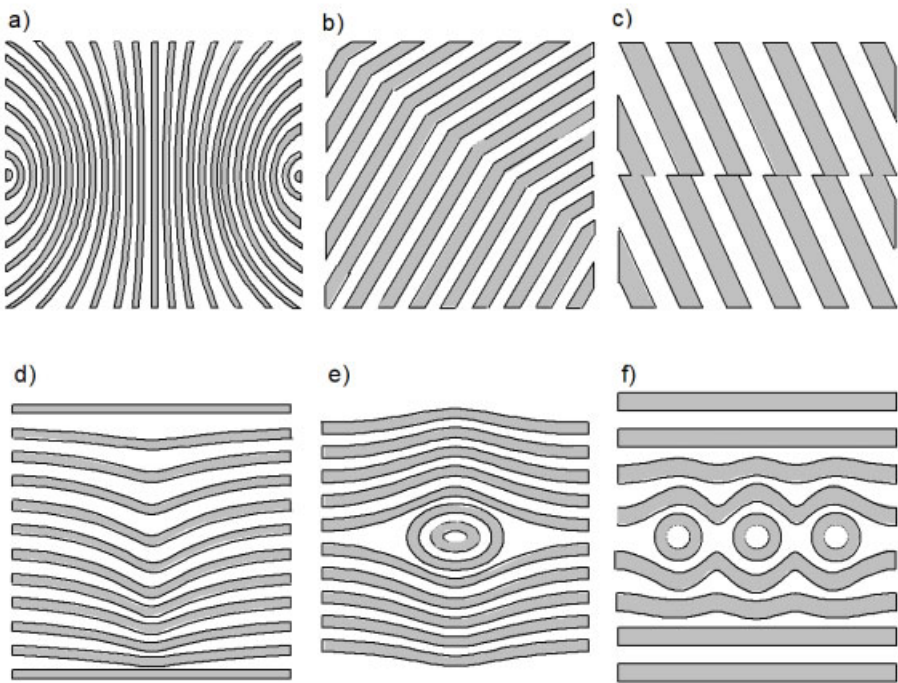


Figure 6.65: Typical defect induced partial fringe patterns: (a) compression, (b) bend, (c) displacement, (d) groove, (e) bull's eye, (f) eye chain.

But for this interpretation one has to guarantee a smooth surface. The same pattern can be produced at the edge of two plane surfaces differing in height. The groove of Fig. 6.65d has a locally varying direction and curvature, it may stem from a subsurface crack. The typical bull's eye pattern, Fig. 6.65e, which is often formed by circular or elliptical closed fringes, is caused by local debonds, voids, or inclusions of various forms and types. The eye chain of Fig. 6.65f with the regular occurrence of comparable partial patterns often specifies systematic errors in the production of the tested material, e. g. in fiber reinforced plastic components.

Of course this list is far from being exhaustive, also the underlying defects cited here are only the most obvious. The actual form not only depends on the type of the defect, but also on its orientation and amplitude, as well as on the loading parameters and the vectorial sensitivity of the holographic arrangement. By preparing specimens with artificial defects, real holographic interference patterns from all the shown classes of partial patterns have been generated, Fig. 6.66 [751].

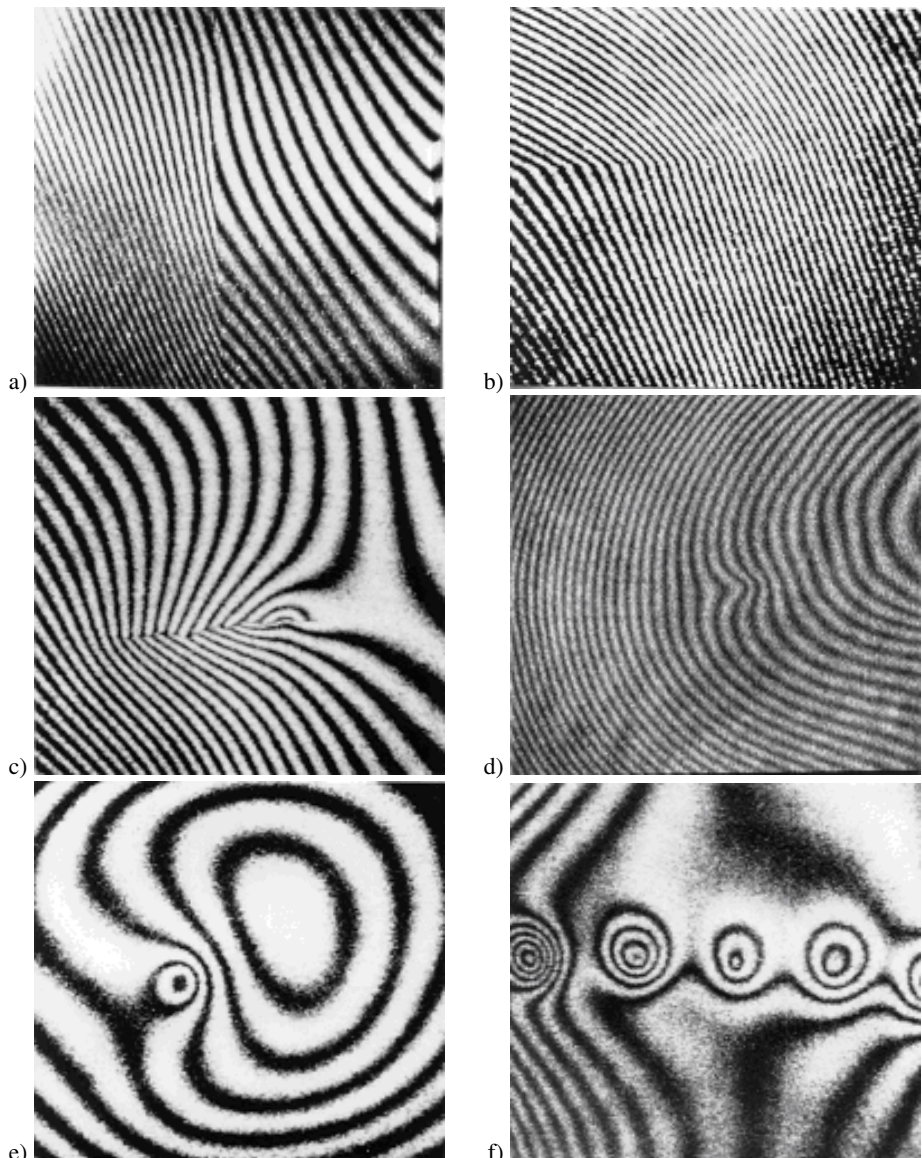


Figure 6.66: Experimentally generated defect induced fringe patterns: (a) compression, (b) bend, (c) displacement, (d) groove, (e) bull's eye, (f) eye chain (Courtesy of W. Osten, BIAS).

6.11.2 Data Reduction for Automatic Qualitative Evaluation

A central step in each solution of a pattern recognition problem is the reduction of the registered input data to a tractable number of parameters, which resemble the significant features of

the input data. In our context we have to reduce from some 10^5 to 10^6 pixels of the recorded holographic interference pattern to a few parameters which still can discriminate interferograms with characteristic partial patterns indicating a material defect from those without. A first stage of data reduction may be the skeletonizing introduced in Section 5.3.

A data reduction strategy that often is successful in digital image processing is to take the 2D Fourier transform. The real amplitude spectrum already is translation invariant. If we describe the amplitude spectrum in polar coordinates and integrate all spectral values along the angles from 0° to 360° (0° to 180° also suffice) at each radius, we get a rotation- as well as translation-invariant 1D spectrum. If needed, a further Fourier transform may produce even a scale-invariant set of features.

Since we are interested only in the existence of a defect induced partial pattern, but not primarily in its location, orientation, or size, translation-, rotation-, and scale-invariant features are exactly what we need. But the outlined Fourier transform based strategy here gives no significant results. The reason is the averaging effect of the global 2D Fourier transform. Small partial patterns may cover only a few pixels of all the pixels of the interferogram. During calculation of each spectral value a weighted sum of the intensities of all pixels is formed, the contribution of a small partial pattern is suppressed by the averaging effect. Especially if some broadband noise is present in the interferogram, a defect induced local pattern will not contribute significantly to the spectrum.

The few published approaches for automatic qualitative evaluation are based on dividing the whole pattern into a number of sections and comparing the fringe densities in these sections. In [752] the interference patterns of pressure vessels are partitioned into squares and the number of fringes in each square is counted. Based on holographic interferograms of proven intact specimens, each square gets a minimum and maximum acceptable fringe count. The fringes are counted automatically in each square, regardless of their orientation. If all fringe counts fall between the predetermined thresholds, the pressure vessel is accepted, otherwise it is rejected as a defective one.

The sections into which the patterns are divided, can even be degenerated rectangles, like rows or columns [244, 753]. In [753] fringe peaks are counted along horizontal lines. If the number of peaks exceeds a threshold in one line, fringes are counted along short vertical columns centering at this horizontal line until again a threshold is reached. To ensure that a closed ring pattern is detected, the fringes are counted along inclined vectors as well. A fault is considered to be detected if the fringe count in each direction is above the threshold value. The process can be repeated to detect multiple defects. The procedure is applied to the detection of brazes in brazed cooling panels.

In [244] Fourier amplitude spectra are calculated one-dimensionally along lines and columns or two-dimensionally in small rectangles. From these spectra an average amplitude spectrum together with an acceptance band broader than its bandwidth is determined. If the spectrum along one line, column, or rectangle differs significantly from the average spectrum, then a locally higher or lower fringe density must have occurred, indicating a defect.

A feature selection scheme that associates parameters to sections of the pattern, which was successfully applied in an artificial neural network approach to qualitative evaluation, is presented in the following. It is based on the fact that the intensity distribution of the defect induced partial patterns, which are searched, is varying more rapidly than the interference pattern in its defect free neighborhood. But the local variation must not be compared to an

averaged global variation, since the fringe density changes continuously even in the non-defect case due to the loading and the varying sensitivity of the holographic arrangement. This change may lead to a higher fringe density in a non-defect area than the density of a defect in a low fringe density area [293]. So the comparison of intensity variation in a small area is restricted to its immediate neighborhood.

For the determination of the intensity variation $I(x, y) \in \{0, 1, \dots, 255\}$ at each pixel (x, y) the slopes a and b of the two-dimensional plane

$$I(x, y) = ax + by + c \quad (6.191)$$

tangential to the intensity distribution $I(x, y)$ are calculated by Gaussian least squares based on its eight neighbors. The slopes are

$$\begin{aligned} a &= \frac{1}{6} [I(x+1, y-1) - I(x-1, y-1) + I(x+1, y) - I(x-1, y) \\ &\quad + I(x+1, y+1) - I(x-1, y+1)] \\ b &= \frac{1}{6} [I(x-1, y+1) - I(x-1, y-1) + I(x, y+1) - I(x, y-1) \\ &\quad + I(x+1, y+1) - I(x+1, y-1)] \end{aligned} \quad (6.192)$$

a and b may have different or equal signs, Fig. 6.67, so the maximum slope at (a, b) is

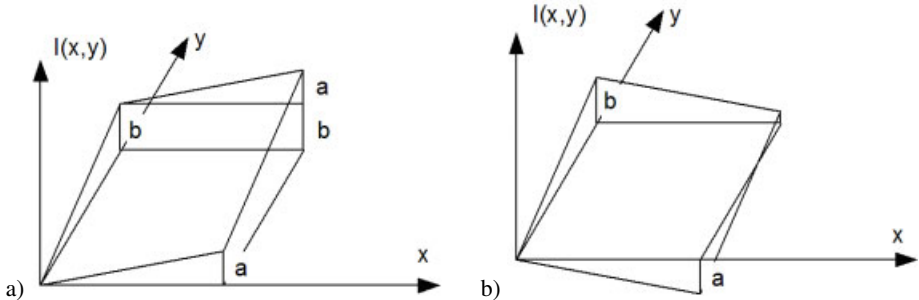


Figure 6.67: Local slope for equal signs of a and b (a), and different signs (b).

approximated by

$$s(x, y) = \max\{|a + b|, |a - b|\}. \quad (6.193)$$

To remain in the range of 8 bits in image processing, we truncate this expression

$$s(x, y) = \min\{\max\{|a + b|, |a - b|\}, 255\}. \quad (6.194)$$

The whole pattern now is partitioned into non-overlapping areas, e. g. the pattern of 512×512 pixels is divided into 8×8 areas of 64×64 pixels each. Each area E gets the parameter $k(E)$, which is the maximal slope of all its pixels

$$k(E) = \max\{s(x, y) : (x, y) \in E\}. \quad (6.195)$$

Figure 6.68a shows an interference pattern with a defect induced local variation in an 8-bit gray-scale display. The parameters $k(E)$ of a partition into 8×8 areas E are given as gray-values in Fig. 6.68b and as numbers in Fig. 6.68c. One can notice the effect of higher fringe density and thus higher slope at the defect-free lower margin of the pattern compared to the defect area in the center of the pattern.

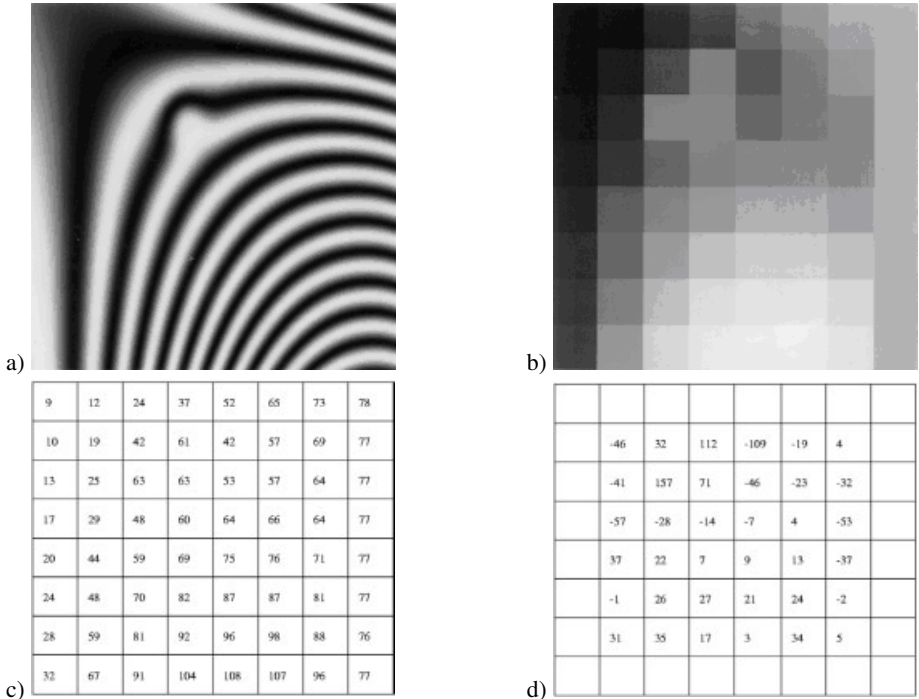


Figure 6.68: Feature selection: (a) interference pattern, (b) maximal slopes in 8×8 areas as gray-values, (c) maximal slopes in 8×8 areas as numbers, (d) Laplace values.

A defect induced local variation of the fringe density is present in area E , if the parameter $k(E)$ differs significantly from the $k(E')$ of the neighboring areas E' . To detect this, we apply a Laplace-filter to the image of area parameters. If the neighboring areas of E are denoted by A to I according to

A	B	C
D	E	F
G	H	I

two possible realizations of the Laplace-filter are

$$f_1(E) = 4k(E) - k(B) - k(D) - k(F) - k(H) \quad (6.196)$$

or

$$f_2(E) = 8k(E) - k(A) - k(B) - k(C) - k(D) - k(F) - k(G) - k(H) - k(I). \quad (6.197)$$

Figure 6.68d shows the Laplace values for all areas having 8 neighboring areas. A defect now is indicated by a high Laplace value. The highest Laplace values of the pattern, regardless where they occur, are translation-invariant as well as rotation-invariant features.

Defects which cause high density fringes even of low contrast are detected by this procedure as long as they are confined to one area or extend over only a few areas.

In a first attempt an automatic defect detection by a threshold comparison of the highest Laplace value over all areas of the tested pattern was carried out. To define the optimal threshold, a sample set of 1000 holographic interferograms was simulated on a computer, see Section 4.1.6, 500 with and 500 without defects. The threshold was chosen at the valley between the two modes of the bimodal histogram of the highest Laplace value of each pattern of the sample set. This approach was feasible as long as the partial patterns did not vary too much. All defect induced partial patterns had to fit into a single area.

Another approach to automatic defect detection is presented in [474]. There the variety of possible interference patterns is limited by experimental modifications, which produce only linear fringes. This holographic fringe linearization is obtained by swinging the object beam between the two exposures. Proper selection of the fringe frequency by adjusting the object beam swing and of the loading force creates a reconstructed image laced with linear fringes that have highly visible fringe shifts at the defect locations. These fringe shifts furthermore have characteristic Fourier signatures different from those of the linear fringe acting as a carrier.

6.11.3 Neural Network Approach to Qualitative Evaluation

The concept of *artificial neural networks* promises a reliable defect detection based on a number of typical examples because a neural network (1) has the intrinsic ability to learn from the input data and to generalize; (2) is nonparametric and makes weaker assumptions about the input data distributions than traditional statistical (Bayesian) methods; and (3) is capable of forming highly nonlinear decision bounds in the feature space.

Each neural network consists of a number of neurons which are the fundamental information processing units, Fig. 6.69. Every *neuron* has a number n of input paths numbered by $i = 1, \dots, n$. The inputs x_i , $i = 1, \dots, n$ are multiplied by *synaptic weights* w_{ji} , where j counts the neurons in the network. The weighted inputs are summed, the result is the internal activity level I_j

$$I_j = \sum_i w_{ji} x_i. \quad (6.198)$$

This activity is modified by a transfer function f which can be a binary (0 and 1) or bipolar (-1 and +1) hard limiter, a threshold function with a linear range, the *sigmoid function* $f(I) =$

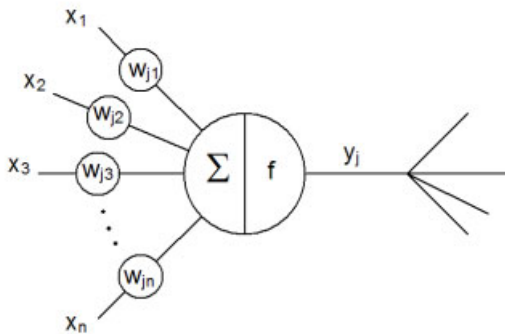


Figure 6.69: Processing element of an artificial neural network.

$[1 + \exp(-I)]^{-1}$, or any nondecreasing bounded function. The result

$$y_j = f \left(\sum_i w_{ji} x_i \right) \quad (6.199)$$

is given to the output path which may be branched to be connected to the input paths of other neurons or it may present the results of the processing of the whole network to the outside.

Usually the neurons of an artificial neural network are organized into groups called layers. A typical network consists of an input layer of source elements, followed by one or more so-called hidden layers, and an output layer, Fig. 6.70. While the basic operation of a neuron

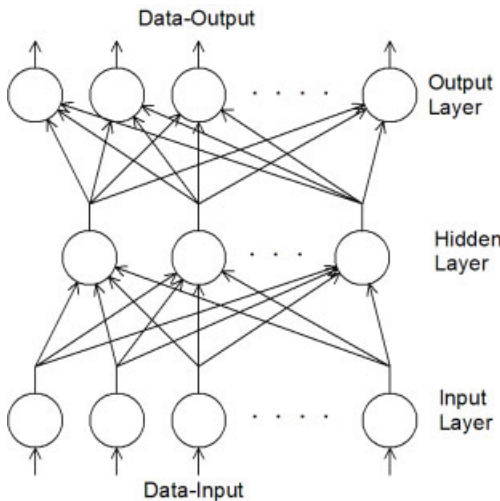


Figure 6.70: Artificial neural network with one hidden layer.

is always the same, the different concepts of neural networks differ in their architecture; that is, the number of inputs and outputs, the number of layers, the number of neurons in each layer, the number of weights in each neuron, the way the neurons and corresponding weights

are linked together within a layer or between the layers, or which neurons receive correction signals. Closely related to the architecture is the way information is fed to the network, its training. Although a single neuron is far from achieving relevant processing of information, it is the network of many interconnected neurons and the information stored in the synaptic weights that exhibits the far reaching problem solving capability. In the brains of living creatures information is processed in parallel by many neurons; this is actually performed sequentially in the computer software realizations of artificial neural networks.

To achieve an automatic detection of the characteristic local patterns of HNDT, a multi-layer network trained by backpropagation learning at sample patterns has been implemented and tested [293, 531, 754]. Since it is not possible to generate the whole training set experimentally – one needs several thousands of holographic interferograms – the training samples are calculated by computer simulation, see Section 4.1.6. For a given application the material and shape of the object, the type of loading, and the typical defects to be detected have first to be examined practically and theoretically. Based on these examinations a restricted number of experiments are performed to check the validity of the simulation program and help to optimize it.

The features of each interference pattern to be presented to the input neurons are the four highest Laplace values introduced in Section 6.11.2, calculated for each partition of the 512×512 pixel pattern into 8×8 , 16×16 , 32×32 , and 64×64 areas. Thus a total of 16 features were to be fed to a neural net with 16 input neurons. The reasons for the advantages of the multiple area partitions are explained with the help of Fig. 6.71. In Fig. 6.71a the defect

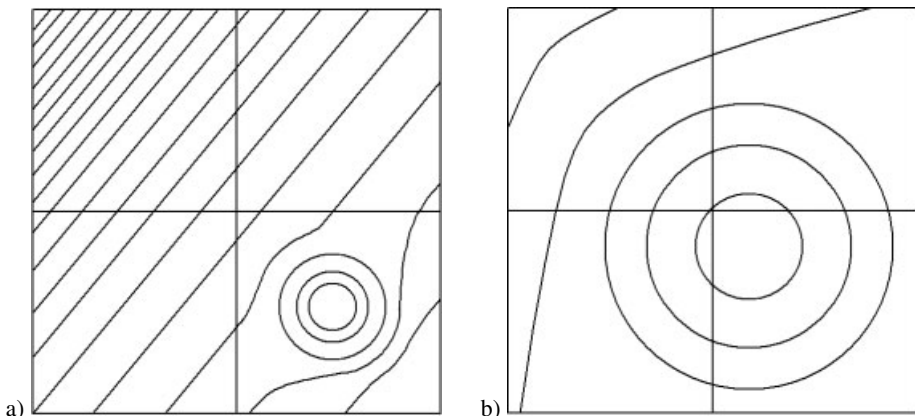


Figure 6.71: Area partitioning and defect size: (a) small defect and large areas, (b) large defect and small areas.

defines the maximum fringe density of its area, but neighboring areas, especially the upper left, also contain high fringe densities, leading to a small Laplace value. Contrary to this, the defect of Fig. 6.71b defines the maximum slopes of several neighboring areas, so the Laplace values representing the difference of slopes between adjacent areas remain small.

The neural network structure that showed optimal performance in this special application is shown in Fig. 6.72. Training of this network was performed by the backpropagation method for supervised learning. This technique, basically a gradient-descent method, propagates the

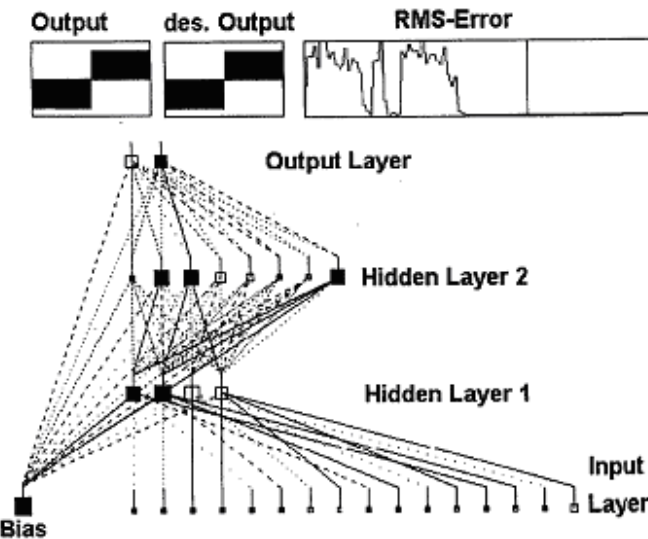


Figure 6.72: Neural network structure.

input through the layers, determining the output according to the actual weights. The output is compared with the output expected for this specific input, which quantifies an error. This error then is propagated back through the network from the output layer to the input layer while modifying the weights with the objective of minimizing the global error. This process is repeated with all input samples of the training set, which are taken each one several times in a stochastic order.

The evaluation of actually measured interference patterns, after the training phase was successfully finished, is shown in Fig. 6.73.

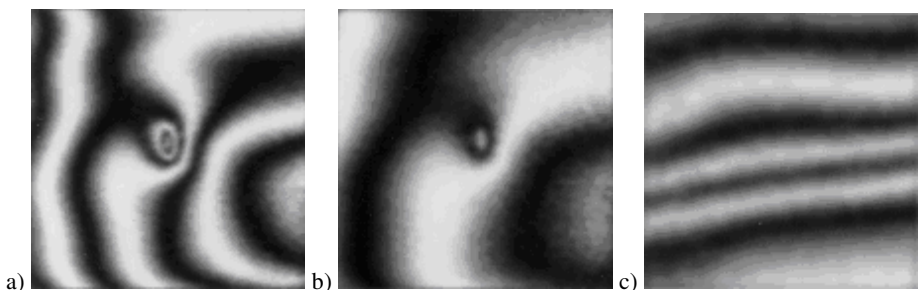


Figure 6.73: Evaluation by neural network: (a–c) interference patterns.

Three interference patterns were generated by digital holography. In a preprocessing step the speckle noise is reduced by low-pass filtering. The three patterns are given in Figs. 6.73a–c, the maximal slopes in gray scale display for 8×8 pixel areas in Fig. 6.73d–f, for 16×16 pixel areas in Figs. 6.73g–i, for 32×32 pixel areas in Figs. 6.73j–l, and for 64×64 pixel

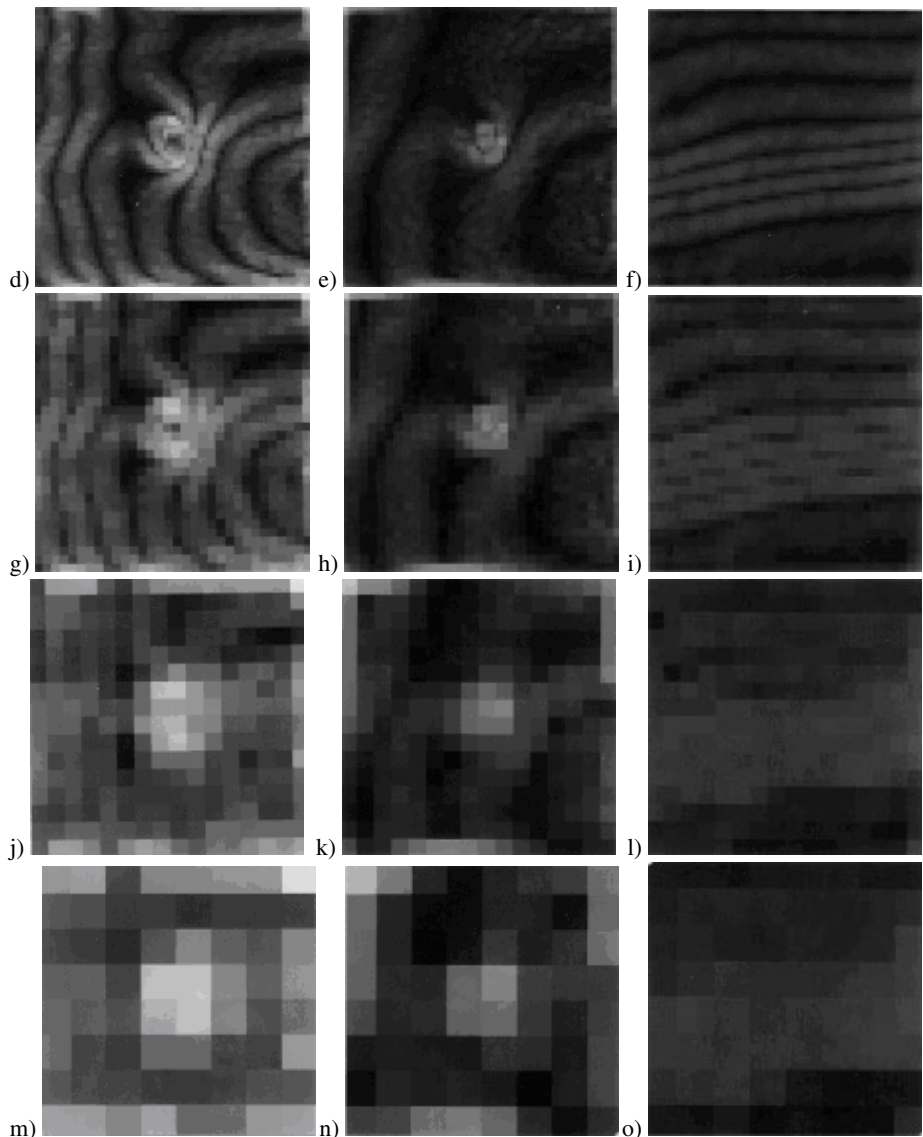


Figure 6.73 (continued): (d–f): Maximal slopes in areas of 8×8 pixels, (g–i): maximal slopes in areas of 16×16 pixels, (j–l): maximal slopes in areas of 32×32 pixels, (m–o): maximal slopes in areas of 64×64 pixels

areas in Figs. 6.73m–o. The corresponding Laplace values in gray scale coding are shown in Figs. 6.73p–A.

The neural network detected a defect in the patterns of Figs. 6.73a and b, and no defect in the pattern of Fig. 6.73c. The same result would have been achieved by a skilled human investigator.

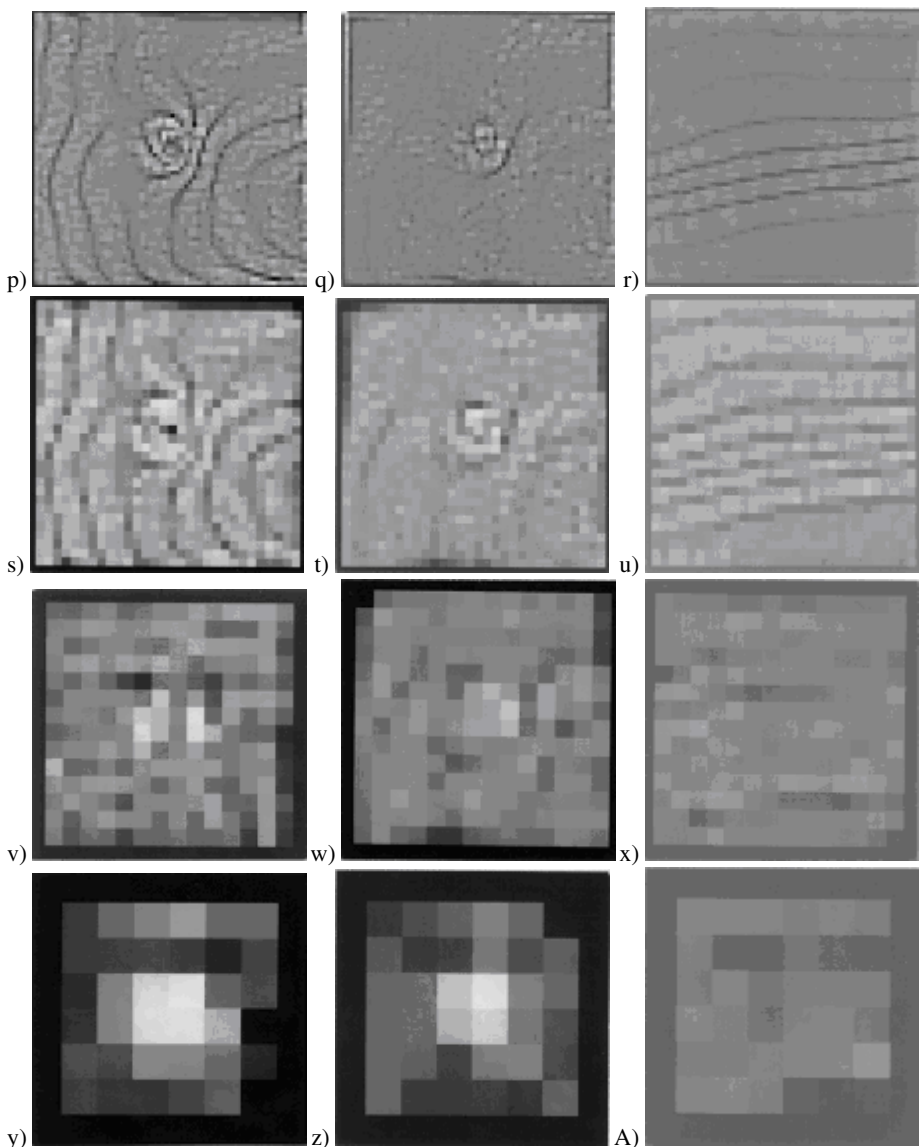


Figure 6.73 (continued): (p–r): Laplace-values in areas of 8×8 pixels, (s–u): Laplace-values in areas of 16×16 pixels, (v–x): Laplace-values in areas of 32×32 pixels, (y–A): Laplace-values in areas of 64×64 pixels

The artificial neural network so far has been applied to find characteristic partial patterns in the holographic interferograms. Another application of an artificial neural network is described in [755, 756] where it processes three-dimensional images obtained by digital holography, aiming at object recognition even for different orientations of the object.

7 Speckle Metrology

In the preceding chapters the speckles which always appear when coherent light is diffusely scattered or reflected were treated as a disturbance to be suppressed or eliminated. On the other hand in coherent optical metrology the speckles can be viewed as the fundamental carriers of information, and thus can be used for specific measurement techniques. A number of methods of speckle metrology are closely related to methods of holographic interferometry. Therefore holographic interferometry and speckle metrology are often presented together in a closed form. A typical example for the close relation between holographic and speckle interferometry is the ESPI/DSPI method, which by several authors is regarded as image plane holography and therefore a holographic interferometric method. For these reasons in the following a brief introduction to the main techniques of speckle metrology is given.

Two principal approaches have to be distinguished in speckle metrology applied to e. g. deformation analysis of opaque diffusely reflecting surfaces: In speckle photography two reflected speckle fields are incoherently superposed to give information about an in-plane displacement; in speckle interferometry two interference fields are compared, each one generated by coherent superposition of the reflected wave field and a reference wave. The two fields to be compared correspond to the object states before and after the deformation.

The nature of the speckles and their statistics, which are of general interest also for holographic interferometry are described in detail in Section 2.5.

7.1 Speckle Photography

In *speckle photography* an opaque diffusely reflecting surface is illuminated by coherent light. The resulting speckle pattern is imaged by the lens of a photo-camera onto photographic film. The exposure results in a pointwise blackening of the film. When the surface point motion has a component in a direction normal to the optical axis, the speckle pattern follows this displacement component. A developed double exposure negative with the two exposures before and after the deformation will consist of a manifold of speckle pairs. The distance between the points of each pair is proportional to the displacement component normal to the optical axis of the corresponding object point, the direction of this lateral displacement component is the same as the direction of the shift of the related speckles.

For reconstruction the double exposure negative, often called *specklegram*, is illuminated in a pointwise manner by an unexpanded laser beam, Fig. 7.1. The point pairs in the small region where the beam passes the specklegram act like the two apertures in *Young's double aperture interferometer*, see Section 2.3.2. We get parallel equispaced fringes with a spacing of $\lambda L/d$ at a screen, which is placed at a distance L from the specklegram. d is the distance

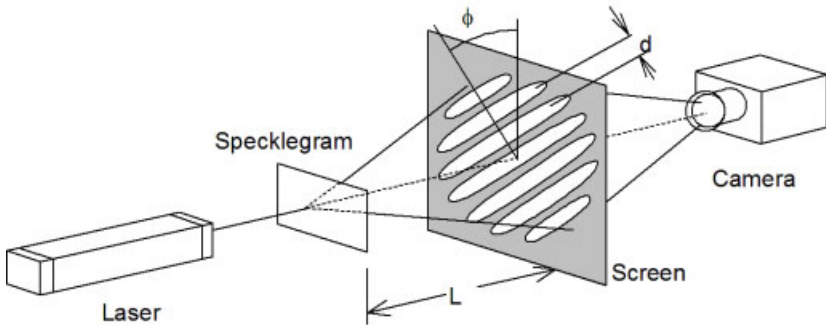


Figure 7.1: Reconstruction of Young's fringes in speckle photography.

in the pointpair in the specklegram, λ the wavelength used. The orientation of the fringes is orthogonal to the direction of the measured displacement component. By scanning the laser spot over the specklegram a two-dimensional field of displacement components can be measured. It should be stressed that from a single specklegram one can get only two pieces of information at each point: The modulus of the displacement projection onto a plane orthogonal to the optical axis, and the direction of this displacement component. The first is given by the distance of the Young's fringes, the second by the orientation of the fringes. In other words, we obtain the x - and y -components of the displacement vector in a coordinate system with the z -axis as the optical axis. There are a number of approaches to determine exactly the spacing and orientation of the fringes [757–759]. Good results have been obtained by locating the primary side lobes in the numerical 2D Fourier spectrum of the fringe pattern [760, 761].

Contrary to the pointwise evaluation and scanning there is a full field measurement method [164], where the specklegram is placed in an optical Fourier processor. A screen with a small hole is placed in the diffraction plane and passes only a small part of the spectrum, ideally a single spatial frequency. The resulting pattern in the image plane after such a filtering shows contours of equal displacement components in the direction given by the position of the filter. The filter position in the spatial frequency domain can now be varied by shifting the hole. It is obvious that in this way the measuring sensitivity can be varied, even after the speckle patterns have been originally recorded.

The main sensitivity of speckle photography is in the direction normal to the optical axis, that means for in-plane displacements of the surface points. The displacements generally have to be larger than the speckle size, which can be controlled by the aperture of the photo-camera.

7.2 Electronic and Digital Speckle Interferometry

The most important technique of speckle interferometry is the *digital speckle pattern interferometry (DSPI)*, originally called *electronic speckle pattern interferometry (ESPI)*, sometimes named *electronic holography* [762], *TV holography* [763–765], or *electro-optic holography* [516, 766, 767], or even *digital holography without wavefront reconstruction* [225] as well as *digital image plane holography* [768–771]. It was invented independently by several

groups [46–48]. The original aim was to overcome the time consuming wet-chemical processing of the silver halide holograms and to use electronic camera tubes instead. To adapt the micro-interference between object and reference wave to the resolution of the cameras, colinear reference and object waves have to be employed and an imaging system has to be used, Fig. 7.2. The object surface is focused onto the camera target, which in conjunction

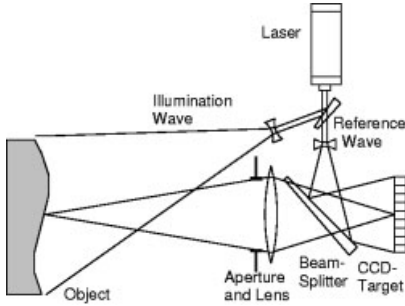


Figure 7.2: Arrangement for digital speckle interferometry.

with the colinear reference wave results in large speckles which now can be resolved by the camera but degrade the resulting interference pattern. This disadvantage is accepted due to the nearly real-time recording and reconstruction, and becomes less severe as CCD-targets get more and smaller pixels. Due to the focusing of the object's surface onto the camera target we record an image plane hologram, contrary to digital holography where only the Fresnel or Fraunhofer diffraction field of the object wavefront is registered, as defined in Chapter 3.

The object wave field in the image plane (x, y) , the plane of the camera target, Fig. 7.2, can be described by

$$E^{(\text{ob})}(x, y) = E_0^{(\text{ob})}(x, y) e^{i\phi^{(\text{ob})}(x, y)} \quad (7.1)$$

where $E_0^{(\text{ob})}(x, y)$ is the real amplitude and $\phi^{(\text{ob})}(x, y)$ is the random phase due to the surface roughness, Fig. 7.3a. The colinear reference wave field

$$E^{(\text{ref})}(x, y) = E_0^{(\text{ref})}(x, y) e^{i\phi^{(\text{ref})}(x, y)} \quad (7.2)$$

is superposed. This reference wave may be a plane wave, a spherical wave, or an arbitrary reflected one, Fig. 7.3b. Only intensities are recorded by the TV target, Fig. 7.3d

$$\begin{aligned} I_A(x, y) &= |E^{(\text{ob})}(x, y) + E^{(\text{ref})}(x, y)|^2 \\ &= I^{(\text{ob})}(x, y) + I^{(\text{ref})}(x, y) + 2\sqrt{I^{(\text{ob})}(x, y) I^{(\text{ref})}(x, y)} \cos \psi(x, y). \end{aligned} \quad (7.3)$$

This is the recorded, digitized, and stored speckle pattern with the stochastic phase difference $\psi(x, y) = \phi^{(\text{ob})}(x, y) - \phi^{(\text{ref})}(x, y)$, Fig. 7.3c. A deformation changes the phase $\phi^{(\text{ob})}(x, y)$ of each point by $\Delta\phi(x, y)$, Fig. 7.3e, so that the wave field after deformation is

$$E^{(\text{ob})'}(x, y) = E_0^{(\text{ob})}(x, y) e^{i[\phi^{(\text{ob})}(x, y) + \Delta\phi(x, y)]}. \quad (7.4)$$

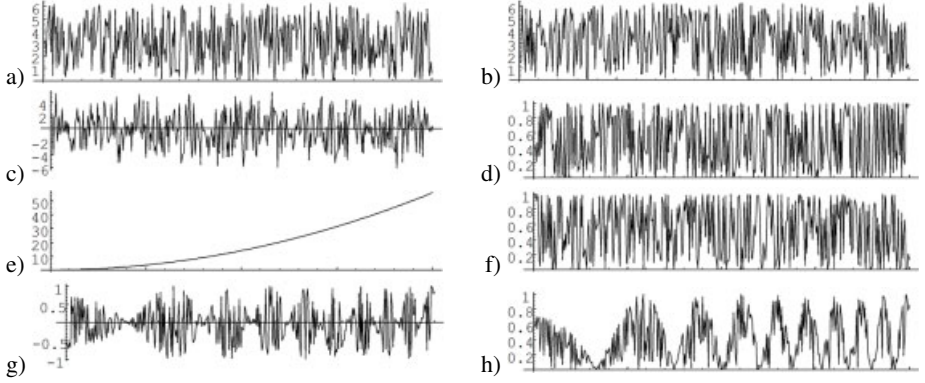


Figure 7.3: Digital speckle interferometry: (a) $\phi^{(\text{ob})}(x)$, (b) $\phi^{(\text{ref})}(x)$, (c) $\phi^{(\text{ob})}(x) - \phi^{(\text{ref})}(x)$, (d) $I_A(x)$, (e) $\Delta\phi(x)$, (f) $I_B(x)$, (g) $I_A(x) - I_B(x)$, (h) $|I_A(x) - I_B(x)|$.

Superposition with the colinear reference wave $E^{(\text{ref})}(x, y)$ leads to $I_B(x, y)$, Fig. 7.3f

$$I_B(x, y) = I^{(\text{ob})'}(x, y) + I^{(\text{ref})}(x, y) + 2\sqrt{I^{(\text{ob})'}(x, y) I^{(\text{ref})}(x, y)} \cos[\psi(x, y) + \Delta\phi(x, y)]. \quad (7.5)$$

In the digital image processing system this second speckle pattern $I_B(x, y)$ is subtracted in a pointwise manner in real time from the stored $I_A(x, y)$, where it is assumed that the deformation changes the phase but not the amplitude, meaning $I^{(\text{ob})'}(x, y) = I^{(\text{ob})}(x, y)$. The resulting difference is, Fig. 7.3g

$$\begin{aligned} & (I_A - I_B)(x, y) \\ &= 2\sqrt{I^{(\text{ob})}(x, y) I^{(\text{ref})}(x, y)} [\cos \psi - \cos \psi \cos \Delta\phi + \sin \psi \sin \Delta\phi](x, y) \quad (7.6) \\ &= 4\sqrt{I^{(\text{ob})}(x, y) I^{(\text{ref})}(x, y)} \sin \left[\psi(x, y) + \frac{\Delta\phi(x, y)}{2} \right] \sin \frac{\Delta\phi(x, y)}{2}. \end{aligned}$$

To display this result in real time on a monitor, positive intensities are obtained by taking the modulus $|I_A - I_B|$ or the square $(I_A - I_B)^2$, Fig. 7.3h. The square root in (7.6) describes the background illumination. The first sine-term gives the stochastic speckle noise which varies randomly from pixel to pixel. This noise is modulated by the sine of the half phase difference induced by the deformation. This low frequency modulation of the high frequency speckle noise is recognized as an interference pattern. The relation between the displacement vector $\mathbf{d}(x, y)$ and the phase difference $\Delta\phi(x, y)$ is as in holographic interferometry, see (4.20) and (4.21)

$$\Delta\phi(x, y) = \frac{2\pi}{\lambda} \mathbf{d}(x, y) \cdot [\mathbf{b}(x, y) - \mathbf{s}(x, y)]. \quad (7.7)$$

An alternative way for determining the phase difference from two speckle interferograms is the Fourier transform method first suggested in [457]. Here both intensities $I_A(x, y)$ and

$I_B(x, y)$ are Fourier transformed. The amplitude spectra in the first and minus first diffraction orders – the first two side-lobes – resemble the aperture, see Fig. 7.2. If the lateral placement of the aperture and the position of the virtual reference source point are properly chosen, the side-lobes do not overlap [306] and a bandpass filter as described in Section 5.6.1 can be applied. A virtual reference source point outside the aperture generates carrier fringes as described in Section 5.6.5. After one side-lobe is isolated by bandpass filtering an inverse Fourier transform is applied and gives complex $c_A(x, y)$ and $c_B(x, y)$. From these the interference phase $\Delta\phi(x, y)$ is calculated as defined in (5.71) by

$$\begin{aligned}\Delta\phi(n, m) &= \arctan \frac{\operatorname{Re}\{c_A(x, y)\}\operatorname{Im}\{c_B(x, y)\} - \operatorname{Re}\{c_B(x, y)\}\operatorname{Im}\{c_A(x, y)\}}{\operatorname{Re}\{c_A(x, y)\}\operatorname{Re}\{c_B(x, y)\} + \operatorname{Im}\{c_A(x, y)\}\operatorname{Im}\{c_B(x, y)\}} \\ &= \arctan \frac{\operatorname{Im}\{c_B(x, y)c_A^*(x, y)\}}{\operatorname{Re}\{c_B(x, y)c_A^*(x, y)\}}.\end{aligned}\quad (7.8)$$

This approach elucidates the close relationship to digital holography, therefore some authors use the term digital image plane holography [768–770].

Equation (7.7) shows that maximum sensitivity of DSPI/ESPI is for out-of-plane displacements. For measuring transversal displacements a modified setup using two illuminations from opposite directions having equal angles to the surface normal is recommended [582, 697, 772]. DSPI/ESPI patterns essentially contain the same information as the corresponding holographic interferograms. Thus their production requires the same precautions concerning vibration isolation and stability during the recording process. The results can be observed in real time, due to the electronic recording there is no problem with an exact repositioning of a hologram plate. The interference phase map quality can be improved by filtering in the spatial or spatial frequency domain [773].

While most applications of digital speckle interferometry are in deformation measurements of opaque surfaces these methods can also be successfully applied in fluid mechanics. Now the flowing transparent medium is seeded with tracer particles which constitute the reflecting object [267]. The particle field may be illuminated from any convenient direction; however, a useful approach is illumination by a thin light sheet as in particle image velocimetry (PIV).

The measurement of transient phenomena like impact studies, vibration analysis, or flow diagnostics is possible using double-pulsed illumination and recording. In this way mechanical amplitude and phase of surface acoustic waves have been measured [774] with interference phase determination by the Fourier transform method. While in this application the surface acoustic waves constitute a spatial carrier frequency by themselves, carrier fringes can be introduced by a tilt between object and reference wave. This allows the use of Fourier transform evaluation, e. g. in the double pulse measurement of brake squeal [775]. The separation of vibration modes using four pulses of a Q-switched ruby laser is described in [776, 777]. Here the method is called digital holography but since the “laser light scattered by the object is collected with an imaging lens that forms the image of the object on each of the three CCD camera faceplates” [776] there clearly an electronic speckle pattern interferometer with out-of-plane sensitivity is employed.

7.3 Electro-optic Holography

Electro-optic holography, also known as *electronic holography* or *TV holography*, is a combination of *phase stepping* and digital speckle interferometry [49, 50, 202]. For static measurements n phase stepped speckle patterns are recorded in the unstressed and n phase stepped speckle patterns in the stressed state. The recorded intensities are, see (7.3)

$$\begin{aligned} I_n(x, y) &= I^{(\text{ob})}(x, y) + I^{(\text{ref})}(x, y) + 2\sqrt{I^{(\text{ob})}(x, y) I^{(\text{ref})}(x, y)} \cos[\psi(x, y) + \phi_{Rn}] \\ I'_n(x, y) &= I^{(\text{ob})'}(x, y) + I^{(\text{ref})}(x, y) \\ &\quad + 2\sqrt{I^{(\text{ob})'}(x, y) I^{(\text{ref})}(x, y)} \cos[\psi(x, y) + \Delta\phi(x, y) + \phi_{Rn}]. \end{aligned} \quad (7.9)$$

The notation is as in Section 7.2, ϕ_{Rn} are the phase shifts. While generally arbitrary phase shifts ϕ_{Rn} can be employed, see Section 5.5, the most used are $\phi_{R1} = 0^\circ$, $\phi_{R2} = 90^\circ$, $\phi_{R3} = 180^\circ$, and $\phi_{R4} = 270^\circ$. This results in

$$\begin{aligned} I_1(x, y) &= I^{(\text{ob})}(x, y) + I^{(\text{ref})}(x, y) + 2\sqrt{I^{(\text{ob})} I^{(\text{ref})}} \cos \psi(x, y) \\ I_2(x, y) &= I^{(\text{ob})}(x, y) + I^{(\text{ref})}(x, y) + 2\sqrt{I^{(\text{ob})} I^{(\text{ref})}} \sin \psi(x, y) \\ I_3(x, y) &= I^{(\text{ob})}(x, y) + I^{(\text{ref})}(x, y) - 2\sqrt{I^{(\text{ob})} I^{(\text{ref})}} \cos \psi(x, y) \\ I_4(x, y) &= I^{(\text{ob})}(x, y) + I^{(\text{ref})}(x, y) - 2\sqrt{I^{(\text{ob})} I^{(\text{ref})}} \sin \psi(x, y) \end{aligned} \quad (7.10)$$

and

$$\begin{aligned} I'_1(x, y) &= I^{(\text{ob})}(x, y) + I^{(\text{ref})}(x, y) + 2\sqrt{I^{(\text{ob})} I^{(\text{ref})}} \cos [\psi(x, y) + \Delta\phi(x, y)] \\ I'_2(x, y) &= I^{(\text{ob})}(x, y) + I^{(\text{ref})}(x, y) + 2\sqrt{I^{(\text{ob})} I^{(\text{ref})}} \sin [\psi(x, y) + \Delta\phi(x, y)] \\ I'_3(x, y) &= I^{(\text{ob})}(x, y) + I^{(\text{ref})}(x, y) - 2\sqrt{I^{(\text{ob})} I^{(\text{ref})}} \cos [\psi(x, y) + \Delta\phi(x, y)] \\ I'_4(x, y) &= I^{(\text{ob})}(x, y) + I^{(\text{ref})}(x, y) - 2\sqrt{I^{(\text{ob})} I^{(\text{ref})}} \sin [\psi(x, y) + \Delta\phi(x, y)] \end{aligned} \quad (7.11)$$

These systems of equations can be solved, see (5.24), yielding $\psi(x, y)$ and $\psi(x, y) + \Delta\phi(x, y)$, whose difference is the interference phase distribution $\Delta\phi(x, y)$. The advantage over conventional DSPI-patterns becomes obvious, when

$$\sqrt{[(I_1 - I_3) + (I'_1 - I'_3)]^2 + [(I_2 - I_4) + (I'_2 - I'_4)]^2} = 8\sqrt{I^{(\text{ob})} I^{(\text{ref})}} \cos(\Delta\phi/2)$$

is displayed. This interference pattern exhibits much less speckle noise than DSPI-patterns.

Besides static deformation measurement electro-optic holography also has been effectively applied to sinusoidally vibrating objects [376]. High quality time average interference patterns can be synthesized from phase stepped recordings. The argument of the Bessel function is determined with high accuracy if the phase of the object or reference wave is modulated at the same frequency and phase as the object vibration [376, 762].

In the described method the four phase shifted patterns were taken one after the other. To get several phase shifted patterns not sequentially in time but spatially separated, the in-line reference wave of digital speckle interferometry must be tilted, which is accomplished by

shifting the focus of the reference wave slightly out of the focus of the camera lens. In [778] this shift was adjusted to produce phase shifts of 120° between subsequent pixels. The three phase shifted images now are coded in neighboring pixels. If the speckles are large enough – about three pixels per speckle – and if the phase to be measured does not vary too much over the speckle size, then the interference phase can be determined for each triple of neighboring pixels by $\Delta\phi = \arctan[\sqrt{3}(I_3 - I_2)/(2I_1 - I_2 - I_3)]$, see Table 5.1. If the angle between object wave and the reference wave tilted in the x -direction is θ , the image plane hologram can be interpreted as a spatial carrier modulated by the object information [779]. The spatial carrier frequency is $f_0 = (\sin \theta)/\lambda$. Let the pixel pitch be Δx , then provided the interference phase $\Delta\phi$ changes slowly, we can calculate $\Delta\phi$ in a pointwise manner by

$$\Delta\phi(x, y) = \arctan\left(\frac{I(x - \Delta x, y) - I(x + \Delta x, y)}{I(x - \Delta x, y) + I(x + \Delta x, y) - 2I(x, y)} \tan(\pi \Delta x f_0)\right). \quad (7.12)$$

A comparison of this approach with digital holography using the Fresnel diffraction field instead of the image plane hologram is given in [64].

The simultaneous use of several reference waves tilted in different directions with respect to the object wave defines various spatial carriers. Each reference wave can be written as [62]

$$R_k(\xi, \eta) = r_k(\xi, \eta) \exp\{-2\pi i(f_{k\xi}\xi + f_{k\eta}\eta)\}. \quad (7.13)$$

Here the $(f_{k\xi}, f_{k\eta})$ describe the spatial carrier frequencies. By considering the dimensions of the imaging aperture and the location of the reference point sources relative to this aperture, the carrier frequencies are separated from each other in the spatial frequency domain and can be isolated by proper filtering. This allows the application of Fourier transform evaluation with carrier [43] as introduced in Section 5.6.1. In this way the three deformation components of a vibrating object are discriminated and measured with simultaneous recording of digital image plane holograms [62].

Furlong [239] uses this technique, there called *optoelectronic holography* (OEH), in conjunction with an *optoelectronic holographic microscope* (OEHM) to characterize shape and deformation of *microelectromechanical systems* (MEMS).

7.4 Speckle Shearography

The requirement of vibration isolation can be dropped to a good extent when using the *speckle-shearing methods*. Here only the spatial variations of the displacement in a predetermined direction are measured, so the methods are rather insensitive to rigid body motions [136, 780]. In the following the method is explained with the example of *digital shearography*, which has attained some economic importance.

Again two wave fields, object and reference, as in DSPI interfere, but now two slightly spatially shifted speckle fields of the rough surface are superposed. The role of the reference wave is taken by one of the two mutually shifted object wave fields, one speaks of *self-reference*. The shifting of the speckle fields is performed by a shearing element, e. g. a glass wedge in front of one half of the imaging lens, two tilted glass plates, a Wollaston prism, or a Michelson interferometer-like arrangement with one mirror slightly tilted, Fig. 7.4.

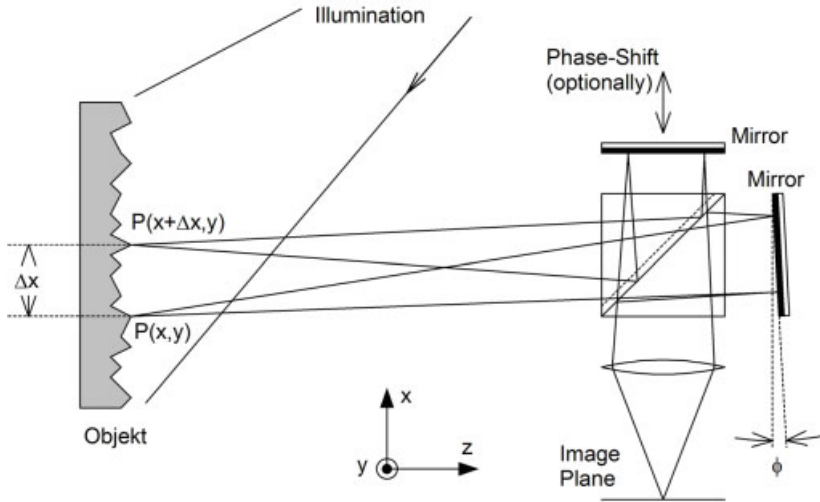


Figure 7.4: Arrangement for digital shearography.

Let the two wave fields be separated laterally by the mutual shearing Δx , then we get the two nearly colinear wave fields

$$\begin{aligned} E_1(x, y) &= E_{01}(x, y) e^{i\phi(x, y)} \\ E_2(x, y) &= E_{02}(x, y) e^{i\phi(x + \Delta x, y)}. \end{aligned} \quad (7.14)$$

Their interference produces the speckle pattern

$$\begin{aligned} I_A(x, y) &= |E_1(x, y) + E_2(x, y)|^2 \\ &= I_1(x, y) + I_2(x, y) + 2\sqrt{I_1(x, y) I_2(x, y)} \cos \psi(x, y) \end{aligned} \quad (7.15)$$

which is recorded, digitized, and stored. $\psi(x, y)$ is the randomly distributed phase difference $\psi(x, y) = \phi(x, y) - \phi(x + \Delta x, y)$. Deformation of the object leads to the wave fields

$$\begin{aligned} E_3(x, y) &= E_{01}(x, y) e^{i[\phi(x, y) + \Delta\phi(x, y)]} \\ E_4(x, y) &= E_{02}(x, y) e^{i[\phi(x + \Delta x, y) + \Delta\phi(x + \Delta x, y)]} \end{aligned} \quad (7.16)$$

whose superposition yields the speckle pattern

$$\begin{aligned} I_B(x, y) &= I_1(x, y) + I_2(x, y) \\ &+ 2\sqrt{I_1(x, y) I_2(x, y)} \cos[\psi(x, y) + \Delta\phi(x, y) - \Delta\phi(x + \Delta x, y)]. \end{aligned} \quad (7.17)$$

Pointwise subtraction gives

$$\begin{aligned}
 (I_A - I_B)(x, y) &= 2\sqrt{I_1 I_2} \{ \cos \psi(x, y) - \cos[\psi(x, y) + \Delta\phi(x, y) - \Delta\phi(x + \Delta x, y)] \} \\
 &= 4\sqrt{I_1 I_2} \sin \left[\psi(x, y) + \frac{\Delta\phi(x, y) - \Delta\phi(x + \Delta x, y)}{2} \right] \\
 &\quad \cdot \sin \frac{\Delta\phi(x, y) - \Delta\phi(x + \Delta x, y)}{2}.
 \end{aligned} \tag{7.18}$$

Positive values may be obtained by taking the modulus or square. Again the term in the root is the background, the first sine-term is the stochastic speckle noise modulated by the second sine-term which stems from the deformation. The displacement vector field $\mathbf{d}(x, y)$ is contained in the argument of this sine by

$$\begin{aligned}
 &\frac{\Delta\phi(x, y) - \Delta\phi(x + \Delta x, y)}{2} \\
 &= \frac{\pi}{\lambda} \{ \mathbf{d}(x, y) \cdot [\mathbf{b}(x, y) - \mathbf{s}(x, y)] - \mathbf{d}(x + \Delta x, y) \cdot [\mathbf{b}(x + \Delta x, y) - \mathbf{s}(x + \Delta x, y)] \} \\
 &\approx \frac{\pi}{\lambda} [\mathbf{d}(x, y) - \mathbf{d}(x + \Delta x, y)] \cdot [\mathbf{b}(x, y) - \mathbf{s}(x, y)] \\
 &= \frac{\pi}{\lambda} \left[\frac{\mathbf{d}(x, y) - \mathbf{d}(x + \Delta x, y)}{\Delta x} \right] \cdot [\mathbf{b}(x, y) - \mathbf{s}(x, y)] \Delta x \\
 &\approx \frac{\partial \mathbf{d}(x, y)}{\partial x} \cdot \frac{\pi \Delta x}{\lambda} [\mathbf{b}(x, y) - \mathbf{s}(x, y)].
 \end{aligned} \tag{7.19}$$

What produces the interference pattern is an approximation to the derivative of the displacement field in the direction of the image shearing, here the x -direction. For rigid body motions we have $\mathbf{d}(x, y) = \text{const}$, implying $\partial \mathbf{d}(x, y) / \partial x = 0$. This explains the insensitivity of the shearing methods to rigid body motions. The sensitivity of the method can be adjusted by controlling the amount of shearing. Besides the shearing in the x -direction we can shear in the y - or other angular directions. Also radial shearing, rotational shearing, inversion shear, or reversal shear can be performed with related optical arrangements [781].

Figure 7.5a presents a DSPI-image of a plate subjected to an out-of-plane deformation by pressing at a central point from the plate's back side. Thus a deformation in the form of a Gaussian bell is produced. The fringes can be interpreted as equi-height lines of the deformed object. For comparison in Fig. 7.5b the same object undergoing the same deformation is investigated by digital shearography. The shear is in the horizontal direction, so the fringes can be explained as equi-contours of the derivative in the horizontal direction with highest fringe order at the locus of steepest slope of the hill. At the top of the hill we have zero slope and thus zero fringe order in the shearographic pattern.

A one-dimensional simulation of speckle shearography is shown in Fig. 7.6. Figure 7.6a displays the random phase $\phi(x)$, while Fig. 7.6b gives the intensity $I_A(x)$ resulting from interference between sheared and unsheared wave fields focused onto the recording target in the image plane. Figure 7.6c shows the assumed additional phase $\Delta\phi(x)$ due to the deformation and in Fig. 7.6d the recorded intensity $I_B(x)$ after deformation is seen. The difference $I_A(x) - I_B(x)$ of the two recorded intensities is given in Fig. 7.6e, and its modulus $|I_A(x) - I_B(x)|$ in Fig. 7.6f.

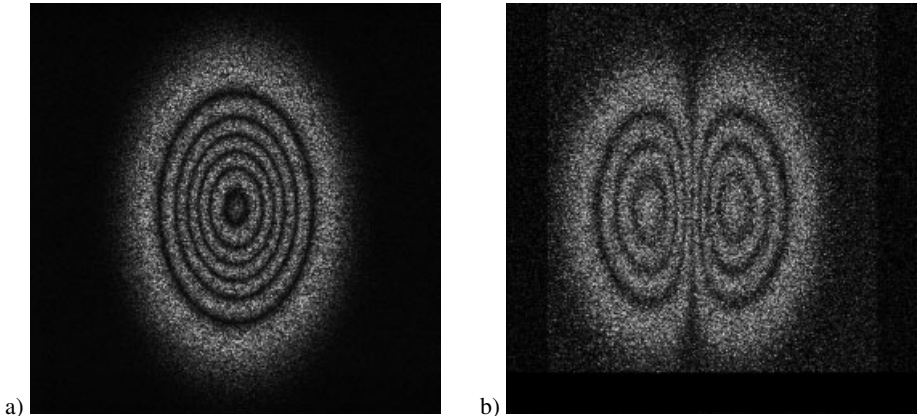


Figure 7.5: DSPI (a) and shearographic (b) patterns of a plate with bell-shaped deformation.

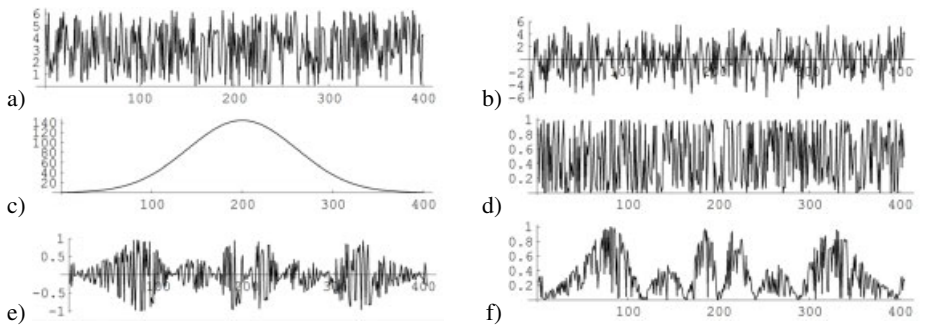


Figure 7.6: Digital speckle shearography: (a) $\phi(x)$, (b) $I_A(x)$, (c) $\Delta\phi(x)$, (d) $I_B(x)$, (e) $I_A(x) - I_B(x)$, (f) $|I_A(x) - I_B(x)|$.

Equations (7.18) and (7.19) show that the fringe density in shearographic patterns depends on the wavelength λ of the light used. So multiple wavelengths, especially when using broadband sources, would decrease the fringe modulation until their total deterioration. However, Falldorf [782] has indicated how the shift of the fringes due to λ can be compensated by employing a dispersive optical component. This component used in [782] is a wedge prism, arranged under a certain angle to the optical axis, that produces a shear Δx proportional to λ . So the factor $\Delta x/\lambda$ in (7.19) becomes a constant, and fringe densities in shearographic measurements are independent from the wavelengths used, provided that the deformation along the shear is linear to the first order.

A Signal Processing Fundamentals

A.1 Overview

Fourier analysis is the most important and appropriate mathematical tool employed in the description of coherent optics and of digital holography. The reasons for this fact are manifold: The propagation of optical fields, e. g. from an object to the recording medium, here the hologram, or from an illuminated hologram to an image plane, which may be the target of an electronic recording device, the retina of an observer's eye, or a virtual plane whose field is calculated and displayed on a monitor, is described in the framework of linear systems theory, where Fourier analysis plays the central role. The optical wave fields used in this book are solutions of the Maxwell equations and as such are superpositions of harmonic functions. Fourier analysis is the adequate tool to deal with those harmonic functions.

Therefore the objective of this appendix is to review the most notable concepts of signal processing, as far as they find applications in optics and especially in digital holography. Of course this remains far from being exhaustive, so the interested reader is referred to a number of excellent textbooks on one- and two-dimensional signal processing, where the topic is introduced systematically, questions regarding the existence of the Fourier transform of classes of signals are discussed, many more theorems are presented, and where proofs, applications, and examples can be found.

The following treatment first introduces the concepts in one dimension, followed by an extension to the two dimensions typical for image processing. At a conceptual level, there is a great deal of similarity between one-dimensional signal processing and two-dimensional image processing. Although in this book we deal with images and two-dimensional patterns the concepts can be described and understood more clearly and easily in one dimension. After this preparation the extension to two dimensions is straightforward

and poses no additional difficulties. Nevertheless also differences already exist between one- and two-dimensional signal processing. For example, many one-dimensional systems are described by ordinary differential equations, while many two-dimensional systems involve partial differential equations, which generally are much more difficult to solve. Another fact is the absence of the fundamental theorem of algebra for two-dimensional polynomials. So two-dimensional polynomials cannot be factored generally into lower-order polynomials, with consequences on filter-design, issues related to system stability, etc. [396]. A basic problem in digital holography refers to sampling of optical two-dimensional signals. That topic is addressed in this appendix as well as the discussion of the chirp function, a function frequently used in digital holography. The following treatment furthermore distinguishes between analog signals, i. e. continuous time and space-signals, and discrete signals. While theory elegantly

deals with continuous infinite functions, in metrologic practice we always have a finite number of sampled discrete data for processing. The differences between signals defined over infinite and finite domains are also identified.

A.2 Definition of the Fourier Transform

Let $f(x)$ be a one-dimensional complex-valued function. The real variable x may stand for a temporal coordinate, e. g. in acoustics or in electronics, or for a spatial coordinate, e. g. in image processing or optics. Then the *Fourier transform* of $f(x)$ is defined as

$$\mathcal{F}\{f(x)\} = F(\xi) = \int_{-\infty}^{\infty} f(x)e^{-i2\pi\xi x} dx. \quad (\text{A.1})$$

The Fourier transform is a linear integral transformation that maps the complex-valued function $f(x)$ to another complex-valued function $F(\xi)$ of the variable ξ . This ξ stands for the *temporal frequency* or the *one-dimensional spatial frequency*.

The *inverse Fourier transform* of a complex-valued function $F(\xi)$ defined in the frequency domain is given by

$$\mathcal{F}^{-1}\{F(\xi)\} = f(x) = \frac{1}{2\pi} \int_{-\infty}^{\infty} F(\xi)e^{i2\pi\xi x} d\xi. \quad (\text{A.2})$$

The *Fourier integral theorem* now states that

$$f(x) = \frac{1}{2\pi} \int_{-\infty}^{\infty} \left[\int_{-\infty}^{\infty} f(x)e^{-i2\pi\xi x} dx \right] e^{i2\pi\xi x} d\xi \quad (\text{A.3})$$

or shortly $f(x) = \mathcal{F}^{-1}\{\mathcal{F}\{f(x)\}\}$, which means that the transformation is reciprocal

$$\mathcal{F}\{f(x)\} = F(\xi) \quad \implies \quad \mathcal{F}^{-1}\{F(\xi)\} = f(x). \quad (\text{A.4})$$

The two functions $f(x)$ and $F(\xi)$ satisfying (A.4) together are called a *Fourier transform pair*. For any $f(x)$, if the Fourier transform exists, $F(\xi)$ is unique and vice versa. From the reciprocity we see that the same amount of information is contained in $f(x)$ described in the spatial (or temporal) domain as is in the complex spectrum $F(\xi)$ represented in the spatial (or temporal) frequency domain.

Since the Fourier transform is an integral transformation, the question of the existence of the infinite limit integrals (A.1) and (A.2) arises. The infinite limits are not the problem, because the Cauchy principal value $\int_{-\infty}^{\infty} f(x) dx = \lim_{A \rightarrow \infty} \int_{-A}^A f(x) dx$ is taken, but on the other hand no direct and simple criterion is known, which is both sufficient and necessary in ensuring that a function has a valid Fourier transform. However in our applications the functions we process generally are digitized images. These are necessarily truncated to a finite spatial extent and furthermore are bounded in their values. Thus they belong to the

class of *transient functions* which fall to zero rapidly enough for large positive and negative arguments so that the integrals in (A.1) and (A.2) exist. If the integral of the absolute value of the function $f(x)$ exists

$$\int_{-\infty}^{\infty} |f(x)| dx < \infty \quad (\text{A.5})$$

and it is either continuous or has only a finite number of discontinuities and these discontinuities are not infinite and furthermore it has at most a finite number of extrema in any finite interval, then its Fourier transform $F(\xi)$ exists for all values of ξ [160,783].

Periodic or *constant functions* do not belong to the class of these transient functions, nevertheless they may be transformable. For their treatment as well as for other purposes the *Dirac delta* or *impulse* $\delta(x)$ is useful. It can be defined as the limit of a sequence of *rectangular functions* $\delta_n(x)$ which are given by

$$\delta(x) = \lim_{n \rightarrow \infty} \delta_n(x) = \lim_{n \rightarrow \infty} n \text{rect}(nx) \quad (\text{A.6})$$

$$\text{rect}(x) = \begin{cases} 1 & \text{for } |x| < \frac{1}{2} \\ 0 & \text{elsewhere.} \end{cases} \quad (\text{A.7})$$

The first components of the sequence $\{\delta_n(x)\}$ are illustrated in Fig. A.1. The limit of this

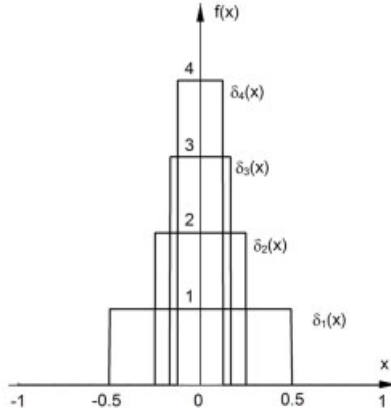


Figure A.1: Rectangular functions converging to the Dirac delta.

sequence of functions is of infinite height but zero width in such a manner that the area is still unity

$$\int_{-\infty}^{\infty} \delta(x) dx = 1. \quad (\text{A.8})$$

The importance of the impulse function is based on the following *sampling property*:

$$\int_{-\infty}^{\infty} f(x) \delta(x - x') dx = f(x') \quad (\text{A.9})$$

where $\delta(x - x')$ denotes an impulse shifted to location $x = x'$. It must be mentioned that from a mathematical standpoint the impulse is not a function in the classic sense. A rigorous treatment uses the calculus of distributions or generalized functions.

Based on the stated properties of the impulse, the Fourier transforms of some constant and periodic functions can be calculated. These transforms are given together with further frequently used Fourier transform pairs in Table A.1. The Fourier transforms of the Gaussian and of the infinite chirp function here are special cases of the correspondence [784]

$$\mathcal{F}\{e^{-sx^2}\} = \sqrt{\frac{\pi}{s}} e^{-\frac{\xi^2}{4s}} \quad \text{for any complex } s \text{ with } \operatorname{Re}\{s\} \geq 0. \quad (\text{A.10})$$

In the first case we set $s = \pi$, and in the second $s = -i\pi$.

A.3 Interpretation of the Fourier Transform

Equation (A.2) indicates that the Fourier transform can be interpreted as a decomposition of the function $f(x)$ into a linear combination of elementary functions, here the complex exponentials of frequencies ξ . Due to the integral this combination consists of a continuum of terms. There are numerous applications where it is much easier to perform a specific processing of each of the simple complex exponentials and to superimpose the individual results to yield the overall result instead of processing the original function $f(x)$.

The frequency decomposition of the Fourier transform can be elucidated by the following argument. Suppose that $f(x)$ is expressed by a number of components of different frequencies

$$f(x) = F_0 + F_1 e^{i2\pi\xi_1 x} + F_2 e^{i2\pi\xi_2 x} + F_3 e^{i2\pi\xi_3 x} + \dots \quad (\text{A.11})$$

Each of these terms rotates with a certain frequency ξ_i . In performing the Fourier transform (A.1) to $f(x)$, each term is multiplied with the factor $e^{-i2\pi\xi x}$. If in a product there is $\xi \neq \xi_i$, the product still rotates and its integral becomes zero. Only where $\xi = \xi_i$, which means that $e^{-i2\pi\xi x}$ rotates with the same frequency but in the other direction, the multiplication stops rotation and the integration gives a value proportional to F_i . Thus the Fourier transform picks the components rotating with specific frequencies. The vanishing integrals are due to the infinite limits and the fact that the real and imaginary parts of the complex exponentials are cosine- and sine-functions $e^{i2\pi\xi x} = \cos 2\pi\xi x + i \sin 2\pi\xi x$, which is the well known *formula of Euler*, Fig. A.2.

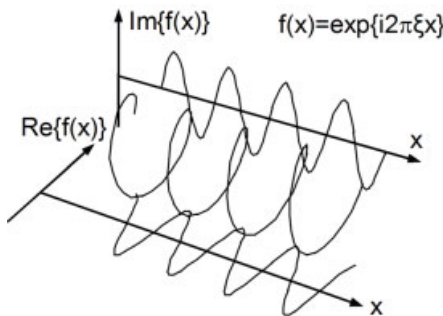


Figure A.2: Projections of complex exponentials.

The functions $F(\xi)$ calculated by (A.1) generally are complex-valued functions. Normally one is not interested in how the values are distributed between the real and imaginary part but in the modulus

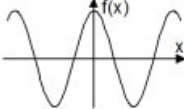
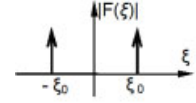
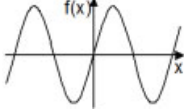
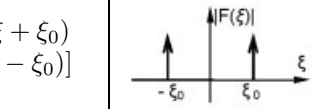
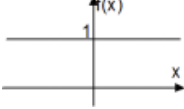
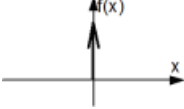
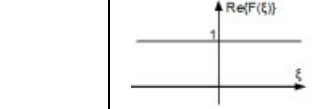
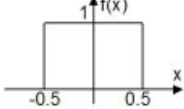
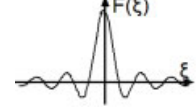
$$|F(\xi)| = \sqrt{\operatorname{Re}^2\{F(\xi)\} + \operatorname{Im}^2\{F(\xi)\}} \quad (\text{A.12})$$

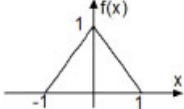
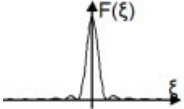
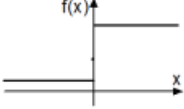
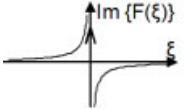
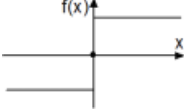
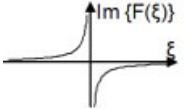
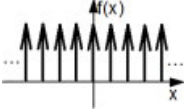
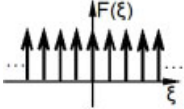
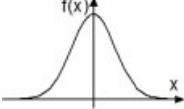
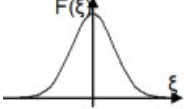
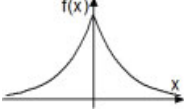
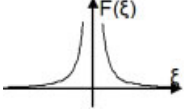
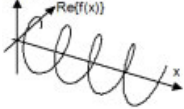
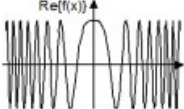
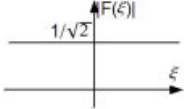
called the *amplitude spectrum* or shortly the amplitude. It should not be confused with the intensity $|F(\xi)|^2$ of an optical wave field $F(\xi)$. The other interesting spectrum is the *phase spectrum* $\phi(\xi)$, shortly called *phase*, which is defined as

$$\phi(\xi) = \arctan \frac{\operatorname{Im}\{F(\xi)\}}{\operatorname{Re}\{F(\xi)\}}. \quad (\text{A.13})$$

The value at frequency zero, $F(0)$, stands for the *average* or *d.c.-component* of the spectrum function, it represents the constant background F_0 in (A.11). F_0 is real if $f(x)$ is a real function.

Table A.1: Useful Fourier transform pairs.

Function in temporal (or 1D spatial) domain	Fourier transform in frequency (spatial frequency) domain
 Cosine $f(x) = \cos(2\pi\xi_0 x)$	$\frac{1}{2} [\delta(\xi + \xi_0) + \delta(\xi - \xi_0)]$ 
 Sine $f(x) = \sin(2\pi\xi_0 x)$	$\frac{i}{2} [\delta(\xi + \xi_0) - \delta(\xi - \xi_0)]$ 
 Constant $f(x) = 1$	$\delta(\xi)$ 
 Dirac delta $f(x) = \delta(x)$	1 
 Rectangular pulse $\operatorname{rect}(x) = \begin{cases} 1 & x < \frac{1}{2} \\ 0 & \text{otherwise} \end{cases}$	$\frac{\sin(\pi\xi)}{\pi\xi} = \operatorname{sinc}(\xi)$ 

Function in temporal (or 1D spatial) domain		Fourier transform in frequency (spatial frequency) domain	
	<p>Triangular pulse</p> $\Lambda(x) = \begin{cases} 1 - x & x < 1 \\ 0 & \text{otherwise} \end{cases}$	$\frac{\sin^2(\pi\xi)}{(\pi\xi)^2} = \text{sinc}^2(\xi)$	
	<p>Unit step</p> $u(x) = \begin{cases} 1 & x > 0 \\ \frac{1}{2} & x = 0 \\ 0 & x < 0 \end{cases}$	$\frac{1}{2} \left[\delta(\xi) - \frac{i}{\pi\xi} \right]$	
	<p>Signum function</p> $\text{sign}(x) = \begin{cases} 1 & x > 0 \\ 0 & x = 0 \\ -1 & x < 0 \end{cases}$	$\frac{1}{i\pi\xi}$	
	<p>Comb function</p> $\text{comb}(x) = \sum_{n=-\infty}^{\infty} \delta(x - n)$	$\text{comb}(\xi)$	
	<p>Gaussian</p> $f(x) = e^{-\pi x^2}$	$e^{-\frac{\xi^2}{4\pi}}$	
	<p>Exponential decay</p> $f(x) = e^{- x }$	$\frac{2}{1 + (2\pi\xi)^2}$	
	<p>Complex exponential</p> $f(x) = e^{i2\pi\xi_0 x}$	$\delta(\xi - \xi_0)$	
	<p>Infinite chirp function</p> $f(x) = e^{i\pi\alpha x^2}$	$\frac{i}{\sqrt{\alpha}} e^{-i\pi \frac{\xi^2}{\alpha}}$	

A.4 Properties of the Fourier Transform

There are a number of properties of the Fourier transform which are frequently used in investigating and processing data in the frequency domain. In the following we see what consequences certain properties of $f(x)$ in the spatial (or temporal) domain have in the frequency domain. The *symmetry properties* are summarized in Table A.2.

Table A.2: Symmetry properties.

$f(x)$	$F(\xi)$
Even [i. e. $f(-x) = f(x)$]	Even
Odd [i. e. $f(-x) = -f(x)$]	Odd
Real [i. e. $\text{Im}\{f(x)\} = 0$]	Hermitean [i. e. $F(\xi) = F^*(-\xi)$]
Real and even	Real and even
Real and odd	Imaginary and odd
Imaginary [i. e. $\text{Re}\{f(x)\} = 0$]	Anti-Hermitean [i. e. $F(\xi) = -F^*(-\xi)$]
Imaginary and even	Imaginary and odd
Imaginary and odd	Real and odd
Even real and odd imaginary	Real
Odd real and even imaginary	Imaginary

The *linearity theorem*, also called *addition theorem*, states that the transform of a weighted sum of two or more functions is the identically weighted sum of the individual transforms

$$\mathcal{F}\{af(x) + bg(x)\} = a\mathcal{F}\{f(x)\} + b\mathcal{F}\{g(x)\} = aF(\xi) + bG(\xi). \quad (\text{A.14})$$

The *shift theorem* specifies that shifting a function in the spatial domain does not alter the amplitude of the Fourier transform but only introduces a phase shift in the frequency domain:

$$\mathcal{F}\{f(x - a)\} = e^{-i2\pi a\xi} F(\xi). \quad (\text{A.15})$$

In optics that means that the intensity of the Fraunhofer diffraction pattern remains unaffected by lateral shifts of the object surface or diffracting transparency.

The *similarity theorem*, also called *scaling theorem*, describes the effect that a change of abscissa scale has on the Fourier transform

$$\mathcal{F}\{f(ax)\} = \frac{1}{|a|} F\left(\frac{\xi}{a}\right). \quad (\text{A.16})$$

This means that if a function is broadened in the temporal or spatial domain, $a < 1$, its transform is contracted in the frequency domain and the amplitude is increased. Contrarily if the function f is narrowed by an $a > 1$, the transform is broadened and the amplitude is flattened.

Differentiation in the temporal or spatial domain corresponds to a multiplication with a linear factor in the frequency domain

$$\mathcal{F} \left\{ \frac{d}{dx} f(x) \right\} = i2\pi\xi F(\xi). \quad (\text{A.17})$$

For functions which are nonzero only over a finite portion of their domain, their *energy* E can be defined by

$$E = \int_{-\infty}^{\infty} |f(x)|^2 dx \quad (\text{A.18})$$

provided the integral exists. *Rayleigh's theorem* states that

$$\int_{-\infty}^{\infty} |f(x)|^2 dx = \int_{-\infty}^{\infty} |F(\xi)|^2 d\xi \quad (\text{A.19})$$

which means that the transform carries the same energy as the original function. Thus Rayleigh's theorem is interpretable as a statement of conservation of energy. It is a special case of *Parseval's theorem*

$$\int_{-\infty}^{\infty} f(x)g(x)^* dx = \int_{-\infty}^{\infty} F(\xi)G(\xi)^* d\xi \quad (\text{A.20})$$

where $*$ denotes the complex conjugate and $\mathcal{F}\{f(x)\} = F(\xi)$ and $\mathcal{F}\{g(x)\} = G(\xi)$ in (A.14) to (A.20).

A.5 Linear Systems

A *system* in the mathematical sense is defined as a mapping of a set of input functions into a set of output functions. This concept is commonly applied in optics where the inputs and outputs can be real-valued functions representing intensity distributions or can be complex-valued functions representing field amplitudes, both defined over two-dimensional spatial coordinates. Characterizing a general system would require the complete knowledge of the outputs for all possible sets of inputs. Knowing the output related to a specific input will tell us nothing about the system's output to another input. But there are restricted, but nevertheless important, classes of systems, where useful relations between input and output are developed and characterization, analysis, and applications of these systems are greatly simplified.

A system L is a *linear system* if

$$L\{af(x) + bg(x)\} = aL\{f(x)\} + bL\{g(x)\} \quad (\text{A.21})$$

where a and b are arbitrary complex numbers and $f(x)$ and $g(x)$ are any input functions. If an input is decomposed into a weighted sum of elementary functions, whose related outputs

can easily be determined, the output of a linear system to this input is just the weighted sum of the elementary outputs. This fact is called the *principle of superposition*.

The sampling property of the Dirac delta (A.9) expresses $f(x)$ as a linear combination of weighted and displaced delta functions. So here the delta functions act as the elementary functions of the decomposition. The response $g(x) = L\{f(x)\}$ of a linear system to the decomposed input $f(x)$ is

$$\begin{aligned} g(x) = L\{f(x)\} &= L \left\{ \int_{-\infty}^{\infty} f(x') \delta(x - x') dx' \right\} \\ &= \int_{-\infty}^{\infty} f(x') L\{\delta(x - x')\} dx'. \end{aligned} \quad (\text{A.22})$$

Here we have taken the $f(x')$ as the weighting factors and extended the linearity property to the continuous case, say from the sum to the integral.

If the response of the system to a Dirac delta is expressed as

$$h(x, x') = L\{\delta(x - x')\} \quad (\text{A.23})$$

we can relate the input and output of the linear system by the so called *superposition integral*

$$g(x) = \int_{-\infty}^{\infty} f(x') h(x, x') dx'. \quad (\text{A.24})$$

Since the Dirac delta alone is used to describe an impulse, the function h is called the *impulse response*. In optics the equivalent to an impulse is a point, therefore the h describing the system that images this point is called a *point spread function*. The linear system now is completely characterized by the responses to the unit impulses for all locations of these impulses in the input plane.

A further important class of systems is that of the invariant systems. A *shift-invariant*, also called *space-invariant* or *isoplanatic system*, L fulfills

$$L\{f(x - x')\} = g(x - x') \quad (\text{A.25})$$

where $g(x) = L\{f(x)\}$ and x' can take any value. For a linear system described by the impulse response $h(x, x')$ the shift invariance gives

$$h(x, x') = h(x - x'). \quad (\text{A.26})$$

For different excitation points x' and response points x the impulse response only depends on the distance $x - x'$ between, but not on the specific location of these points on the x -axis. In this way the linear shift-invariant system is completely characterized by the function $h(x)$ depending on a single variable.

The superposition integral (A.24) now takes the simple form

$$g(x) = \int_{-\infty}^{\infty} f(x') h(x - x') dx'. \quad (\text{A.27})$$

The operation on two functions expressed on the right-hand side of (A.27) is called a *convolution* and is written shortly by

$$f(x) \star h(x) = \int_{-\infty}^{\infty} f(x') h(x - x') dx'. \quad (\text{A.28})$$

The integrand in (A.27) is the product of $f(x')$ and $h(x')$ with the latter shifted by x giving $h(x' - x)$ and then rotated by 180° yielding $h(x - x')$. The calculation of the convolution of a triangular pulse $f(x) = \{x \text{ for } x \in [0., 1.], 2 - x \text{ for } x \in [1., 2.], 0. \text{ elsewhere}\}$ and a rectangular pulse $h(x) = \{1 \text{ for } |x| < 0.25, 0. \text{ elsewhere}\}$ is illustrated in Fig. A.3. Figures A.3a and b display the functions $f(x)$ and $h(x)$, and the shaded areas in Figs. A.3c

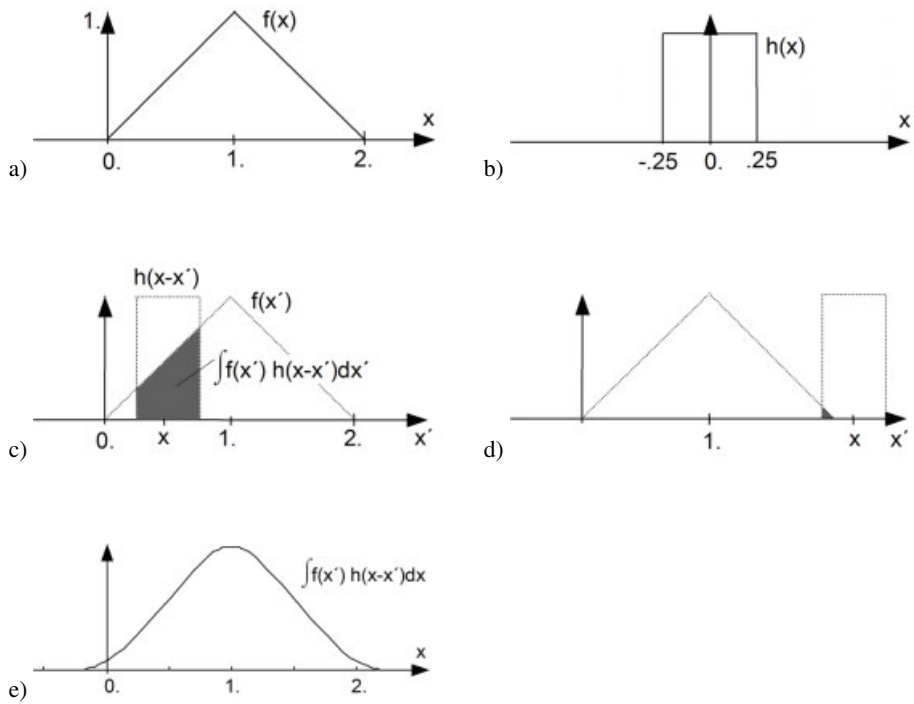


Figure A.3: Calculation of convolution.

and d indicate the values of the convolution for the specific x . Figure A.3d shows that even for $x > 2$, where $f(x) = 0$ and $h(x) = 0$, there is still a non-vanishing convolution. In fact $f(x) \star h(x)$ in this case has non-vanishing values in the range $-0.25 < x < 2.25$. The result shown in Fig. A.3e indicates that the rectangular pulse acts as a low-pass filter smearing out the sharp edges of the triangle. The 180° rotation is not explicitly shown because in this example $h(x)$ is an even function.

The convolution operation has a number of useful properties such as *commutativity*

$$f(x) \star g(x) = g(x) \star f(x), \quad (\text{A.29})$$

associativity

$$[f(x) \star g(x)] \star h(x) = f(x) \star [g(x) \star h(x)], \quad (\text{A.30})$$

and *distributivity*

$$f(x) \star [g(x) + h(x)] = [f(x) \star g(x)] + [f(x) \star h(x)]. \quad (\text{A.31})$$

Extremely useful is the *convolution theorem* which states that the Fourier transform of a convolution is the product of the individual Fourier transforms

$$\mathcal{F}\{f(x) \star g(x)\} = \mathcal{F}\{f(x)\} \cdot \mathcal{F}\{g(x)\}. \quad (\text{A.32})$$

This theorem allows one to replace the often tedious operation of convolution by the much more simpler and more economic operations of Fourier transform and multiplication $f(x) \star g(x) = \mathcal{F}^{-1}\{\mathcal{F}\{f\} \cdot \mathcal{F}\{g\}\}$.

The linear shift-invariant system now can be characterized by its impulse response $h(x)$ with which the input function is convolved, or by the function $H(\xi) = \mathcal{F}\{h(x)\}$, the Fourier transform of the input is multiplied with to yield the Fourier transform of the result. The function $H(\xi)$ is called the system's *transfer function*. In other words, a harmonic input of complex amplitude $F(\xi)$ produces a harmonic output of the same spatial frequency with complex amplitude $G(\xi) = F(\xi) \cdot H(\xi)$. Either of the impulse response or the transfer function characterizes the linear shift-invariant system completely and enables us to determine the output corresponding to an arbitrary input.

A concept for analyzing mutual relationships or similarities between two deterministic as well as probabilistic functions is *correlation analysis*. Let $f(x)$ and $g(x)$ be two real- or complex-valued functions, then their *cross-correlation function* is defined as

$$\begin{aligned} \gamma_{fg}(x) &= \int_{-\infty}^{\infty} f^*(x' - x)g(x') dx' \\ &= \gamma_{gf}^*(-x). \end{aligned} \quad (\text{A.33})$$

It is the average product of f and g for each shift x of the one relative to the other. Note that for real functions the cross correlation differs from the convolution in that before taking the product of the two mutually shifted functions no 180° rotation is performed.

The analog to the convolution theorem now reads

$$\mathcal{F}\{\gamma_{fg}(x)\} = \mathcal{F}\{f(x)\}^* \cdot \mathcal{F}\{g(x)\} \quad (\text{A.34})$$

which allows the calculation of the correlation by $\gamma_{fg}(x) = \mathcal{F}^{-1}\{\mathcal{F}\{f\}^* \cdot \mathcal{F}\{g\}\}$. The $*$ here denotes the complex conjugate.

If both function agree, we get the *autocorrelation function*

$$\begin{aligned} R(x) &= \int_{-\infty}^{\infty} f^*(x' - x)f(x') dx' \\ &= \int_{-\infty}^{\infty} f(x' + x)f^*(x') dx' \end{aligned} \quad (\text{A.35})$$

which indicates how much a function matches its own shifted replicas. The autocorrelation plays an important role in the investigation of periodic and of random functions. It is always even and has its maximum at $x = 0$. The *autocorrelation theorem* states that

$$\int_{-\infty}^{\infty} R(x) dx = \left[\int_{-\infty}^{\infty} f(x') dx' \right]^2. \quad (\text{A.36})$$

Every function has a unique autocorrelation function but the converse is not true. From (A.34) directly follows the *Wiener-Khinchine theorem* which is expressed as

$$\mathcal{F}\{R(x)\} = \mathcal{F}\{f(x) \star f(-x)\} = |F(u)|^2. \quad (\text{A.37})$$

For deterministic functions $f(x)$, $|F(u)|^2$ is the *power spectrum*. The Wiener-Khinchine theorem states that the power spectrum is the Fourier transform of the autocorrelation function.

A.6 Fourier Analysis of Sampled Functions

In technical applications, e. g. in measurements, we have no access to the continuous functions, but only to sampled values of a signal at discrete temporal or spatial instants. Furthermore we cannot measure from the infinite past to the infinite future, in the same way in the spatial domain we cannot record signals of infinite extent. Therefore we have to deal with a finite number of discrete signals. In the following the Fourier theory is extended to discrete sampled signals as well as to finite signals.

Let a continuous function $f(x)$ be defined for $X_1 \leq x \leq X_2$. This function can be expressed as

$$f(x) = \sum_{k=-\infty}^{\infty} a_k e^{i2\pi k f_0 x} \quad (\text{A.38})$$

where $f_0 = 1/X$ with $X = X_2 - X_1$. Here $f(x)$ is represented by an infinite linear combination of sines and cosines, the so called *sinusoids*, which oscillate with $k f_0$ cycles per unit of x .

$$e^{i2\pi k f_0 x} = \cos(2\pi k f_0 x) + i \sin(2\pi k f_0 x). \quad (\text{A.39})$$

The frequencies of all sinusoids are integer multiples of the *fundamental frequency* f_0 , the first four components of which are displayed in Fig. A.4. Each coefficient a_k is called the

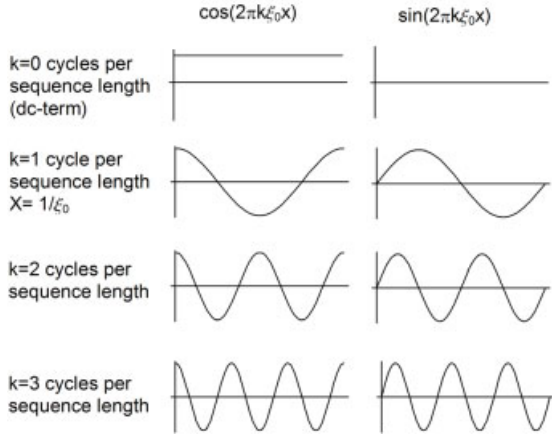


Figure A.4: First four components of a Fourier series.

complex amplitude of the k -th component, and these coefficients are obtained by

$$a_k = \frac{1}{X} \int_{X_1}^{X_2} f(x) e^{-i2\pi k \frac{x}{X}} dx. \quad (\text{A.40})$$

The representation (A.38) with the a_k defined by (A.40) is called the *Fourier series*.

The difference between the continuous Fourier transform and the Fourier series is that we have all frequencies between $-\infty$ and ∞ in the sinusoids of the continuous Fourier transform but only integer multiples of the fundamental frequency f_0 for the Fourier series. The series representation is contained in the continuous Fourier transform representation especially if $f(x)$ is assumed to be zero outside $[X_1, X_2]$, which restricts the range of integration in (A.1). The additional information in $F(\xi)$ for $\xi \neq kf_0$ in the continuous reconstruction (A.2) is necessary to constrain the values of the reconstructed $f(x) = \mathcal{F}^{-1}\{F(\xi)\}$ outside the interval $[X_1, X_2]$. If we reconstruct $f(x)$ only from the a_k by (A.38) we will of course obtain the correct values of $f(x)$ within $[X_1, X_2]$, but we will get *periodic replications* of the original $f(x)$ outside the interval $[X_1, X_2]$. Contrarily, using $F(\xi)$ and (A.2) for reconstruction, we will obtain $f(x)$ exactly within $[X_1, X_2]$ and the correct zero everywhere outside.

As in the continuous case a discrete function may also be given a frequency domain representation. Let $\{f_n\}$ be the discrete samples of a continuous function $f(x)$ at all points $n\Delta x$, spaced by the sampling interval Δx

$$f_n = f(n\Delta x) \quad n = \dots, -1, 0, 1, \dots \quad (\text{A.41})$$

Then the *discrete Fourier transform* is defined by

$$F(\xi) = \sum_{n=-\infty}^{\infty} f_n e^{-i2\pi\xi n \Delta x}. \quad (\text{A.42})$$

From the discrete Fourier transform the function $f(x)$ can be recovered by

$$f(n\Delta x) = \frac{\Delta x}{2\pi} \int_{-\pi/\Delta x}^{\pi/\Delta x} F(\xi) e^{i2\pi\xi n\Delta x} d\xi \quad (\text{A.43})$$

which gives the discrete function $f_n = f(n\Delta x)$ by integration over weighted sinusoids.

Although this discrete but still infinite Fourier transform is useful for many theoretical discussions, for practical purposes the following *finite Fourier transform* is actually calculated. Let the discrete function

$$f(0), f(\Delta x), f(2\Delta x), \dots, f((N-1)\Delta x) \quad (\text{A.44})$$

be N elements long and be written as $\{f_0, f_1, f_2, \dots, f_{N-1}\}$. Then the finite Fourier transform is defined as

$$F_k = \frac{1}{N} \sum_{n=0}^{N-1} f_n e^{-i2\pi \frac{kn}{N}} \quad k = 0, 1, 2, \dots, N-1. \quad (\text{A.45})$$

The F_k are samples of the continuous function $F(\xi)$ of (A.42) for $\xi = \frac{k}{N\Delta x}$ with $k = 0, 1, \dots, N-1$, as can be proven by rewriting (A.45) with these ξ . This implies that if (A.45) is used to compute the frequency domain representation of a discrete function, a sampling interval of Δx in the x -domain corresponds to a sampling interval of $\Delta\xi = 1/(N\Delta x)$ in the frequency domain.

If $f(x)$ is a real function, or in the finite case f_n is a real sequence, then the d.c.-term F_0 is real. It is calculated by

$$F_0 = \frac{1}{N} \sum_{n=0}^{N-1} f_n. \quad (\text{A.46})$$

The value F_1 stands for the sinusoid of 1 cycle per sequence length. The value F_k represents k cycles per sequence length, as long as $k \leq N/2$. For higher values we must recognize the periodicity property $F_{-k} = F_{N-k}$, so that for $k > N/2$ the F_k represents $-(N-k)$ cycles per sequence length. But since an output where the negative axis information follows the positive axis information is somewhat unnatural to look at, the output should be rearranged. Normally looking finite Fourier transform outputs with the d.c.-component at the center, as for the well known optical diffraction patterns in the Fraunhofer region, can be produced by merely reordering the result or by multiplying the sequence to be transformed f_n with $(-1)^n$

$$f'_n = f_n (-1)^n \quad (\text{A.47})$$

prior to calculating the finite Fourier transform.

The *inverse finite Fourier transform* is

$$f_n = \sum_{k=0}^{N-1} F_k e^{i2\pi \frac{kn}{N}}. \quad (\text{A.48})$$

Both (A.45) and (A.48) define sequences that are periodically replicated due to the discrete nature. Since $e^{i(2\pi/N)Nm} = 1$ for all integers m we see that

$$\begin{aligned} F_{Nm+i} &= F_i \quad \text{for all } m \in \mathbb{Z} \\ \text{and } f_{Nm+i} &= f_i \quad \text{for all } m \in \mathbb{Z}. \end{aligned} \quad (\text{A.49})$$

The four types of Fourier transforms are summarized in Table A.3 [785].

Table A.3: Types of Fourier transforms.

		Continuous Space/Time	Discrete Space/Time
Continuous Frequency	Name: Forward: Inverse: Periodicity:	Continuous Fourier Transform $F(\xi) = \int_{-\infty}^{\infty} f(x)e^{-i2\pi\xi x} dx$ $f(x) = \frac{1}{2\pi} \int_{-\infty}^{\infty} F(\xi)e^{i2\pi\xi x} d\xi$ none	Discrete Fourier Transform $F(\xi) = \sum_{n=-\infty}^{\infty} f_n e^{-i2\pi\xi n \Delta x}$ $f_n = \frac{\Delta x}{2\pi} \int_{-\pi/\Delta x}^{\pi/\Delta x} F(\xi)e^{i2\pi\xi n \Delta x} d\xi$ $F(\xi) = F(\xi + m(2\pi/\Delta x))$
Discrete Frequency	Name: Forward: Inverse: Periodicity:	Fourier Series $F_k = \frac{1}{X} \int_{X_1}^{X_2} f(x)e^{-i2\pi k \frac{x}{X}} dx$ $f(x) = \sum_{k=-\infty}^{\infty} F_k e^{i2\pi k \frac{x}{X}}$ $f(x) = f(x + mX)$	Finite Fourier Transform $F_k = \frac{1}{N} \sum_{n=0}^{N-1} f_n e^{-i2\pi \frac{kn}{N}}$ $f_n = \sum_{k=0}^{N-1} F_k e^{i2\pi \frac{kn}{N}}$ $f_i = f_{i+Nm} \quad \text{and} \quad F_i = F_{i+Nm}$

A.7 The Sampling Theorem and Data Truncation Effects

In the definitions of the discrete infinite as well as finite Fourier transforms a sequence of numbers $\{f_n\}$ was used to approximate a continuous function $f(x)$. The question arises as to how finely must the data be sampled in order to accurately represent the original signal. The answer is given by the *sampling theorem*: If a signal $f(x)$ has a Fourier transform $F(\xi)$ such that

$$F(\xi) = 0 \quad \text{for } \xi \geq \frac{\xi_N}{2} \quad (\text{A.50})$$

then sampling of f at any rate greater than ξ_N is sufficient in order to ensure an exact reconstruction of $f(x)$ from the samples. That means if Δx is the interval between consecutive samples, it must be $2\pi/\Delta x > \xi_N$. Equation (A.50) implies that the sampling frequency ξ must be higher than twice the largest frequency contained in $F(\xi)$, which is estimated to ξ_N . The frequency ξ_N is known as the *Nyquist rate* or *Nyquist frequency*. Functions $f(x)$ for

which an upper bound of frequencies as in (A.50) exists and which have finite energy, i. e. the energy E defined in (A.18) fulfills $E < \infty$, are called *band-limited functions*.

To consider the consequences of sampling at below the Nyquist rate, the sampled version $f_s(x)$ of a function $f(x)$ is expressed by a multiplication of the original continuous signal $f(x)$ with the sampling function $h(x)$ given by

$$h(x) = \sum_{n=-\infty}^{\infty} \delta(x - n\Delta x). \quad (\text{A.51})$$

Since $h(x)$ is periodic, its Fourier transform is computed via the Fourier series to

$$H(\xi) = \frac{2\pi}{\Delta x} \sum_{n=-\infty}^{\infty} \delta\left(\xi - \frac{2\pi n}{\Delta x}\right). \quad (\text{A.52})$$

Converting the multiplication into a convolution in the frequency domain we get the transform

$$F_s(\xi) = \frac{2\pi}{\Delta x} \sum_{n=-\infty}^{\infty} F\left(\xi - \frac{2\pi n}{\Delta x}\right) \quad (\text{A.53})$$

which is a sum of shifted functions $F(\xi)$. The formula of the Fourier transform of a function f sampled at $n\Delta x$ is

$$F_s(\xi) = \frac{2\pi}{\Delta x} \sum_{n=-\infty}^{\infty} f(n\Delta x) e^{-i2\pi\xi n\Delta x}. \quad (\text{A.54})$$

Figure A.5 shows the results of over- and undersampling. Figure A.5a gives the amplitude spectrum $|F(\xi)|$, Fig. A.5b displays the result after sampling at a rate faster than the Nyquist rate, i. e. $\Delta x < 2\pi/\xi_N$, meaning that the sampling theorem is fulfilled. Figure A.5c is the spectrum after sampling at exactly the Nyquist rate, and Fig. A.5d shows the overlap resulting from sampling at less than the Nyquist rate. An inverse Fourier transform of the spectrum in Fig. A.5d would produce an erroneous signal, the error is known generally as *aliasing* or as *moiré pattern* in two-dimensional image processing.

In many applications we have only a finite number of samples over a finite time or space while the signal extends beyond the limits of this interval. Nevertheless we assume that all the significant transitions of the signal occur in this base interval. Let the signal $f_n = f(x_n)$ be defined for all n . The true discrete Fourier transform of this signal is

$$F(\xi) = \sum_{n=-\infty}^{\infty} f_n e^{-i2\pi\xi n\Delta x}. \quad (\text{A.55})$$

Suppose we take only an N -element transform meaning that of all the $x_n = n\Delta x$ we will retain only those going from $-(N/2 - 1)\Delta x$ to $(N/2)\Delta x$. It is assumed that N is even. The discrete Fourier transform of the *truncated data* is

$$\begin{aligned} F'(\xi) &= \sum_{n=-(N/2-1)}^{N/2} f_n e^{-i2\pi\xi n\Delta x} \\ &= \sum_{n=-\infty}^{\infty} f_n h_N(n) e^{-i2\pi\xi n\Delta x} \end{aligned} \quad (\text{A.56})$$

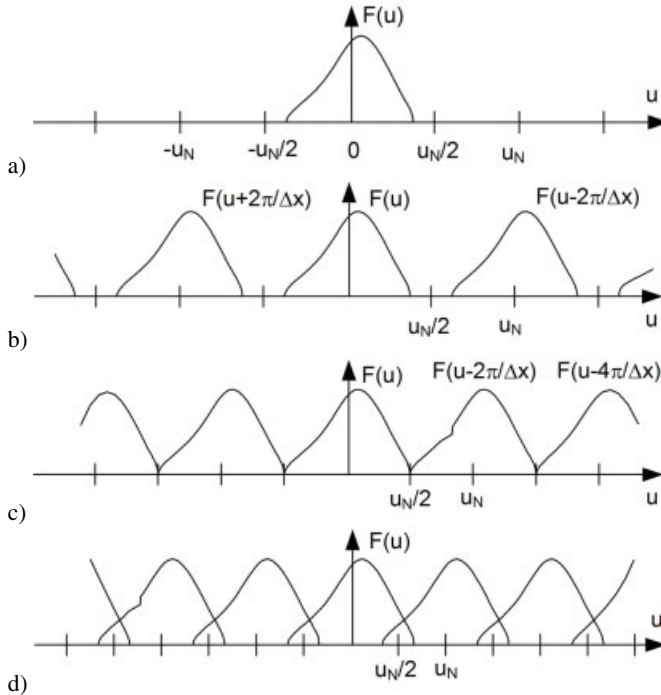


Figure A.5: Examples of over- and undersampling.

where $h_N(n)$ is the function that is equal to 1 for n between $-(N/2 - 1)$ and $N/2$, and zero outside. The transform of $h_N(n)$ is

$$\begin{aligned}
 H_N(\xi) &= \sum_{n=-(N/2-1)}^{N/2} e^{-i2\pi\xi n \Delta x} \\
 &= e^{-i2\pi\xi \frac{\Delta x}{2}} \frac{\sin \frac{2\pi\xi N \Delta x}{2}}{\sin \frac{2\pi\xi \Delta x}{2}}. \tag{A.57}
 \end{aligned}$$

By the convolution theorem we have

$$F'(\xi) = \frac{\Delta x}{2\pi} F(\xi) * H_N(\xi). \tag{A.58}$$

The function $H_N(\xi)$ is displayed in Fig. A.6, it illustrates the nature of distortion introduced by *data truncation*.

The interpretation of $H_N(\xi)$ leads to the general statement that a function which vanishes outside a finite interval will yield a smooth transform with infinite extent: A function of bounded support cannot be band-limited and vice versa.

Closely related to the truncation effect is the *leakage* effect. Consider a periodic continuous signal that is truncated to a finite interval. If the length of the interval is not an integer

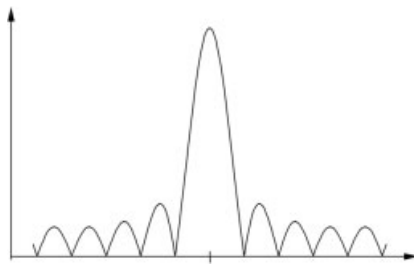


Figure A.6: Convolution function resulting from data truncation.

multiple of the period, a periodic continuation by putting the left end of the interval at the right end would produce discontinuities and would destroy the original periodicity. The components of $f(x)$ not periodic over the interval appear to leak out into portions of the spectrum adjacent to the correct spatial frequency value.

The truncation of a function to an interval can be represented by multiplication with a *rectangular window function* $w_r(x)$

$$w_r(x) = \begin{cases} 1 & : \text{for } x \in [x_1, x_2] \\ 0 & : \text{elsewhere.} \end{cases} \quad (\text{A.59})$$

A method for reducing the error by leakage is the smoothing of the sharp corners of $w_r(x)$. Thus the function $f(x)$ can be multiplied by a smooth window $w(x)$ before calculating the finite Fourier transform. Often used is the so called *Hanning window* $w_H(x)$

$$w_H(x) = \frac{1}{2} \left(1 - \cos \frac{2\pi(x - x_1)}{x_2 - x_1} \right). \quad (\text{A.60})$$

Its effect is shown in Fig. A.7. In Fig. A.7a we have a continuous signal and the correspond-

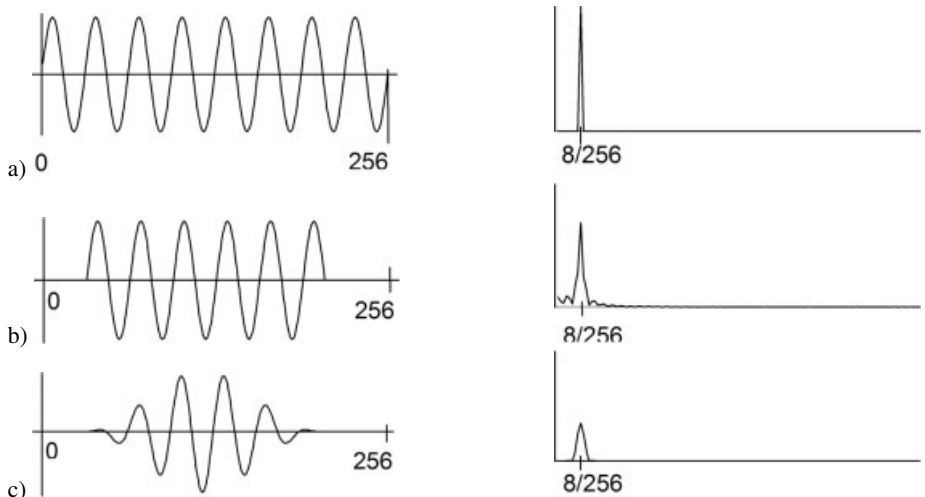


Figure A.7: Reduction of leakage by Hanning window.

ing amplitude spectrum. The leakage by the rectangular window is displayed in Fig. A.7b, where there are sidelobes besides the peak at frequency 8/256 in the amplitude spectrum. In Fig. A.7c we recognize the significant reduction of leakage by the Hanning window. Although the main peak is broadened slightly, the sidelobes are suppressed significantly. Other window functions are known, like the Hamming, Bartlett, and cosine-taper window, to name just a few.

The multiplication of a function $F(\xi)$ in the frequency domain with a window function $W(\xi)$ which is zero for $|\xi| > \xi_W$ also leads to consequences: The inverse transform of $[F \cdot W](\xi)$ is a band-limited approximation to $f(x)$, the inverse transform of the transform $F_s(\xi)$ of a sampled function $f(n\Delta x)$ multiplied with the window $[F_s \cdot W](\xi)$ gives an interpolated version of $f(n\Delta x)$. If the function $f(x)$ is band-limited and sampled with Δx fulfilling the sampling theorem, then a window $W(\xi)$ with $W(\xi) = 0$ for $|\xi| > 1/(2\Delta x)$ will cause no disturbing effects. Applying the same window to the transform of a function which is not band-limited will give rise to aliasing.

From the above discussion it follows that a band-limited function cannot be perfectly space-limited and vice-versa. However in practice there are functions which are band-limited and have significant values only over a finite region. Then it is possible to represent this function with good accuracy by a finite number of sample points [160]. Let such a function $g(x)$ have significant values in the region $-L \leq x < L$ and $g(x)$ is sampled, in accord with the sampling theorem, with spacing $\Delta x = \frac{1}{2B}$. Then the total number M of significant samples required to represent $g(x)$ is

$$M = 4LB \quad (\text{A.61})$$

which is called the *space-bandwidth product* of function g . This value can be regarded as the number of degrees of freedom of function g or as a measure of its complexity. The ability of an optical system to accurately handle inputs and outputs having large space-bandwidth products is a measure of performance, and is directly related to the quality of the system [160].

A.8 Interpolation and Resampling

Discrete signal interpolation is a common operation in digital signal and image processing. In the context of digital holography it is required e. g. when translating a digital hologram by a fraction of a pixel period, or in transforming a digital hologram of $N_1 \times M_1$ pixels into one of $N_2 \times M_2$ pixels. In both cases we have to apply first an interpolation from the discrete values followed by a resampling.

If the spacing of the sampling points obeys the *Whittaker-Shannon sampling theorem* then this theorem implies that exact recovery of a band-limited function can be achieved from the sampled values by injecting at each sampling point an interpolating sinc-function. Each of these interpolating sinc-functions is weighted according to the sampled value at the corresponding point [160]. Let Δx be the sampling interval in one dimension and $\{a_n\}$ the sampled values, then the continuous band-limited signal $a(x)$ is restored by

$$a(x) = \sum_{n=-\infty}^{\infty} a_n \operatorname{sinc}\left(\frac{x}{\Delta x} - n\right) = \sum_{n=-\infty}^{\infty} a_n \frac{\sin[\pi(\frac{x}{\Delta x} - n)]}{\pi(\frac{x}{\Delta x} - n)}. \quad (\text{A.62})$$

Normally we have only a finite number of N samples a_0, a_1, \dots, a_{N-1} , then we interpolate by

$$a(x) = \sum_{n=0}^{N-1} a_n \frac{\sin \left[\frac{\pi M}{N} \left(\frac{x}{\Delta x} - n \right) \right]}{N \sin \left[\frac{\pi}{N} \left(\frac{x}{\Delta x} - n \right) \right]} = \sum_{n=0}^{N-1} a_n \text{sincd} \left[M; N; \pi \left(\frac{x}{\Delta x} - n \right) \right]. \quad (\text{A.63})$$

Here we have defined the discrete sinc-function $\text{sincd} [M; N; x]$ in which the parameter M can take values $M \in \{N-1, N, N+1\}$.

The commonly used method of discrete sinc-interpolation is zero-padding. It is implemented by padding the discrete Fourier spectrum of the signal with an appropriate number of zeros and performing the inverse transformation of the padded spectrum. This leads to a signal of kN values instead of the original N values, then each k -th value is taken of the kN values. This approach exhibits several shortcomings and restrictions, especially it requires an amount of cumbersome programming, computation, and memory. But all these obstacles can be circumvented by an elegant algorithm presented by Yaroslavsky [786, 787]. This algorithm is based on the shifted discrete Fourier-transform (SDFT) and its inverse (SDFT^{-1})

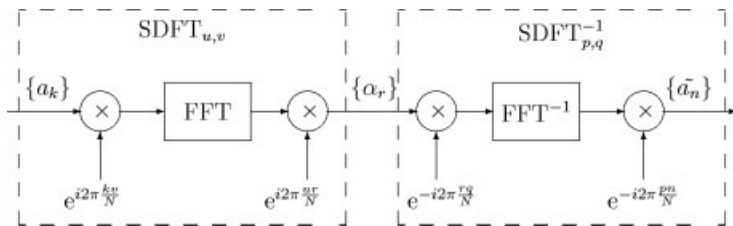
$$\text{SDFT}_{u,v}\{a_n\} = \frac{1}{\sqrt{N}} \sum_{n=0}^{N-1} a_n e^{i2\pi \frac{nv}{N}} e^{i2\pi \frac{(n+u)r}{N}} = \alpha_r \quad (\text{A.64})$$

$$\text{SDFT}_{u,v}^{-1}\{\alpha_r\} = \frac{1}{\sqrt{N}} \sum_{n=0}^{N-1} \alpha_r e^{-i2\pi \frac{nv}{N}} e^{i2\pi \frac{(n+u)r}{N}} = a_r. \quad (\text{A.65})$$

Here the u, v and p, q are the shifts in the signal and in the spectral range, respectively, which are fractions of the discretization intervals. The concept of interpolation now is that the SDFT and its inverse can be performed using different shifts. The signal flow



is implemented by performing the following multiplications and Fourier transforms



In this form with $M = N$ and the desired shift p this procedure results in a signal of N values, which are shifted by $p\Delta x$ with respect to the original $\{a_n\}$ and are found as the real parts of $\{\tilde{a}_n\}$. Further details on this useful algorithm are given in [788].

A.9 Two-Dimensional Image Processing

For processing images like digital holograms or holographic interference patterns some of the aforementioned signal processing concepts are extended to two dimensions in the following. A *picture* or *image* is nothing more than a real-valued function $f(x, y)$ of two *spatial coordinates*. The values of this function can be interpreted as *gray-values*, so $f(x, y)$ gives the brightness distribution of, say, a black and white photograph.

Let L be an operation that maps an image f into another image $L[f]$. L is called *linear* if for all constants a, b and all images f, g

$$L[af + bg] = aL[f] + bL[g]. \quad (\text{A.66})$$

For the analysis of two-dimensional linear operations we need the concept of a *point source*, the two-dimensional equivalent to the delta impulse. Over the *two-dimensional rectangular function*

$$\text{rect}(x, y) = \begin{cases} 1 & : \text{ for } |x| \leq \frac{1}{2} \text{ and } |y| \leq \frac{1}{2} \\ 0 & : \text{ elsewhere} \end{cases} \quad (\text{A.67})$$

and

$$\delta_n(x, y) = n^2 \text{rect}(nx, ny) \quad n = 1, 2, \dots \quad (\text{A.68})$$

the point source δ is defined by

$$\delta(x, y) = \lim_{n \rightarrow \infty} \delta_n(x, y) \quad (\text{A.69})$$

which has the properties known from one dimension

$$\int_{-\infty}^{\infty} \int_{-\infty}^{\infty} \delta(x, y) dx dy = 1 \quad (\text{A.70})$$

and

$$\int_{-\infty}^{\infty} \int_{-\infty}^{\infty} f(x, y) \delta(x - a, y - b) dx dy = f(a, b). \quad (\text{A.71})$$

Although the same notation except of the two variables is used for the impulse and the point source, no confusion should arise.

A linear operation L is called *shift invariant* if

$$L[f(x - a, y - b)] = L[f](x - a, y - b); \quad (\text{A.72})$$

in other words, if the input f is shifted by (a, b) then the output $L[f]$ is also merely shifted by (a, b) . Using the representation (A.71) and the linearity of L we get

$$\begin{aligned} L[f(x, y)] &= L \left[\int_{-\infty}^{\infty} \int_{-\infty}^{\infty} f(x', y') \delta(x' - x, y' - y) dx' dy' \right] \\ &= \int_{-\infty}^{\infty} \int_{-\infty}^{\infty} f(x', y') L[\delta(x' - x, y' - y)] dx' dy' \\ &= \int_{-\infty}^{\infty} \int_{-\infty}^{\infty} f(x', y') h_L(x' - x, y' - y) dx' dy' \end{aligned} \quad (\text{A.73})$$

where the last equality uses the shift invariance of L , and h_L denotes the response of δ under L , the *point spread function*. The last expression in (A.73) defines the *two-dimensional convolution* $L[f] = f \star h_L = h_L \star f$. The *two-dimensional Fourier transform* $F(\xi, \eta)$ of the image $f(x, y)$ is defined by

$$F(\xi, \eta) = \int_{-\infty}^{\infty} \int_{-\infty}^{\infty} f(x, y) e^{-i2\pi(\xi x + \eta y)} dx dy. \quad (\text{A.74})$$

The two-dimensional Fourier transform can be considered as a one-dimensional transform with respect to, say, x , performed for all y , followed by the one-dimensional transform with respect to y , performed for all x

$$F(\xi, \eta) = \int_{-\infty}^{\infty} \left[\int_{-\infty}^{\infty} f(x, y) e^{-i2\pi\xi x} dx \right] e^{-i2\pi\eta y} dy. \quad (\text{A.75})$$

This *separability* is used in the *two-dimensional Fourier transform algorithm* where first all rows are replaced by their one-dimensional transforms and then all columns are transformed one-dimensionally or vice versa and the one-dimensional transforms are calculated by the effective FFT-procedure, see Section A.10. The discrete finite two-dimensional Fourier transform is

$$F(k, l) = \frac{1}{N^2} \sum_{m=0}^{N-1} \left[\sum_{n=0}^{N-1} f(n, m) W_N^{kn} \right] W_N^{lm} \quad (\text{A.76})$$

with $k = 0, 1, \dots, N - 1$, $l = 0, 1, \dots, N - 1$ numbering the sample points in the spatial frequency domain and $W_N = \exp\{-i2\pi/N\}$.

The properties of the one-dimensional Fourier transform translate to two dimensions in a natural way, some additional properties due to the two dimensions arise. Some of these properties are summarized in Table A.4. Here $f(x, y)$, $f_1(x, y)$, $f_2(x, y)$ are functions in the spatial domain and $F(\xi, \eta)$, $F_1(\xi, \eta)$, $F_2(\xi, \eta)$ are the corresponding transformed functions in the spatial frequency domain. a and b are scalar numbers. (r, Θ) are polar coordinates in the

Table A.4: Properties of the two-dimensional Fourier transform.

Name	Function in the Spatial Domain	Transformed Function in the Spatial Frequency Domain
<i>Linearity</i>	$af_1(x, y) + bf_2(x, y)$	$aF_1(\xi, \eta) + bF_2(\xi, \eta)$
<i>Scaling</i>	$f(ax, by)$	$\frac{1}{ ab } F\left(\frac{\xi}{a}, \frac{\eta}{b}\right)$
<i>Shifting</i>	$f(x - x_0, y - y_0)$ $e^{i2\pi(\xi_0 x + \eta_0 y)} f(x, y)$	$e^{-i2\pi(\xi x_0 + \eta y_0)} F(\xi, \eta)$ $F(\xi - \xi_0, \eta - \eta_0)$
<i>Differentiation</i>	$\left(\frac{\partial}{\partial x}\right)^m \left(\frac{\partial}{\partial y}\right)^n f(x, y)$	$(i2\pi\xi)^m (i2\pi\eta)^n F(\xi, \eta)$
<i>Laplacian</i>	$\nabla^2 f(x, y) = \left(\frac{\partial^2}{\partial x^2} + \frac{\partial^2}{\partial y^2}\right) f(x, y)$	$-4\pi^2(\xi^2 + \eta^2) F(\xi, \eta)$
<i>Rotation</i>	$f(r, \Theta + \alpha)$	$F(p, \phi + \alpha)$
<i>Rotational Symmetry</i>	$f(r, \Theta) = f(r)$	$F(p, \phi) = F(p)$ $= 2\pi \int_0^\infty r f(r) J_0(2\pi rp) dr$
<i>Convolution</i>	$f_1(x, y) * f_2(x, y)$ $f_1(x, y) f_2(x, y)$	$F_1(\xi, \eta) F_2(\xi, \eta)$ $F_1(\xi, \eta) * F_2(\xi, \eta)$
<i>Separability</i>	$f(x, y) = f_1(x) f_2(y)$	$F(\xi, \eta) = F_1(\xi) F_2(\eta)$
<i>Parseval's Theorem</i>	$\int_{-\infty}^{\infty} \int_{-\infty}^{\infty} f_1(x, y) f_2^*(x, y) dx dy = \int_{-\infty}^{\infty} \int_{-\infty}^{\infty} F_1(\xi, \eta) F_2^*(\xi, \eta) d\xi d\eta$	
<i>Conservation of Energy</i>	$\int_{-\infty}^{\infty} \int_{-\infty}^{\infty} f(x, y) ^2 dx dy = \int_{-\infty}^{\infty} \int_{-\infty}^{\infty} F(\xi, \eta) ^2 d\xi d\eta$	

spatial domain and (p, ϕ) polar coordinates in the spatial frequency domain. α is an angular coordinate, x_0, y_0, u_0, v_0 are fixed spatial coordinates and spatial frequencies, respectively. The transform $F(p)$ of the rotationally symmetric function $f(r)$ in line 7 of the table is called a *Hankel transform*. It contains the zero-order *Bessel function* of the first kind J_0 .

If a two-dimensional Fourier transform of $f(x, y)$ is computed as described above (A.76), the zero peak at the spatial frequency $(0, 0)$ will not occur at the center of the array, as one is used to from the Fraunhofer diffraction patterns, but in the upper leftmost corner. A manipulation to force the frequency domain origin to approximately the center of the array (a precise center coordinate component does not exist if N is an even number) is the multiplication of the data with $(-1)^{m+n}$ before the transform

$$f'(m, n) = f(m, n)(-1)^{m+n}. \quad (\text{A.77})$$

The *two-dimensional sampling theorem* states the following [789]: A function $f(x, y)$ whose Fourier transform $F(\xi, \eta)$ vanishes over all but a bounded region in the spatial frequency domain can be reproduced everywhere from its values taken over a lattice of points

$(m(\Delta x_1, \Delta y_1) + n(\Delta x_2, \Delta y_2))$, $m, n = 0, \pm 1, \pm 2, \dots$ in the spatial domain provided the vectors $(\Delta x_1, \Delta y_1)$ and $(\Delta x_2, \Delta y_2)$ are small enough to ensure nonoverlapping of the spectrum $F(\xi, \eta)$ with its images on a periodic lattice of points $(l(\Delta \xi_1, \Delta \eta_1) + k(\Delta \xi_2, \Delta \eta_2))$, $k, l = 0, \pm 1, \pm 2, \dots$ in the spatial frequency domain, where the vectors $(\Delta \xi_i, \Delta \eta_i)$, $i = 1, 2$, depend on the $(\Delta x_i, \Delta y_i)$, $i = 1, 2$, by

$$\Delta x_i \Delta \xi_j + \Delta y_i \Delta \eta_j = \begin{cases} 0 & : i \neq j \\ 1 & : i = j. \end{cases} \quad (\text{A.78})$$

The definition of the sampling lattices over the two vectors reflects the fact that it is not necessary to sample in a rectangular grid. This is illustrated in Fig. A.8. Figure A.8a displays the sampling points in the spatial domain, Fig. A.8b depicts a boundary of the transform $F(\xi, \eta)$ of a band-limited two-dimensional function, and Fig. A.8c shows the nonoverlapping copies of $F(\xi, \eta)$.

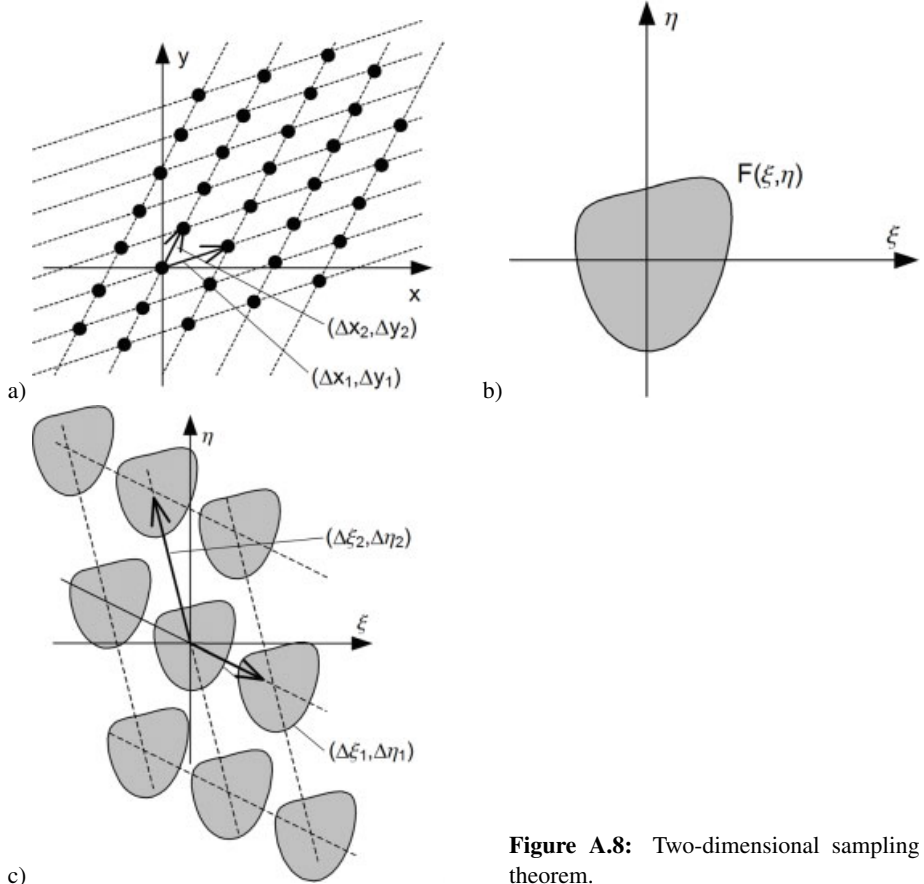


Figure A.8: Two-dimensional sampling theorem.

The effects of sampling without and with violation of the sampling theorem are shown in Figs. A.9 and A.10. The sinusoidal pattern of Fig. A.9a is sampled by discrete points at a rate

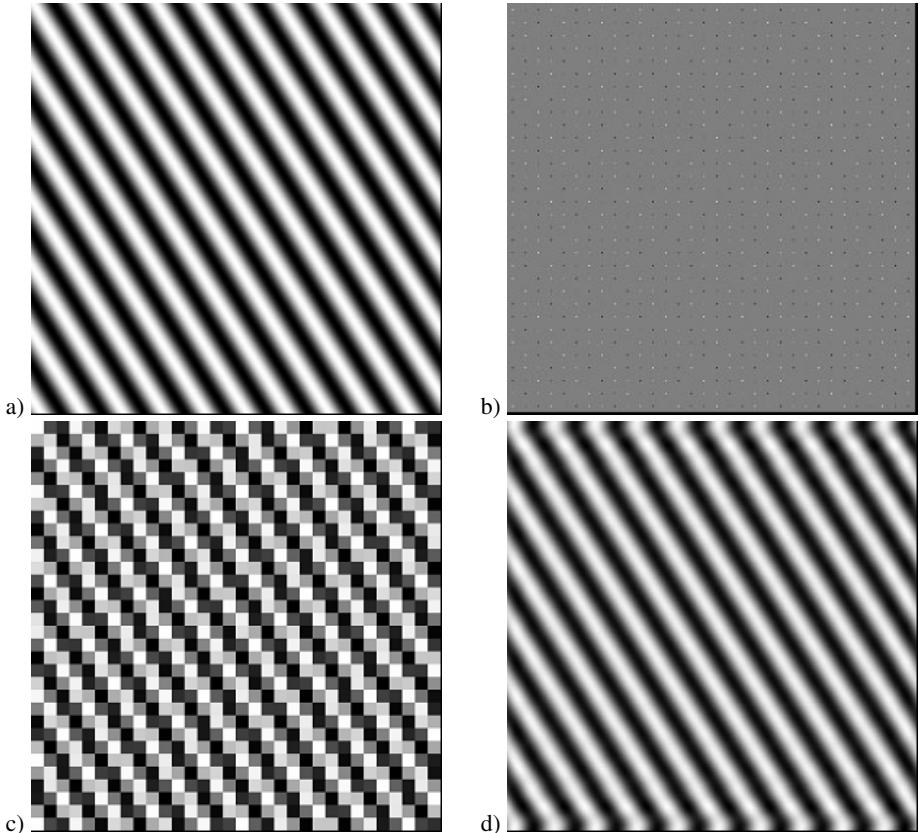


Figure A.9: Sampling above the Nyquist rate.

higher than the Nyquist rate, Fig. A.9b. The area between the samples is displayed in gray, so some samples cannot be recognized since they have intensity gray, too. If the sampled points are spread to squares with constant intensities, we get the pattern of Fig. A.9c. In Fig. A.9d the sampled data of Fig. A.9b are low-pass filtered at the Nyquist rate, which means that all frequencies higher than the Nyquist frequency are suppressed. Direction and frequency of the sinusoid have been reconstructed correctly. We only recognize the leakage effect at the upper and lower edges of Fig. A.9d, due to a non-smooth continuation of the periodic replicas of the original sinusoids.

On the other hand we have a high-frequency sinusoid in Fig. A.10a, which is sampled at the same rate as that of Fig. A.9. Figure A.10b gives the sinusoid sampled at a rate much lower than the Nyquist rate. The expanded sampled points are displayed in Fig. A.10c. In Fig. A.10d we see the sampled data low-pass filtered at the Nyquist rate of the pattern of Fig. A.10a, but the direction and frequency of the sinusoid have changed due to aliasing.

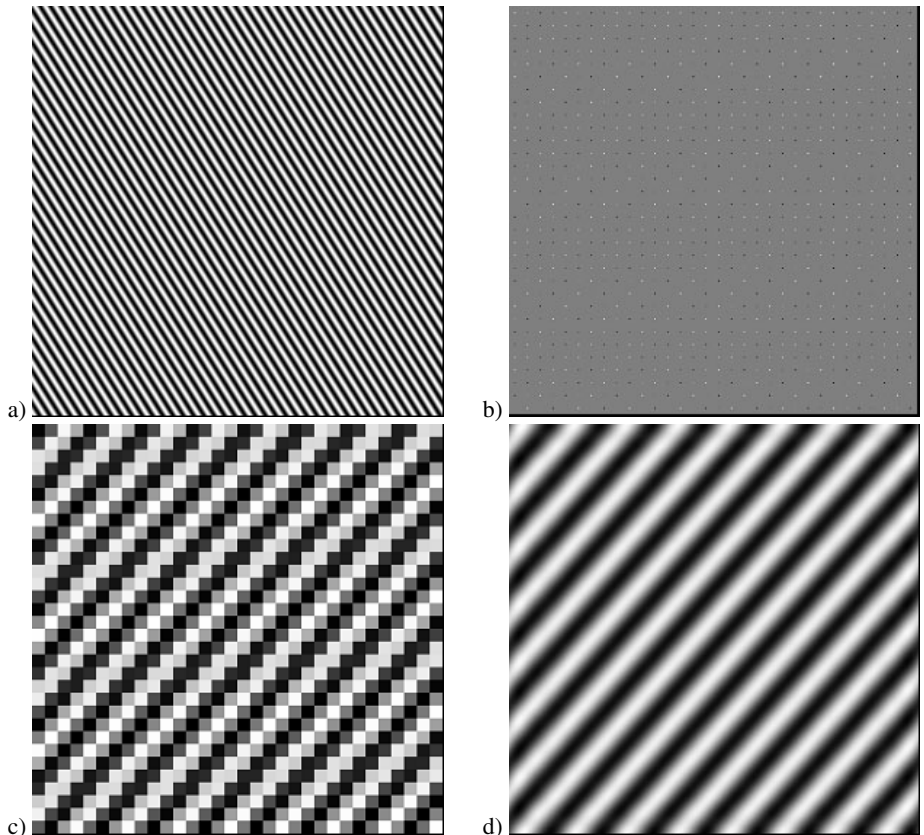


Figure A.10: Sampling below the Nyquist rate.

A.10 The Fast Fourier Transform

The growing importance of the Fourier transform in practical applications of digital signal processing over the last decades is mainly based on the effective algorithm to compute the finite Fourier transform known as the *fast Fourier transform, FFT*.

A simple measure for the amount of computations in (A.45) is the number of complex multiplications. For the N elements of F_k there are N sums each with N products, so that for a straightforward determination of the one-dimensional finite discrete Fourier transform N^2 products would be required to compute the whole set $\{F_k : k = 0, 1, \dots, N-1\}$. To simplify the notation, in the finite Fourier transform (A.45) let W_N represent the invariant part of the exponential term, i. e.

$$W_N = e^{-i\frac{2\pi}{N}} \quad (\text{A.79})$$

so that (A.45) now becomes

$$F_k = \frac{1}{N} \sum_{n=0}^{N-1} f_n W_N^{kn} \quad k = 0, 1, \dots, N-1. \quad (\text{A.80})$$

The cyclic character of the coefficients W_N^{kn} is illustrated in Fig. A.11 for $N = 8$. The

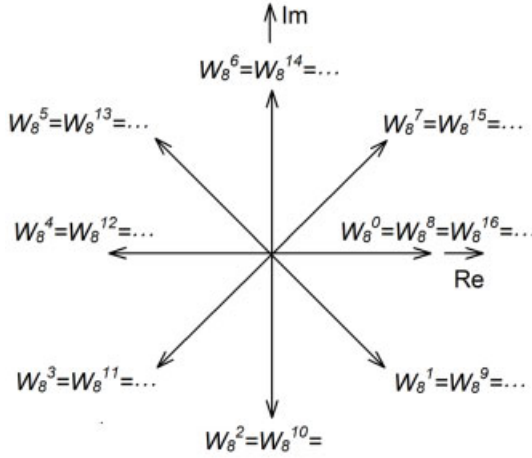


Figure A.11: Equivalence of different powers of W_N for $N = 8$.

redundancy shown in this representation, namely the equality of many different powers of W_N and half of all powers differing only by the sign, is used in the FFT algorithm in an intelligent way to save complex multiplications. Especially if N is a power of 2, the necessary computations are subdivided into basic transformations to the base $N = 2$. The corresponding signal-flow diagram for $N = 2$ often is called a *butterfly*, Fig. A.12. A possible signal flow graph for calculation of an 8-point FFT is shown in Fig. A.13.

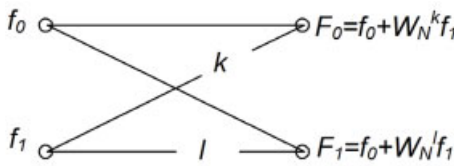


Figure A.12: Basic butterfly for FFT.

A careful analysis of the *FFT algorithm* shows that now at most only $(N/2) \log_2 N$ complex products have to be calculated for an N -element Fourier transform, with N a power of 2. This number can be further reduced by recognizing trivial multiplications as with $W_N^0 = (1, 0)$. As an example take $N = 512$: Instead of $N^2 = 262,144$ complex multiplications now we need at most $(N/2) \log_2 N = 2,304$ complex multiplications. The advantage is obvious.

For practical implementations more savings are possible. The sines and cosines of W_N^{kn} should be taken from a look-up-table prepared once before the main computation. Furthermore multiplications with unity or zero can be avoided. If a real sequence is to be trans-

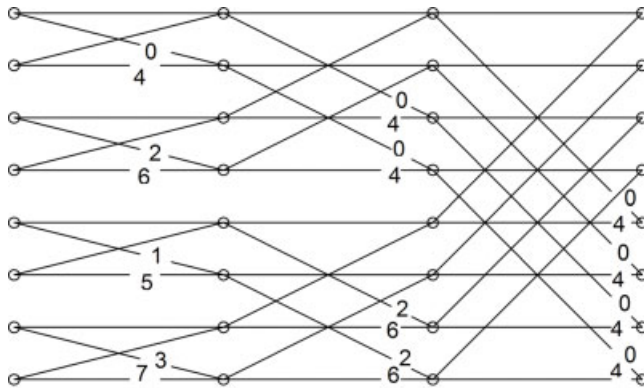


Figure A.13: Signal flow graph for FFT with $N = 8$.

formed, nearly half of the computations can be saved by recognizing the Hermitean property, Table A.2.

A short *FFT-subroutine* in FORTRAN is given here, which may easily be translated into other programming languages:

```

SUBROUTINE FFT(FR,FI,K,IFLAG)
C - FAST FOURIER TRANSFORM
C - DATA IN FR (REAL) AND FI (IMAGINARY) ARRAYS
C - IF IFLAG=1: (FR,FI) IS REPLACED BY ITS DISCRETE FOURIER TRANSFORM
C - IF IFLAG=-1: SAME BY ITS INVERSE DISCRETE FOURIER TRANSFORM
C - NUMBER OF POINTS IS N=2**K; FR,FI DIMENSIONED IN MAIN PROGRAM
      DIMENSION FR(1),FI(1)
      N=2**K
      MR=0
      NM1=N-1
      DO 1 M=1,NM1
      L=N
2     L=L/2
      IF (MR+L.GT.NM1) GOTO 2
      MR=MOD(MR,L)+L
      IF (MR.LE.M) GOTO 1
      TEMP=FR(M+1)
      FR(M+1)=FR(MR+1)
      FR(MR+1)=TEMP
      TEMP=FI(M+1)
      FI(M+1)=FI(MR+1)
      FI(MR+1)=TEMP
1     CONTINUE
      L=1
3     IF (L.GE.N) RETURN
      ISTEP=2*L
      EL=L
      DO 4 M=1,L
      A=IFLAG*3.1415926535*FLOAT(1-M)/EL
      WR=COS(A)
      WI=SIN(A)
      DO 4 I=M,N,ISTEP

```

```

J=I+L
TEMPL=WR*FR(J)-WI*FI(J)
TEMPI=WR*FI(J)+WI*FR(J)
FR(J)=FR(I)-TEMPL
FI(J)=FI(I)-TEMPI
FR(I)=FR(I)+TEMPL
FI(I)=FI(I)+TEMPI
4    CONTINUE
L=ISTEP
GOTO 3
END

```

This should help for initial tests. More efficient programs should systematically avoid multiplications by zero and one, and should merge the multiplications by $\sqrt{2}$, or can be based on the Hartley transform. Detailed discussions of the FFT algorithms can be found in [790, 791].

A.11 Fast Fourier Transform for $N \neq 2^n$

Occasionally one needs to compute large DFTs of size $N \neq 2^n$ which can be done by combining several small DFTs of sizes N_1, N_2, \dots, N_l , which are relative prime factors of N . Here we only consider the simple case of a DFT of size N , where N is the product of two mutually prime factors N_1 and N_2 . The objective is to convert this one-dimensional DFT into a two-dimensional DFT of size $N_1 \times N_2$. In order to do this, one must convert the indices n and k in (A.80), defined modulo N , into two sets of indices n_1, k_1 and n_2, k_2 , defined, respectively, modulo N_1 and modulo N_2 . This can be done by the Chinese remainder theorem or by use of simple permutations [792]. Thus we arrive at the index transformations

$$\begin{aligned} n &\equiv N_1 n_2 + N_2 n_1 \text{ modulo } N \\ k &\equiv N_1 k_2 + N_2 k_1 \text{ modulo } N \\ n_1, k_1 &= 0, \dots, N_1 - 1 \\ n_2, k_2 &= 0, \dots, N_2 - 1. \end{aligned} \tag{A.81}$$

This is valid only for $(N_1, N_2) = 1$. Now we substitute n and k in (A.80) and using the fact $N_1 N_2 \equiv 0$ modulo N we obtain

$$F_{N_1 k_2 + N_2 k_1} = \frac{1}{N} \sum_{n_1=0}^{N_1-1} \sum_{n_2=0}^{N_2-1} f_{N_1 n_2 + N_2 n_1} W_1^{N_2 n_1 k_1} W_2^{N_1 n_2 k_2} \tag{A.82}$$

with

$$W_1 = e^{-i\frac{2\pi}{N_1}} \quad W_2 = e^{-i\frac{2\pi}{N_2}}. \tag{A.83}$$

In order to obtain a two-dimensional DFT in the conventional lexicographic order, it is convenient to replace k_1 and k_2 by their permuted values $t_2 k_1$ and $t_1 k_2$ such that $N_2 t_2 \equiv 1$ modulo N_1 and $N_1 t_1 \equiv 1$ modulo N_2 . This is equivalent to replacing the mapping of k given by (A.82) with its Chinese remainder equivalent

$$k \equiv N_1 t_1 k_2 + N_2 t_2 k_1 \text{ modulo } N. \tag{A.84}$$

Now we have

$$F_{N_1 t_1 k_2 + N_2 t_2 k_1} = \frac{1}{N} \sum_{n_1=0}^{N_1-1} \sum_{n_2=0}^{N_2-1} f_{N_1 n_2 + N_2 n_1} W_1^{n_1 k_1} W_2^{n_2 k_2} \quad (\text{A.85})$$

which is the usual representation of a DFT of size $N_1 \times N_2$. Thus by using for n the permutation defined by (A.85), and for k the Chinese remainder correspondence defined by (A.84) (or vice versa), we are able to map a one-dimensional DFT of length $N_1 N_2$ into a two-dimensional DFT of size $N_1 \times N_2$. The same method can be used recursively to define a one to many multidimensional mapping, as is shown explicitly in [792].

In the following a subroutine based on this approach is presented. It is for the case $N = 3072 = N_1 N_2 = 1024 \cdot 3$, which is used e. g. for processing the images recorded with the CMOS-arrays of Canon having 3072×2048 pixels. This subroutine contains a 3-point transform in one direction and calls a radix-2 transform as given in the previous subroutine.

```

SUBROUTINE FFT3072(FR,FI,IFLAG)
DIMENSION FR(3072),FI(3072)
DIMENSION GR1(1024),GI1(1024),GR2(1024),GI2(1024),GR3(1024),GI3(1024)
VA=SQRT(2.)/2.
S3=SQRT(3.)/2.
DO 1 I=1,1024
  GR1(I)=FR(3*I-2)
  GI1(I)=FI(3*I-2)
  GR2(I)=FR(MOD(3*I+1021,3072)+1)
  GI2(I)=FI(MOD(3*I+1021,3072)+1)
  GR3(I)=FR(MOD(3*I+2045,3072)+1)
  GI3(I)=FI(MOD(3*I+2045,3072)+1)
1 CONTINUE
CALL FFT(GR1,GI1,10,IFLAG)
CALL FFT(GR2,GI2,10,IFLAG)
CALL FFT(GR3,GI3,10,IFLAG)
DO 2 I=1,1024
  A=GR1(I)+GR2(I)+GR3(I)
  B=GI1(I)+GI2(I)+GI3(I)
  IF (IFLAG.EQ.1) THEN
    C=GR1(I)-GR2(I)/2.+S3*GI2(I)-GR3(I)/2.-S3*GI3(I)
    D=GI1(I)-S3*GR2(I)-GI2(I)/2.+S3*GR3(I)-GI3(I)/2.
    E=GR1(I)-GR2(I)/2.-3*GI2(I)-GR3(I)/2.+S3*GI3(I)
    F=GI1(I)+S3*GR2(I)-GI2(I)/2.-S3*GR3(I)-GI3(I)/2.
  ELSE
    C=GR1(I)-GR2(I)/2.-S3*GI2(I)-GR3(I)/2.+S3*GI3(I)
    D=GI1(I)+S3*GR2(I)-GI2(I)/2.-S3*GR3(I)-GI3(I)/2.
    E=GR1(I)-GR2(I)/2.+3*GI2(I)-GR3(I)/2.-S3*GI3(I)
    F=GI1(I)-S3*GR2(I)-GI2(I)/2.+S3*GR3(I)-GI3(I)/2.
  ENDIF
  GR1(I)=A/S3
  GI1(I)=B/S3
  GR2(I)=C/S3
  GI2(I)=D/S3
  GR3(I)=E/S3
  GI3(I)=F/S3
2 CONTINUE
DO 3 I=1,1024

```

```

FR (MOD (2049* (I-1) , 3072)+1)=GR1 (I)
FR (MOD (2049* (I-1) +1024, 3072)+1)=GR2 (I)
FR (MOD (2049* (I-1) +2048, 3072)+1)=GR3 (I)
FI (MOD (2049* (I-1) , 3072)+1)=GI1 (I)
FI (MOD (2049* (I-1) +1024, 3072)+1)=GI2 (I)
FI (MOD (2049* (I-1) +2048, 3072)+1)=GI3 (I)
3    CONTINUE
      RETURN
      END

```

A.12 Cosine and Hartley Transform

The Fourier transform considered so far has a complex kernel, the complex exponentials. There are transforms with real kernels, which draw advantage from some of the symmetries pointed out in Table A.2.

If $f(x)$ is even, meaning $f(x) = f(-x)$ for all (x, y) , or $f(x, y) = f(-x, -y)$ in the two-dimensional case, then its Fourier transform is reduced to the *cosine transform*

$$\mathcal{C}\{f(x)\}(\xi) = \int_0^\infty f(x) \cos(2\pi\xi x) dx \quad (\text{A.86})$$

or in two dimensions

$$\mathcal{C}\{f(x, y)\}(\xi, \eta) = \int_0^\infty \int_0^\infty f(x, y) \cos[2\pi(\xi x + \eta y)] dx dy. \quad (\text{A.87})$$

If the two-dimensional signal also is axially symmetric

$$f(x, y) = f(-x, y) = f(x, -y) = f(-x, -y) \quad (\text{A.88})$$

then its two-dimensional Fourier transform is reduced to the *separable cosine transform* [786]

$$\mathcal{C}\{f(x, y)\}(\xi, \eta) = \int_0^\infty \int_0^\infty f(x, y) \cos(2\pi\xi x) \cos(2\pi\eta y) dx dy. \quad (\text{A.89})$$

The inverse cosine transform is identical to the cosine transform.

Another transform with a real-valued kernel like the cosine transform is the *Hartley transform* that is defined in one dimension as

$$\begin{aligned}
\mathcal{H}\{f(x)\}(\xi) &= \int_{-\infty}^{\infty} f(x) [\cos(2\pi\xi x) + \sin(2\pi\xi x)] dx \\
&= \frac{\sqrt{2}}{2} \int_{-\infty}^{\infty} f(x) \cos(2\pi\xi x - \frac{\pi}{4}) dx.
\end{aligned} \quad (\text{A.90})$$

Like the cosine transform, the forward Hartley transform and its inverse are identical. Although the Hartley transform is defined for both real and complex functions $f(x)$, or sequences f_n in the discrete case, its practical value arises from the way in which it takes advantage of the symmetry in the Fourier transform of a real function or sequence [793]. The Fourier spectra and the Hartley spectra of real-valued functions $f(x)$ are related by [102]

$$\begin{aligned}\mathcal{H}\{f(x)\}(\xi) &= \frac{1}{2i} [(i+1)\mathcal{F}\{f(x)\}(\xi) + (i-1)\mathcal{F}\{f(x)\}(-\xi)] \\ &= \text{Re}\mathcal{F}\{f(x)\}(\xi) + \text{Im}\mathcal{F}\{f(x)\}(\xi)\end{aligned}\quad (\text{A.91})$$

and

$$\begin{aligned}\mathcal{F}\{f(x)\}(\xi) &= \frac{1}{2} [\mathcal{H}\{f(x)\}(\xi) + \mathcal{H}\{f(x)\}(-\xi)] \\ &\quad - \frac{i}{2} [\mathcal{H}\{f(x)\}(\xi) - \mathcal{H}\{f(x)\}(-\xi)].\end{aligned}\quad (\text{A.92})$$

Thus the real part of the Fourier transform is the even part of the Hartley transform, while the imaginary part of the Fourier transform is the odd part of the Hartley transform.

As in the case of the cosine transform, two possible versions of the two-dimensional Hartley transform exist, namely the *separable Hartley transform* [786]

$$\mathcal{H}_s\{f(x,y)\}(\xi, \eta) = \int_{-\infty}^{\infty} \int_{-\infty}^{\infty} f(x,y) \cos\left(2\pi\xi x - \frac{\pi}{4}\right) \cos\left(2\pi\eta y - \frac{\pi}{4}\right) dx dy \quad (\text{A.93})$$

and the *inseparable Hartley transform*

$$\mathcal{H}_i\{f(x,y)\}(\xi, \eta) = \int_{-\infty}^{\infty} \int_{-\infty}^{\infty} f(x,y) \cos[2\pi(\xi x + \eta y) - \frac{\pi}{4}] dx dy. \quad (\text{A.94})$$

The two-dimensional Fourier-Hartley relation with $H_i(\xi, \eta)$ standing for $\mathcal{H}_i\{f(x,y)\}(\xi, \eta)$ and $F(\xi, \eta) = \mathcal{F}\{f(x,y)\}(\xi, \eta)$ is

$$F(\xi, \eta) = \frac{1}{2} [H_i(\xi, \eta) + H_i(-\xi, -\eta)] - \frac{i}{2} [H_i(\xi, \eta) - H_i(-\xi, -\eta)]. \quad (\text{A.95})$$

This relation, which is valid for the inseparable Hartley transform, forms a natural extension of the one-dimensional transform (A.92). But unfortunately due to the lack of separability there is no efficient algorithm for calculating the 2D transform by a cascaded processing of fast 1D transforms along lines and columns.

For the separable Hartley transform on the other hand the Fourier transform is expressed as

$$F(\xi, \eta) = \frac{1}{2} [H_s(\xi, -\eta) + H_s(-\xi, \eta)] - \frac{i}{2} [H_s(\xi, \eta) - H_s(-\xi, -\eta)]. \quad (\text{A.96})$$

Now we have gained separability but paid the price that the simple relation $F = \{\text{Even part of } H\} - i\{\text{Odd part of } H\}$, which is valid for the one-dimensional and the inseparable two-dimensional Hartley transform, no longer holds, instead (A.96) must be used [793].

A.13 The Chirp Function and the Fresnel Transform

In Table A.1 we have already met the quadratic phase exponential, also called the *chirp function*

$$f(x) = e^{i\pi\beta x^2} \quad (\text{A.97})$$

which has the Fourier transform

$$F(\xi) = \frac{i}{\sqrt{\beta}} e^{-i\pi\frac{\xi^2}{\beta}}. \quad (\text{A.98})$$

The special importance of the chirp function stems from its property that it is an oscillatory signal, where the frequency of oscillation linearly depends on the spatial coordinate. Thus it is interesting from a theoretical standpoint. Furthermore it appears in the Fresnel transform, which is extensively used in diffraction theory and in digital holography. Therefore it is of great interest in optics. The chirp function got its name from applications in testing transmission systems for acoustic signals. In Table A.1 the real part of the chirp function is displayed, the modulus is constant $|f(x)| = 1.0$, since it is a pure phase function. Its Fourier transform is again a scaled chirp function with constant amplitude.

The above mentioned facts hold for the chirp function of infinite extent, but things dramatically change if we investigate the finite chirp function, which represents only a section of the infinite one, now defined in a finite interval. Let this interval be $[-L, L]$, then the finite chirp function can be expressed as

$$g(x) = e^{i\pi\beta x^2} \operatorname{rect}\left(\frac{x}{2L}\right). \quad (\text{A.99})$$

Its Fourier spectrum has to be calculated by

$$G(\xi) = \int_{-L}^L e^{i\pi\beta x^2} e^{-i2\pi\xi ux} dx. \quad (\text{A.100})$$

By completing the square in the exponent and changing the variables of integration from x to $t = \sqrt{2\beta}(x - \xi/\beta)$ we get

$$G(\xi) = \frac{1}{\sqrt{2\beta}} e^{-i\pi\frac{\xi^2}{\beta}} \int_{-\sqrt{2\beta}(L+\frac{\xi}{\beta})}^{\sqrt{2\beta}(L-\frac{\xi}{\beta})} e^{i\pi\frac{t^2}{2}} dt. \quad (\text{A.101})$$

The integral can be expressed in terms of the tabulated Fresnel integrals, which are defined by

$$C(z) = \int_0^z \cos\left(\frac{\pi t^2}{2}\right) dt \quad S(z) = \int_0^z \sin\left(\frac{\pi t^2}{2}\right) dt. \quad (\text{A.102})$$

Here the spectrum $G(\xi)$ is

$$\begin{aligned} G(\xi) = & \frac{e^{-i\pi\xi^2/\beta}}{\sqrt{2\beta}} \left\{ C\left(\sqrt{2\beta}\left(L - \frac{\xi}{\beta}\right)\right) - C\left(\sqrt{2\beta}\left(-L - \frac{\xi}{\beta}\right)\right) \right. \\ & \left. + iS\left(\sqrt{2\beta}\left(L - \frac{\xi}{\beta}\right)\right) - iS\left(\sqrt{2\beta}\left(-L - \frac{\xi}{\beta}\right)\right) \right\}. \end{aligned} \quad (\text{A.103})$$

Figure A.14 shows the real part of the one-dimensional finite chirp function for $N = 2L = 512$ points with $\beta = 0.0004$. The plot of $|G(\xi)|$ is displayed in Fig. A.14b. As can be seen, the spectrum is almost flat over the region $[-2\pi\beta L, 2\pi\beta L]$ and almost zero outside that region. In the named region the values of $|G(\xi)|$ oscillate around $\sqrt{1/\beta}$ [784].

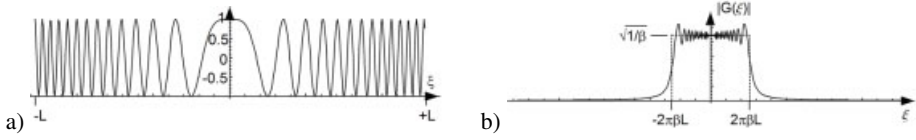


Figure A.14: The finite chirp function (a) and its amplitude spectrum (b).

A shifted version of the finite chirp function

$$g'(x) = e^{i\pi\beta(x - x_0)^2} \operatorname{rect}\left(\frac{x}{2L}\right) \quad (\text{A.104})$$

in the interval $[-L, L]$ has a shifted spectrum, see Fig. A.15. Figure A.15a displays the real

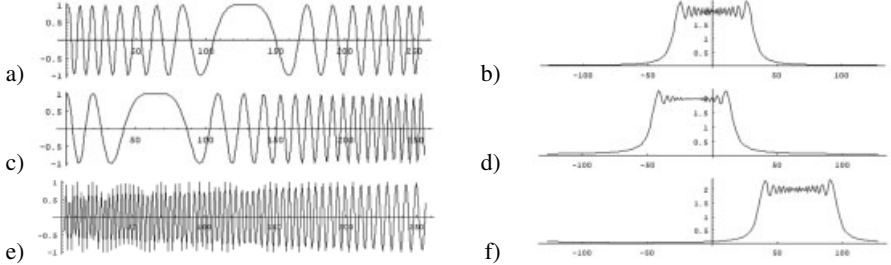


Figure A.15: Shifted chirp functions and their amplitude spectra.

part of a finite chirp function whose central part containing the frequency zero is central in the sampling interval. Its amplitude spectrum is shown in Fig. A.15b. A shifted finite chirp function is given in Fig. A.15c with its amplitude spectrum in Fig. A.15d. The finite chirp function of Fig. A.15e is shifted so far that only positive frequencies are contained in the sampling interval. This is reflected in the spectrum, Fig. A.15f, which almost totally lies in the positive part of the frequency domain. This clearly illustrates the differences between the finite and the infinite chirp functions and their corresponding Fourier transforms. While in the infinite case the amplitude spectrum is a constant, which is not altered by a shift of the

function, now in the finite case the amplitude spectrum varies. A shift of the infinite chirp function leads to a spectrum which is multiplied by a pure phase factor, on the other hand a shift of the finite sampling interval over the chirp function results in a shift of the amplitude spectrum. This behavior also can be explained using the concept of *local frequencies*. Let $g(x)$ be generally defined as $g(x) = a(x) \exp[i\phi(x)]$, then the local frequency f_{loc} at point x is defined by

$$f_{loc}(x) = \frac{1}{2\pi} \frac{\partial}{\partial x} \phi(x). \quad (\text{A.105})$$

If we examine $g(x) = \exp[i\pi\beta x^2]$ with regard to its local frequencies, we obtain

$$f_{loc}(x) = \frac{1}{2\pi} \frac{\partial}{\partial x} \pi\beta x^2 = \beta x. \quad (\text{A.106})$$

This means that in the interval $[-L, L]$ the chirp function $g(x)$ carries local frequencies from $-\beta L$ to βL . For the shifted function $g'(x) = \exp[i\pi\beta(x - x_0)^2]$ the local frequency is $f_{loc}(x) = \beta(x - x_0)$. In the interval $[-L, L]$ the local frequencies now vary from $-\beta(L - x_0)$ to $+\beta(L - x_0)$, which is obviously reflected in the amplitude spectrum, Fig. A.15.

In Section 2.4.2 the Fresnel approximation for calculating the diffraction integral has been introduced. Under certain conditions (2.79) the complex optical field in one plane as diffracted from the field in another plane can be determined by the Fresnel transform (2.73). The prominent role the Fresnel transform plays in optics justifies the presentation of some often used properties [129] in this section.

The Fresnel transform \mathcal{FR}_τ with parameter $\tau > 0$ of a function $f(x) \in L_2(\mathbb{R})$ is defined as the convolution

$$\mathcal{FR}_\tau\{f(x)\} = f(x) \star k_\tau(x) \quad (\text{A.107})$$

where $k_\tau(x)$ is the well known chirp function

$$k_\tau(x) = \frac{1}{\tau} e^{i\pi(\frac{x}{\tau})^2}. \quad (\text{A.108})$$

If we compare with the first line of (2.73) we recognize that $\tau = \lambda z$ in optical applications. The Fresnel transform is unitary so we have a *Parseval equality*

$$\int_{-\infty}^{\infty} f(x) g^*(x) dx = \int_{-\infty}^{\infty} \mathcal{FR}_\tau\{f(x)\}(\xi) (\mathcal{FR}_\tau\{g(x)\})^*(\xi) d\xi \quad (\text{A.109})$$

for all $f, g \in L_2(\mathbb{R})$ and all $\tau > 0$

and for $f = g$ a *Plancherel equality*

$$\|f\| = \|\mathcal{FR}_\tau\{f\}\| \quad \text{for all } f \in L_2(\mathbb{R}) \text{ and all } \tau > 0. \quad (\text{A.110})$$

The inverse Fresnel transform is given by

$$f(x) = \mathcal{FR}_\tau\{f\}(\xi) \star k_\tau^{-1}(\xi) \text{ with } k_\tau^{-1}(\xi) = k_\tau^*(\xi) = \frac{1}{\tau} e^{-i\pi(\frac{\xi}{\tau})^2}. \quad (\text{A.111})$$

For computation of the inverse of the Fresnel transform the duality relation can be used

$$f^*(x) = \mathcal{FR}_\tau \{ \mathcal{FR}_\tau \{ f(x) \}^*(\xi) \}(x) \quad \text{for all } f \in L_2(\mathbb{R}) \text{ and all } \tau > 0. \quad (\text{A.112})$$

As the Fresnel transform is a convolution operator it is shift invariant

$$\mathcal{FR}_\tau \{ f(x - x_0) \}(\xi) = \mathcal{FR}_\tau \{ f(\xi) \}(x - x_0) \quad \text{for any } x_0 \in \mathbb{R}. \quad (\text{A.113})$$

The scaling property is

$$\mathcal{FR}_\tau \left\{ f \left(\frac{x}{s} \right) \right\}(\xi) = \mathcal{FR}_{\tau/s} \{ f(\xi) \} \left(\frac{\xi}{s} \right). \quad (\text{A.114})$$

This means that the parameter τ Fresnel transform of the dilated function $f(x/s)$ is the dilated version of the parameter τ' Fresnel transform of f with the rescaled parameter $\tau' = \tau/s$.

Since holography is in essence a lensless process, it tends to spread out sharp details like object edges over the entire image plane. This issue of resolution is quantified by a Heisenberg-like uncertainty relation, which also guides us in the search for a suitable wavelet basis when we try to employ the wavelet concept in digital holography, see Section 3.4.3.

Let μ_f be the average of the squared modulus of an L_2 -function f

$$\mu_f = \frac{1}{\|f\|^2} \int_{-\infty}^{\infty} x |f(x)|^2 dx \quad (\text{A.115})$$

and σ_f^2 its variance

$$\sigma_f^2 = \frac{1}{\|f\|^2} \int_{-\infty}^{\infty} (x - \mu_f) |f(x)|^2 dx. \quad (\text{A.116})$$

Then we have the following *uncertainty relation* for the Fresnel transform, the proof of which can be found in [129]. If $f \in L_2(\mathbb{R})$ and $\tilde{f} = \mathcal{FR}_\tau \{ f(x) \}$, then we have

$$\sigma_f^2 \sigma_{\tilde{f}}^2 \geq \frac{\tau^4}{16\pi^2} \quad (\text{A.117})$$

with equality if and only if there exist $x_0, \omega_0, b \in \mathbb{R}$, and $a \in \mathbb{C}$ such that

$$f(x) = ae^{i\omega_0 x} e^{-b(x - x_0)^2} e^{-i\pi(\frac{x}{\tau})^2}. \quad (\text{A.118})$$

If $f(x)$ is real-valued, the relation

$$\sigma_f^2 \sigma_{\tilde{f}}^2 \geq \frac{\tau^4}{16\pi^2} + \sigma_f^4 \quad (\text{A.119})$$

holds, with equality if and only if there exist x_0, a , and $b \in \mathbb{R}$, such that

$$f(x) = ae^{-b(x - x_0)^2}. \quad (\text{A.120})$$

This allows one to give a lower bound on the variance of \tilde{f} that is independent of f [129]

$$\sigma_{\tilde{f}}^2 \geq \frac{\tau^2}{2\pi}. \quad (\text{A.121})$$

It should be noted that signals can be represented as a linear combination of elementary functions of the form (A.118), which constitutes the so-called *Gabor transform*, another result [794] of the inventor of holography.

The translation of the Fresnel transform to two dimensions is straightforward. The 2D kernel is

$$k_{\tau}^{(2)}(x, y) = \frac{1}{\tau^2} e^{i\pi \left(\frac{\sqrt{x^2+y^2}}{\tau}\right)^2} \quad (\text{A.122})$$

but since it is separable $k_{\tau}^{(2)}(x, y) = k_{\tau}(x)k_{\tau}(y)$, most mathematical analysis can be performed in one dimension.

The free-space propagation of light as given in (2.73) now can be expressed

$$\begin{aligned} E(\xi, \eta) &= \frac{e^{ikz}}{i\lambda z} \int_{-\infty}^{\infty} \int_{-\infty}^{\infty} U(x, y) e^{\frac{i\pi}{\lambda z} [(\xi - x)^2 + (\eta - y)^2]} dx dy \\ &= -ie^{ikz} \mathcal{FR}_{\sqrt{\lambda z}}^{(2)} \{U(x, y)\}(\xi, \eta). \end{aligned} \quad (\text{A.123})$$

B Computer Aided Tomography

In holographic interferometry of refractive index fields the interference phase is given by the integral over the refractive index distribution along the illuminating ray passing the measurement volume, (4.22). Therefore, except for very simple problems, we have to reconstruct the distribution of the refractive index from a sufficient number of projections, a problem first addressed by Radon [795]. Since the extensive use of this approach in medical diagnosis using X-rays, this so called field of *computer aided tomography* has emerged rapidly: signals from a diversity of sources from the whole electromagnetic spectrum are used [796], and the theoretical background of the computer evaluation algorithms has been refined.

Here only a very basic introduction to the main approaches to computer aided tomography is given to constitute a background for the evaluation techniques used in holographic interferometric measurements at transparent refracting objects, see Section 6.10.

B.1 Mathematical Preliminaries

The measurement of the three-dimensional distribution of a physical quantity like the X-ray attenuation in human tissue or the *refractive index* in a transparent medium is simplified by the treatment of the measurement volume cut into two-dimensional plane slices. After an evaluation many of such slices are stacked to build the three-dimensional result. So here we only have to consider a two-dimensional distribution of a physical quantity $f(x, y)$ in a single plane. Without loss of generality we can assume that $f(x, y)$ is spatially bounded. Then by proper scaling and shifting we can ensure $f(x, y) = 0$ outside the unit circle Ω in the Cartesian coordinate system, Fig. B.1.

For the description of line integrals and projections the use of *polar coordinates* (t, ϕ) is advantageous, Fig. B.1:

$$f(x, y) = f(t \cos \phi, t \sin \phi). \quad (\text{B.1})$$

A line in the plane now can be described by the two parameters s and θ : s is the signed distance of the line to the origin of the coordinate system and θ is the angle between the line and the y -axis, Fig. B.1. The projections of $f(x, y)$ along lines are called the *Radon transforms* $r(s, \theta)$, defined as

$$r(s, \theta) = \int_{-T}^T f(s \cos \theta - t \sin \theta, s \sin \theta + t \cos \theta) dt \quad (\text{B.2})$$

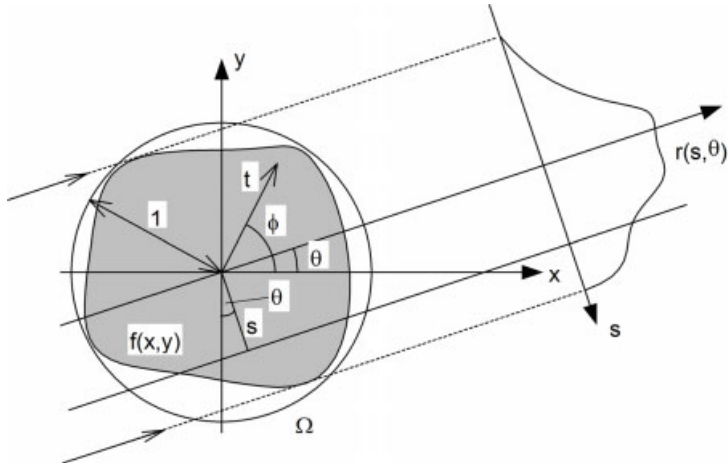


Figure B.1: Projection through a refractive index field.

or employing the delta function

$$r(s, \theta) = \int_{-\infty}^{\infty} \int_{-\infty}^{\infty} f(x, y) \delta(x \cos \theta + y \sin \theta - s) dx dy. \quad (\text{B.3})$$

The T of (B.2) can be set to $T(s) = (1 - s^2)^{1/2}$ since by assumption $f(s, \theta) = 0$ for $|s| > 1$, which is outside the unit-circle.

(s, θ) and $(-s, \theta + \pi)$ represent the same line in the plane, therefore this is true for the projections

$$r(s, \theta) = r(-s, \theta + \pi). \quad (\text{B.4})$$

In the following some reconstruction methods will be introduced. This outline will be restricted to parallel projections, all rays establishing the projections are parallel. The case of fan beam projection is discussed in the literature [785].

What is measured in practical experiments are the estimated projections $r(s, \theta)$ for discrete values of s and θ . From these projections the distribution $f(x, y)$ has to be reconstructed, which should be a two-dimensional array of numbers, each representing the physical quantity to be measured in an elementary cell.

Algorithms become more easy, if r is uniformly sampled in s and θ . Therefore we assume a set of projections in N angular directions separated by $\Delta\theta$, each of these consisting of M equidistant beams separated by Δs , Fig. B.2.

B.2 The Generalized Projection Theorem

Let $f(x, y)$ be a function as in Section B.1 and $r(s, \theta)$ its Radon transform. Let further $w(s)$ be any function of a single variable such that the following integrals exist. Then for all angles

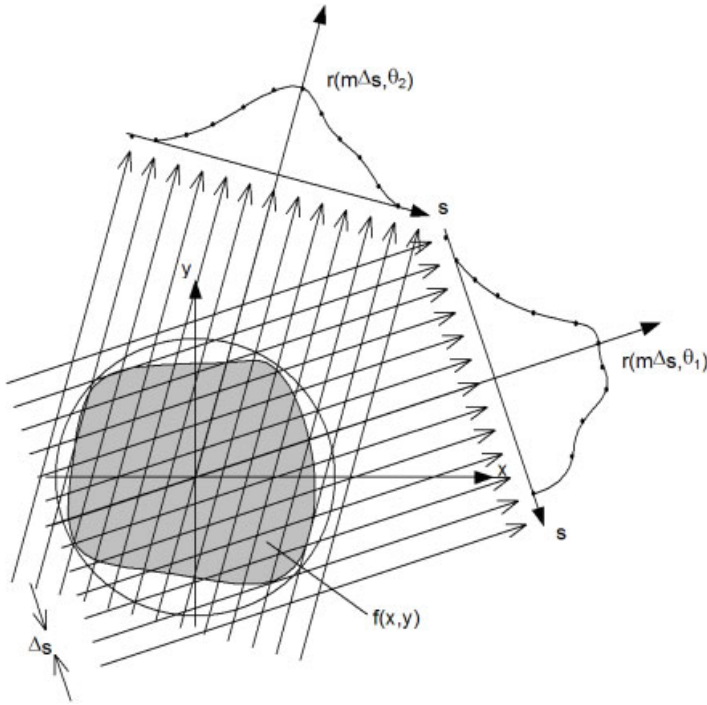


Figure B.2: Projections along parallel equidistant rays.

θ we have

$$\int_{-1}^1 r(s, \theta) w(s) ds = \iint_{\Omega} f(x, y) w(x \cos \theta + y \sin \theta) dx dy. \quad (\text{B.5})$$

This theorem is proved by replacing $r(s, \theta)$ by its definition (B.2) and a change of the integration variables from the rotating coordinates (s, t) to fixed coordinates (x, y) :

$$\begin{aligned} \int_{-1}^1 r(s, \theta) w(s) ds &= \int_{-1}^1 \int_{-T}^T f(s \cos \theta - t \sin \theta, s \sin \theta + t \cos \theta) dt w(s) ds \\ &= \iint_{\Omega} f(x, y) w(x \cos \theta + y \sin \theta) dx dy. \end{aligned} \quad (\text{B.6})$$

The change of variables is $x = s \cos \theta - t \sin \theta$, $y = s \sin \theta + t \cos \theta$, or conversely $s = x \cos \theta + y \sin \theta$, $t = y \cos \theta - x \sin \theta$, and $ds dt = dx dy$ since the Jacobian is 1.

This *generalized projection theorem* states the equivalence of an operation on the projection r with a related operation on the object f itself.

By taking $w(s) = \exp(-2\pi i \rho s)$ we obtain the *projection theorem for Fourier transforms*, also called *Fourier slice theorem* [785]:

$$R(\rho, \theta) = F(\rho \cos \theta, \rho \sin \theta) \quad (\text{B.7})$$

with $R(\rho, \theta) = \mathcal{F}\{r(s, \theta)\}$ and $F(u, v) = \mathcal{F}\{f\}(u, v)$. This theorem states that the Fourier transform of a parallel projection of $f(x, y)$, taken at a fixed angle θ , gives a one-dimensional slice of the Fourier transform $F(u, v)$, subtending an angle θ with the v -axis. In Fig. B.3 the Fourier transform of the projection $r(s, \theta)$ gives the values of $F(u, v)$ along line l . The angular coordinate in the spatial frequency domain, expressed by Θ , here coincides with θ .

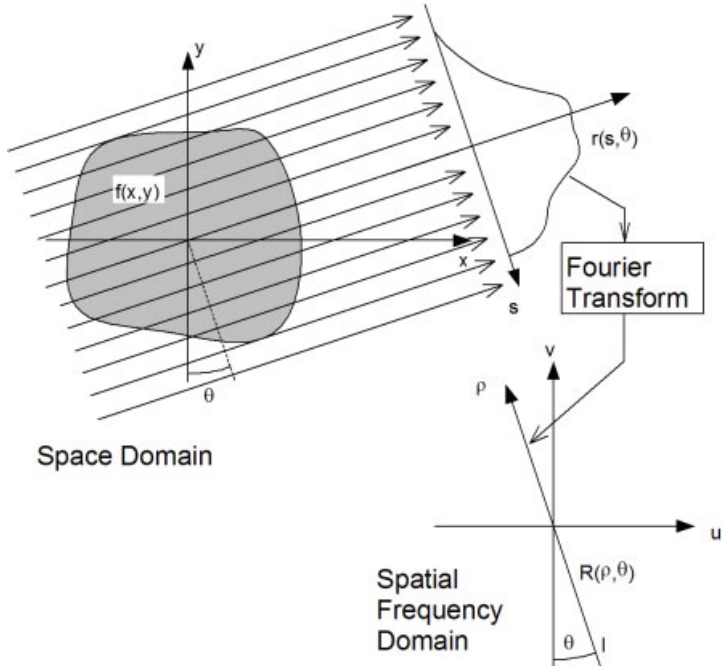


Figure B.3: Projection theorem for Fourier transforms.

A direct approach to reconstruction based on the projection theorem for Fourier transforms would consist of collecting enough slices in the frequency domain, which are produced by transforming the projections along a sufficient number of angles, and to compute the inverse transform of the compiled two-dimensional frequency spectrum. But the inverse transform requires rectangularly sampled data, while the slices yield samples along radial lines, Fig. B.4. To obtain data in a square grid, a sort of nearest neighbor, linear, or bilinear interpolation must be performed. Since the data points become sparser as they are further away from the center, Fig. B.4, the interpolation error increases. That means high frequency components of the reconstructed image are more likely to be degraded than are low frequency items. Altogether this approach has only theoretical value, in practice the filtered backprojection method, which also is based on the projection theorem for Fourier transforms, is the one most frequently applied.

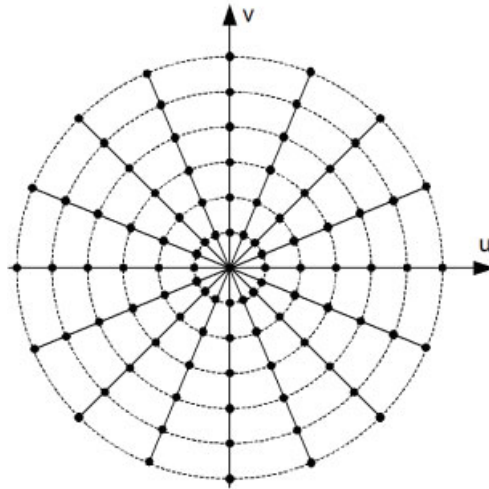


Figure B.4: Slices in the frequency domain.

B.3 Reconstruction by Filtered Backprojection

The function $f(x, y)$ to be reconstructed can be written as the inverse Fourier transform of its transform $F(u, v)$, which expressed in polar coordinates in the frequency domain is

$$\begin{aligned} f(x, y) &= \int_{-\infty}^{\infty} \int_{-\infty}^{\infty} F(u, v) e^{i2\pi(ux + vy)} du dv \\ &= \int_0^{2\pi} \int_0^{\infty} F(\rho, \Theta) e^{i2\pi(\rho x \cos \Theta + \rho y \sin \Theta)} \rho d\rho d\Theta \end{aligned} \quad (\text{B.8})$$

with $u = \rho \cos \Theta$, $v = \rho \sin \Theta$, and $du dv = \rho d\rho d\Theta$. The integral is split into two and employing the property $F(\rho, \Theta + \pi) = F(-\rho, \Theta)$ we get

$$\begin{aligned} f(x, y) &= \int_0^{\pi} \int_0^{\infty} F(\rho, \Theta) e^{i2\pi\rho(x \cos \Theta + y \sin \Theta)} \rho d\rho d\Theta \\ &+ \int_0^{\pi} \int_{-\infty}^0 F(\rho, \Theta + \pi) e^{i2\pi\rho(x \cos(\Theta + \pi) + y \sin(\Theta + \pi))} (-\rho) d\rho d\Theta \\ &= \int_0^{\pi} \left\{ \int_{-\infty}^{\infty} F(\rho, \Theta) |\rho| e^{i2\pi\rho t} d\rho \right\} d\Theta \end{aligned} \quad (\text{B.9})$$

with the abbreviation $t = x \cos \Theta + y \sin \Theta$.

The Fourier transform for each angle Θ is the corresponding transformed projection, so we get

$$f(x, y) = \int_0^\pi \left\{ \int_{-\infty}^{\infty} R(\rho, \Theta) |\rho| e^{i2\pi\rho t} d\rho \right\} d\Theta. \quad (\text{B.10})$$

If we introduce the quantity

$$q_\Theta(t) = \int_{-\infty}^{\infty} R(\rho, \Theta) |\rho| e^{i2\pi\rho t} d\rho \quad (\text{B.11})$$

(B.10) reads

$$f(x, y) = \int_0^\pi q_\Theta(x \cos \Theta + y \sin \Theta) d\Theta. \quad (\text{B.12})$$

These last two equations, (B.11) and (B.12), are the heart of the *reconstruction by filtered backprojection*. Equation (B.11) represents a filtering operation applied to the projection $R(\rho, \Theta)$, where the frequency response of the filter is given by $|\rho|$, so we name $q_\Theta(t)$ the *filtered projection*. The filtered projections $q_\Theta(t)$ for different angles Θ then are backprojected in the spatial domain to form an estimate of $f(x, y)$, which is the content of (B.12). This can be imagined with the help of Fig. B.5. For a given angle Θ_i the filtered projection contributes

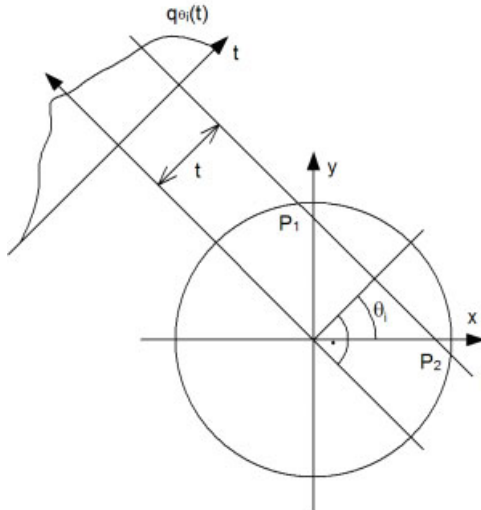


Figure B.5: Backprojection of the filtered projection.

its value $q_{\Theta_i}(t)$ to all points (x, y) in the image plane, for which $t = x \cos \Theta_i + y \sin \Theta_i$. Thus the filtered projection for t is smeared back over all points along the projection line l of Fig. B.5. Since here we assume a circular area of interest in the image plane, $q_{\Theta_i}(t)$ is smeared over all points between P_1 and P_2 . Altogether this is done for all the $q_{\Theta_i}(t)$ over all t as well as for all angles Θ_i .

B.4 Practical Implementation of Filtered Backprojection

In practice the energy contained in the spectra above a certain frequency is negligible, which means for practical purposes the projection may be considered as band-limited. If ρ_{\max} is higher than the highest significant frequency component in each projection, the projections can be sampled error-free at intervals of $\Delta t = 1/(2\rho_{\max})$. We assume further that the projection data are zero for large $|t|$, then the M samples of a projection are

$$r(m\Delta t, \Theta) \quad \text{with} \quad m = -M/2, \dots, +M/2 - 1. \quad (\text{B.13})$$

Now the FFT algorithm can be used to calculate the Fourier transforms $R(\rho, \Theta)$ of the projections

$$R(\rho, \Theta) \approx R\left(m \frac{2\rho_{\max}}{M}, \Theta\right) = \frac{1}{2\rho_{\max}} \sum_{k=-M/2}^{M/2-1} r\left(\frac{k}{2\rho_{\max}}, \Theta\right) e^{-i2\pi \frac{mk}{M}}. \quad (\text{B.14})$$

This projection now has to be filtered according to (B.11)

$$q_{\Theta}(t) \approx \frac{2\rho_{\max}}{M} \sum_{m=-M/2}^{M/2-1} R\left(m \frac{2\rho_{\max}}{M}, \Theta\right) \left|m \frac{2\rho_{\max}}{M}\right| e^{i2\pi(2\rho_{\max}/M)t}. \quad (\text{B.15})$$

The multiplication in the frequency domain before taking the inverse transform is equivalent to a convolution in the spatial, the t -domain

$$q_{\Theta}(t) = \int r(s, \theta) h(t-s) ds \quad (\text{B.16})$$

where $h(t)$ is the inverse Fourier transform of the function $|\rho|$ multiplied with a window function in the frequency domain. A simple window function $B(\rho)$ only reflects the band-limitness, so that the convolution kernel is the inverse transform of

$$H(\rho) = |\rho| B(\rho) \quad (\text{B.17})$$

with $B(\rho) = 1$ for $|\rho| < \rho_{\max}$ and zero otherwise. The impulse response of $H(\rho)$ is

$$\begin{aligned} h(t) &= \int_{-\infty}^{\infty} H(\rho) e^{i2\pi\rho t} d\rho \\ &= \frac{1}{2\Delta t} \frac{\sin 2\pi t/(2\Delta t)}{2\pi t/(2\Delta t)} - \frac{1}{4(\Delta t)^2} \frac{\sin \pi t/(2\Delta t)}{\pi t/(2\Delta t)}. \end{aligned} \quad (\text{B.18})$$

The projection data are measured with the sampling interval Δt , consequently we only need $h(t)$ at the sampled points. These values are

$$h(m\Delta t) = \begin{cases} \frac{1}{4(\Delta t)^2} & m = 0 \\ 0 & m \text{ even} \\ -\frac{1}{m^2\pi^2(\Delta t)^2} & m \text{ odd.} \end{cases} \quad (\text{B.19})$$

This is the well known *Ramachandran-Lakshminarayanan kernel*. Another frequently used kernel is the *Shepp-Logan kernel* [797]

$$h(m\Delta t) = \frac{-2}{\pi^2(\Delta t)^2(4m^2 - 1)}. \quad (\text{B.20})$$

Unfortunately the values of $x \cos \theta_i + y \sin \theta_i$ do not always correspond to the sampled points $m\Delta t$. Therefore the filtered projection $q_\Theta(t)$ must be interpolated between the sampling points. Linear interpolation in most applications is adequate.

Altogether a practical implementation of the filtered backprojection method consists of the following steps:

- Choice of parameters: These are the number M of sampling points in each projection, the number N of angular projections, the sampling interval Δt , the angular separation $\Delta\theta = \pi/N$, the cutoff frequency $\rho_{\max} = 1/(2\Delta t)$, the number of pixels $K \times L$ in the reconstructed image, the pixel distances Δx and Δy in the reconstructed image, the interpolation procedure (e. g. piecewise linear), the type of convolution kernel (e. g. Shepp-Logan).
- Projection data input: These are N vectors each having M components.
- Convolution of each projection with the kernel: This is performed in the spatial domain or by multiplication in the frequency domain.
- Interpolation of the filtered projections.
- Backprojection.
- Display of results.

A very simple example is shown in Fig. B.6. The function $f(x, y)$ to be reconstructed from four projections in the directions $\theta = 0^\circ, 45^\circ, 90^\circ$, and 135° is, Fig. B.6a

$$f(x, y) = \begin{cases} 1 & 0 \leq x \leq 0.25 \text{ and } 0 \leq y \leq 0.25 \\ 0.5 & 0.25 \leq x \leq 0.5 \text{ and } 0 \leq y \leq 0.5 \\ 0.5 & 0.25 \leq y \leq 0.5 \text{ and } 0 \leq x \leq 0.25 \\ 0 & \text{elsewhere.} \end{cases} \quad (\text{B.21})$$

The four projections are shown in Figs. B.6c to f, the Shepp-Logan-kernel to be applied to the projections in Fig. B.6b. The filtered and interpolated projections are given in Figs. B.6g to j. The resulting $f(x, y)$ after backprojection is displayed in pseudo 3D in Fig. B.6k and in gray-values in Fig. B.6l. It must be admitted that this example is far from practical because four projections are never sufficient.

B.5 Algebraic Reconstruction Techniques

The *algebraic reconstruction techniques*, also known as *series expansion reconstruction methods*, principally differ from the transformation based methods as the filtered backprojection

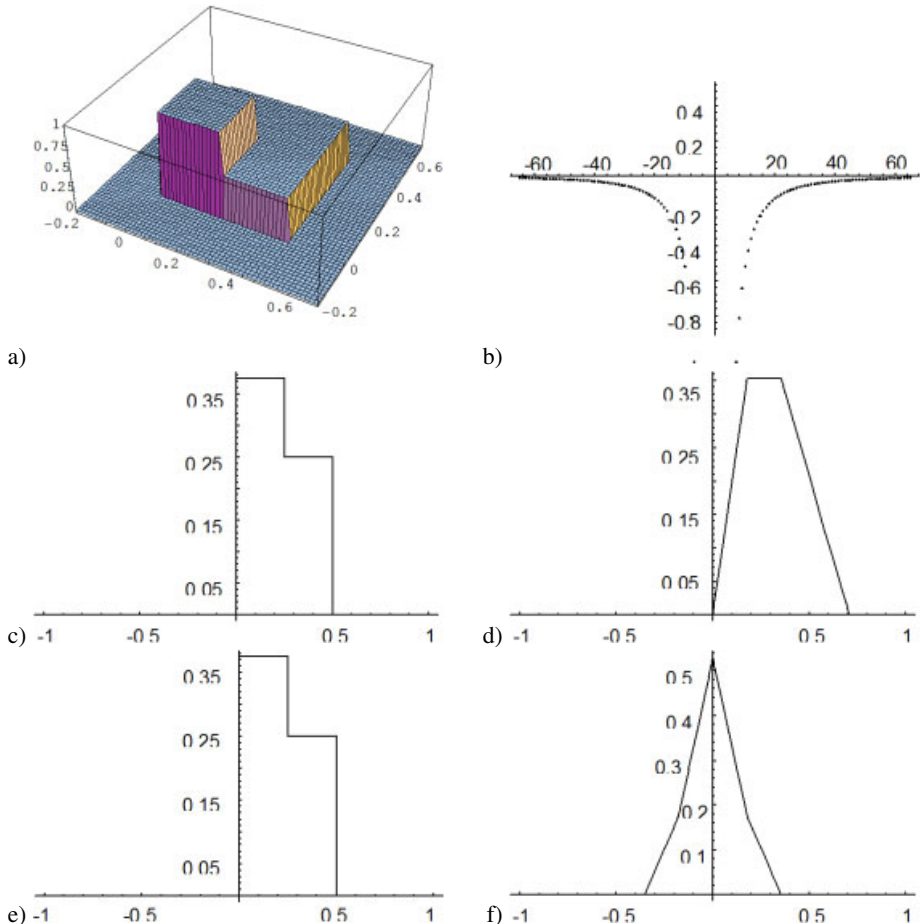


Figure B.6: Numerical example for reconstruction by filtered backprojection: (a) 2D test function $f(x, y)$, (b) Shepp-Logan convolution kernel, (c – f) projections of $f(x, y)$, (c) $\theta = 0^\circ$, (d) $\theta = 45^\circ$, (e) $\theta = 90^\circ$, (f) $\theta = 135^\circ$.

reconstruction. While in the transform methods the problem is treated as a continuous one until it is discretized for computational implementation, the algebraic reconstructions are discretized from the beginning [798–801]. The following short outline again only deals in two dimensions.

The interesting area is partitioned into a Cartesian grid of square cells, the pixels, numbered consecutively from 1 to N , Fig. B.7.

It is assumed that the function $f(x, y)$ to be reconstructed is constant in each cell, f_j being its value in cell j . Let M rays probe the area, one of these rays being indicated in Fig. B.7. The rays now have a finite thickness. The different portions each ray i intercepts with each

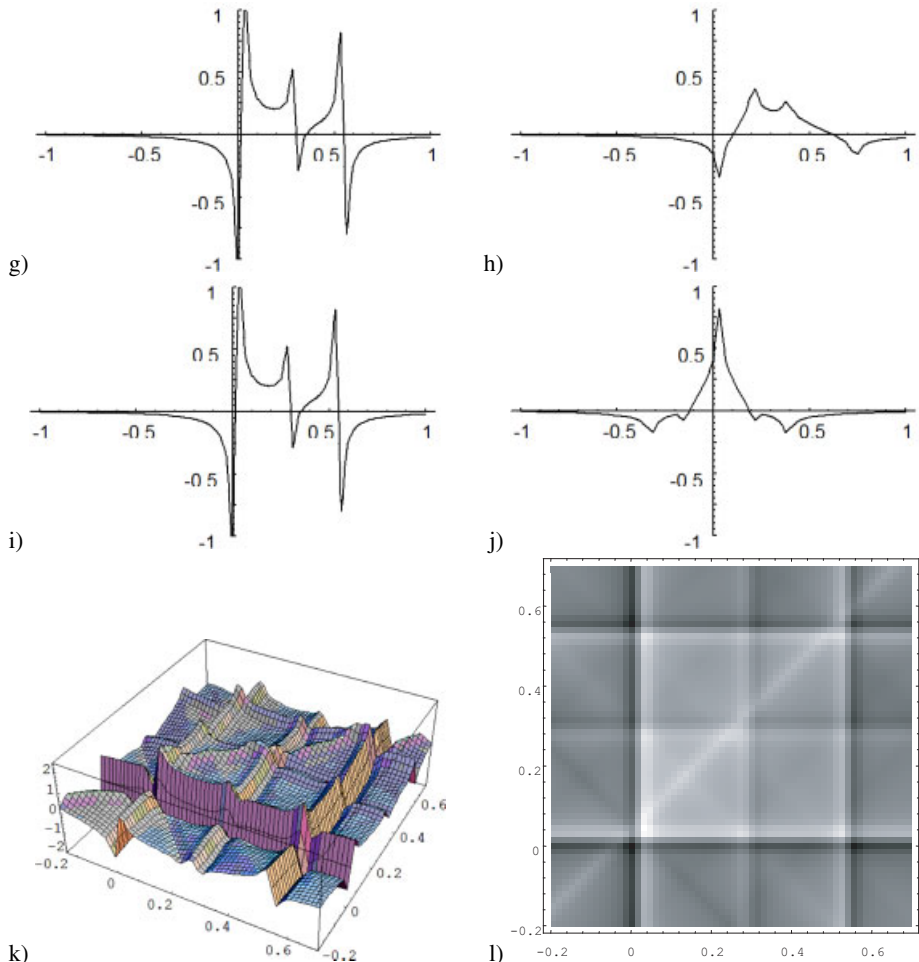


Figure B.6 (continued): (g – j) filtered and interpolated projections, (k, l) reconstructed function, (k) pseudo 3D display, (l) gray-scale display.

cell j are quantified by w_{ij} . After running through the grid the integrated signal p_i of ray i is the sum of the values f_j of all subtended pixels weighted with the area of the cell w_{ij} the ray covers:

$$p_i = \sum_{j=1}^N w_{ij} f_j \quad i = 1, \dots, M. \quad (\text{B.22})$$

This system of linear equations can be written in matrix form $\mathbf{p} = \mathbf{W} \cdot \mathbf{f}$. Since for each ray only the intercepted pixels yield $w_{ij} \neq 0$, \mathbf{W} is a sparsely occupied matrix, but its size frequently is of the order $10^6 \times 10^6$.

A solution by direct matrix inversion is not feasible because of the size of the problem, sometimes the system is underdetermined with less projections than cells, often the system

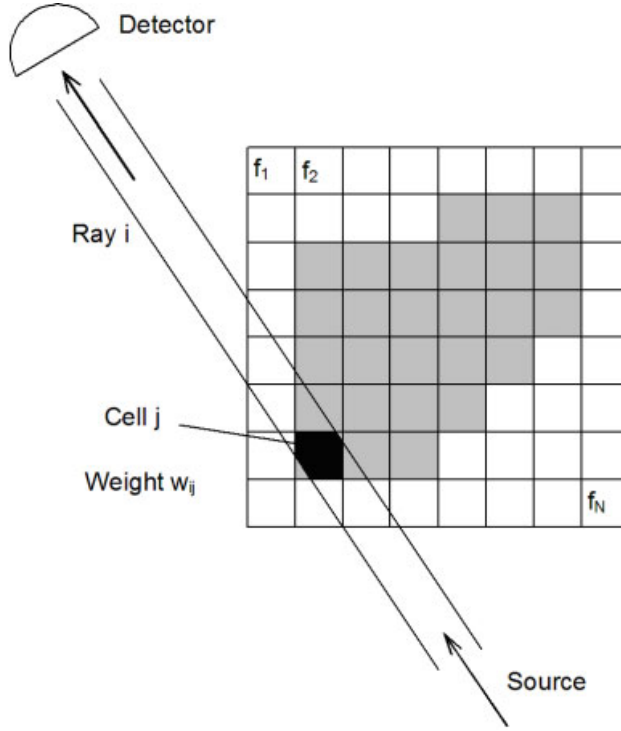


Figure B.7: Geometry for algebraic reconstruction.

is overdetermined and inconsistent, and generally all projections are measured with limited accuracy. Instead one has to look for appropriate iterative solutions.

The primary algebraic reconstruction technique is based on the Kaczmarz algorithm for solving a system of linear equations [798]: Beginning with an arbitrary initial guess, the solutions are iteratively refined by taking into account the measurements along one ray during one iteration step. Convergence of the iteration is forced by introduction of relaxation parameters.

Another approach replaces the equalities (B.22) by inequalities

$$p_i - \varepsilon_i \leq \sum_{j=1}^N w_{ij} f_j \leq p_i + \varepsilon_i \quad i = 1, \dots, M \quad (\text{B.23})$$

where the tolerances ε_i reflect the limited measurement accuracy. The iteration looks for a vector in the intersection of all hyperslabs defined by the inequalities (B.23).

Other methods use the concepts of entropy optimization, quadratic optimization, least squares regularization or statistical techniques [785, 798].

This short outline should be finished by the observation that still today most commercial equipment works with transform methods. But due to the versatility and flexibility of the algebraic reconstruction techniques and the enormous increase in computer speed these methods have good prospects for the future.

C Bessel Functions

Bessel functions arise in solving differential equations for systems with cylindrical symmetry. The *Bessel functions* $J_n(z)$ and $Y_n(z)$ are linearly independent solutions to the differential equation

$$z^2 \frac{d^2y}{dz^2} + z \frac{dy}{dz} + (z^2 - n^2)y = 0. \quad (\text{C.1})$$

$J_n(z)$ is called the *Bessel function of the first kind*, $Y_n(z)$ is referred to as the *Bessel function of the second kind*. For integer n , the $J_n(z)$ are regular at $z = 0$, the $Y_n(z)$ have a logarithmic divergence at $z = 0$.

Alternatively the Bessel function of the first kind can be defined over the integral

$$J_n(z) = \frac{1}{2\pi} \int_0^{2\pi} \cos(z \sin t - nt) dt \quad z \in C, \quad n = 0, 1, 2, \dots \quad (\text{C.2})$$

or as the power series

$$\begin{aligned} J_n(z) &= \frac{z^n}{2^n 0! n!} - \frac{z^{n+2}}{2^{n+2} 1! (n+1)!} + \frac{z^{n+4}}{2^{n+4} 2! (n+2)!} - \frac{z^{n+6}}{2^{n+6} 3! (n+3)!} + \dots \\ &= \sum_{i=0}^{\infty} \frac{(-1)^i z^{n+2i}}{2^{n+2i} i! (n+i)!} \quad \text{for} \quad |z| < \infty. \end{aligned} \quad (\text{C.3})$$

Since the absolute values of the coefficients of this power series decrease very rapidly, this representation is useful for a practical calculation even for large $|z|$.

By proper combination of the power series components and using the Euler formula one obtains the useful formula

$$\sum_{n=-\infty}^{\infty} J_n(z) e^{in\phi} = e^{iz \sin \phi}. \quad (\text{C.4})$$

We see in (C.3) that for real x $J_n(x)$ is also real and an even function for even n and an odd function if n is odd. Figure C.1 shows the first four real Bessel functions $J_0(x), \dots, J_3(x)$. All real Bessel functions are bounded by the functions $\pm \sqrt{2/(\pi x)}$ which also are shown in Fig. C.1. We recognize the damped oscillation of all curves as well as the distribution of the zeroes becoming more and more regular with increasing x .

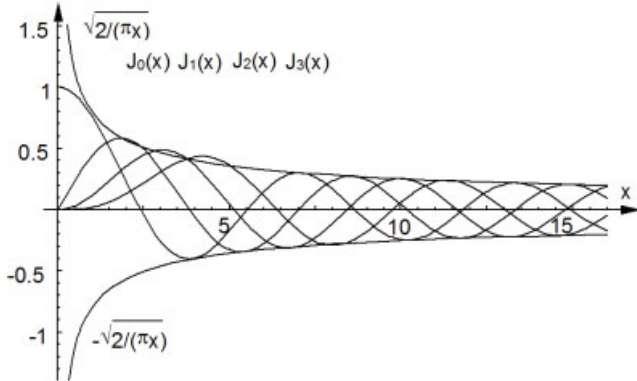


Figure C.1: Real Bessel functions of the first kind.

The most interesting Bessel function in holographic interferometry is the real Bessel function of the first kind and zero order $J_0(x)$ because it describes the intensity distribution resulting from the *time average method* for analyzing harmonically vibrating objects. The zeros b_m , $J_0(b_m) = 0$, $m = 1, 2, \dots$, can be approximated for sufficiently large m by

$$b_m^* = \left(m - \frac{1}{4}\right)\pi. \quad (\text{C.5})$$

Accordingly an approximating function to $J_0(x)$ for large x is

$$J_0^*(x) = \sqrt{\frac{2}{\pi x}} \cos\left(x - \frac{\pi}{4}\right). \quad (\text{C.6})$$

For higher order n we have

$$J_n^*(x) = \sqrt{\frac{2}{\pi x}} \cos\left(x - \frac{2n+1}{4}\pi\right). \quad (\text{C.7})$$

A table of the first 30 zeros of $J_0(x)$ together with the approximating b_m^* is given with a precision of five decimal places in Table C.1.

At this point it should be mentioned that the n -th order Bessel functions of the first kind also appear in the Zernike description of wavefronts in optical testing: A data spectrum $D(u, v)$ is described by a sum of Zernike terms

$$Z_{m,n}(r, \Theta) = R_{m,n}(r)e^{im\Theta}, \quad m, n \in N, \quad n > 0, \quad m < n, \quad m+n \text{ even} \quad (\text{C.8})$$

where $R_{m,n}(r)$ are *Zernike polynomials*. The Zernike terms form a complete orthogonal set of functions over the unit circle. The Fourier transforms of $Z_{m,n}(r, \Theta)$ are

$$\mathcal{F}\{Z_{m,n}(r, \Theta)\} = \mathcal{Z}_{m,n}(\rho, \theta) = (-1)^n A_n(\rho) e^{im\theta} \quad (\text{C.9})$$

Table C.1: Zeroes of the real Bessel function of the first kind and zero order.

m	b_m	b_m^*	m	b_m	b_m^*
1	2.40483	2.35619	16	49.48261	49.48008
2	5.52008	5.49779	17	52.62405	52.62168
3	8.65373	8.63938	18	55.76551	55.76327
4	11.79153	11.78097	19	58.90698	58.90486
5	14.93092	14.92257	20	62.04847	62.04645
6	18.07106	18.06416	21	65.18996	65.18805
7	21.21164	21.20575	22	68.33147	68.32964
8	24.35247	24.34734	23	71.47298	71.47123
9	27.49348	27.48894	24	74.61450	74.61283
10	30.63461	30.63053	25	77.75603	77.75442
11	33.77582	33.77212	26	80.89756	80.89601
12	36.91710	36.91371	27	84.03909	84.03760
13	40.05843	40.05531	28	87.18063	87.17920
14	43.19979	43.19690	29	90.32217	90.32078
15	46.34119	46.33849	30	93.46372	93.46238

where

$$A_n(\rho) = \frac{1}{\rho} J_{n+1}(2\pi\rho) \quad (\text{C.10})$$

with (ρ, θ) being the spatial frequency coordinates in polar form [481].

Bibliography

- [1] D. Gabor. A new microscopic principle. *Nature*, 161:777–778, 1948. {3, 37, 169}
- [2] D. Gabor. Microscopy by reconstructed wavefronts. *Proc. Royal Society A*, 197:454–487, 1949. {3, 37, 169}
- [3] D. Gabor. Microscopy by reconstructed wavefronts: II. *Proc. Royal Society B*, 64:449–469, 1951. {3, 37}
- [4] G. L. Rogers. Experiments in diffraction microscopy. *Proc. Roy. Soc. Edinb.*, 63A:193–221, 1952. {3}
- [5] H. M. A. El-Sum and P. Kirkpatrick. Microscopy by reconstructed wavefronts. *Phys. Rev.*, 85:763, 1952. {3}
- [6] A. W. Lohmann. Optische Einseitenbandübertragung angewandt auf das Gabor-Mikroskop. *Optica Acta*, 3:97–99, 1956. {3}
- [7] E. N. Leith and J. Upatnieks. Wavefront reconstruction with diffused illumination and three-dimensional objects. *Journ. Opt. Soc. Amer.*, 54:1295–1301, 1964. {3, 42, 45, 169}
- [8] E. N. Leith and J. Upatnieks. Wavefront reconstruction with continuous-tone objects. *Journ. Opt. Soc. Amer.*, 53:1377–1381, 1963. {3, 42, 45, 169}
- [9] E. N. Leith and J. Upatnieks. Wavefront reconstruction with diffused illumination and three-dimensional objects. *Journ. Opt. Soc. Amer.*, 54:1295–1301, 1964. {3, 42, 45}
- [10] Y. N. Denisyuk. Photographic reconstruction of the optical properties of an object in its own scattered field. *Sov. Phys. Dokl.*, 7:543, 1962. {3}
- [11] A. W. Lohmann and D. P. Paris. Binary Fraunhofer holograms generated by computer. *Appl. Opt.*, 6:1739–1748, 1967. {4}
- [12] W. H. Lee. Sampled Fourier transform hologram generated by computer. *Appl. Opt.*, 9:639–643, 1970. {4}
- [13] W. H. Lee. Binary synthetic holograms. *Appl. Opt.*, 13:1677–1682, 1974. {4}
- [14] J. F. Heanue, M. C. Bashaw, and L. Hesselink. Volume holographic storage and retrieval of digital data. *Science*, 265:749–752, 1994. {4}
- [15] <http://www.aprilisinc.com/>. Homepage of Aprilis, Inc. {4}
- [16] R. L. Powell and K. A. Stetson. Interferometric vibration analysis by wavefront reconstruction. *Journ. Opt. Soc. Amer.*, 55:1593–1598, 1965. {4, 323, 326}
- [17] K. A. Stetson and R. L. Powell. Interferometric hologram evaluation of real-time vibration analysis of diffuse objects. *Journ. Opt. Soc. Amer.*, 55:1694–1695, 1965. {4, 332}

- [18] R. J. Collier, E. T. Doherty, and K. S. Pennington. New method for generating depth contours holographically. *Appl. Phys. Lett.*, 7(8):223–225, 1965. {4}
- [19] R. E. Brooks, L. O. Hefflinger, and R. F. Wuerker. Interferometry with a holographically reconstructed comparison beam. *Appl. Phys. Lett.*, 7:248–249, 1965. {4, 195}
- [20] L. O. Hefflinger, R. F. Wuerker, and R. E. Brooks. Holographic interferometry. *Journ. Appl. Phys.*, 37:642–649, 1966. {4, 195}
- [21] K. A. Haines and B. P. Hildebrand. Surface-deformation measurement using the wavefront reconstruction technique. *Appl. Opt.*, 5:595–602, 1966. {4, 45, 214}
- [22] K. A. Haines and B. P. Hildebrand. Interferometric measurements on diffuse surfaces by holographic techniques. *IEEE Trans., IM* 15:149–161, 1966. {4, 45, 214}
- [23] K. A. Haines and B. P. Hildebrand. Contour generation by wavefront reconstruction. *Phys. Lett.*, 19:10–11, 1965. {4, 333}
- [24] L. O. Hefflinger and R. F. Wuerker. Holographic contouring via multifrequency lasers. *Appl. Phys. Lett.*, 15:28–30, 1969. {4, 333}
- [25] B. P. Hildebrand and K. A. Haines. The generation of three-dimensional contour maps by wavefront reconstruction. *Phys. Lett.*, 21:422–423, 1966. {4, 333}
- [26] B. P. Hildebrand and K. A. Haines. Multiple-wavelength and multiple-source holography applied to contour generation. *Journ. Opt. Soc. Amer.*, 57(2):155–162, 1967. {4, 333}
- [27] T. Tsuruta, N. Shiotake, J. Tsujiuchi, and K. Matsuda. Holographic generation of contour map of diffusely reflecting surface by using immersion method. *Jap. J. Appl. Phys.*, 6:661–662, 1967. {4, 336}
- [28] J. S. Zelenka and J. R. Varner. New method for generating depth contours holographically. *Appl. Opt.*, 7:2107–2110, 1968. {4, 333}
- [29] M. H. Horman. An application of wavefront reconstruction to interferometry. *Appl. Opt.*, 4(2):333–336, 1965. {4}
- [30] D. W. Sweeney and C. M. Vest. Reconstruction of three dimensional refractive index fields from multidirectional interferometric data. *Appl. Opt.*, 12(11):2649–2663, 1973. {4, 379–382}
- [31] K. A. Stetson. A rigorous treatment of the fringes of hologram interferometry. *Optik*, 29(4):386–400, 1969. {4, 215}
- [32] N. E. Molin and K. A. Stetson. Measurement of fringe loci and localization in hologram interferometry for pivot motion, in-plane rotation and in-plane translation. Part I. *Optik*, 31:157–177, 1970. {4, 215}
- [33] N. E. Molin and K. A. Stetson. Measurement of fringe loci and localization in hologram interferometry for pivot motion, in-plane rotation and in-plane translation. Part II. *Optik*, 31:281–291, 1970. {4, 215}
- [34] N. E. Molin and K. A. Stetson. Fringe localization in hologram interferometry of mutually independent and dependent rotations around orthogonal, non-intersecting axes. *Optik*, 33:399–422, 1970. {4, 215}
- [35] K. A. Stetson. The argument of the fringe function in hologram interferometry of general deformations. *Optik*, 31(6):576–591, 1970. {4, 214, 215, 222, 318}

- [36] E. B. Aleksandrov and A. M. Bonch-Bruevich. Investigation of surface strains by the hologram technique. *Sov. Phys. - Tech. Phys.*, 12(2):258–265, 1967. {4}
- [37] A. E. Ennos. Measurement of in-plane surface strain by hologram interferometry. *Journ. Phys. E: Scient. Instr.*, 1:731–734, 1968. {4, 266, 267}
- [38] W. Osten, R. Höfling, and J. Saedler. Two computer-aided methods for data reduction from interferograms. In W. F. Fagan, editor, *Industrial Optoelectronic Measurement Systems using Coherent Light*, volume 863 of *Proc. of Soc. Photo-Opt. Instr. Eng.*, pages 105–113, 1987. {4, 229}
- [39] P. Carre. Installation et utilisation du comparateur photoelectrique et interferentiel du Bureau International des Poids et Mesures. *Metrologia*, 2(1):13–23, 1966. {4, 248}
- [40] J. H. Bruning, J. G. Gallagher, D. P. Rosenfeld, D. A. White, D. J. Brangaccio, and D. R. Herriott. Digital wavefront measuring interferometer for testing optical surfaces and lenses. *Appl. Opt.*, 13:2693, 1974. {4}
- [41] B. Fischer and W. Jüptner. Automatisierte Auswertung holografischer Interferenzmuster mit dem Zeilen-Scan-Verfahren (Automatic evaluation of holographic interference patterns with the line-scan method). In *Spring School of Holographic Interferometry in Technology and Medicine*, 1978. (In German). {4}
- [42] Th. Kreis, B. Fischer, W. Jüptner, and G. Sepold. Automatisierte Auswertung holografischer Interferenzmuster bei der Untersuchung von Zugproben (Automatic evaluation of holographic interference patterns in the investigation of tensile test specimen). In W. Waidelich, editor, *Laser 81 – Optoelektronik in der Technik*, pages 105–110. Springer-Verlag, 1981. (In German). {4}
- [43] M. Takeda, H. Ina, and S. Kobayashi. Fourier-transform method of fringe-pattern analysis for computer-based topography and interferometry. *Journ. Opt. Soc. Amer.*, 72(1):156–160, 1982. {4, 256, 263, 405}
- [44] Th. Kreis. Digital holographic interference-phase measurement using the Fourier-transform method. *Journ. Opt. Soc. Amer. A*, 3(6):847–855, 1986. {4, 256, 261}
- [45] J. A. Leendertz. Interferometric displacement measuring on scattering surfaces utilizing speckle effect. *J. Phys. E: Sci. Instrum.*, 3:214–218, 1970. {5}
- [46] J. N. Butters and J. A. Leendertz. Holographic and video techniques applied to engineering measurement. *J. Meas. Control*, 4:349–354, 1971. {5, 401}
- [47] A. Macovski, D. Ramsey, and L. F. Schaefer. Time lapse interferometry and contouring using television systems. *Appl. Opt.*, 10:2722–2727, 1971. {5, 401}
- [48] O. Schwomma. Austrian Patent No. 298830, 1972. {5, 401}
- [49] K. Creath. Phase shifting speckle interferometry. *Appl. Opt.*, 24:3053–3058, 1985. {5, 404}
- [50] K. A. Stetson and W. R. Brohinsky. Electro-optic holography and its application to hologram interferometry. *Appl. Opt.*, 24(21):3631–3637, 1985. {5, 404}
- [51] J. W. Goodman and R. W. Lawrence. Digital image formation from electronically detected holograms. *Appl. Phys. Lett.*, 11(3):77–79, 1967. {5, 6}
- [52] T. S. Huang. Digital holography. *Proc. IEEE*, 59(9):1335–1346, 1971. {5, 6}
- [53] M. A. Kronrod, N. S. Merzlyakov, and L. P. Yaroslavskii. Reconstruction of holograms with a computer. *Sov. Phys.-Tech. Phys.*, 17:333–334, 1972. {6}

- [54] T. H. Demetrikopoulos and R. Mittra. Digital and optical reconstruction of images from suboptical diffraction patterns. *Appl. Opt.*, 13:665–670, 1974. {6}
- [55] L. P. Yaroslavskii and N. S. Merzlyakov. *Methods of Digital Holography*. Consultants Bureau, New York, 1980. {6}
- [56] U. Schnars. Direct phase determination in hologram interferometry with use of digitally recorded holograms. *Journ. Opt. Soc. Amer. A*, 11(7):2011–2015, 1994. {6, 269}
- [57] U. Schnars and W. Jüptner. Direct recording of holograms by a CCD target and numerical reconstruction. *Appl. Opt.*, 33(2):179–181, 1994. {6}
- [58] U. Schnars and W. Jüptner. Digital recording and reconstruction of holograms in hologram interferometry and shearography. *Appl. Opt.*, 33(20):4373–4377, 1994. {6}
- [59] U. Schnars, Th. Kreis, and W. Jüptner. Digital recording and numerical reconstruction of holograms: Reduction of the spatial frequency spectrum. *Opt. Eng.*, 35(4):977–982, 1995. {6, 85}
- [60] U. Schnars, Th. Kreis, and W. Jüptner. CCD-recording and numerical reconstruction of holograms and holographic interferograms. In M. Kujawinska, R. J. Pryputniewicz, and M. Takeda, editors, *Interferometry VII: Techniques and Analysis*, volume 2544 of *Proc. of Soc. Photo-Opt. Instr. Eng.*, pages 57–63, 1995. {6, 85}
- [61] Y. Zou, G. Pedrini, and H. Tiziani. Surface contouring in a video frame by changing the wavelength of a diode laser. *Opt. Eng.*, 35(4):1074–1079, 1996. {6}
- [62] St. Schedin, G. Pedrini, H. J. Tiziani, and F. Mendoza Santoyo. Simultaneous three-dimensional dynamic deformation measurements with pulsed digital holography. *Appl. Opt.*, 38(34):7056–7062, 1999. {6, 282, 405}
- [63] G. Pedrini, Y. L. Zou, and H. J. Tiziani. Digital double-pulsed holographic interferometry for vibration analysis. *Journ. Modern Opt.*, 42(2):367–374, 1995. {6}
- [64] G. Pedrini, Y. L. Zou, and H. J. Tiziani. Comparison of two reflecting surfaces by using digital holographic interferometry. *Opt. Comm.*, 118:186–192, 1995. {6, 405}
- [65] G. Pedrini, Ph. Fröning, H. Fessler, and H. J. Tiziani. In-line digital holographic interferometry. *Appl. Opt.*, 37(26):6262–6269, 1998. {6, 332}
- [66] Th. Kreis and U. Schnars. Internal Reports, BMFT-Project HOLOMETEC, 1993+1994. {6}
- [67] F. Dubois, L. Joannes, and J. C. Legros. Improved three-dimensional imaging with a digital holography microscope with a source of partial spatial coherence. *Appl. Opt.*, 38(34):7085–7094, 1999. {6}
- [68] F. Dubois, L. Joannes, O. Dupont, J. L. Dewandel, and J. C. Legros. An integrated optical set-up for fluid-physics experiments under microgravity conditions. *Meas. Sci. & Techn.*, 10(10):934–945, 1999. {6, 385}
- [69] F. Dubois, O. Monnom, C. Yourassowsky, and J.-C. Legros. Border processing in digital holography by extension of the digital hologram and reduction of the higher spatial frequencies. *Appl. Opt.*, 41(14):2621–2626, 2002. {6, 180}
- [70] F. Dubois, C. Minetti, O. Monnom, C. Yourassowsky, J.-C. Legros, and P. Kischel. Pattern recognition with a digital holographic microscope working in partially coherent illumination. *Appl. Opt.*, 41(20):4108–4119, 2002. {6}

- [71] A. Albertazzi Jr. and A. Vieira Fantin. Digital complex holography using a shearing interferometer: principles and early results. In K. Creath and J. Schmit, editors, *Interferometry XI: Techniques and Analysis*, volume 4777 of *Proc. of Soc. Photo-Opt. Instr. Eng.*, pages 57–68, 2002. {6, 127, 128}
- [72] H. J. Kreuzer and R. A. Pawlitzek. Fast implementation of in-line holography for high resolution shape measurement. In Z. Füzesi, W. Jüptner, and W. Osten, editors, *Simulation and Experiment in Laser Metrology*, pages 61–66, 1996. {6, 175}
- [73] H. J. Kreuzer and R. A. Pawlitzek. Numerical reconstruction for in-line holography in reflection and under glancing incidence. In W. Jüptner and W. Osten, editors, *Fringe '97, Automatic Processing of Fringe Patterns*, pages 364–367, 1997. {6, 175}
- [74] M. R. A. Shegelski, S. Faltus, Th. Clark, and H. J. Kreuzer. Improvements in the reconstruction of in-line holograms by energy sampling and tomography. *Ultramicroscopy*, 74:169–178, 1998. {6, 179}
- [75] H. J. Kreuzer, N. Pomerleau, K. Blagrave, and M. H. Jericho. Digital in-line holography with numerical reconstruction. In M. Kujawinska, editor, *Interferometry 99: Techniques and Technology*, volume 3744 of *Proc. of Soc. Photo-Opt. Instr. Eng.*, pages 65–74, 1999. {6, 175}
- [76] H. J. Kreuzer, M. J. Jericho, I. A. Meinertzhangen, and W. Xu. Digital in-line holography with photons and electrons. *J. Phys.: Condens. Matter*, 13:10729–10741, 2001. {6, 174}
- [77] W. Xu, M. H. Jericho, I. A. Meinertzhangen, and H. J. Kreuzer. Digital in-line holography for biological applications. *PNAS*, 98(20):11301–11305, 2001. {6, 169}
- [78] W. Xu, M. H. Jericho, I. A. Meinertzhangen, and H. J. Kreuzer. Digital in-line holography of microspheres. *Appl. Opt.*, 41(25):5367–5375, 2002. {6, 169}
- [79] W. Xu, M. H. Jericho, H. J. Kreuzer, and I. A. Meinertzhangen. Tracking particles in four dimensions with in-line holographic microscopy. *Opt. Lett.*, 28(3):164–166, 2003. {6, 169}
- [80] C.-S. Guo, L. Zhang, H.-T. Wang, J. Liao, and Y. Y. Zhu. Phase-shifting error and its elimination in phase-shifting digital holography. *Opt. Lett.*, 27(19):1687–1689, 2002. {6, 126}
- [81] Ch. Liu, Y. Li, X. Cheng, Zh. Liu, F. Bo, and J. Zhu. Elimination of zero-order diffraction in digital holography. *Opt. Eng.*, 41(10):2434–2437, 2002. {6, 106}
- [82] H. Sekanina and J. Posposil. Digital holography using a digital photo-camera. *Journ. Modern Opt.*, 49(13):2083–2092, 2002. {6, 139}
- [83] R. Binet, J. Colineau, and J.-C. Lehureau. Short-range synthetic aperture imaging at 633 nm by digital holography. *Appl. Opt.*, 41(23):4775–4782, 2002. {6, 137}
- [84] F. Le Clerc, L. Collot, and M. Gross. Numerical heterodyne holography with two-dimensional photodetector arrays. *Opt. Lett.*, 25(10):716–718, 2000. {6, 127, 242}
- [85] F. Le Clerc, L. Collot, and M. Gross. Selection of ballistic photons in diffusing media by numerical heterodyne holography. In P. Jacquot and J.-M. Fournier, editors, *Interferometry in Speckle Light*, pages 243–248, 2000. {6, 127}
- [86] F. Le Clerc, L. Collot, and M. Gross. Numerical heterodyne holography. In P. Jacquot and J.-M. Fournier, editors, *Interferometry in Speckle Light*, pages 235–242, 2000. {6, 127}

- [87] F. Le Clerc, M. Gross, and L. Collot. Synthetic-aperture experiment in the visible with on-axis digital heterodyne holography. *Opt. Lett.*, 26(20):1550–1552, 2001. {6, 137}
- [88] S. Coetmellec, C. Buraga-Lefebvre, D. Lebrun, and C. Özkul. Application of in-line digital holography to multiple plane velocimetry. *Meas. Sci. & Techn.*, 12:1392–1397, 2001. {6, 166}
- [89] S. Coetmellec, D. Lebrun, and C. Özkul. Application of the two-dimensional fractional-order Fourier transformation to particle field digital holography. *Journ. Opt. Soc. Amer. A*, 19:1537–1546, 2002. {6, 162}
- [90] L. Yu and L. Cai. Iterative algorithm with a constraint condition for numerical reconstruction of a three-dimensional object from its hologram. *Journ. Opt. Soc. Amer. A*, 18(5):1033–1045, 2001. {6, 161}
- [91] L. Yu and L. Cai. Multidimensional data encryption with digital holography. *Opt. Comm.*, 215:271–284, 2003. {6, 183}
- [92] E. Allaria, S. Brugioni, S. De Nicola, P. Ferraro, S. Grilli, and R. Meucci. Digital holography at 10.6 μm . *Opt. Comm.*, 215:257–262, 2003. {6, 57, 60, 357}
- [93] S. Grilli, P. Ferraro, S. De Nicola, A. Finizio, G. Pierattini, and R. Meucci. Whole optical wavefields reconstruction by digital holography. *Opt. Expr.*, 9(6):294–302, 2001. {6, 136}
- [94] S. De Nicola, P. Ferraro, A. Finizio, and G. Pierattini. Compensation of aberrations in Fresnel off-axis digital holography. In W. Osten and W. Jüptner, editors, *Fringe 2001*, pages 407–412, 2001. {6, 62, 114}
- [95] S. De Nicola, P. Ferraro, A. Finizio, and G. Pierattini. Correct-image reconstruction in the presence of severe anamorphism by means of digital holography. *Opt. Lett.*, 26:974–976, 2001. {6, 114}
- [96] S. Murata and N. Yasuda. Potential of digital holography in particle measurement. *Opt. Laser Technol.*, 32:567–574, 2000. {6, 161}
- [97] O. Matoba, T. J. Naughton, Y. Frauel, N. Bertaux, and B. Javidi. Real-time three-dimensional object reconstruction by use of a phase-encoded digital hologram. *Appl. Opt.*, 41(29):6187–6192, 2002. {6, 127}
- [98] O. Matoba and B. Javidi. Optical retrieval of encrypted digital holograms for secure real-time display. *Opt. Lett.*, 27(5):321–323, 2002. {6, 183}
- [99] N. Takai, M. Yamada, and T. Idogawa. Holographic interferometry using a reference wave with a sinusoidally modulated amplitude. *Opt. Laser Technol.*, 8:21–23, 1976. {6, 330}
- [100] Y. Takaki and H. Ohzu. Fast numerical reconstruction technique for high-resolution hybrid holographic microscopy. *Appl. Opt.*, 38(11):2204–2211, 1999. {6, 170, 171, 173}
- [101] Y. Takaki, H. Kawai, and H. Ohzu. Hybrid holographic microscopy free of conjugate and zero-order images. *Appl. Opt.*, 38(23):4990–4996, 1999. {6, 105, 108}
- [102] M. Takeda, K. Taniguchi, T. Hirayama, and H. Kohgo. Single-transform Fourier/Hartley fringe analysis for holographic interferometry. In Z. Füzesi, W. Jüptner, and W. Osten, editors, *Simulation and Experiment in Laser Metrology*, pages 67–73, 1996. {6, 384, 385, 440}

- [103] I. Yamaguchi and T. Zhang. Phase-shifting digital holography. *Opt. Lett.*, 22(16):1268–1270, 1997. {6, 125, 126}
- [104] T. Zhang and I. Yamaguchi. Three-dimensional microscopy with phase-shifting digital holography. *Opt. Lett.*, 23(15):1221–1223, 1998. {6, 125, 126}
- [105] T. Zhang and I. Yamaguchi. 3-D microscopy with phase-shifting digital holography. In *Laser Interferometry IX: Applications*, volume 3479 of *Proc. of Soc. Photo-Opt. Instr. Eng.*, pages 152–159, 1998. {6, 126}
- [106] I. Yamaguchi, J.-I. Kato, S. Ohta, and J. Mizuno. Image formation in phase-shifting digital holography. In G. M. Brown, W. Jüptner, and R. J. Pryputniewicz, editors, *Laser Interferometry X: Applications*, volume 4101 of *Proc. of Soc. Photo-Opt. Instr. Eng.*, pages 330–338, 2000. {6, 171}
- [107] I. Yamaguchi, S. Ohta, and J.-I. Kato. Surface contouring by phase-shifting digital holography and noise reduction. In P. Jacquot and J.-M. Fournier, editors, *Interferometry in Speckle Light*, pages 249–256, 2000. {6, 343}
- [108] I. Yamaguchi, J.-I. Kato, S. Ohta, and J. Mizuno. Image formation in phase-shifting digital holography and applications to microscopy. *Appl. Opt.*, 40(34):6177–6186, 2001. {6, 171}
- [109] I. Yamaguchi, O. Inomoto, and J.-I. Kato. Surface shape measurement by phase-shifting digital holography. In W. Osten and W. Jüptner, editors, *Fringe 2001*, pages 365–372, 2001. {6, 343}
- [110] I. Yamaguchi, T. Matsumura, and J.-I. Kato. Phase-shifting color digital holography. *Opt. Lett.*, 27(13):1108–1110, 2002. {6, 129}
- [111] S. Pasko and R. Jozwicki. Novel Fourier approach to digital holography. *Opto-Electron. Rev.*, 10(2):89–95, 2002. {6, 107}
- [112] Y. Xu, C. M. Vest, and J. D. Murray. Holographic interferometry used to demonstrate a theory of pattern formation in animal coats. *Appl. Opt.*, 22(22):3479–3483, 1983. {6, 326}
- [113] L. Xu, X. Peng, J. Miao, and A. Asundi. Digital micro-holo-interferometry for microstructure studies. In G. M. Brown, W. Jüptner, and R. J. Pryputniewicz, editors, *Laser Interferometry X: Applications*, volume 4101 of *Proc. of Soc. Photo-Opt. Instr. Eng.*, pages 543–548, 2000. {6, 179, 311}
- [114] L. Xu, X. Peng, J. Miao, and A. Asundi. Studies of digital microscopic holography with applications to microstructure testing. *Appl. Opt.*, 40(28):5046–5051, 2001. {6, 179, 311}
- [115] B. Nilsson and T. E. Carlsson. Simultaneous measurement of shape and deformation using digital light-in-flight recording by holography. *Opt. Eng.*, 39(1):244–253, 2000. {6, 346, 347}
- [116] B. Nilsson and T. E. Carlsson. Direct three-dimensional shape measurement by digital light-in-flight holography. *Appl. Opt.*, 37(34):7954–7959, 1998. {6, 346}
- [117] T. E. Carlsson. Measurement of three-dimensional shapes using light-in-flight recording by holography. *Opt. Eng.*, 32(10):2587–2592, 1993. {6, 339}

- [118] B. Nilsson and T. E. Carlsson. Resolution improvements of the digital light-in-flight recording by holography method. In G. M. Brown, W. Jüptner, and R. J. Pryputniewicz, editors, *Laser Interferometry X: Applications*, volume 4101 of *Proc. of Soc. Photo-Opt. Instr. Eng.*, pages 369–377, 2000. {6, 346, 348}
- [119] B. Skarman, J. Becker, and K. Wozniak. Simultaneous 3D-PIV and temperature measurements using a new CCD-based holographic interferometer. *Flow Meas. Instrum.*, 7(1):1–6, 1996. {6, 127}
- [120] M. Jacquot, P. Sandoz, and G. Tribillon. Digital holography with improved resolution by spatial sampling of holograms. In P. Jacquot and J.-M. Fournier, editors, *Interferometry in Speckle Light*, pages 219–226, 2000. {6, 84, 137}
- [121] M. Jacquot, P. Sandoz, and G. Tribillon. High resolution digital holography. *Opt. Comm.*, 190:87–94, 2001. {6, 84, 137}
- [122] T. Colomb, P. Dahlgren, E. Cuche, D. Beguin, and Chr. Depeursinge. A method for polarisation imaging using digital holography. In P. Jacquot and J.-M. Fournier, editors, *Interferometry in Speckle Light*, pages 227–234, 2000. {6, 314}
- [123] T. Colomb, P. Dahlgren, D. Beguin, E. Cuche, P. Marquet, and Chr. Depeursinge. Polarization imaging by use of digital holography. *Appl. Opt.*, 41(1):27–37, 2002. {6, 314}
- [124] D. E. Cuche. Determination of the Poisson's ratio by the holographic moire technique. In W. Jüptner, editor, *Holography Techniques and Applications*, volume 1026 of *Proc. of Soc. Photo-Opt. Instr. Eng.*, pages 165–170, 1988. {6, 176, 178, 179, 318, 359}
- [125] D. Beguin, E. Cuche, P. Dahlgren, C. Depeursinge, G. Delacretaz, and R. P. Salathe. Single acquisition polarisation imaging with digital holography. *Electron. Lett.*, 35(23):2053–2055, 1999. {6, 314}
- [126] D. Cuche and W. Schumann. Fringe modification with amplification in holographic interferometry and application of this to determine strain and rotation. In W. F. Fagan, editor, *Industrial Applications of Laser Technology*, volume 398 of *Proc. of Soc. Photo-Opt. Instr. Eng.*, pages 35–45, 1983. {6, 317}
- [127] E. Cuche, P. Marquet, and C. Depeursinge. Spatial filtering for zero-order and twin-image elimination in digital off-axis holography. *Appl. Opt.*, 39(23):4070–4075, 2000. {6, 107}
- [128] E. Cuche, P. Marquet, P. Dahlgren, and Chr. Depeursinge. Digital holographic microscopy, a new method for simultaneous amplitude- and quantitative phase-contrast imaging. In P. Jacquot and J.-M. Fournier, editors, *Interferometry in Speckle Light*, pages 213–218, 2000. {6, 176}
- [129] M. Liebling, Th. Blu, and M. Unser. Fresnelets: New multiresolution wavelet bases for digital holography. *IEEE Trans. on Image Proc.*, 12(1):29–43, 2003. {6, 133, 134, 443–445}
- [130] L. Onural and P. D. Scott. Digital decoding of in-line holograms. *Opt. Eng.*, 26(11):1124–1132, 1987. {6, 105, 108}
- [131] L. Onural and M. T. Özgen. Extraction of three-dimensional object-location information directly from in-line holograms using Wigner analysis. *Journ. Opt. Soc. Amer. A*, 9(2):252–260, 1992. {6, 108}

- [132] L. Onural. Sampling of the diffraction field. *Appl. Opt.*, 39(32):5929–5935, 2000. {6, 146}
- [133] Y. Frauel and B. Javidi. Digital three-dimensional image correlation by use of computer-reconstructed integral imaging. *Appl. Opt.*, 41(26):5488–5496, 2002. {6}
- [134] E. Tajahuerce and B. Javidi. Encrypting three-dimensional information with digital holography. *Appl. Opt.*, 39(35):6595–6601, 2000. {6, 180, 182}
- [135] E. Tajahuerce, O. Matoba, S. C. Verrall, and B. Javidi. Optoelectronic information encryption with phase-shifting interferometry. *Appl. Opt.*, 39(14):2313–2320, 2000. {6, 180, 183}
- [136] Y. Y. Hung and C. Y. Liang. Image-shearing camera for direct measurement of surface strain. *Appl. Opt.*, 18(7):1046–1051, 1979. {6, 405}
- [137] G. Indebetouw and P. Klysubun. Imaging through scattering media with depth resolution by use of low-coherence gating in spatiotemporal digital holography. *Opt. Lett.*, 25(4):212–214, 2000. {6, 179, 180}
- [138] G. Indebetouw and P. Klysubun. Space-time digital holography: A three-dimensional microscopic imaging scheme with an arbitrary degree of spatial coherence. *Adv. Phys. Lett.*, 75(14):2017–2019, 1999. {6, 179}
- [139] T.-C. Poon, T. Kim, G. Indebetouw, B. W. Schilling, M. H. Wu, K. Shinoda, and Y. Suzuki. Twin-image elimination experiments for three-dimensional images in optical scanning holography. *Opt. Lett.*, 25(4):215–217, 2000. {6, 127}
- [140] M. K. Kim. Wavelength-scanning digital interference holography for optical section imaging. *Opt. Lett.*, 24(23):1693–1695, 1999. {6, 137}
- [141] M. K. Kim. Tomographic three-dimensional imaging of a biological specimen using wavelength-scanning digital interference holography. *Optics Expr.*, 7(9):305–310, 2000. {6, 137}
- [142] S. Lai and M. A. Neifeld. Digital wavefront reconstruction and its application to image encryption. *Opt. Comm.*, 178(4-6):283–289, 2000. {6, 183, 263}
- [143] G. Lai and T. Yatagai. Dual-reference holographic interferometry with a double pulsed laser. In F.-P. Chiang, editor, *International Conference on Photomechanics and Speckle Metrology*, volume 814 of *Proc. of Soc. Photo-Opt. Instr. Eng.*, pages 346–351, 1987. {6, 47, 202}
- [144] Z. Liu, M. Centurion, G. Panotopoulos, J. Hong, and D. Psaltis. Holographic recording of fast events on a CCD camera. *Opt. Lett.*, 27(1):22–24, 2002. {6, 286}
- [145] J. H. Milgram and W. Li. Computational reconstruction of images from holograms. *Appl. Opt.*, 41(5):853–864, 2002. {6, 169}
- [146] R. B. Owen and A. A. Zozulya. In-line digital holographic sensor for monitoring and characterizing marine particulates. *Opt. Eng.*, 39(8):2187–2197, 2000. {6, 385}
- [147] R. B. Owen, A. A. Zozulya, M. R. Benoit, and D. M. Klaus. Microgravity materials and life sciences research applications of digital holography. *Appl. Opt.*, 41(19):3927–3935, 2002. {6, 385}
- [148] R. B. Owen and A. A. Zozulya. Comparative study with double-exposure digital holographic interferometry and a shack-hartmann sensor to characterize transparent materials. *Appl. Opt.*, 41(28):5891–5895, 2002. {6, 385}

- [149] M.R. Benoit, D. M. Klaus, and R. B. Owen. Quantifying extracellular mass transport using digital holography. *ASGSB 2001 Abstracts*, 2001. {6}
- [150] G. Pan and H. Meng. Digital in-line holographic PIV for 3D particulate flow diagnostics. In *4th International Symposium on Particle Image Velocimetry, Göttingen*, 2001. {6, 160}
- [151] X. Xiao and I. K. Puri. Digital recording and numerical reconstruction of holograms: an optical diagnostic for combustion. *Appl. Opt.*, 41(19):3890–3899, 2002. {6, 384}
- [152] L. Yaroslavsky. Digital holography: 30 years later. In *Practical Holography XVI*, volume 4659 of *Proc. of Soc. Photo-Opt. Instr. Eng.*, pages 1–11, 2002. {6}
- [153] L. Yaroslavsky. *Digital Holography and Digital Image Processing*. Kluwer Academic Publishers, 2003. {6}
- [154] P. Hariharan. Laser interferometry: current trends and future prospects. In R. J. Pryputniewicz, editor, *Laser Interferometry IV: Computer-Aided Interferometry*, volume 1553 of *Proc. of Soc. Photo-Opt. Instr. Eng.*, pages 2–11, 1991. {7}
- [155] H. Rottenkolber and W. Jüptner. Holographic interferometry in the next decade. In R. J. Pryputniewicz, editor, *Laser Interferometry: Quantitative Analysis of Interferograms*, volume 1162 of *Proc. of Soc. Photo-Opt. Instr. Eng.*, pages 2–15, 1989. {7}
- [156] H. J. Tiziani. Optical methods for precision measurements. *Opt. Quantum Electron.*, 21:253–282, 1989. {7}
- [157] J. Durnin. Exact solutions for nondiffracting beams. I. The scalar theory. *Journ. Opt. Soc. Amer. A*, 4:651–654, 1987. {12}
- [158] J. W. Goodman. *Introduction to Fourier Optics*. McGraw-Hill, 1968. {17, 19}
- [159] W. Lauterborn, T. Kurz, and M. Wiesenfeldt. *Coherent Optics*. Springer, 1993. (In German). {17–19, 52, 61}
- [160] J. W. Goodman. *Introduction to Fourier Optics*. McGraw-Hill, New York, second edition, 1996. {21–23, 25, 27–29, 101, 140, 141, 143, 171, 178, 411, 427}
- [161] K. Iizuka. *Engineering Optics*. Springer Verlag, Berlin, Heidelberg, New York, second edition, 1987. {28}
- [162] B. E. A. Saleh and M. C. Teich. *Fundamentals of Photonics*. John Wiley and Sons, 1991. {29}
- [163] J. W. Goodman. Statistical properties of laser speckle patterns. In J. C. Dainty, editor, *Laser Speckle and Related Phenomena*, volume 9 of *Springer Series Topics in Applied Physics*, pages 9–75, 1975. {30, 33, 35}
- [164] K. J. Gasvik. *Optical Metrology*. John Wiley and Sons, 1987. {36, 306, 400}
- [165] E. B. Champagne. Non-paraxial imaging, magnification and aberration properties in holography. *Journ. Opt. Soc. Amer.*, 57:51–55, 1967. {44, 47}
- [166] R. W. Meier. Magnification and third-order aberrations in holography. *Journ. Opt. Soc. Amer.*, 55:987–992, 1965. {44, 45, 47}
- [167] J. F. Miles. Imaging and magnification properties in holography. *Optica Acta*, 19:165–186, 1972. {44}
- [168] D. B. Neumann. Geometrical relationships between the original object and the two images of a hologram reconstruction. *Journ. Opt. Soc. Amer.*, 56:858–861, 1966. {44}

- [169] W. Schumann and M. Dubas. On the motion of holographic images caused by movements of the reconstruction light source, with the aim of application to deformation analysis. *Optik*, 46(4):377–392, 1976. {44}
- [170] C. M. Vest. *Holographic Interferometry*. John Wiley and Sons, 1979. {45, 185, 195, 204, 206, 211, 214, 224, 311, 313–315, 318, 329, 330, 367, 370, 372, 374, 376, 383}
- [171] E. N. Leith and J. Upatnieks. Reconstructed wavefronts and communication theory. *Journ. Opt. Soc. Amer.*, 52:1123–1130, 1962. {45}
- [172] P. Hariharan. *Optical Holography: Principles, Techniques and Applications*. Cambridge University Press, 1984. {45–47, 50, 58, 59, 160, 329}
- [173] P. Hariharan. Basic principles. In P. K. Rastogi, editor, *Holographic Interferometry*, volume 68 of *Springer Series in Optical Sciences*, pages 7–32, 1994. {46}
- [174] D. Paoletti, S. Amadesi, and A. D’Altorio. A fringe control method for real time HNDT. *Opt. Comm.*, 49(2):98–102, 1984. {47}
- [175] J. N. Latta. Computer-based analysis of hologram imagery and aberrations. I. Hologram types and their nonchromatic aberrations. *Appl. Opt.*, 10:599–608, 1971. {47}
- [176] J. N. Latta. Computer-based analysis of hologram imagery and aberrations. II. Aberrations induced by a wavelength shift. *Appl. Opt.*, 10:609–618, 1971. {47}
- [177] J. N. Latta. Computer-based analysis of holography using ray tracing. *Appl. Opt.*, 10:2698–2710, 1971. {47}
- [178] J. F. Miles. Evaluation of the wavefront aberration in holography. *Optica Acta*, 20:19–31, 1973. {47}
- [179] G. W. Stroke and A. E. Labeyrie. White light reconstruction of holographic images using the Lippmann-Bragg diffraction effect. *Phys. Lett.*, 20(4):368–370, 1966. {51}
- [180] Yu. I. Ostrovsky, M. M. Butusov, and G. V. Ostrovskaia. *Interferometry by Holography*. Springer-Verlag, 1980. {52, 386}
- [181] R. T. Pitlak and R. Page. Pulsed lasers for holographic interferometry. *Opt. Eng.*, 24(4):639–644, 1985. {56}
- [182] A. J. Decker. Holographic interferometry with an injection seeded Nd:YAG laser and two reference beams. *Appl. Opt.*, 29(18):2697–2700, 1990. {57}
- [183] G. Hüttmann, W. H. Lauterborn, and E. Schmitz. Holography with a frequency-doubled Nd:YAG laser. In W. Jüptner, editor, *Holography Techniques and Applications*, volume 1026 of *Proc. of Soc. Photo-Opt. Instr. Eng.*, pages 14–21, 1988. {57}
- [184] L. Crawforth, C.-K. Lee, and A. C. Munce. Application of pulsed laser holographic interferometry to the study of magnetic disc drive component motions. In K. Stetson and R. Pryputniewicz, editors, *International Conference on Hologram Interferometry and Speckle Metrology*, pages 404–412, 1990. {57}
- [185] P. Hariharan. High-precision, digital, phase-stepping interferometry with laser diode. In R. J. Pryputniewicz, editor, *Laser Interferometry: Quantitative Analysis of Interferograms*, volume 1162 of *Proc. of Soc. Photo-Opt. Instr. Eng.*, pages 86–91, 1989. {57}
- [186] Y. Ishii, J. Chen, and K. Murata. Digital phase-measuring interferometry with a tunable laser diode. *Opt. Lett.*, 12(4):233–235, 1987. {57}

- [187] R. J. Parker. A quarter century of thermoplastic holography. In K. Stetson and R. Pryputniewicz, editors, *International Conference on Hologram Interferometry and Speckle Metrology*, pages 217–224, 1990. {59}
- [188] M. Georges, C. Thizy, V. Scauflaire, S. Ryhon, G. Pauliat, P. Lemaire, and G. Roosen. Dynamic holographic interferometry with photorefractive crystals: review of applications and advanced techniques. In K. Gastinger, O. Løkberg, and S. Winther, editors, *Speckle Metrology 2003*, volume 4933 of *Proc. of Soc. Photo-Opt. Instr. Eng.*, pages 250–255, 2003. {60}
- [189] J. P. Herriau, A. Delboulbe, and J. P. Huignard. Non-destructive testing using real time holographic interferometry in BSO crystals. In W. F. Fagan, editor, *Industrial Applications of Laser Technology*, volume 398 of *Proc. of Soc. Photo-Opt. Instr. Eng.*, pages 123–129, 1983. {60}
- [190] H. J. Tiziani. Real-time metrology with BSO crystals. *Optica Acta*, 29(4):463–470, 1982. {60}
- [191] X. Wang, R. Magnusson, and A. Haji-Sheikh. Real-time interferometry with photorefractive reference holograms. *Appl. Opt.*, 32(11):1983–1986, 1993. {60}
- [192] D. H. Barnhart, N. Hampp, N. A. Halliwell, and J. M. Coupland. Digital holographic velocimetry with bacteriorhodopsin (BR) for real-time recording and numeric reconstruction. In *11th International Symposium on Applications of Laser Techniques to Fluid Mechanics, Lisbon*, 2002. {61}
- [193] J. P. Bentley. *Principles of Measurement Systems*, chapter 15: Optical measurement systems, pages 364–405. Longman Scientific and Technical, 2nd edition, 1988. {61}
- [194] G. O. Reynolds, J. B. DeVelis, G. B. Parrent, and B. J. Thompson. *The New Physical Optics Notebook: Tutorials in Fourier Optics*. SPIE Optical Engineering Press, 1989. {61}
- [195] J. A. Gilbert, D. R. Mattheys, and Ch. M. Hendren. Displacement analysis of the interior walls of a pipe using panoramic holo-interferometry. In F. P. Chiang, editor, *Second International Conference on Photomechanics and Speckle Metrology*, volume 1554 of *Proc. of Soc. Photo-Opt. Instr. Eng.*, pages 128–134, 1991. {61}
- [196] N. Abramson. *The Making and Evaluation of Holograms*. Academic Press, 1981. {61, 337, 365}
- [197] B. E. Jones. Optical fibre sensors and systems for industry. *Journ. Phys. E: Sci. Instr.*, 18:770–782, 1985. {61}
- [198] F. Solitro, L. Gatti, F. Bedarida, and L. Michetti. Multidirectional holographic interferometer (MHOI) with fiber optics for study of crystal growth in microgravity. In R. J. Pryputniewicz, editor, *Laser Interferometry: Quantitative Analysis of Interferograms*, volume 1162 of *Proc. of Soc. Photo-Opt. Instr. Eng.*, pages 62–65, 1989. {61, 377}
- [199] J. A. Gilbert, T. D. Dudderar, M. E. Schultz, and A. J. Boehlein. The monomode fiber – a new tool for holographic interferometry. *Exp. Mech.*, 23(2):190–195, 1983. {62}
- [200] J. A. Gilbert, T. D. Dudderar, and A. Nose. Remote deformation field measurement through different media using fiber optics. *Opt. Eng.*, 24(4):628–631, 1985. {62}

- [201] S. Pflüger, R. Noll, J. Hertzberg, V. Sturm, and W. Meesters. Pulsed holography with elongated q-switch pulse. In VDI-Technology Centre, editor, *Holographic-Interferometric Metrology*, Laser-Research and Laser-Technology, pages 131–145, 1995. (In German). **{62}**
- [202] K. Creath. Phase-shifting holographic interferometry. In P. K. Rastogi, editor, *Holographic Interferometry*, volume 68 of *Springer Series in Optical Sciences*, pages 109–150, 1994. **{62, 242, 404}**
- [203] G. E. Sommargren. Double exposure holographic interferometry using commonpath reference waves. *Appl. Opt.*, 16(6):1736–1741, 1977. **{63, 245}**
- [204] M. Kujawinska and D. W. Robinson. Automatic fringe pattern analysis for holographic measurement of transient event. In W. Jüptner, editor, *Holography Techniques and Applications*, volume 1026 of *Proc. of Soc. Photo-Opt. Instr. Eng.*, pages 93–103, 1988. **{65}**
- [205] M. Kujawinska and D. W. Robinson. Multichannel phase-stepped holographic interferometry. *Appl. Opt.*, 27:312–320, 1988. **{65, 243}**
- [206] C. R. Mercer and G. Beheim. Fiber optic phase stepping system for interferometry. *Appl. Opt.*, 30(7):729–734, 1991. **{65}**
- [207] M. Takeda and M. Kitoh. Spatio-temporal frequency-multiplex heterodyne interferometry. In R. J. Pryputniewicz, editor, *Laser Interferometry IV: Computer-Aided Interferometry*, volume 1553 of *Proc. of Soc. Photo-Opt. Instr. Eng.*, 1991. **{65, 265}**
- [208] Th. V. Higgins. The technology of image capture. *Laser Focus World*, 30(12):53–60, 1994. **{66}**
- [209] W. S. Boyle and G. E. Smith. Charge coupled semiconductor devices. *Bell Systems Tech. Journ.*, 49:587–593, 1970. **{66}**
- [210] G. C. Holst. *CCD Arrays, Cameras, and Displays*. SPIE Optical Engineering Press, 1996. **{66, 68, 71, 72, 74, 76}**
- [211] R. Spooren. Standard charge-coupled device cameras for video speckle interferometry. *Opt. Eng.*, 33(3):889–896, 1994. **{69, 73}**
- [212] Th. Baumbach, W. Osten, C. Falldorf, and W. Jüptner. Remote interferometry by digital holography for shape control. In W. Osten, editor, *Interferometry XI*, volume 4778 of *Proc. of Soc. Photo-Opt. Instr. Eng.*, pages 338–349, 2002. **{73, 354, 356}**
- [213] <http://www.extremetech.com/article2/0,3973,474239,00.asp>. **{73}**
- [214] J. Adams, K. Parulski, and K. Spaulding. Color processing in digital cameras. *IEEE Micro*, 18(6):20–29, 1998. **{77}**
- [215] D. Merrill. The next generation digital camera. *Optics and Photonics News*, Jan.:26–33, 2003. **{77}**
- [216] D. Alleysson, S. Süsstrunk, and J. Herault. Color demosaicing by estimating luminance and opponent chromatic signals in the Fourier domain. In *Proc. IS&T/SID 10th Color Imaging Conference*, pages 331–336, 2002. **{77, 79}**
- [217] R. Ramanath, W. E. Snyder, G. L. Bilbro, and W. A. Sander III. Demosaicing methods for Bayer color arrays. *Journ. Electronic Imaging*, 11(3):306–315, 2002. **{79}**
- [218] P. Longere, X. Zhang, P. DelaHunt, and D. Brainard. Perceptual assessment of demosaicing algorithm performance. *Proc. IEEE*, 90(1):123–132, 2002. **{80}**

- [219] J. P. Allebach, N. C. Gallagher, and B. Liu. Aliasing error in digital holography. *Appl. Opt.*, 15(9):2183–2188, 1976. **{81}**
- [220] M. Young. *Optics and Lasers: An Engineering Physics Approach*. Springer-Verlag, 1977. **{86, 371}**
- [221] P. Rastogi and A. Sharma. Systematic approach to image formation in digital holography. *Opt. Eng.*, 42(5):1208–1214, 2003. **{88, 102, 141}**
- [222] G. Pedrini, S. Schedin, and H. J. Tiziani. Lensless digital-holographic interferometry for the measurement of large objects. *Opt. Comm.*, 171:29–36, 1999. **{88, 102}**
- [223] A. F. Doval, C. Trillo, O. Lopez, D. Cernadas, C. Lopez, B. V. Dorrio, J. L. Fernandez, and M. Perez-Amor. Lensless zooming Fourier-transform digital holography. In K. Gastinger, O. Løkberg, and S. Winther, editors, *Speckle Metrology 2003*, volume 4933 of *Proc. of Soc. Photo-Opt. Instr. Eng.*, pages 111–116, 2003. **{89, 102}**
- [224] S. De Nicola, P. Ferraro, A. Finizio, S. Grilli, and G. Pierattini. Experimental demonstration of the longitudinal image shift in digital holography. *Opt. Eng.*, 42(6):1625–1630, 2003. **{91}**
- [225] M. Y. Y. Hung, H. M. Shang, and L. Yang. Unified approach for holography and shearography in surface deformation measurement and nondestructive testing. *Opt. Eng.*, 42(5):1197–1207, 2003. **{92, 400}**
- [226] E. Torres and J. Guerrero Bermudez. Digital Fourier holography: recording and optical reconstruction. *Revista Colombiana de Fisica*, 35(1):168–171, 2003. **{93}**
- [227] Th. Kreis, P. Aswendt, and R. Höfling. Hologram reconstruction using a digital micromirror device. *Opt. Eng.*, 40(6):926–933, 2001. **{93, 146}**
- [228] E. Cuche, F. Bevilacqua, and C. Depeursinge. Digital holography for quantitative phase-contrast imaging. *Opt. Lett.*, 24(5):291–293, 1999. **{96}**
- [229] C. Wagner, S. Seebacher, W. Osten, and W. Jüptner. Digital recording and numerical reconstruction of lensless Fourier holograms in optical metrology. *Appl. Opt.*, 38(22):4812–4820, 1999. **{101}**
- [230] N. Demoli, J. Mestrovic, and I. Sovic. Subtraction digital holography. *Appl. Opt.*, 42:798–804, 2003. **{105, 108, 385}**
- [231] Th. Kreis and W. Jüptner. Suppression of the dc term in digital holography. *Opt. Eng.*, 36(8):2357–2360, 1997. **{105}**
- [232] Ø . Skotheim. Holovision – a software package for reconstruction and analysis of digitally sampled holograms. In K. Gastinger, O. Løkberg, and S. Winther, editors, *Speckle Metrology 2003*, volume 4933 of *Proc. of Soc. Photo-Opt. Instr. Eng.*, pages 311–316, 2003. **{106, 124}**
- [233] S. Pasko and R. Jozwicki. Improvement methods of reconstruction process in digital holography. *Opto-Electron. Rev.*, 11(3):203–209, 2003. **{107}**
- [234] G. Liu. Object reconstruction from noisy holograms. *Opt. Eng.*, 29(1):19–24, 1990. **{107}**
- [235] G. Pedrini, P. Fröning, H. Fessler, and H. J. Tiziani. In-line digital holographic interferometry. *Appl. Opt.*, 37(26):6262–6269, 1998. **{108}**
- [236] A. Stadelmeier and J. H. Massing. Compensation of lens aberrations in digital holography. *Opt. Lett.*, 25:1630–1632, 2000. **{114}**

- [237] Th. Kreis. *Holographic Interferometry: Principles and Methods*. Wiley-VCH, 1996. **{126, 332, 342}**
- [238] S.-G. Kim, B. Lee, and E.-S. Kim. Removal of bias and the conjugate image in incoherent on-axis triangular holography and real-time reconstruction of the complex hologram. *Appl. Opt.*, 36(20):4784–4791, 1997. **{127}**
- [239] C. Furlong and R. J. Pryputniewicz. Optoelectronic characterization of shape and deformation of MEMS accelerometers used in transportation applications. *Opt. Eng.*, 42(5):1223–1231, 2003. **{127, 311, 405}**
- [240] A. Albertazzi Jr. and A. Vieira Fantin. Digital complex holography using a shearing interferometer: improvements and recent results. In K. Gastinger, O. Løkberg, and S. Winther, editors, *Speckle Metrology 2003*, volume 4933 of *Proc. of Soc. Photo-Opt. Instr. Eng.*, pages 42–47, 2003. **{127, 128}**
- [241] M. Liebling, Th. Blu, E. Cuche, P. Marquet, Chr. Depeursinge, and M. Unser. Local amplitude and phase retrieval method for digital holography applied to microscopy. In *Conference on Biomedical Optics 2003*, volume 5143 of *Proc. of Soc. Photo-Opt. Instr. Eng.*, 2003. **{130, 132}**
- [242] M. Liebling, Th. Blu, and M. Unser. Complex-wave retrieval from a single off-axis hologram. *Journ. Opt. Soc. Amer. A*, 21(3):367–377, 2004. **{130}**
- [243] M. Liebling, Th. Blu, E. Cuche, P. Marquet, Chr. Depeursinge, and M. Unser. A novel non-diffractive reconstruction method for digital holographic microscopy. In *Proc. of the First 2002 IEEE International Symposium on Biomedical Imaging: Macro to Nano*, pages 625–628, 2002. **{130}**
- [244] Th. Kreis. *Auswertung holografischer Interferenzmuster mit Methoden der Ortsfrequenzanalyse (Evaluation of holographic interference patterns using methods of spatial frequency analysis)*. Fortschritt-Berichte VDI, Reihe 8, Nr. 108. VDI-Verlag, 1986. (In German). **{132, 390}**
- [245] M. Liebling, Th. Blu, and M. Unser. Non-linear Fresnellet approximation for interference term suppression in digital holography. In *Wavelets: Applications in Signal and Image Processing X*, Proc. of Soc. Photo-Opt. Instr. Eng., 2003. **{134}**
- [246] S. Belaid, D. Lebrun, and C. Özkul. Application of two-dimensional wavelet transform to hologram analysis: visualization of glass fibers in a turbulent flame. *Opt. Eng.*, 36(7):1947–1951, 1997. **{134}**
- [247] M. Malek, S. Coetmellec, D. Allano, and D. Lebrun. Formulation of in-line holography process by a linear shift invariant system: application to the measurement of fiber diameter. *Opt. Comm.*, 223:263–271, 2003. **{134}**
- [248] D. Lebrun, S. Belaid, and C. Özkul. Hologram reconstruction by use of optical wavelet transform. *Appl. Opt.*, 38(17):3730–3734, 1999. **{134}**
- [249] S. Soontaranon, J. Widjaja, and T. Asakura. Direct analysis of in-line particle holograms by using wavelet transform and envelope reconstruction method. *Optik*, 113(11):489–494, 2002. **{134}**
- [250] L. Onural and M. Kocatepe. Family of scaling chirp functions, diffraction, and holography. *IEEE Trans. Signal Proc.*, 43(71):1568–1578, 1995. **{134}**
- [251] L. Onural. Diffraction from a wavelet point of view. *Opt. Lett.*, 18(11):846–848, 1993. **{134}**

- [252] Th. Kreis, M. Adams, and W. Jüptner. Methods of digital holography: A comparison. In *European Symposium on Lasers and Optics in Manufacturing*, volume 3098 of *Proc. of Soc. Photo-Opt. Instr. Eng.*, pages 224–233, 1997. **{134}**
- [253] Th. Kreis and W. Jüptner. Principles of digital holography. In W. Jüptner and W. Osten, editors, *Fringe '97*, pages 353–363, 1997. **{136, 162}**
- [254] J. W. Goodman. Statistical properties of laser speckle patterns. In J. C. Dainty, editor, *Laser Speckle and Related Phenomena*, volume 9 of *Topics in Applied Physics*, pages 9–75, 1975. **{136}**
- [255] Th. Kreis, M. Adams, and W. Jüptner. Aperture synthesis in digital holography. In K. Creath and J. Schmitt, editors, *Laser Interferometry XI: Techniques and Analysis*, volume 4777 of *Proc. of Soc. Photo-Opt. Instr. Eng.*, pages 69–76, 2002. **{137}**
- [256] Th. Kreis. Frequency analysis of digital holography. *Opt. Eng.*, 41(4):771–778, 2002. **{141}**
- [257] Th. Kreis. Frequency analysis of digital holography with reconstruction by convolution. *Opt. Eng.*, 41(8):1829–1839, 2002. **{141}**
- [258] L. Xu, J. Miao, and A. Asundi. Properties of digital holography based on in-line configuration. *Opt. Eng.*, 39(12):3214–3219, 2000. **{146, 179}**
- [259] M. L. Huebschman, B. Munjuluri, and H. R. Garner. Dynamic holographic 3-D image projection. *Opt. Expr.*, 11(5):437–445, 2003. **{146}**
- [260] E. Tajahuerce, O. Matoba, and B. Javidi. Shift-invariant three-dimensional object recognition by means of digital holography. *Appl. Opt.*, 40(23):3877–3886, 2001. **{159}**
- [261] Th. Kreis, M. Adams, and W. Jüptner. Digital in-line holography in particle measurement. In M. Kujawinska, editor, *Interferometry 99: Techniques and Technology*, volume 3744 of *Proc. of Soc. Photo-Opt. Instr. Eng.*, pages 54–64, 1999. **{160, 165}**
- [262] Th. Kreis. Digital holography for metrologic applications. In P. Jacquot and J.-M. Fournier, editors, *Interferometry in Speckle Light*, pages 205–212, 2000. **{160, 333, 348}**
- [263] G. Pan and H. Meng. Digital holography of particle fields: reconstruction by use of complex amplitude. *Appl. Opt.*, 42(5):827–833, 2003. **{160}**
- [264] C. Fournier, C. Ducottet, and Th. Fournel. Digital in-line holography: influence of the reconstruction function on the axialprofile of a reconstructed particle image. *Meas. Sci. & Techn.*, 15:686–693, 2004. **{160}**
- [265] M. Adams, Th. Kreis, and W. Jüptner. Particle size and position measurement with digital holography. In *European Symposium on Lasers and Optics in Manufacturing*, volume 3098 of *Proc. of Soc. Photo-Opt. Instr. Eng.*, pages 234–240, 1997. **{160, 162, 165}**
- [266] Th. Kreis, W. Jüptner, and J. Geldmacher. Digital holography: Methods and applications. In *International Conference on Applied Optical Metrology*, volume 3407 of *Proc. of Soc. Photo-Opt. Instr. Eng.*, pages 169–177, 1998. **{162}**
- [267] J. Lobera, N. Andres, and M. P. Arroyo. Digital image plane holography as a three-dimensional flow velocimetry technique. In K. Gastinger, O. Løkberg, and S. Winther, editors, *Speckle Metrology 2003*, volume 4933 of *Proc. of Soc. Photo-Opt. Instr. Eng.*, pages 279–284, 2003. **{166, 403}**

- [268] S. Lai, B. King, and M. A. Neifeld. Wavefront reconstruction by means of phase-shifting digital in-line holography. *Opt. Comm.*, 173:155–160, 2000. {167}
- [269] S. Lai, B. Kemper, and G. von Bally. Off-axis reconstruction of in-line holograms for twin-image elimination. *Opt. Comm.*, 169:37–43, 1999. {167}
- [270] H. Sun, H. Dong, M. A. Player, J. Watson, D. M. Paterson, and R. Perkins. In-line digital video holography for the study of erosion processes in sediments. *Meas. Sci. & Techn.*, 13:L7–L12, 2002. {168}
- [271] Y. Takaki and H. Ohzu. Hybrid holographic microscopy: visualization of three-dimensional object information by use of viewing angles. *Appl. Opt.*, 39(29):5302–5308, 2000. {174}
- [272] L. Yu, Y. An, and L. Cai. Numerical reconstruction of digital holograms with variable viewing angles. *Opt. Expr.*, 10(22):1250–1257, 2002. {174}
- [273] D. Lebrun, A. M. Benkouider, S. Coetmellec, and M. Malek. Particle field digital holographic reconstruction in arbitrary tilted planes. *Opt. Expr.*, 11(3):224–229, 2003. {174}
- [274] E. Cuche, P. Marquet, and Chr. Depeursinge. Simultaneous amplitude-contrast and quantitative phase-contrast microscopy by numerical reconstruction of Fresnel off-axis holograms. *Appl. Opt.*, 38(34):6994–7001, 1999. {178}
- [275] P. Ferraro, S. De Nicola, A. Finizio, G. Coppola, S. Grilli, C. Magro, and G. Pierattini. Compensation of the inherent wave front curvature in digital holographic coherent microscopy for quantitative phase-contrast imaging. *Appl. Opt.*, 42:1938–1946, 2003. {178}
- [276] L. Xu, X. Peng, A. Asundi, and J. Miao. Digital microholointerferometer: development and validation. *Opt. Eng.*, 42(8):2218–2224, 2003. {179}
- [277] G. Pedrini and H. J. Tiziani. Short-coherence digital microscopy by use of a lensless holographic imaging system. *Appl. Opt.*, 41(22):4489–4496, 2002. {180}
- [278] G. Pedrini, S. Schedin, and H. J. Tiziani. Aberration compensation in digital holographic reconstruction of microscopic objects. *Journ. Modern Opt.*, 48(6):1035–1041, 2001. {180}
- [279] G. Pedrini, S. Schedin, and H. J. Tiziani. Spatial filtering in digital holographic microscopy. *Journ. Modern Opt.*, 47(8):1447–1454, 2000. {180}
- [280] Th. J. Naughton, J. B. McDonald, and B. Javidi. Efficient compression of Fresnel fields for internet transmission of three-dimensional images. *Appl. Opt.*, 42:4758–4764, 2003. {180}
- [281] B. Javidi and T. Nomura. Securing information by use of digital holography. *Opt. Lett.*, 25(1):28–30, 2000. {180}
- [282] N. Takai and Y. Mifune. Digital watermarking by a holographic technique. *Appl. Opt.*, 41(5):865–873, 2002. {183}
- [283] S. Kishk and B. Javidi. Watermarking of three-dimensional objects by digital holography. *Opt. Lett.*, 28(3):167–169, 2003. {183}
- [284] R. W. Larson, J. S. Zelenka, and E. L. Johansen. Microwave radar imagery. In *Proceedings of Symposium on Engineering Applications of Holography*, Proc. of Soc. Photo-Opt. Instr. Eng., page 14, 1972. {185}

- [285] K. Suzuki and B. P. Hildebrand. Holographic interferometry with acoustic waves. In N. Booth, editor, *Acoustical Holography*, volume 6, pages 577–595. Plenum Press, New York, 1975. {185}
- [286] J. E. Sollid and J. B. Swint. A determination of the optimum beam ratio to produce maximum contrast photographic reconstructions from double-exposure holographic interferograms. *Appl. Opt.*, 9(12):2717–2719, 1970. {186}
- [287] J. E. Sollid. Holographic interferometry applied to measurements of small static displacements of diffusely reflecting surfaces. *Appl. Opt.*, 8(8):1587–1595, 1969. {191, 266, 301}
- [288] R. Pawluczyk and Z. Kraska. Diffuse illumination in holographic double-aperture interferometry. *Appl. Opt.*, 24(18):3072–3078, 1985. {194}
- [289] J. D. Trolinger. The holography of phase objects. In N. A. Massie, editor, *Interferometric Metrology, Critical Reviews*, volume 816 of *Proc. of Soc. Photo-Opt. Instr. Eng.*, pages 128–139, 1987. {194}
- [290] N. L. Hecht, J. E. Minardi, D. Lewis, and R. L. Fusek. Quantitative theory for predicting fringe pattern formation in holographic interferometry. *Appl. Opt.*, 12(11):2665–2676, 1973. {196}
- [291] J. Janta and M. Miler. Model interferogram as an aid for holographic interferometry. *J. Optics*, 8(5):301–307, 1977. {196}
- [292] R. Höfling and W. Osten. Displacement measurement by image processed speckle patterns. *Journ. Modern Opt.*, 34:607–617, 1987. {196}
- [293] Th. Kreis, W. Jüptner, and R. Biedermann. Neural network approach to holographic nondestructive testing. *Appl. Opt.*, 34(8):1407–1415, 1995. {197, 387, 391, 395}
- [294] D. I. Farrant and J. N. Petzing. Sensitivity errors in interferometric deformation metrology. *Appl. Opt.*, 42:5634–5641, 2003. {198, 200}
- [295] G. S. Rightley, L. K. Matthews, and G. P. Mulholland. Holographic analysis and experimental error. In K. Stetson and R. Pryputniewicz, editors, *International Conference on Hologram Interferometry and Speckle Metrology*, pages 343–350, 1990. {200}
- [296] W. Jüptner, K. Ringer, and H. Welling. The evaluation of interference fringes for holographic strain and translation measurement (in German). *Optik*, 38:437–448, 1973. {200}
- [297] N. Abramson. The holo-diagram: A practical device for making and evaluating holograms. *Appl. Opt.*, 8:1235–1240, 1969. {200}
- [298] N. Abramson. The holo-diagram II: A practical device for information retrieval in hologram interferometry. *Appl. Opt.*, 9:97–101, 1970. {200}
- [299] N. Abramson. The holo-diagram III: A practical device for predicting fringe patterns in hologram interferometry. *Appl. Opt.*, 9:2311–2320, 1970. {200}
- [300] N. Abramson. The holo-diagram IV: A practical device for simulating fringe patterns in hologram interferometry. *Appl. Opt.*, 10:2155–2161, 1971. {200}
- [301] N. Abramson. The holo-diagram V: A device for practical interpreting of hologram fringes. *Appl. Opt.*, 11:1143–1147, 1972. {200}
- [302] S. Toyooka. Holographic interferometry with increased sensitivity for diffusely reflecting objects. *Appl. Opt.*, 16(4):1054–1057, 1977. {201}

- [303] R. Dändliker, E. Marom, and F. M. Mottier. Two-reference-beam holographic interferometry. *Journ. Opt. Soc. Amer.*, 66(1):23–30, 1976. {201, 235}
- [304] R. Dändliker. Two-reference-beam holographic interferometry. In P. K. Rastogi, editor, *Holographic Interferometry*, volume 68 of *Springer Series in Optical Sciences*, pages 75–108, 1994. {201, 202}
- [305] R. Dändliker, R. Thalmann, and J.-F. Willemin. Fringe interpolation by two-reference-beam holographic interferometry: reducing sensitivity to hologram misalignment. *Opt. Comm.*, 42(5):301–306, 1982. {203, 235, 242}
- [306] S. Schedin, G. Pedrini, H. J. Tiziani, and F. Mendoza Santoyo. Simultaneous three-dimensional dynamic deformation measurements with pulsed digital holography. *Appl. Opt.*, 38(34):7056–7062, 1999. {203, 282, 403}
- [307] S. Walles. On the concept of homologous rays in holographic interferometry of diffusely reflecting surfaces. *Optica Acta*, 17:899–913, 1970. {204, 215}
- [308] K. A. Stetson. Use of fringe vectors in hologram interferometry to determine fringe localization. *Journ. Opt. Soc. Amer.*, 66(6):626–627, 1976. {205}
- [309] P. K. Rastogi. Techniques to measure displacements, derivatives and surface shapes. extension to comparative holography. In P. K. Rastogi, editor, *Holographic Interferometry*, volume 68 of *Springer Series in Optical Sciences*, pages 213–292, 1994. {206, 227, 335, 336, 351, 359, 360}
- [310] R. Jones and C. Wykes. *Holographic and Speckle Interferometry*. Cambridge University Press, second edition, 1989. {206, 208, 227}
- [311] J. Blanco-Garcia, J. L. Fernandez, and M. Perez-Amor. Fringe localization control in holographic interferometry. *Appl. Opt.*, 31(4):488–496, 1992. {210}
- [312] K. A. Stetson. Fringe interpolation for hologram interferometry of rigid-body motions and homogeneous deformations. *Journ. Opt. Soc. Amer.*, 64(1):1–10, 1974. {215, 318}
- [313] K. A. Stetson. Fringe vectors and observed fringe vectors in hologram interferometry. *Appl. Opt.*, 14(2):272–273, 1975. {215, 318}
- [314] K. A. Stetson. Holographic strain analysis by fringe localization planes. *Journ. Opt. Soc. Amer.*, 66:627, 1976. {215}
- [315] P. M. Boone and R. Verbiest. Applications of hologram interferometry and translation measurement. *Optica Acta*, 16:555–567, 1969. {215}
- [316] M. A. Machado Gama. Fringe localization and visibility in hologram and classical broad source interferometry. *Opt. Comm.*, 8(4):362–365, 1973. {215}
- [317] T. Tsuruta, N. Shiotake, and Y. Itoh. Formation and localization of holographically produced interference fringes. *Optica Acta*, 16:723–733, 1969. {215}
- [318] W. T. Welford. Fringe visibility and localization in hologram interferometry. *Opt. Comm.*, 1(3):123–125, 1969. {215}
- [319] W. T. Welford. Fringe visibility and localization in hologram interferometry with parallel displacement. *Opt. Comm.*, 1(7):311–314, 1970. {215}
- [320] P. K. Rastogi. Visualization and measurement of slope and curvature fields using holographic interferometry: an application to flaw detection. *Journ. Modern Opt.*, 38(7):1251–1263, 1991. {215}

- [321] E. Schnack and P. A. Klumpp. Shearographic and holographic defect detection for composite materials. In R. J. Pryputniewicz, editor, *Laser Interferometry IV: Computer-Aided Interferometry*, volume 1553 of *Proc. of Soc. Photo-Opt. Instr. Eng.*, 1991. {215}
- [322] H. Steinbichler, S. Leidenbach, J. Engelsberger, E.-H. Nösekabel, and J. Sun. Optical measuring systems help to find constructional weak spots. In R. J. Pryputniewicz, editor, *Laser Interferometry IV: Computer-Aided Interferometry*, volume 1553 of *Proc. of Soc. Photo-Opt. Instr. Eng.*, pages 240–249, 1991. {215}
- [323] G. Birnbaum and C. M. Vest. Holographic nondestructive evaluation: status and future. *Intern. Adv. in Nondestructive Testing*, 9:257–282, 1983. {215, 218}
- [324] S. Amadesi, A. D’Altorio, and D. Paoletti. Single-two hologram interferometry: a combined method for dynamic tests on painted wooden statues. *J. Optics*, 14(5):243–246, 1983. {216}
- [325] G. M. Brown. Computer automated holometry for automotive applications. In W. F. Fagan, editor, *Industrial Optoelectronic Measurement Systems using Coherent Light*, volume 863 of *Proc. of Soc. Photo-Opt. Instr. Eng.*, pages 213–222, 1987. {216, 221, 321}
- [326] G. Cavaccini, A. Ciliberto, L. D’Antonio, P. Ferraro, A. Ortona, and C. Sabatino. Holographic interferometry used for structural analysis of bonded structures in aerospace industry. In K. Stetson and R. Pryputniewicz, editors, *International Conference on Hologram Interferometry and Speckle Metrology*, pages 379–384, 1990. {216}
- [327] J. Gryzagoridis. Holographic non-destructive testing of composites. *Opt. Laser Technol.*, 21(2):113–116, 1989. {216}
- [328] Y. Y. Hung. Shearography versus holography in nondestructive evaluation of tires and composites. In F.-P. Chiang, editor, *International Conference on Photomechanics and Speckle Metrology*, volume 814 of *Proc. of Soc. Photo-Opt. Instr. Eng.*, pages 433–442, 1987. {216}
- [329] H. Kasprzak, H. Podbielska, and G. von Bally. Human tibia rigidity examined in bending and torsion loading by using double-exposure holographic interferometry. In W. Jüptner, editor, *Holography Techniques and Applications*, volume 1026 of *Proc. of Soc. Photo-Opt. Instr. Eng.*, pages 196–201, 1988. {216}
- [330] H. G. Leis. Vibration analysis of an 8-cylinder V-engine by time-averaged holographic interferometry. In W. F. Fagan, editor, *Industrial Applications of Laser Technology*, volume 398 of *Proc. of Soc. Photo-Opt. Instr. Eng.*, pages 90–94, 1983. {216}
- [331] J. W. Newman. Production and field inspection of advanced materials with holographic and speckle interferometry. In F.-P. Chiang, editor, *International Conference on Photomechanics and Speckle Metrology*, volume 814 of *Proc. of Soc. Photo-Opt. Instr. Eng.*, pages 421–427, 1987. {216}
- [332] B. Ovryn. Holographic interferometry. *CRC Crit. Rev. in Biomed. Eng.*, 16(4):269–322, 1989. {216}
- [333] P. Paulet. Holographic measuring of the deformations of various internal combustion engine parts. In W. F. Fagan, editor, *Industrial Applications of Laser Technology*, volume 398 of *Proc. of Soc. Photo-Opt. Instr. Eng.*, pages 30–34, 1983. {216}

- [334] C. A. Sciammarella and B. Subbaraman. Application of holographic interferometry to the NDE of composites. In SEM, editor, *Optical Methods in Composites*, Proc. of the 1986 SEM Fall Conference on Experimental Mechanics, pages 11–16, 1986. {216}
- [335] P. Zanetta, G. P. Solomos, M. Zürn, and A. C. Lucia. Holographic detection of defects in composites. *Opt. Laser Technol.*, 25(2):97–102, 1993. {216}
- [336] J. E. Sollid and K. A. Stetson. Strains from holographic data. *Exp. Mech.*, 18(6):208–214, 1978. {216, 311, 317}
- [337] K. D. Hinsch. Holographic interferometry of surface deformations of transparent fluids. *Appl. Opt.*, 17(19):3101–3107, 1978. {216}
- [338] C. M. E. Holden, S. C. J. Parker, and P. J. Bryanston-Cross. Quantitative three-dimensional holographic interferometry for flow field analysis. *Opt. Lasers in Eng.*, 19:285–298, 1993. {217}
- [339] T. A. W. M. Lanen. Digital holographic interferometry in flow research. *Opt. Comm.*, 79(5):386–396, 1990. {217}
- [340] T. A. W. M. Lanen, P. G. Bakker, and P. J. Bryanston-Cross. Digital holographic interferometry in high-speed flow research. *Exp. Fluids*, 13:56–62, 1992. {217}
- [341] T. A. W. M. Lanen, C. Nebbeling, and J. L. van Ingen. Phase-stepping holographic interferometry in studying transparent density fields around 2-D objects of arbitrary shape. *Opt. Comm.*, 76(3/4):268–275, 1990. {217}
- [342] J. D. Trolinger, N. Brock, P. DeBarber, J. Hsu, and J. Millerd. Recent developments in optical flow diagnostics. In *Proc. of 32nd Aerospace Sciences Meeting and Exhibit*, pages 1–21, 1994. {217}
- [343] J. D. Trolinger. The new methods in holographic flow diagnostics. In K. Stetson and R. Pryputniewicz, editors, *International Conference on Hologram Interferometry and Speckle Metrology*, pages 488–493, 1990. {217}
- [344] R. D. Matulka and D. J. Collins. Determination of three-dimensional density fields from holographic interferograms. *Journ. Appl. Phys.*, 42:1109–1119, 1971. {217}
- [345] M. J. Ehrlich and J. W. Wagner. Investigation of transient acoustic wave and shock wave propagation in bulk materials using high speed pulsed holographic interferometry and computer assisted optical tomography. In K. Stetson and R. Pryputniewicz, editors, *International Conference on Hologram Interferometry and Speckle Metrology*, pages 422–428, 1990. {217}
- [346] R. J. Parker. Extraction of 3-d flow data from transsonic flow holograms. In W. F. Fagan, editor, *Industrial Optoelectronic Measurement Systems using Coherent Light*, volume 863 of *Proc. of Soc. Photo-Opt. Instr. Eng.*, pages 78–85, 1987. {217}
- [347] R. J. Parker and M. Reeves. Holographic flow visualization in rotating turbomachinery. In K. Stetson and R. Pryputniewicz, editors, *International Conference on Hologram Interferometry and Speckle Metrology*, pages 500–507, 1990. {217}
- [348] M. Watanabe, A. Abe, R. T. Casey, and K. Takayama. Holographic interferometric observation of shock wave phenomena. In R. J. Pryputniewicz, editor, *Laser Interferometry IV: Computer-Aided Interferometry*, volume 1553 of *Proc. of Soc. Photo-Opt. Instr. Eng.*, pages 418–426, 1991. {217}
- [349] D. W. Watt and C. M. Vest. Digital interferometry for flow visualization. *Exp. Fluids*, 5:401–406, 1987. {217}

- [350] D. W. Watt and C. M. Vest. Turbulent flow visualization by interferometric integral imaging and computed tomography. *Exp. Fluids*, 8:301–311, 1990. {217}
- [351] J. S. Steckenrider, M. J. Ehrlich, and J. W. Wagner. Pulsed holographic recording of very high speed transient events. In F. P. Chiang, editor, *Second International Conference on Photomechanics and Speckle Metrology*, volume 1554 of *Proc. of Soc. Photo-Opt. Instr. Eng.*, pages 106–112, 1991. {217}
- [352] B. Lu, X. Yang, H. Abendroth, H. Eggers, and E. Ziolkowski. Measurement of a three-dimensional temperature field applying ESPI and CT techniques. *Opt. Comm.*, 69(1):6–10, 1988. {217, 362}
- [353] W. Merzkirch. Calculation of fluid density from holographic interferograms. In P. Smigelski, editor, *Deuxieme Colloque Franco-Allemand sur les Applications de l'Holographie*, pages 195–207, 1989. {217}
- [354] N. Rubayi, J. Yeakle, and M. A. Wright. Holographic investigation of various stressing techniques for detecting flaws in composite laminates. In *Optical Methods in Composites*, Proc. of the 1986 SEM Fall Conference on Experimental Mechanics, pages 1–10, 1986. {218}
- [355] D. L. Mader. Holographic interferometry on pipes: precision interpretation by least-squares fitting. *Appl. Opt.*, 24(22):3784–3790, 1985. {218, 303}
- [356] P. Del Vo and M. L. Rizzi. Vibrational testing of an X-ray concentrator by holographic interferometry. In F.-P. Chiang, editor, *International Conference on Photomechanics and Speckle Metrology*, volume 814 of *Proc. of Soc. Photo-Opt. Instr. Eng.*, pages 357–364, 1987. {219}
- [357] H.-A. Crostack, E. H. Meyer, and K.-J. Pohl. Holographic interferometric ultrasound imaging – technique and application in nondestructive testing. In W. Jüptner, editor, *Holography Techniques and Applications*, volume 1026 of *Proc. of Soc. Photo-Opt. Instr. Eng.*, pages 123–132, 1988. {219}
- [358] K.-J. Pohl and H.-A. Crostack. Holographic visualization of laser-induced ultrasonic Rayleigh waves. In K. Stetson and R. Pryputniewicz, editors, *International Conference on Hologram Interferometry and Speckle Metrology*, pages 449–456, 1990. {219}
- [359] P. Gren and R. Olsson. Deformation during impact on an orthotropic composite plate. In K. Stetson and R. Pryputniewicz, editors, *International Conference on Hologram Interferometry and Speckle Metrology*, pages 429–434, 1990. {219}
- [360] D. Fraile, F. Gascon, and A. Varade. Fringe pattern in holographic interferometry for thermal expansion characterization of anisotropic bodies. *Appl. Opt.*, 31(34):7371–7374, 1992. {219}
- [361] D. W. Watt, T. S. Gross, and S. D. Hening. Three-illumination-beam phase-shifted holographic interferometry study of thermally induced displacements on a printed wiring board. *Appl. Opt.*, 30(13):1617–1623, 1991. {219}
- [362] A. Choudry. Digital holographic interferometry of convective heat transport. *Appl. Opt.*, 20(7):1240–1244, 1981. {221}
- [363] A. Choudry. Automated fringe reduction techniques. In N. A. Massie, editor, *Interferometric Metrology, Critical Reviews*, volume 816 of *Proc. of Soc. Photo-Opt. Instr. Eng.*, pages 49–55, 1987. {221}

- [364] A. Choudry, H. Dekker, and D. Enard. Automated interferometric evaluation of optical components at the European Southern Observatory (ESO). In W. F. Fagan, editor, *Industrial Applications of Laser Technology*, volume 398 of *Proc. of Soc. Photo-Opt. Instr. Eng.*, pages 66–72, 1983. **{221}**
- [365] A. C. Gillies. Image processing approach to fringe patterns. *Opt. Eng.*, 27(10):861–866, 1988. **{221}**
- [366] F. Ginesu and F. Bertolino. Numerical analysis of fringe patterns for structural engineering problems. In R. J. Pryputniewicz, editor, *Laser Interferometry IV: Computer-Aided Interferometry*, volume 1553 of *Proc. of Soc. Photo-Opt. Instr. Eng.*, pages 313–324, 1991. **{221}**
- [367] J. M. Huntley. Fringe analysis today and tomorrow. In K. Gastinger, O. Løkberg, and S. Winther, editors, *Speckle Metrology 2003*, volume 4933 of *Proc. of Soc. Photo-Opt. Instr. Eng.*, pages 167–174, 2003. **{221}**
- [368] Th. Kreis. Computer aided evaluation of fringe patterns. *Opt. Lasers in Eng.*, 19:221–240, 1993. **{221}**
- [369] M. Kujawinska. The architecture of a multipurpose fringe pattern analysis system. *Opt. Lasers in Eng.*, 19:261–268, 1993. **{221}**
- [370] G. E. Maddux. Video/computer techniques for static and dynamic experimental mechanics. In R. J. Pryputniewicz, editor, *Industrial Laser Interferometry*, volume 746 of *Proc. of Soc. Photo-Opt. Instr. Eng.*, pages 52–57, 1987. **{221}**
- [371] R. J. Pryputniewicz. Review of methods for automatic analysis for fringes in hologram interferometry. In N. A. Massie, editor, *Interferometric Metrology, Critical Reviews*, volume 816 of *Proc. of Soc. Photo-Opt. Instr. Eng.*, pages 140–148, 1987. **{221}**
- [372] G. T. Reid. Automatic fringe pattern analysis: A review. *Opt. Lasers in Eng.*, 7:37–68, 1986. **{221}**
- [373] D. W. Robinson and G. T. Reid, editors. *Interferogram Analysis: Digital Fringe Pattern Measurement Techniques*. Institute of Physics, Bristol and Philadelphia, 1993. **{221}**
- [374] C. A. Sciammarella and G. Bhat. Computer assisted techniques to evaluate fringe patterns. In R. J. Pryputniewicz, editor, *Laser Interferometry IV: Computer-Aided Interferometry*, volume 1553 of *Proc. of Soc. Photo-Opt. Instr. Eng.*, pages 252–262, 1991. **{221}**
- [375] J. S. Sirkis, Y.-M. Chen, H. Singh, and A. Y. Cheng. Computerized optical fringe pattern analysis in photomechanics: a review. *Opt. Eng.*, 31(2):304–314, 1992. **{221}**
- [376] R. J. Pryputniewicz. Quantitative determination of displacements and strains from holograms. In P. K. Rastogi, editor, *Holographic Interferometry*, volume 68 of *Springer Series in Optical Sciences*, pages 33–74, 1994. **{222, 318, 329, 404}**
- [377] N. Abramson. The rose of error or the importance of sign. In *Technical Digest of Topical Meeting On Hologram Interferometry and Speckle Metrology*. Opt. Soc. Amer., 1980. **{222}**
- [378] Th. Kreis. Computer-aided evaluation of holographic interferograms. In P. K. Rastogi, editor, *Holographic Interferometry*, volume 68 of *Springer Series in Optical Sciences*, pages 151–212, 1994. **{222}**

- [379] D. R. Matthys, J. A. Gilbert, T. D. Dudderar, and K. W. Koenig. A windowing technique for the automated analysis of holo-interferograms. *Opt. Lasers in Eng.*, 8:123–136, 1988. {224}
- [380] P. D. Plotkowski, M. Y. Y. Hung, J. D. Hovanesian, and G. Gerhardt. Improved fringe carrier techniques for unambiguous determination of holographically recorded displacements. *Opt. Eng.*, 24(5):754–756, 1985. {224}
- [381] J. Petkovsek and K. Rankel. Measurement of three-dimensional displacement by four small holograms. In P. Meyrueis and M. Grosmann, editors, *2nd European Congress on Optics Applied to Metrology*, volume 210 of *Proc. of Soc. Photo-Opt. Instr. Eng.*, pages 173–177, 1979. {224, 299}
- [382] N. Eichhorn and W. Osten. An algorithm for the fast derivation of line structures from interferograms. *Journ. Modern Opt.*, 35(10):1717–1725, 1988. {225, 229, 231}
- [383] W. Osten. *Digital Processing and Evaluation of Interference Images*. Akademie-Verlag, Berlin, 1991. (In German). {226}
- [384] W. Luth. *Isolation of Moving Objects in Digital Image Sequences*. Academy of Sciences of the GDR, 1989. (In German). {226}
- [385] K. Creath. Submicron linewidth measurement using an interferometric optical profiler. In W. H. Arnold, editor, *Integrated Circuit Metrology, Inspection, and Process Control*, volume 1464 of *Proc. of Soc. Photo-Opt. Instr. Eng.*, pages 474–483, 1991. {228}
- [386] K. Creath. Holographic contour and deformation measurement using a 1.4 million element detector array. *Appl. Opt.*, 28(11):2170–2175, 1989. {228, 333}
- [387] K. Creath. Phase-measurement interferometry: Beware these errors. In R. J. Pryputniewicz, editor, *Laser Interferometry IV: Computer-Aided Interferometry*, volume 1553 of *Proc. of Soc. Photo-Opt. Instr. Eng.*, pages 213–220, 1991. {228, 255}
- [388] K. Freischlad and C. L. Koliopoulos. Fourier description of digital phase-measuring interferometry. *Journ. Opt. Soc. Amer. A*, 7(4):542–551, 1990. {228, 255}
- [389] C. P. Brophy. Effect of intensity error correlation on the computed phase of phase shifting interferometry. *Journ. Opt. Soc. Amer. A*, 7(4):537–541, 1990. {228, 255}
- [390] O. A. Skydan, F. Lilley, M. J. Lalor, and D. R. Burton. Quantization error of CCD cameras and their influence on phase calculation in fringe pattern analysis. *Appl. Opt.*, 42:5302–5307, 2003. {228}
- [391] W. R. J. Funnell. Image processing applied to the interactive analysis of interferometric fringes. *Appl. Opt.*, 20(18):3245–3250, 1981. {229, 231, 233, 235, 374}
- [392] W. Osten, J. Saedler, and H. Rottenkolber. Interpretation of interferometric fringe patterns using digital image processing (in German). *Technisches Messen tm*, 54:285–290, 1988. {229}
- [393] T. Yatagai. Intensity based analysis methods. In D. W. Robinson and G. T. Reid, editors, *Interferogram Analysis: Digital Fringe Pattern Measurement Techniques*, pages 72–93. Institute of Physics, Bristol and Philadelphia, 1993. {229, 231, 235}
- [394] Th. Kreis and H. Kreitlow. Quantitative evaluation of holographic interference patterns under image processing aspects. In P. Meyrueis and M. Grosmann, editors, *2nd European Congress on Optics Applied to Metrology*, volume 210 of *Proc. of Soc. Photo-Opt. Instr. Eng.*, pages 196–202, 1979. {230, 231, 287}

- [395] A. K. Jain and C. R. Christensen. Digital processing of images in speckle noise. In W. H. Carter, editor, *Applications of Speckle Phenomena*, volume 243 of *Proc. of Soc. Photo-Opt. Instr. Eng.*, pages 46–50, 1980. {230}
- [396] J. S. Lim and H. Nawab. Techniques for speckle noise removal. *Opt. Eng.*, 20(3):472–480, 1981. {230, 409}
- [397] F. A. Sadjadi. Perspectives on techniques for enhancing speckled imagery. *Opt. Eng.*, 29(1):25–30, 1990. {230}
- [398] T. R. Crimmins. Geometric filter for speckle reduction. *Appl. Opt.*, 24(10):1438–1443, 1985. {230}
- [399] T. R. Crimmins. Geometric filter for reducing speckle. *Opt. Eng.*, 25(5):651–654, 1986. {230}
- [400] E. Bieber and W. Osten. Improvement of speckled fringe patterns by Wiener filtration. In Z. Jaroszewicz and M. Pluta, editors, *Interferometry 89*, volume 1121 of *Proc. of Soc. Photo-Opt. Instr. Eng.*, pages 393–399, 1989. {230}
- [401] Y. Katzir, I. Glaser, A. A. Friesem, and B. Sharon. On-line acquisition and analysis for holographic nondestructive evaluation. *Opt. Eng.*, 21:1016, 1982. {231}
- [402] F. Becker, G. E. A. Meier, and H. Wegner. Automatic evaluation of interferograms. In A. G. Tescher, editor, *Applications of Digital Image Processing*, volume 359 of *Proc. of Soc. Photo-Opt. Instr. Eng.*, pages 386–393, 1982. {231}
- [403] F. Becker and Y. H. Yu. Digital fringe reduction technique applied to the measurement of three-dimensional transonic flow fields. *Opt. Eng.*, 24(3):429–434, 1985. {231, 234, 235}
- [404] J. Budzinski. SNOP: a method for skeletonization of a fringe pattern along a fringe direction. *Appl. Opt.*, 31(16):3109–3113, 1992. {231, 233}
- [405] S. Nakadate, N. Magome, T. Honda, and J. Tsujiuchi. Hybrid holographic interferometer for measuring three-dimensional deformations. *Opt. Eng.*, 20(2):246–252, 1981. {231, 235}
- [406] T. Yatagai, S. Nakadate, M. Idesawa, and H. Saito. Automatic fringe analysis using digital image processing techniques. *Opt. Eng.*, 21(3):432–435, 1982. {231, 235}
- [407] E. A. Mnatsakanyan and S. V. Nefyodov. Skeletonizing of interferometric images for finding maximum and minimum centres of fringes. In K. Stetson and R. Pryputniewicz, editors, *International Conference on Hologram Interferometry and Speckle Metrology*, pages 351–355, 1990. {231}
- [408] H. Winter, S. Unger, and W. Osten. The application of adaptive and anisotropic filtering for the extraction of fringe pattern skeletons. In W. Osten, R. J. Pryputniewicz, G. T. Reid, and H. Rottenkolber, editors, *Fringe '89, Automatic Processing of Fringe Patterns*, Physical Research, pages 158–166. Akademie-Verlag, Berlin, 1989. {231}
- [409] J. A. Aparicio, J. L. Molpeceres, A. M. de Frutos, C. de Castro, S. Caceres, and F. A. Frechoso. Improved algorithm for the analysis of holographic interferograms. *Opt. Eng.*, 32(5):963–969, 1993. {233}
- [410] F. Bertolino and F. Ginesu. Semiautomatic approach of grating techniques. *Opt. Lasers in Eng.*, 19:313–323, 1993. {233}

- [411] A. E. Ennos, D. W. Robinson, and D. C. Williams. Automatic fringe analysis in holographic interferometry. *Optica Acta*, 32(2):135–145, 1985. {233}
- [412] S. Krishnaswamy. Algorithm for computer tracing of interference fringes. *Appl. Opt.*, 30(13):1624–1628, 1991. {233}
- [413] R. Nübel. Computer-aided evaluation method for interferograms. *Exp. Fluids*, 12:166–172, 1992. {233}
- [414] G. W. Johnson, D. C. Leiner, and D. T. Moore. Phase-locked interferometry. *Opt. Eng.*, 18(1):46–52, 1979. {233}
- [415] G. A. Mastin and D. C. Ghiglia. Digital extraction of interference fringe contours. *Appl. Opt.*, 24(12):1727–1728, 1985. {234}
- [416] V. Srinivasan, S.-T. Yeo, and P. Chaturvedi. Fringe processing and analysis with a neural network. *Opt. Eng.*, 33(4):1166–1171, 1994. {234}
- [417] K. H. Womack, K. L. Underwood, and D. Forbes. Microprocessor-based video interferogram analysis system. In *Minicomputers and Microprocessors in Optical Systems*, volume 230 of *Proc. of Soc. Photo-Opt. Instr. Eng.*, pages 168–179, 1980. {235}
- [418] A. Colin and W. Osten. Automatic support for consistent labelling of skeletonized fringe patterns. *Journ. Modern Opt.*, 42:945–954, 1995. {235}
- [419] J. B. Schemm and C. M. Vest. Fringe pattern recognition and interpolation using non-linear regression analysis. *Appl. Opt.*, 22(18):2850–2853, 1983. {235}
- [420] U. Mieth and W. Osten. Three methods for the interpolation of phase values between fringe pattern skeletons. In W. Osten, R. J. Pryputniewicz, G. T. Reid, and H. Rottenkolber, editors, *Fringe '89, Automatic Processing of Fringe Patterns*, Physical Research, pages 118–123. Akademie-Verlag, Berlin, 1989. {235}
- [421] R. Dändliker, B. Ineichen, and F. M. Mottier. High resolution hologram interferometry by electronic phase measurement. *Opt. Comm.*, 9:412–416, 1973. {235}
- [422] P. V. Farrell, G. S. Springer, and C. M. Vest. Heterodyne holographic interferometry: concentration and temperature measurements in gas mixtures. *Appl. Opt.*, 21(9):1624–1627, 1982. {235}
- [423] R. J. Pryputniewicz. Heterodyne holography, applications in studies of small components. *Opt. Eng.*, 24(5):849–854, 1985. {235, 387}
- [424] R. Thalmann and R. Dändliker. Strain measurement by heterodyne holographic interferometry. *Appl. Opt.*, 26(10):1964–1971, 1987. {235}
- [425] Th. Kreis, J. Geldmacher, and R. Biedermann. Theoretical and experimental investigations of the accuracy of diverse methods for evaluating interference patterns. In *Report on DFG-Project Kr953/2-1*, 1993. (In German). {239}
- [426] Th. Kreis, J. Geldmacher, and W. Jüptner. A comparison of interference phase determination methods with respect to achievable accuracy. In W. Jüptner and W. Osten, editors, *Fringe '93*, pages 51–59, 1993. {241}
- [427] B. Breuckmann and W. Thieme. Computer-aided analysis of holographic interferograms using the phase-shift method. *Appl. Opt.*, 24(14):2145–2149, 1985. {242}
- [428] R. Dändliker and R. Thalmann. Heterodyne and quasi-heterodyne holographic interferometry. *Opt. Eng.*, 24(5):824–831, 1985. {242}

- [429] P. Hariharan. Quasi-heterodyne hologram interferometry. *Opt. Eng.*, 24(4):632–638, 1985. {242}
- [430] P. Hariharan, B. F. Oreb, and N. Brown. A digital phase-measurement system for real-time holographic interferometry. *Opt. Comm.*, 41(6):393–396, 1982. {242}
- [431] R. Thalmann and R. Dändliker. Automated evaluation of 3-D displacement and strain by quasi-heterodyne holographic interferometry. In W. F. Fagan, editor, *Optics in Engineering Measurement*, volume 599 of *Proc. of Soc. Photo-Opt. Instr. Eng.*, pages 141–148, 1985. {242}
- [432] O. Y. Kwon and D. M. Shough. Multichannel grating phase-shift interferometers. In W. F. Fagan, editor, *Optics in Engineering Measurements*, volume 599 of *Proc. of Soc. Photo-Opt. Instr. Eng.*, page 273, 1985. {243}
- [433] J. E. Greivenkamp. Generalized data reduction for heterodyne interferometry. *Opt. Eng.*, 23(4):350–352, 1984. {245}
- [434] P. L. Wizinowich. Phase shifting interferometry in the presence of vibration: a new algorithm and system. *Appl. Opt.*, 29(22):3271–3279, 1990. {246}
- [435] D. P. Towers, P. J. Bryanston-Cross, and C. E. Towers. The automatic quantitative analysis of phase stepped interferograms. In K. Stetson and R. Pryputniewicz, editors, *International Conference on Hologram Interferometry and Speckle Metrology*, pages 480–483, 1990. {248}
- [436] W. Jüptner, Th. Kreis, and H. Kreitlow. Automatic evaluation of holographic interferograms by reference beam phase shifting. In W. F. Fagan, editor, *Industrial Applications of Laser Technology*, volume 398 of *Proc. of Soc. Photo-Opt. Instr. Eng.*, pages 22–29, 1983. {248}
- [437] J. Novak. Five-step phase-shifting algorithms with unknown values of phase shift. *Optik*, 114(2):63–68, 2003. {250}
- [438] V. A. Deason and G. D. Lassahn. Novel approaches to automated reduction of phase shifted interferograms. In R. J. Pryputniewicz, editor, *Laser Interferometry IV: Computer-Aided Interferometry*, volume 1553 of *Proc. of Soc. Photo-Opt. Instr. Eng.*, pages 569–582, 1991. {251}
- [439] X.-Y. Su, A. M. Zarubin, and G. von Bally. Modulation analysis of phase-shifted holographic interferograms. *Opt. Comm.*, 105(5,6):379–387, 1994. {251}
- [440] M. Chang, Ch.-P. Hu, P. Lam, and J. C. Wyant. High precision deformation measurement by digital phase shifting interferometry. *Appl. Opt.*, 24(22):3780–3783, 1985. {255}
- [441] Th. Kreis. Quantitative evaluation of interference patterns. In W. F. Fagan, editor, *Industrial Optoelectronic Measurement Systems using Coherent Light*, volume 863 of *Proc. of Soc. Photo-Opt. Instr. Eng.*, pages 68–77, 1987. {255}
- [442] Y. Y. Cheng and J. C. Wyant. Phase shifter calibration in phase-shifting interferometry. *Appl. Opt.*, 24:3049–3052, 1985. {255}
- [443] J. Schwider, R. Burow, K.-E. Elssner, J. Grzanna, R. Spolaczyk, and K. Merkel. Digital wave-front measuring interferometry: some systematic error sources. *Appl. Opt.*, 22(21):3421–3432, 1983. {255, 365}

- [444] J. van Wingerden, H. J. Frankena, and C. Smorenburg. Linear approximation for measurement errors in phase shifting interferometry. *Appl. Opt.*, 30:2718–2729, 1991. **{255}**
- [445] K. Kinnstaetter, A. W. Lohmann, J. Schwider, and N. Streibl. Accuracy of phase shifting interferometry. *Appl. Opt.*, 27:5082–5089, 1988. **{256}**
- [446] P. J. de Groot. Derivation of algorithms for phase-shifting interferometry using the concept of a data-sampling window. *Appl. Opt.*, 34(22):4723–4730, 1995. **{256}**
- [447] P. J. de Groot. Vibration in phase-shifting interferometry. *Journ. Opt. Soc. Amer. A*, 12(2):354–365, 1995. **{256}**
- [448] K. G. Larkin and B. F. Oreb. Design and assessment of symmetrical phase-shifting algorithms. *Journ. Opt. Soc. Amer. A*, 9(10):1740–1748, 1992. **{256}**
- [449] D. R. Burton and M. J. Lalor. Managing some of the problems of Fourier fringe analysis. In G. T. Reid, editor, *Fringe Pattern Analysis*, volume 1163 of *Proc. of Soc. Photo-Opt. Instr. Eng.*, pages 149–160, 1989. **{256}**
- [450] Th. Kreis. Fourier-transform evaluation of holographic interference patterns. In F.-P. Chiang, editor, *International Conference on Photomechanics and Speckle Metrology*, volume 814 of *Proc. of Soc. Photo-Opt. Instr. Eng.*, pages 365–371, 1987. **{256, 260}**
- [451] Th. Kreis and W. Jüptner. Fourier-transform evaluation of interference patterns: the role of filtering in the spatial-frequency domain. In R. J. Pryputniewicz, editor, *Laser Interferometry: Quantitative Analysis of Interferograms*, volume 1162 of *Proc. of Soc. Photo-Opt. Instr. Eng.*, pages 116–125, 1989. **{256, 258}**
- [452] Th. Kreis and W. Jüptner. Fourier-transform evaluation of interference patterns: de-modulation and sign-ambiguity. In R. J. Pryputniewicz, editor, *Laser Interferometry IV: Computer-Aided Interferometry*, volume 1553 of *Proc. of Soc. Photo-Opt. Instr. Eng.*, pages 263–273, 1991. **{256, 261, 289}**
- [453] A. A. Malcolm and D. R. Burton. The relationship between Fourier fringe analysis and the FFT. In R. J. Pryputniewicz, editor, *Laser Interferometry IV: Computer-Aided Interferometry*, volume 1553 of *Proc. of Soc. Photo-Opt. Instr. Eng.*, pages 286–297, 1991. **{256}**
- [454] Q.-S. Ru, T. Honda, J. Tsujiuchi, and N. Ohyama. Fringe analysis by using 2-D-Fresnel transforms. *Opt. Comm.*, 66(1):21–24, 1988. **{256}**
- [455] Q.-S. Ru, N. Ohyama, T. Honda, and J. Tsujiuchi. Constant radial shearing interferometry with circular gratings. *Appl. Opt.*, 28(15):3350–3353, 1989. **{256}**
- [456] D. Lovric, Z. Vucic, J. Gladic, N. Demoli, S. Mitrovic, and M Milas. Refined Fourier-transform method of analysis of full two-dimensional digitized interferograms. *Appl. Opt.*, 42(8):1477–1484, 2003. **{260}**
- [457] Th. Kreis. Automatic evaluation of interference patterns. In W. Jüptner, editor, *Holography Techniques and Applications*, volume 1026 of *Proc. of Soc. Photo-Opt. Instr. Eng.*, pages 80–89, 1988. **{261, 402}**
- [458] K. E. Perry Jr. and J. McKelvie. A comparison of phase shifting and Fourier methods in the analysis of discontinuous fringe patterns. *Opt. Lasers in Eng.*, 19:269–284, 1993. **{261}**

- [459] P. Zanetta, D. Albrecht, G. Schirripa Spagnolo, and D. Paoletti. Application of fast fourier transform techniques to the quantitative analysis of holographic and TV-holographic interferograms. *Optik*, 97(2):47–52, 1994. {261}
- [460] N. Ohyama, S. Kinoshita, A. Cornejo-Rodriguez, T. Honda, and J. Tsujiuchi. Accuracy of phase determination with unequal reference phase shift. *Journ. Opt. Soc. Amer. A*, 5(12):2019–2025, 1988. {263}
- [461] D. J. Bone, H.-A. Bachor, and R. J. Sandeman. Fringe-pattern analysis using 2-D Fourier transform. *Appl. Opt.*, 25(10):1653–1660, 1986. {263}
- [462] P. J. Bryanston-Cross, C. Quan, and T. R. Judge. Application of the FFT method for the quantitative extraction of information from high-resolution interferometric and photoelastic data. *Opt. Laser Technol.*, 26(3):147–155, 1994. {263}
- [463] D. R. Burton and M. J. Lalor. The precision measurement of engineering form by computer analysis of optically generated contours. In D. W. Braggins, editor, *Industrial Inspection*, volume 1010 of *Proc. of Soc. Photo-Opt. Instr. Eng.*, pages 17–24, 1989. {263}
- [464] C. Gorecki. Interferogram analysis using a Fourier transform method for automatic 3D surface measurement. *Pure Appl. Opt.*, 1:103–110, 1992. {263}
- [465] J. Gu and F. Chen. Fast Fourier transform, iteration, and least-squares-fit demodulation image processing for analysis of single-carrier fringe pattern. *Journ. Opt. Soc. Amer. A*, 12(10):2159–2164, 1995. {263}
- [466] K. A. Nugent. Interferogram analysis using an accurate fully automatic algorithm. *Appl. Opt.*, 24(18):3101–3105, 1985. {263}
- [467] D. Paoletti and G. Schirripa Spagnolo. Fourier transform for sandwich holograms evaluation. *J. Optics*, 25(1):17–23, 1994. {263}
- [468] R. Preater and R. Swain. Fourier transform fringe analysis of ESPI fringes from rotating components. In G. M. Brown, K. G. Harding, and H. Stahl, editors, *Industrial Applications of Optical Inspection, Metrology, and Sensing*, volume 1821 of *Proc. of Soc. Photo-Opt. Instr. Eng.*, pages 82–100, 1992. {263}
- [469] C. Roddier and F. Roddier. Interferogram analysis using Fourier transform techniques. *Appl. Opt.*, 26(9):1668–1673, 1987. {263}
- [470] M. Takeda. Spatial-carrier fringe-pattern analysis and its applications to precision interferometry and profilometry: An overview. *Industrial Metrology*, 1(2):79–99, 1990. {263}
- [471] M. Takeda. Spatial carrier heterodyne techniques for precision interferometry and profilometry: An overview. In Z. Jaroszewicz and M. Pluta, editors, *Interferometry '89*, volume 1121 of *Proc. of Soc. Photo-Opt. Instr. Eng.*, pages 73–88, 1989. {263}
- [472] M. Takeda and Z. Tung. Subfringe holographic interferometry by computer-based spatial-carrier fringe-pattern analysis. *J. Optics*, 16(3):127–131, 1985. {263}
- [473] S. Toyooka, H. Nishida, and J. Takezaki. Automatic analysis of holographic and shearographic fringes to measure flexural strains in plates. *Opt. Eng.*, 28(1):55–60, 1989. {263}
- [474] G. O. Reynolds, D. A. Servaes, L. Ramos-Izquierdo, J. B. DeVelis, D. C. Peirce, P. D. Hilton, and R. A. Mayville. Holographic fringe linearization interferometry for defect detection. *Opt. Eng.*, 24(5):757–768, 1985. {263, 393}

- [475] D. R. Matthys, T. D. Dudderar, and J. A. Gilbert. Automated analysis of holointerferograms for the determination of surface displacement. *Exp. Mech.*, 28:86–91, 1988. {263}
- [476] J. D. Trolinger. Application of generalized phase control during reconstruction to flow visualization holography. *Appl. Opt.*, 18:766–774, 1979. {263}
- [477] D. Tentori and D. Salazar. Hologram interferometry: carrier fringes. *Appl. Opt.*, 30(35):5157–5158, 1991. {264}
- [478] P. Long, D. Hsu, and B. Wang. Cylindrical fringe carrier technique in holographic interferometry. *Opt. Eng.*, 27(10):867–869, 1988. {264}
- [479] W. W. Macy Jr. Two-dimensional fringe-pattern analysis. *Appl. Opt.*, 22(23):3898–3901, 1983. {265}
- [480] P. L. Ransom and J. V. Kokal. Interferogram analysis by a modified sinusoid fitting technique. *Appl. Opt.*, 25(22):4199–4204, 1986. {265}
- [481] K. H. Womack. Frequency domain description of interferogram analysis. *Opt. Eng.*, 23(4):396–400, 1984. {265, 303, 461}
- [482] K. H. Womack. Interferometric phase measurement using spatial synchronous detection. *Opt. Eng.*, 23(4):391–395, 1984. {265}
- [483] M. J. Landry and C. M. Wise. Automatic data reduction of certain holographic interferograms. *Appl. Opt.*, 12(10):2320–2327, 1973. {266, 268}
- [484] E. B. Aleksandrov and A. M. Bonch-Bruevich. Investigation of surface strains by the hologram technique. *Sov. Phys.–Tech. Phys.*, 12(2):258–265, 1967. {266}
- [485] L. Ek and K. Biedermann. Analysis of a system for hologram interferometry with a continuously scanning reconstruction beam. *Appl. Opt.*, 16(9):2535–2542, 1977. {268}
- [486] V. Fossati Bellani and A. Sona. Measurement of three-dimensional displacements by scanning a double-exposure hologram. *Appl. Opt.*, 13(6):1337–1341, 1974. {268}
- [487] L. Ek and K. Biedermann. Implementation of hologram interferometry with a continuously scanning reconstruction beam. *Appl. Opt.*, 17(11):1727–1732, 1978. {268}
- [488] R. Peralta-Fabi. Measurements of microdisplacements by holographic image processing. In W. F. Fagan, editor, *Industrial Applications of Laser Technology*, volume 398 of *Proc. of Soc. Photo-Opt. Instr. Eng.*, pages 169–173, 1983. {268}
- [489] H. Rytz. Holographic measurement of three dimensional displacements by means of a holographic plate. In W. F. Fagan, editor, *Industrial Applications of Laser Technology*, volume 398 of *Proc. of Soc. Photo-Opt. Instr. Eng.*, pages 53–58, 1983. {268}
- [490] Th. Kreis. Digital holographic interferometry. In P. Rastogi and D. Inaudi, editors, *Trends in Optical Nondestructive Testing*, pages 113–127, 2000. {269, 340}
- [491] Th. Kreis, W. Jüptner, and J. Geldmacher. Principles of digital holographic interferometry. In *Laser Interferometry IX: Techniques and Analysis*, volume 3478 of *Proc. of Soc. Photo-Opt. Instr. Eng.*, pages 45–54, 1998. {279}
- [492] Th. Kreis. Digital holography and holographic interferometry. *Machine Graphic and Vision*, 8(4):611–624, 1999. {279}
- [493] B. Gombkötö, J. Kornis, Z. Füzesy, M. Kiss, and P. Kovacs. Difference displacement measurement by digital holography by use of simulated wave fronts. *Appl. Opt.*, 43(8):1621–1624, 2004. {279}

- [494] G. Schönebeck. New holographic means to exactly determine coefficients of elasticity. In W. F. Fagan, editor, *Industrial Applications of Laser Technology*, volume 398 of *Proc. of Soc. Photo-Opt. Instr. Eng.*, pages 130–136, 1983. {280, 317}
- [495] G. Schönebeck. Holography and torsional problems. In W. F. Fagan, editor, *Industrial Optoelectronic Measurement Systems using Coherent Light*, volume 863 of *Proc. of Soc. Photo-Opt. Instr. Eng.*, pages 173–177, 1987. {280, 317}
- [496] P. Picart, E. Moisson, and D. Mounier. Mechanical measurement using multiplexing/demultiplexing of digital Fresnel holograms. In K. Gastinger, O. Løkberg, and S. Winther, editors, *Speckle Metrology 2003*, volume 4933 of *Proc. of Soc. Photo-Opt. Instr. Eng.*, pages 346–354, 2003. {282}
- [497] P. Picart, E. Moisson, and D. Mounier. Twin sensitivity measurement by spatial multiplexing of digitally recorded holograms. *Appl. Opt.*, 42:1947–1957, 2003. {282}
- [498] G. Pedrini and H. J. Tiziani. Quantitative evaluation of two-dimensional dynamic deformations using digital holography. *Opt. Laser Technol.*, 29(5):249–256, 1997. {283}
- [499] J. M. Huntley and J. R. Buckland. Characterization of sources of 2π phase discontinuity in speckle interferograms. *Journ. Opt. Soc. Amer. A*, 12(9):1990–1996, 1995. {287}
- [500] W. Osten and R. Höfling. The inverse modulo process in automatic fringe analysis – problems and approaches. In K. Stetson and R. Pryputniewicz, editors, *International Conference on Hologram Interferometry and Speckle Metrology*, pages 301–309, 1990. {287}
- [501] J. Munoz, G. Paez, and M. Strojnik. Two-dimensional phase unwrapping of subsampled phase-shifted interferograms. *Journ. Modern Opt.*, 51(1):49–63, 2004. {287, 292}
- [502] J. Munoz, M. Strojnik, and G. Paez. Phase recovery from a single undersampled interferograms. *Appl. Opt.*, 42(34):6846–6852, 2003. {287}
- [503] D. R. Burton and M. J. Lalor. Multichannel Fourier fringe analysis as an aid to automatic phase unwrapping. *Appl. Opt.*, 33(14):2939–2948, 1994. {288}
- [504] D. J. Bone. Fourier fringe analysis: the two-dimensional phase unwrapping problem. *Appl. Opt.*, 30(25):3627–3632, 1991. {288, 292}
- [505] K. Itoh. Analysis of the phase unwrapping algorithm. *Appl. Opt.*, 21(14):2470, 1982. {289}
- [506] J. M. Triboulet. A new phase unwrapping algorithm. *IEEE Trans. on Acoust., Speech, and Signal Proc.*, 25(2):170–177, 1977. {289}
- [507] D. W. Robinson. Phase unwrapping methods. In D. W. Robinson and G. T. Reid, editors, *Interferogram Analysis: Digital Fringe Pattern Measurement Techniques*, pages 194–229. Institute of Physics, Bristol and Philadelphia, 1993. {289, 292}
- [508] M. Takeda. Fringe formula for projection type moire topography. *Opt. Lasers in Eng.*, 1(3):45–52, 1982. {289}
- [509] D. W. Robinson and D. C. Williams. Digital phase stepping speckle interferometry. *Opt. Comm.*, 57(1):26–30, 1986. {289}
- [510] H. A. Vrooman and A. A. M. Maas. Image processing in digital speckle interferometry. In H. Halliwell, editor, *Fringe Analysis 89*, FASIG, 1989. {289}
- [511] K. Andresen and Q. Yu. Robust phase unwrapping by spin filtering using a phase direction map. In W. Jüptner and W. Osten, editors, *Fringe '93*, pages 154–156, 1993. {289}

- [512] P. J. Bryanston-Cross and C. Quan. Examples of automatic phase unwrapping applied to interferometric and photoelastic images. In W. Jüptner and W. Osten, editors, *Fringe '93*, pages 121–135, 1993. {289}
- [513] D. G. Ghiglia and L. A. Romero. Robust two-dimensional weighted and unweighted phase unwrapping that uses fast transforms and iterative methods. *Journ. Opt. Soc. Amer. A*, 11(1):107–117, 1994. {289, 295}
- [514] T. R. Judge, Ch. Quan, and P. J. Bryanston-Cross. Holographic deformation measurements by Fourier transform technique with automatic phase unwrapping. *Opt. Eng.*, 31(3):533–543, 1992. {289}
- [515] J. A. Quiroga and E. Bernabeu. Phase-unwrapping algorithm for noisy phase-map processing. *Appl. Opt.*, 33(29):6725–6731, 1994. {289}
- [516] G. Schirripa Spagnolo, D. Ambrosini, D. Paoletti, and R. Borghi. High-speed digital processing of electro-optic holography images for a quantitative analysis. *J. Opt.*, 28:118–124, 1997. {289, 400}
- [517] J. Schörner, A. Ettemeyer, U. Neupert, H. Rottenkolber, C. Winter, and P. Obermeier. New approaches in interpreting holographic images. *Opt. Lasers in Eng.*, 14:283–291, 1991. {289}
- [518] R. Cusack, J. M. Huntley, and H. T. Goldrein. Improved noise-immune phase-unwrapping algorithm. *Appl. Opt.*, 34(5):781–789, 1995. {290}
- [519] J. M. Huntley. Noise-immune phase unwrapping algorithm. *Appl. Opt.*, 28(15):3268–3270, 1989. {290, 295}
- [520] J. J. Gierloff. Phase unwrapping by regions. In R. E. Fischer and W. J. Smith, editors, *Current Developments in Optical Engineering II*, volume 818 of *Proc. of Soc. Photo-Opt. Instr. Eng.*, pages 2–9, 1987. {292}
- [521] O. Y. Kwon. Advanced wavefront sensing at Lockheed. In N. A. Massie, editor, *Interferometric Metrology*, volume 816 of *Proc. of Soc. Photo-Opt. Instr. Eng.*, pages 196–211, 1987. {292}
- [522] D. Winter, R. Ritter, and H. Sadewasser. Evaluation of modulo 2π phase-images with regional discontinuities: area based unwrapping. In W. Jüptner and W. Osten, editors, *Fringe '93*, pages 157–159, 1993. {292}
- [523] P. Stephenson, D. R. Burton, and M. J. Lalor. Data validation techniques in a tiled phase unwrapping algorithm. *Opt. Eng.*, 33(11):3703–3708, 1994. {292}
- [524] D. P. Towers, T. Judge, and P. J. Bryanston-Cross. A quasi heterodyne holographic technique and automatic algorithms for phase unwrapping. In G. T. Reid, editor, *Fringe Pattern Analysis*, volume 1163 of *Proc. of Soc. Photo-Opt. Instr. Eng.*, pages 95–119, 1989. {292}
- [525] D. P. Towers, T. R. Judge, and P. J. Bryanston-Cross. Automatic interferogram analysis techniques applied to quasi-heterodyne holography and ESPI. *Opt. Lasers in Eng.*, 14:239–281, 1991. {292}
- [526] A. Baldi. Phase unwrapping by region growing. *Appl. Opt.*, 42(14):2498–2505, 2003. {292}
- [527] D. G. Ghiglia, G. A. Mastin, and L. A. Romero. Cellular-automata method for phase unwrapping. *Journ. Opt. Soc. Amer. A*, 4(1):267–280, 1987. {292, 294}

- [528] A. Spik and D. W. Robinson. Investigation of the cellular automata method for phase unwrapping and its implementation on an array processor. *Opt. Lasers in Eng.*, 14:25–37, 1991. {292, 294}
- [529] R. J. Green and J. G. Walker. Phase unwrapping using a priori knowledge about the band limits of a function. In D. W. Braggins, editor, *Industrial Inspection*, volume 1010 of *Proc. of Soc. Photo-Opt. Instr. Eng.*, pages 36–43, 1989. {294}
- [530] R. J. Green, J. G. Walker, and D. W. Robinson. Investigation of the Fourier-transform method of fringe pattern analysis. *Opt. Lasers in Eng.*, 8:29–44, 1988. {294}
- [531] Th. Kreis, R. Biedermann, and W. Jüptner. Evaluation of holographic interference patterns by artificial neural networks. In M. Kujawinska, R. J. Pryputniewicz, and M. Takeda, editors, *Interferometry VII: Techniques and Analysis*, volume 2544 of *Proc. of Soc. Photo-Opt. Instr. Eng.*, pages 11–24, 1995. {294, 395}
- [532] M. Takeda, K. Nagatome, and Y. Watanabe. Phase unwrapping by neural network. In W. Jüptner and W. Osten, editors, *Fringe '93*, pages 136–141, 1993. {294}
- [533] J. M. Huntley, R. Cusack, and H. Saldner. New phase unwrapping algorithms. In W. Jüptner and W. Osten, editors, *Fringe '93*, pages 148–153, 1993. {295}
- [534] J. M. Huntley and H. Saldner. Temporal phase-unwrapping algorithm for automated interferogram analysis. *Appl. Opt.*, 32(17):3047–3052, 1993. {295}
- [535] G. Pedrini, I. Alexeenko, W. Osten, and H. J. Tiziani. Temporal phase unwrapping of digital hologram sequences. *Appl. Opt.*, 42:5846–5854, 2003. {295}
- [536] J. S. Lim. *Two-Dimensional Signal and Image Processing*. Prentice-Hall Intern., 1990. {295}
- [537] J. Arines. Least-squares modal estimation of wrapped phases: application to phase unwrapping. *Appl. Opt.*, 42:3373–3378, 2003. {295}
- [538] J. Ebbeni. Measurement of mechanical deformations from holographic interferograms. In P. Smigelski, editor, *Deuxieme Colloque Franco-Allemand sur les Applications de l'Holographie*, pages 1–18, 1989. {298}
- [539] Z. Füzessey and N. Abramson. Measurement of 3-D displacement: sandwich holography and regulated path length interferometry. *Appl. Opt.*, 21(2):260–264, 1982. {298}
- [540] E. Müller, V. Hrdliczka, and D. E. Cuche. Computer-based evaluation of holographic interferograms. In W. F. Fagan, editor, *Industrial Applications of Laser Technology*, volume 398 of *Proc. of Soc. Photo-Opt. Instr. Eng.*, pages 46–52, 1983. {298}
- [541] R. J. Pryputniewicz and W. W. Bowley. Techniques of holographic displacement measurement: an experimental comparison. *Appl. Opt.*, 17(11):1748–1756, 1978. {299}
- [542] K. A. Stetson. Use of sensitivity vector variations to determine absolute displacements in double exposure hologram interferometry. *Appl. Opt.*, 29(4):502–504, 1990. {300}
- [543] Z. Füzessey. Application of double-pulse holography for the investigations of machines and systems. In G. Frankowski, N. Abramson, and Z. Füzessey, editors, *Application of Metrological Laser Methods in Machines and Systems*, volume 15 of *Physical Research*, pages 75–107. Akademie Verlag, Berlin, 1991. {301}
- [544] Z. Füzessey and F. Gyimesi. Difference holographic interferometry: displacement measurement. *Opt. Eng.*, 23(6):780–783, 1984. {301, 350, 351}

- [545] Z. Füzesy and P. Wesolowski. Simplified static holographic evaluation method omitting the zero-order fringe. *Opt. Eng.*, 24(6):1023–1025, 1985. {301}
- [546] W. Jüptner, J. Geldmacher, Th. Bischof, and Th. Kreis. Measurement of the deformation of a pressure vessel above a weld point. In R. J. Pryputniewicz, G. M. Brown, and W. Jüptner, editors, *Interferometry: Applications*, volume 1756 of *Proc. of Soc. Photo-Opt. Instr. Eng.*, pages 98–105, 1992. {301, 305}
- [547] Th. Kreis and W. Jüptner. Determination of defects by combination of holographic interferometry and finite-element-method. *VDI-Berichte*, 631:139–151, 1987. (In German). {301, 321, 322}
- [548] M. Medhat. Computer analysis of interferograms by fitting quadratic forms. *Journ. Modern Opt.*, 38(1):121–128, 1991. {303}
- [549] J. D. Trolinger, D. C. Weber, G. C. Pardo, G. T. Gunnarsson, and W. F. Fagan. Application of long-range holography in earthquake engineering. *Opt. Eng.*, 30(9):1315–1319, 1991. {304}
- [550] W. Jüptner and H. Kreitlow. Holographic recording of non-vibration protected objects (in German). In W. Waidelich, editor, *Laser 77 Opto-Electronics*, pages 420–425. ipc science and technology press, 1977. {304}
- [551] D. B. Neumann and H. W. Rose. Improvement of recorded holographic fringes by feedback control. *Appl. Opt.*, 6(6):1097–1104, 1967. {304}
- [552] V. Kebbel, H.-J. Hartmann, W. Jüptner, U. Schnars, L. Gatti, and J. Becker. Detection and compensation of misalignment for interferometric diagnostic tools applied in space-borne facilities. In G. M. Brown, W. Jüptner, and R. Pryputniewicz, editors, *Interferometry X: Applications*, volume 4101 of *Proc. of Soc. Photo-Opt. Instr. Eng.*, pages 468–476, 2000. {304, 385}
- [553] H. W. Rose and H. D. Pruett. Stabilization of holographic fringes by FM feedback. *Appl. Opt.*, 7(1):87–89, 1968. {304, 305}
- [554] H. Kreitlow, Th. Kreis, and W. Jüptner. Holographic interferometry with reference beams modulated by the object motion. *Appl. Opt.*, 26(19):4256–4262, 1987. {305, 331}
- [555] F. M. Mottier. Holography of randomly moving objects. *Appl. Phys. Lett.*, 15(2):44–45, 1969. {305}
- [556] J. P. Waters. Object motion compensation by speckle reference beam interferometry. *Appl. Opt.*, 11:630–636, 1972. {305, 331}
- [557] D. B. Neumann and R. C. Penn. Object motion compensation using reflection holography. *Journ. Opt. Soc. Amer.*, 62:1373, 1972. {305}
- [558] N. Abramson. Sandwich hologram interferometry: A new dimension in holographic comparison. *Appl. Opt.*, 13:2019–2025, 1974. {305}
- [559] N. Abramson. Sandwich hologram interferometry 2: Some practical calculations. *Appl. Opt.*, 14:981–984, 1975. {305}
- [560] N. Abramson. Sandwich hologram interferometry 4: Holographic studies of two milling machines. *Appl. Opt.*, 16:2521–2531, 1977. {305}
- [561] N. Abramson and H. Bjelkhagen. Industrial holographic measurements. *Appl. Opt.*, 12:2792–2796, 1973. {305}

- [562] N. Abramson and H. Bjelkhagen. Pulsed sandwich holography 2: Practical application. *Appl. Opt.*, 17:187–191, 1978. {305}
- [563] N. Abramson and H. Bjelkhagen. Sandwich hologram interferometry 5: Measurement of in-plane displacement and compensation for rigid body motion. *Appl. Opt.*, 18:2870–2880, 1979. {305}
- [564] N. Abramson, H. Bjelkhagen, and P. Skande. Sandwich holography for storing information interferometrically with a high degree of security. *Appl. Opt.*, 18:2017–2021, 1979. {305}
- [565] H. Bjelkhagen. Pulsed sandwich holography. *Appl. Opt.*, 16:1727–1731, 1977. {305}
- [566] G. Lai and T. Yatagai. Dual-reference holographic interferometry with a double pulsed laser. *Appl. Opt.*, 27(18):3855–3858, 1988. {305}
- [567] A. Stimpfing and P. Smigelski. New method for compensating and measuring any motion of three-dimensional objects in holographic interferometry. *Opt. Eng.*, 24(5):821–823, 1985. {305}
- [568] P. Smigelski. New possibilities of holographic interferometry. In W. Jüptner, editor, *Holography Techniques and Applications*, volume 1026 of *Proc. of Soc. Photo-Opt. Instr. Eng.*, pages 90–92, 1988. {305}
- [569] B. Lutz and W. Schumann. Approach to extend the domain of visibility of recovered modified fringes when holographic interferometry is applied to large deformations. *Opt. Eng.*, 34(7):1879–1886, 1995. {305}
- [570] W. Schumann. Holographic interferometry applied to the case of large deformations. *Journ. Opt. Soc. Amer. A*, 6(11):1738–1747, 1989. {305}
- [571] S. Toyooka. Holographic interferometer, proof against external vibrations. *Optica Acta*, 29(6):861–865, 1982. {305}
- [572] P. Cielo. *Optical Techniques for Industrial Inspection*. Academic Press, 1988. {306}
- [573] R. J. Pryputniewicz. Determination of the sensitivity vectors directly from holograms. *Journ. Opt. Soc. Amer.*, 67(10):1351–1353, 1977. {306}
- [574] R. J. Pryputniewicz and K. A. Stetson. Determination of sensitivity vectors in hologram interferometry from two known rotations of the object. *Appl. Opt.*, 19(13):2201–2205, 1980. {307}
- [575] D. Vogel, V. Grosser, W. Osten, J. Vogel, and R. Höfling. Holographic 3d-measurement technique based on a digital image processing system. In W. Jüptner and W. Osten, editors, *Fringe '89*, pages 33–42, 1989. {307}
- [576] R. Dändliker and R. Thalmann. Determination of 3-D displacement and strain by holographic interferometry for non-plane objects. In W. F. Fagan, editor, *Industrial Applications of Laser Technology*, volume 398 of *Proc. of Soc. Photo-Opt. Instr. Eng.*, pages 11–16, 1983. {308}
- [577] S. K. Dhir and J. P. Sikora. An improved method for obtaining the general displacement field from a holographic interferogram. *Exp. Mech.*, 12:323–327, 1972. {311}
- [578] P. W. King III. Holographic interferometry technique utilizing two plates and relative fringe orders for measuring micro-displacements. *Appl. Opt.*, 13:231–233, 1974. {311}
- [579] C. A. Sciammarella and T. Y. Chang. Holographic interferometry applied to the solution of a shell problem. *Exp. Mech.*, 14:217–224, 1974. {311}

- [580] C. A. Sciammarella and J. A. Gilbert. Strain analysis of a disk subjected to diametral compression by means of holographic interferometry. *Appl. Opt.*, 12:1951–1956, 1973. **{311}**
- [581] G. Coppola, S. De Nicola, P. Ferraro, A. Finizio, S. Grilli, M. Iodice, C. Magro, and G. Pierattini. Evaluation of residual stress in MEMS structures by digital holography. In K. Gastinger, O. Løkberg, and S. Winther, editors, *Speckle Metrology 2003*, volume 4933 of *Proc. of Soc. Photo-Opt. Instr. Eng.*, pages 226–231, 2003. **{311}**
- [582] C. A. Sciammarella and F. M. Sciammarella. Measurement of mechanical properties of materials in the micrometer range using electronic holographic moire. *Opt. Eng.*, 42(5):1215–1222, 2003. **{311, 403}**
- [583] W. Schumann, J.-P. Zürcher, and D. Cuche. *Holography and Deformation Analysis*. Springer-Verlag, 1985. **{311}**
- [584] M. Y. Y. Hung, L. Lin, and H. M. Shang. Simple method for direct determination of bending strains by use of digital holography. *Appl. Opt.*, 40(25):4514–4518, 2001. **{317}**
- [585] C. A. Sciammarella and R. Narayanan. The determination of the components of the strain tensor in holographic interferometry. *Exp. Mech.*, 24:257–264, 1984. **{317}**
- [586] K. A. Stetson. The relationship between strain and derivatives of observed displacement in coherent optical metrology. *Exp. Mech.*, 7:273–275, 1981. **{317}**
- [587] L. H. Taylor and G. B. Brandt. An error analysis of holographic strains determined by cubic splines. *Exp. Mech.*, 12:543–548, 1972. **{317}**
- [588] R. J. Pryputniewicz and K. A. Stetson. Holographic strain analysis: extension of fringe vector method to include perspective. *Appl. Opt.*, 15(3):725–728, 1976. **{318}**
- [589] R. J. Pryputniewicz. Holographic strain analysis: an experimental implementation of the fringe-vector theory. *Appl. Opt.*, 17(22):3613–3618, 1978. **{318}**
- [590] K. A. Stetson. Homogeneous deformations: determination by fringe vectors in hologram interferometry. *Appl. Opt.*, 14:2256–2259, 1975. **{318}**
- [591] F. Chen, G. M. Brown, M. M. Marchi, and M. Dale. Recent advances in brake noise and vibration engineering using laser metrology. *Opt. Eng.*, 42(5):1359–1369, 2003. **{321, 323}**
- [592] G. M. Brown. Fringe analysis for automotive applications. *Opt. Lasers in Eng.*, 19:203–220, 1993. **{321}**
- [593] W. Jüptner and Th. Kreis, editors. *An External Interface for Processing 3-D Holographic and X-Ray Images*. Research Reports ESPRIT. Springer-Verlag, 1989. **{321}**
- [594] A. S. Kobayashi. Hybrid experimental-numerical stress analysis. *Exp. Mech.*, 23(3):338–347, 1983. **{321}**
- [595] M. M. Ratnam and W. T. Evans. Comparison of measurement of piston deformation using holographic interferometry and finite elements. *Exp. Mech.*, 12:336–342, 1993. **{321}**
- [596] J. M. Weathers, W. A. Foster, W. F. Swinson, and J. L. Turner. Integration of laser-speckle and finite-element techniques of stress analysis. *Exp. Mech.*, 3:60–65, 1985. **{321}**

- [597] K. Oh and R. J. Pryputniewicz. Application of electro-optic holography in the study of cantilever plate vibration with concentrated masses. In K. Stetson and R. Pryputniewicz, editors, *International Conference on Hologram Interferometry and Speckle Metrology*, pages 245–253, 1990. {321}
- [598] H. Borner, M. Schulz, J. Villain, and H. Steinbichler. Application of holographic interferometry supported by FEM-calculations during the development of a new assembly technique. In W. Jüptner, editor, *Holography Techniques and Applications*, volume 1026 of *Proc. of Soc. Photo-Opt. Instr. Eng.*, pages 171–175, 1988. {321}
- [599] M. A. Caponero, A. De Angelis, V. R. Filetti, and S. Gammella. Structural analysis of an aircraft turbine blade prototype by use of holographic interferometry. In R. J. Pryputniewicz, G. M. Brown, and W. Jüptner, editors, *Interferometry VI: Applications*, volume 2004 of *Proc. of Soc. Photo-Opt. Instr. Eng.*, pages 150–161, 1993. {321}
- [600] X. Bohineust, V. Linet, and F. Dupuy. Development and application of holographic modal decomposition techniques to acoustic analysis of vehicle structures. In R. J. Pryputniewicz, G. M. Brown, and W. Jüptner, editors, *Interferometry VI: Applications*, volume 2004 of *Proc. of Soc. Photo-Opt. Instr. Eng.*, pages 118–129, 1993. {321}
- [601] R. J. Pryputniewicz. Holographic and finite element studies of vibrating beams. In W. F. Fagan, editor, *Optics in Engineering Measurement*, volume 599 of *Proc. of Soc. Photo-Opt. Instr. Eng.*, pages 54–62, 1985. {321}
- [602] Th. Bischof and W. Jüptner. Investigation of the stress distribution in intact bonds by holographic interferometry and finite element method. In R. J. Pryputniewicz, editor, *Laser Interferometry IV: Computer-Aided Interferometry*, volume 1553 of *Proc. of Soc. Photo-Opt. Instr. Eng.*, pages 326–331, 1991. {321}
- [603] G. C. Brown and R. J. Pryputniewicz. Holographic microscope for measuring displacements of vibrating microbeams using time-averaged, electro-optic holography. *Opt. Eng.*, 37(5):1398–1405, 1998. {321}
- [604] W. Jüptner, Th. Kreis, J. Geldmacher, and Th. Bischof. Detection of defects in adhesion bonds using holographic interferometry (in German). *Qualität und Zuverlässigkeit*, 36(7):417–423, 1991. {321}
- [605] J. Balas, J. Sladek, and M. Drzik. Stress analysis by combination of holographic interferometry and boundary-integral method. *Exp. Mech.*, 83:196–202, 1983. {322}
- [606] C. A. Sciammarella. Contributions of interferometry to the field of fracture mechanics. In R. J. Pryputniewicz, G. M. Brown, and W. Jüptner, editors, *Interferometry VI: Applications*, volume 2004 of *Proc. of Soc. Photo-Opt. Instr. Eng.*, pages 204–214, 1993. {323}
- [607] J. M. Huntley and L. R. Benckert. Measurement of dynamic crack tip displacement field by speckle photography and interferometry. *Opt. Lasers in Eng.*, 19:299–312, 1993. {323}
- [608] L. W. Meyer, W. Jüptner, and H.-D. Steffens. Fracture toughness investigations using holographic interferometry. In W. Waideich, editor, *Laser 75 Opto-Electronics*, pages 203–205. IPC Science and Technology Press, 1975. {323}
- [609] A. J. Moore and J. R. Tyrer. The evaluation of fracture mechanics parameters from electronic speckle pattern interferometric fringe patterns. *Opt. Lasers in Eng.*, 19:325–336, 1993. {323}

- [610] W. Jüptner, K. Grünwald, R. Zirn, and H. Kreitlow. Measurement of the stress intensity factor k_i in large specimens by means of holographic interferometry. In D. Vukicevic, editor, *Holographic Data Nondestructive Testing*, volume 370 of *Proc. of Soc. Photo-Opt. Instr. Eng.*, pages 62–65, 1982. {323}
- [611] P. Will, W. Totzauer, and B. Michel. Generalized J-integral of fracture mechanics from holographic data. *Phys. Stat. Sol. (a)*, 95:K113–K116, 1986. {323}
- [612] K. A. Stetson and I. R. Harrison. Computer-aided holographic vibration analysis for vectorial displacements of bladed disks. *Appl. Opt.*, 17(11):1733–1738, 1978. {323}
- [613] K. A. Stetson. Holographic vibration analysis. In R. K. Erf, editor, *Holographic Non-Destructive Testing*, pages 181–220. Academic Press, 1974. {323}
- [614] J. Janta and M. Miler. Time average holographic interferometry of damped oscillations. *Optik*, 36:185–195, 1972. {324}
- [615] P. C. Gupta and K. Singh. Time-average hologram interferometry of periodic, non-cosinusoidal vibrations. *Appl. Phys.*, 6:233–240, 1975. {324}
- [616] P. C. Gupta and K. Singh. Characteristic fringe function for time-average holography of periodic nonsinusoidal vibrations. *Appl. Opt.*, 14:129–133, 1975. {324}
- [617] P. C. Gupta and K. Singh. Hologram interferometry of vibrations represented by the square of a Jacobian elliptic function. *Nouv. Rev. Opt.*, 7:95–100, 1976. {324}
- [618] P. Hariharan, B. F. Oreb, and C. H. Freund. Stroboscopic holographic interferometry: measurements of vector components of a vibration. *Appl. Opt.*, 26(18):3899–3903, 1987. {325}
- [619] P. Sajenko and C. D. Johnson. Stroboscopic holographic interferometry. *Appl. Phys. Lett.*, 13:44–46, 1968. {326}
- [620] S. Nakadate, H. Saito, and T. Nakajima. Vibration measurement using phase-shifting stroboscopic holographic interferometry. *Optica Acta*, 33(10):1295–1309, 1986. {326}
- [621] B. Ineichen and J. Mastner. Vibration analysis by stroboscopic two-reference-beam heterodyne holographic interferometry. In P. Meyrueis and M. Grosmann, editors, *2nd European Congress on Optics Applied to Metrology*, volume 210 of *Proc. of Soc. Photo-Opt. Instr. Eng.*, pages 207–212, 1979. {326, 331}
- [622] K. A. Stetson. Method of vibration measurements in heterodyne interferometry. *Opt. Lett.*, 7:233–234, 1982. {326, 331}
- [623] P. Hariharan. Application of holographic subtraction to time-average hologram interferometry of vibrating objects. *Appl. Opt.*, 12:143–146, 1973. {326}
- [624] R. J. Pryputniewicz. Time-average holography in vibration analysis. *Opt. Eng.*, 24:843–848, 1985. {326}
- [625] R. Tonin and D. A. Bies. Analysis of 3-D vibrations from time-averaged holograms. *Appl. Opt.*, 17(23):3713–3721, 1978. {326}
- [626] R. Tonin and D. A. Bies. General theory of time-averaged holography for the study of three-dimensional vibrations at a single frequency. *Journ. Opt. Soc. Amer.*, 68(7):924–931, 1978. {326}
- [627] K. Antropius. Fundamentals of time-average holographic interferometry and its applications to vibration measurements. In G. Frankowski, N. Abramson, and Z. Füzesi, editors, *Application of Metrological Laser Methods in Machines and Systems*, volume 15 of *Physical Research*, pages 167–194. Akademie Verlag, Berlin, 1991. {327}

- [628] C. S. Vikram. Study of vibrations. In P. K. Rastogi, editor, *Holographic Interferometry*, volume 68 of *Springer Series in Optical Sciences*, pages 293–318, 1994. [\[329\]](#)
- [629] M. Ueda, S. Miida, and T. Sato. Signal-to-noise ratio and smallest detectable vibration amplitude in frequency translated holography – an analysis. *Appl. Opt.*, 15:2690–2694, 1976. [\[330\]](#)
- [630] C. C. Aleksoff. Temporally modulated holography. *Appl. Opt.*, 10(6):1329–1341, 1971. [\[330\]](#)
- [631] J. W. Goodman. Temporal filtering properties of holograms. *Appl. Opt.*, 6:857–859, 1967. [\[330\]](#)
- [632] D. B. Neumann, C. F. Jacobsen, and G. M. Brown. Holographic technique for determining the phase of vibrating objects. *Appl. Opt.*, 9:1357–1368, 1970. [\[330\]](#)
- [633] C. C. Aleksoff. Time average holography extended. *Appl. Phys. Lett.*, 14:23–24, 1969. [\[330\]](#)
- [634] J. A. Levitt and K. A. Stetson. Mechanical vibrations: mapping their phase with hologram interferometry. *Appl. Opt.*, 15:195–199, 1976. [\[331\]](#)
- [635] C. S. Vikram. Mechanical vibrations: mapping their phase with hologram interferometry. *Appl. Opt.*, 16:1140–1141, 1977. [\[331\]](#)
- [636] J. Politch. Spectroscopic holography: a new method for mode analysis of randomly excited structures. *Journ. Opt. Soc. Amer. A*, 7(8):1355–1361, 1990. [\[331\]](#)
- [637] P. Hariharan and B. F. Oreb. Stroboscopic holographic interferometry: application of digital techniques. *Opt. Comm.*, 59(2):83–86, 1986. [\[331\]](#)
- [638] S. Nakadate. Vibration measurement using phase-shifting time-average holographic interferometry. *Appl. Opt.*, 25:4155–4161, 1986. [\[331\]](#)
- [639] K. A. Stetson. Fringe-shifting technique for numerical analysis of time-average holograms of vibrating objects. *Journ. Opt. Soc. Amer. A*, 5:1472–1476, 1988. [\[331, 332\]](#)
- [640] G. Pedrini, H. J. Tiziani, and I. Alexeenko. Digital-holographic interferometry with an image-intensifier system. *Appl. Opt.*, 41(4):648–653, 2002. [\[332\]](#)
- [641] G. Pedrini, P. Fröning, H. Fessler, and H. J. Tiziani. Transient vibration measurements using multi-pulse digital holography. *Opt. Laser Technol.*, 29(8):505–511, 1997. [\[333\]](#)
- [642] H. E. Cline, A. S. Holik, and W. E. Lorensen. Computer-aided surface reconstruction of interference contours. *Appl. Opt.*, 21(24):4481–4488, 1982. [\[333\]](#)
- [643] H. E. Cline, W. E. Lorensen, and A. S. Holik. Automatic moire contouring. *Appl. Opt.*, 23(10):1454–1459, 1984. [\[333\]](#)
- [644] G. Pedrini, P. Fröning, H. J. Tiziani, and M. E. Gusev. Pulsed digital holography for high-speed contouring that uses a two-wavelength method. *Appl. Opt.*, 38(16):3460–3467, 1999. [\[333\]](#)
- [645] A. A. Friesem and U. Levy. Fringe-formation in two-wavelength contour holography. *Appl. Opt.*, 15:3009–3020, 1976. [\[333\]](#)
- [646] R. P. Tatam, J. C. Davies, C. H. Buckberry, and J. D. C. Jones. Holographic surface contouring using wavelength modulation of laser diodes. *Opt. Laser Technol.*, 22(5):317–321, 1990. [\[333\]](#)
- [647] J. R. Varner. Simplified multiple-frequency holographic contouring. *Appl. Opt.*, 10:212–213, 1971. [\[333\]](#)

- [648] J. S. Zelenka and J. R. Varner. Multiple-index holographic contouring. *Appl. Opt.*, 8:1431–1434, 1969. {336}
- [649] N. Abramson. Holographic contouring by translation. *Appl. Opt.*, 15:1018–1022, 1976. {338}
- [650] P. K. Rastogi and L. Pflug. A holographic technique featuring broad range sensitivity to contour diffuse objects. *Journ. Modern Opt.*, 38(9):1673–1683, 1991. {338}
- [651] P. Carelli, D. Paoletti, G. Schirripa Spagnolo, and A. D’Altorio. Holographic contouring method: application to automatic measurements of surface defects in artwork. *Opt. Eng.*, 30(9):1294–1298, 1991. {338}
- [652] P. DeMatta and V. Fossati-Bellani. Holographic contouring by displacing the object and the illumination beam. *Opt. Comm.*, 26(1):17–21, 1978. {338}
- [653] M. Yonemura. Holographic contour generation by spatial frequency modulation. *Appl. Opt.*, 21(20):3652–3658, 1982. {338}
- [654] N. Abramson. Sandwich hologram interferometry 3: Contouring. *Appl. Opt.*, 15:200–205, 1976. {338}
- [655] N. Abramson. Light-in-flight recording: High-speed holographic motion pictures of ultrafast phenomena. *Appl. Opt.*, 22(2):215–232, 1983. {338, 377}
- [656] N. Abramson. Light-in-flight recording. 2: Compensation for the limited speed of the light used for observation. *Appl. Opt.*, 23(10):1481–1492, 1984. {338}
- [657] N. Abramson. Light-in-flight recording. 3: Compensation for optical relativistic effects. *Appl. Opt.*, 23(22):4007–4014, 1984. {338}
- [658] N. Abramson. Light-in-flight recording. 4: Visualizing optical relativistic phenomena. *Appl. Opt.*, 24(20):3323–3329, 1985. {338}
- [659] N. Abramson. Time reconstructions in light-in-flight recording by holography. *Appl. Opt.*, 30(10):1242–1252, 1991. {338}
- [660] N. Abramson and K. G. Spears. Single pulse light-in-flight recording by holography. *Appl. Opt.*, 28(10):1834–1841, 1989. {338}
- [661] T. Kubota and Y. Awatsuji. Observation of light propagation by holography with a picosecond pulsed laser. *Opt. Lett.*, 2(10):815–817, 2002. {338}
- [662] G. Tribillon and R. Salazar. Holographic reconstruction of a synthesised subpicosecond pulse. In W. F. Fagan, editor, *Industrial Applications of Laser Technology*, volume 398 of *Proc. of Soc. Photo-Opt. Instr. Eng.*, pages 181–184, 1983. {338}
- [663] H. Hinrichs, K. D. Hinsch, J. Kickstein, and M. Böhmer. Light-in-flight holography for visualization and velocimetry in three-dimensional flows. *Opt. Lett.*, 22(11):828–830, 1997. {339}
- [664] S. Seebacher, W. Osten, and W. Jüptner. Measuring shape and deformation of small objects using digital holography. In *Laser Interferometry IX: Applications*, volume 3479 of *Proc. of Soc. Photo-Opt. Instr. Eng.*, pages 104–115, 1998. {340}
- [665] I. Yamaguchi, J.-I. Kato, and H. Matsuzaki. Measurement of surface shape and deformation by phase-shifting image digital holography. *Opt. Eng.*, 42(5):1267–1271, 2003. {343}
- [666] C. Wagner, W. Osten, and S. Seebacher. Direct shape measurement by digital wavefront reconstruction and multiwavelength contouring. *Opt. Eng.*, 39(1):79–85, 2000. {343}

- [667] W. Osten. Active metrology by digital holography. In K. Gastinger, O. Løkberg, and S. Winther, editors, *Speckle Metrology 2003*, volume 4933 of *Proc. of Soc. Photo-Opt. Instr. Eng.*, pages 96–110, 2003. **{343, 354, 387}**
- [668] J. Pomerico, U. Schnars, H.-J. Hartmann, and W. Jüptner. Digital recording and numerical reconstruction of holograms: a new method for displaying light in flight. *Appl. Opt.*, 34(35):8095–8099, 1995. **{346}**
- [669] T. E. Carlsson, B. Nilsson, and J. Gustafsson. System for acquisition of three-dimensional shape and movement using digital light-in flight holography. *Opt. Eng.*, 40(1):67–75, 2001. **{346}**
- [670] P. K. Rastogi. Comparative holographic interferometry: A nondestructive inspection system for detection of flaws. *Exp. Mech.*, 25:325–337, 1985. **{350, 360}**
- [671] D. B. Neumann. Comparative holography. In *Technical Digest of Topical Meeting on Hologram Interferometry and Speckle Metrology*, pages MB2–1–MB2–4. Opt. Soc. Amer., 1980. **{350}**
- [672] D. B. Neumann. Comparative holography: a technique for eliminating background fringes in holographic interferometry. *Opt. Eng.*, 24(4):625–627, 1985. **{350}**
- [673] Z. Füzessey and F. Gyimesi. Difference holographic interferometry. In W. F. Fagan, editor, *Industrial Applications of Laser Technology*, volume 398 of *Proc. of Soc. Photo-Opt. Instr. Eng.*, pages 240–243, 1983. **{350}**
- [674] Z. Füzessey, F. Gyimesi, and I. Banyasz. Difference holographic interferometry (DHI): single reference beam technique. *Opt. Comm.*, 68(6):404–407, 1984. **{350}**
- [675] F. Gyimesi and Z. Füzessey. Difference holographic interferometry: theory. *Journ. Modern Opt.*, 35(10):1699–1716, 1988. **{350}**
- [676] Z. Füzessey, F. Gyimesi, and J. Kornis. Comparison of two filament lamps by difference hologram interferometry. *Opt. Laser Technol.*, 18(6):318–320, 1986. **{351}**
- [677] Z. Füzessey. Measurement of 3D-displacement by regulated path length interferometry. In W. F. Fagan, editor, *Industrial Applications of Laser Technology*, volume 398 of *Proc. of Soc. Photo-Opt. Instr. Eng.*, pages 17–21, 1983. **{351}**
- [678] F. Gyimesi and Z. Füzessey. Difference holographic interferometry (DHI): two-refractive-index contouring. *Opt. Comm.*, 53(1):17–22, 1985. **{351}**
- [679] Z. Füzessey and F. Gyimesi. Difference holographic interferometry (DHI): phase object measurement. *Opt. Comm.*, 57(1):31–33, 1986. **{351}**
- [680] P. K. Rastogi. Comparative holographic moire interferometry in real time. *Appl. Opt.*, 23(6):924–927, 1984. **{352, 353}**
- [681] P. K. Rastogi. Interferometric comparison of diffuse objects using comparative holography. *Opt. Eng.*, 34(7):1923–1929, 1995. **{352}**
- [682] E. Simova and V. Sainov. Comparative holographic moire interferometry for nondestructive testing: comparison with conventional holographic interferometry. *Opt. Eng.*, 28(3):261–266, 1989. **{352}**
- [683] G. H. Kaufmann and P. K. Rastogi. Comparative holographic interferometry using a phase shifting technique. In K. Stetson and R. Pryputniewicz, editors, *International Conference on Hologram Interferometry and Speckle Metrology*, pages 180–183, 1990. **{353}**

- [684] P. K. Rastogi, M. Barillot, and G. H. Kaufmann. Comparative phase shifting holographic interferometry. *Appl. Opt.*, 30(7):722–728, 1991. {353}
- [685] E. S. Simova and K. N. Stoev. Automated Fourier transform fringe-pattern analysis in holographic moire. *Opt. Eng.*, 32(9):2286–2294, 1993. {353, 360}
- [686] W. Osten, T. Baumbach, and W. Jüptner. Comparative digital holography. *Opt. Lett.*, 27(20):1764–1766, 2002. {356}
- [687] W. Osten, T. Baumbach, S. Seebacher, and W. Jüptner. Remote shape control by comparative digital holography. In W. Osten and W. Jüptner, editors, *Fringe 2001*, pages 373–382, 2001. {356}
- [688] J. C. Wyant. Testing aspherics using two-wavelength holography. *Appl. Opt.*, 10(9):2113–2118, 1971. {357, 358}
- [689] C. Polhemus. Two-wavelength interferometry. *Appl. Opt.*, 12(9):2071–2074, 1973. {358}
- [690] R. Dändliker, R. Thalmann, and D. Prongue. Two-wavelength laser interferometry using superheterodyne detection. *Opt. Lett.*, 13(5):339–341, 1988. {358}
- [691] P. Lam, J. D. Gaskill, and J. C. Wyant. Two-wavelength holographic interferometer. *Appl. Opt.*, 23:3079–3081, 1984. {358}
- [692] N. Ninane and M. P. Georges. Holographic interferometry using two-wavelength holography for the measurement of large deformations. *Appl. Opt.*, 34(11):1923–1928, 1995. {358}
- [693] W. Jüptner, Th. Kreis, and J. Geldmacher. Determination of absolute fringe order in hologram interferometry with wavelength controlled lasers. In M. Y. Y. Hung and R. J. Pryputniewicz, editors, *Industrial Laser Interferometry II*, volume 955 of *Proc. of Soc. Photo-Opt. Instr. Eng.*, pages 143–146, 1988. {358}
- [694] D. C. Holloway, A. M. Patacca, and W. L. Fourney. Direction-sensitive displacement analysis by multiple frequency holographic interferometry. *Appl. Opt.*, 17(8):1213–1219, 1978. {358}
- [695] C. A. Sciammarella. Holographic moire, an optical tool for the determination of displacements, strains, contours, and slopes of surfaces. *Opt. Eng.*, 21(4):447–457, 1982. {359}
- [696] P. Rastogi and J.-L. Sandoz. Mechanical evaluation of finger-jointed timber assemblies using holographic moire interferometry. *Journ. Opt. Soc. Amer. A*, 14(8):1742–1753, 1997. {359, 360}
- [697] C. A. Sciammarella and J. A. Gilbert. A holographic-moire technique to obtain separate patterns for components of displacement. *Exp. Mech.*, 16:215–220, 1976. {360, 403}
- [698] C. A. Sciammarella and J. A. Gilbert. Holographic interferometry applied to the measurement of displacements of the interior points of transparent bodies. *Appl. Opt.*, 15:2176–2182, 1976. {360}
- [699] M Spajer, P. K. Rastogi, and J. Monneret. In plane displacement and strain measurement by speckle interferometry and moire derivation. *Appl. Opt.*, 20(19):3392–3402, 1981. {360}
- [700] C. A. Sciammarella and S. K. Chawla. Holographic moire technique to obtain displacement components and derivatives. *Exp. Mech.*, 18:373–381, 1978. {360}

- [701] S. K. Chawla and C. A. Sciammarella. *Exp. Mech.*, 20:240, 1980. {360}
- [702] M.-A. Beeck. Pulsed holographic vibration analysis on high-speed rotating objects: fringe formation, recording techniques, and practical applications. In W. Jüptner, editor, *Holography Techniques and Applications*, volume 1026 of *Proc. of Soc. Photo-Opt. Instr. Eng.*, pages 186–195, 1988. {360}
- [703] M.-A. Beeck. Pulsed holographic vibration analysis on high-speed rotating objects: fringe formation, recording techniques, and practical applications. *Opt. Eng.*, 31(3):553–561, 1992. {360}
- [704] J. P. Sikora and F. T. Mendenhall. Holographic vibration study of a rotating propeller blade. *Exp. Mech.*, 14(6):230–232, 1974. {360}
- [705] T. Tsuruta and Y. Itoh. Holographic interferometry for rotating subject. *Appl. Phys. Lett.*, 17:85–87, 1970. {360}
- [706] T. E. Carlsson, B. Nilsson, J. Gustafsson, and N. Abramson. Practical system for time-resolved holographic interferometry. *Opt. Eng.*, 30(7):1017–1022, 1991. {360}
- [707] J. Geldmacher, H. Kreitlow, P. Steinlein, and G. Sepold. Comparison of vibration mode measurements on rotating objects by different holographic methods. In W. F. Fagan, editor, *Industrial Applications of Laser Technology*, volume 398 of *Proc. of Soc. Photo-Opt. Instr. Eng.*, pages 101–110, 1983. {361}
- [708] E. Vogt, J. Geldmacher, B. Dirr, and H. Kreitlow. Hybrid-vibration mode analysis of rotating turbine-blade models. *Exp. Mech.*, 25:161–170, 1985. {361}
- [709] K. A. Stetson. The use of an image derotator in hologram interferometry and speckle photography of rotating objects. *Exp. Mech.*, 18:67–73, 1978. {362}
- [710] H. J. Tiziani. Holographic interferometry and speckle metrology: a review of the present state. In W. F. Fagan, editor, *Industrial Applications of Laser Technology*, volume 398 of *Proc. of Soc. Photo-Opt. Instr. Eng.*, pages 2–10, 1983. {362}
- [711] P. Waddell. Stopping rotary motion with a prism. *Machine Design*, 45:151–152, 1973. {362}
- [712] Lasermet Ltd. The Lasermet Rotoviewer. Technical information sheet. {363}
- [713] U. Haupt and M. Rautenberg. Investigation of blade vibration of radial impellers by means of telemetry and holographic interferometry. *Trans. ASME: J. Eng. Power*, 104:838–843, 1982. {363}
- [714] C. Perez Lopez, F. Mendoza Santoyo, G. Pedrini, S. Schedin, and H. Tiziani. Pulsed digital holographic interferometry for dynamic measurement of rotating objects with an optical derotator. *Appl. Opt.*, 40:5106–5110, 2001. {364}
- [715] C. Perez Lopez, F. Mendoza Santoyo, and J. A. Guerrero. Decoupling the x , y and z displacement components in a rotating disc using three-dimensional pulsed digital holography. *Meas. Sci. & Techn.*, 14:97–100, 2003. {364}
- [716] M. Yonemura, T. Nishisaka, and H. Machida. Endoscopic hologram interferometry using fiber optics. *Appl. Opt.*, 20:1664–1667, 1981. {364}
- [717] E. Kolenovic, W. Osten, R. Klattenhoff, S. Lai, Chr. von Kopylow, and W. Jüptner. Miniaturized digital holography sensor for distal three-dimensional endoscopy. *Appl. Opt.*, 42:5167–5172, 2003. {364, 365}

- [718] S. Schedin, G. Pedrini, H. J. Tiziani, A. K. Aggarwal, and M. E. Gusev. Comparative study of various endoscopes for pulsed digital holographic interferometry. *Appl. Opt.*, 40:2692–2697, 2001. {364}
- [719] S. Schedin, G. Pedrini, H. J. Tiziani, and F. Mendoza Santoyo. All-fibre pulsed digital holography. *Opt. Comm.*, 165(4-6):183–188, 1999. {364}
- [720] G. Pedrini, I. Alexeenko, and H. J. Tiziani. Pulsed endoscopic digital holographic interferometry for investigation of hidden surfaces. In K. Gastinger, O. Løkberg, and S. Winther, editors, *Speckle Metrology 2003*, volume 4933 of *Proc. of Soc. Photo-Opt. Instr. Eng.*, pages 123–128, 2003. {364}
- [721] P. M. Boone and P. Jacquot. Use of an all-holographic desensitized white-light interferometer for visualization of plastic zones. In K. Stetson and R. Pryputniewicz, editors, *International Conference on Hologram Interferometry and Speckle Metrology*, pages 494–499, 1990. {365, 366}
- [722] S. S. Cha and C. M. Vest. Tomographic reconstruction of strongly refracting fields and its applications to interferometric measurements of boundary layers. *Appl. Opt.*, 20:2787–2794, 1981. {369, 382, 383}
- [723] W. Hauf and U. Grigull. *Optical Methods in Heat Transfer*, volume 6 of *Advances in Heat Transfer*. Academic Press, 1970. {372, 376}
- [724] D. Vukicevic, T. Neger, H. Jäger, J. Woisetschläger, and H. Philipp. Optical tomography by heterodyne holographic interferometry. In P. Greguss and T. H. Jeong, editors, *Holography*, volume IS 8 of *SPIE Institute Series*, pages 160–193, 1990. {374, 384}
- [725] C. M. Vest. Interferometry of strongly refracting axisymmetric phase objects. *Appl. Opt.*, 14(7):1601–1606, 1975. {376}
- [726] R. Ladenburg, J. Winkler, and C. C. Van Voorhis. Interferometric study of faster than sound phenomena, Part I. *Phys. Rev.*, 73:1359–1377, 1948. {377}
- [727] R. Barakat. Solution of an Abel integral equation for band-limited functions by means of sampling theorems. *J. Math. Phys.*, 43:325–331, 1964. {377}
- [728] D. W. Sweeney. A comparison of Abel integral inversion schemes for interferometric applications. *Journ. Opt. Soc. Amer.*, 64:559, 1974. {377}
- [729] M. Kalal and K. A. Nugent. Abel inversion using fast Fourier transforms. *Appl. Opt.*, 27(10):1956–1959, 1988. {377}
- [730] C. M. Vest. Holographic interferometry of transparent media. In VDI, editor, *VDI Symposium on Holographic Interferometry*, 1983. {377}
- [731] I. H. Lira and Ch. M. Vest. Refraction correction in holographic interferometry and tomography of transparent objects. *Appl. Opt.*, 26(18):3919–3928, 1987. {378}
- [732] D. D. Verhoeven. Application of holographic interferometry and computer tomography to full-field measurement of asymmetric refractive index distributions. In W. Jüptner, editor, *Holography Techniques and Applications*, volume 1026 of *Proc. of Soc. Photo-Opt. Instr. Eng.*, pages 111–122, 1988. {379}
- [733] M. V. Berry and D. F. Gibbs. The interpretation of optical projections. *Proc. Roy. Soc. London*, A314:143–152, 1970. {379}
- [734] H. G. Junginger and W. van Haeringen. Calculation of three-dimensional refractive-index field using phase integrals. *Opt. Comm.*, 5:1–4, 1972. {379}

- [735] C. M. Vest. Tomography for properties of materials that bend rays: a tutorial. *Appl. Opt.*, 24(23):4089–4094, 1985. {383, 384}
- [736] R. Snyder and L. Hesselink. Optical tomography for flow visualization of the density around a revolving helicopter rotor blade. *Appl. Opt.*, 23(20):3650–3656, 1984. {383}
- [737] S. J. Norton and M. Linzer. Correcting for ray refraction in velocity and attenuation tomography. *Ultrason. Imaging*, 4:201, 1982. {383}
- [738] K. Iwata and R. Nagata. Calculation of refractive index distribution from interferograms using the Born and Rytov's approximation. *Jpn. J. Appl. Phys.*, 14(1):379, 1975. {383}
- [739] S. K. Kenue and J. F. Greenleaf. Limited angle multifrequency diffraction tomography. *IEEE Trans. Son. Ultrason.*, 29:213, 1982. {383}
- [740] S. S. Cha and H. Sun. Tomography for reconstructing continuous fields from ill-posed multidirectional interferometric data. *Appl. Opt.*, 29(2):251–258, 1990. {383}
- [741] I. Prikryl and C. M. Vest. Holographic interferometry of transparent media using light scattered by embedded test objects. *Appl. Opt.*, 21(14):2554–2557, 1982. {383}
- [742] S. E. Reichenbach, J. C. Burton, and K. W. Miller. Comparison of algorithms for computing the two-dimensional discrete Hartley transform. *Journ. Opt. Soc. Amer. A*, 6:818–821, 1989. {385}
- [743] V. Kebbel, H. J. Hartmann, and W. Jüptner. Characterization of micro-optics using digital holography. In G. M. Brown, W. Jüptner, and R. Pryputniewicz, editors, *Laser Interferometry X: Applications*, volume 4101 of *Proc. of Soc. Photo-Opt. Instr. Eng.*, pages 477–487, 2000. {385}
- [744] V. Kebbel, M. Adams, H. J. Hartmann, and W. Jüptner. Digital holography as a versatile optical diagnostic method for microgravity experiments. *Meas. Sci. & Techn.*, 10(10):893–899, 1999. {385}
- [745] N. Demoli, D. Vukicevic, and M. Torzynski. Dynamic digital holographic interferometry with three wavelengths. *Opt. Expr.*, 11(7):767–774, 2003. {385}
- [746] J. D. Trolinger and J. C. Hsu. Flowfield diagnostics by holographic interferometry and tomography. In W. Jüptner and W. Osten, editors, *Fringe '93*, pages 423–439, 1993. {386}
- [747] B. A. Tozer, R. Glanville, A. L. Gordon, M. J. Little, J. M. Webster, and D. G. Wright. Holography applied to inspection and measurement in an industrial environment. *Opt. Eng.*, 24(5):746–753, 1985. {387}
- [748] H. Hong, D. B. Sheffer, and C. W. Loughry. Detection of breast lesions by holographic interferometry. *J. Biomed. Opt.*, 4(03):368–375, 1999. {387}
- [749] J. Woisetschläger, D. B. Sheffer, C. W. Loughry, K. Somasundaram, S. K. Chawla, and P. J. Wesolowski. Phase-shifting holographic interferometry for breast cancer detection. *Appl. Opt.*, 33:5011–5015, 1994. {387}
- [750] M. A. Schulze, M. A. Hunt, E. Voelkl, J. D. Hickson, W. Usry, R. G. Smith, R. Bryant, and C. E. Thomas Jr. Semiconductor wafer defect detection using digital holography. In *Process and Materials Characterization and Diagnostics in IC Manufacturing II*, Proc. of Soc. Photo-Opt. Instr. Eng., 2003. {387}
- [751] U. Mieth, W. Osten, and W. Jüptner. Knowledge assisted fault detection based on line features of skeletons. In W. Jüptner and W. Osten, editors, *Fringe '93*, Physical Research, pages 367–373. Akademie-Verlag, Berlin, 1993. {388}

- [752] D. A. Tichenor and V. P. Madsen. Computer analysis of holographic interferograms for nondestructive testing. *Opt. Eng.*, 18(5):469–472, 1979. {390}
- [753] D. W. Robinson. Automatic fringe analysis with a computer image-processing system. *Appl. Opt.*, 22(14):2169–2176, 1983. {390}
- [754] J. Kornis and G. Vasarhelyi. Application of artificial neural network in holographic and speckle interferometry. In K. Gastinger, O. Løkberg, and S. Winther, editors, *Speckle Metrology 2003*, volume 4933 of *Proc. of Soc. Photo-Opt. Instr. Eng.*, pages 212–217, 2003. {395}
- [755] Y. Frauel and B. Javidi. Neural network for three-dimensional object recognition based on digital holography. *Opt. Lett.*, 26(19):1478–1480, 2001. {398}
- [756] Y. Frauel, E. Tajahuerce, M.-A. Castro, and B. Javidi. Distortion-tolerant three-dimensional object recognition with digital holography. *Appl. Opt.*, 40(23):3887–3893, 2001. {398}
- [757] N. A. Halliwell and C. J. Pickering. Analysis methods in laser speckle photography and particle image velocimetry. In D. W. Robinson and G. T. Reid, editors, *Interferogram Analysis: Digital Fringe Pattern Measurement Techniques*, pages 230–261. Institute of Physics, Bristol and Philadelphia, 1993. {400}
- [758] B. Ineichen, P. Eglin, and R. Dändliker. Hybrid optical and electronic image processing for strain measurements by speckle photography. *Appl. Opt.*, 19:2191–2195, 1980. {400}
- [759] H. Kreitlow and Th. Kreis. Automatic evaluation of Young’s fringes related to the study of in-plane-deformations by speckle techniques. In P. Meyrueis and M. Grosmann, editors, *2nd European Congress on Optics Applied to Metrology*, volume 210 of *Proc. of Soc. Photo-Opt. Instr. Eng.*, pages 18–24, 1979. {400}
- [760] J. M. Huntley. Speckle photography fringe analysis by the Walsh transform. *Appl. Opt.*, 25:382–386, 1986. {400}
- [761] H. Kreitlow, Th. Kreis, and W. Jüptner. Optimierung der automatisierten Auswertung von Specklegrammen beim Einsatz eines schnellen Fouriertransformators (Optimization of automatic evaluation of specklegrams using a fast Fourier-transformer). In W. Waidelich, editor, *Laser 83 - Optoelektronik in der Technik*, pages 159–164. Springer-Verlag, 1983. (In German). {400}
- [762] K. A. Stetson. K100 electronic holography system and HG7000 interferometric computer: instruments for automotive component analysis. *Opt. Eng.*, 42(5):1348–1353, 2003. {400, 404}
- [763] R. Mattsson, P. Gren, and A. Wåhlin. Laser ignition of pre-mixed gases studies by pulse TV holography. In K. Gastinger, O. Løkberg, and S. Winther, editors, *Speckle Metrology 2003*, volume 4933 of *Proc. of Soc. Photo-Opt. Instr. Eng.*, pages 285–290, 2003. {400}
- [764] P. Gren. Bending wave propagation in rotating objects measured by pulsed TV holography. *Appl. Opt.*, 41(34):7237–7240, 2002. {400}
- [765] P. Gren. Pulsed TV holography combined with digital speckle photography restores lost interference phase. *Appl. Opt.*, 40(14):2304–2309, 2001. {400}

- [766] G. Schirripa Spagnolo, D. Ambrosini, and G. Guattari. Electro-optic holography system and digital image processing for in situ analysis of microclimate variation on artworks. *J. Opt.*, 28:99–106, 1997. {400}
- [767] G. Schirripa Spagnolo, G. Guattari, E. Grinzato, P. G. Bison, D. Paoletti, and D. Ambrosini. Frescoes diagnostics by electro-optic holography and infrared thermography. *NDT.net*, 5(1), 2000. <http://www.ndt.net/article/v05n01/schirripa/schirrip.htm>. {400}
- [768] S. Schedin, G. Pedrini, and H. J. Tiziani. Pulsed digital holography for deformation measurements on biological tissues. *Appl. Opt.*, 39(16):2853–2857, 2000. {400, 403}
- [769] G. Pedrini, H. J. Tiziani, and M. E. Gusev. Pulsed digital holographic interferometry with 694- and 347-nm wavelengths. *Appl. Opt.*, 39(2):246–249, 2000. {400, 403}
- [770] S. Schedin, G. Pedrini, H. J. Tiziani, A. K. Aggarwal, and M. E. Gusev. Highly sensitive pulsed digital holography for built-in defect analysis with a laser excitation. *Appl. Opt.*, 40:100–117, 2001. {400, 403}
- [771] E. Marquardt and J. Richter. Digital image holography. *Opt. Eng.*, 37(5):1514–1519, 1998. {400}
- [772] P. Aswendt, R. Höfling, and W. Totzauer. Digital speckle pattern interferometry applied to thermal strain measurements of metal-ceramic compounds. *Opt. Laser Technol.*, 22(4):278–282, 1990. {403}
- [773] A. Shulev, I. Russev, and V. Sainov. New automatic FFT filtration method for phase maps and its application in speckle interferometry. In K. Gastinger, O. Løkberg, and S. Winther, editors, *Speckle Metrology 2003*, volume 4933 of *Proc. of Soc. Photo-Opt. Instr. Eng.*, pages 323–327, 2003. {403}
- [774] C. Trillo, A. F. Doval, D. Cernadas, O. Lopez, C. Lopez, B. V. Dorrio, J. L. Fernandez, and M. Perez-Amor. Measurement of the mechanical amplitude and phase of transient surface acoustic waves using double pulsed TV holography and the spatial Fourier transform method. In K. Gastinger, O. Løkberg, and S. Winther, editors, *Speckle Metrology 2003*, volume 4933 of *Proc. of Soc. Photo-Opt. Instr. Eng.*, pages 66–71, 2003. {403}
- [775] R. Krupka, Th. Walz, and A. Ettemeyer. Fast and full-field measurement of brake squeal using pulsed ESPI technique. *Opt. Eng.*, 42(5):1354–1358, 2003. {403}
- [776] P. Fröning, G. Pedrini, H. J. Tiziani, and F. Mendoza Santoyo. Vibration mode separation of transient phenomena using multi-pulse digital holography. *Opt. Eng.*, 38(12):2062–2068, 1999. {403}
- [777] F. Mendoza Santoyo, G. Pedrini, S. Schedin, and H. J. Tiziani. 3D displacement measurements of vibrating objects with multi-pulse digital holography. *Meas. Sci. & Technol.*, 10(12):1305–1308, 1999. {403}
- [778] S. Leidenbach. The direct phase measurement – a new method for determination of a phase image from a single intensity image (in German). In W. Waidelech, editor, *Laser 91 - Optoelektronik Mikrowellen*, pages 68–72, 1991. {405}
- [779] H. O. Saldner, N.-E. Molin, and K. A. Stetson. Fourier transform evaluation of phase data in spatially phase-biased TV holograms. *Appl. Opt.*, 35(2):332–336, 1996. {405}

- [780] Y. Y. Hung. Electronic shearography versus ESPI for nondestructive evaluation. In F.-P. Chiang, editor, *Moiré Techniques, Holographic Interferometry, Optical NDT, and Applications to Fluid Mechanics*, volume 1554B of *Proc. of Soc. Photo-Opt. Instr. Eng.*, pages 692–700, 1991. {405}
- [781] A. R. Ganesan, D. K. Sharma, and M. P. Kothiyal. Universal digital speckle shearing interferometer. *Appl. Opt.*, 27(22):4731–4734, 1988. {407}
- [782] C. Falldorf, S. G. Hanson, W. Osten, and W. Jüptner. Fringe compensation in multi-band speckle shearography using a wedge prism. In K. Gastinger, O. Løkberg, and S. Winther, editors, *Speckle Metrology 2003*, volume 4933 of *Proc. of Soc. Photo-Opt. Instr. Eng.*, pages 82–89, 2003. {408}
- [783] D. C. Champeney. *A Handbook of Fourier Theorems*. Cambridge University Press, 1987. {411}
- [784] A. Papoulis. *Signal Analysis*. McGraw-Hill International Book Company, 1977. {412, 442}
- [785] A. C. Kak and M. Slaney. *Principles of Computerized Tomographic Imaging*. IEEE Press, 1988. {423, 448, 450, 457}
- [786] L. P. Yaroslavsky. Efficient algorithm for discrete sinc interpolation. *Appl. Opt.*, 36(2):460–463, 1997. {428, 439, 440}
- [787] L. Yaroslavsky. Boundary effect free and adaptive discrete signal sinc-interpolation algorithms for signal and image resampling. *Appl. Opt.*, 42(20+32):4166–4175+6495, 2003. {428}
- [788] L. Yaroslavsky and M. Eden. *Fundamentals of Digital Optics*. Birkhäuser, 1996. {428}
- [789] A. Rosenfeld and A. C. Kak. *Digital Picture Processing*. Academic Press, 2nd edition, 1982. {431}
- [790] E. O. Brigham. *The Fast Fourier Transform*. Prentice-Hall, 1974. {437}
- [791] S. D. Stearns. *Digital Signal Analysis*. Hayden Book Comp., 1975. {437}
- [792] H. J. Nussbaumer. *Fast Fourier Transform and Convolution Algorithms*. Springer Series in Information Sciences, Vol. 2. 1982. {437, 438}
- [793] A. B. Watson and A. Poirson. Separable two-dimensional discrete Hartley transform. *Journ. Opt. Soc. Amer. A*, 3(12):2001–2004, 1986. {440}
- [794] D. Gabor. Theory of communication. *J. Inst. Electr. Eng. (London)*, 93:429–457, 1946. {445}
- [795] J. Radon. Über die Bestimmung von Funktionen durch ihre Integralwerte längs gewisser Mannigfaltigkeiten. *Ber. der Sächs. Akad. der Wissensch., Math.-Phys. Klasse*, 69:262–277, 1917. {447}
- [796] R. H. T. Bates, K. L. Garden, and T. M. Peters. Overview of computerized tomography with emphasis on future developments. *Proc. IEEE*, 71(3):356–372, 1983. {447}
- [797] R. M. Lewitt. Reconstruction algorithms: transform methods. *Proc. IEEE*, 71(3):390–408, 1983. {454}
- [798] Y. Censor. Finite series-expansion reconstruction methods. *Proc. IEEE*, 71(3):409–419, 1983. {455, 457}

- [799] A. L. Collins, M. W. Collins, and J. Hunter. The application of tomographic reconstruction techniques to the extraction of data from holographic interferograms. In R. J. Pryputniewicz, G. M. Brown, and W. Jüptner, editors, *Interferometry VI: Applications*, volume 2004 of *Proc. of Soc. Photo-Opt. Instr. Eng.*, pages 234–243, 1993. {455}
- [800] H. Tan and D. Modarress. Algebraic reconstruction technique code for tomographic interferometry. *Opt. Eng.*, 24:435–440, 1985. {455}
- [801] D. D. Verhoeven. MART-type CT algorithms for the reconstruction of multidirectional interferometric data. In R. J. Pryputniewicz, editor, *Laser Interferometry IV: Computer-Aided Interferometry*, volume 1553 of *Proc. of Soc. Photo-Opt. Instr. Eng.*, pages 376–387, 1991. {455}

Author Index

- Abe, A., see Watanabe, M. [348]
Abendroth, H., see Lu, B. [352]
Abramson, N. [196, 297–301, 377, 558–564, 649, 654–660]
—, see Carlsson, T. E. [706]
—, see Füzesy, Z. [539]
Adams, J. [214]
Adams, M. [265]
—, see Kebbel, V. [744]
—, see Kreis, Th. [252, 255, 261]
Aggarwal, A. K., see Schedin, S. [718, 770]
Albertazzi Jr., A. [71, 240]
Albrecht, D., see Zanetta, P. [459]
Aleksandrov, E. B. [36, 484]
Aleksoff, C. C. [630, 633]
Alexeenko, I., see Pedrini, G. [535, 640, 720]
Allano, D., see Malek, M. [247]
Allaria, E. [92]
Allebach, J. P. [219]
Alleysson, D. [216]
Amadesi, S. [324]
—, see Paoletti, D. [174]
Ambrosini, D., see Spagnolo, G. Schirripa [516, 766, 767]
An, Y., see Yu, L. [272]
Andres, N., see Lobera, J. [267]
Andresen, K. [511]
Angelis, A. De, see Caponero, M. A. [599]
Antropius, K. [627]
Aparicio, J. A. [409]
Arines, J. [537]
Arroyo, M. P., see Lobera, J. [267]
Asakura, T., see Soontaranon, S. [249]
Asundi, A., see Xu, L. [113, 114, 258, 276]
Aswendt, P. [772]
—, see Kreis, Th. [227]
Awatsuji, Y., see Kubota, T. [661]

Bachor, H.-A., see Bone, D. J. [461]
Bakker, P. G., see Lanen, T. A. W. M. [340]
Balas, J. [605]
Baldi, A. [526]
Banyasz, I., see Füzesy, Z. [674]
Barakat, R. [727]
Barillot, M., see Rastogi, P. K. [684]
Barnhart, D. H. [192]
Bashaw, M. C., see Heanue, J. F. [14]
Bates, R. H. T. [796]
Baumbach, T., see Osten, W. [686, 687]
Baumbach, Th. [212]
Becker, F. [402, 403]
Becker, J., see Kebbel, V. [552]
—, see Skarman, B. [119]
Bedarida, F., see Solitro, F. [198]
Beeck, M.-A. [702, 703]
Beguin, D. [125]
—, see Colomb, T. [122, 123]
Beheim, G., see Mercer, C. R. [206]
Belaid, S. [246]
—, see Lebrun, D. [248]
Benckert, L. R., see Huntley, J. M. [607]
Benkouider, A. M., see Lebrun, D. [273]
Benoit, M. R., see Owen, R. B. [147]
Benoit, M.R. [149]
Bentley, J. P. [193]
Bermudez, J. Guerrero, see Torres, E. [226]
Bernabeu, E., see Quiroga, J. A. [515]
Berry, M. V. [733]
Bertaux, N., see Matoba, O. [97]
Bertolino, F. [410]
—, see Ginesu, F. [366]
Bevilacqua, F., see Cuche, E. [228]
Bhat, G., see Sciammarella, C. A. [374]
Bieber, E. [400]
Biedermann, K., see Ek, L. [485, 487]

- Biedermann, R.*, see Kreis, Th. [293, 425, 531]
Bies, D. A., see Tonin, R. [625, 626]
Bilbro, G. L., see Ramanath, R. [217]
Binet, R. [83]
Birnbaum, G. [323]
Bischof, Th. [602]
—, see Jüptner, W. [546, 604]
Bison, P. G., see Spagnolo, G. Schirripa [767]
Bjelkhagen, H. [565]
—, see Abramson, N. [561–564]
Blaggrave, K., see Kreuzer, H. J. [75]
Blanco-Garcia, J. [311]
Blu, Th., see Liebling, M. [129, 241–243, 245]
Bo, F., see Liu, Ch. [81]
Boehnlein, A. J., see Gilbert, J. A. [199]
Bohineust, X. [600]
Böhmer, M., see Hinrichs, H. [663]
Bonch-Bruevich, A. M., see Aleksandrov, E. B. [36, 484]
Bone, D. J. [461, 504]
Boone, P. M. [315, 721]
Borghi, R., see Spagnolo, G. Schirripa [516]
Borner, H. [598]
Bowley, W. W., see Pryputniewicz, R. J. [541]
Boyle, W. S. [209]
Brainard, D., see Longere, P. [218]
Brandt, G. B., see Taylor, L. H. [587]
Brangaccio, D. J., see Bruning, J. H. [40]
Breuckmann, B. [427]
Brigham, E. O. [790]
Brock, N., see Trolinger, J. D. [342]
Brohinsky, W. R., see Stetson, K. A. [50]
Brooks, R. E. [19]
—, see Heflinger, L. O. [20]
Brophy, C. P. [389]
Brown, G. C. [603]
Brown, G. M. [325, 592]
—, see Chen, F. [591]
—, see Neumann, D. B. [632]
Brown, N., see Hariharan, P. [430]
Brugioni, S., see Allaria, E. [92]
Bruning, J. H. [40]
Bryanston-Cross, P. J. [462, 512]
—, see Holden, C. M. E. [338]
—, see Judge, T. R. [514]
—, see Lanen, T. A. W. M. [340]
Bryanston-Cross, P. J., see Towers, D. P. [525]
Bryant, R., see Schulze, M. A. [750]
Buckberry, C. H., see Tatam, R. P. [646]
Buckland, J. R., see Huntley, J. M. [499]
Budzinski, J. [404]
Buraga-Lefebvre, C., see Coetmellec, S. [88]
Burow, R., see Schwider, J. [443]
Burton, D. R. [449, 463, 503]
—, see Malcolm, A. A. [453]
—, see Skydan, O. A. [390]
—, see Stephenson, P. [523]
Burton, J. C., see Reichenbach, S. E. [742]
Butters, J. N. [46]
Butusov, M. M., see Ostrovsky, Yu. I. [180]
Caceres, S., see Aparicio, J. A. [409]
Cai, L., see Yu, L. [90, 91, 272]
Caponero, M. A. [599]
Carelli, P. [651]
Carlsson, T. E. [117, 669, 706]
—, see Nilsson, B. [115, 116, 118]
Carre, P. [39]
Casey, R. T., see Watanabe, M. [348]
Castro, M.-A., see Frauel, Y. [756]
Cavaccini, G. [326]
Censor, Y. [798]
Centurion, M., see Liu, Z. [144]
Cernadas, D., see Doval, A. F. [223]
—, see Trillo, C. [774]
Cha, S. S. [722, 740]
Champagne, E. B. [165]
Champeney, D. C. [783]
Chang, M. [440]
Chang, T. Y., see Sciammarella, C. A. [579]
Chaturvedi, P., see Srinivasan, V. [416]
Chawla, S. K. [701]
—, see Sciammarella, C. A. [700]
—, see Woisetschläger, J [749]
Chen, F. [591]
—, see Gu, J. [465]
Chen, J., see Ishii, Y. [186]
Chen, Y.-M., see Sirkis, J. S. [375]
Cheng, A. Y., see Sirkis, J. S. [375]
Cheng, X., see Liu, Ch. [81]
Cheng, Y. Y. [442]
Choudry, A. [362–364]
Christensen, C. R., see Jain, A. K. [395]
Cielo, P. [572]
Ciliberto, A., see Cavaccini, G. [326]
Clark, Th., see Shegelski, M. R. A. [74]
Clerc, F. Le [84]
Cline, H. E. [642, 643]

- Coetmellec, S. [88, 89]
—, see Lebrun, D. [273]
—, see Malek, M. [247]
Colin, A. [418]
Colineau, J., see Binet, R. [83]
Collier, R. J. [18]
Collins, A. L. [799]
Collins, D. J., see Matulka, R. D. [344]
Collins, M. W., see Collins, A. L. [799]
Collot, L., see Clerc, F. Le [84]
—, see Le Clerc, F. [85–87]
Colomb, T. [122, 123]
Coppola, G. [581]
—, see Ferraro, P. [275]
Cornejo-Rodríguez, A., see Ohyama, N. [460]
Coupland, J. M., see Barnhart, D. H. [192]
Crawforth, L. [184]
Creath, K. [49, 202, 385–387]
Crimmins, T. R. [398, 399]
Crostack, H.-A. [357]
—, see Pohl, K.-J. [358]
Cuche, D. [126]
Cuche, D. E. [124]
—, see Müller, E. [540]
Cuche, D., see Schumann, W. [583]
Cuche, E. [127, 128, 228, 274]
—, see Beghuin, D. [125]
—, see Colomb, T. [122, 123]
—, see Liebling, M. [241, 243]
Cusack, R. [518]
—, see Huntley, J. M. [533]
- Dahlgren, P.*, see Beghuin, D. [125]
—, see Colomb, T. [122, 123]
—, see Cuche, E. [128]
Dale, M., see Chen, F. [591]
D'Altorio, A., see Amadesi, S. [324]
D'Altorio, A., see Carelli, P. [651]
D'Altorio, A., see Paoletti, D. [174]
Dändliker, R. [303–305, 421, 428, 576, 690]
—, see Ineichen, B. [758]
—, see Thalmann, R. [424, 431]
D'Antonio, L., see Cavaccini, G. [326]
Davies, J. C., see Tatam, R. P. [646]
de Castro, C., see Aparicio, J. A. [409]
de Frutos, A. M., see Aparicio, J. A. [409]
de Groot, P. J. [446, 447]
Deason, V. A. [438]
DeBarber, P., see Trolinger, J. D. [342]
- Decker, A. J. [182]
Dekker, H., see Choudry, A. [364]
Delacretaz, G., see Beghuin, D. [125]
DelaHunt, P., see Longere, P. [218]
Delboulbe, A., see Herriau, J. P. [189]
DeMatta, P. [652]
Demetrakopoulos, T. H. [54]
Demoli, N. [230, 745]
—, see Lovric, D. [456]
Denisyuk, Y. N. [10]
Depeursinge, C., see Beghuin, D. [125]
—, see Cuche, E. [127, 228]
Depeursinge, Chr., see Colomb, T. [122, 123]
—, see Cuche, E. [128, 274]
—, see Liebling, M. [241, 243]
DeVelis, J. B., see Reynolds, G. O. [194, 474]
Dewandel, J. L., see Dubois, F. [68]
Dhir, S. K. [577]
Dirr, B., see Vogt, E. [708]
Doherty, E. T., see Collier, R. J. [18]
Dong, H., see Sun, H. [270]
Dorrio, B. V., see Doval, A. F. [223]
—, see Trillo, C. [774]
Doval, A. F. [223]
—, see Trillo, C. [774]
Drzik, M., see Balas, J. [605]
Dubas, M., see Schumann, W. [169]
Dubois, F. [67–70]
Ducottet, C., see Fournier, C. [264]
Dudderar, T. D., see Gilbert, J. A. [199, 200]
—, see Matthys, D. R. [379, 475]
Dupont, O., see Dubois, F. [68]
Dupuy, F., see Bohineust, X. [600]
Durnin, J. [157]
- Ebbeni, J. [538]
Eden, M., see Yaroslavsky, L. [788]
Eggers, H., see Lu, B. [352]
Eglin, P., see Ineichen, B. [758]
Ehrlich, M. J. [345]
—, see Steckenrider, J. S. [351]
Eichhorn, N. [382]
Ek, L. [485, 487]
El-Sum, H. M. A. [5]
Elssner, K.-E., see Schwider, J. [443]
Enard, D., see Choudry, A. [364]
Engelsberger, J., see Steinbichler, H. [322]
Ennos, A. E. [37, 411]
Ettemeyer, A., see Krupka, R. [775]

- , see Schörner, J. [517]
Evans, W. T., see Ratnam, M. M. [595]
- Fagan, W. F.*, see Trolinger, J. D. [549]
Falldorf, C. [782]
—, see Baumbach, Th. [212]
Faltus, S., see Shegelski, M. R. A. [74]
Fantin, A. Vieira, see Albertazzi Jr., A. [71, 240]
Farrant, D. I. [294]
Farrell, P. V. [422]
Fernandez, J. L., see Blanco-Garcia, J. [311]
—, see Doval, A. F. [223]
—, see Trillo, C. [774]
Ferraro, P. [275]
—, see Allaria, E. [92]
—, see Cavaccini, G. [326]
—, see Coppola, G. [581]
—, see Grilli, S. [93]
—, see Nicola, S. De [94, 95, 224]
Fessler, H., see Pedrini, G. [65, 235, 641]
Filetti, V. R., see Caponero, M. A. [599]
Finizio, A., see Coppola, G. [581]
—, see Ferraro, P. [275]
—, see Grilli, S. [93]
—, see Nicola, S. De [94, 95, 224]
Fischer, B. [41]
—, see Kreis, Th. [42]
Forbes, D., see Womack, K. H. [417]
Fossati Bellani, V. [486]
Fossati-Bellani, V., see DeMattia, P. [652]
Foster, W. A., see Weathers, J. M. [596]
Fournel, Th., see Fournier, C. [264]
Fourney, W. L., see Holloway, D. C. [694]
Fournier, C. [264]
Fraile, D. [360]
Frankena, H. J., see van Wingerden, J. [444]
Frauel, Y. [133, 755, 756]
—, see Matoba, O. [97]
Frechosso, F. A., see Aparicio, J. A. [409]
Freischlad, K. [388]
Freund, C. H., see Hariharan, P. [618]
Friesem, A. A. [645]
—, see Katzir, Y. [401]
Fröning, P. [776]
—, see Pedrini, G. [235, 641, 644]
Fröning, Ph., see Pedrini, G. [65]
Funnell, W. R. J. [391]
Furlong, C. [239]
Fusek, R. L., see Hecht, N. L. [290]
Füzessy, Z. [539, 543–545, 673, 674, 676, 677, 679]
—, see Gombkötö, B. [493]
—, see Gyimesi, F. [675, 678]
Gabor, D. [1–3, 794]
Gallagher, J. G., see Bruning, J. H. [40]
Gallagher, N. C., see Allebach, J. P. [219]
Gammella, S., see Caponero, M. A. [599]
Ganesan, A. R. [781]
Garden, K. L., see Bates, R. H. T. [796]
Garner, H. R., see Huebschman, M. L. [259]
Gascon, F., see Fraile, D. [360]
Gaskill, J. D., see Lam, P. [691]
Gasvik, K. J. [164]
Gatti, L., see Kebbel, V. [552]
—, see Solitro, F. [198]
Geldmacher, J. [707]
—, see Jüptner, W. [546, 604, 693]
—, see Kreis, Th. [266, 425, 426, 491]
—, see Vogt, E. [708]
Georges, M. [188]
Georges, M. P., see Ninane, N. [692]
Gerhardt, G., see Plotkowski, P. D. [380]
Ghiglia, D. C., see Mastin, G. A. [415]
Ghiglia, D. G. [513, 527]
Gibbs, D. F., see Berry, M. V. [733]
Gierloff, J. J. [520]
Gilbert, J. A. [195, 199, 200]
—, see Matthys, D. R. [379, 475]
—, see Sciammarella, C. A. [580, 697, 698]
Gillies, A. C. [365]
Ginesu, F. [366]
—, see Bertolino, F. [410]
Gladic, J., see Lovric, D. [456]
Glanville, R., see Tozer, B. A. [747]
Glaser, I., see Katzir, Y. [401]
Goldrein, H. T., see Cusack, R. [518]
Gombkötö, B. [493]
Goodman, J. W. [51, 158, 160, 163, 254, 631]
Gordon, A. L., see Tozer, B. A. [747]
Gorecki, C. [464]
Green, R. J. [529, 530]
Greenleaf, J. F., see Kenue, S. K. [739]
Greivenkamp, J. E. [433]
Gren, P. [359, 764, 765]
—, see Mattsson, R. [763]
Grigull, U., see Hauf, W. [723]
Grilli, S. [93]

- , see Allaria, E. [92]
 —, see Coppola, G. [581]
 —, see Ferraro, P. [275]
 —, see Nicola, S. De [224]
Grinzato, E., see Spagnolo, G. Schirripa [767]
Gross, M., see Clerc, F. Le [84]
 —, see Le Clerc, F. [85–87]
Gross, T. S., see Watt, D. W. [361]
Grosser, V., see Vogel, D. [575]
Gruenewald, K., see Jüptner, W. [610]
Gryzagoridis, J. [327]
Grzanna, J., see Schwider, J. [443]
Gu, J. [465]
Guattari, G., see Spagnolo, G. Schirripa [766, 767]
Guerrero, J. A., see Lopez, C. Perez [715]
Gunnarsson, G. T., see Trolinger, J. D. [549]
Guo, C.-S. [80]
Gupta, P. C. [615–617]
Gusev, M. E., see Pedrini, G. [644, 769]
 —, see Schedin, S. [718, 770]
Gustafsson, J., see Carlsson, T. E. [669, 706]
Gyimesi, F. [675, 678]
 —, see Füzessy, Z. [544, 673, 674, 676, 679]
- Haines, K. A.* [21–23]
 —, see Hildebrand, B. P. [25, 26]
Haji-Sheikh, A., see Wang, X. [191]
Hallowell, N. A. [757]
 —, see Barnhart, D. H. [192]
Hampp, N., see Barnhart, D. H. [192]
Hanson, S. G., see Falldorf, C. [782]
Hariharan, P. [154, 172, 173, 185, 429, 430, 618, 623, 637]
Harrison, I. R., see Stetson, K. A. [612]
Hartmann, H. J., see Kebbel, V. [743, 744]
Hartmann, H.-J., see Pomarico, J. [668]
Hauf, W. [723]
Haupt, U. [713]
Heanue, J. F. [14]
Hecht, N. L. [290]
Heflinger, L. O. [20, 24]
 —, see Brooks, R. E. [19]
Hendren, Ch. M., see Gilbert, J. A. [195]
Hening, S. D., see Watt, D. W. [361]
Herault, J., see Alleysson, D. [216]
Herriau, J. P. [189]
Herriott, D. R., see Bruning, J. H. [40]
Hertzberg, J., see Pfleger, S. [201]
- Hesselink, L.*, see Heanue, J. F. [14]
 —, see Snyder, R. [736]
Hickson, J. D., see Schulze, M. A. [750]
Higgins, Th. V. [208]
Hildebrand, B. P. [25, 26]
 —, see Haines, K. A. [21–23]
 —, see Suzuki, K. [285]
Hilton, P. D., see Reynolds, G. O. [474]
Hinrichs, H. [663]
Hinsch, K. D. [337]
 —, see Hinrichs, H. [663]
Hirayama, T., see Takeda, M. [102]
Höfling, R. [292]
 —, see Aswendt, P. [772]
 —, see Kreis, Th. [227]
 —, see Osten, W. [38, 500]
 —, see Vogel, D. [575]
Holden, C. M. E. [338]
Holik, A. S., see Cline, H. E. [642, 643]
Holloway, D. C. [694]
Holst, G. C. [210]
Honda, T., see Nakadate, S. [405]
 —, see Ohyama, N. [460]
 —, see Ru, Q.-S. [454, 455]
Hong, H. [748]
Hong, J., see Liu, Z. [144]
Horman, M. H. [29]
Hovanesian, J. D., see Plotkowski, P. D. [380]
Hrdliczka, V., see Müller, E. [540]
Hsu, D., see Long, P. [478]
Hsu, J. C., see Trolinger, J. D. [746]
Hsu, J., see Trolinger, J. D. [342]
Hu, Ch.-P., see Chang, M. [440]
Huang, T. S. [52]
Huebschman, M. L. [259]
Huignard, J. P., see Herriau, J. P. [189]
Hung, M. Y. Y. [225, 584]
 —, see Plotkowski, P. D. [380]
Hung, Y. Y. [136, 328, 780]
Hunt, M. A., see Schulze, M. A. [750]
Hunter, J., see Collins, A. L. [799]
Huntley, J. M. [367, 499, 519, 533, 534, 607, 760]
 —, see Cusack, R. [518]
Hüttmann, G. [183]
- Idesawa, M.*, see Yatagai, T. [406]
Idogawa, T., see Takai, N. [99]
III, P. W. King [578]
Iizuka, K. [161]

- Ina, H.*, see Takeda, M. [43]
Indebetouw, G. [137, 138]
 —, see Poon, T.-C. [139]
Ineichen, B. [621, 758]
 —, see Dändliker, R. [421]
Inomoto, O., see Yamaguchi, I. [109]
Iodice, M., see Coppola, G. [581]
Ishii, Y. [186]
Itoh, K. [505]
Itoh, Y., see Tsuruta, T. [317, 705]
Iwata, K. [738]
- Jacobsen, C. F.*, see Neumann, D. B. [632]
Jacquot, M. [120, 121]
Jacquot, P., see Boone, P. M. [721]
Jäger, H., see Vukicevic, D. [724]
Jain, A. K. [395]
Janta, J. [291, 614]
Javidi, B. [281]
 —, see Frauel, Y. [133, 755, 756]
 —, see Kishk, S. [283]
 —, see Matoba, O. [97, 98]
 —, see Naughton, Th. J. [280]
 —, see Tajahuerce, E. [134, 135, 260]
Jericho, M. H., see Kreuzer, H. J. [75]
 —, see Xu, W. [77–79]
Jericho, M. J., see Kreuzer, H. J. [76]
Joannes, L., see Dubois, F. [67, 68]
Johansen, E. L., see Larson, R. W. [284]
Johnson, C. D., see Sajenko, P. [619]
Johnson, G. W. [414]
Jones, B. E. [197]
Jones, J. D. C., see Tatam, R. P. [646]
Jones, R. [310]
Jozwicki, R., see Pasko, S. [111, 233]
Jr., C. E. Thomas, see Schulze, M. A. [750]
Judge, T. R. [514]
 —, see Bryanston-Cross, P. J. [462]
 —, see Towers, D. P. [525]
Judge, T., see Towers, D. P. [524]
Junginger, H. G. [734]
Jüptner, W. [296, 436, 546, 550, 604, 610, 693]
 —, see Adams, M. [265]
 —, see Baumbach, Th. [212]
 —, see Bischof, Th. [602]
 —, see Falldorf, C. [782]
 —, see Fischer, B. [41]
 —, see Kebbel, V. [552, 743, 744]
 —, see Kolenovic, E. [717]
- , see Kreis, Th. [42, 231, 252, 253, 255, 261, 266, 293, 426, 451, 452, 491, 531, 547]
 —, see Kreitlow, H. [554, 761]
 —, see Meyer, L. W. [608]
 —, see Mieth, U. [751]
 —, see Osten, W. [686, 687]
 —, see Pomarico, J. [668]
 —, see Rottenkolber, H. [155]
 —, see Schnars, U. [57–60]
 —, see Seebacher, S. [664]
 —, see Wagner, C. [229]
- Kak, A. C.* [785]
 —, see Rosenfeld, A. [789]
Kalal, M. [729]
Kasprzak, H. [329]
Kato, J.-I., see Yamaguchi, I. [106–110, 665]
Katzir, Y. [401]
Kaufmann, G. H. [683]
 —, see Rastogi, P. K. [684]
Kawai, H., see Takaki, Y. [101]
Kebbel, V. [552, 743, 744]
Kemper, B., see Lai, S. [269]
Kenue, S. K. [739]
Kickstein, J., see Hinrichs, H. [663]
Kim, E.-S., see Kim, S.-G. [238]
Kim, M. K. [140, 141]
Kim, S.-G. [238]
Kim, T., see Poon, T.-C. [139]
King, B., see Lai, S. [268]
Kinnstaetter, K. [445]
Kinoshita, S., see Ohyama, N. [460]
Kirkpatrick, P., see El-Sum, H. M. A. [5]
Kischel, P., see Dubois, F. [70]
Kishk, S. [283]
Kiss, M., see Gombkötö, B. [493]
Kitoh, M., see Takeda, M. [207]
Klattenhoff, R., see Kolenovic, E. [717]
Klaus, D. M., see Benoit, M.R. [149]
 —, see Owen, R. B. [147]
Klumpp, P. A., see Schnack, E. [321]
Klysubun, P., see Indebetouw, G. [137, 138]
Kobayashi, A. S. [594]
Kobayashi, S., see Takeda, M. [43]
Kocatepe, M., see Onural, L. [250]
Koenig, K. W., see Matthys, D. R. [379]
Kohgo, H., see Takeda, M. [102]
Kokal, J. V., see Ransom, P. L. [480]
Kolenovic, E. [717]

- Koliopoulos, C. L., see Freischlad, K. [388]
Kornis, J. [754]
—, see Füzesi, Z. [676]
—, see Gombkötö, B. [493]
Kothiyal, M. P., see Ganesan, A. R. [781]
Kovacs, P., see Gombkötö, B. [493]
Kraska, Z., see Pawluczyk, R. [288]
Kreis, Th. [42, 44, 66, 227, 231, 237, 244, 252,
253, 255–257, 261, 262, 266, 293, 368, 378,
394, 425, 426, 441, 450–452, 457, 490–492,
531, 547]
—, see Adams, M. [265]
—, see Jüptner, W. [436, 546, 604, 693]
—, see Kreitlow, H. [554, 759, 761]
—, see Schnars, U. [59, 60]
Kreitlow, H. [554, 759, 761]
—, see Geldmacher, J. [707]
—, see Jüptner, W. [436, 550, 610]
—, see Kreis, Th. [394]
—, see Vogt, E. [708]
Kreuzer, H. J. [72, 73, 75, 76]
—, see Shegelski, M. R. A. [74]
—, see Xu, W. [77–79]
Krishnaswamy, S. [412]
Kronrod, M. A. [53]
Krupka, R. [775]
Kubota, T. [661]
Kujawinska, M. [204, 205, 369]
Kurz, T., see Lauterborn, W. [159]
Kwon, O. Y. [432, 521]
- Labeyrie, A. E., see Stroke, G. W. [179]
Ladenburg, R. [726]
Lai, G. [143, 566]
Lai, S. [142, 268, 269]
—, see Kolenovic, E. [717]
Lalor, M. J., see Burton, D. R. [449, 463, 503]
—, see Skydan, O. A. [390]
—, see Stephenson, P. [523]
Lam, P. [691]
—, see Chang, M. [440]
Landry, M. J. [483]
Lanen, T. A. W. M. [339–341]
Larkin, K. G. [448]
Larson, R. W. [284]
Lassahn, G. D., see Deason, V. A. [438]
Latta, J. N. [175–177]
Lauterborn, W. [159]
Lauterborn, W. H., see Hüttmann, G. [183]
- Lawrence, R. W., see Goodman, J. W. [51]
Le Clerc, F. [85–87]
Lebrun, D. [248, 273]
—, see Belaid, S. [246]
—, see Coetmellec, S. [88, 89]
—, see Malek, M. [247]
Lee, B., see Kim, S.-G. [238]
Lee, C.-K., see Crawforth, L. [184]
Lee, W. H. [12, 13]
Leendertz, J. A. [45]
—, see Butters, J. N. [46]
Legros, J.-C., see Dubois, F. [69, 70]
Lehureau, J.-C., see Binet, R. [83]
Leidenbach, S. [778]
—, see Steinbichler, H. [322]
Leiner, D. C., see Johnson, G. W. [414]
Leis, H. G. [330]
Leith, E. N. [7–9, 171]
Lemaire, P., see Georges, M. [188]
Levitt, J. A. [634]
Levy, U., see Friesem, A. A. [645]
Lewis, D., see Hecht, N. L. [290]
Lewitt, R. M. [797]
Li, W., see Milgram, J. H. [145]
Li, Y., see Liu, Ch. [81]
Liang, C. Y., see Hung, Y. Y. [136]
Liao, J., see Guo, C.-S. [80]
Liebling, M. [129, 241–243, 245]
Lilley, F., see Skydan, O. A. [390]
Lim, J. S. [396, 536]
Lin, L., see Hung, M. Y. Y. [584]
Linet, V., see Bohineust, X. [600]
Linzer, M., see Norton, S. J. [737]
Lira, I. H. [731]
Little, M. J., see Tozer, B. A. [747]
Liu, B., see Allebach, J. P. [219]
Liu, Ch. [81]
Liu, G. [234]
Liu, Z. [144]
Liu, Zh., see Liu, Ch. [81]
Lobera, J. [267]
Lohmann, A. W. [6, 11]
—, see Kinnstaetter, K. [445]
Long, P. [478]
Longere, P. [218]
Lopez, C. Perez [714, 715]
Lopez, C., see Doval, A. F. [223]
—, see Trillo, C. [774]
Lopez, O., see Doval, A. F. [223]

- , see Trillo, C. [774]
Lorenzen, W. E., see Cline, H. E. [642, 643]
Loughry, C. W., see Hong, H. [748]
 —, see Woisetschläger, J [749]
Lovric, D. [456]
 Ltd., Lasermet [712]
Lu, B. [352]
Lucia, A. C., see Zanetta, P. [335]
Luth, W. [384]
Lutz, B. [569]
- Maas, A. A. M.*, see Vrooman, H. A. [510]
Machado Gama, M. A. [316]
Machida, H., see Yonemura, M. [716]
Macovski, A. [47]
Macy Jr., W. W. [479]
Maddux, G. E. [370]
Mader, D. L. [355]
Madsen, V. P., see Tichenor, D. A. [752]
Magnusson, R., see Wang, X. [191]
Magome, N., see Nakadate, S. [405]
Magro, C., see Coppola, G. [581]
 —, see Ferraro, P. [275]
Malcolm, A. A. [453]
Malek, M. [247]
 —, see Lebrun, D. [273]
Marchi, M. M., see Chen, F. [591]
Marom, E., see Dändliker, R. [303]
Marquardt, E. [771]
Marquet, P., see Colomb, T. [123]
 —, see Cuche, E. [127, 128, 274]
 —, see Liebling, M. [241, 243]
Massing, J. H., see Stadelmeier, A. [236]
Mastin, G. A. [415]
 —, see Ghiglia, D. G. [527]
Mastner, J., see Ineichen, B. [621]
Matoba, O. [97, 98]
 —, see Tajahuerce, E. [135, 260]
Matsuda, K., see Tsuruta, T. [27]
Matsumura, T., see Yamaguchi, I. [110]
Matsuzaki, H., see Yamaguchi, I. [665]
Matthews, L. K., see Rightley, G. S. [295]
Matthys, D. R. [379, 475]
 —, see Gilbert, J. A. [195]
Mattsson, R. [763]
Matulka, R. D. [344]
Mayville, R. A., see Reynolds, G. O. [474]
McDonald, J. B., see Naughton, Th. J. [280]
McKelvie, J., see Perry Jr., K. E. [458]
- Medhat, M. [548]
Meesters, W., see Pflüger, S. [201]
Meier, G. E. A., see Becker, F. [402]
Meier, R. W. [166]
Meinertzhangen, I. A., see Kreuzer, H. J. [76]
 —, see Xu, W. [77–79]
Mendenhall, F. T., see Sikora, J. P. [704]
Meng, H., see Pan, G. [150, 263]
Mercer, C. R. [206]
Merkel, K., see Schwider, J. [443]
Merrill, D. [215]
Merzkirch, W. [353]
Merzlyakov, N. S., see Kronrod, M. A. [53]
 —, see Yaroslavskii, L. P. [55]
Mestrovic, J., see Demoli, N. [230]
Meucci, R., see Allaria, E. [92]
 —, see Grilli, S. [93]
Meyer, E. H., see Crostack, H.-A. [357]
Meyer, L. W. [608]
Miao, J., see Xu, L. [113, 114, 258, 276]
Michel, B., see Will, P. [611]
Michetti, L., see Solitro, F. [198]
Mieth, U. [420, 751]
Mifune, Y., see Takai, N. [282]
Miida, S., see Ueda, M. [629]
Milas, M., see Lovric, D. [456]
Miler, M., see Janta, J. [291, 614]
Miles, J. F. [167, 178]
Milgram, J. H. [145]
Miller, K. W., see Reichenbach, S. E. [742]
Millerd, J., see Trolinger, J. D. [342]
Minardi, J. E., see Hecht, N. L. [290]
Minetti, C., see Dubois, F. [70]
Mitrovic, S., see Lovric, D. [456]
Mitra, R., see Demetrikopoulos, T. H. [54]
Mizuno, J., see Yamaguchi, I. [106, 108]
Mnatsakanyan, E. A. [407]
Modarress, D., see Tan, H. [800]
Moisson, E., see Picart, P. [496, 497]
Molin, N. E. [32–34]
Molin, N.-E., see Saldner, H. O. [779]
Molpeceres, J. L., see Aparicio, J. A. [409]
Monneret, J., see Spajer, M [699]
Monnom, O., see Dubois, F. [69, 70]
Moore, A. J. [609]
Moore, D. T., see Johnson, G. W. [414]
Mottier, F. M. [555]
 —, see Dändliker, R. [303, 421]
Mounier, D., see Picart, P. [496, 497]

- Mulholland, G. P.*, see Rightley, G. S. [295]
Müller, E. [540]
Munce, A. C., see Crawforth, L. [184]
Munjuluri, B., see Huebschman, M. L. [259]
Munoz, J. [501, 502]
Murata, K., see Ishii, Y. [186]
Murata, S. [96]
Murray, J. D., see Xu, Y. [112]
- Nagata, R.*, see Iwata, K. [738]
Nagatome, K., see Takeda, M. [532]
Nakadate, S. [405, 620, 638]
—, see Yatagai, T. [406]
Nakajima, T., see Nakadate, S. [620]
Narayanan, R., see Sciammarella, C. A. [585]
Naughton, T. J., see Matoba, O. [97]
Naughton, Th. J. [280]
Nawab, H., see Lim, J. S. [396]
Nebbeling, C., see Lanen, T. A. W. M. [341]
Nefyodov, S. V., see Mnatsakanyan, E. A. [407]
Neger, T., see Vukicevic, D. [724]
Neifeld, M. A., see Lai, S. [142, 268]
Neumann, D. B. [168, 551, 557, 632, 671, 672]
Neupert, U., see Schörner, J. [517]
Newman, J. W. [331]
Nicola, S. De [94, 95, 224]
—, see Allaria, E. [92]
—, see Coppola, G. [581]
—, see Ferraro, P. [275]
—, see Grilli, S. [93]
Nilsson, B. [115, 116, 118]
—, see Carlsson, T. E. [669, 706]
Ninane, N. [692]
Nishida, H., see Toyooka, S. [473]
Nishisaka, T., see Yonemura, M. [716]
Noll, R., see Pflüger, S. [201]
Nomura, T., see Javidi, B. [281]
Norton, S. J. [737]
Nose, A., see Gilbert, J. A. [200]
Nösekabel, E.-H., see Steinbichler, H. [322]
Novak, J. [437]
Nübel, R. [413]
Nugent, K. A. [466]
—, see Kalal, M. [729]
Nussbaumer, H. J. [792]
- Obermeier, P.*, see Schörner, J. [517]
Oh, K. [597]
Ohta, S., see Yamaguchi, I. [106–108]
- Ohyama, N.* [460]
—, see Ru, Q.-S. [454, 455]
Ohzu, H., see Takaki, Y. [100, 101, 271]
Olsson, R., see Gren, P. [359]
Onural, L. [130–132, 250, 251]
Oreb, B. F., see Hariharan, P. [430, 618, 637]
—, see Larkin, K. G. [448]
Ortona, A., see Cavaccini, G. [326]
Osten, W. [38, 383, 392, 500, 667, 686, 687]
—, see Baumbach, Th. [212]
—, see Bieber, E. [400]
—, see Colin, A. [418]
—, see Eichhorn, N. [382]
—, see Falldorf, C. [782]
—, see Höfling, R. [292]
—, see Kolenovic, E. [717]
—, see Mieth, U. [420, 751]
—, see Pedrini, G. [535]
—, see Seebacher, S. [664]
—, see Vogel, D. [575]
—, see Wagner, C. [229, 666]
—, see Winter, H. [408]
Ostrovskaya, G. V., see Ostrovsky, Yu. I. [180]
Ostrovsky, Yu. I. [180]
Ovryn, B. [332]
Owen, R. B. [146–148]
—, see Benoit, M.R. [149]
Özgen, M. T., see Onural, L. [131]
Özkul, C., see Belaid, S. [246]
—, see Coetmellec, S. [88, 89]
—, see Lebrun, D. [248]
- Paez, G.*, see Munoz, J. [501, 502]
Page, R., see Pitlak, R. T. [181]
Pan, G. [150, 263]
Panotopoulos, G., see Liu, Z. [144]
Paoletti, D. [174, 467]
—, see Amadesi, S. [324]
—, see Carelli, P. [651]
—, see Spagnolo, G. Schirripa [516, 767]
—, see Zanetta, P. [459]
Papoulis, A. [784]
Pardoen, G. C., see Trolinger, J. D. [549]
Paris, D. P., see Lohmann, A. W. [11]
Parker, R. J. [187, 346, 347]
Parker, S. C. J., see Holden, C. M. E. [338]
Parrent, G. B., see Reynolds, G. O. [194]
Parulski, K., see Adams, J. [214]
Pasko, S. [111, 233]

- Patacca, A. M.*, see Holloway, D. C. [694]
Paterson, D. M., see Sun, H. [270]
Paulet, P. [333]
Pauliat, G., see Georges, M. [188]
Pawlitzek, R. A., see Kreuzer, H. J. [72, 73]
Pawluczyk, R. [288]
Pedrini, G. [63–65, 222, 235, 277–279, 498, 535, 640, 641, 644, 720, 769]
—, see Fröning, P. [776]
—, see Lopez, C. Perez [714]
—, see Santoyo, F. Mendoza [777]
—, see Schedin, S. [306, 718, 719, 768, 770]
—, see Schedin, St. [62]
—, see Zou, Y. [61]
Peirce, D. C., see Reynolds, G. O. [474]
Peng, X., see Xu, L. [113, 114, 276]
Penn, R. C., see Neumann, D. B. [557]
Pennington, K. S., see Collier, R. J. [18]
Peralta-Fabi, R. [488]
Perez-Amor, M., see Blanco-Garcia, J. [311]
Perez-Amor, M., see Doval, A. F. [223]
—, see Trillo, C. [774]
Perkins, R., see Sun, H. [270]
Perry Jr., K. E. [458]
Peters, T. M., see Bates, R. H. T. [796]
Petkovsek, J. [381]
Petzing, J. N., see Farrant, D. I. [294]
Pflug, L., see Rastogi, P. K. [650]
Pflüger, S. [201]
Philipp, H., see Vukicevic, D. [724]
Picart, P. [496, 497]
Pickering, C. J., see Halliwell, N. A. [757]
Pierattini, G., see Coppola, G. [581]
—, see Ferraro, P. [275]
—, see Grilli, S. [93]
—, see Nicola, S. De [94, 95, 224]
Pitlak, R. T. [181]
Player, M. A., see Sun, H. [270]
Plotkowski, P. D. [380]
Podbielska, H., see Kasprzak, H. [329]
Pohl, K.-J. [358]
—, see Crostack, H.-A. [357]
Poirson, A., see Watson, A. B. [793]
Polhemus, C. [689]
Politch, J. [636]
Pomarico, J. [668]
Pomerleau, N., see Kreuzer, H. J. [75]
Poon, T.-C. [139]
Posposil, J., see Sekanina, H. [82]
Powell, R. L. [16]
—, see Stetson, K. A. [17]
Preater, R. [468]
Prikryl, I. [741]
Prongue, D., see Dändliker, R. [690]
Pruett, H. D., see Rose, H. W. [553]
Pryputniewicz, R. J. [371, 376, 423, 541, 573, 574, 588, 589, 601, 624]
—, see Brown, G. C. [603]
—, see Furlong, C. [239]
—, see Oh, K. [597]
Psaltis, D., see Liu, Z. [144]
Puri, I. K., see Xiao, X. [151]
Quan, C., see Bryanston-Cross, P. J. [462, 512]
Quan, Ch., see Judge, T. R. [514]
Quiroga, J. A. [515]
Radon, J. [795]
Ramanath, R. [217]
Ramos-Izquierdo, L., see Reynolds, G. O. [474]
Ramsey, D., see Macovski, A. [47]
Rankel, K., see Petkovsek, J. [381]
Ransom, P. L. [480]
Rastogi, P. [221, 696]
Rastogi, P. K. [309, 320, 650, 670, 680, 681, 684]
—, see Kaufmann, G. H. [683]
—, see Spajer, M [699]
Ratnam, M. M. [595]
Rautenberg, M., see Haupt, U. [713]
Reeves, M., see Parker, R. J. [347]
Reichenbach, S. E. [742]
Reid, G. T. [372]
Reynolds, G. O. [194, 474]
Richter, J., see Marquardt, E. [771]
Rightley, G. S. [295]
Ringer, K., see Jüptner, W. [296]
Ritter, R., see Winter, D. [522]
Rizzi, M. L., see Vo, P. Del [356]
Robinson, D. W. [507, 509, 753]
—, see Ennos, A. E. [411]
—, see Green, R. J. [530]
—, see Kujawinska, M. [204, 205]
—, see Spik, A. [528]
Roddier, C. [469]
Roddier, F., see Roddier, C. [469]
Rogers, G. L. [4]
Romero, L. A., see Ghiglia, D. G. [513, 527]
Roosen, G., see Georges, M. [188]

- Rose, H. W. [553]
—, see Neumann, D. B. [551]
- Rosenfeld, A. [789]
Rosenfeld, D. P., see Bruning, J. H. [40]
- Rottenkolber, H. [155]
—, see Osten, W. [392]
- , see Schörner, J. [517]
- Ru, Q.-S. [454, 455]
- Rubayi, N. [354]
- Russev, I.*, see Shulev, A. [773]
- Ryhon, S.*, see Georges, M. [188]
- Rytz, H. [489]
- Sabatino, C.*, see Cavaccini, G. [326]
- Sadewasser, H.*, see Winter, D. [522]
- Sadjadi, F. A. [397]
- Saedler, J.*, see Osten, W. [38, 392]
- Sainov, V.*, see Shulev, A. [773]
—, see Simova, E. [682]
- Saito, H.*, see Nakadate, S. [620]
—, see Yatagai, T. [406]
- Sajenko, P. [619]
- Salathe, R. P.*, see Beguin, D. [125]
- Salazar, D.*, see Tentori, D. [477]
- Salazar, R.*, see Tribillon, G. [662]
- Saldner, H. O. [779]
- Saldner, H.*, see Huntley, J. M. [533, 534]
- Saleh, B. E. A. [162]
- Sandeman, R. J.*, see Bone, D. J. [461]
- Sander III, W. A.*, see Ramanath, R. [217]
- Sandoz, J.-L.*, see Rastogi, P. [696]
- Sandoz, P.*, see Jacquot, M. [120, 121]
- Santoyo, F. Mendoza [777]
—, see Fröning, P. [776]
- , see Lopez, C. Perez [714, 715]
- , see Schedin, S. [306, 719]
- , see Schedin, St. [62]
- Sato, T.*, see Ueda, M. [629]
- Scauflaire, V.*, see Georges, M. [188]
- Schaefer, L. F.*, see Macovski, A. [47]
- Schedin, S. [306, 718, 719, 768, 770]
—, see Lopez, C. Perez [714]
- , see Pedrini, G. [222, 278, 279]
- , see Santoyo, F. Mendoza [777]
- Schedin, St. [62]
- Schemm, J. B. [419]
- Schilling, B. W.*, see Poon, T.-C. [139]
- Schmitz, E.*, see Hüttmann, G. [183]
- Schnack, E. [321]
- Schnars, U. [56–60]
—, see Kebbel, V. [552]
- , see Kreis, Th. [66]
- , see Pomarico, J. [668]
- Schönebeck, G. [494, 495]
- Schörner, J. [517]
- Schultz, M. E.*, see Gilbert, J. A. [199]
- Schulz, M.*, see Borner, H. [598]
- Schulze, M. A. [750]
- Schumann, W. [169, 570, 583]
—, see Cuche, D. [126]
- , see Lutz, B. [569]
- Schwider, J. [443]
—, see Kinnstaetter, K. [445]
- Schwomma, O. [48]
- Sciammarella, C. A. [334, 374, 579, 580, 582, 585, 606, 695, 697, 698, 700]
—, see Chawla, S. K. [701]
- Sciammarella, F. M.*, see Sciammarella, C. A. [582]
- Scott, P. D.*, see Onural, L. [130]
- Seebacher, S. [664]
—, see Osten, W. [687]
- , see Wagner, C. [229, 666]
- Sekanina, H. [82]
- Sepold, G.*, see Geldmacher, J. [707]
—, see Kreis, Th. [42]
- Servaes, D. A.*, see Reynolds, G. O. [474]
- Shang, H. M.*, see Hung, M. Y. Y. [225, 584]
- Sharma, A.*, see Rastogi, P. [221]
- Sharma, D. K.*, see Ganesan, A. R. [781]
- Sharon, B.*, see Katzir, Y. [401]
- Sheffer, D. B.*, see Hong, H. [748]
—, see Woisetschläger, J [749]
- Shegelski, M. R. A. [74]
- Shinoda, K.*, see Poon, T.-C. [139]
- Shiotake, N.*, see Tsuruta, T. [27, 317]
- Shough, D. M.*, see Kwon, O. Y. [432]
- Shulev, A. [773]
- Sikora, J. P. [704]
—, see Dhir, S. K. [577]
- Simova, E. [682]
- Simova, E. S. [685]
- Singh, H.*, see Sirkis, J. S. [375]
- Singh, K.*, see Gupta, P. C. [615–617]
- Sirkis, J. S. [375]
- Skande, P.*, see Abramson, N. [564]
- Skarman, B. [119]
- Skotheim, Ø. [232]

- Skydan, O. A. [390]
Sladek, J., see Balas, J. [605]
Slaney, M., see Kak, A. C. [785]
 Smigelski, P. [568]
 —, see Stimpfling, A. [567]
Smith, G. E., see Boyle, W. S. [209]
Smith, R. G., see Schulze, M. A. [750]
Smorenburg, C., see van Wingerden, J. [444]
 Snyder, R. [736]
Snyder, W. E., see Ramanath, R. [217]
 Solitro, F. [198]
 Sollid, J. E. [286, 287, 336]
Solomos, G. P., see Zanetta, P. [335]
Somasundaram, K., see Woisetschläger, J [749]
 Sommargren, G. E. [203]
Sona, A., see Fossati Bellani, V. [486]
 Soontaranon, S. [249]
Sovic, I., see Demoli, N. [230]
 Spagnolo, G. Schirripa [516, 766, 767]
 —, see Carelli, P. [651]
 —, see Paoletti, D. [467]
 —, see Zanetta, P. [459]
 Spajer, M [699]
Spaulding, K., see Adams, J. [214]
Spears, K. G., see Abramson, N. [660]
 Spik, A. [528]
Spolaczyk, R., see Schwider, J. [443]
 Spooren, R. [211]
Springer, G. S., see Farrell, P. V. [422]
 Srinivasan, V. [416]
 Stadelmeier, A. [236]
 Stearns, S. D. [791]
 Steckenrider, J. S. [351]
Steffens, H.-D., see Meyer, L. W. [608]
 Steinbichler, H. [322]
 —, see Borner, H. [598]
Steinlein, P., see Geldmacher, J. [707]
 Stephenson, P. [523]
 Stetson, K. A. [17, 31, 35, 50, 308, 312–314, 542,
 586, 590, 612, 613, 622, 639, 709, 762]
 —, see Levitt, J. A. [634]
 —, see Molin, N. E. [32–34]
 —, see Powell, R. L. [16]
 —, see Pryputniewicz, R. J. [574, 588]
 —, see Saldner, H. O. [779]
 —, see Sollid, J. E. [336]
 Stimpfling, A. [567]
Stoev, K. N., see Simova, E. S. [685]
Streibl, N., see Kinnstaetter, K. [445]
Strojnik, M., see Munoz, J. [501, 502]
 Stroke, G. W. [179]
Sturm, V., see Pflüger, S. [201]
 Su, X.-Y. [439]
Subbaraman, B., see Sciammarella, C. A. [334]
 Sun, H. [270]
 —, see Cha, S. S. [740]
Sun, J., see Steinbichler, H. [322]
Süssstrunk, S., see Alleysson, D. [216]
 Suzuki, K. [285]
Suzuki, Y., see Poon, T.-C. [139]
Swain, R., see Preater, R. [468]
 Sweeney, D. W. [30, 728]
Swinson, W. F., see Weathers, J. M. [596]
Swint, J. B., see Sollid, J. E. [286]
 Tajahuerce, E. [134, 135, 260]
 —, see Frauel, Y. [756]
 Takai, N. [99, 282]
 Takaki, Y. [100, 101, 271]
Takayama, K., see Watanabe, M. [348]
 Takeda, M. [43, 102, 207, 470–472, 508, 532]
Takezaki, J., see Toyooka, S. [473]
 Tan, H. [800]
Taniguchi, K., see Takeda, M. [102]
 Tatam, R. P. [646]
 Taylor, L. H. [587]
Teich, M. C., see Saleh, B. E. A. [162]
 Tentori, D. [477]
 Thalmann, R. [424, 431]
 —, see Dändliker, R. [305, 428, 576, 690]
Thieme, W., see Breuckmann, B. [427]
Thizy, C., see Georges, M. [188]
Thompson, B. J., see Reynolds, G. O. [194]
 Tichenor, D. A. [752]
Tiziani, H. J. [156, 190, 710]
 —, see Fröning, P. [776]
 —, see Pedrini, G. [63–65, 222, 235, 277–279,
 498, 535, 640, 641, 644, 720, 769]
 —, see Santoyo, F. Mendoza [777]
 —, see Schedin, S. [306, 718, 719, 768, 770]
 —, see Schedin, St. [62]
Tiziani, H., see Lopez, C. Perez [714]
 —, see Zou, Y. [61]
 Tonin, R. [625, 626]
 Torres, E. [226]
Torzymski, M., see Demoli, N. [745]
Totzauer, W., see Aswendt, P. [772]
 —, see Will, P. [611]

- Towers, C. E., see Towers, D. P. [435]
Towers, D. P. [435, 524, 525]
Toyooka, S. [302, 473, 571]
Tozer, B. A. [747]
Tribillon, G. [662]
—, see Jacquot, M. [120, 121]
Tribolet, J. M. [506]
Trillo, C. [774]
—, see Doval, A. F. [223]
Trolinger, J. D. [289, 342, 343, 476, 549, 746]
Tsujiuchi, J., see Nakadate, S. [405]
—, see Ohyama, N. [460]
—, see Ru, Q.-S. [454, 455]
—, see Tsuruta, T. [27]
Tsuruta, T. [27, 317, 705]
Tung, Z., see Takeda, M. [472]
Turner, J. L., see Weathers, J. M. [596]
Tyrer, J. R., see Moore, A. J. [609]
- Ueda, M. [629]
Underwood, K. L., see Womack, K. H. [417]
Unger, S., see Winter, H. [408]
Unser, M., see Liebling, M. [129, 241–243, 245]
Upatnieks, J., see Leith, E. N. [7–9, 171]
Usry, W., see Schulze, M. A. [750]
- van Haeringen, W.*, see Junginger, H. G. [734]
van Ingen, J. L., see Lanen, T. A. W. M. [341]
van Wingerden, J. [444]
Varade, A., see Fraile, D. [360]
Varner, J. R. [647]
—, see Zelenka, J. S. [28, 648]
Vasarhelyi, G., see Kornis, J. [754]
Verbiest, R., see Boone, P. M. [315]
Verhoeven, D. D. [732, 801]
Verrall, S. C., see Tajahuerce, E. [135]
Vest, C. M. [170, 725, 730, 735]
—, see Birnbaum, G. [323]
—, see Cha, S. S. [722]
—, see Farrell, P. V. [422]
—, see Prikryl, I. [741]
—, see Schemm, J. B. [419]
—, see Sweeney, D. W. [30]
—, see Watt, D. W. [349, 350]
—, see Xu, Y. [112]
Vest, Ch. M., see Lira, I. H. [731]
Vikram, C. S. [628, 635]
Villain, J., see Borner, H. [598]
Vo, P. Del [356]
- Voelkl, E.*, see Schulze, M. A. [750]
Vogel, D. [575]
Vogel, J., see Vogel, D. [575]
Vogt, E. [708]
von Bally, G., see Kasprzak, H. [329]
—, see Lai, S. [269]
—, see Su, X.-Y. [439]
von Kopylow, Chr., see Kolenovic, E. [717]
Voorhis, C. C. Van, see Ladenburg, R. [726]
Vrooman, H. A. [510]
Vucic, Z., see Lovric, D. [456]
Vukicevic, D. [724]
—, see Demoli, N. [745]
- Waddell, P. [711]
Wagner, C. [229, 666]
Wagner, J. W., see Ehrlich, M. J. [345]
—, see Steckenrider, J. S. [351]
Walker, J. G., see Green, R. J. [529, 530]
Walles, S. [307]
Walz, Th., see Krupka, R. [775]
Wang, B., see Long, P. [478]
Wang, H.-T., see Guo, C.-S. [80]
Wang, X. [191]
Watanabe, M. [348]
Watanabe, Y., see Takeda, M. [532]
Waters, J. P. [556]
Watson, A. B. [793]
Watson, J., see Sun, H. [270]
Watt, D. W. [349, 350, 361]
Weathers, J. M. [596]
Weber, D. C., see Trolinger, J. D. [549]
Webster, J. M., see Tozer, B. A. [747]
Wegner, H., see Becker, F. [402]
Welford, W. T. [318, 319]
Welling, H., see Jüptner, W. [296]
Wesolowski, P. J., see Woisetschläger, J [749]
Wesolowski, P., see Füzesy, Z. [545]
White, D. A., see Bruning, J. H. [40]
Widjaja, J., see Soontaranon, S. [249]
Wiesenfeldt, M., see Lauterborn, W. [159]
Will, P. [611]
Willemin, J.-F., see Dändliker, R. [305]
Williams, D. C., see Ennos, A. E. [411]
—, see Robinson, D. W. [509]
Winkler, J., see Ladenburg, R. [726]
Winter, C., see Schörner, J. [517]
Winter, D. [522]
Winter, H. [408]

- Wise, C. M.*, see Landry, M. J. [483]
Wizinowich, P. L. [434]
Woisetschläger, J. [749]
Woisetschläger, J., see Vukicevic, D. [724]
Womack, K. H. [417, 481, 482]
Wozniak, K., see Skarman, B. [119]
Wählin, A., see Mattsson, R. [763]
Wright, D. G., see Tozer, B. A. [747]
Wright, M. A., see Rubayi, N. [354]
Wu, M. H., see Poon, T.-C. [139]
Wuerker, R. F., see Brooks, R. E. [19]
—, see Heflinger, L. O. [20, 24]
Wyant, J. C. [688]
—, see Chang, M. [440]
—, see Cheng, Y. Y. [442]
—, see Lam, P. [691]
Wykes, C., see Jones, R. [310]
- Xiao, X.* [151]
Xu, L. [113, 114, 258, 276]
Xu, W. [77–79]
—, see Kreuzer, H. J. [76]
Xu, Y. [112]
- Yamada, M.*, see Takai, N. [99]
Yamaguchi, I. [103, 106–110, 665]
—, see Zhang, T. [104, 105]
Yang, L., see Hung, M. Y. Y. [225]
Yang, X., see Lu, B. [352]
Yaroslavskii, L. P. [55]
—, see Kronrod, M. A. [53]
- Yaroslavsky, L.* [152, 153, 787, 788]
Yaroslavsky, L. P. [786]
Yasuda, N., see Murata, S. [96]
Yatagai, T. [393, 406]
—, see Lai, G. [143, 566]
Yeakle, J., see Rubayi, N. [354]
Yeo, S.-T., see Srinivasan, V. [416]
Yonemura, M. [653, 716]
Young, M. [220]
Yourassowsky, C., see Dubois, F. [69, 70]
Yu, L. [90, 91, 272]
Yu, Q., see Andresen, K. [511]
Yu, Y. H., see Becker, F. [403]
- Zanetta, P.* [335, 459]
Zarubin, A. M., see Su, X.-Y. [439]
Zelenka, J. S. [28, 648]
—, see Larson, R. W. [284]
Zhang, L., see Guo, C.-S. [80]
Zhang, T. [104, 105]
—, see Yamaguchi, I. [103]
Zhang, X., see Longere, P. [218]
Zhu, J., see Liu, Ch. [81]
Zhu, Y. Y., see Guo, C.-S. [80]
Ziolkowski, E., see Lu, B. [352]
Zirn, R., see Jüptner, W. [610]
Zou, Y. [61]
Zou, Y. L., see Pedrini, G. [63, 64]
Zozulya, A. A., see Owen, R. B. [146–148]
Zürcher, J.-P., see Schumann, W. [583]
Ziern, M., see Zanetta, P. [335]

Subject Index

- 2 π ambiguity 224
1/f noise 72
2+1-technique 246
- Abel transform 376
aberrations 47
abnormal dispersion 386
absolute phase 224
absorption coefficient 385
acoustooptic modulator 304
acoustooptical modulator 65, 236
addition theorem 415
adhesive bonding 321
aerodynamics 370
algebraic reconstruction technique 454
algorithm, FFT 234, 256, 435
algorithm, two-dimensional FFT 430
aliasing 424
ambiguity, 2 π 224
ambiguity, sign 222, 224, 238, 255, 257, 261
amplitude division 17, 37
amplitude hologram 39, 58
amplitude modulation holography 330
amplitude spectrum 256, 413
amplitude spectrum, Fourier 390
amplitude, complex 421
amplitude, real 10
amplitude, vibration 217
analog-to-digital converter 228
analysis, correlation 419
analysis, particle 160
anamorphism 114
angular frequency 10
angular magnification 46
anti-phase 14
antinodes 324
approach, convolution 115
- approximation, Fresnel 24
approximation, paraxial 27
arctan-function 222
arctan-function, principal value of 222
argon-ion laser 57
arrangement, in-line 47, 118
arrangement, off-axis 47
array, Bayer 77
artificial neural network 234, 393
associativity 419
astigmatism 114, 115
asymmetric refractive index field 377
autocorrelation function 420
autocorrelation theorem 420
automata, cellular 292
automatic qualitative evaluation 390
average component 413
- B-spline 133
background variations 258
backprojection, filtered 164
backprojection, reconstruction by filtered 452
bacteriorhodopsin 60
band-limited function 424
bandlimit demodulation 294
bandpass filter 256
bandpass filtering 257
bandwidth, effective 381
Bayer array 77
beam 314
beam, cantilever 314
beam, laser 54
beam, nondiffracting 12
beat frequency 15, 235
bending moment 216, 218
bending waves 217
Bessel function 190, 326, 431, 459
Bessel function of the first kind 459

- Bessel function of the second kind 459
 Bessel wave 12
 bilinear interpolation 235, 308, 309
 birefringent 218
 blooming 69
 bonding, adhesive 321
 boundary element method 322
 boundary of object 231
 Bragg cell 65
 Bragg reflection 52
 BSO 60
 butterfly 435
- camera, consumer still 139
 camera, pyroelectric 60
 camera-tubes, TV 61
 cantilever beam 314
 capacity, well 66
 Carre formula 248
 carrier frequency 263
 cascaded reconstruction 150
 cavity 55
 CCD-target 61
 cell, Bragg 65
 cell, Pockels 56
 cellular automata 292
 central reconstruction formula of digital holography 96
 centrifugal force 360
 chamber, pressure 218
 chamber, vacuum 218
 characteristic function 329
 charge coupled devices 66
 check, consistency 294
 chirp function 145, 441
 chrominance 79
 circular symmetric phase object 376
 CMOS 73
 coefficient, absorption 385
 coefficient, thermal expansion 216
 coefficients, stress-optical 373
 coherence function, spatial 21
 coherence function, spatio-temporal 21
 coherence length 18
 coherence time 18
 coherence, degree of 18
 coherence, mutual degree of 21
 coherence, self 18
 coherence, spatial 19
- coherence, temporal 17
 coherent superposition 13
 color filter detector, lateral 77
 color filter detector, vertical 77
 color matching function 77
 color sensor 76
 commutativity 419
 comparative holographic interferometry 350
 comparative holographic moiré interferometry 352
 comparative holography, digital 354
 complementary metal oxide semiconductor (CMOS) 73
 complex amplitude 421
 complex exponential function 414
 component, average 413
 component, d.c. 413
 computer aided tomography 377, 447
 computerized tomography 164
 concentration, mass 217
 concentration, species 386
 condition number, Hadamard 310
 condition of a system of linear equations 310
 conjugated image 41
 conservation of energy 431
 consistency check 294
 constant function 411
 constant, Gladstone-Dale 370
 consumer still camera 139
 continuation 224, 287
 contour measurement 306
 contouring 339
 contouring by refractive index variation 336
 contouring, digital holographic 340
 contouring, holographic 333
 contouring, projected fringe 338
 contours 335
 contours, three-dimensional 218
 contrast 16
 contrast, speckle pattern 33
 control, feedback 304
 control, integration time 72
 converging lens 27
 converter, analog-to-digital 228
 convolution 230, 418, 431
 convolution approach 115
 convolution kernel 230
 convolution theorem 419
 convolution, two-dimensional 430

- coordinate, spatial 429
coordinates, polar 447
correction, shading 229, 230
correlation analysis 419
cosine transform 439
cosine transform, separable 439
crack 322
crack propagation 217, 323
cross-correlation function 419
cross-reconstructions 201
crystals, photorefractive 60
current, dark 71
cutoff frequency 256, 258
CW laser 304
CW-laser 57
- d.c.-term 102
damped vibration 217
dark current 71
data encryption 180
data truncation 425
data, truncated 424
decorrelation, speckle 227
defect detection 321
defect validation 322
deformation 191
deformation gradient matrix 319
deformation, homogeneous 318
deformations 216
degree of coherence 18
degree of coherence, mutual 21
degree of transmission 39
delta, Dirac 411
demodulation 224, 287
demodulation, bandlimit 294
demodulation, path dependent 288
demodulation, path independent 288, 289
demosaicking 79
density, electron 217
density, energy 60
dependent object motions 325
derivative, second 317
derotator, image 362
desensitized holographic interferometer 365
detection, defect 321
detection, spatial synchronous 265
detector, lateral color filter 77
detector, vertical color filter 77
devices, charge coupled 66
- diagnostics, flow 217
diagnostics, plasma 217, 374
diagram, holo- 200
dichromated gelatin 58
difference holographic interferometry 350
difference, frequency 235
difference, interference phase 188
differences, finite 317
differentiation 416, 431
differentiation, numerical 317
diffraction efficiency 60
diffraction formula, Fresnel-Kirchhoff 22
diffraction grating 65, 243
diffractive optical element 365
diffuse illumination holographic interferometry 195
- digital comparative holography 354
digital holographic contouring 340
digital holographic microscopy 170
digital holography 61, 81
digital holography without wavefront reconstruction 400
digital holography, central reconstruction formula of 96
digital holography, phase-shifting 127
digital image plane holography 400
digital shearography 405
digital speckle pattern interferometry 400
digitization 227
diode laser 57
Dirac delta 411
Dirac delta impulse 48
direct inversion 379
discrete Fourier transform 421
dispersion 217
dispersion, abnormal 386
displacement vector 192
displacement vector field 297
displacement, dynamic 216
displacement, known reference 298
displacement, one-dimensional 216
displacement, rigid body 307
displacement, static 216
displacement, three-dimensional 216
displacement, unknown reference 299
distortion, perspective 298, 308
distortions of holographic interferogram 225
distributed loads 219
distribution, refractive index 194

- distributivity 419
 diverging lens 27
 division, amplitude 17, 37
 division, wavefront 19, 37
 domain, spatial frequency 257
 Doppler shift 15
 double aperture interferometer, Young's 399
 double exposure hologram 266
 double exposure method 186, 235, 242
 doubly refractive prism 92
 DSPI 400
 dye laser 57
 dynamic displacement 216
 dynamic evaluation 301
 dynamic evaluation method 266
 dynamic load 219
 dynamic range 72
 dynamics, fluid 217
 effect, stress-optical 217, 373
 effective bandwidth 381
 effective refractive index 374
 efficiency, diffraction 60
 efficiency, quantum 71
 elasticity, modulus of 314, 373
 elasticity, shear modulus of 315
 electric field strength 9
 electro-optic holography 400, 404
 electron density 217
 electron gas 217
 electronic holography 400, 404
 electronic noise 226
 electronic speckle pattern interferometry 400
 emission, spontaneous 53
 emission, stimulated 53
 emulsions, photographic 58
 encryption, data 180
 endoscopic holographic interferometry 364
 energy 416
 energy density 60
 energy, conservation of 431
 enhancement, image 258
 equality, Parseval 443
 equality, Plancherel 443
 equation, Gladstone-Dale 217, 370
 equation, ideal gas 217, 371
 equation, Lorentz-Lorenz 217, 372
 equation, phase sampling 242
 equation, ray 367
 equations, holographic imaging 45
 equations, system of 298
 equivalent wavelength 358
 ESPI 400
 ESPI methods 61
 etalon 55
 Euler formula 11, 412
 evaluation method, dynamic 266
 evaluation method, static 266
 evaluation, automatic qualitative 390
 evaluation, dynamic 301
 evaluation, Fourier transform 256
 evaluation, phase sampling 242
 evaluation, qualitative 215
 evanescent wave 29
 event, transient 242
 events, transient 217
 exposure, noise equivalent 72
 exposure, saturation equivalent 72
 exposure, time of 38
 Fabry-Perot interferometer 55
 factor, stress intensity 322
 far-field region 50
 fast Fourier transform 434
 feature map, self organizing 234
 feedback control 304
 FFT 434
 FFT algorithm 234, 256, 435
 FFT algorithm, two-dimensional 430
 FFT-subroutine 436
 fibers, monomode 62
 fibers, multimode 62
 fibers, optical 61
 field strength, electric 9
 field, speckle 30
 field, strongly refracting refractive index 382
 fill-factor 74
 filter, bandpass 256
 filter, finite impulse response 230
 filter, linear low-pass 230
 filter, median 230, 274
 filter, nonlinear 230
 filter, nonrecursive 230
 filter, recursive 230
 filter, spatial 61
 filtered backprojection 164
 filtered backprojection, reconstruction by 452
 filtered projection 452

- filtering, bandpass 257
finite differences 317
finite discrete Fourier transform 258
finite element method 321
finite Fourier transform 422
finite fringe interferogram 224
finite fringes 224
finite impulse response filter 230
fixed pattern noise 72
flexural rigidity 317
flow diagnostics 217
flow visualization 217, 370
fluid dynamics 217
focal length 27
force 312
force, centrifugal 360
formula of Euler 412
formula, Carre 248
formula, of Euler 11
Fourier amplitude spectrum 390
Fourier integral theorem 410
Fourier series 421
Fourier slice theorem 379, 450
Fourier spectrum 234
Fourier synthesis 379
Fourier transform 410
Fourier transform evaluation 256
Fourier transform hologram 48
Fourier transform holography 47
Fourier transform holography, lensless 49, 91, 100
Fourier transform pair 410
Fourier transform, discrete 421
Fourier transform, fast 434
Fourier transform, finite 422
Fourier transform, finite discrete 258
Fourier transform, inverse 257, 410
Fourier transform, inverse finite 422
Fourier transform, short time 132
fracture mechanics 322
fracture toughness 322
frame transfer 68
Fraunhofer diffraction region 50
Fraunhofer hologram 50
free space propagation, transfer function of 29
free-space propagation, impulse response of 29
frequency 10
frequency difference 235
frequency domain, spatial 257
frequency modulation 304
frequency plane restoration 380
frequency shift 62, 65
frequency translated holography 329
frequency, angular 10
frequency, beat 15, 235
frequency, carrier 263
frequency, cutoff 256, 258
frequency, fundamental 420
frequency, local 443
frequency, Nyquist 423
frequency, one-dimensional spatial 410
frequency, spatial 234, 260
frequency, temporal 410
Fresnel approximation 24
Fresnel diffraction region 50
Fresnel hologram 50
Fresnel-Kirchhoff diffraction formula 22
Fresnelets 133
fringe locus function 222, 318
fringe numbering 234
fringe order 234
fringe tensor 319
fringe tracking 229
fringe-vector 307, 318
fringes, finite 224
fringes, infinite 224
fringes, interference 14
function, arctan- 222
function, autocorrelation 420
function, band-limited 424
function, Bessel 190, 326, 431, 459
function, Bessel of the first kind 459
function, Bessel of the second kind 459
function, characteristic 329
function, chirp 145, 441
function, color matching 77
function, complex exponential 414
function, constant 411
function, cross-correlation 419
function, fringe locus 222, 318
function, Gaussian 414
function, harmonic spatial 256
function, modulation transfer 74
function, periodic 411
function, point spread 141, 227, 417, 430
function, rectangular 411
function, rectangular pulse 414

- function, rectangular window 426
 function, sensitivity 200
 function, sigmoid 393
 function, spatial coherence 21
 function, spatio-temporal coherence 21
 function, transfer 29, 419
 function, transient 411
 function, triangular pulse 414
 function, two-dimensional rectangular 429
 function, unit-step 414
 fundamental frequency 420

 Gabor transform 445
 gas laser 57
 gas, density of 217
 gas, electron 217
 Gaussian function 414
 Gaussian least squares 301
 gelatin, dichromated 58
 generalized phase shifting interferometry 263
 generalized projection theorem 449
 Gladstone-Dale constant 370
 Gladstone-Dale equation 217, 370
 global iteration 293
 gradient matrix, deformation 319
 gradient operator 367
 grating, diffraction 65, 243
 grating, radial 65
 gravity 218
 gray-values 227, 429
 grid method 380
 grog method 337
 ground state 54

 Hadamard condition number 310
 Hankel transform 431
 Hanning window 426
 harmonic spatial function 256
 harmonic vibration 190, 217, 323
 harmonic wave 10
 Hartley transform 439
 Hartley transform, inseparable 440
 Hartley transform, separable 440
 heat transfer 217
 helium-cadmium laser 57
 helium-neon laser 57
 Hermitean 256
 heterodyne holographic interferometry 235,
 326
 heterodyne holography, numerical 127
 heterodyne method 62, 201
 heterodyne method, quasi 242
 heterodyning, spatial 263
 heterodyning, temporal 235
 HNDT 215
 holo-diagram 200
 hologram 38, 40
 hologram interferometry, sandwich 305, 338
 hologram, amplitude 39, 58
 hologram, double exposure 266
 hologram, Fourier transform 48
 hologram, Fraunhofer 50
 hologram, Fresnel 50
 hologram, image 50
 hologram, in-line- 42
 hologram, multiplexed 280
 hologram, off-axis 42
 hologram, phase 39, 58
 hologram, rainbow 53
 hologram, three-dimensional 52
 hologram, volume 52
 hologram, white light 51
 holographic contouring 333
 holographic contouring, digital 340
 holographic imaging equations 45
 holographic interference pattern 185
 holographic interferogram 185
 holographic interferogram, distortions of 225
 holographic interferometer, desensitized 365
 holographic interferometric metrology 303
 holographic interferometry 185
 holographic interferometry, comparative 350
 holographic interferometry, difference 350
 holographic interferometry, diffuse illumination 195
 holographic interferometry, endoscopic 364
 holographic interferometry, heterodyne 235,
 326
 holographic interferometry, real-time 188,
 236, 260, 326
 holographic interferometry, stroboscopic 325
 holographic interferometry, time average 326
 holographic interferometry, two-wavelength
 357
 holographic microscope, optoelectronic 405
 holographic moiré 359
 holographic moiré interferometry,comparative
 352

- holographic nondestructive testing 215, 303, 387
holographic vibration analysis 190
holography, amplitude modulation 330
holography, digital 61, 81
holography, digital comparative 354
holography, digital image plane 400
holography, digital without wavefront reconstruction 400
holography, electro-optic 400, 404
holography, electronic 400, 404
holography, Fourier transform 47
holography, frequency translated 329
holography, lensless Fourier transform 49, 91, 100
holography, numerical heterodyne 127
holography, optoelectronic 405
holography, phase modulation 330
holography, phase-shifting digital 127
holography, rainbow 53
holography, sandwich 276
holography, single beam 47
holography, spectroscopic 331
holography, split beam 47
holography, stroboscopic 304
holography, TV 400, 404
holography, two beam 47
holography, two reference beam 201, 235, 242, 255
homogeneous deformation 318
homogeneous medium 367
homologous points 204
homologous rays 204
Hopfield network 294
Huygens principle 12
hybrid method 321

ideal gas equation 217, 371
ill-conditioned matrix 310
illumination point 192, 306
image 429
image derotator 362
image enhancement 258
image hologram 50
image plane holography, digital 400
image, conjugated 41
image, orthoscopic 42
image, pseudoscopic 42
image, real 42, 97

image, virtual 42, 98
images, twin 98
imaging equations, holographic 45
imaging, polarization 314
immersion method 336
impulse 411
impulse load 219
impulse response 141, 230, 417
impulse response filter, finite 230
impulse response of free-space propagation 29
impulse, Dirac delta 48
in-line arrangement 47, 118
in-line-hologram 42
in-phase 14
in-plane strains 216
incoherent part 16
incoherent superposition 16
independent object motions 325
index, refractive 366, 385, 447
infinite fringe interferogram 224
infinite fringes 224
inseparable Hartley transform 440
integral theorem, Fourier 410
integral, superposition 417
integration time 67
integration time control 72
intensity 12
intensity modulation 251
intensity, short time 13
intensity, speckle pattern 33
interference 13
interference fringes 14
interference pattern 14
interference pattern, holographic 185
interference pattern, macroscopic 185
interference pattern, microscopic 185
interference phase 188
interference phase difference 188
interferogram, distortions of holographic 225
interferogram, finite fringe 224
interferogram, holographic 185
interferogram, infinite fringe 224
interferogram, space-time 265
interferometer, desensitized holographic 365
interferometer, Fabry-Perot 55
interferometer, Michelson 17
interferometer, reflective grating 114
interferometer, rotating 361

- interferometer, Twyman-Green 17
 interferometer, Young's double aperture 19, 399
 interferometric metrology, holographic 303
 interferometry digital speckle pattern 400
 interferometry, comparative holographic 350
 interferometry, comparative holographic moiré 352
 interferometry, difference holographic 350
 interferometry, diffuse illumination holographic 195
 interferometry, electronic speckle pattern 400
 interferometry, endoscopic holographic 364
 interferometry, generalized phase shifting 263
 interferometry, heterodyne holographic 235, 326
 interferometry, holographic 185
 interferometry, Mach-Zehnder 217
 interferometry, real-time holographic 188, 236, 260, 326
 interferometry, sandwich hologram 305, 338
 interferometry, stroboscopic holographic 325
 interferometry, time average holographic 326
 interferometry, two-wavelength holographic 357
 interline transfer 68
 interpolation 235
 interpolation by triangulation 235
 interpolation, bilinear 235, 308, 309
 interpolation, one-dimensional spline 235
 invariant, shift 429
 inverse finite Fourier transform 422
 inverse Fourier transform 257, 410
 inversion, direct 379
 inversion, population 54
 isoplanatic system 417
 isotropic material, optically 218
 iteration, global 293
 iteration, local 292

 J-integral 323
 jitter 73
 Jones matrices 62

 kernel, convolution 230
 kernel, Ramachandran-Lakshminarayanan 454
 kernel, Shepp-Logan 454
 krypton laser 57

 Laplace operator 9
 Laplacian 431
 laser 53
 laser beam 54
 laser, argon-ion 57
 laser, CW 57, 304
 laser, diode 57
 laser, dye 57
 laser, gas 57
 laser, helium-cadmium 57
 laser, helium-neon 57
 laser, krypton 57
 laser, neodymium:YAG 57
 laser, pulsed 56, 304
 laser, ruby 56
 lateral color filter detector 77
 lateral magnification 46
 law, Maxwell-Neumann stress-optical 218, 373
 law, Snell's 367
 leakage 425
 least squares method 299
 least squares phase unwrapping 295
 least squares, Gaussian 301
 length, coherence 18
 length, focal 27
 lens formula 86
 lens, converging 27
 lens, diverging 27
 lens, negative 27
 lens, positive 27
 lens, thin 26
 lensless Fourier transform holography 49, 91, 100
 level, trigger 237
 light, speed of 9, 366
 light-in-flight recording 338, 377
 limit, refractionless 377
 line address transfer 67
 line integral transform 370
 linear 429
 linear low-pass filter 230
 linear system 416
 linearity 431
 linearity theorem 415
 liquids 372
 load, dynamic 219
 load, impulse 219

- load, periodic 219
load, point 218, 219
load, static 219
load, tensile 323
load, thermal 219, 321
load, transient 219
load, vibrational 219
loading, pressure 218
loads, distributed 219
local frequency 443
local iteration 292
localization 205
longitudinal magnification 46
longitudinal modes 55
Lorentz-Lorenz equation 217, 372
low-pass filter, linear 230
luminance 79
- Mach-Zehnder interferometry 217
macroscopic interference pattern 185
magnification formula 86
magnification, angular 46
magnification, lateral 46
magnification, longitudinal 46
mass concentration 217
mass transfer 217
material, optically isotropic 218
materials, recording 58
matrix, deformation gradient 319
matrix, ill-conditioned 310
matrix, sensitivity 299, 306
matrix, singular 310
Maxwell-Neumann stress-optical law 218, 373
measurement, contour 306
measurement, temperature 371
measuring time 13
mechanical stressing 218
mechanics, fracture 322
media, transparent 194
median filter 230, 274
medium, homogeneous 367
medium, nonhomogeneous 367
MEMS 405
method, boundary element 322
method, double exposure 235, 242
method, dynamic evaluation 266
method, finite element 321
method, grid 380
method, grog 337
method, heterodyne 201
method, hybrid 321
method, immersion 336
method, least squares 299
method, phase lock 233
method, phase shift 201, 242
method, phase step 201, 242
method, quasi heterodyne 242
method, real-time 255
method, static evaluation 266
method, time average 191, 333, 460
method, two-wavelength 333
metrology, holographic interferometric 303
Michelson interferometer 17
microelectromechanical systems 311, 405
microscope, optoelectronic holographic 405
microscopic interference pattern 185
microscopy, digital holographic 170
mode, vibration 217, 360
mode-shape 324
mode-shapes 324
modes, longitudinal 55
modes, transverse 55
modulation transfer function 74
modulation, frequency 304
modulation, intensity 251
modulator, acoustooptic 304
modulator, acoustooptical 65, 236
modulo 2π 224
modulus of elasticity 314, 373
moiré pattern 424
moiré, holographic 359
moment, bending 216, 218
monomode fibers 62
mother wavelet 133
multimode fibers 62
multiplexed hologram 280
mutual degree of coherence 21
- NDT 215
near-field region 50
negative lens 27
neodymium:YAG laser 57
network, artificial neural 234, 393
network, Hopfield 294
network, neural 294
neural network 294
neural network, artificial 234, 393

- neuron 234, 393
 nodes 324
 noise equivalent exposure 72
 noise, 1/f 72
 noise, electronic 226
 noise, fixed pattern 72
 noise, quantization 72
 noise, reset 72
 noise, shot 72
 noise, speckle 258
 noise, white 72
 non-vibration isolated object 304
 nondestructive testing 215
 nondestructive testing, holographic 215, 303, 387
 nondiffracting beam 12
 nonhomogeneous medium 367
 nonlinear filter 230
 nonlinear vibration 217
 nonrecursive filter 230
 nonuniformity, photoresponse 72
 normal strain 311
 normal stress 312
 number, Hadamard condition 310
 numbering, fringe 234
 numerical differentiation 317
 numerical heterodyne holography 127
 numerical reconstruction 93
 Nyquist frequency 423
 Nyquist rate 423

 object motions, dependent 325
 object motions, independent 325
 object motions, separable 324
 object related triggering 304, 361
 object wave 37
 object, boundary of 231
 object, circular symmetric phase 376
 object, non-vibration isolated 304
 object, phase 194
 object, rotating 360
 object, transparent 194
 objective speckles 35
 objects, transparent 217
 observation point 192, 306
 observer projection theorem 214, 268
 off-axis arrangement 47
 off-axis-hologram 42
 one-dimensional displacement 216

 one-dimensional spatial frequency 410
 one-dimensional spline interpolation 235
 operator, gradient 367
 operator, Laplace 9
 optical element, diffractive 365
 optical fibers 61
 optical path difference 191
 optically isotropic material 218
 optoelectronic holographic microscope 405
 optoelectronic holography 405
 order, fringe 234
 orthogonally polarized wave 16
 orthoscopic image 42

 pair, Fourier transform 410
 parallelly polarized wave 16
 parameter, scale 132
 parameter, translation 132
 paraxial approximation 27
 Parseval equality 443
 Parseval's theorem 416, 431
 particle analysis 118, 160
 path dependent demodulation 288
 path difference, optical 191
 path independent demodulation 288
 path length transform 370
 pattern, holographic interference 185
 pattern, interference 14
 pattern, moiré 424
 pattern, speckle 30
 period 10
 periodic function 411
 periodic load 219
 periodic replications 421
 perspective distortion 298, 308
 phase 10, 413
 phase conjugated wave 42
 phase hologram 39, 58
 phase lock method 233
 phase modulation holography 330
 phase object 194, 217
 phase object, circular symmetric 376
 phase relations 217
 phase sampling 62
 phase sampling equation 242
 phase sampling evaluation 242
 phase shift 62
 phase shift method 201, 242
 phase shifting 62, 244

- phase shifting interferometry, generalized 263
phase spectrum 413
phase step method 201, 242
phase stepping 244, 404
phase unwrapping 224, 287
phase unwrapping, least squares 295
phase unwrapping, temporal 295
phase velocity 11
phase, absolute 224
phase, relative 10
phase, speckle pattern 33
phase-shifting digital holography 127
photochromics 59
photographic emulsions 58
photography, speckle 399
photopolymers 58
photorefractive crystals 60
photoresists 58
photoresponse nonuniformity 72
photothermoplastics 59
picture 429
piezoelectric transducer 65
pinhole 61
pixel number 74
pixel size 74
pixels 227
Plancherel equality 443
plane polarized wave 10
plane stress 216, 314
plane wave 11
plasma diagnostics 217, 374
plastic zone 323
plate 316
Pockels cell 56
point load 218, 219
point source 429
point spread function 141, 227, 417, 430
point, illumination 306
point, observation 306
points, homologous 204
Poisson ratio 216, 315, 373
polar coordinates 447
polarization 9, 61
polarization imaging 314
pollution, wrap-around 258
polynomial, Zernike 303, 460
population inversion 54
positive lens 27
power spectrum 420
pressure 217
pressure chamber 218
pressure loading 218
pressure vessel 305
principal value of arctan-function 222
principle of superposition 417
principle, Huygens 12
prism, doubly refractive 92
prism, wavelength selector 55
prism, Wollaston 92
problem, random walk 30
processing, regional 292
processing, tile 292
product, space-bandwidth 73, 427
projected fringe contouring 338
projection theorem for Fourier transforms 450
projection theorem, generalized 449
projection, filtered 452
propagation, crack 217, 323
propagation, impulse response of free-space 29
propagation, transfer function of free space 29
property, sampling 411
property, symmetry 415
pseudoscopic image 42
pulsed laser 56, 304
pumping 54
pyroelectric camera 60
Q-switch 56
qualitative evaluation 215
qualitative evaluation, automatic 390
quantization 227, 258
quantization noise 72
quantum efficiency 71
quasi heterodyne method 242
radial grating 65
Radon transform 370, 447
rainbow hologram 53
rainbow holography 53
Ramachandran-Lakshminarayanan kernel 454
random walk problem 30
range, dynamic 72
rate, Nyquist 423
ratio, Poisson 216, 315, 373
ratio, signal-to-noise 226
ray equation 367
Rayleigh's theorem 416

- rays, homologous 204
 real amplitude 10
 real image 42, 97
 real-time holographic interferometry 188, 236, 260, 326
 real-time method 255
 reconstruction 40
 reconstruction by filtered backprojection 452
 reconstruction technique, algebraic 454
 reconstruction, cascaded 150
 reconstruction, numerical 93
 reconstruction, series expansion 454
 recording materials 58
 recording, light-in-flight 338, 377
 rectangular function 411
 rectangular function, two-dimensional 429
 rectangular pulse function 414
 rectangular window function 426
 recursive filter 230
 reference displacement, known 298
 reference displacement, unknown 299
 reference wave 37, 89
 reflection, Bragg 52
 reflective grating interferometer 114
 refractionless limit 377
 refractive index 366, 385, 447
 refractive index distribution 194
 refractive index field, asymmetric 377
 refractive index field, strongly refracting 382
 refractive index variation 217
 refractive index variation, contouring 336
 refractive index, effective 374
 refractivity, specific 372
 region, far-field 50
 region, Fraunhofer diffraction 50
 region, Fresnel diffraction 50
 region, near-field 50
 regional processing 292
 relation, uncertainty 444
 relative phase 10
 replications, periodic 421
 reset noise 72
 resolution, spatial 40, 74, 255
 resonance 385
 response, impulse 141, 230, 417
 responsivity 72
 responsivity, spectral 71
 restoration, frequency plane 380
 rigid body displacement 307
 rigid body rotation 208
 rigid body rotations 216
 rigid body translation 208, 300
 rigid body translations 216
 rigidity, flexural 317
 rotating interferometer 361
 rotating object 360
 rotation 312, 431
 rotation, rigid body 208
 rotational symmetry 431
 rotations, rigid body 216
 ruby laser 56
 sampling property 411
 sampling theorem 82, 228, 379, 423
 sampling theorem, two-dimensional 431
 sampling theorem, Whittaker-Shannon 427
 sampling, phase 62
 sandwich hologram interferometry 305, 338
 sandwich holography 276
 saturation 258
 saturation equivalent exposure 72
 scalar wave equation 10
 scale parameter 132
 scaling 431
 scaling theorem 415
 second derivative 317
 segmentation 229, 231
 self coherence 18
 self organizing feature map 234
 self-reference 405
 sensitivity function 200
 sensitivity matrix 299, 306
 sensitivity vector 193, 299, 306
 sensitivity vector, varying 300
 sensor, color 76
 separability 430, 431
 separable cosine transform 439
 separable Hartley transform 440
 separable object motions 324
 series expansion reconstruction 454
 series, Fourier 421
 shading correction 229, 230
 shear modulus of elasticity 315
 shear strain 311
 shear stress 312
 shearography, digital 405
 Shepp-Logan kernel 454
 shift invariant 429

- shift theorem 415
shift, Doppler 15
shift, frequency 62, 65
shift, phase 62
shift-invariant system 417
shifting 431
shifting, phase 62, 244
shock waves 217
short time Fourier transform 132
short time intensity 13
shot noise 72
sigmoid function 393
sign ambiguity 222, 224, 238, 255, 257, 261
signal-to-noise ratio 226
silver halide 58
similarity theorem 415
single beam holography 47
singular matrix 310
sinusoidal vibration 323
sinusoids 420
size, pixel 74
size, speckle 34
skeletonizing 229
smoothing 229
Snell's law 367
solids, transparent 373
source, point 429
space-bandwidth product 73, 427
space-invariant system 417
space-time interferogram 265
spatial coherence 19
spatial coherence function 21
spatial coordinate 429
spatial filter 61
spatial frequency 234, 260
spatial frequency domain 257
spatial frequency, one-dimensional 410
spatial heterodyning 263
spatial resolution 40, 74, 255
spatial synchronous detection 265
spatial transform 308
spatio-temporal coherence function 21
species concentration 386
specific refractivity 372
speckle decorrelation 227
speckle field 30
speckle noise 258
speckle pattern 30
speckle pattern contrast 33
speckle pattern intensity 33
speckle pattern interferometry, digital 400
speckle pattern interferometry, electronic 400
speckle photography 399
speckle size 34
speckle-shearing methods 405
specklegram 399
speckles 30
speckles, objective 35
speckles, subjective 35
spectral responsivity 71
spectroscopic holography 331
spectrum manipulating method 183
spectrum, amplitude 256, 413
spectrum, Fourier 234
spectrum, Fourier amplitude 390
spectrum, phase 413
spectrum, power 420
speed of light 9, 366
spherical wave 12
spline interpolation, one-dimensional 235
split beam holography 47
spontaneous emission 53
state, ground 54
static displacement 216
static evaluation method 266
static load 219
stepping, phase 244
STFT 132
still camera, consumer 139
stimulated emission 53
strain 216, 311
strain, in-plane 216
strain, normal 311
strain, shear 311
streamlines 217
stress 217, 312
stress intensity factor 322
stress tensor 312
stress, normal 312
stress, plane 216, 314
stress, shear 312
stress, tangential 312
stress, tensile 218
stress, torsional 218
stress-optical coefficients 373
stress-optical effect 217, 373
stress-optical law, Maxwell-Neumann 218,
373

- stresses 216
 stressing, mechanical 218
 stroboscopic holographic interferometry 325
 stroboscopic holography 304
 strongly refracting refractive index field 382
 subjective speckles 35
 subroutine, FFT 436
 superposition integral 417
 superposition principle 10
 superposition, coherent 13
 superposition, incoherent 16
 superposition, principle of 417
 surface tension 216
 symmetry property 415
 symmetry, rotational 431
 synaptic weight 393
 synthesis, Fourier 379
 synthetic wavelength 358
 system 416
 system of equations 298
 system of linear equations, condition of 310
 system, isoplanatic 417
 system, linear 416
 system, shift-invariant 417
 system, space-invariant 417
 systems, microelectromechanical 311, 405

 tangential stress 312
 target, CCD- 61
 technique, 2+1- 246
 temperature 217
 temperature measurement 371
 temporal coherence 17
 temporal frequency 410
 temporal heterodyning 235
 temporal phase unwrapping 295
 tensile load 323
 tensile stress 218
 tension, surface 216
 tensor, fringe 319
 tensor, stress 312
 testing, holographic nondestructive 303, 387
 testing, nondestructive 215
 theorem, addition 415
 theorem, autocorrelation 420
 theorem, convolution 419
 theorem, Fourier integral 410
 theorem, Fourier slice 379, 450
 theorem, generalized projection 449

 theorem, linearity 415
 theorem, observer projection 214, 268
 theorem, Parseval's 416, 431
 theorem, projection, for Fourier transforms 450
 theorem, Rayleigh's 416
 theorem, sampling 228, 379, 423
 theorem, scaling 415
 theorem, shift 415
 theorem, similarity 415
 theorem, two-dimensional sampling 431
 theorem, Whittaker-Shannon sampling 427
 theorem, Wiener-Kinchine 420
 thermal expansion coefficient 216
 thermal load 219, 321
 thin lens 26
 three-dimensional contours 218
 three-dimensional displacement 216
 three-dimensional hologram 52
 tile processing 292
 time average holographic interferometry 326
 time average method 191, 333, 460
 time of exposure 38
 tomography, computer aided 377, 447
 tomography, computerized 164
 torsional stress 218
 toughness, fracture 322
 tracking, fringe 229
 transducer, piezoelectric 65
 transfer function 29, 419
 transfer function of free space propagation 29
 transfer, frame 68
 transfer, heat 217
 transfer, interline 68
 transfer, line address 67
 transfer, mass 217
 transform pair, Fourier 410
 transform, Abel 376
 transform, cosine 439
 transform, discrete Fourier 421
 transform, fast Fourier 434
 transform, finite discrete Fourier 258
 transform, finite Fourier 422
 transform, Fourier 410
 transform, Gabor 445
 transform, Hankel 431
 transform, Hartley 439
 transform, inseparable Hartley 440
 transform, inverse finite Fourier 422

- transform, inverse Fourier 257, 410
transform, line integral 370
transform, path length 370
transform, Radon 370, 447
transform, separable cosine 439
transform, separable Hartley 440
transform, spatial 308
transform, wavelet 132
transient event 242
transient events 217
transient function 411
transient load 219
translation parameter 132
translation, rigid body 208, 216, 300
transmission, degree of 39
transparent media 194
transparent object 194, 217
transparent solids 373
transverse modes 55
transverse wave 9
triangular pulse function 414
triangulation, interpolation by 235
trigger level 237
triggering, object related 304, 361
tristimulus value 77
truncated data 424
truncation, data 425
TV camera-tubes 61
TV holography 400, 404
twin images 98
two beam holography 47
two reference beam holography 201, 235, 242, 255
two-dimensional convolution 430
two-dimensional FFT algorithm 430
two-dimensional rectangular function 429
two-dimensional sampling theorem 431
two-wavelength holographic interferometry 357
two-wavelength method 333
Twyman-Green interferometer 17

uncertainty relation 444
unit-step function 414
unwrapping, least squares phase 295
unwrapping, phase 224, 287
unwrapping, temporal phase 295

vacuum chamber 218

validation, defect 322
value, tristimulus 77
variation, refractive index 217
variations, background 258
vector field, displacement 297
vector, displacement 192
vector, sensitivity 193, 299, 306
vector, varying sensitivity 300
velocity, phase 11
vertical color filter detector 77
vessel, pressure 305
vibration amplitude 217
vibration analysis, holographic 190
vibration mode 217, 360
vibration, damped 217
vibration, harmonic 190, 217, 323
vibration, nonlinear 217
vibration, sinusoidal 323
vibrational load 219
vibrations 217
virtual image 42, 98
visibility 16
visualization, flow 217, 370
volume hologram 52

watermarking 183
wave equation 9
wave equation, scalar 10
wave number 10
wave vector 11
wave, Bessel 12
wave, evanescent 29
wave, harmonic 10
wave, object 37
wave, orthogonally polarized 16
wave, parallelly polarized 16
wave, phase conjugated 42
wave, plane 11
wave, plane polarized 10
wave, reference 37, 89
wave, spherical 12
wave, transverse 9
wavefront 11
wavefront division 19, 37
wavefront reconstruction, digital holography without 400
wavelength 10
wavelength selector prism 55
wavelength, equivalent 358

- wavelength, synthetic 358
wavelet transform 132
waves, bending 217
waves, shock 217
weight, synaptic 393
well capacity 66
white light hologram 51
white noise 72
Whittaker-Shannon sampling theorem 427
Wiener-Khinchine theorem 420
window function, rectangular 426
window, Hanning 426
Wollaston prism 92
wrap-around pollution 258
Young's double aperture interferometer 19, 399
Zernike polynomial 303, 460
zone, plastic 323